Linear Elastodynamic Analysis

Andersen, Lars

Publication date:
2006

Document Version
Publisher's PDF, also known as Version of record

Linear Elastodynamic Analysis

Lars Andersen

ISSN 1901-7286
DCE Lecture Notes No. 3

AALBORG UNIVERSITY
Department of Civil Engineering

Aalborg University
Department of Civil Engineering
Water and Soil

DCE Lecture Notes No. 3

Linear Elastodynamic Analysis

by

Lars Andersen

December 2006

Scientific Publications at the Department of Civil Engineering

Technical Reports are published for timely dissemination of research results and scientific work carried out at the Department of Civil Engineering (DCE) at Aalborg University. This medium allows publication of more detailed explanations and results than typically allowed in scientific journals.

Technical Memoranda are produced to enable the preliminary dissemination of scientific work by the personnel of the DCE where such release is deemed to be appropriate. Documents of this kind may be incomplete or temporary versions of papers—or part of continuing work. This should be kept in mind when references are given to publications of this kind.

Contract Reports are produced to report scientific work carried out under contract. Publications of this kind contain confidential matter and are reserved for the sponsors and the DCE. Therefore, Contract Reports are generally not available for public circulation.

Lecture Notes contain material produced by the lecturers at the DCE for educational purposes. This may be scientific notes, lecture books, example problems or manuals for laboratory work, or computer programs developed at the DCE.

Theses are monograms or collections of papers published to report the scientific work carried out at the DCE to obtain a degree as either PhD or Doctor of Technology. The thesis is publicly available after the defence of the degree.

Latest News is published to enable rapid communication of information about scientific work carried out at the DCE. This includes the status of research projects, developments in the laboratories, information about collaborative work and recent research results.

Published 2006 by
Aalborg University
Department of Civil Engineering
Sohngaardsholmsvej 57,
DK-9000 Aalborg, Denmark

Printed in Denmark at Aalborg University

ISSN 1901-7286 DCE Lecture Notes No. 3

Preface

This book is intended for use as lecturing material on the graduate and licentiate level in Civil Engineering. It contains a general introduction to soil dynamics and the solution of viscoelastic wave-propagation problems by means of numerical methods. This includes the finite-element method, the boundary-element method and the domain-transformation method. Applications are ground-borne vibrations from stationary sources such as machines and pile ramming. Further, specialised numerical schemes for the analysis of moving sources are presented. These methods are useful for the analysis of road and railway traffic.

The first chapter of the book gives an overview of the basic theory of stress waves propagating in viscoelastic media. In particular, the effect of surfaces and interfaces in a viscoelastic material is studied, and different mechanisms influencing the wave propagation are discussed. This includes dispersion as well as material and geometrical dissipation of waves in viscoelastic materials. Finally, brief introduction to wave propagation in saturated porous media is included. Generally, all mathematical derivations are presented in index notation. For readers who are unfamiliar with this formulation of partial differential equations, a short introduction is provided in Appendix A.

Subsequently, Chapter 2 deals with the finite element formulation of elastodynamics. The emphasis of the chapter lies on the discussion of time integration and spatial discretization of wave-propagation problems. Further, a formulation is given of transmitting boundary conditions which must be applied at the artificial boundaries of the numerical model. Finally, the treatment of moving sources, *e.g.* vehicles, in a finite element model is discussed.

Chapters 3 and 4 deal with the boundary-element method, which is an alternative to the finite-element and particularly useful for open or unbounded domains, *e.g.* soil. Firstly, Chapter 3 presents the theoretical background in terms of integral equations. A key issue in this regard is the so-called Green's function which is applied as a weight function in the boundary-integral equations. The Green's functions and the corresponding integral identities are derived in time and frequency domain, and special solutions are provided for plane strain and antiplane shear.

An introduction to the numerical aspects of the boundary-element method is given in Chapter 4. Two- and three-dimensional elastodynamics is considered, and different orders of spatial interpolation are presented. Only the so-called direct boundary-element method is concerned. However, both frequency- and time-domain schemes are included in the presentation. Finally, different approaches to the coupling of boundary-element and finite-element schemes are discussed.

The finite-element and boundary-element methods is very adaptable; but the solution of large soil domains is computationally expensive. Thus, in Chapter 5, an alternative semi-analytic

method is derived, which may be applied for the analysis of layered half-spaces subject to moving or stationary loads. This method is based on the so-called Thompson–Haskel approach and involves a double Fourier transformation from the horizontal spatial coordinates into the corresponding wavenumber domain. At the end of the chapter, examples are given of how to apply the method to the analysis of surface footings.

The discussion of foundation modelling continues in Chapter 6 which deals with the formulation of lumped-parameter models. The main idea of these models is to reduce a finite-element, or similar, model to a mechanical system with a few degrees of freedom. This is ideal in the case of foundations, since a rigourous modelling of the soil may by very inefficient if only the structural response is of interest. At the beginning of the chapter, simple models for an axisymmetric footing are presented. Subsequently, the so-called consistent lumped-parameter model is discussed, and examples are given in which the models are calibrated to the response of the models presented in Chapters 2 and 5.

At the end of the book, a number of exercises are included. Some of these exercises provide "hands-on" examples of the different numerical methods and may be used as mini projects, *e.g.* for evaluation of an MSc or PhD course based on these lecture notes.

I would like to thank my colleagues, in particular Morten A. Liingaard and my former PhD supervisor Søren R.K. Nielsen, for their valuable contributions to this book.

Aalborg, December 2006 Lars Andersen

Contents

CHAPTER 1
The basics of elastodynamics

In this chapter, the basic theory for waves propagating in elastic solids is described. Firstly, the theory for pressure and shear waves propagating through the elastic body is explained, and the influence of free surfaces or interfaces is discussed with focus on reflection and refraction of waves. Secondly, the Rayleigh wave propagating on the surface of a half-space is considered. Subsequently, the dispersion and dissipation of different wave types are discussed. The derivations and descriptions of elastic waves in this chapter form a theoretical basis for the formulation of numerical solutions in the subsequent chapters.

1.1 Introduction

Wave propagation in elastic or viscoelastic media is a problem which is encountered in many fields of engineering, both mechanical and civil engineering. One of the first fields of application for the theory of waves in elastic media was earthquakes. Still earth tremors are subject to extensive research, both from an experimental and a theoretical approach. In particular, over the last decades there has been an increasing interest in man-made ground vibration. Examples include ramming of sheet piles, traffic induced vibration and noise from machine foundation. Some typical sources to ground borne noise are illustrated in Fig. 1–1.

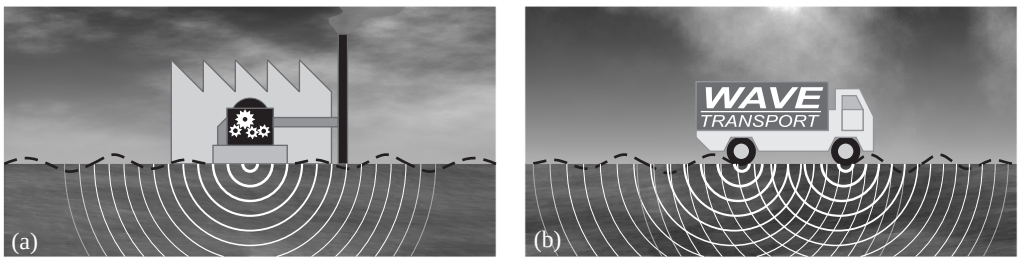

Figure 1–1 Ground borne vibration from (a) a machine foundation and (b) a moving vehicle.

The reason for the interest in ground vibration is its impact on people and buildings. At low frequencies, typically up till 80 Hz, vibrations may be felt as whole-body vibrations. Further, low-frequent waves in soil may cause whole buildings on the surface to vibrate at their lower eigenfrequencies. Vibrations at higher frequencies, about 20–250 Hz, may result in structure borne noise, which may be heard by people working or living in buildings. Some examples of ground borne vibration and structure borne noise are shown in Fig. 1–2. The resonance frequencies are taken from the work by Jones (1994).

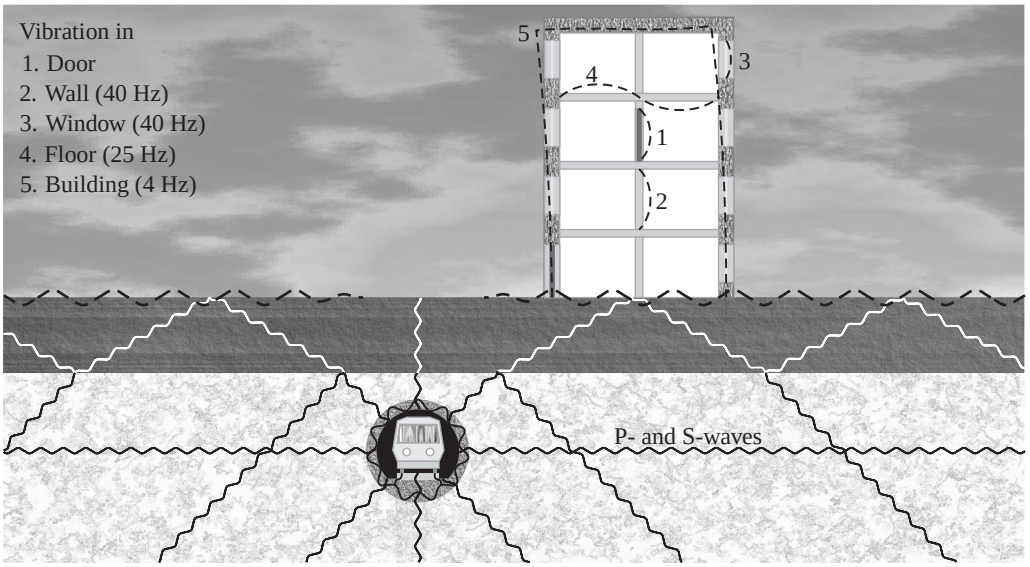

Figure 1–2 Ground borne vibration and structure borne noise from a train in a tunnel. Typical resonance frequencies are given in parentheses..

1.1.1 Wave types in an elastic medium

Measurements of the response of the ground to earthquakes or man-made vibration sources indicate that three different waves are usually encountered in the soil. A schematic time series of the horizontal response at an observation point on the surface of the ground is illustrated in Fig. 1–3. A qualitative description of the three waves indicated by P, S and R is given below, while a theoretical explanation of the various wave types may be found in Sections 1.2 and 1.4. A further discussion of some basic properties of wave propagation is carried out in Section 1.6.

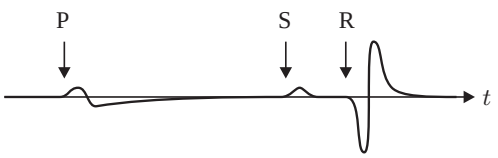

Figure 1–3: Schematic time series of horizontal displacements measured at the surface of the ground. The arrival times of the P-, the S- and the Rayleigh wave are indicated.

The P-wave is the first wave to arrive at an observation point. Hence it is denoted the *primary wave*. The particle motion is pure dilatation, or pressure, and the wave propagates through space with the phase velocity c_P, cf. Fig. 1–4. The P-wave corresponds to the acoustic waves in a fluid, *e.g.* in air.

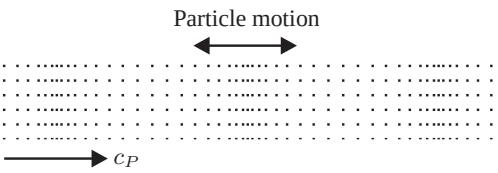

Figure 1–4: Plane P-wave.

The S-wave arrives after the P-wave and is therefore referred to as the *secondary wave*. Here the particle motion happens as equivoluminal shear as illustrated in Fig. 1–5. Similarly to the P-wave, the S-wave travels through space. The phase velocity c_S is typically about $0.5\,c_P$

but may be much lower in, for example, organic soils. The S-wave is usually decomposed into two components: the SV-wave and the SH-wave. The H and V denote *horizontal* and *vertical*, respectively, and refer to the direction of the particle motion as illustrated in Fig. 1–6. It is noted that at a free surface, or at an interface between two materials, a partial transition from P-waves into S-waves and vice versa may take place. A further discussion of this and other phenomena may be found in the next section.

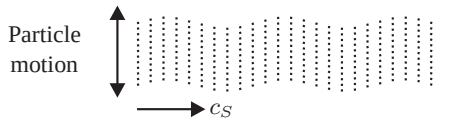

Figure 1–5: Plane S-wave.

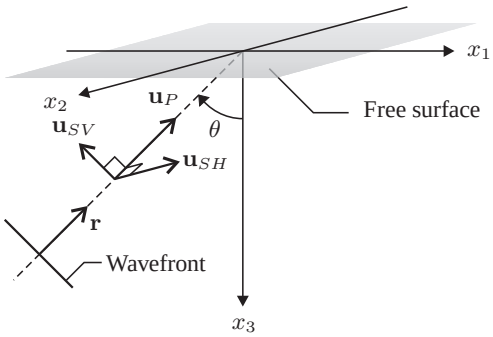

Figure 1–6: Components of the displacement field in a plane elastic wave.

The Rayleigh wave runs on the surface of a half-space, *i.e.* on the ground surface. This wave is somewhat slower than the S-wave, typically with a phase speed of around $c_R = 0.9c_S$. In contrast to the P- and S-waves, the Rayleigh wave contains both pressure and shear components in the displacement field. A derivation of the theory for Rayleigh waves may be found in Section 1.4.

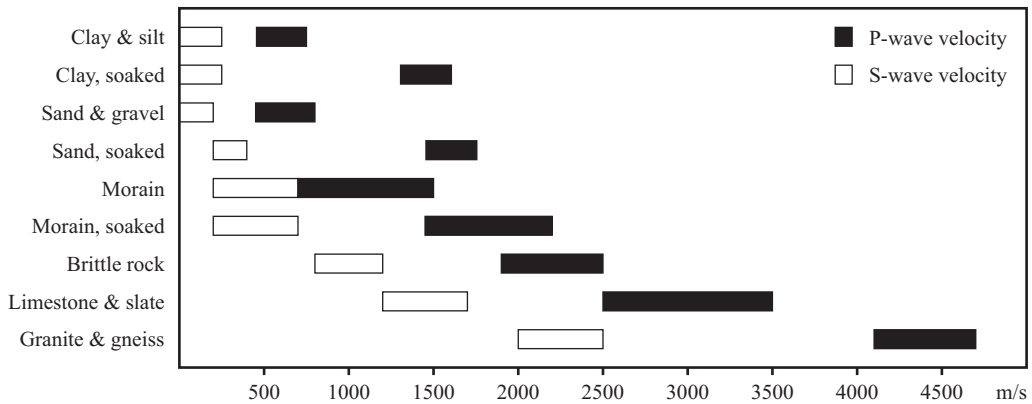

Figure 1–7 Typical propagation velocities of P- and S-waves (*Soil and rock mechanics*. The Royal Swedish Academy of Engineering Science, Report 225, Stockholm, 1979).

The P-, S- and Rayleigh waves are the waves that were first observed in nature, and for which a theoretical explanation was first given. Other wave types exist, some of which will be discussed in the following sections and chapters. However, in a given material no wave exists which is faster than the P-wave. Typical propagation velocities of P- and S-waves are given in Fig. 1–7. For comparison, the velocity of acoustic waves in air and water, *i.e.* the speed of sound, is 344 m/s (at 20 °C) and about 1500 m/s, respectively. It is noted that soaked sand and clay, treated as elastic media, have a only one phase, *i.e.* both the soil and the pore water are treated as a single material with a Poisson ratio close to 0.5. This explains the great difference between the P- and S-wave speeds in these materials as will be further explained in the following sections. On the other hand, rock and limestone show a high degree of cementation. This results in Poisson ratios of about 0.15. Finally, drained sandy soil typically has a Poisson ratio of 0.2 to 0.3.

Geometrical damping

It has been observed that at great distances from the epicentre of an earthquake, or far away from a source to man-made ground vibration, the Rayleigh wave leads to strong vibrations, whereas P- and S-waves vanish. A part of the explanation may be that the majority of the energy transmitted to the ground by a surface source leads to the generation of Rayleigh waves.

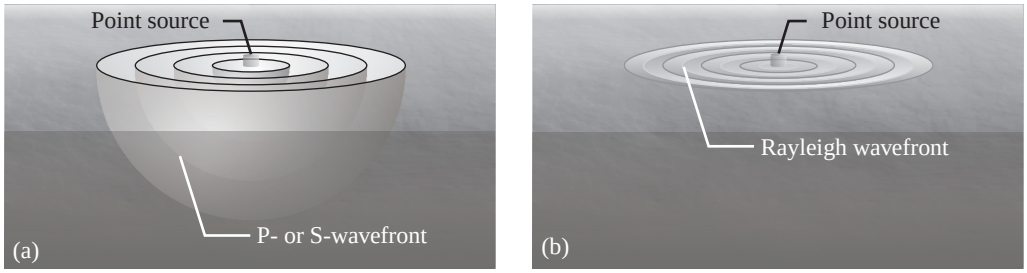

Figure 1–8 Geometrical damping of waves emanating from a point source on the surface of a half-space: (a) P- and S-waves, (b) the Rayleigh wave.

However, another reason lies in the fact that the P- and S-waves spread over the volume, thus forming spherical wavefronts, whereas Rayleigh waves are bound to the surface, thus spreading like "rings on water", cf. Fig. 1–8. This implies a faster decay of the energy, and hence the displacement amplitudes, in the P- and S-waves with the distance from the source than is observed for the Rayleigh wave. The decay of the amplitude of a wave due to spreading of the energy over a larger area or volume is denoted *geometrical damping*. Obviously, the geometrical damping of P- and S-waves is stronger than that of Rayleigh waves. We shall return to the discussion of geometrical damping in Subsection 1.6.2.

1.1.2 The linear (visco)elastic model for stress wave propagation

Most materials show a very complex behaviour. Mechanical properties may vary, both on a micro and macro scale, and they may change due to the deformation and load history. Thus, in nature most materials show some degree of nonlinear *elastoplastic* response, *inhomogeneity* and *anisotropy*. This may be vere pronounce for granular, possibly cemented materials such as soil and rock, whereas many materials show little variation of the properties with the localization, level and orientation of deformation.

In order to fully describe the behaviour of a material, a vast amount of properties need to be known. This implies two complications. Firstly, the determination of the material properties requires that several field tests and/or laboratory tests are carried out. Secondly, a numerical or analytical model facilitating a very complex material behaviour may lead to advanced computations, which are very demanding in terms of computation power—or they may simply be impossible. Hence, in the classic elastodynamic theories, we are only concerned with linear material behaviour, and most often the materials are assumed to be isotropic and homogeneous. The shortcomings of this approach are discussed below.

Linear elasticity vs. nonlinear elastoplastic behaviour

Close to the epicentre of earthquakes, very large strains are observed in the ground. However, farther away the strains are smaller. This is also the situation for ground vibrations due to human

activity, *e.g.* road and railway traffic, and in structural materials such as steel and concrete, the strains associated with dynamic loads, *i.e.* structure borne noise and vibration, are often inside the elastic range.

Hence, even for soil, which is in other fields of engineering regarded as a strongly nonlinear material, it may be reasonable to implement a linear model. The range of application of different material models is illustrated in Fig. 1–9. The linear model may be a pure elastic model, or a viscoelastic model may be utilized. The inclusion of viscosity, *i.e.* material damping, in the model complicates the computations of the response to dynamic excitation but usually provides a much better description of the material.

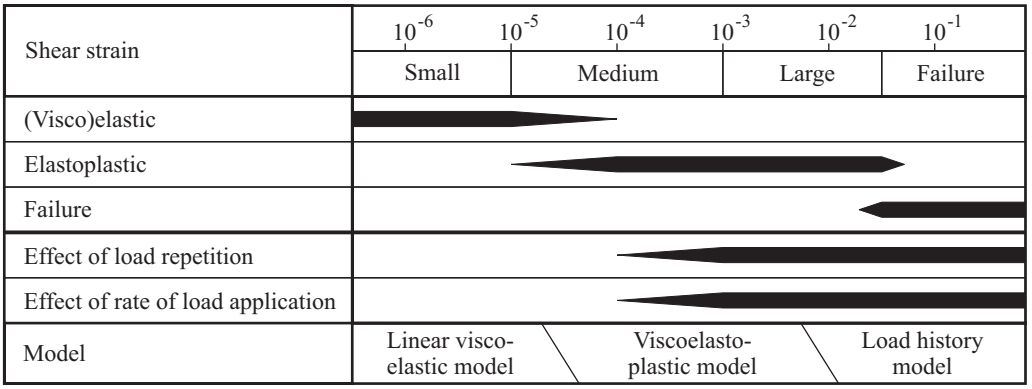

Figure 1–9 Material behaviour of soil at different magnitudes of the shear strain (Krätzig and Niemann 1996). The figure indicates whether load repetition and the rate of load application are important at different levels of strain and which kind of model that describes the material with sufficient accuracy.

Of course, problems exist in which the nonlinear behaviour of soil cannot be disregarded, *i.e.* when the excitation leads to large strains. Further, in several problems concerning saturated soil, *e.g.* liquefaction, it is necessary to model soil as a two-phase system with an additional set of equations describing the pore water.

Inhomogeneous vs. homogeneous materials

Steel and other metals/alloys may be regarded as homogeneous, even on a microscopic scale. However, concrete and most rocks are clearly inhomogeneous. This also applies to soil. Here the particles, whether mineral or organic, may vary significantly in size and shape as illustrated in Fig. 1–10, and the material density on macro scale varies due to variation of the void ratio.

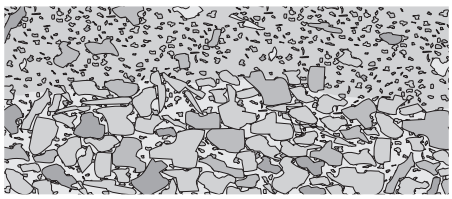

Figure 1–10: Inhomogeneous soil. Note the interface between two layers.

Nevertheless, the *local* variations of the density and the strength of a material are of little importance to wave propagation. By local inhomogeneities we understand the variation of material properties over a distance that is much smaller than the characteristic wave length. Hence, for low frequencies, only inhomogeneities such as layers of different soil deposits, also known as *strata*, are important. Here is interesting to know that the Rayleigh wave speed in most soils is above 100 m/s. Therefore, at 100 Hz the wave lengths are 1 m or more, whereas the grain

size is typically much smaller, around 1 mm. At very high frequencies, or for coarsely grained materials, the size and shape of the individual grains may influence the wave propagation; but here the applicability of a continuum model may in any case be doubtful.

A similar division into local and global inhomogeneities applies to the dynamics of structures. Here, details such as welding seems, joints and bolts have a weak influence on the lower eigenfrequencies and vibration modes. However, the response is strongly influenced by, for example, the variations of the bending stiffness of beams.

It is noted that in any real soil deposit, the elastic strength properties vary over depth due to prestressing from overlaying soil (or ice etc.). In practice, when dealing with wave propagation, smooth variations of the strength over depth may be modelled as stepwise variations by means of a number of layers. Typically, just one or two layers overlaying a homogeneous half-space are sufficient for the description of wave propagation in soil.

Anisotropic vs. isotropic materials

Wood is by nature an anisotropic material with very different strength in the directions parallel and orthogonal to the fibres. This also applies to many kinds of rock and most sedimentary soil. Even sand shows an anisotropic behaviour, which is a result of the way in which the grains are initially deposited. In elastodynamics, the main difference between isotropic and anisotropic materials is the fact that in an isotropic material, the speed of wave propagation is the same in all directions, whereas in anisotropic materials the wave speed varies. The anisotropy may influence all, or only some of the wave types in a medium.

Figure 1–11: An anisotropic material, *e.g.* soil, rock or wood. The shear strength is low in the x_1-direction and high in the x_3-direction.

In situ stresses in materials

In materials such as soil, nonzero in situ stresses are often present due to a prestressing of the material. However, wave propagation and vibration in general is related to stress variations. Hence, whereas in situ stresses play a significant part in the evaluation of failure loads, they may be disregarded in elstodynamics—at least for small variations of the strain.

However, the stiffness of granular soil deposits as well as clay has been recorded to increase significantly with the overburden pressure and thus with depth. This increase of stiffness may need to be accounted for in a model of the ground, *e.g.* by treating the soil as a number of homogeneous layers with different modules of elasticity. Further, field and laboratory test show that increasing pressure leads to cementation, resulting in a decrease of the Poisson ratio. Hence, typically the P- and S-wave speeds in deep soil deposits lie relatively close to each other, whereas at shallow depths, the P-wave speed may be much higher than the S-wave speed—in particular in fully saturated, undrained clayey and sandy soils.

1.2 Volume waves in elastic solids

An infinite elastic domain is considered, and a formulation of the equations of motion is to be

given in the Cartesian coordinates $\mathbf{x} = \{x_1, x_2, x_3\}^T$. A cubic infinitesimal element with the dimensions $\mathrm{d}x_1 \times \mathrm{d}x_2 \times \mathrm{d}x_3$, situated in the interior of the domain, is subject to the volume forces $\rho\mathbf{b}$ and surface traction as illustrated in Fig. 1–12. Here, $\rho = \rho(\mathbf{x})$ is the mass density, and $\mathbf{b} = \mathbf{b}(\mathbf{x}, t)$ is the vector with the components $b_i(\mathbf{x}, t)$, $i = 1, 2, 3$, expressing the body forces per unit mass. The traction vector $\mathbf{p} = \mathbf{p}(\mathbf{x}, t)$ has the components $p_j(\mathbf{x}, t) = \sigma_{ij} n_j$, where σ_{ij} is the *Cauchy stress tensor*, and n_j, $j = 1, 2, 3$, are the components of the outward unit normal vector $\mathbf{n}$. The summation convention applies so that summation is carried out over repeated indices, in this case the index j. Since the normal vectors on the surfaces of the infinitesimal element are parallel with the coordinate axes, the traction vectors $\mathbf{p}_i$ have the components σ_{ij}. The negative sign of $\mathbf{p}_i$ on three of the surface in Fig. 1–12 is due to the direction of the unit normal on these surfaces. In the general case, the full Taylor expansion is employed in order to find the difference between the stresses on two opposing sides of the cube. Here, however, we are only concerned with the linear contributions; hence any higher order terms are disregarded.

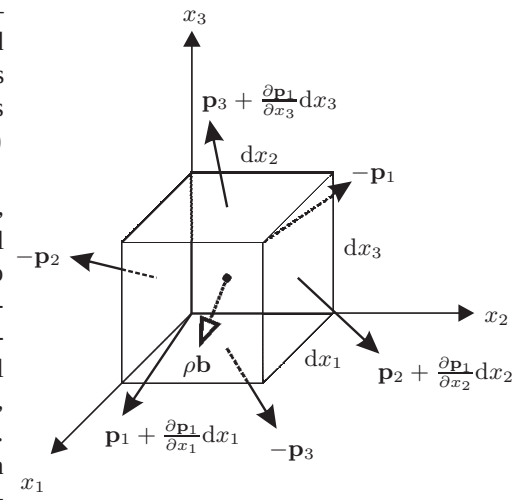

Figure 1–12: Forces on infinitesimal element.

Thus summation of the linear contributions from the external forces in each coordinate direction and use of Newton's second law yields the equation

$$\frac{\partial \sigma_{ij}}{\partial x_j} + \rho b_i = \rho \frac{\partial^2 u_i}{\partial t^2}, \tag{1–1}$$

which is identified as the *Cauchy equation of motion*. Here, $u_i = u_i(\mathbf{x}, t)$ are the components of the displacement field, and consequently the second partial derivative of u_i with respect to time is the acceleration at the material coordinate $\mathbf{x}$. Note that at this stage, no assumptions have been made with respect to material behaviour.

Assuming that the material is linear elastic, and that only small deformations are present in the domain, the stress may be expressed in terms of the strains according to the *generalised Hooke's law*,

$$\sigma_{ij} = E_{ijkl} \epsilon_{kl}, \tag{1–2}$$

where $E_{ijkl} = E_{ijkl}(\mathbf{x})$ is the *elasticity tensor*, and $\epsilon_{kl} = \epsilon_{kl}(\mathbf{x}, t)$ is the *infinitesimal strain tensor*, in which any higher order terms in the Taylor expansions for the displacements around a point $\mathbf{x}$ are disregarded,

$$\epsilon_{ij}(\mathbf{x}, t) = \frac{1}{2}\left(\frac{\partial u_i(\mathbf{x}, t)}{\partial x_j} + \frac{\partial u_j(\mathbf{x}, t)}{\partial x_i} \right). \tag{1–3}$$

Apparently, E_{ijkl} has 81 components. However, only 27 of these components are independent, which is due to the following reasons:

- The Cauchy stress tensor σ_{ij} is symmetric in indices i and j, because the angular accelerations are small of higher order, and therefore the first order contributions to the angular moments around the centre of the infinitesimal element must be in equilibrium.
- The small train tensor ϵ_{kl} is symmetric in indices k and l, which follows immediately from the definition in Eq. (1–3).
- It is assumed that a positive definite strain energy function $\mathcal{U} = \mathcal{U}(\epsilon_{ij})$ exists, which is defined so that $\sigma_{ij} = \partial\mathcal{U}/\partial\epsilon_{ij}$.

Hence, E_{ijkl} is subject to the symmetry properties

$$E_{ijkl} = E_{jikl}, \qquad E_{ijkl} = E_{ijlk}, \qquad E_{ijkl} = E_{klij}. \tag{1–4}$$

Equations (1–1), (1–2) and (1–3) are occasionally referred to as the *dynamic*, the *physical* and the *geometrical* conditions, respectively.

Homogeneity of the material implies that the mass density ρ and the elasticity tensor E_{ijkl} are independent of $\mathbf{x}$. Further, assuming that the material is isotropic, the stress–strain relationship simplifies to

$$\sigma_{ij} = \lambda\Delta\delta_{ij} + 2\mu\epsilon_{ij}, \tag{1–5}$$

where $\Delta = \Delta(\mathbf{x}, t)$ is the *dilation*,

$$\Delta(\mathbf{x}, t) = \frac{\partial u_k(\mathbf{x}, t)}{\partial x_k}, \tag{1–6}$$

δ_{ij} is the *Kronecker delta*,

$$\delta_{ij} = \begin{cases} 1 & \text{for} \quad i = j \\ 0 & \text{for} \quad i \neq j \end{cases} \tag{1–7}$$

and λ and μ are the so-called *Lamé constants*, which are related to the Young's modulus E and the Poisson ratio ν as

$$\lambda = \frac{\nu E}{(1+\nu)(1-2\nu)}, \qquad \mu = \frac{E}{2(1+\nu)}. \tag{1–8}$$

The inverse relationships are given as

$$E = \frac{\mu(3\lambda + 2\mu)}{\lambda + \mu}, \qquad \nu = \frac{\lambda}{2(\lambda + \mu)}. \tag{1–9}$$

Since the material is homogeneous, λ and μ are independent of $\mathbf{x}$. The Lamé constant μ is also identified as the *shear modulus*, which is often denoted G.

For the linear elastic homogeneous isotropic medium, the Cauchy equation of motion reduces to the *Navier equations*,

$$(\lambda + \mu)\frac{\partial^2 u_j}{\partial x_i \partial x_j} + \mu\frac{\partial^2 u_i}{\partial x_j \partial x_j} + \rho b_i = \rho\frac{\partial^2 u_i}{\partial t^2}. \tag{1–10}$$

In the following, it is understood that only the stress deviations from the state of static equilibrium are considered. These are the stresses that propagate through the solid as elastic waves. In this context, the body forces stemming from gravity are to be neglected.

It is noted that Eq. (1–10) with the Lamé constants defined by Eq. (1–8) is valid for three-dimensional wave propagation in elastic solids as well as plane strain. However, in the case of *plane stress* the governing equations of motion achieve a slightly different form when expressed in terms of Young's modulus and the Poisson ratio. This may be treated by introduction of the alternative Lamé constants

$$\bar{\lambda} = \frac{\nu E}{1-\nu^2}, \qquad \bar{\mu} = \frac{E}{2\,(1+\nu)}, \qquad \text{(plane stress)} \qquad (1\text{–}11)$$

where the usual definitions of E and ν apply, and the Navier equations read:

$$\left(\bar{\lambda}+\bar{\mu}\right)\frac{\partial^2 u_j}{\partial x_i \partial x_j} + \bar{\mu}\frac{\partial^2 u_i}{\partial x_j \partial x_j} + \rho b_i = \rho\frac{\partial^2 u_i}{\partial t^2}. \qquad \text{(plane stress)} \qquad (1\text{–}12)$$

Equation (1–12) is identical to Eq. (1–10) except for the application of $\bar{\lambda}$ and $\bar{\nu}$ instead of λ and μ. It is left to the reader to prove this.

1.2.1 Derivation of the P- and S-wave speeds

Two different wave types propagate in an infinite elastic medium. These waves are denoted body waves or volume waves, and the nature of each wave type is revealed in the following subsections.

Dilatational waves

In the absence of body forces, the Navier equations read

$$(\lambda+\mu)\frac{\partial^2 u_j}{\partial x_i \partial x_j} + \mu\frac{\partial^2 u_i}{\partial x_j \partial x_j} = \rho\frac{\partial^2 u_i}{\partial t^2}. \qquad (1\text{–}13)$$

Taking the divergence of Eq. (1–13) yields the scalar equation

$$(\lambda+\mu)\frac{\partial^3 u_j}{\partial x_i \partial x_j \partial x_i} + \mu\frac{\partial^3 u_i}{\partial x_j \partial x_j \partial x_i} = \rho\frac{\partial^3 u_i}{\partial t^2 \partial x_i},$$

which after a substitution and reordering of terms involving repeated indices yields

$$(\lambda+\mu)\frac{\partial^3 u_k}{\partial x_k \partial x_i \partial x_i} + \mu\frac{\partial^3 u_k}{\partial x_k \partial x_i \partial x_i} = \rho\frac{\partial^3 u_k}{\partial t^2 \partial x_k},$$

In terms of the dilatation, defined in Eq. (1–6), this equation is recast as

$$(\lambda+2\mu)\frac{\partial^2 \Delta}{\partial x_i \partial x_i} = \rho\frac{\partial^2 \Delta}{\partial t^2} \qquad \Rightarrow$$

$$\frac{\partial^2 \Delta}{\partial x_i \partial x_i} = \frac{1}{c_P^2}\frac{\partial^2 \Delta}{\partial t^2}, \qquad c_P = \sqrt{\frac{\lambda+2\mu}{\rho}}. \qquad (1\text{–}14)$$

This equation is recognized as the wave equation in three dimensions with c_P defining the phase speed of the wave propagation. For the isotropic elastic continuum, the problem defined by Eq. (1–14) is spherically symmetric.

Rotational waves

Taking the rotation of Eq. (1–13) yields the three equations

$$(\lambda+\mu)\,\varepsilon_{ijk}\frac{\partial^3 u_l}{\partial x_l \partial x_k \partial x_j}+\mu\varepsilon_{ijk}\frac{\partial^3 u_k}{\partial x_l \partial x_l \partial x_j}=\rho\varepsilon_{ijk}\frac{\partial^3 u_k}{\partial t^2 \partial x_j}. \tag{1–15}$$

Here ε_{ijk} is the *permutation symbol*;

$$\varepsilon_{ijk}=\begin{cases} 1 & \text{if } ijk \text{ is a subsequence of } 12312,\\ -1 & \text{if } ijk \text{ is a subsequence of } 32132,\\ 0 & \text{otherwise.}\end{cases} \tag{1–16}$$

The term $\partial^3 u_l/\partial x_l \partial x_k \partial x_j$ is symmetric in the indices j and k, whereas the permutation symbol ϵ_{ijk} is antisymmetric. Hence, the first term appearing in Eq. (1–15) vanishes. This corresponds to the well-known property that the rotation of the divergence of a vector field (and vice versa) is equal to zero. Making use of this result, Eq. (1–15) reduces to

$$\frac{\partial^2 w_i}{\partial x_j \partial x_j}=\frac{1}{c_S^2}\frac{\partial^2 w_i}{\partial t^2}, \qquad c_S=\sqrt{\frac{\mu}{\rho}}, \tag{1–17}$$

which is the three-dimensional wave equation with phase speed c_S. The quantity $w_j=w_j(\mathbf{x},t)$ is the rotation of the displacement field,

$$w_i=\frac{1}{2}\,\varepsilon_{ijk}\frac{\partial u_k}{\partial x_j}=\frac{1}{2}\,\varepsilon_{ijk}W_{kj}, \qquad W_{ij}=\frac{1}{2}\left(\frac{\partial u_i}{\partial x_j}-\frac{\partial u_j}{\partial x_i}\right). \tag{1–18}$$

Here $W_{ij}=W_{ij}(\mathbf{x},t)$ is identified as the *infinitesimal rotation tensor*. Note that the infinitesimal strain and rotation tensors are actually the symmetric and antisymmetric parts of the gradient of the displacement field, so that

$$\frac{\partial u_i}{\partial x_j}=\epsilon_{ij}+W_{ij}. \tag{1–19}$$

1.2.2 Naming convention for the volume waves

It is now evident that the displacement may be decomposed into a dilatational part $u_{P,i}$ and a rotational part $u_{S,i}$, so that the total displacements are given as

$$u_i=u_{P,i}+u_{S,i}. \tag{1–20}$$

The two parts of the displacement field propagate as waves with the phase speeds c_P and c_S, respectively. For any real materials, the Lamé constants are both real positive quantities, and therefore $c_P>c_S$. As a consequence of this, dilatational waves reach and observer before the rotational waves, for what reason the denotations *primary* waves (P-waves) and *secondary* waves (S-waves) have been coined. Accordingly, c_P and c_S are referred to as the P- and S-wave speed, respectively.

As already mentioned, the rotation of the divergence of a vector field and the divergence of the rotation of a vector field both vanish. Therefore, the P-wave field corresponds to *irrotational*

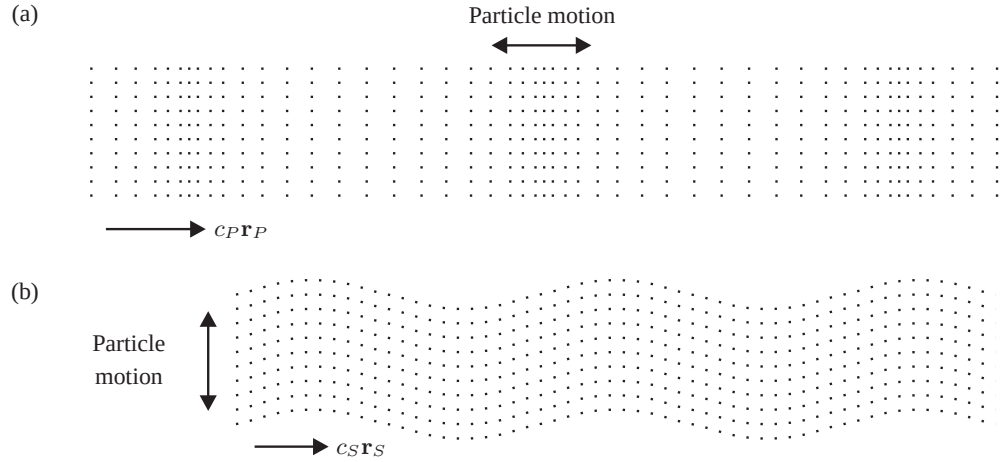

Figure 1–13 The particle motion in (a) P-waves and (b) S-waves. The unit vectors $\mathbf{r}_P$ and $\mathbf{r}_S$ denote the directions of P- and S-wave propagation, respectively.

waves, only consisting of changes in the volume. On the other hand, the S-wave field is free of divergence, implying that these waves are *equivoluminal* waves. The two wave types are illustrated in Fig. 1–13. Alternatively, the two wave types are referred to as *pressure* (or *compressional*) and *shear* waves. These names correspond well with the original denotations described above. Note that the phase speeds are occasionally referred to as c_1 and c_2 rather than c_P and c_S, which is the notation used in this text.

1.3 Reflection and transmission of waves

In the previous section, the basic theory for wave propagation in an infinite homogeneous linear elastic medium has been put forward. It was found that P- and S-waves propagate independently of one another in these circumstances. However, most problems in geodynamics involve bounded domains and possibly domains with inhomogeneities, *e.g.* soil layers or buried structures. When waves hit an obstacle or a boundary, full or partial reflection of the waves will occur. The nature of reflection is strongly dependent on the boundary conditions, which may be demonstrated by the following simple example.

Example 1.1 Reflection of one-dimensional waves at a free or a fixed boundary

The one-dimensional wave propagation problem is considered. Let ρ denote the mass density of a given material. The displacement field $u = u(x,t)$ is then governed by the wave equation

$$\frac{\partial^2 u}{\partial x^2} + \frac{\rho b}{c^2} = \frac{1}{c^2}\frac{\partial^2 u}{\partial t^2}, \tag{a}$$

where $b = b(x,t)$ are the body forces applied per unit length in the x-direction. Further, c is the wave velocity which depends on the mass density ρ and some stiffness property of the material. Note that Eq. (a) is equivalent to Eqs. (1–14) and (1–17) for dilatation and shear waves, respectively. *(continued)*

The material domain is now defined by $x \geq 0$. When the waves hit the boundary at $x = 0$, reflection will occur. Thus the total wave field consists of the incident wave propagating in the positive x-direction and a reflected wave propagating in the negative x-direction. Assuming that the wave does not change shape or amplitude as it propagates through the material, the displacement field may be written as

$$u(x,t) = U^i f(ct + x) + U^r f(ct - x), \tag{b}$$

where U^i and U^r are the constant amplitudes of the incoming and reflected waves, respectively. Further, f is some function describing the shape and propagation of the waves; it should be at least twice differentiable with respect to its argument. Other notations may be applied, *e.g.* $f(ct+x) = g(t+x/c)$. Only the sign and the relative scaling of the time and space coordinates via the wave speed c are important. It is easily verified that the wave field (b) is a valid solution to the wave equation (a).

Two different kinds of boundary conditions are applied, that is

- Dirichlet conditions, *i.e.* natural boundary conditions, of the kind $u(0,t) = 0$,
- Neumann conditions, *i.e.* mechanical boundary conditions, of the kind $-\partial u/\partial x = 0$.

The first case corresponds to a fixed boundary. This may, for example, represent a soil layer over bedrock. Here it may be assumed that the soil is completely fixed at the interface. Since the stresses are given in terms of the spatial derivatives of the displacements, the second case corresponds to a free surface with no traction applied.

Application of the boundary condition $u(0,t) = 0$ to the solution given by Eq. (b) provides the result

$$u(0,t) = U^i f(ct) + U^r f(ct) = 0. \tag{c}$$

In order for this equation to hold at any instance of time, t, it follows that

$$U^i + U^r = 0 \quad \Rightarrow \quad U^r = C_r U^i \quad \text{where} \quad C_r = -1. \qquad \text{(fixed boundary)} \tag{d}$$

Here C_r is denoted the reflection coefficient. The change in sign indicates a phase shift of π between the incident and the reflected wave. Standing waves occur with the amplitude $2U^i$ a quarter of the wavelength away from the fixed boundary. At $x = 0$, the amplitude of the total wave field is 0. The incoming waves, the reflected waves and the total, or resulting, wave field are illustrated in Fig. Aa.

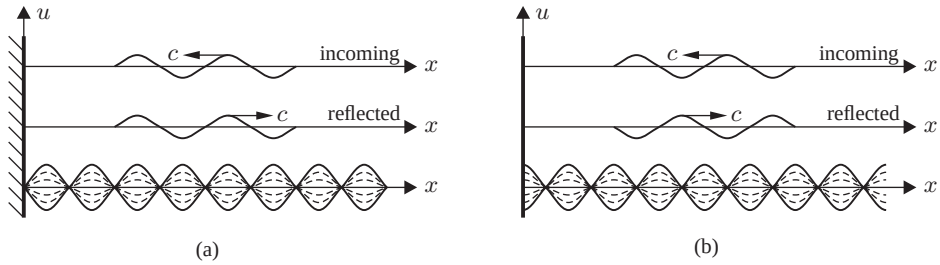

(a) (b)

Figure A Reflection of waves at a boundary: (a) fixed and (b) free boundary.

Next, when the Neumann condition is applied, the following result is obtained:

$$-\left.\frac{\partial u}{\partial x}\right|_{x=0} = \left. U^i f'(ct - x)\right|_{x=0} - \left. U^r f'(ct + x)\right|_{x=0} = 0, \tag{e}$$

where the prime denotes differentiation with respect to the argument. Again, in order for this equation to hold for arbitrary t it follows that *(continued)*

$$U^i - U^r = 0 \quad \Rightarrow \quad U^r = C_r U^i \quad \text{where} \quad C_r = 1. \qquad \text{(free boundary)} \qquad \text{(f)}$$

Hence, when the boundary is free of traction, the reflected wave is in phase with the incident wave. Consequently, standing waves are generated with the amplitude $2U^i$ at $x = 0$, while the total displacement is equal to 0 a quarter of the wavelength away from the free boundary. The incoming, the reflected and the total wave fields are shown in Fig. Ab. □

As illustrated by the example above, both a free and a fixed boundary lead to full reflection of incident waves back into the domain occupied by the material. The amplitudes of the resulting wave field are equal in the two situations, *i.e.* the only difference lies in the phase shifts. On the other hand when an an interface between two different materials is considered, *e.g.* between two soil layers, a part of the energy may be transmitted from one material to the other and only the remaining part of the energy is reflected. Furthermore, mixing of different wave types may take place at a boundary or an interface. This will be discussed in Subsections 1.3.2 and 1.3.3. Firstly, however, the terminology *mechanical impedance* will be introduced.

1.3.1 Mechanical impedance and transmission coefficients

In the case of direct electrical current, the relationship between the voltage, U, and the current, I, is given in terms of Ohm's law, $U = RI$. Here R is denoted the *ohmic resistance*. When an alternating current is considered, additional resistance arises due to the reactance, X. In the frequency domain, the complex notation $\hat{U} = (R + \mathrm{i}X)\hat{I} = Z\hat{I}$ applies, where the hat indicates the amplitudes of the respective quantities. The combined resistance Z is referred to as the *electrical impedance*.

Based on similar principles, the *acoustic impedance* z is defined as the ratio between the pressure, p, and the particle velocity, v, on an imaginary surface in a sound wave, *i.e.* $p = zv$. Acoustic impedance is measured in *rayls* (1 rayl = 1 Ns/m^3).

As demonstrated in Example 1.2 below, the acoustic impedance is ρc, where ρ is the mass density of the material and c is a characteristic phase velocity of wave propagation in the material. Thus, in contrast to the electrical impedance which is a complex quantity in the frequency domain, the acoustic impedance is real valued.

Example 1.2 Mechanical impedance in one-dimensional wave propagation

Let ρ denote the mass density of a given material. The stiffness modulus M is defined so that

$$c = \sqrt{M/\rho} \quad \Rightarrow \quad M = c^2\rho. \qquad \text{(a)}$$

Here c is the phase velocity of waves propagating through the material. A comparison of Eq. (a) with Eqs. (1–14) and (1–17) reveals that $M = \lambda + 2\mu$ for P-waves, whereas $M = \mu$ for S-waves.

Next, consider a homogeneous half-space defined by $x \leq 0$ and occupied by this material. No loads are applied in the interior of the domain. However, the half-space is subject to the traction $p(t)$, which is distributed uniformly over the entire surface $x = 0$ and applied either normal or tangential to the surface. In any case the problem reduces to one-dimensional wave propagation governed by the equation

$$\frac{\partial^2 u}{\partial x^2} = \frac{1}{c^2}\frac{\partial^2 u}{\partial t^2}. \qquad \text{(b)}$$

(continued)

The direction of displacements and the value of the phase velocity c depend on the direction, in which the traction is applied. Thus, if a tangential traction is applied, S-waves are generated in the half-space, whereas a traction in the direction of the normal generates P-waves. However, in both cases the waves will propagate in the negative x-direction, *i.e.* into the half-space. Hence, assuming that the amplitude and the shape of the waves are constant as the waves propagate through the half-space, the displacement field may be described as $u(x,t) = Uf(ct+x)$. The particle velocity v and the stress related to the wave propagation are

$$\dot{u}(x,t) = \frac{\partial u}{\partial t} = cUf'(ct+x), \quad \sigma(x,t) = M\frac{\partial u}{\partial x} = MUf'(ct+x) \tag{c}$$

where prime denotes differentiation with respect to the argument. In the general three-dimensional case, the traction p_i is defined as $p_i = \sigma_{ij}n_j$, where n_j are the components of the outward unit normal, and σ_{ij} is the stress tensor. In the present one-dimensional case the outward normal to the surface $x = 0$ points in the positive x-direction. Hence, the traction is $p(t) = \sigma(0,t)$. Further, defining $v(t) = \dot{u}(0,t)$ as the particle velocity at the boundary, this leads to the following conclusion:

$$\left.\begin{array}{rcl} v(t) &=& cUf'(ct) \\ p(t) &=& MUf'(ct) \end{array}\right\} \quad \Rightarrow \quad p(t) = \frac{Mc}{c^2}v(t) \quad \Rightarrow \quad p(t) = zv(t) \quad \text{where} \quad z = \rho c, \tag{d}$$

where use has been made of the fact that $c^2 = M/\rho$. The quantity $z = \rho c$ is denoted the *mechanical impedance* and is a fundamental property in the dynamics of materials. It provides the particle velocity which is generated in the material due to a unit traction applied over a surface. Evidently, if c corresponds to the phase velocity of sound through the material, the quantity z is identified as the *acoustic impedance*.

Finally it is noted that the result provided in Eq. (d) would also be achieved if the half-space defined by $x \geq 0$ was considered. In this case the displacement field due to wave propagation would be defined as $u(x,t) = Uf(ct-x)$. However, the resulting change of sign on the stress according to Eq. (c), implying that $\sigma(0,t) = -zv(t)$, would be counteracted by the corresponding change of sign in the direction of the outward normal, *i.e.* $p(t) = -\sigma(0,t)$ on the boundary of the half-space defined by $x \geq 0$. □

In three-dimensional elastodynamics involving both P- and S-waves, the mechanical impedance is a second order tensor, z_{ij}, defining the relationship between the traction $p_i(\mathbf{x},t)$ and the particle velocity $v_j(\mathbf{x},t)$. With S denoting the surface subject to the traction,

$$p_i(\mathbf{x},t) = z_{ij}v_j(\mathbf{x},t), \quad \mathbf{x} \in S. \tag{1–21}$$

Thus, the mechanical impedance may be considered a generalisation of the acoustic impedance. Obviously, in the case of plane stress or strain, the indices $i,j = 1,2$.

The impedance of elastic continua on the particle level is further discussed in the next chapter with regard to the formulation of transmitting boundaries in finite element models. Here, the key issue is that the impedance mismatch between two materials is closely related to the transmission of energy via their common interface. This is demonstrated in the following example in the case of one-dimensional wave propagation.

Example 1.3 Reflection and transmission coefficients in one-dimensional wave propagation

Consider two homogeneous half-spaces with the common interface $x = 0$. The half-space defined by $x \leq 0$ is occupied by a material with the impedance $z_1 = \rho_1 c_1$, and a material with the impedance $z_2 = \rho_2 c_2$ occupies the half-space defined by $x > 0$. Here ρ_1 and ρ_2 are the mass densities of the two materials, whereas c_1 and c_2 are the corresponding phase velocities of wave propagation. *(continued)*

A wave impinges on the interface from the half-space $x \leq 0$. A part of the energy in the incoming wave is transmitted through the interface into the adjacent half-space. The remaining part of the energy is reflected back into the half-space $x \leq 0$. Hence,

$$u(x,t) = \begin{cases} u^i(x,t) + u^r(x,t) & \text{for} \quad x \leq 0 \\ u^t(x,t) & \text{for} \quad x > 0 \end{cases} \tag{a}$$

where the superscripts i, r and t refer to *incoming*, *reflected* and *transmitted* waves, respectively. Assuming that the amplitude and the shape of each wave component are constant as the waves travel through the respective materials, the displacement fields may be written

$$u^i(x,t) = U^i f(c_1 t - x), \quad u^r(x,t) = U^r f(c_1 t + x), \quad u^t(x,t) = U^t f(c_2 t - x). \tag{b}$$

The incoming and the transmitted wave both travel in the positive x-direction, whereas Eq. (b) defines a reflected wave moving in the negative x-direction. The situation is shown in Fig. A.

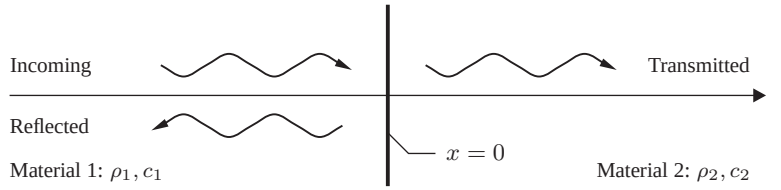

Figure A Reflection and transmission of one-dimensional waves at an interface.

Continuity of the displacement at the interface $x = 0$ between the two materials involves that

$$u(0,t) = u^i(0,t) + u^r(0,t) = u^t(0,t). \tag{c}$$

Likewise, the particle velocity should be continuous across the interface. This implies that

$$v^i(t) + v^r(t) = v^t(t), \quad v(t) = \left.\frac{\partial u}{\partial t}\right|_{x=0} \tag{d}$$

Furthermore, since no exterior forces are applied at the interface $x = 0$, the stress resultant should be equal to zero. As pointed out in Example 1.2, the stress provided by a wave travelling in the positive x-direction is $\sigma(0,t) = zv(t)$, whereas a wave travelling in the negative x-direction implies the stress $\sigma(0,t) = -zv(t)$. Therefore,

$$\sigma^i(0,t) + \sigma^r(0,t) = \sigma^t(0,t) \quad \Rightarrow \quad z_1 v^i(t) - z_1 v^r(t) = z_2 v^t(t), \tag{e}$$

where use has been made of the fact that the incoming and the reflected waves both propagate in the material with the impedance $z_1 = \rho_1 c_1$, whereas the transmitted wave propagates in the material with the impedance $z_2 = \rho_2 c_2$. Combination of Eqs. (d) and (e) provides the result

$$z_1 v^i(t) - z_1 \left(v^t(t) - v^i(t) \right) = z_2 v^t(t) \quad \Rightarrow$$

$$C_r = \frac{v^r(t)}{v^i(t)} = 1 - C_t, \quad C_t = \frac{v^t(t)}{v^i(t)} = \frac{2z_1}{z_1 + z_2} = \frac{2}{1 + \varrho}, \quad \varrho = \frac{z_2}{z_1}. \tag{f}$$

Here C_r and C_t are identified as the reflection and transmission coefficients with regard to the particle velocities, and therefore also the displacements, in the two adjacent materials. The fraction $\varrho = z_2/z_1$ is coined the *impedance mismatch*. Obviously, the reflection and transmission coefficients only depend on the relative values of the impedances of the adjacent material domains expressed via ϱ, see Fig. B.

(continued)

Next, no net energy should be generated at the interface. This implies that the instantaneous rate of work, *i.e.* the *power*, per unit area of the surface should be equal to zero, that is $p(t)v(t) = 0$. Hence, the power generated by the incoming wave should be counterbalanced by the power consumed by the reflected and the transmitted wave, *i.e.*

$$\sigma^i(0,t)v^i(t) + \sigma^r(0,t)v^r(t) = \sigma^t(0,t)v^t(t) \quad \Rightarrow \quad z_1\{v^i(t)\}^2 = z_1\{v^r(t)\}^2 + z_2\{v^t(t)\}^2. \tag{g}$$

Division of Eq. (g) by $z_1\{v^i(t)\}^2$ and insertion of Eq. (b) leads to the result:

$$1 = E_r + E_t, \quad E_r = C_r^2 = 1 - E_t, \quad E_t = \frac{z_2}{z_1}C_t^2 = \frac{4z_1z_2}{(z_1+z_2)^2} = \frac{4\varrho}{(1+\varrho)^2}, \quad \varrho = \frac{z_2}{z_1}. \tag{h}$$

Here E_r is the *energy-reflection coefficient*, and E_t is the *energy-transmission coefficient*.

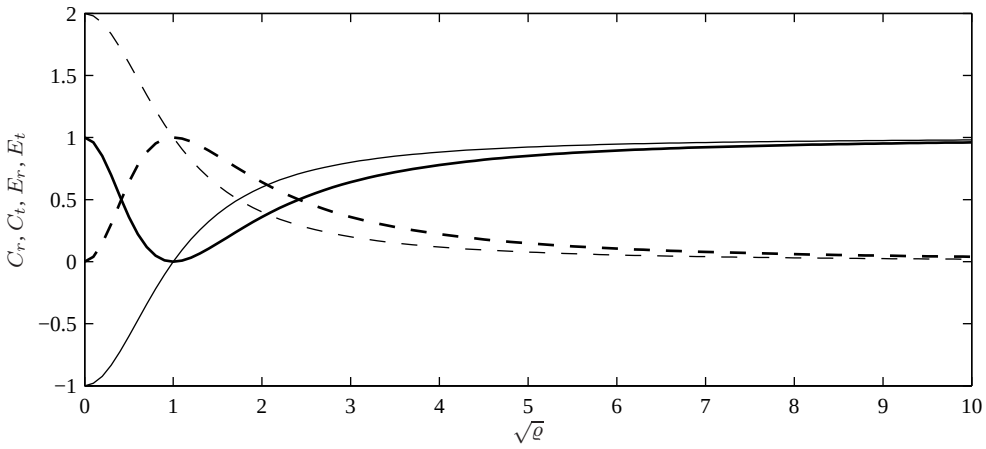

Figure B Velocity-reflection coefficient C_r (——), velocity-transmisson coefficient C_t (— —), energy-reflection coefficient E_r (——) and energy-transmission coefficient E_t (— —) as functions of the impedance mismatch ϱ.

It may be interesting to note that the energy-reflection coefficient is simply the square of the amplitude-reflection coefficient. On the other hand, the energy-transmission coefficient E_t and the velocity-transmission coefficient C_t are different in nature, especially for low values of ϱ as illustrated in Fig. B. Evidently, if $\varrho = 1$ all the energy is transmitted since $E_t = 1$. However, if $\varrho \to 0$ it follows that $E_t \to 0$. This situation corresponds to a free boundary, *i.e.* an interface between a dense solid medium and a very light and flexible material, *e.g.* air. Finally, if $\varrho \to \infty$, full reflection takes place back into the light and flexible material, since

$$E_t = \frac{4\varrho}{(1+\varrho)^2} \to \frac{4}{\varrho} \to 0 \quad \text{for} \quad \varrho = \frac{z_2}{z_1} \to \infty. \tag{i}$$

This corresponds to a fixed boundary, *e.g.* between a soil layer and bedrock. □

It is finally noted that the terminology “impedance” is also applied to structures. Whereas Eq. (1–21) suggests a real value of the impedance in frequency space on the particle level, the impedances of, for example, surface footings on an elastic half-space are complex. Only in the high-frequency range does the “impedance” reduce to a pure relationship between the traction and the velocity. A further discussion may be found in Chapter 3.

1.3.2 Reflection of volume waves at a free surface

At a free surface a coupling, or transformation, takes place between P-waves and certain S-waves, whereas other S-waves are simply reflected at the boundary in the same way as acoustic waves, *i.e.* as waves of the same kind. This phenomenon is discussed in the following.

The half-space defined by $x_3 > 0$ is considered. Thus, the free surface is situated in the x_1–x_2 plane and the outward unit normal vector points in the negative x_3-direction as illustrated in Fig. 1–14. Plane waves are assumed to propagate in the direction defined by the unit vector $\mathbf{r}$ and with the phase speed c. The particle motion is given as

$$u_i(\mathbf{x}, t) = A_i f(x_i r_i - ct), \tag{1–22}$$

where A_i are the components of the amplitude vector $\mathbf{A}$, r_i are the components of $\mathbf{r}$ and f is a continuous function which is assumed to be at least twice differentiable with respect to the argument. Insertion of the plane wave field into the homogeneous Navier equations (1–13) reveals that only the phase speeds $c = c_P$ and $c = c_S$ are permissible. For the plane P-wave, the amplitude vector $\mathbf{A}$ is in the direction of wave propagation, *i.e.* $A_i = r_i|\mathbf{A}|$. The amplitude vector for the plane S-wave is orthogonal to $\mathbf{r}$, so that $A_i\, r_i = 0$. Further, plane S-waves are polarized whence it follows that $\mathbf{A}$ does not change with time. The S-wave is divided into two components as shown in Fig. 1–14. The indices H and V denote *horizontal* and *vertical* motion, and the corresponding wave components are referred to as SH- and SV-waves.

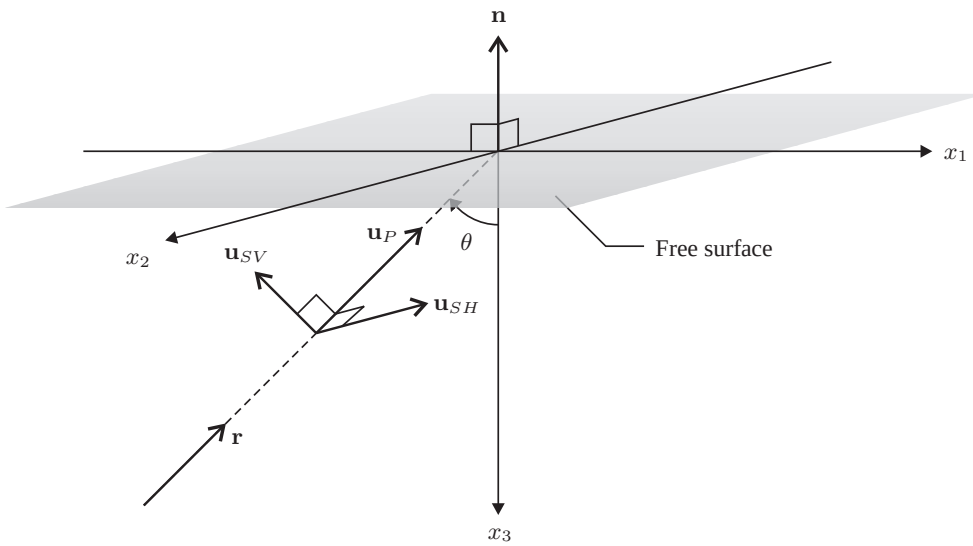

Figure 1–14 Components of a plane wave field in a half-space and position of the free surface.

The direction of the plane wave propagation is defined by

$$r_i\, n_i = \cos\theta, \qquad r_i\, e_i^{(2)} = 0, \tag{1–23}$$

where $e_i^{(2)}$ are the components of the unit vector in the x_2-direction and θ is the angle of incidence, measured in the x_1–x_3-plane. Note that the chosen directions of $\mathbf{n}$ and $\mathbf{r}$ simplify the

computations. However, there is no loss of generality as any other orientation of the free surface and the incoming wave field may be achieved by a rotation of the coordinate system.

Helmholtz decomposition of a vector field

In order to study the reflection of P- and S-waves at the free surface of a half-space, it is convenient to apply the concept of Helmholtz decomposition, which will be briefly described in this subsection.

Let $f_i(\mathbf{x})$ denote a piecewise continuous vector field defined on the closed domain Ω. Any such field may be decomposed into the gradient of a scalar field and the rotation, or curl, of a divergence free vector field,

$$f_i(\mathbf{x}) = \frac{\partial \Phi(\mathbf{x})}{\partial x_i} + \varepsilon_{ijk}\frac{\partial \Psi_k(\mathbf{x})}{\partial x_j}, \tag{1–24}$$

where

$$\Phi(\mathbf{x}) = -\frac{\partial F_j(\mathbf{x})}{\partial x_j}, \qquad \Psi_i(\mathbf{x}) = \varepsilon_{ijk}\frac{\partial F_k(\mathbf{x})}{\partial x_j}, \qquad F_i(\mathbf{x}) = \frac{1}{4\pi}\int_\Omega \frac{f_i(\mathbf{y})}{|\mathbf{x}-\mathbf{y}|}\,\mathrm{d}\Omega(\mathbf{y}). \tag{1–25}$$

The scalar field Φ and the vector field Ψ_i are referred to as *Helmholtz potentials*, and the property that the vector field $\Psi_i(\mathbf{x})$ is divergence free stems from fact that $\Psi_i(\mathbf{x})$ is the rotation of the vector field $F_j(\mathbf{x})$. Further, inserting the scalar and vector fields defined in Eq. (1–25) into Eq. (1–24), and making use of the δ–ε identity,

$$\varepsilon_{ijk}\varepsilon_{klm} = \delta_{il}\delta_{jm} - \delta_{im}\delta_{jl}, \tag{1–26}$$

it becomes clear, that the two fields $f_i(\mathbf{x})$ and $F_i(\mathbf{x})$ are related via the Poisson equation,

$$\frac{\partial^2 F_i}{\partial x_j \partial x_j} + f_i = 0. \tag{1–27}$$

A formal proof of the Helmholtz decomposition theorem is given in Appendix A.

The Helmholtz decomposition theorem stated above is valid even for infinite, or open, domains, provided that the vector field f_i vanishes with a rate of at least $a/|\mathbf{x}|^2$ for $|\mathbf{x}| \to \infty$, where a is a constant. This property of f_i is a necessary condition for the integral in Eq. (1–25) to exist.

Conditions at the free surface

The displacement field is now decomposed by means of Helmholtz decomposition,

$$u_i(\mathbf{x},t) = \frac{\partial \varphi(\mathbf{x},t)}{\partial x_i} + \varepsilon_{ijk}\frac{\partial \psi_k(\mathbf{x},t)}{\partial x_j}. \tag{1–28}$$

Since the scalar field $\varphi(\mathbf{x},t)$ is rotation free, whereas the vector field $\psi_i(\mathbf{x},t)$ is divergence free, it comes as no surprise that insertion of the decomposed displacement field (1–28) into the homogeneous Navier equations (1–13) provides the four equations

$$\frac{\partial^2 \varphi}{\partial x_j \partial x_j} = \frac{1}{c_P^2}\frac{\partial^2 \varphi}{\partial t^2}, \qquad \frac{\partial^2 \psi_i}{\partial x_j \partial x_j} = \frac{1}{c_S^2}\frac{\partial^2 \psi_i}{\partial t^2}. \tag{1–29}$$

Apparently, the Helmholtz potentials φ and ψ_i are all decoupled. However, this is only the case in a infinite medium, whereas a coupling between the respective potential fields take place at an inter face or at the free surface of a half-space.

The boundary conditions at $x_3 = 0$ are

$$\sigma_{33} = \sigma_{13} = \sigma_{23} = 0. \tag{1–30}$$

Applying these conditions, insertion of the plane wave field with the direction of propagation defined by Eq. (1–23) in the stress–strain relation (1–5) yields

$$\sigma_{13} = \mu \left(2\frac{\partial^2 \varphi}{\partial x_1 \partial x_3} + \frac{\partial^2 \psi_2}{\partial x_1^2} - \frac{\partial^2 \psi_2}{\partial x_3^2} \right) = 0, \tag{1–31}$$

$$\sigma_{23} = \mu \left(\frac{\partial^2 \psi_1}{\partial x_3^2} - \frac{\partial^2 \psi_3}{\partial x_1 \partial x_3} \right) = 0, \tag{1–32}$$

$$\sigma_{33} = (\lambda + 2\mu) \left(\frac{\partial^2 \varphi}{\partial x_1^2} + \frac{\partial^2 \varphi}{\partial x_3^2} \right) - 2\mu \left(\frac{\partial^2 \varphi}{\partial x_1^2} - \frac{\partial^2 \psi_2}{\partial x_1 \partial x_3} \right) = 0. \tag{1–33}$$

Any terms involving derivatives in the x_2-direction vanish because the definition of the plane wave field implies that the particle motion is constant along any line parallel with the x_2-axis. By inspection of Eqs. (1–31) to (1–33) it becomes evident that there are two uncoupled problems with respect to wave interference and reflection at the free surface:

1 P- and SV-waves, plane strain, $u_2 = 0$, governed by the wave equations

$$\frac{\partial^2 \varphi}{\partial x_j \partial x_j} = \frac{1}{c_P^2} \frac{\partial^2 \varphi}{\partial t^2}, \qquad \frac{\partial^2 \psi_2}{\partial x_j \partial x_j} = \frac{1}{c_S^2} \frac{\partial^2 \psi_2}{\partial t^2}, \tag{1–34}$$

and with the boundary conditions given by Eqs. (1–31) and (1–33).

2 SH-waves, $u_1 = u_3 = 0$, governed by the wave equations

$$\frac{\partial^2 \psi_1}{\partial x_j \partial x_j} = \frac{1}{c_S^2} \frac{\partial^2 \psi_1}{\partial t^2}, \qquad \frac{\partial^2 \psi_3}{\partial x_j \partial x_j} = \frac{1}{c_S^2} \frac{\partial^2 \psi_3}{\partial t^2}, \tag{1–35}$$

and with the boundary condition given by Eq. (1–32).

The two problems are dealt with in the following subsections. For simplicity, only the situation of harmonically varying particle motion is considered.

Reflection of plane harmonic P- and SV-waves

Harmonic variation of the displacement field with time implies a wave field in the form

$$u_i(\mathbf{x}, t) = U_i(\mathbf{x}, \omega) \mathrm{e}^{\mathrm{i}\omega t}, \tag{1–36}$$

where $U_i(\mathbf{x}, \omega)$ is an amplitude function and $\omega = 2\pi/T$ is the circular frequency of the variation. Here T is the period. The wavelength of a wave with the phase speed c and the period T is $L = cT$. However, in the case of harmonic waves, the spatial variation may advantageously be

described in terms of the wavenumber $k = 2\pi/L = \omega/c$. Moreover, in order to account for the direction of wave propagation, $\mathbf{r}$, a wavenumber vector $\mathbf{k}$ may be defined with the components

$$k_i = r_i \frac{\omega}{c}. \tag{1–37}$$

With these definitions of the temporal and spatial variations, it becomes clear that harmonic plane waves are given by Eq. (1–22) with $f = \mathrm{e}^{\mathrm{i}(k_j x_j - \omega t)}$, *i.e.*

$$u_i(\mathbf{x}, t) = A_i \mathrm{e}^{\mathrm{i}(k_j x_j - \omega t)}. \tag{1–38}$$

It is noted that this definition corresponds to Fourier transforms of the kind

$$\bar{U}_i(\mathbf{k}, \omega) = \iiint_{-\infty}^{\infty} U_i(\mathbf{x}, \omega) \mathrm{e}^{-\mathrm{i}k_j x_j} \mathrm{d}\mathbf{x}, \quad U_i(\mathbf{x}, \omega) = \int_{-\infty}^{\infty} u_i(\mathbf{x}, t) \mathrm{e}^{+\mathrm{i}\omega t} \mathrm{d}t, \tag{1–39}$$

with the inverse transforms given as

$$u_i(\mathbf{x}, t) = \frac{1}{2\pi} \int_{-\infty}^{\infty} U_i(\mathbf{x}, \omega) \mathrm{e}^{-\mathrm{i}\omega t} \mathrm{d}\omega, \quad U_i(\mathbf{x}, \omega) = \frac{1}{2\pi} \iiint_{-\infty}^{\infty} \bar{U}_i(\mathbf{k}, \omega) \mathrm{e}^{+\mathrm{i}k_j x_j} \mathrm{d}\mathbf{k}. \tag{1–40}$$

Comparison of Eqs. (1–38) and (1–39) reveals that $\bar{U}_i(\mathbf{k}, \omega) = A_i$ for the harmonically varying plane wave field. It is noted that the harmonic variation of type $\mathrm{e}^{+\mathrm{i}\omega t}$ is not standard in Fourier transformation (Eq. (1–39)). However, the temporal and spatial transformations defined by Eqs. (1–39) and (1–40) imply the nice property that wave propagation actually occurs in the positive direction of the wavenumber vector, whereas standard Fourier transformation with respect to time would imply wave propagation in the negative $\mathbf{k}$-direction.

In this subsection, the reflection of harmonic P- and SV-waves is studied. The analysis of the plane strain situation is carried out for two situations:

1 the incoming wave is a P-wave travelling in the direction $\mathbf{r}_P$,

2 the incoming wave is an S-wave travelling in the direction $\mathbf{r}_S$.

Here, the term *incoming* refers to an observer situated at the free surface. Accordingly, any wave reflected from the surface is referred to as *outgoing*. It is noted that any mixture of incoming P- and SV-waves may be treated, simply by summing the outgoing wave fields from the incoming P-wave and the incoming SV-wave. This is due to the fact that the problem is linear and that, furthermore, the P- and S-waves only interact at the boundary.

Incoming P-waves are described by the wavenumber vector $\mathbf{k}_P^i$ with the components

$$k_{P\,i}^i = r_{P\,i} \frac{\omega}{c_P}. \tag{1–41}$$

Similarly, the outgoing P- and SV-waves are defined by the wavenumber vectors $\mathbf{k}_P^r$ and $\mathbf{k}_S^r$ with the components

$$k_{P\,i}^r = r_{P\,j} \left(\delta_{ij} - 2n_i n_j\right) \frac{\omega}{c_P}, \qquad k_{S\,i}^r = r_{S\,j} \left(\delta_{ij} - 2n_i n_j\right) \frac{\omega}{c_S}, \tag{1–42}$$

respectively, where the superscript r stands for *reflected*. The operation in the parenthesis defines the reflection of the wavenumber vector around the boundary with outward unit normal n_i. The component parallel to the boundary is the same after the transformation, but the component orthogonal to the boundary is mirrored. Since $\mathbf{r}$ and $\mathbf{n}$ are both unit vectors, it follows immediately from Eq. (1–42) that

$$k_P\, c_P = k_S\, c_S = \omega, \tag{1–43}$$

where $k_P = |\mathbf{k}_P^i| = |\mathbf{k}_P^r|$ and $k_S = |\mathbf{k}_S^r|$.

The wave equations (1–34) are satisfied by the harmonically varying fields

$$\varphi(\mathbf{x},t) = A_P^i \mathrm{e}^{\mathrm{i}(k_{P\,j}^i x_j - \omega t)} + A_P^r \mathrm{e}^{\mathrm{i}(k_{P\,j}^r x_j - \omega t)}, \qquad \psi_2(\mathbf{x},t) = A_S^r \mathrm{e}^{\mathrm{i}(k_{S\,j}^r x_j - \omega t)}. \tag{1–44}$$

Here A_P^i and A_P^r are the amplitudes of the incoming and the reflected P-waves, respectively, and A_S^r is the amplitude of the reflected SH-wave.

Insertion of the potentials defined by Eq. (1–44) into the boundary conditions (1–31) and (1–33) for $x_3 = 0$ yields

$$\begin{aligned} &k_P^2 \left(2\sin^2\theta_P - \alpha^2\right)\left(A_P^i + A_P^r\right)\mathrm{e}^{\mathrm{i}k_P(\sin\theta_P x_1 - c_P t)} \\ &\quad - k_S^2 \sin 2\theta_S A_S^r \mathrm{e}^{\mathrm{i}k_S(\sin\theta_S x_1 - c_S t)} = 0, \end{aligned} \tag{1–45}$$

$$k_P^2 \sin^2 2\theta_P \left(A_P^i + A_P^r\right)\mathrm{e}^{\mathrm{i}k_P(\sin\theta_P x_1 - c_P t)} - k_S^2 \sin 2\theta_S A_S^r \mathrm{e}^{\mathrm{i}k_S(\sin\theta_S x_1 - c_S t)} = 0, \tag{1–46}$$

where θ_P and θ_S are the angles between the normal vector $\mathbf{n}$ and the reflected P- and S-waves, respectively, according to the definitions in Fig. 1–15. The parameter α is the ratio between the phase speeds c_P and c_S,

$$\alpha = \frac{c_P}{c_S} = \frac{k_S}{k_P} = \sqrt{\frac{\lambda + 2\mu}{\mu}}. \tag{1–47}$$

In order for the boundary conditions (1–45) and (1–46) to be satisfied for any instant of time and for any point on the boundary, *i.e.* for any combination of t and x_1, the phase in the P- and SV-wave terms must be identical. Making use of Eq. (1–43) it becomes evident that this involves the identity $k_P \sin\theta_P = k_S \sin\theta_S$, or

$$\frac{k_S}{k_P} = \frac{\sin\theta_P}{\sin\theta_S} = \alpha, \tag{1–48}$$

which is the equivalent of *Snell's law* for elastic waves. It is noticed that the reflected S-wave leaves the surface at an angle, which is less oblique than that of the P-wave.

Since the phase of P- and S-waves are identical, they vanish in the computation of the amplitudes of the plane reflected wave fields. Hence, for a given amplitude of the incoming P-wave, the relative amplitudes of the reflected P- and S-waves, or the *reflection coefficients*, become

$$\frac{A_P^r}{A_P^i} = \frac{\sin 2\theta_P \sin 2\theta_S - \alpha^2 \cos^2 2\theta_S}{\sin 2\theta_P \sin 2\theta_S + \alpha^2 \cos^2 2\theta_S}, \qquad \frac{A_S^r}{A_P^i} = \frac{2\sin 2\theta_P \cos 2\theta_S}{\sin 2\theta_P \sin 2\theta_S + \alpha^2 \cos^2 2\theta_S}. \tag{1–49}$$

The angle θ_S and the wavenumber k_S are determined by Eq. (1–48). Further, from Eq. (1–49) it follows that an incoming P-wave propagating in the direction perpendicular to the boundary, *i.e.* $\mathbf{r}_P = \mathbf{n}$, is reflected as a pure P-wave. The amplitude of the reflected P-wave is $A_P^r = -A_P^i$. The negative sign indicates a phase shift of π between the particle motion in the incoming and the reflected wave field. In Fig. 1–16 the relative amplitudes of reflected P- and SV-waves are plotted as functions of the angle of incidence, θ_P, and the Poisson ratio for the material in the half-space. Note that by Eqs. (1–8) and (1–47) it follows that

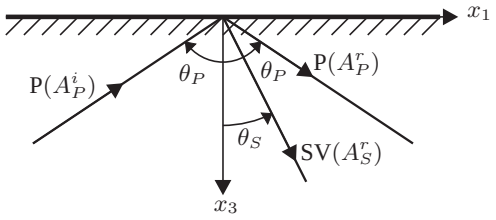

Figure 1–15: Reflection of an incoming P-wave at a free boundary. Note that $\theta_P > \theta_S$.

$$\alpha^2 = \frac{2-2\nu}{1-2\nu}. \tag{1–50}$$

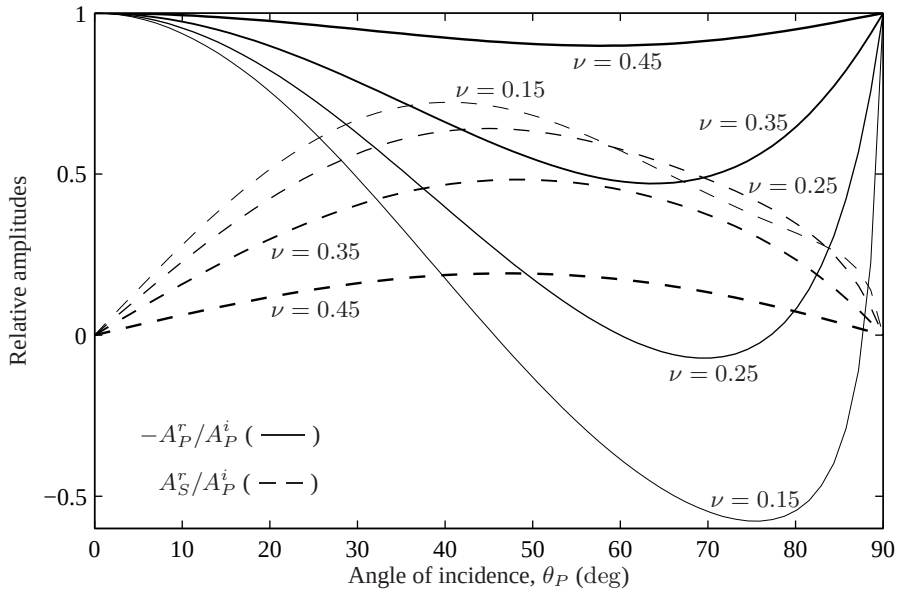

Figure 1–16 Relative amplitudes of reflected waves from a free surface for incoming P-waves with different angles of incident, θ_P, and for various Poisson ratios, ν.

Incoming SV-waves impinging on the boudary under the angle θ_S are reflected as SV-waves and possibly also P-waves. The situation is illustrated in Fig. 1–17. For a known amplitude of the incoming SV-wave, the amplitudes of reflected P- and SV-waves may be computed in the same manner as described for incoming P-waves in the previous paragraph. Only the main results are given, *i.e.* the relative amplitudes,

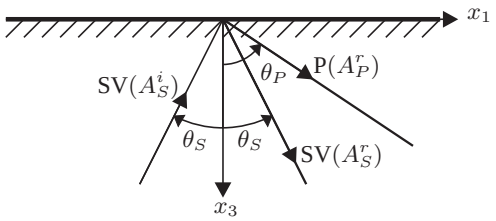

Figure 1–17: Reflection of an incoming SV-wave at a free boundary. Note that $\theta_P > \theta_S$.

$$\frac{A_S^r}{A_S^i} = \frac{\sin 2\theta_P \, \sin 2\theta_S \, - \, \alpha^2 \, \cos^2 2\theta_S}{\sin 2\theta_P \, \sin 2\theta_S \, + \, \alpha^2 \, \cos^2 2\theta_S}, \qquad \frac{A_P^r}{A_S^i} = \frac{-2\alpha^2 \sin 2\theta_S \, \cos 2\theta_S}{\sin 2\theta_P \, \sin 2\theta_S \, + \, \alpha^2 \, \cos^2 2\theta_S}, \quad (1\text{–}51)$$

which may alternatively be denoted the reflection coefficients. The angle θ_P and the wavenumber k_P are defined by Eq. (1–48). In Fig. 1–18 the relative amplitudes are plotted as functions of the angle of incidence, θ_S, and for different Poisson ratio of the half-space material.

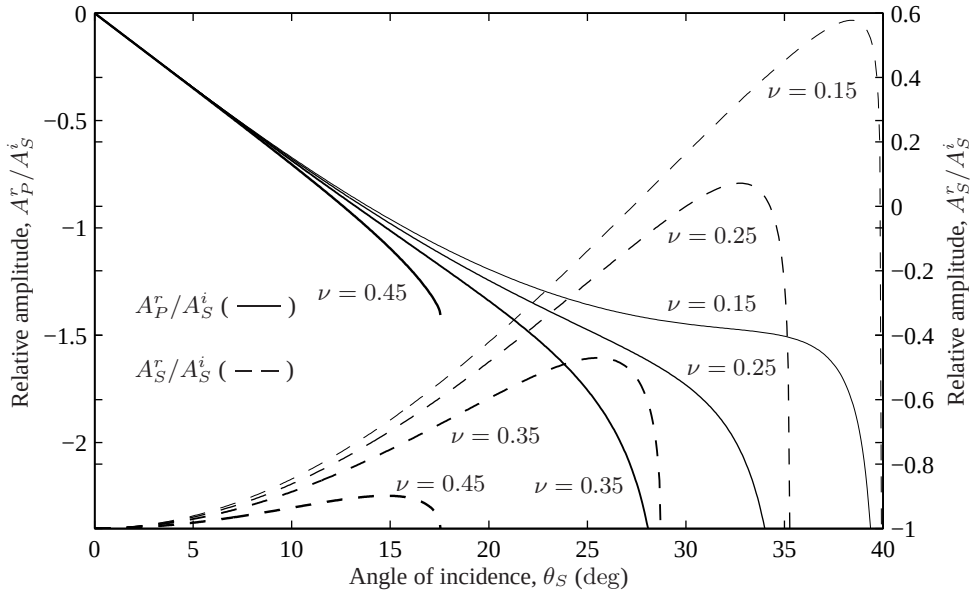

Figure 1–18 Relative amplitudes of reflected waves from a free surface for incoming SV-waves with different angles of incident, θ_S, and for various Poisson ratios, ν.

Inspection of Eq. (1–48) reveals that a critical angle, $\theta_S = \theta_c$, exists for which the reflected P-wave propagates parallel with the boundary, *i.e.* $\sin\theta_P = \alpha \, \sin\theta_c = 1$. For $\alpha = c_P/c_S = 2$, the critical angle becomes $30°$. If the incident SH-wave impinges on the free boundary at an angle $\theta_S > \theta_c$, only an SV-wave is reflected. The energy that for smaller angles is reflected as a P-wave is in stead captured as a surface wave with exponential decay of the amplitude in the x_3-direction, see Fig. 1–19. The nature of surface waves is further discussed in the next section with special reference to the *Rayleigh wave*.

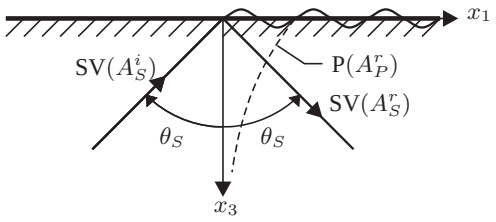

Figure 1–19: Total reflection of SV-wave for $\theta_S > \theta_c$. The P-waves are captured in the surface.

Reflection of harmonic SH-waves

The particle motion in SH-waves is exclusively in the x_2-direction, *i.e.* in the direction orthogonal to the plane, in which the plane strain problem is defined. Thus, SH-waves do not interact with P- and SV-waves at a free surface and they may therefore be treated independently thereof.

Plane SH-waves that are solution to the wave equations (1–35) are identified as

$$\psi_1(\mathbf{x},t) = B_1^i \mathrm{e}^{\mathrm{i}(k_{S\,j}^i x_j - \omega t)} + B_1^r \mathrm{e}^{\mathrm{i}(k_{S\,j}^r x_j - \omega t)}, \tag{1–52}$$

$$\psi_2(\mathbf{x},t) = B_2^i \mathrm{e}^{\mathrm{i}(k_{S\,j}^i x_j - \omega t)} + B_2^r \mathrm{e}^{\mathrm{i}(k_{S\,j}^r x_j - \omega t)}, \tag{1–53}$$

where $k_{S\,j}^i$ are the components of the wavenumber vector for the incoming SH-waves, whereas $k_{S\,j}^r$ are the components of the wavenumber vector for the reflected SH-waves.

Apparently, the problem of SH-wave reflection involves four amplitudes, B_1^i, B_1^r, B_2^i and B_2^r. However, by insertion of the solutions (1–52) and (1–53) into the condition

$$\frac{\partial \psi_i}{\partial x_i} = 0, \tag{1–54}$$

which follows from the fact that the divergence of the rotation of a vector field vanishes, it becomes clear that

$$\mathrm{i}\left(k_{S\,1}^i B_1^i\right) \mathrm{e}^{\mathrm{i}(k_{S\,j}^i x_j - \omega t)} + \mathrm{i}\left(k_{S\,1}^r B_1^r\right) \mathrm{e}^{\mathrm{i}(k_{S\,j}^r x_j - \omega t)} = 0. \tag{1–55}$$

Equation (1–55) is only satisfied for an arbitrary point on the surface $x_3 = 0$ and for any instant of time t if

$$k_{S\,1}^i\, B_1^i = -k_{S\,2}^i B_2^i, \qquad k_{S\,1}^r\, B_1^r = -k_{S\,2}^r B_2^r, \tag{1–56}$$

which defines the amplitudes

$$A_{SH}^i = B_1^i = -\frac{k_{S\,2}^i}{k_{S\,1}^i}\, B_2^i, \qquad A_{SH}^r = B_1^r = -\frac{k_{S\,2}^r}{k_{S\,1}^r}\, B_2^r. \tag{1–57}$$

Hence, the boundary condition (1–32) yields

$$\{k_{S\,2}^i\}^2 \left(A_{SH}^i + A_{SH}^r\right) + \{k_{S\,1}^i\}^2 \left(A_{SH}^i + A_{SH}^r\right) = 0, \tag{1–58}$$

where use has been made of the fact that $k_{S\,2}^r = -k_{S\,2}^i$ and $k_{S\,1}^r = k_{S\,1}^i$. This follows from Eq. (1–42) with $\mathbf{r}_S$ denoting the direction of wave propagation of the incoming SH-wave.

The static case $k_{S\,i} = 0$ is not of interest. Further, since $k_{S\,i}$ defines a real vector, $\{k_{S\,1}^i\}^2 + \{k_{S\,2}^i\}^2 > 0$, and therefore Eq. (1–58) involves that the amplitude of the reflected SH-wave is

$$A_{SH}^r = -A_{SH}^i. \tag{1–59}$$

Thus, all the energy in the incoming SH-wave is reflected as an outgoing SH-wave. The particle motion in the outgoing wave has a phase shift of π relative to that of the incoming wave.

1.3.3 Reflection and refraction at an interface

An interface is defined as the common boundary between two layers or half-spaces with different material properties. An incoming wave hitting such an interface is reflected back into the medium whence it came as discussed in the previous subsection. However, in addition to this the waves are refracted so that a part of the energy propagates into the adjacent layer. This problem is treated in the following for harmonic elastic waves with the circular frequency ω. Again, the problem is divided into the decoupled problems involving plane strain and SH-wave propagation, respectively.

P- and SV-waves

A plane harmonic wave incoming from $x_3 \to \infty$ is considered, and with no loss of generality the interface is situated at $x_3 = 0$. Further, the wave propagation is assumed to take place in the x_1–x_3-plane. The wave propagation and the material properties in the bottommost half-space defined by $x_3 > 0$ are given as λ, μ, ρ, c_P, c_S, σ_{ij}, φ, ψ_i and u_i. Likewise, the wave propagation and the material properties in the uppermost half-space defined by $x_3 < 0$ are given as $\breve{\lambda}$, $\breve{\mu}$, $\breve{\rho}$, $\breve{c}_P$, $\breve{c}_S$, $\breve{\sigma}_{ij}$, $\breve{\varphi}$, $\breve{\psi}_i$ and $\breve{u}_i$. The solutions to Eq. (1–34) for the lower and upper half-space achieve the form

$$\varphi(\mathbf{x},t) = A_P^i \mathrm{e}^{\mathrm{i}(k_{P\,j}^i x_j - \omega t)} + A_P^r \mathrm{e}^{\mathrm{i}(k_{P\,j}^r x_j - \omega t)}, \tag{1–60}$$

$$\psi_2(\mathbf{x},t) = A_S^i \mathrm{e}^{\mathrm{i}(k_{S\,j}^i x_j - \omega t)} + A_S^r \mathrm{e}^{\mathrm{i}(k_{S\,j}^r x_j - \omega t)}, \tag{1–61}$$

$$\breve{\varphi}(\mathbf{x},t) = \breve{A}_P^r \mathrm{e}^{\mathrm{i}(\breve{k}_{P\,j}^r x_j - \omega t)}, \qquad \breve{\psi}_2(\mathbf{x},t) = \breve{A}_S^r \mathrm{e}^{\mathrm{i}(\breve{k}_{S\,j}^r x_j - \omega t)}, \tag{1–62}$$

It is noticed that there are only refracted waves (denoted by the superscript r) in the upper half-space, whereas there are both incoming and reflected waves in the lower half-space. As an alternative to the wavenumber vectors $\mathbf{k}_P^i$, $\mathbf{k}_S^i$, $\mathbf{k}_P^r$, $\mathbf{k}_s^r$, $\breve{\mathbf{k}}_P^r$ and $\breve{\mathbf{k}}_S^r$, the direction of wave propagation may be defined by the angles θ_P, θ_S, $\breve{\theta}_P$ and $\breve{\theta}_S$, see Fig. 1–20.

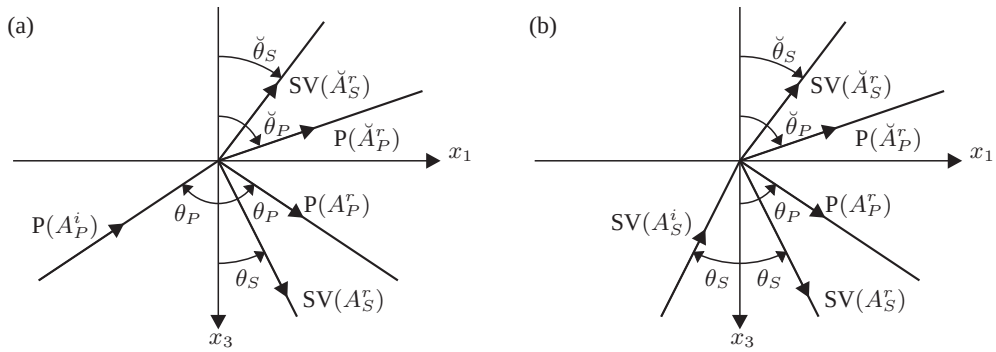

Figure 1–20 Reflection and refreaction of plane waves at the interface $x_3 = 0$ for (a) P-waves incoming from the lower half-space and (b) SV-waves incoming from the lower half-space.

The boundary conditions at the interface are only satisfied for arbitrary x_1-coordinates and instants of time if all the incoming and refracted waves propagate in phase. Since the wavenumber satisfy conditions of the kind (1–43), it follows that $k_P \sin\theta_P = k_S \sin\theta_S = \breve{k}_P \sin\breve{\theta}_P = \breve{k}_S \sin\breve{\theta}_S$, or

$$\frac{\breve{k}_P}{k_P} = \frac{\sin\theta_P}{\sin\breve{\theta}_P} = \frac{c_P}{\breve{c}_P}, \qquad \frac{\breve{k}_S}{k_S} = \frac{\sin\theta_S}{\sin\breve{\theta}_S} = \frac{c_S}{\breve{c}_S}, \tag{1–63}$$

$$\frac{\breve{k}_S}{k_P} = \frac{\sin\theta_P}{\sin\breve{\theta}_S} = \frac{c_P}{\breve{c}_S}, \qquad \frac{\breve{k}_P}{k_S} = \frac{\sin\theta_S}{\sin\breve{\theta}_P} = \frac{c_S}{\breve{c}_P}. \tag{1–64}$$

Together, Eqs. ((1–63) and (1–64) constitute the Snell's law for reflection and refraction of plane harmonic elastic P- and SV-waves at an interface. In same manner as for the reflection of SV-waves at a free surface, it is noted that waves may be trapped in the interface. Depending on

the material properties in the two layers and the nature and angle of incidence of the incoming wave, this may happen for the reflected and/or refracted P-wave and possibly also the refracted SV-wave. Waves propagating along an interface in the form of captured body waves with an exponential decay of the amplitude away from the interface are referred to as Stonely wave.

A computation of the amplitudes of the reflected and refracted wave fields that arise when an incoming P- or SV-wave is considered is based on the assumption that the displacements are continuous across the boundary whereas there is equilibrium of the forces. This implies that

$$u_1 = \breve{u}_1, \qquad u_3 = \breve{u}_3, \qquad \sigma_{13} = \breve{\sigma}_{13}, \qquad \sigma_{33} = \breve{\sigma}_{33} \qquad \text{for} \qquad x_3 = 0. \tag{1–65}$$

The derivation of the relative amplitudes is left to the reader.

SH-waves

In the case of incoming SH-waves the situation simplifies significantly as only one reflected and refracted wave is present. The situation is illustrated in Fig. 1–21. The reflected wave leaves the interface under the angle of inclination θ_S of the incoming wave. The refracted wave leaves the interface under an angle $\breve{\theta}_S$ defined by the Snell's law

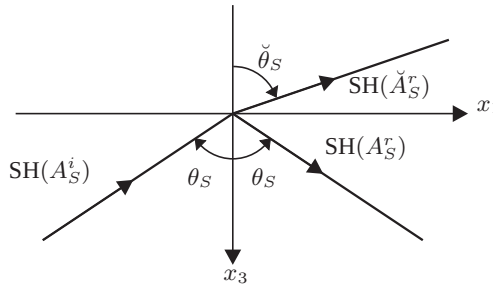

Figure 1–21: Reflection and refraction of an SH-wave at an interface.

$$\frac{\breve{k}_S}{k_S} = \frac{\sin\theta_S}{\sin\breve{\theta}_S} = \frac{c_S}{\breve{c}_S}. \tag{1–66}$$

The relative amplitudes of the reflected and refracted SH-waves when compared to that of the incoming SH-wave will not be derived.

Love waves may arise due to multiple reflections of SH-waves between two interfaces. Thus, a stratified medium is considered, and in one of the layers the phase speed c_S is lower than that in the surrounding layers. In geodynamics this may, for example, be the case when a soft clay or an organic soil material overlays limestone or rock. In either case the mass density in the two layers is of the same order of magnitude whereas the shear strengths given by μ may be significantly different from one another. The layer with the relatively low phase speed c_S is denoted the *soft layer*.

An SH-wave source is assumed to be present inside the soft layer. The waves propagate away from the source and will eventually hit one of the interfaces bounding the layer, one of which may be a free surface. This leads to reflection and refraction as illustrated in Fig. 1–22. It is noticed that beyond a certain distance, l, from the source only reflection occurs. This is a result of the fact that $\sin\breve{\theta}_S \leq 1$. Thus the soft layer acts as a *wave guide* for the SH-waves. The layer wave resulting from the SH-waves captured in the layer is referred to as the *Love wave*, or the L-wave, and is attributed to A.E.H. Love who put forward the theory in 1911.

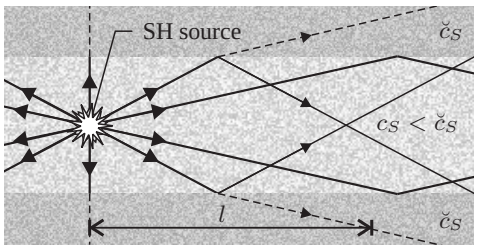

Figure 1–22: Generation of a Love wave in a soft layer. The SH-waves captured in the layer are denoted L.

1.4 The Rayleigh wave on a homogeneous half-space

In the previous section it has been shown that two different waves may propagate through the interior of an unbounded elastic domain, namely P- and S-waves. However, when an interface or a free surface is present, some mixing of the two wave types will take place, and the possibility of waves being trapped in the surface/interface arises. Further, observations of earth tremors lead to the conclusion that waves may propagate along the surface of a half-space other than the P- and S-waves. These waves were first described by Lord Rayleigh in 1885 and they are accordingly referred to as *Rayleigh waves*. In this section we shall prove that Rayleigh waves are also mathematically permissible solutions to the Navier equations.

1.4.1 Potential field for plane Rayleigh waves

Consider the homogeneous isotropic linear elastic half-space defined by $x_3 > 0$. The particle motion in plane strain is then given by the previously defined wave equations

$$\frac{\partial^2 \varphi}{\partial x_j \partial x_j} = \frac{1}{c_P^2}\frac{\partial^2 \varphi}{\partial t^2}, \qquad \frac{\partial^2 \psi_2}{\partial x_j \partial x_j} = \frac{1}{c_S^2}\frac{\partial^2 \psi_2}{\partial t^2}, \tag{1–34}$$

given in terms of the potentials φ and ψ_2.

The particle motion is assumed to vary harmonically with time. Since the aim of this analysis is to prove the existence of a surface wave, no wave propagation is allowed in the x_3-direction, *i.e.* over depth. Moreover, only wave propagation in the positive x_1-direction is allowed; hence, solutions to the wave equations (1–34) are sought in the form

$$\varphi(x_1, x_3, t) = \Phi(x_3)\mathrm{e}^{\mathrm{i}k_P(\sin\theta_P x_1 - c_P t)}, \qquad \psi_2(x_1, x_3, t) = \Psi_2(x_3)\mathrm{e}^{\mathrm{i}k_S(\sin\theta_S x_1 - c_S t)}. \tag{1–67}$$

Here $\Phi(x_3)$ and $\Psi_2(x_3)$ are amplitude functions describing the variation of the particle motion over depth. These amplitudes must decay with depth so that a finite amount of mechanical energy is present per unit surface area of the half-space due to the wave motion. k_P and k_S are the previously defined wavenumbers of P- and S-waves, and θ_P and θ_S are angles of incidence of the two wave types. Insertion of the potentials (1–67) into Eq. (1–34) leads to two ordinary differential equations in x_3,

$$\frac{\partial^2 \Phi}{\partial x_3^2} + \left(1 - \sin^2\theta_P\right) k_P^2 \Phi = 0, \qquad \frac{\partial^2 \Psi_2}{\partial x_3^2} + \left(1 - \sin^2\theta_S\right) k_S^2 \Psi_2 = 0. \tag{1–68}$$

Next, the wavenumber k_R and the phase speed c_R for the Rayleigh wave are introduced,

$$k_R = k_P \sin\theta_P = k_S \sin\theta_S, \qquad k_P c_P = k_S c_S = \omega = k_R c_R. \tag{1–69}$$

The fact that $k_P \sin\theta_P = k_S \sin\theta_S$ follows from Eq. (1–48), whereas the definition of c_R for a known value of k_R stems from Eq. (1–43). Equation (1–68) may now conveniently be rewritten as

$$\frac{\partial^2 \Phi}{\partial x_3^2} - \gamma_P^2 \Phi = 0, \qquad \frac{\partial^2 \Psi_2}{\partial x_3^2} - \gamma_S^2 \Psi_2 = 0, \tag{1–70}$$

where the "reduced wavenumbers" γ_P and γ_S are introduced,

$$\gamma_P^2 = k_R^2\left(1-\frac{c_R^2}{c_P^2}\right), \quad \gamma_S^2 = k_R^2\left(1-\frac{c_R^2}{c_S^2}\right). \tag{1–71}$$

γ_P^2 and γ_S^2 are assumed to be positive real quantities. Physically, this involves that $c_R < c_S$, *i.e.* the Rayleigh wave speed is smaller than the S-wave speed, and therefore also the P-wave speed. This is in good accordance with observations in the nature.

Solutions to the homogeneous ordinary differential equations (1–71) are in the form

$$\Phi(x_3) = A_P \mathrm{e}^{-\gamma_P x_3} + B_P \mathrm{e}^{\gamma_P x_3}, \qquad \Psi(x_3) = A_S \mathrm{e}^{-\gamma_S x_3} + B_S \mathrm{e}^{\gamma_S x_3}. \tag{1–72}$$

Given the restrictions on γ_P and γ_S, the A and B terms describe amplitude functions, which decrease and increase exponentially with depth, respectively, that is for $x_3 \to \infty$. The terms involving increasing amplitudes with depth a invalid from a physical point of view. On the other hand, the A terms make sense, as integration of an exponentially decreasing function from $x_3 = 0$ to $x_3 \to \infty$ provides a finite value. Hence, the potential fields (1–67) become

$$\varphi(x_1, x_3, t) = A_P \mathrm{e}^{-\gamma_P x_3} \mathrm{e}^{\mathrm{i}k_R(x_1 - c_R t)}, \qquad \psi_2(x_1, x_3, t) = A_S \mathrm{e}^{-\gamma_S x_3} \mathrm{e}^{\mathrm{i}k_R(x_1 - c_R t)}, \tag{1–73}$$

where the wavenumbers are substituted by application of Eq. (1–69). The fact that γ_P^2 and γ_S^2 must be positive real values now becomes evident. Complex and negative values of γ_P^2 and γ_S^2 correspond to damped and undamped wave propagation in the x_3 direction, respectively, and the definition of the surface wave is that wave propagation is restricted to the horizontal x_1-direction.

It is noted that the Rayleigh wave described by these potential fields corresponds to the situation in which both P- and SV-waves are trapped in a small zone in the vicinity of the surface. The situation of trapped P-waves for grazing SV-waves has previously been discussed.

1.4.2 Particle motion in the Rayleigh wave field

The u_1 and u_3 components of the plane displacement field follow from Eq. (1–28). Subsequently the stress components on the surface $x_3 = 0$ may be found by means of Eq. (1–5). Hence,

$$u_1 = \left(\gamma_S A_S \mathrm{e}^{-\gamma_S x_3} + \mathrm{i}k_R A_P \mathrm{e}^{-\gamma_P x_3}\right) \mathrm{e}^{\mathrm{i}k_R(x_1 - c_R t)}, \tag{1–74}$$

$$u_3 = -\left(\gamma_P A_P \mathrm{e}^{-\gamma_P x_3} - \mathrm{i}k_R A_S \mathrm{e}^{-\gamma_S x_3}\right) \mathrm{e}^{\mathrm{i}k_R(x_1 - c_R t)}, \tag{1–75}$$

$$\sigma_{11} = \mu\left\{\left(\gamma_S^2 - k_R^2 - 2\gamma_P^2\right) A_P \mathrm{e}^{-\gamma_P x_3} - 2\mathrm{i}\gamma_S k_R A_S \mathrm{e}^{-\gamma_S x_3}\right\} \mathrm{e}^{\mathrm{i}k_R(x_1 - c_R t)}, \tag{1–76}$$

$$\sigma_{13} = -\mu\left\{2\mathrm{i}\gamma_P k_R A_P \mathrm{e}^{-\gamma_P x_3} + \left(\gamma_S^2 + k_R^2\right) A_S \mathrm{e}^{-\gamma_S x_3}\right\} \mathrm{e}^{\mathrm{i}k_R(x_1 - c_R t)}, \tag{1–77}$$

$$\sigma_{33} = -\mu\left\{\left(\gamma_S^2 + k_R^2\right) A_P \mathrm{e}^{-\gamma_P x_3} + 2\mathrm{i}\gamma_S k_R A_S \mathrm{e}^{-\gamma_S x_3}\right\} \mathrm{e}^{\mathrm{i}k_R(x_1 - c_R t)}, \tag{1–78}$$

The boundary conditions at the free surface $x_3 = 0$ now involves that

$$\sigma_{13} = \sigma_{33} = 0 \quad \text{for} \quad x_3 = 0. \tag{1–79}$$

Insertion of the stresses given by Eqs. (1–77) and (1–78) into Eq. (1–79) yields

$$\left(\gamma_S^2 + k_R^2\right) A_P - 2\mathrm{i}\gamma_S k_R A_S = 0, \tag{1–80}$$

$$2\mathrm{i}\gamma_P k_R A_P + \left(\gamma_S^2 + k_R^2\right) A_S = 0. \tag{1–81}$$

Equations (1–80) and (1–81) yield the trivial solution $A_P = A_S = 0$, which is not very interesting since in this case $u_1 = u_3 = 0$. Non-trivial solutions exist if the determinant of the coefficient matrix for the system of equations defined by Eqs. (1–80) and (1–81) is equal to zero. This leads to the *Rayleigh wave frequency relation*

$$\left(\gamma_S^2 + k_R^2\right)^2 - 4\gamma_P\gamma_S k_R^2 = 0. \tag{1–82}$$

The amplitude ratio between the P- and S-wave parts of the Rayleigh wave field may be expressed by means of either Eq. (1–80) or Eq. (1–81),

$$\frac{A_P}{A_S} = \frac{2\mathrm{i}\gamma_S k_R}{\gamma_S^2 + k_R^2} = -\frac{\gamma_S^2 + k_R^2}{2\mathrm{i}\gamma_P k_R}. \tag{1–83}$$

Substitution of Eq. (1–83) into Eqs. (1–74) and (1–75) yields

$$u_1 = \mathrm{i}A_P\left(k_R\mathrm{e}^{-\gamma_P x_3} - \frac{\gamma_S^2 + k_R^2}{2k_R}\mathrm{e}^{-\gamma_S x_3}\right)\mathrm{e}^{\mathrm{i}k_R(x_1 - c_R t)}, \tag{1–84}$$

$$u_3 = A_P\left(-\gamma_P\mathrm{e}^{-\gamma_P x_3} + \frac{\gamma_S^2 + k_R^2}{2\gamma_S}\mathrm{e}^{-\gamma_S x_3}\right)\mathrm{e}^{\mathrm{i}k_R(x_1 - c_R t)}. \tag{1–85}$$

The presence of the imaginary unit i in the expression for u_1 involves that the horizontal displacement component is $\pi/2$ out of phase with the vertical displacement component u_3, in which the imaginary unit does not occur. Therefore the trajectories of the particles are ellipses. In opposition to gravitation waves on the surface of a fluid, the horizontal displacement amplitude at any depth is smaller than that of the vertical displacement component. In particular, $u_1 = 0$ for $x_3 = x_3^c \approx 0.19L_R$, where $L_R = 2\pi/k_R$ is the Rayleigh wavelength. Furthermore, at shallow depths, *i.e.* for $x_3 < x_3^c$, the particle motion in the Rayleigh wave field is *retrograde*. This means that the particle motion is counterclockwise for a wave propagating to the right. However, for depths greater than x_3^c, the particle motion is reversed. The nature of the wave field is sketched in Fig. 1–23, and Fig. 1–24 shows the relative amplitudes of the vertical and horizontal displacements for various Poisson ratios. Note that a computation of the relative amplitudes implies that c_R is known. The phase speed of the Rayleigh wave is derived in the following subsection.

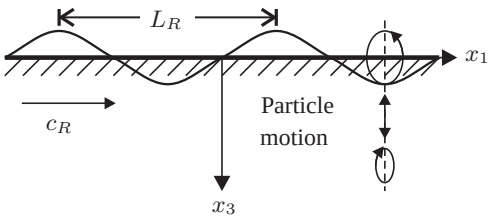

Figure 1–23: Particle motion and wave propagation in the plane Rayleigh wave.

1.4.3 Derivation of the Rayleigh wave speed

Insertion of γ_P^2 and γ_S^2 as defined by Eq. (1–71) into the frequency relation (1–82) provides the so-called *Rayleigh equation*,

$$\left(2 - \frac{c_R^2}{c_S^2}\right)^2 = 4\left(1 - \frac{c_R^2}{c_P^2}\right)^{\frac{1}{2}}\left(1 - \frac{c_R^2}{c_S^2}\right)^{\frac{1}{2}}, \tag{1–86}$$

which defines c_R for known values of c_P and c_S. Equation (1–86) may alternatively be written as a fourth order polynomial equation in c_R^2/c_S^2,

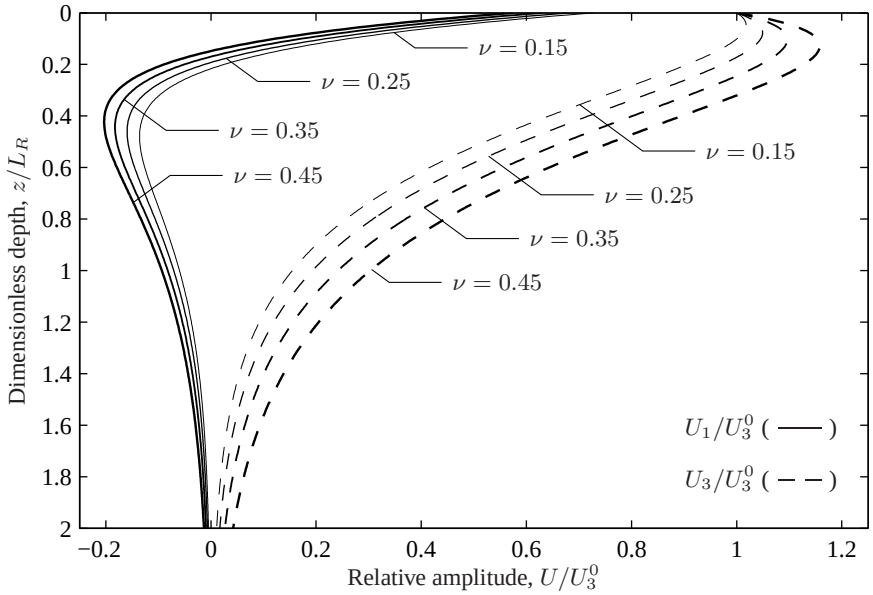

Figure 1–24 Relative amplitudes of vertical and horizontal displacements in plane Rayleigh wave for various Poisson ratios, ν. L_R denotes the Rayleigh wavelength.

$$\left(\frac{c_R}{c_S}\right)^2 \left\{ \left(\frac{c_R}{c_S}\right)^6 - 8\left(\frac{c_R}{c_S}\right)^4 + \left(24 - 16\alpha^{-2}\right)\left(\frac{c_R}{c_S}\right)^2 - 16\left(1 - \alpha^{-2}\right) \right\} = 0, \tag{1–87}$$

where $\alpha = c_P/c_S$, cf. Eq. (1–47). The root $c_R^2/c_S^2 = 0$ has no physical meaning, since this would correspond to a case in which the Rayleigh wave does not propagate. Thus, Eq. (1–87) reduces to a third order polynomial equation in c_R^2/c_S^2,

$$\left(\frac{c_R}{c_S}\right)^6 - 8\left(\frac{c_R}{c_S}\right)^4 + \left(24 - 16\alpha^{-2}\right)\left(\frac{c_R}{c_S}\right)^2 - 16\left(1 - \alpha^{-2}\right) = 0. \tag{1–88}$$

Mathematically, Eq. (1–88) has three roots c_R^2/c_S^2. However, only one of these is physically valid. According to Eq. (1–50), α may be expressed in terms of the Poisson ratio, and it turns out that the number of real and complex roots are:

- $\nu > 0.263$: 1 real positive root and two complex conjugate roots,
- $\nu < 0.263$: 3 real positive roots.

Inspection of Eqs. (1–84) and (1–85) expressing the displacement field reveals that the complex roots would correspond to a response that is either decreasing or increasing with time. However, a harmonically varying solution is sought, *i.e.* the amplitudes must be constant in time. Hence, the complex roots are invalid, and for $\nu > 0.263$ c_R is given as the square root of the real positive root. For $\nu < 0.263$, three positive roots exist. However, as discussed earlier the condition $c_R/c_S < 1$ must be met. Otherwise the Rayleigh wave is not a surface wave. For Poisson ratios on the interval $\nu \in [0, 0.5]$, *i.e.* for any real material, only one of the roots satisfies

this condition. Hence, the Rayleigh wave speed is uniquely defined for any Poisson ratio and increases monotonically from $c_R \approx 0.862 c_S$ for $\nu = 0$ to $c_R \approx 0.955 c_S$ for $\nu = 0.5$ as illustrated in Fig. 1–25.

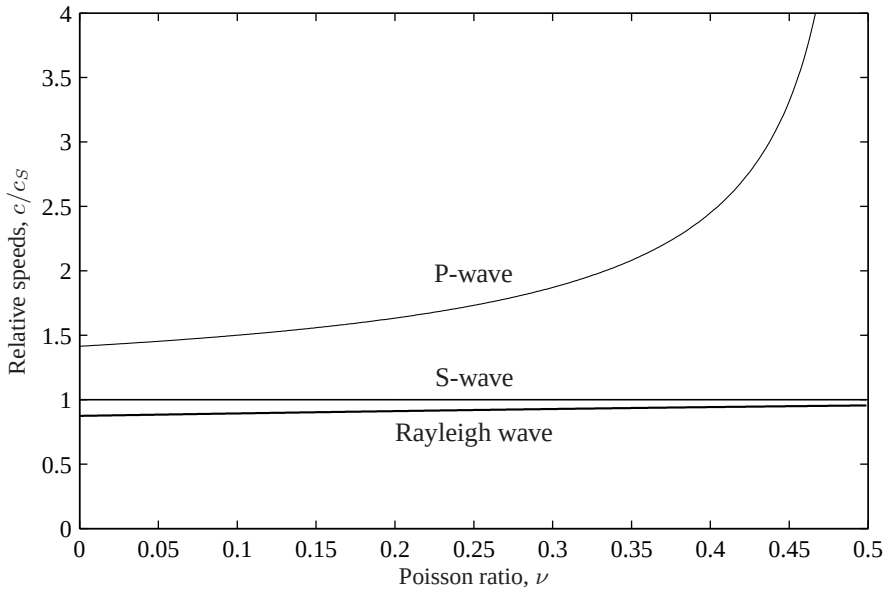

Figure 1–25 Relative speeds of P-, S- and Rayleigh waves as functions of the Poisson ratio.

Finally it is mentioned that a wave similar to the Rayleigh wave may exist at the interface between two adjacent homogeneous half-spaces. This so-called *Stonely wave* describes a displacement field with harmonic variation along the interface and exponential decay of the amplitudes away from the interface. Sometimes this wave is referred to as the *generalised Rayleigh wave*. The displacements must be continuous and the stresses must be in equilibrium across the interface. This leads to a frequency relation for the Stonely wave that is much more complicated than Eq. (1–82) for the Rayleigh wave. A full derivation of the Stonely wave field is beyond the scope of this text. However, it should be noted that the existence of the Stonely wave depends on relative shear strengths and the densities of the two media in contact. Thus, only for a certain interval of the ratios $\mu/\breve{\mu}$ and $\rho/\breve{\rho}$ does the Stonely wave exist.

1.5 Wave propagation in poroelastic materials

In the first sections of this chapter, soil has been treated as a viscoelastic material, applying a linear elastic continuum model. This simplified approach may provide results of an acceptable quality for dry granular materials, which may adequately be described as a single-phase system, *i.e.* wave propagation only takes place as shear and dilation in the grain skeleton. However, in saturated porous materials (*e.g.* soil, rock or concrete below the phreatic level) the pore pressure in the fluid phase interacts with the stresses carried by the solid phase, *i.e.* the effective stresses. This results in a second P-wave in addition to the P-wave that is identified in a single-phase

elastic material. The influence and importance of the second P-wave are highly dependent on the frequency of excitation and the permeability of the bulk material constituted by the grain skeleton and the pore fluid. Thus, the material may be fully drained at low frequencies and undrained at high frequencies, whereas it is partially (un)drained in the middle frequency range.

In the following, the continuum model for a fully saturated porous material is presented. The theory is mainly due to M.A. Biot, who developed the theory for wave propagation in saturated porous materials in a series of papers (Biot 1941; Biot 1955; Biot 1956a; Biot 1956c). This theory has later been generalised to multi-phase systems by Carcione *et al.* (2004). The theory is applicable to wave propagation at frequencies where the the wavelengths are much longer than the characteristic length of the voids and grains in the soil skeleton. For (much) smaller wavelengths, such phenomena as resonance of the pore pressure waves inside a single void have to be considered. A theory for wave propagation in the high-frequency range was formulated by Biot (1956b). However, as pointed out by Biot himself, the high-frequency range formulation is almost solely of academic interest.

Thus, in this section we shall only consider a two-phase system consisting of a solid skeleton and a single pore fluid, *e.g.* water, and only the low to medium-frequency range will be considered. Further, the theory is restricted to small deformations, *i.e.* a linear model for a poroelastic medium is described. It is demonstrated that the second P-wave in a fully saturated porous medium propagates at a speed which is much lower than the usual P- and S-wave speeds. Hence, it is often referred to as the *slow P-wave*. Furthermore, the limitations of the single-phase model described in the previous sections will be outlined, and guidelines are given for situations in which the simple viscoelastic model may be applied.

1.5.1 Basic definitions in poroelasticity

A porous material, or matrix, with the total volume V is considered. The material is fully saturated and the pores are assumed to be distributed randomly in space so that the material on a macroscopic level may be described as a continuum. The volume is divided into two parts,

$$V = V_s + V_f, \tag{1–89}$$

where V_s is the volume of the solid phase, *i.e.* the grain skeleton, and V_f is the volume of fluid. In geotechnical engineering, the subscript f is generally substituted by the subscript w, since the pore fluid is usually water. In any case, it is noted that only the volume of interconnected pores is included in the definition of V_f. In saturated porous materials, *e.g.* soil, a part of the pore fluid is constrained. For example, a part of the water in clay is chemically bound to the clay mineral, and in rock or granular soil, some of the water may be trapped in cracks that are not connected to the primary system of pores. This part of the fluid belongs to the solid phase, *i.e.* to V_s, since it cannot move relatively to the solid matrix. Unfortunately, in real soil or concrete etc. it may be difficult to determine which part of the pore fluid that is free to move relatively to the solid skeleton.

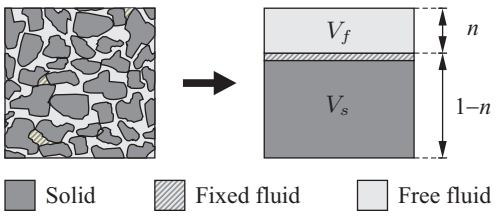

Figure 1–26: Definition of the porosity, n, in a saturated porous material. The volume of the free fluid in the interconnected pores is $V_f = nV$, and the volume of the solid (including fixed fluid) is $V_s = (1 - n)V$.

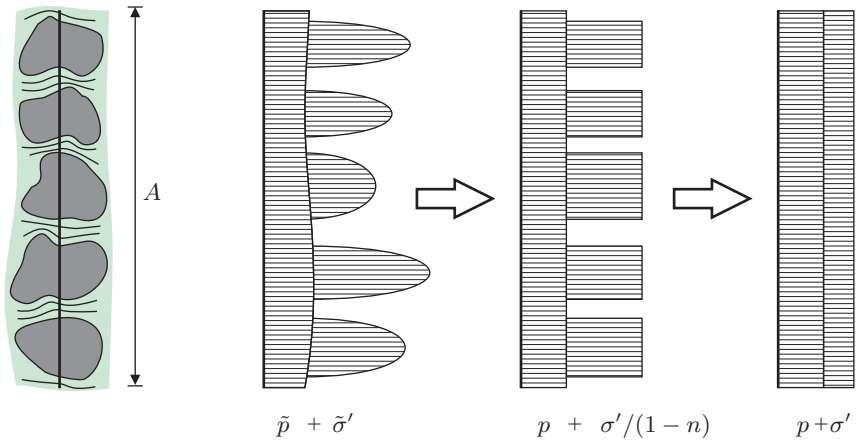

Figure 1–27 Stresses acting on a cross section in a poroelastic medium.

The *porosity* of the porous material, or matrix, is defined as

$$n = V_f/V, \tag{1–90}$$

i.e. as the volume fraction taken up by interconnected pores. Occasionally, in the international literature on porous materials, the porosity is denoted f, ϕ or β, but in the Danish geotechnical literature the symbol n is usually applied. Given that the soil is fully saturated, the mass density of the matrix material constituted by the solid and the fluid becomes

$$\rho = (1-n)\rho_s + n\rho_f, \tag{1–91}$$

where ρ_s is the mass density of the solid phase and ρ_f is the mass density of the fluid phase. In standard geotechnical engineering ρ_s is most often the average density of the minerals constituting the grains in the soil. This is not the case in the present formulation, since any fluid that is not allowed to move freely between the grains is considered part of the solid phase as illustrated in Fig. 1–26. In other words, n is the volume fraction of interconnected pores. With this definition, n is occasionally referred to as the *effective porosity*.

In the present theory, it is assumed that the pores are distributed randomly, so that the matrix material may be considered both homogeneous and isotropic on a macroscopic level. Hence, for any cross section with the total area A inside the material, the area $A_f = nA$ will be constituted by the free pore fluid (see Fig. 1–26), whereas the solid phase (including fixed pore water) constitutes the area $A_s = (1-n)A$.

Next, we define the pore pressure, $p = p(\mathbf{x}, t)$, as the pressure which is present inside the pore fluid in the interconnected voids. Whereas the mean total stress, $\sigma = \sigma_{kk}$, is defined as positive in tension, the pore pressure is positive in compression. This definition is common practice in geotechnical engineering. The total stresses σ_{ij} are now divided into two parts,

$$\sigma_{ij} = \sigma'_{ij} - p\delta_{ij}. \tag{1–92}$$

Here p is the pore pressure in the fluid constituent, and σ'_{ij} are referred to as the effective stresses. While the pore pressure is present in both the fluid and the solid phase, the effective stresses are

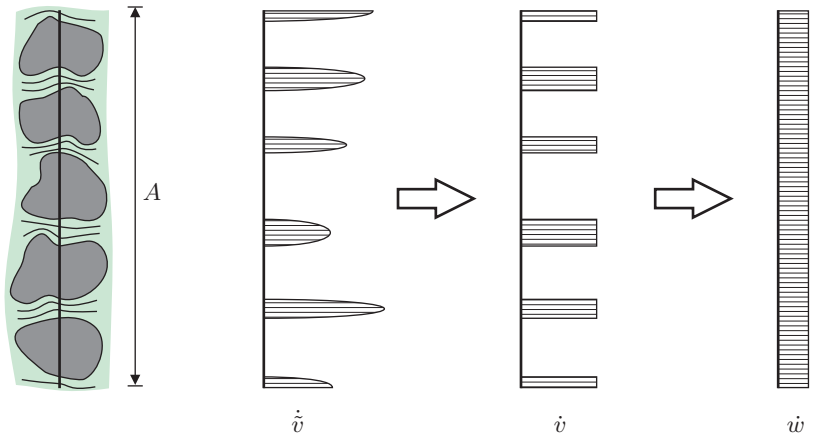

Figure 1–28 Flow velocity over a cross section in a poroelastic medium.

carried solely by the solid skeleton. Given that the solid phase only constitutes the fraction $1-n$ of the entire matrix, the total stress in the solid phase is actually $\sigma'_{ij}/(1-n) - p\delta_{ij}$, whereas the total stress in the pore fluid is $-p\delta_{ij}$. In Example 1.4 the definition of the effective stress is further discussed, in particular with respect to the formulation of constitutive laws.

The displacements of the grain skeleton and the fluid in the interconnected pores are denoted u_i and v_i, respectively. In addition to the full displacement of the pore fluid, a relative velocity is introduced in the form

$$\dot{w}_i = \frac{\partial w_i}{\partial t} = n\left(\frac{\partial v_i}{\partial t} - \frac{\partial u_i}{\partial t}\right), \qquad w_i = n\,(v_i - u_i)\,. \tag{1–93}$$

The quantity $\dot{w}_i = \dot{w}_i(\mathbf{x}, t)$ is referred to as the *seepage velocity*. Evidently, $\dot{w}_i$ is the average relative velocity of the fluid flow in the matrix including both the fluid and the solid phase. Thus, in the particular case $u_i = 0$ the definition $\dot{w}_i = q_i/A$ applies, where q_i is the fluid flow, or flux, through the cross-sectional area A in coordinate direction i, cf. Fig. 1–28.

1.5.2 Constitutive laws in poroelasticity

The effective stresses are provided by the constitutive law for the porous matrix, *i.e.* the grain skeleton. Assuming a linear isotropic material behaviour, the stress–strain relationship is similar to Eq. (1–5). However, it must be taken into consideration that a change in the pore pressure will lead to a change in the volume of the solid constituent, *i.e.* the grains or the porous solid, which does not involve a change in the effective stresses. Hence,

$$\sigma'_{ij} = \lambda\epsilon'_{kk}\delta_{ij} + 2\mu\epsilon'_{ij}, \qquad \text{where} \qquad \epsilon'_{ij} = \epsilon_{ij} - \frac{1}{3}\Delta_s^p\delta_{ij}, \quad \Delta_s^p = -\frac{p}{K_s}. \tag{1–94}$$

Here ϵ_{ij} are the components of the small strain tensor given by Eq. (1–3), and λ and μ are the Lamé constants of the matrix material. Note that these may be substantially different from the Lamé constants λ_s and μ_s of the solid material as further discussed below. Finally, Δ_s^p is the dilation in the solid phase due to the pore pressure (positive in expansion) and K_s is the bulk

Table 1–1 Compressibility of soil, rock and concrete.

	Bulk Modulus[a] (MPa)		
Material	K	K_s	$\beta = (1 - K/K_s)$
Quartzitic Sandstone	17,000	37,000	0.54
Quincy Granite (30 m deep)	13,000	52,000	0.75
Vermont Marble	5,600	71,000	0.92
Concrete (approximately)	5,000	40,000	0.88
Dense Sand	56	36,000	0.9985
Loose Sand	11	36,000	0.9997
London Clay (over consolidated)	13	50,000	0.99975
Gosport Clay (normally consolidated)	1.7	50,000	0.99997

[a] Bulk moduli at $p = 98$ kPa (atmospheric pressure); water: $K_f = 2040$ MPa.

modulus of the solid constituent. The following relationship applies between K_s and the Lamé constants λ_s and μ_s of the solid constituent, *e.g.* the grains or the rock material:

$$K_s = \lambda_s + \frac{2}{3}\mu_s. \tag{1–95}$$

In granular materials such as residual soils, λ_s and μ_s are typically much greater than λ and μ, *e.g.* the Lamé constants of sand are much smaller than those of quarts crystal. Hence, the reduction in the volume of the solid phase resulting from an increase of the pore pressure is generally negligible. In this situation Δ_s^p may be disregarded and the approximation $\epsilon'_{ij} \approx \epsilon_{ij}$ applies. On the other hand, in concrete, intact rock and similar cemented materials the bulk modulus of the solid constituent, K_s, and that of the matrix material, K, are typically of the same order of magnitude, cf. Table 1–1 (Skempton 1960). Therefore, in these materials Δ_s^p becomes significant, and the full definition provided by Eq. (1–94) applies. Finally, it is noted that in the general nonlinear case, an additional contribution to the total strains ϵ_{ij}, but not to ϵ'_{ij}, stems from creep and thermoelastic behaviour. However, this nonreversible term is disregarded in the present theory.

For the pore pressure, a constitutive equation equivalent to Eq. (1–94) is achieved by consideration of the volumetric strain of the matrix, *i.e.* the dilatation. Making use of Eqs. (1–3) and (1–93), the total dilatation may be expressed as

$$\Delta = (1-n)\Delta_s + n\Delta_f = \frac{\partial u_k}{\partial x_k} + \frac{\partial w_k}{\partial x_k}, \qquad \text{where} \qquad \Delta_s = \frac{\partial u_k}{\partial x_k}, \quad \Delta_f = \frac{\partial v_k}{\partial x_k}. \tag{1–96}$$

Defining K_f as the bulk modulus of the fluid, the following constitutive laws are obtained with regard to the volumetric strains of the solid and the fluid phase, respectively:

$$\Delta_s = \frac{1}{1-n}\frac{\sigma'}{K_s} - \frac{p}{K_s} = \Delta'_s + \Delta_s^p, \qquad \text{where} \qquad \sigma' = \frac{\sigma'_{kk}}{3}, \quad \Delta_f = -\frac{p}{K_f}. \tag{1–97}$$

Here σ' is the mean effective stress, and $\sigma'/(1-n) - p$ is identified as the actual mean stress in the solid phase, given that the effective stresses are carried by the solid skeleton alone.

Insertion of Eq. (1–97) into Eq. (1–96) provides a relation which defines the pore pressure in terms of the matrix displacements u_i and the seepage displacements w_i,

$$\Delta = \frac{\partial u_k}{\partial x_k} + \frac{\partial w_k}{\partial x_k} = \frac{\sigma'}{K_s} - (1-n)\frac{p}{K_s} - n\frac{p}{K_f} \approx -n\frac{p}{K_f}. \tag{1–98}$$

Note that only the volume strain, *i.e.* the dilation, occurs in Eq. (1–98), that is the constitutive law for the pore fluid is independent of any shear deformations in the solid constituent or the fluid. On the right-hand side of Eq. (1–98) it has been assumed that the volumetric strain in the solid phase is much smaller than the dilatation in the pore fluid. This approximation is valid for most granular materials such as soil, given that $nK_s \gg (1-n)K_f$. This is the case for sand, where n is typically around 0.2 to 0.3 and $K_s \approx 20K_f$ ($K_f \approx 2$ GPa for water). However, for rock-like materials n may be close to zero, and in this case the contributions to the total dilatation from the solid phase and the fluid phase may be of the same order of magnitude, or the main contribution may come from the solid phase.

Example 1.4 Alternative definition of effective stress—Biot theory

The total stresses, σ_{ij}, may be divided into the pore pressure, p and the so-called effective stresses, σ'_{ij}. According to Eq. (1–92)

$$\sigma'_{ij} = \sigma_{ij} + p\delta_{ij}. \qquad \text{(Terzaghi effective stresses)} \tag{a}$$

This definition of the effective stress was proposed by K. Terzaghi, and the components σ'_{ij} are occasionally referred to as the *Terzaghi effective stresses*. It is noted that p is positive in compression, whereas the stresses are defined as positive in tension.

With the definition given by Eq. (a), the constitutive law for the effective stresses is given in terms of "effective strains" according to the relation

$$\sigma'_{ij} = \lambda\epsilon'_{kk}\delta_{ij} + 2\mu\epsilon'_{ij}, \qquad \text{where} \qquad \epsilon'_{ij} = \epsilon_{ij} - \frac{1}{3}\Delta_s^p\delta_{ij}, \quad \Delta_s^p = -\frac{p}{K_s}. \tag{1–94}$$

Equation (1–94) implies that the volumetric strain of the solid skeleton due to a change in the pore pressure will not provide any change in the effective stresses.

Alternatively, one may define the effective stress as

$$\sigma''_{ij} = \lambda\epsilon_{kk}\delta_{ij} + 2\mu\epsilon_{ij}, \tag{b}$$

i.e. in terms of the *total* strains. However, Eq. (b) implies that in the general case $\sigma''_{ij} \neq \sigma_{ij} + p\delta_{ij}$, that is Terzaghi's definition of effective stresses does not hold when the constitutive equation is defined in terms of effective stresses and total strains. In order to prove this, the mean effective stress σ' is computed from Eq. (1–94). Making use of the fact that $\delta_{kk} = 3$, the following result is obtained:

$$\sigma' = \frac{1}{3}\sigma'_{kk} = \frac{1}{3}\lambda\epsilon'_{ii}\delta_{kk} + \frac{2}{3}\mu\epsilon'_{kk} = K\epsilon'_{kk} = K\left(\epsilon_{kk} + \frac{p}{K_s}\right). \tag{c}$$

Here K and K_s are the bulk moduli of the matrix material and the solid constituent, respectively,

$$K = \lambda + \frac{2}{3}\mu, \qquad K_s = \lambda_s + \frac{2}{3}\mu_s. \tag{d}$$

(continued)

Similarly to Eq. (c), the mean effective stress σ'' is found as

$$\sigma'' = \frac{1}{3}\sigma''_{kk} = \frac{1}{3}\lambda\epsilon_{ii}\delta_{kk} + \frac{2}{3}\mu\epsilon_{kk} = K\epsilon_{kk}. \tag{e}$$

Comparison of Eqs. (c) and (e) provides the result that $\sigma'' = \sigma' - (K/K_s)p$, suggesting that

$$\sigma''_{ij} = \sigma'_{ij} - \delta_{ij}\frac{K}{K_s}p. \tag{f}$$

Therefore, as an alternative to the Terzaghi effective stresses given by Eq. (f), one may apply the definition

$$\sigma''_{ij} = \sigma_{ij} + \beta p\delta_{ij}, \qquad \beta = 1 - K/K_s. \qquad \text{(Biot effective stresses)} \tag{g}$$

This formulation was originally proposed by Biot. A comparison of Eqs. (1–94) and (b) suggests that the *Biot effective stresses* lead to much simpler constitutive models than the Terzaghi effective stresses which must be defined in terms of "effective" strains.

It is worthwhile to note that for both granular soil and clay saturated with water, the bulk modulus of the minerals constituting the solid part of the material is much greater than the bulk modulus of the matrix, *i.e.* $K_s \gg K$. In particular, for normally or under consolidated clayey soil with large water contents $\beta \approx 1$, see Table 1–1. Hence, the Biot and the Terzaghi effective stresses are equivalent.

Finally, in saturated porous rock and concrete, K and K_s are of the same order of magnitude, and values of β as low as 0.5 may be expected. This fact is often neglected in geotechnical engineering practice. Here Eqs. (a) and (b) are usually applied with the erroneous assumption that $\sigma''_{ij} = \sigma'_{ij}$. It is noted that the Terzaghi effective normal stresses provided by Eq. (a) are smaller than, or equal to, the Biot effective normal stresses given by Eq. (g). The difference may be significant in the case of rock. □

1.5.3 Quasi-static flow in porous materials—Darcy's law

As the pore fluid flows through the interconnected voids of the solid skeleton, the two constituents interact. In the case of quasi-static flow, the equilibrium of forces for the fluid phase is provided by the equation

$$-\frac{\partial w_i}{\partial t} = k_{ij}\left(\frac{\partial p}{\partial x_j} + \rho_f b_j\right), \tag{1–99}$$

where $b_i = b_i(\mathbf{x}, t)$ are the specific body forces, and $k_{ij} = k_{ij}(\mathbf{x})$ are the components of a second order tensor with the SI units ($\mathrm{m}^3{\cdot}\mathrm{s}{\cdot}\mathrm{kg}^{-1}$) representing the permeability of the material. In the general case k_{ij} is fully populated and asymmetric. However, in orthotropic materials only the diagonal terms have none-zero values. Typically, in stratified soil $k_{11} = k_{22} \neq k_{33}$, *i.e.* the vertical permeability is different from the horizontal permeability. In the particularly simple case of isotropic porous materials $k_{ij} = \delta_{ij}k$, *i.e.* the permeability is defined by a single parameter, k.

Equation (1–99) is identified as the generalised Darcy's law for fluid flow in a porous medium. It is observed that a gradient in the pore pressure, p, which is not counterbalanced by external forces, b_i, will lead to seepage with the velocity w_i. The speed of the fluid flow increases with the permeability of the matrix. Further, in anisotropic materials the flow may not necessarily be in the opposite direction of the gradient. This is evidently the case for isotropic and orthotropic materials, since k_{ij} only contains diagonal terms.

Table 1–2 Permeability of various soil and rock materials.

Relative Permeability	Pervious				Semi-Pervious			Impervious					
Unconsolidated Sand & Gravel	Well Sorted Gravel		Well Sorted Sand or Sand & Gravel		Very Fine Sand, Silt Loess, Loam								
Unconsolidated Clay & Organic					Peat		Layered Clay			Fat / Unweathered Clay			
Consolidated Rocks	Highly Fractured Rock				Oil Reservoir Rocks			Fresh Sandstone		Fresh Limestone, Dolomite		Fresh Granite	
κ (cm^2)	10^{-3}	10^{-4}	10^{-5}	10^{-6}	10^{-7}	10^{-8}	10^{-9}	10^{-10}	10^{-11}	10^{-12}	10^{-13}	10^{-14}	10^{-15}
κ (milli-darcies)	10^8	10^7	10^6	10^5	10^4	10^3	100	10	1	0.1	0.01	10^{-3}	10^{-4}

In contrast to the *hydraulic conductivity*, $\chi = g\rho_f k$, with SI units (m·s^{-1}), the parameter k is independent of the fluid density and the gravitational acceleration, g. However, the components of k_{ij} still depend on the dynamic viscosity of the pore fluid, μ_f, with the SI units (kg·m^{-1}·s^{-1}). An alternative measure of the permeability that only depends on the geometry of the soil skeleton may be defined as

$$\kappa = \mu_f k. \tag{1–100}$$

This parameter is coined the *permeability coefficient* and has the SI units (m^2), but it is usually measured in *darcy* (d), or more commonly *milli-darcy* (md) (1 darcy $\sim 10^{-12}$ m^2). Typical values for soil and rock are listed in Table 1–2 which is taken from (**?**).

In the following we shall restrict ourselves to the case of isotropic materials, *i.e.* $k_{ij} = \delta_{ij} k$. Furthermore, disregarding body forces, Eq. (1–99) simplifies to

$$\frac{\partial p}{\partial x_i} + \frac{1}{k}\frac{\partial w_i}{\partial t} = 0. \tag{1–101}$$

1.5.4 Governing equations in poroelasticity

When rapid motion is considered, additional terms arise in Eq. (1–101), which account for the forces of inertia. Thus, in coordinate direction i the balance of forces acting on the fluid part of a unit volume in a fully saturated porous medium, *i.e.* a fluid mass with the volume n, becomes:

$$-n\frac{\partial p}{\partial x_i} - \phi\frac{\partial w_i}{\partial t} = n\rho_f \frac{\partial^2 v_i}{\partial t^2} - n\rho_a \left(\frac{\partial^2 v_i}{\partial t^2} - \frac{\partial^2 u_i}{\partial t^2} \right). \tag{1–102}$$

In the quasi-static case, $\phi = n/k$. However, in wave propagation problems it has been found that the permeability of soil depends on the frequency of excitation, *i.e.* $\phi = \phi(\omega)$. This is similar to the coefficient of drag forces on immersed bodies being dependent on Reynold's number, *i.e.* the flow velocity. The second term on the right-hand side of Eq. (1–102) accounts for added mass from the solid skeleton. This term is further addressed below. By use of Eq. (1–93), the balance of momentum in the pore fluid may conveniently be rewritten into the form

$$-n\frac{\partial p}{\partial x_i} - \phi\frac{\partial w_i}{\partial t} = n\rho_f \frac{\partial^2 u_i}{\partial t^2} + (\rho_f - \rho_a)\frac{\partial^2 w_i}{\partial t^2}. \qquad \text{(fluid momentum)} \tag{1–103}$$

In the case of problems involving large displacements, a term of the form $(\partial \dot{w}_i/\partial x_j)\dot{w}_j$ should be included on the right-hand side of Eq. (1–103) to account for the exchange of momentum due to convection. However, the present formulation in terms of linear wave theory is restricted to small displacements. Hence, this term is disregarded.

Next, for the solid phase constituting the specific volume $(1-n)$, the balance of forces acting per unit volume achieves the form:

$$\frac{\partial \sigma'_{ij}}{\partial x_j} - (1-n)\frac{\partial p}{\partial x_i} + \phi \frac{\partial w_i}{\partial t} = (1-n)\rho_s \frac{\partial^2 u_i}{\partial t^2} + \rho_a \frac{\partial^2 w_i}{\partial t^2}. \qquad \text{(solid momentum)} \qquad (1\text{–}104)$$

Here it is noted that the actual stresses in the solid phase (not distribute over the entire matrix) are $\sigma'_{ij}/(1-n) - p\delta_{ij}$, since the effective stresses are carried solely by the solid skeleton. In accordance with Newton's third law, the viscous forces stemming from seepage and the inertia forces due to added mass enter this equation with the opposite sign compared with Eq. (1–103). With the present sign convention, a positive value of the quantities ϕ and ρ_a lead to viscous damping and positive added mass with regard to the motion of the solid skeleton. However, Berryman (1980) suggested that $\rho_a = \rho_f(1-a)$ with $a = (1+1/n)/2$, which provides a negative value of ρ_a. Further, with this definition the same value of ρ_a is obtained for all soils with a given effective porosity, n—independently of the shape of the interconnected voids.

For the total matrix, including both the solid phase and the pore fluid, the balance of momentum on a unit volume is obtained by addition of Eqs. (1–103) and (1–104),

$$\frac{\partial \sigma_{ij}}{\partial x_j} = \rho \frac{\partial^2 u_i}{\partial t^2} + \rho_f \frac{\partial^2 w_i}{\partial t^2}, \qquad \text{(total momentum)} \qquad (1\text{–}105)$$

where

$$\rho = (1-n)\rho_s + n\rho_f, \qquad \sigma_{ij} = \sigma'_{ij} - p\delta_{ij} = \sigma''_{ij} - \beta p \delta_{ij}, \qquad \beta = 1 - K/K_s, \qquad (1\text{–}106)$$

with K and K_s defining the bulk moduli of the matrix and the solid constituent, respectively, cf. Table 1–1. It is observed that the viscous forces due to seepage and the inertia forces stemming from the added mass vanish in the total balance of momentum. These forces act as internal forces between the two phases, *i.e.* the solid and the fluid phase.

The total stresses on the left-hand side of Eq. (1–105) act on the entire matrix, but according to Eq. (1–106) it may be split into the Terzaghi or Biot effective stresses, *i.e.* σ'_{ij} or σ''_{ij}, and the pore pressure, p. As suggested by Example 1.4, a formulation in terms of the Biot effective stresses may be preferred, since this provides a constitutive law in terms of the total strains. In the particular case of isotropic elastic materials,

$$\sigma''_{ij} = \lambda \epsilon_{kk}\delta_{ij} + 2\mu\epsilon_{ij}, \qquad (1\text{–}107)$$

which is much simpler to apply than Eq. (1–94).

Together with Eq. (1–98), the balance equantions (1–103) and (1–104) (or alternatively Eq. (1–105)) form a system of seven coupled equations of motion for the fully saturated porous material. The seven unknown quantities are: the total displacements of the solid, $u_i(\mathbf{x},t)$, $i = 1,2,3$, the seepage velocity, $\dot{w}_i(\mathbf{x},t)$, $i = 1,2,3$, and the pore pressure, $p(\mathbf{x},t)$. However, in certain situations, *e.g.* drained or undrained conditions, the system of equations is simplified and the number of unknowns is reduced. This is demonstrated in the example below.

Example 1.5 Wave propagation in perfectly drained or undrained soil

Drained soil

In a perfectly drained material, the average velocity of the pore fluid is equal to zero. The pore fluid simply moves around the grains, but there is no net flow of fluid through the matrix. Thus, the average total displacement of the fluid is $v_i = 0$, *i.e.*

$$w_i = -nu_i \qquad \Rightarrow \qquad \frac{\partial w_i}{\partial t} = -n\frac{\partial u_i}{\partial t} \qquad \Rightarrow \qquad \frac{\partial^2 w_i}{\partial t^2} = -n\frac{\partial^2 u_i}{\partial t^2}. \tag{a}$$

Furthermore, the coefficient of permeability, and thus k, is assumed to approach infinity. In this case, the equation of motion for the fluid phase, *i.e.* Eq. (1–103), reduces to

$$\frac{\partial p}{\partial x_i} = \frac{n}{k}\frac{\partial u_i}{\partial t} - \rho_f \left(\frac{\partial^2 u_i}{\partial t^2} - \frac{n}{n}\frac{\partial^2 u_i}{\partial t^2} \right) = \frac{n}{k}\frac{\partial u_i}{\partial t} \to 0 \quad \text{for} \quad k \to \infty. \tag{b}$$

This result was to be expected. Since both viscous and inertia forces are disregarded, the pore fluid cannot sustain a gradient in the pore pressure, *i.e.* the pore water is immediately drained away.

Making use of the result given by Eq. (b), and further making use of Eq. (1–91), the equation of motion for the total matrix (1–105) reduces to

$$\frac{\partial \sigma''_{ij}}{\partial x_j} = \rho_d \frac{\partial^2 u_i}{\partial t^2}, \qquad \rho_d = (1-n)\rho_s. \tag{c}$$

Thus, in perfectly drained porous materials, the internal forces provided by the effective stresses are counterbalanced by the inertia of the solid skeleton. In geotechnical engineering ρ_d is usually referred to as the *drained mass density*.

Undrained soil

Next, in all situations involving rapid transient or cyclic loading, *i.e.* including wave propagation problems, clay acts as an undrained material. In this case the fluid constituent cannot move relatively to the solid skeleton, which implies that

$$w_i = 0 \qquad \Rightarrow \qquad \frac{\partial w_i}{\partial t} = \frac{\partial^2 w_i}{\partial t^2} = 0. \tag{d}$$

Insertion of this result into Eq. (1–103) provides the pore pressure gradient

$$-\frac{\partial p}{\partial x_i} = \rho_f \frac{\partial^2 u_i}{\partial t^2}. \tag{e}$$

The equation of motion for the total matrix follows by insertion of Eqs. (d) and (e) into Eq. (1–105),

$$\frac{\partial \sigma_{ij}}{\partial x_j} = \rho \frac{\partial^2 u_i}{\partial t^2} \qquad \Leftrightarrow \qquad \frac{\partial \sigma'_{ij}}{\partial x_j} = \rho' \frac{\partial^2 u_i}{\partial t^2}, \qquad \rho' = \rho - \rho_f. \tag{f}$$

In geotechnical engineering ρ' is referred to as the *reduced*, or *effective*, mass density of the soil. As indicated by Eq. (f), the dynamic equilibrium for a fully saturated and perfectly undrained porous material may be expressed in terms of either full or effective stresses. In the first case, a constitutive law providing the relationship between σ_{ij} and ϵ_{ij} must be applied, whereas in the second case Eq. (1–94) applies to an isotropic elastic solid material. Typically, for undrained clay the governing equation is expressed in terms of total stresses and densities. □

1.6 Dispersion and dissipation of elastic waves

In order to fully describe elastic wave propagation, the terms *dispersion* and *dissipation* need to be defined. A lookup in the dictionary may lead to the conclusion that the words are synonymous, both meaning "spreading". However, in the context of wave propagation dispersion and dissipation describe two very different characteristics of the displacement field.

Dispersion — *Waves propagate with different phase speeds for different wavenumbers, i.e.* for different frequencies. Therefore, a short broad banded pulse emanating from a source point will not arrive as a short pulse at an observation far away. Instead the pulse will be spread over time since the waves with different frequencies travel with different speeds.

Dissipation — *Waves are attenuated, i.e.* damped, over time and/or space. This may be due to a combination of *geometrical dissipation* (spreading of the energy over a larger volume) and *material dissipation* (local damping due to a conversion from mechanical energy into heat).

In the subsections below, the phenomena of dispersion and geometrical/material dissipation are discussed in detail.

1.6.1 Dispersion

If the phase speed of wave depends on the wavenumber, the wave is defined as *dispersive*. On the other hand, if the phase speed is not dependent of the wavenumber, the wave is *non-dispersive*.

Equations (1–14) and (1–17) state that the phase speeds c_P and c_S are functions of the material properties λ, μ and ρ, *i.e.* the stiffness and the mass density of the material. These quantities are not frequency dependent, and hence it is concluded that P- and S-waves in an elastic continuum are non-dispersive.

From the Rayleigh equation (1–86) it is observed that c_R is independent of the wavenumber, both explicitly and implicitly as neither of c_P and c_S are wavenumber dependent. Therefore it is concluded that the Rayleigh wave is non-dispersive. In a similar manner it may be shown that also the Stonely wave at an interface between two elastic half-spaces is non-dispersive.

Whereas the volume and the surface waves in a homogeneous elastic material are all non-dispersive, this is generally not the case for waves propagating in a stratum, *i.e.* a layered medium. For example it has been observed that only vibrations with a frequency above a certain frequency, ω_c, give rise to wave propagation in a soft soil layer over bedrock. Different authors refer to this frequency is either the *cut-on frequency* or the *cut-off frequency*. It is noted that whereas wavefronts propagate with the previously defined *phase speed*

$$c(k) = \frac{\omega}{k}, \tag{1–108}$$

the energy propagates with the so-called *group velocity*,

$$c_g(k) = \frac{\partial \omega}{\partial k}. \tag{1–109}$$

The name "group velocity" originates from studies of surface waves on water. Here it has been observed that waves form groups travelling along the surface. Each individual wave travels with a speed, $c(k)$, which is faster than the speed of the group, c_g. Hence, apparently the waves rise at

the tail of the group and diminish at the head of the group. Similar observations can be made for waves travelling along a wave guide in elastic media, *e.g.* the Love wave. The fact that the energy travels at the group velocity will not be proved here. A detailed derivation of the group velocity, or the speed of energy propagation, may be found, for example, in the book by Achenbach (1973) for different wave types including SH-waves trapped in a surface layer. As a result of the fact that waves with different wavenumbers propagate with different speeds, the shape of a pulse will change as the pulse propagates through a medium. This has been illustrated in Fig. 1–29.

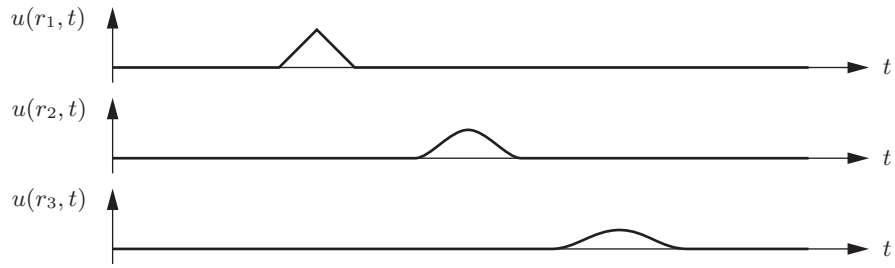

Figure 1–29 Pulse propagating along a bar—change of the shape due to dispersion. Displacement time series at three distances from a source, $r_1 < r_2 < r_3$.

The number and nature of waves propagating in a medium, or in a structure, may advantageously be illustrated in a *dispersion diagram* or a *slowness diagram*.

The dispersion diagram — The quantities k and ω are plotted along the axes of the diagram, typically with ω along the abscissa. P-, S- and Rayleigh waves are non-dispersive and therefore they form straight lines in the dispersion diagram with a slope equal to c_P^{-1}, c_S^{-1} and c_R^{-1}, respectively. On the other hand, dispersive waves form curved lines as illustrated in Fig. 1–30a. At any point the slope of the tangent is equal to the group velocity c_g.

The slowness diagram — Here the quantities plotted along the axes are the frequency ω and the *slowness* $s = c^{-1} = k/\omega$. Hence a curve in a slowness diagram depicts the slope of a curve in the corresponding dispersion diagram. A non-dispersive wave results in a straight line with slopes equal to zero, since the phase velocity c is constant, *i.e.* independent of the wavenumber. The slowness diagram is sketched in Fig. 1–30b.

It is noted that for non-dispersive waves $c_g = c$, so that the energy propagates at the same speed as the wavefronts. However, for dispersive waves the group velocity and the phase velocity are generally different. In Fig. 1–30 the dashed curve represents a dispersive wave which is only present in the system for frequencies beyond ω_c. The group velocity of this wave goes to zero in the limit as $\omega \to \omega_c$. The group and phase velocities become identical in the high frequency limit. Here they asymptotically approach a value between c_R and c_S. In Chapter 5 we shall return to the dispersion diagram and its use for the description of waves in a stratum.

1.6.2 Geometrical dissipation of waves

When a wave propagates through an elastic medium it may be attenuated due to spreading of the mechanical energy over a larger volume. This mechanism is known as *geometrical dissipation* or *geometrical damping*. It is noted that the geometrical damping of the mechanical energy is

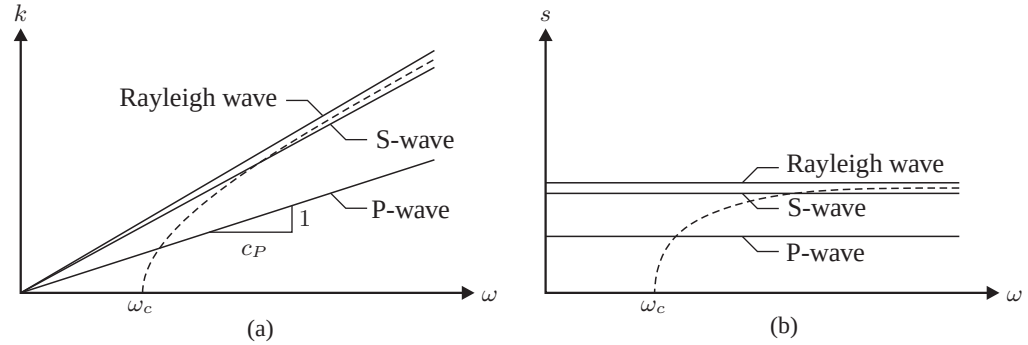

Figure 1–30 Different ways of illustrating dispersion of waves: (a) *dispersion diagram* and (b) *slowness diagram*. The dashed lines represent a dispersive wave.

proportional to the square of the damping of the displacement amplitudes. This is due to the fact the the mechanical energy $\mathcal{H}$ is defined as

$$\mathcal{H} = \mathcal{U} + \mathcal{K}, \tag{1–110}$$

where $\mathcal{U}$ is the potential energy, *i.e.* the strain energy, and $\mathcal{K}$ is the kinetic energy,

$$\mathcal{U} = \frac{1}{2}\sigma_{ij}\epsilon_{ij} = \frac{1}{2}E_{ijkl}\epsilon_{kl}\epsilon_{ij}, \qquad \mathcal{K} = \frac{1}{2}\rho\frac{\partial u_j}{\partial t}\frac{\partial u_j}{\partial t}. \tag{1–111}$$

For a given shape of the displacement field, *e.g.* a plane P-wave field, both the strain and the particle velocity are proportional to the displacement.

The degree of geometrical damping depends on the "geometry of the wavefronts". Thus the essential property of the waves is whether they spread in one, two or three dimensions. The following possibilities exist:

***"Three-dimensional waves"* —** P- and S-waves emanating from a point source spread in three dimensions. They form spherical wavefronts with the surface area $4\pi r^2$, where r is the distance from the source to the observer. Since the same energy must be present in the wavefront, independently of the distance from the source, the energy per unit volume spreads as $1/r^2$, and the displacement amplitudes decrease as $1/r$ with the distance.

***"Two-dimensional waves"* —** P- and S-waves emanating from a line source spread as cylindrical wavefronts with the surface area $2\pi r$ per unit length of the source. Hence, in plane strain the P- and S-wave energy at a given distance r from the line source is proportional to $1/r$, and the amplitude of the displacement amplitudes are proportional to $\sqrt{1/r}$. The same degree of geometrical dissipation applies to the Rayleigh wave generated by a point source on the surface of a half-space. Here the energy is contaminated in the vicinity of the surface, thus forming circular wavefronts with the circumference $2\pi r$. In the same way it may be reasoned that the displacement amplitudes in layer waves generated by point sources decay as $\sqrt{1/r}$ due to geometrical damping.

***"One-dimensional waves"* —** Plane P- or S-waves propagate as one-dimensional waves in a well-defined direction. The purely elastic waves are defined so that the amplitudes do not

change as the waves propagate through the medium. Therefore they are not subject to geometrical damping. This also applies to the plane Rayleigh wave, *i.e.* the Rayleigh wave emanating from a line load. This is due to the fact that the mechanical energy in the Rayleigh wave is bound to the surface, and in the case of plane strain, no spreading is possible in the out-of-the-plane direction. Similarly, layer waves in plane strain, or waves travelling along a one-dimensional wave guide, are not damped geometrically.

The degree of geometrical damping of the various wave types is critical in the design of numerical models which may be used for the analysis of, for example, dynamic soil–structure interaction. This will be further discussed in the next chapter.

Example 1.6 Geometrical damping of P- and S-waves from a harmonic point source

As an example of geometrical damping, let us consider the spreading of P- and S-waves from a unit amplitude harmonic point source. The load is applied at the *source point* $\mathbf{y}$ and acting in coordinate direction l, and we seek the response at the receiver or *observation point* $\mathbf{x}$ in direction i. According to the discussion above, we expect a displacement amplitude decay proportional to $1/r$, where $r = |\mathbf{x} - \mathbf{y}|$ is the distance between the observation point and the source point.

A description of the point force in terms of a distributed load that may be integrated over space is achieved by utilization of the three-dimensional Dirac delta function $\delta(\mathbf{x})$,

$$\delta(\mathbf{x}) = \delta(x_1)\,\delta(x_2)\,\delta(x_3), \qquad \int_{-\infty}^{\infty} \delta(x-y) f(y) \mathrm{d}y = f(x), \tag{a}$$

where $\delta(x)$ is the Dirac delta function in one dimension. In the time domain, the harmonic point source may now be described as $\rho b_i(\mathbf{x},t) = \rho B^*_{il}(\mathbf{x},\omega;\mathbf{y})\,\mathrm{e}^{\mathrm{i}\omega t}$, where the amplitude is given as $\rho B^*_{il}(\mathbf{x},\omega;\mathbf{y}) = \delta(\mathbf{x}-\mathbf{y})\delta_{il}$.

In the steady state, the influence of initial conditions vanishes, and hence the displacement field varies harmonically with time as $u_i(\mathbf{x},t) = U^*_{il}(\mathbf{x},\omega;\mathbf{y})\,\mathrm{e}^{\mathrm{i}\omega t}$. Inserting the displacement field and the body forces corresponding to the harmonic point source into the Navier equations (1–10), and skipping the exponential term $\mathrm{e}^{\mathrm{i}\omega t}$, we arrive at the partial differential equations

$$(\lambda+\mu)\,\frac{\partial^2}{\partial x_i \partial x_j} U^*_{jl}(\mathbf{x},\omega;\mathbf{y}) + \mu \frac{\partial^2}{\partial x_j \partial x_j} U^*_{il}(\mathbf{x},\omega;\mathbf{y}) + \delta(\mathbf{x}-\mathbf{y})\delta_{il} = -\rho\omega^2 U^*_{il}(\mathbf{x},\omega;\mathbf{y}). \tag{b}$$

The subscript l indicates that there is not one, but *three* times three equations of motion, *i.e.* three for each $l = 1, 2, 3$. We bear in mind that the subscript l indicates the coordinate direction of the harmonic point force. The amplitude function $U^*_{il}(\mathbf{x},\omega;\mathbf{y})$ is denoted the frequency-domain *Green's function* or *fundamental solution* for the elastic full-space. It may be regarded as a generalised dynamic influence function since the response to any other excitation may be found be linear superposition of a number of (read integration over infinitely many) point sources. In order to find the displacement Green's function, the principle of Helmholtz decomposition is utilized, cf. Subsection 1.3.2. This implies that each of the fields $B^*_{il}(\mathbf{x},\omega;\mathbf{y})$ and $U^*_{il}(\mathbf{x},\omega;\mathbf{y})$, defined on the domain D, may be written as the sum of the gradient to a scalar field and the rotation of a vector field, *i.e.*

$$B^*_{il}(\mathbf{x},\omega;\mathbf{y}) = \frac{\partial \Phi_l(\mathbf{x},\omega;\mathbf{y})}{\partial x_i} + \varepsilon_{ijk} \frac{\partial \Psi_{kl}(\mathbf{x},\omega;\mathbf{y})}{\partial x_j}, \tag{c}$$

$$U^*_{il}(\mathbf{x},\omega;\mathbf{y}) = \frac{\partial \varphi_l(\mathbf{x},\omega;\mathbf{y})}{\partial x_i} + \varepsilon_{ijk} \frac{\partial \psi_{kl}(\mathbf{x},\omega;\mathbf{y})}{\partial x_j}, \tag{d}$$

(continued)

where ε_{ijk} is the permutation symbol, cf. Eq. (1–16). The three scalar fields $\Phi_l(\mathbf{x},\omega;\mathbf{y})$ (one for each coordinate direction of the load, l) and the vector fields $\Psi_{il}(\mathbf{x},\omega;\mathbf{y})$ are derived from the load field as

$$\Phi_l(\mathbf{x},\omega;\mathbf{y}) = -\frac{1}{4\pi}\frac{\partial}{\partial x_i}\int_\Omega \frac{1}{|\mathbf{x}-\mathbf{z}|}B^*_{il}(\mathbf{z},\omega;\mathbf{y})d\mathbf{z} = -\frac{1}{4\pi}\frac{\partial}{\partial x_l}\left(\frac{1}{r}\right), \tag{e}$$

$$\Psi_{il}(\mathbf{x},\omega;\mathbf{y}) = \frac{1}{4\pi}\varepsilon_{ijk}\frac{\partial}{\partial x_j}\int_\Omega \frac{1}{|\mathbf{x}-\mathbf{z}|}B^*_{kl}(\mathbf{z},\omega;\mathbf{y})d\mathbf{z} = \frac{1}{4\pi}\varepsilon_{ijl}\frac{\partial}{\partial x_j}\left(\frac{1}{r}\right). \tag{f}$$

Taking the divergence and rotation, respectively, of Eq. (b) the following inhomogeneous frequency-domain equivalents of the wave equation are produced,

$$c_P^2\frac{\partial^2\varphi_l}{\partial x_j^2} - \frac{1}{4\pi\rho}\frac{\partial}{\partial x_l}\left(\frac{1}{r}\right) = -\omega^2\varphi_l, \qquad c_S^2\frac{\partial^2\psi_{il}}{\partial x_j^2} + \frac{1}{4\pi\rho}\varepsilon_{ijl}\frac{\partial}{\partial x_j}\left(\frac{1}{r}\right) = -\omega^2\psi_{il}. \tag{g}$$

Next, the substitutions

$$\varphi_l(\mathbf{x},\omega;\mathbf{y}) = -\frac{\partial}{\partial x_l}p(\mathbf{x},\omega;\mathbf{y}), \quad \psi_{il}(\mathbf{x},\omega;\mathbf{y}) = \varepsilon_{ijl}\frac{\partial}{\partial x_j}s(\mathbf{x},\omega;\mathbf{y}) \tag{h}$$

are introduced. Furthermore, making use of the fact that $k_P = \omega/c_P$ and $k_S = \omega/c_S$, Eq. (g) may be written as

$$\frac{\partial^2 p}{\partial x_j^2} + \frac{1}{4\pi\rho c_P^2 r} = -k_P^2 p, \qquad \frac{\partial^2 s}{\partial x_j^2} + \frac{1}{4\pi\rho c_S^2 r} = -k_S^2 s. \tag{i}$$

Noting that $c_P^2k_P^2 = c_S^2k_S^2 = \omega^2$, the particular solutions to Eq. (i) both become $p_p(\mathbf{x},\omega;\mathbf{y}) = s_p(\mathbf{x},\omega;\mathbf{y}) = -1/\left(4\pi\rho\omega^2 r\right)$, whereas the complimentary solutions are $p_c(\mathbf{x},\omega;\mathbf{y}) = c_1\,(1/r)\,\mathrm{e}^{\mathrm{i}k_P r} + c_2\,(1/r)\,\mathrm{e}^{-\mathrm{i}k_P r}$, $s_c(\mathbf{x},\omega;\mathbf{y}) = d_1\,(1/r)\,\mathrm{e}^{\mathrm{i}k_S r} + d_2\,(1/r)\,\mathrm{e}^{-\mathrm{i}k_S r}$. With the given definition of the harmonic time variation, *i.e.* a variation of the kind $\mathrm{e}^{\mathrm{i}\omega t}$, the first term of each of the complimentary solutions corresponds to waves coming in from infinity. We recall the fact that P- and S-waves are non-dispersive, so that the energy propagates in the direction of the waves for any frequency. Hence, for physical reasons $c_1 = d_1 = 0$, since energy must propagate away from the source.

Subsequently, as the solution must be finite for $r \to 0$, the full solutions are derived as:

$$p(\mathbf{x},\omega;\mathbf{y}) = \frac{1}{4\pi\rho\omega^2 r}\left(\mathrm{e}^{-\mathrm{i}k_P r} - 1\right), \quad s(\mathbf{x},\omega;\mathbf{y}) = \frac{1}{4\pi\rho\omega^2 r}\left(\mathrm{e}^{-\mathrm{i}k_S r} - 1\right). \tag{j}$$

By differentiation of the solutions (j) as defined by Eq. (h) and subsequently Eqs. (c) and (d), the following Green's function is finally obtained for the amplitudes of the time-harmonic displacements,

$$U^*_{il}(\mathbf{x},\omega;\mathbf{y}) = \frac{1}{4\pi\rho c_S^2}\left(\alpha\delta_{il} - \beta\frac{\partial r}{\partial x_i}\frac{\partial r}{\partial x_l}\right), \tag{k}$$

where $\partial r/\partial x_i$ are identified as the direction cosines of the vector $\mathbf{r} = \mathbf{x} - \mathbf{y}$, and

$$\alpha = \left(\frac{1}{r} + \frac{1}{\mathrm{i}k_S r^2} - \frac{1}{k_S^2 r^3}\right)\mathrm{e}^{-\mathrm{i}k_S r} - \frac{c_S^2}{c_P^2}\left(\frac{1}{\mathrm{i}k_P r^2} - \frac{1}{k_P^2 r^3}\right)\mathrm{e}^{-\mathrm{i}k_P r}, \tag{l}$$

$$\beta = \left(\frac{1}{r} + \frac{3}{\mathrm{i}k_S r^2} - \frac{3}{k_S^2 r^3}\right)\mathrm{e}^{-\mathrm{i}k_S r} - \frac{c_S^2}{c_P^2}\left(\frac{1}{r} + \frac{3}{\mathrm{i}k_P r^2} - \frac{3}{k_P^2 r^3}\right)\mathrm{e}^{-\mathrm{i}k_P r}. \tag{m}$$

Clearly, the term with the lowest degree of geometrical damping in either of α and β has a decay proportional to $1/r$ as initially proposed. □

1.6.3 Material dissipation of waves

By the notion "material damping" we understand the transformation of mechanical energy into thermic energy, *i.e.* heat. From thermodynamics this transition is known to be a one-way process. The nature of material damping is closely related to such mechanisms as friction between particles or grains, molecular collisions or irreversible intercrystal heat flux. In the continuum model, this involves that material damping is related to the motion at material points.

Experiments have shown that the energy dissipation in some materials is strongly dependent of the frequency and the temperature. A linear variation with the frequency is observed for fluids. However, for most solid materials, a linear viscous model overestimates the frequency dependence. For example, for polymers and elastomers, which are often used in absorbers and resilient mounts, a dependency with the square root of the frequency has been found to be descriptive (Gaul 1999), and in many kinds of soil the damping is almost independent of the frequency in the frequency range relevant to ground-borne noise (Aki and Richards 1980). Thus, there is a need of material dissipation models that are able to provide different degrees of frequency dependence. Such models are discussed below

Before we turn to the discussion of how a material model which includes damping is formulated, it should be realized that a material model must posses two key features.

- The model must be *causal*. This means that a disturbance is not recorded before the load is applied.
- The model must not provide negative material damping.

These requirements may seem trivial, but actually they are not met by some material models which are often applied in engineering.

Hereditary versus differential approach

By the so-called *hereditary approach*, any linear viscoelastic material model may be written in terms of an integral relationship between the stress and the strain. In the one-dimensional case the relationship reads

$$\sigma(t) = \int_{-\infty}^{t} G(t-\tau)\,\mathrm{d}\epsilon(\tau), \qquad \epsilon(t) = \int_{-\infty}^{t} J(t-\tau)\,\mathrm{d}\sigma(\tau), \tag{1–112}$$

where the upper integration limits are due to the requirement of causality. $G(t)$ is known as the *relaxation modulus*, whereas $J(t)$ is denoted the *creep compliance*. A physical interpretation of $G(t)$ and $J(t)$ is given below. The relations (1–112) allow jumps, *i.e.* discontinuities, in the stress and stain histories. Further, $\sigma(t)$ and $\epsilon(t)$ need not be differentiable. Therefore the integrals in Eq. (1–112) are so-called *Stieltjes* integrals.

In the general three-dimensional case, the relaxation modulus and the creep compliance are replaced with the fourth order tensors $G_{ijkl}(t)$ and $J_{ijkl}(t)$, respectively. Thus, the hereditary approach yields the three-dimensional equivalent of Eq. (1–112),

$$\sigma_{ij}(t) = \int_{-\infty}^{t} G_{ijkl}(t-\tau)\,\mathrm{d}\epsilon_{kl}(\tau), \qquad \epsilon_{ij}(t) = \int_{-\infty}^{t} J_{ijkl}(t-\tau)\,\mathrm{d}\sigma_{kl}(\tau). \tag{1–113}$$

If the stress and strain histories are both assumed to be smooth continuous functions, the one-dimensional viscoelastic stress–strain relationship (1–112) may alternatively be written

$$\sigma(t) = \int_{-\infty}^{t} G(t-\tau)\frac{\mathrm{d}\epsilon(\tau)}{\mathrm{d}\tau}\,\mathrm{d}\tau, \qquad \epsilon(t) = \int_{-\infty}^{t} J(t-\tau)\frac{\mathrm{d}\sigma(\tau)}{\mathrm{d}\tau}\,\mathrm{d}\tau. \tag{1–114}$$

Here the integrals are identified as *Riemann* integrals. Other names are *Duhamel* integrals and *convolution* integrals. Evidently there must exist a unique relationship between $G(t)$ and $J(t)$ in order for Eq. (1–114) to be satisfied. Thus it may be shown that the two functions must satisfy the integral relationship

$$\frac{\mathrm{d}}{\mathrm{d}t}\int_{0}^{t} G(t)J(t-\tau)\,\mathrm{d}\tau = 1. \tag{1–115}$$

A proof of Eq. (1–115) will not be given here. However, it will be shown that the rule applies to some of the standard viscoelastic models that are applied in the analysis of *e.g.* soil dynamics. For the three-dimensional case, an integral identity similar to Eq. (1–115) defines a unique relationship between $G_{ijkl}(t)$ and $J_{ijkl}(t)$.

In order to provide a physical interpretation of the creep compliance, let us consider the case of a constant stress applied at the time $t = 1$. Given that no stress has previously been applied to the material, the stress history is given as $\sigma(t) = \sigma_0\, H(t)$, where $H(t)$ is the *Heaviside function*,

$$H(t) = \begin{cases} 0 & \text{for} \quad t < 0 \\ 1 & \text{for} \quad t \geq 0 \end{cases} . \tag{1–116}$$

It is noted that formally, derivation of the Heaviside function with respect to time yields the Dirac delta function, *i.e.* $\sigma_0\,\mathrm{d}H(t)/\mathrm{d}t = \sigma_0\,\delta(t)$. Insertion of this result into Eq. (1–114) leads to the conclusion that $\epsilon(t) = \sigma_0\, J(t)$ for a constant stress σ_0 applied at $t = 0$. Therefore we get the following definition.

Definition 1.1 Creep compliance

$J(t)$ is the development of the strain over time for a unit stress applied at time zero.

Next, if a constant strain is applied to a one-dimensional member at the time $t = 0$, *i.e.* $\epsilon(t) = \epsilon_0 H(t)$. Hence, from Eq. (1–114) it follows that the stress will vary over time as $\sigma(t) = \epsilon_0\, G(t)$. The relaxation modulus may thus be given the following physical interpretation.

Definition 1.2 Relaxation modulus

$G(t)$ is the development of the stress over time for a unit strain applied at time zero.

Whereas the hereditary approach is very adaptable in the sense that any material behaviour can be modelled, it is not very convenient from a computational point of view. Thus we would like a material model that works locally in time, so that the convolution may be avoided. An introduction to the formulation of such models is provided in the following examples. As we shall see, the findings in Examples 1.7 and 1.8 hint that for certain simple choices of the relaxation

modulus and the creep compliance, the hereditary form may be reformulated in terms of local time derivatives. In the general case we refer to this as the *differential approach*.

Example 1.7 One-dimensional linear elasticity

We assume that the relaxation modulus is given as $G(t) = E$, and that the strain vanishes in the limit as $t \to -\infty$. Hence, the stress–strain relationship in Eq. (1–114) yields

$$\sigma(t) = \int_{-\infty}^{t} E \frac{\mathrm{d}\epsilon(\tau)}{\mathrm{d}\tau}\,\mathrm{d}\tau = E\left\{\epsilon(t) - \epsilon(-\infty)\right\} = E\epsilon(t). \tag{a}$$

This is the Hooke's law for one-dimensional elasticity. E may be the Young's modulus of a bar. If a bar with the length L and the cross section area A is considered, EA/L is the "spring stiffness". Similarly, $G_{ijkl}(t) = E_{ijkl}$ yields the pure elastic relationship provided by the generalised Hooke's law (1–2). Alternatively, Eq. (a) may be written $\epsilon(t) = E^{-1}\sigma(t)$, which yields the creep compliance $J(t) = E^{-1}$. It is evident that $G(t) = E$ and $J(t) = E^{-1}$ fulfill Eq. (1–115). □

Example 1.8 One-dimensional linear viscosity

Let us assume that the relaxation modulus is given as $G(t) = \eta\,\delta(t)$. Then Eq. (1–114) provides the stress–strain relationship

$$\sigma(t) = \int_{-\infty}^{t} \eta\,\delta(t-\tau)\frac{\mathrm{d}\epsilon(\tau)}{\mathrm{d}\tau}\,\mathrm{d}\tau = \eta\,\frac{\mathrm{d}\epsilon(\tau)}{\mathrm{d}\tau}\bigg|_{\tau=t} = \eta\frac{\mathrm{d}\epsilon(t)}{\mathrm{d}t}. \tag{a}$$

Thus, we get a relationship between $\sigma(t)$ and $\epsilon(t)$ which is *local* in time, *i.e.* no convolution is necessary in order to compute the stress for a given instantaneous value of the strain. When η is a real positive quantity, the model leads to linear viscous damping and η is denoted the viscous damping constant. This model is descriptive for many fluids and the damping has a linear dependency of the frequency. Thus, in the frequency domain, assuming a harmonic variation of the kind $\mathrm{e}^{\mathrm{i}\omega t}$, we get $\hat{\sigma}(\omega) = \mathrm{i}\omega\hat{\epsilon}(\omega)$. Here the hat denotes Fourier transformation with respect to time.

In order to find the creep compliance corresponding to the relaxation modulus $G(t) = \eta\,\delta(t)$, we first rewrite the stress–strain relationship as

$$\frac{\mathrm{d}\epsilon(t)}{\mathrm{d}t} = \frac{1}{\eta}\,\sigma(t). \tag{b}$$

Integration over time provides the hereditary form

$$\epsilon(t) = \int_{-\infty}^{t} \frac{\mathrm{d}\epsilon(\tau)}{\mathrm{d}\tau}\,\mathrm{d}\tau = \int_{-\infty}^{t} \frac{\sigma(\tau)}{\eta}\,\mathrm{d}\tau = \int_{-\infty}^{t} \frac{t-\tau}{\eta}\,\frac{\mathrm{d}\sigma(\tau)}{\mathrm{d}\tau}\,\mathrm{d}\tau. \tag{c}$$

which in contrast to Eq. (a) is *global* in time. That the last reformulation is valid may easily be checked,

$$\int_{-\infty}^{t} \frac{t-\tau}{\eta}\,\frac{\mathrm{d}\sigma(\tau)}{\mathrm{d}\tau}\,\mathrm{d}\tau = \frac{t-\tau}{\eta}\,\sigma(\tau)\bigg|_{-\infty}^{t} + \int_{-\infty}^{t} \frac{\sigma(\tau)}{\eta}\,\mathrm{d}\tau, \tag{d}$$

which follows by the rule of partial integration. We now state that $\sigma(t)$ should vanish in the limit as $t \to -\infty$. Further, since the stress must be finite for the time $\tau = t$, the first term of the right hand side of Eq. (d) becomes zero. Hence we have proved that the creep compliance for the linear viscous damping model is $J(t) = t/\eta$. Finally, the following integral identity is achieved, *(continued)*

$$\frac{\mathrm{d}}{\mathrm{d}t}\int_0^t \eta\,\delta(t)\,\frac{t-\tau}{\eta}\,\mathrm{d}\tau = \frac{\mathrm{d}}{\mathrm{d}t}\,t = 1. \tag{e}$$

Hence, $G(t) = \eta\,\delta(t)$ and $J(t) = t/\eta$ fulfill the condition (1–115). □

In order to provide more complex models, a combination of the linear elastic "spring" and the linear viscous "dashpot" models may be proposed. The two simplest combination of a spring and a dashpot are shown in Fig. 1–31. The *Maxwell model* consists of a spring and a dashpot in series, whereas the the *Kelvin model* assumes a parallel coupling of a spring and a dashpot.

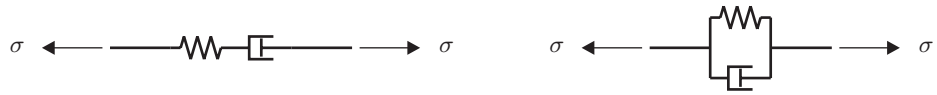

(a) (b)

Figure 1–31 Simple viscoelastic models: (a) the *Maxwell model* and (b) the *Kelvin model*.

In the Maxwell model, it is evident that the total strain ϵ and the total stress are given as

$$\epsilon = \epsilon_e + \epsilon_v, \qquad \sigma = \sigma_e = \sigma_v, \qquad \text{(Maxwell} \sim \text{series coupling)} \tag{1–117}$$

where ϵ_e and ϵ_v are the strains in the elastic part and the viscous part of the system, respectively. Likewise σ_e and σ_v are stresses in the elastic and the viscous parts of the system, respectively. On the other hand, in the Kelvin model, the stress and strain become

$$\epsilon = \epsilon_e = \epsilon_v, \qquad \sigma = \sigma_e + \sigma_v, \qquad \text{(Kelvin} \sim \text{parallel coupling)} \tag{1–118}$$

A comparison of Eqs. (1–114) and (1–117) reveals that the creep compliance of the Maxwell model is achieved as the sum of the creep compliances for the subsystems, *i.e.* $J(t) = J_e(t) + J_v(t)$. Analogously, for the Kelvin model Eq. (1–118) involves that the relaxation modulus is given as the sum of the relaxation moduli of the subsystems, *i.e.* $G(t) = G_e(t) + G_v(t)$. Hence, making use of the results in Examples 1.7 and 1.8, the following quantities are identified:

$$J(t) \;=\; J_e(t) \,+\, J_v(t) \;=\; \frac{1}{E} \,+\, \frac{t}{\eta}, \qquad \text{(Maxwell} \sim \text{series coupling)} \tag{1–119}$$

$$G(t) \;=\; G_e(t) \,+\, G_v(t) \;=\; E \,+\, \eta\,\delta(t), \qquad \text{(Kelvin} \sim \text{parallel coupling)} \tag{1–120}$$

These results may be generalised as follows:

Definition 1.3 Series coupling

For two models placed in series, $J(t) = J_1(t) + J_2(t)$ holds.

Definition 1.4 Parallel coupling

For two models placed in parallel, $G(t) = G_1(t) + G_2(t)$ holds.

In hereditary form, the stress–strain relationships for the Maxwell and Kelvin models read

$$\epsilon(t) \;=\; \int_{-\infty}^{t} \left(\frac{1}{E} \,+\, \frac{t-\tau}{\eta} \right) \frac{\mathrm{d}\sigma(\tau)}{\mathrm{d}\tau}\, \mathrm{d}\tau, \qquad \text{(Maxwell} \sim \text{series coupling)} \quad \text{(1–121)}$$

$$\sigma(t) \;=\; \int_{-\infty}^{t} \left(E \,+\, \eta\, \delta(t-\tau) \right) \frac{\mathrm{d}\epsilon(\tau)}{\mathrm{d}\tau}\, \mathrm{d}\tau, \qquad \text{(Kelvin} \sim \text{parallel coupling)} \quad \text{(1–122)}$$

In terms of local time derivatives, this is equivalent to the formulations

$$\frac{\mathrm{d}\epsilon(t)}{\mathrm{d}t} \;=\; \frac{1}{E}\, \frac{\mathrm{d}\sigma(t)}{\mathrm{d}t} \,+\, \frac{1}{\eta}\sigma(t), \qquad \text{(Maxwell} \sim \text{series coupling)} \quad \text{(1–123)}$$

$$\sigma(t) \;=\; E\,\epsilon \,+\, \eta\, \frac{\mathrm{d}\epsilon(t)}{\mathrm{d}t}, \qquad \text{(Kelvin} \sim \text{parallel coupling)} \quad \text{(1–124)}$$

The reformulation of Eqs. (1–121) and (1–122) into Eqs. (1–123) and (1–124) holds if the stress and strain, and their temporal derivatives, respectively, both vanish in the limit as $t \to -\infty$.

Rational approximations to viscoelasticity

Inspection of the stress–strain relationships for the Maxwell and the Kelvin models, given in differential operator form, suggests that a class of viscoelastic models may be achieved in the form of the *rational approximation*

$$\sum_{i=0}^{n} a_i\, \frac{\mathrm{d}^i \sigma(t)}{\mathrm{d}t^i} = \sum_{j=0}^{m} b_j\, \frac{\mathrm{d}^j \epsilon(t)}{\mathrm{d}t^j}. \qquad \text{(1–125)}$$

This class of damping models work locally in time, which provides a good model in terms of computation speed. However, the restriction to relaxation moduli and creep compliances that result in the local time dependence between $\sigma(t)$ and $\epsilon(t)$ may lead to the necessity of several terms n and m in order to achieve a useful model for a given material.

In Eq. (1–125) a_i, $i = 0, 1, ..., n$ and b_j, $j = 0, 1, ...m$, are material constants which are all real quantities. For the Maxwell model we identify the parameters $a_0/b_1 = \eta$ and $a_1/b_1 = E$, which are definitely real, given that b_1 is selected as an arbitrary real number. All other parameters a_i, b_j in the Maxwell model are equal to zero. Likewise, in the Kelvin model the nonzero parameters are $b_0/a_0 = E$ and $b_1/a_0 = \eta$ with a_0 chosen as an arbitrary real number.

In the general case, we would like to know the $n + m + 2$ parameters in Eq. (1–125) for a material. These should be determined from a number of laboratory or field tests. However, the time-domain approach leads to a complicated calibration of a_i and b_i. Hence, in practice the calibration is carried out in the frequency domain. Here Eq. (1–125) yields

$$\sum_{i=0}^{n} a_i\, (\mathrm{i}\omega)^i\, \hat{\sigma}(\omega) = \sum_{j=0}^{m} b_j\, (\mathrm{i}\omega)^j\, \hat{\epsilon}(\omega), \qquad \text{(1–126)}$$

which may alternatively be written as

$$\hat{\sigma}(\omega) = \hat{G}(\omega)\, \hat{\epsilon}(\omega), \qquad \hat{G}(\omega) = \frac{\sum_{j=0}^{m} b_j\, (\mathrm{i}\omega)^j}{\sum_{i=0}^{n} a_i\, (\mathrm{i}\omega)^i}. \qquad \text{(1–127)}$$

The function $\hat{G}(\omega)$ is denoted a *rational filter*, and it is realized that $\hat{G}(\omega)$ is the Fourier transform of the relaxation modulus $G(t)$ with respect to time for a harmonic variation of the kind $\mathrm{e}^{\mathrm{i}\omega t}$. $\hat{G}(\omega)$ may be interpreted as a complex frequency dependent stiffness modulus of the material. We may write this complex stiffness as

$$\hat{G}(\omega) = G(\omega)\left\{1 + \mathrm{i}\eta(\omega)\right\}, \tag{1–128}$$

where the real part $G(\omega)$ is the stiffness, whereas the imaginary part $\mathrm{i}\eta(\omega)\,G(\omega)$ should define material dissipation. This prohibits certain combinations of the values of the parameters a_i and b_j. Thus, if the measured frequency spectrum is fitted uncritically by a rational filter of the kind (1–127), a "viscoelastic" model may be obtained that introduces negative material damping. Further, as noted in the previous subsection the rational filter should provide a material model that is causal. A further discussion hereof is beyond the scope of these course notes.

Fractional time derivatives in viscoelasticity

In the previous subsection we confined ourselves to rational approximations of the stress-strain relationship. This has the advantage that the governing equations in the time domain become partial differential equations which are local in time. However, a great number of parameters may be needed in a model in order to get a satisfactory fit to experimental results. We might suspect that this is due to the fact that the viscoelastic behaviour that is modelled with the rational approach does not correspond to the real behaviour of a material. Thus, for some polymers it has been found that the stiffness and damping of the material depend on the square root of the frequency. Evidently this frequency dependence is not easily provided by a rational filter.

A greater degree of freedom in fitting viscoelastic models to experimental results is achieved if we allow the utilization of so-called *fractional time derivatives* to appear in the differential equations stating the stress–strain relationship. The rather abstract notion of a fractional time derivative of the order α involves the application of a differential operator in the form

$$\mathcal{D}^{\alpha} f(t) = \frac{\mathrm{d}^{\alpha} f(t)}{\mathrm{d}t^{\alpha}} = \frac{1}{\Gamma(1-\alpha)} \frac{\mathrm{d}}{\mathrm{d}t} \int_{a=0}^{t} \frac{f(\tau)}{(t-\tau)^{\alpha}}\,\mathrm{d}\tau, \qquad \alpha \in \,]0,1[\,, \tag{1–129}$$

which is nonlocal in time. $\Gamma(1-\alpha)$ is the gamma function,

$$\Gamma(1-\alpha) = \int_0^{\infty} \mathrm{e}^{-\tau}\tau^{-\alpha}\,\mathrm{d}\tau. \tag{1–130}$$

For integer arguments, $\Gamma(n) = (n-1)!$. The fractional derivative $\mathcal{D}^{\alpha} f(t)$ of any noninteger order may be computed as $\mathcal{D}^{n}(\mathcal{D}^{\beta} f(t))$, where $n \in N$ and $\beta \in \,]0,1[$ so that $\alpha = n + \beta$.

The time-domain formulation provided by Eq. (1–129) is attributed to Riemann and Liouville (Oldham and Spanier 1974). Due to its complexity, the convolution operator is not suited for application to practical problems. Instead, a solution is sought in Laplace domain, employing the principle of elastic–viscoelastic correspondence. The Laplace transform of $\mathcal{D}^{\alpha} f(t)$ is found as

$$\mathcal{L}\{\mathcal{D}^{\alpha} f(t)\} = s^{\alpha}\,\bar{f}(s), \qquad \bar{f}(s) = \mathcal{L}\{f(t)\}, \tag{1–131}$$

where $\mathcal{L}$ is the Laplace operator, and the Laplace transform is defined as

$$\mathcal{L}\{f(t)\} = \int_0^{\infty} f(t)\,\mathrm{e}^{-st}\,\mathrm{d}t. \tag{1–132}$$

Alternatively, for the evaluation of harmonic vibration or wave propagation, a change of the lower integration limit in Eq. (1–129) to $a = -\infty$ provides the Fourier transformation over time

$$\mathcal{F}\{\mathcal{D}^\alpha f(t)\} = (\mathrm{i}\omega)^\alpha\, \bar{f}(\omega), \qquad \bar{f}(\omega) = \mathcal{F}\{f(t)\}\,. \tag{1–133}$$

The Fourier transformation, here denoted by $\mathcal{F}\{\cdot\}$, is defined as

$$\mathcal{F}\{f(t)\} = \int_{-\infty}^{\infty} f(t)\, \mathrm{e}^{\mathrm{i}\omega t}\, \mathrm{d}t. \tag{1–134}$$

With this definition of the fractional time derivative in the time and frequency domains, a generalization of Eqs. (1–125) and (1–126) yields

$$\sum_{i=0}^{n} a_i\, \mathcal{D}^{\alpha_i} \sigma(t) = \sum_{j=0}^{m} b_j\, \mathcal{D}^{\beta_j} \epsilon(t), \tag{1–135}$$

$$\sum_{i=0}^{n} a_i\, (\mathrm{i}\omega)^{\alpha_i}\, \hat{\sigma}(\omega) = \sum_{j=0}^{m} b_j\, (\mathrm{i}\omega)^{\beta_j}\, \hat{\epsilon}(\omega), \tag{1–136}$$

respectively, where it is understood that $\alpha_0 = \beta_0 = 0$.

Example 1.9 A fractional derivative model with four parametres

A relatively simple, but quite adaptable viscoelastic model is achieved by inclusion of a single fractional time derivative on either side of Eq. (1–135). Letting $a_0 = 1$, $b_0 = E_0$, $a_1 = \tau_\sigma^\alpha$, $b_1 = \tau_\epsilon^\alpha$ and $\alpha_1 = \beta_1 = \alpha$, the model may be written

$$(1 + \tau_\sigma^\alpha D^\alpha)\, \sigma(t) - (1 + \tau_\epsilon^\alpha D^\alpha)\, E_0\, \epsilon(t) = 0. \tag{a}$$

Here E_0 is the static stiffness modulus, while τ_σ^α and τ_ϵ^α may be interpreted as time scales for the stress and strain, respectively.

In the frequency domain, Eq. (a) yields

$$\hat{\sigma}(\omega) = E(\omega)\, \hat{\epsilon}(\omega), \qquad E(\omega) = E_0\, \frac{1 + (\tau_\epsilon \mathrm{i}\omega)^\alpha}{1 + (\tau_\sigma \mathrm{i}\omega)^\alpha}. \tag{b}$$

The low and high frequency limits of the stiffness $E(\omega)$ are, respectively,

$$E(0) = E_0, \qquad E_\infty = \lim_{\omega \to \infty} E(\omega) = E_0 \left(\frac{\tau_\epsilon}{\tau_\sigma}\right)^\alpha, \tag{c}$$

where it has been found that most materials become stiffer with increasing frequency, *i.e.* $E_\infty/E_0 > 1$ or $\tau_\epsilon > \tau_\sigma$. We may say that a material "better remembers the strain than the stress".

It is evident that the low and high frequency limits of $E(\omega)$ provided by Eq. (b) are purely elastic. Thus, material damping is only present in the medium frequency range. The variation of the complex stiffness with the frequency is illustrated in Fig. A for three different values of α and for $E_\infty/E_0 = 2$.

(continued)

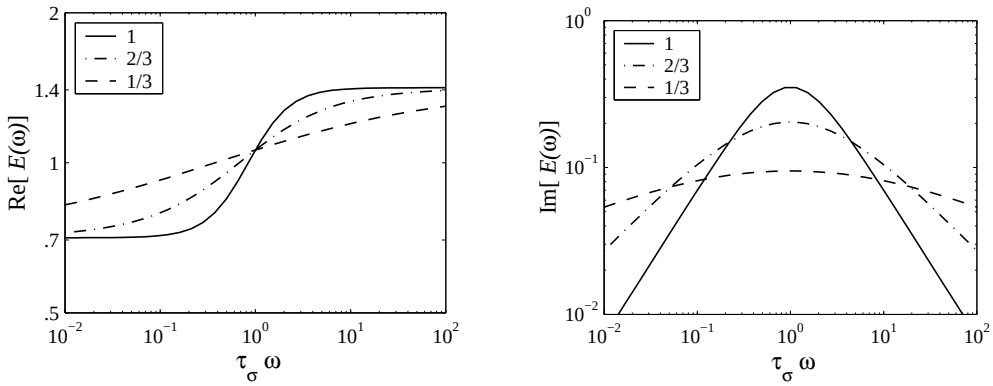

Figure A Frequency dependent elastic modulus, $E_\infty/E_0 = 2$.

When $\alpha = 1$, we obtain a viscoelastic behaviour resembling that of a combined Maxwell and Kelvin model. This follows from a comparison of Eq. (a) with Eqs. (1–122) and (1–123). On the other hand, when α approaches 0, the model approaches the *hysteretic material model*, in which the imaginary term, *i.e.* the damping, is represented by the step function $\mathrm{sign}(\omega)$. The sign of the frequency is important when the time domain solution is established by means of double-sided inverse Fourier transformation. □

Dispersion related to dissipation

Material dissipation implies that the phase velocities of waves propagation are different from the values in a perfectly elastic material as illustrated by the following example.

Example 1.10 Dispersion in a one-dimensional viscoelastic model

Let us consider the propagation of viscoelastic waves in a one-dimensional model. This may correspond to the case of elongation waves propagating through a bar or the propagation of plane P-waves in an elastic continuum along the x-axis. In the absence of body forces, the problem is defined by the one-dimensional homogeneous Cauchy equation,

$$\frac{\partial \sigma(x,t)}{\partial x} = \rho \frac{\partial^2 u(x,t)}{\partial t^2}, \tag{a}$$

A viscoelastic stress–strain relationship is now assumed in the form

$$\hat{\sigma}(\omega) = E(\omega)\,\hat{\epsilon}(\omega). \tag{b}$$

Since the strain in one dimension is $\epsilon = \partial u/\partial x$, Eq. (a) may be rewritten in the frequency domain as

$$E(\omega)\frac{\partial^2 \hat{u}(x,\omega)}{\partial x^2} = -\omega^2 \rho\, \hat{u}(x,\omega) \qquad \Rightarrow$$

$$\frac{\partial^2 \hat{u}(x,\omega)}{\partial x^2} + \left(\frac{\omega}{c}\right)^2 \hat{u}(x,\omega) = 0, \qquad c = c(\omega) = \sqrt{\frac{E(\omega)}{\rho}}, \tag{c}$$

(continued)

where $\hat{u}(x,\omega)$ is the Fourier transform of the displacement with respect to time and $c(\omega)$ is identified as the phase velocity of the waves. Evidently, the phase velocity is frequency dependent when the complex stiffness modulus $E(\omega)$ is frequency dependent. Therefore, a viscoelastic model with frequency dependent stiffness and/or material damping leads to dispersive wave propagation, and further in the frequency domain the phase velocity is generally a complex quantity.

Since the waves are dispersive we may suspect that the group velocity of the waves is no longer equal to the phase velocity. In order to show that this is actually so, we first establish the solution to Eq. (c),

$$\hat{u}(x,\omega) = A_1(\omega)\,\mathrm{e}^{\mathrm{i}k(\omega)x} + A_2(\omega)\,\mathrm{e}^{-\mathrm{i}kx}, \qquad k = k(\omega) = \frac{\omega}{c} = \omega\sqrt{\frac{\rho}{E(\omega)}}. \tag{d}$$

Here $k(\omega)$ is the wavenumber. The imaginary part of k due to a complex stiffness modulus $E(\omega)$ leads to attenuation of the waves which comes as no surprise since we are dealing with a model that contains material dissipation. With a harmonic time variation of the kind $\mathrm{e}^{\mathrm{i}\omega t}$, the two terms describe wave propagation in the negative and positive x-direction, respectively.

From the definition of the wavenumber in Eq. (d), the group velocity of the waves in the one-dimensional viscoelastic model is found as

$$c_g(\omega) = \frac{\mathrm{d}\omega}{\mathrm{d}k} = c(\omega)\left(1 - \frac{\omega}{2E(\omega)}\,\frac{\mathrm{d}E(\omega)}{\mathrm{d}\omega}\right)^{-1}. \tag{e}$$

It is observed that $c_g(0) = c(0)$. Further, if the stiffness modulus approaches a constant value asymptotically in the high frequency limit $\omega \to \infty$, we find that $c_g(\infty) = c(\infty)$. However, for any intermediate frequency, the group and phase velocities may be different. □

From Eq. (d) of Example 1.10 it is noted that the wavenumber becomes complex in the presence of material dissipation. Therefore, material dissipation in the frequency domain formulation leads to an exponential decay of the displacement amplitudes with the distance from a given source. Herein lies a difference when compared with geometrical damping, which implies an amplitude decrease with distance defined be some potential function. Consequently, in the near-field the geometrical damping is more important than material damping, whereas in the far-field the material damping becomes the more significant source to wave dissipation.

Further, in Example 1.10 we find that the group velocity is frequency dependent for all frequencies $\omega \neq 0$ unless the complex stiffness modulus is independent of the frequency. This is the situation in the so-called *hysteretic material model*, which is defined by the complex stiffness modulus

$$E(\omega) \;=\; E_0\,(1 + \mathrm{i}\,\eta\,\mathrm{sign}(\omega))\,, \qquad \text{(Hysteretic damping)} \quad \text{(1–137)}$$

where η is denoted the *loss factor*. The frequency dependence is only present via the sign function $\mathrm{sign}(\omega)$. However, it may be shown that the hysteretic model is not causal. Therefore, use of this model should generally be avoided. Nevertheless, utilization of this model is quite widespread. The main reason is that the model provides a simple means of introducing material damping. Often, the wave speeds in a material have been measured, but no reliable information exist about the energy loss. It may then be convenient to estimate a loss factor of, for example, 10%. Further, in soil the frequency dependency of the material damping and stiffness is very small, and it may be shown that the non-causal response appearing before the application of a load is very small when the damping is low. However, the material behaviour is better modelled in a physically sound manner by the application of a fractional derivative model of low order α.

1.7 Summary

In this chapter, the basic theory for wave propagation in viscoelastic media has been discussed. The analysis has been confined to the case of homogeneous and isotropic materials, and the continuum model has been adopted. The main results of the chapter are listed below.

P-waves (primary/compression/dilational/rotation free waves) propagate through an elastic medium with the phase velocity c_P. The particle motion is in the same direction as the wave propagation. In a linear elastic medium the P-waves are non-dispersive.

S-waves (secondary/shear/rotarional/equivoluminal) waves propagate through an elastic medium with the phase velocity $c_S < c_P$. The particle motion is orthogonal to the direction of wave propagation. Like the P-waves, the S-waves are non-dispersive in a linear elastic material.

SH-waves are "horizontally" polarized shear waves, *i.e.* S-waves with particle motion parallel to a free surface or layer interface.

SV-waves are "vertically" polarized shear waves. They describe the remaining part of the S-wave field not accounted for in the SH-wave.

Rayleigh waves travel on the surface of a homogeneous linear elastic half-space with the frequency independent phase velocity $c_R \approx 0.9\, c_S$. The particle motion is elliptical and retrograde near the surface.

Mechanical impedance is the ratio of traction over a surface and the particle velocity it generates. The terminology is borrowed from acoustics, where impedance provides the particle velocity due to an applied pressure over a given surface.

Impedance mismatch between two adjacent materials is the key issue with regard to energy reflection and transmission. If the impedance of two materials are identical, all energy will be transmitted through their common interface. On the other hand, if there is a strong impedance mismatch, almost all the energy is reflected.

Reflection and conversion of P- and S-waves takes place at a free surface of a half-space. The P- and SV-waves are coupled, whereas an SH-wave is reflected as an SH-wave.

Reflection, refraction and conversion of P- and S-waves happens at an interface between two half-spaces or layers. Again, only the P- and SV-parts of the wave field are coupled.

Love waves may travel along a soft layer over a half-space. They consist of SH-waves trapped within the layer because refraction into the adjacent layer(s) cannot take place.

Porous media consist of two or more phases. In a fully saturated porous material, *e.g.* soil below the phreatic level, the pore pressure in the fluid phase interacts with the stresses in the solid phase. In the general case, this results in seven equations with seven unknowns.

Effective stresses are carried solely by the solid skeleton in a porous material. For rock and concrete, the effective stress measure proposed by Biot should be applied instead of the Terzaghi effective stresses to obtain a simpler formulation of constitutive equations.

Pore pressures in fully saturated porous materials are carried by the pore fluid and the solid skeleton, *i.e.* the same pore pressure is present in both constituents.

Dispersion of waves involve that waves travel with a phase velocity that is frequency dependent. This may happen due to geometrical or material reasons. Thus, waves travelling in a wave guide, or a layer, are dispersive because certain frequencies lead to "eigenmodes" in the layer. Material dissipation generally leads to dispersion.

Geometrical dissipation or damping takes place due to the spreading of the energy over a surface or a volume. P- and S-waves spread in three dimensions from a point source. They are therefore subject to stronger geometrical damping than Rayleigh waves or Love waves, which only spread in two dimensions. Geometrical damping is described by a potential function of the distance from a source.

Material dissipation or damping exists in all real materials. The material damping is related to particle motion and is therefore frequency dependent. Material damping leads to exponential decay of the displacement amplitudes over distance.

Causality involves that there will be no response before a load has been applied. In order to ensure that this will be the case in a mathematical model, one should be careful when selecting a material model. It is noted that the hysteretic material model is not causal. Yet it remains one of the "most popular" models for soil and some other materials.

As stated in the introduction, the theory explained in this chapter will serve as a foundation for the numerical and analytic framework in the subsequent chapters.

CHAPTER 2
Finite-element analysis of elastodynamic problems

The finite-element method is a powerful numerical solution technique for problems governed by differential equations within a bounded region. In particular the method is advantageous in the analysis of problems involving local inhomogeneities and nonlinearities. However, in order to formulate a finite element solution for an unbounded domain, special care must be shown at the artificial boundaries that arise in the numerical model in order to ensure, for example, radiation of waves or heat into the infinite region. Different ways of formulating radiating, or transmitting, boundary conditions are discussed in this chapter with an emphasis on wave propagation in elastic media. Firstly, however, a short introduction is given to the formulation of the finite-element method in time and frequency domain.

2.1 Introduction to the finite-element method

The *finite-element method* (FEM) is well-suited for the analysis of finite structures and closed interior domains. However, in the analysis of open, or infinite, domains, the problem arises that only a finite part can be modelled with the finite-element method. Therefore, artificial boundaries must be introduced at a given distance from the area of interest. The use of Dirichlet and Neumann boundary conditions at the artificial boundaries implies a reflection of the outgoing waves back into the computational domain, or the FEM model. Instead so-called transmitting boundary conditions (TBCs) should be implemented, which ensure that the energy leaves the model through the artificial boundary. Various formulations of such transmitting boundary conditions for both elastic wave propagation and wave propagation in structural elements will be discussed in Section 2.5.

Firstly, however, the formulation of the FEM for a closed interior domain will be resumed in the next section. In particular, the various steps in the FEM formulation will be described. Examples will be given of the finite element analysis of problems involving stationary sources, such as machine foundations. In Section 2.4, it will be discussed how an FEM model should be adjusted in order to compute the steady state response to a moving source, *e.g.* a vehicle moving on the surface of a road. Further, before the discussion of transmitting boundary conditions in Section 2.5, the FEM solution of elastodynamic problems in time and frequency domain will be discussed in Sections 2.2 and 2.3.

2.1.1 The basic steps of the finite-element method

The offset of the finite-element method is the so-called *weak formulation* of a problem. The weak formulation is obtained from the *strong formulation—i.e.* the original partial or ordinary differential equation—by multiplication with an arbitrary virtual field and integration over the volume (in three-dimensional continuum problems), the area (in two-dimensional continuum problems, plate and shell problems) or the length (beam and rod problems). Afterwards the continuous physical field is discretized into the values at a finite number of points in the interior and on the surface of the considered bounded domain. These points are referred to as *nodes*. This means that all the spatial dimensions are kept in the discretization process. This is an essential difference from the *boundary element method* (BEM) formulation, in which only the boundary of the domain is discretized. A description of the BEM is beyond the scope of these notes. The formulation and several examples of application of the BEM in elastodynamics may be found in the book by Domínguez (1993).

In elastostatic problems, the finite element mesh is usually refined—*i.e.* smaller elements are used—in the vicinity of an applied force and in other regions, in which large gradients of the stress are expected. In wave propagation problems, however, the regions with large gradients will change over time. Therefore the elements have to be relatively small in the entire model. Furthermore, the elements have to be able to describe a travelling wave. This puts an upper limit on the size of the elements. The number of elements that are required per wavelength as a minimum depends on the kind of elements being used as will be discussed later.

In the FEM, the field quantities at any point inside the domain other than the nodes are found by interpolation between the nodal values. The interpolation functions are selected on a local basis, so that contributions are only present from the nodes adjacent to the point in question. This procedure differs from the Rayleigh-Ritz Method, in which approximative shape functions are identified for the entire domain, and from the BEM, in which the fundamental solutions are used as the influence functions. For the three-dimensional elastodynamic harmonic wave propagation problem, the Green's function was derived in Example 1.6. Consequently, in the FEM the original domain, D, is transformed into a number of small sub-domains, D_j, referred to as *finite elements*, see Fig. 2–1. The geometry of these elements is defined by the nodes and the interpolation, or shape, functions, which are also used to compute field quantities at interior points in the elements. Usually, polynomial functions are used as shape functions. Depending on the degree of the polynomials, the interpolation is referred to as linear, quadratic or cubic, etcetera. In any case, the spatial shape functions must fulfill the criterion that the FEM solution *converges*. This means that the approximative FEM solution must become infinitely close to the exact solution as the element size goes to zero. Convergence is assured if the requirements of *completeness* and *compatibility* (or the *conforming requirement*) are met:

Completeness — The approximation must be able to describe arbitrary constant values of the field quantity (*e.g.* the displacements) and the spatial derivatives thereof (*e.g.* the strains), which are present in the weak formulation of the problem.

Compatibility — The shape functions must provide a continuous, non-overlapping approximation of the field quantity and possibly also the derivatives, so that each integral in the weak formulation is well defined, not only in each individual element, but also over the boundaries.

Compatibility involves that the same shape functions are used for contiguous elements so that, for example, the displacements are not only identical at the common nodes, but also along

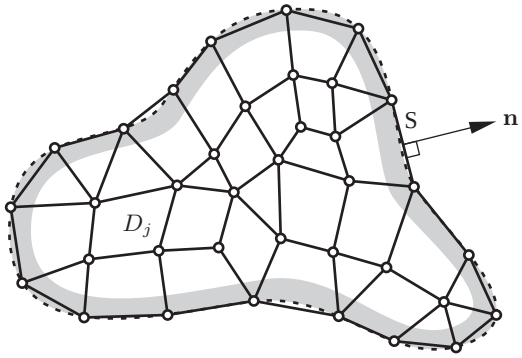

Figure 2–1 Discretization of the domain into finite elements, each representing the sub-domain D_j.

the common element surface. However, it turns out that reasonable results may in some cases be achieved in FEM codes, where non-conforming elements are used. This is, for example, the case in most FEM analysis of plates.

After the discretization of the integral equation corresponding to the weak formulation, the volume and surface integrals for the entire domain/surface are divided into sub-integrals over each finite element. Each of these integrals over a finite element constitutes an *element matrix*, or an *element vector*. Examples include the mass and stiffness matrices for continuum finite elements in linear elasticity or acoustics. It is noted that in this process, the traction applied to the surface of an element is transformed into equivalent *nodal forces*.

After the matrices for the individual elements have been computed, they are *assembled* into a global system of equations—one equation for each degree of freedom. In three-dimensional elasticity there are typically *three* degrees of freedom per node, *i.e.* the displacement in each spatial coordinate direction. In a plane SH-wave propagation FEM problem, there is only one degree of freedom at each node, namely the out-of-plane displacement component. In the assembly of the system matrices, contributions from all elements to each single node are added. This implies that adjacent elements have common nodes.

As a final step in the FEM, the boundary conditions for the entire domain are introduced via nodal forces or forced nodal displacements. The matrix system of equations is then solved either in frequency domain or in time domain. A frequency-domain solution is straight forward, while time-domain solutions demand the use of *time-integration algorithms*. Some of these are briefly discussed in the next section. Finally, based on the shape functions, interior values of the field quantity, or the strains/stresses, can be found inside each element. Thus, to summarize, the usual steps in the finite element formulation of a problem are the following:

1. establish the strong formulation of the problem,
2. establish the weak formulation of the problem,
3. discretize the continuous field into a finite number of nodal values,
4. select the shape functions for the physical and the virtual field,
5. compute the element matrices,

6 assemble the element matrices into a global system of equations,

7 apply nodal forces and introduce boundary conditions,

8 solve global system of equations in matrix form,

9 compute, if necessary, interior values or gradients by interpolation.

Rather than discussing the various steps of the FEM any further from a general point of view, a few examples will be given in the following subsections in order to illustrate the formulation of the method.

2.1.2 Finite element formulation of an elastic continuum

Consider the elastic body D having the surface $S = S_0 \cup S_1$ with the outward unit normal vector $\mathbf{n}$ with components n_j. With reference to Section 1.2, the *strong formulation* of the problem is given by the Cauchy equation of motion (1–1), which is repeated here for convenience

$$\frac{\partial \sigma_{ij}(\mathbf{x},t)}{\partial x_j} + \rho(\mathbf{x})\, b_i(\mathbf{x},t) = \rho(\mathbf{x})\, \frac{\partial^2 u_i(\mathbf{x},t)}{\partial t^2}. \tag{1–1}$$

$\sigma_{ij}(\mathbf{x},t)$ is the Cauchy stress tensor, $u_i(\mathbf{x},t)$ is the displacement field, $\rho(\mathbf{x})$ is the mass density and $b_i(\mathbf{x},t)$ is the load per unit mass. Vector $\mathbf{x}$ is the position in space and t is the time. Equation (1–1) is subject to the boundary and initial conditions

$$u_j(\mathbf{x},t) = \bar{u}_j(\mathbf{x},t) \quad \text{for} \quad \mathbf{x} \in S_0 \quad \text{and} \quad p_j(\mathbf{x},t) = \bar{p}_j(\mathbf{x},t) \quad \text{for} \quad \mathbf{x} \in S_1, \tag{2–1}$$

$$u_j(\mathbf{x},0) = \mathring{u}_j(\mathbf{x}) \quad \text{for} \quad \mathbf{x} \in D \quad \text{and} \quad \frac{\partial}{\partial t} u_j(\mathbf{x},0) = \mathring{v}_j(\mathbf{x}) \quad \text{for} \quad \mathbf{x} \in D, \tag{2–2}$$

i.e. geometrical boundary conditions are prescribed along the boundary S_0 and mechanical boundary conditions are provided for S_1, where $p_i(\mathbf{x},t) = \sigma_{ij}(\mathbf{x},t)\, n_j$ is the surface traction.

In what follows, engineering strains, *i.e.* linear deformations, are assumed, but the material is allowed to be inhomogeneous and anisotropic. This means that the material density is generally a function of the spatial coordinates, whereas the stress–strain relationship, *i.e.* the constitutive relationship, is given by the generalized Hooke's law, Eq. (1–2).

The *weak formulation* of the field equations for the continuum is obtained by multiplication of Eq. (1–1) with the virtual field $\delta u_i(\mathbf{x},t)$ and integration over the volume. $\delta u_i(\mathbf{x},t)$ is a variation of the displacement field and must fulfill the geometric boundary conditions along the boundary S_0. Otherwise it is arbitrary. Applying Green's theorem and making use of the fact that δu vanishes along S_0, the following integral equation is obtained for the domain D:

$$\begin{aligned} &\int_D \delta\varepsilon_{ij}(\mathbf{x},t)\sigma_{ij}(\mathbf{x},t)\mathrm{d}V(\mathbf{x}) + \int_D \delta u_i(\mathbf{x},t)\rho(\mathbf{x})\frac{\partial^2 u_i(\mathbf{x},t)}{\partial t^2}\mathrm{d}V(\mathbf{x}) \\ &\quad = \int_{S_1} \delta u_i(\mathbf{x},t) p_i(\mathbf{x},t)\mathrm{d}S(\mathbf{x}) + \int_D \delta u_i(\mathbf{x},t)\rho(\mathbf{x}) b_i(\mathbf{x},t)\mathrm{d}V(\mathbf{x}). \end{aligned} \tag{2–3}$$

Here $\delta\varepsilon_{ij}(\mathbf{x},t)$ is the strain related to the virtual field $\delta u_i(\mathbf{x},t)$, and use has been made of the fact that $\sigma_{ij}(\mathbf{x},t) = \sigma_{ji}(\mathbf{x},t)$ so that $(\partial u_i(\mathbf{x},t)/\partial x_j)\sigma_{ij}(\mathbf{x},t) = (\partial u_j(\mathbf{x},t)/\partial x_i)\sigma_{ij}(\mathbf{x},t)$.

The next step in the FE approach is to *discretize* the domain into a number of finite elements as illustrated in Fig. 2–1. Let $\mathbf{u}_e(t)$ and $\delta\mathbf{u}_e(t)$ be two $(3n_e \times 1)$ vectors storing the nodal displacements in the physical and the variational field, respectively, for the n_e nodes in element e. Further, defining $\mathbf{x}_e$ as the $(3n_e \times 1)$ coordinate vector for the element nodes, the displacement field and the virtual field over the element volume D_e may be described in vector form,

$$\mathbf{u}(\mathbf{x},t) = \mathbf{\Phi}_e(\mathbf{x})\mathbf{u}_e(t), \qquad \delta\mathbf{u}(\mathbf{x},t) = \mathbf{\Psi}_e(\mathbf{x})\delta\mathbf{u}_e(t), \tag{2–4}$$

where $\mathbf{x}$ is a point (x_1, x_2, x_3) in the interior D_e of the element and $\mathbf{\Phi}_e(\mathbf{x})$, $\mathbf{\Psi}_e(\mathbf{x})$ are two $(3 \times 3n_e)$ matrices storing the *shape functions* and the *weight functions* for the element, respectively. Note that summation convention does not apply with regard to repeated indices e on vectors and matrices. This index simply indicates the number of the element in question.

For the physical field quantities, the following definition applies:

$$\mathbf{\Phi}_j(\mathbf{x}) = \begin{bmatrix} \phi_1 & 0 & 0 & \phi_2 & 0 & 0 & \cdots & \phi_{n_e} & 0 & 0 \\ 0 & \phi_1 & 0 & 0 & \phi_2 & 0 & \cdots & 0 & \phi_{n_e} & 0 \\ 0 & 0 & \phi_1 & 0 & 0 & \phi_2 & \cdots & 0 & 0 & \phi_{n_e} \end{bmatrix}. \tag{2–5}$$

Each of the components ϕ_n, $n = 1, 2, \ldots, n_e$, is the shape function belonging to the nth element node and depends on the position $\mathbf{x}$ inside the element, $\phi_n = \phi_n(\mathbf{x})$. The shape functions are selected so that the total contributions from all nodes/shape functions of an element add up to a total of 1 at any given point interior to the element. In particular, the shape function ϕ_n should be equal to 1 at node n and achieve the value 0 at any other node. Further, the shape functions should be selected so that neighbouring elements are compatible. Examples are given below.

When selecting the weight functions, which may be considered as the shape functions for the virtual field, one may either use the shape functions which are also used for the physical field, or other interpolation functions may be used. Here, the *Galerkin method* is used, implying that the weight and shape functions are identical, *i.e.* $\mathbf{\Psi}_e(\mathbf{x}) \equiv \mathbf{\Phi}_e(\mathbf{x})$. Later, the use of other weight functions will be discussed.

For the individual element, the material is described by the mass density ρ^e and the elasticity tensor E^e_{iklm}. These properties may, or may not, vary over the element volume. In any case, the properties may be selected differently for adjacent elements in order to model local inhomogeneities. The resulting discretized equation of motion for element e may conveniently be written in the form

$$\begin{aligned} &\{\delta\mathbf{u}_e(t)\}^T \left(\int_{D_e} \{\bar{\mathbf{\nabla}}\mathbf{\Phi}_j(\mathbf{x})\}^T \mathbf{E}_e \bar{\mathbf{\nabla}}\mathbf{\Phi}_e(\mathbf{x}) \mathrm{d}V \; \mathbf{u}_e(t) + \int_{D_e} \{\mathbf{\Phi}_e(\mathbf{x})\}^T \rho_e \mathbf{\Phi}_e(\mathbf{x}) \mathrm{d}V \; \frac{\mathrm{d}^2\mathbf{u}_e(t)}{\mathrm{d}t^2} \right) \\ &\quad = \{\delta\mathbf{u}_e(t)\}^T \left(\int_{S_e} \{\mathbf{\Phi}_e(\mathbf{x})\}^T \mathbf{p}(\mathbf{x},t) \mathrm{d}S + \int_{D_e} \{\mathbf{\Phi}_e(\mathbf{x})\}^T \rho^e \mathbf{b}(\mathbf{x},t) \mathrm{d}V \right), \end{aligned} \tag{2–6}$$

where $\mathbf{p}(\mathbf{x},t)$ and $\mathbf{b}(\mathbf{x},t)$ are the surface traction and the body force with the components $p_i(\mathbf{x},t)$ and $b_i(\mathbf{x},t)$, $i = 1, 2, 3$, respectively. $\bar{\mathbf{\nabla}}$ is a matrix differential operator defined as

$$\bar{\mathbf{\nabla}} = \begin{bmatrix} \frac{\partial}{\partial x_1} & 0 & 0 & \frac{\partial}{\partial x_2} & \frac{\partial}{\partial x_3} & 0 \\ 0 & \frac{\partial}{\partial x_2} & 0 & \frac{\partial}{\partial x_1} & 0 & \frac{\partial}{\partial x_3} \\ 0 & 0 & \frac{\partial}{\partial x_3} & 0 & \frac{\partial}{\partial x_1} & \frac{\partial}{\partial x_2} \end{bmatrix}^T, \tag{2–7}$$

and $\mathbf{E}_e$ is the elasticity tensor rearranged in matrix form,

$$\mathbf{E}_e = \begin{bmatrix} E^j_{1111} & E^j_{1122} & E^j_{1133} & E^j_{1112} & E^j_{1113} & E^j_{1123} \\ E^j_{2211} & E^j_{2222} & E^j_{2233} & E^j_{2212} & E^j_{2213} & E^j_{2223} \\ E^j_{3311} & E^j_{3322} & E^j_{3333} & E^j_{3312} & E^j_{3313} & E^j_{3323} \\ E^j_{1211} & E^j_{1222} & E^j_{1233} & E^j_{1212} & E^j_{1213} & E^j_{1223} \\ E^j_{1311} & E^j_{1322} & E^j_{1333} & E^j_{1312} & E^j_{1313} & E^j_{1323} \\ E^j_{2311} & E^j_{2322} & E^j_{2333} & E^j_{2312} & E^j_{2313} & E^j_{2323} \end{bmatrix}. \tag{2–8}$$

Here, use has been made of the symmetry conditions (1–4). In particular, for a locally homogeneous and isotropic material with the Young's modulus E^e and the Poisson ratio ν^e occupying element e, the rearranged elasticity tensor is given as

$$\mathbf{E}_e = \frac{E^e}{(1+\nu^e)(1-2\nu^e)} \begin{bmatrix} 1-\nu^e & \nu^e & \nu^e & 0 & 0 & 0 \\ \nu^e & 1-\nu^e & \nu^e & 0 & 0 & 0 \\ \nu^e & \nu^e & 1-\nu^e & 0 & 0 & 0 \\ 0 & 0 & 0 & (\frac{1}{2}-\nu^e) & 0 & 0 \\ 0 & 0 & 0 & 0 & (\frac{1}{2}-\nu^e) & 0 \\ 0 & 0 & 0 & 0 & 0 & (\frac{1}{2}-\nu^e) \end{bmatrix}. \tag{2–9}$$

In this case, the Cauchy equations of motion reduce to the Navier equations, Eq. (1–10).

The stationarity condition implies that Eq. (2–6) must hold for any $\delta\mathbf{u}_e(t)$. This leads to the final FE form of the equation of motion for a single finite element,

$$\mathbf{K}_e\mathbf{u}_e(t) + \mathbf{M}_e\frac{\mathrm{d}^2\mathbf{u}_e(t)}{\mathrm{d}t^2} = \mathbf{f}_e(t). \tag{2–10}$$

$\mathbf{K}_e$ and $\mathbf{M}_e$ are the *element static stiffness matrix* and the *element mass matrix*, respectively, and $\mathbf{f}_e(t)$ represents the nodal forces applied to element e. The definitions of $\mathbf{K}_e$, $\mathbf{M}_e$ and $\mathbf{f}_e(t)$ are readily determined by a comparison of Eqs. (2–6) and (2–10). In addition to the stiffness and mass matrices, damping may be accounted for in the system. Linear viscous damping implies the introduction of an additional term proportional to the particle velocity, *i.e.*

$$\mathbf{K}_e\mathbf{u}_e(t) + \mathbf{C}_e\frac{\mathrm{d}\mathbf{u}_e(t)}{\mathrm{d}t} + \mathbf{M}_e\frac{\partial^2}{\partial t^2}\mathbf{u}_e(t) = \mathbf{f}_e(t), \tag{2–11}$$

where $\mathbf{C}_e$ is referred to as the *element damping matrix*. Usually, proportional damping is assumed, meaning that $\mathbf{C}_e$ is introduced as $\mathbf{C}_e = \eta^e\mathbf{K}_e$. This corresponds to a Kelvin model, cf. Eq. (1–122). In structural dynamics, material damping may alternatively be applied as Rayleigh damping, $\mathbf{C}_e = \alpha_e\mathbf{K}_e + \beta_e\mathbf{M}_e$. A model of this kind may not always be physically reasonable, but it provides a means of calibration to measurements.

The *assembly* of the local systems of equations is carried out by adding the contributions from all elements sharing the same degrees of freedom. This produces the system matrices $\mathbf{K}$, $\mathbf{C}$ and $\mathbf{M}$ for the entire domain, D. Thus, for a domain discretized with finite elements, the equation of motion reads

$$\mathbf{K}\mathbf{u}(t) + \mathbf{C}\dot{\mathbf{u}}(t) + \mathbf{M}\ddot{\mathbf{u}}(t) = \mathbf{f}(t), \quad \mathbf{u}(0) = \mathbf{u}_0, \quad \dot{\mathbf{u}}(0) = \dot{\mathbf{u}}_0, \tag{2–12}$$

where $\dot{\mathbf{u}}(t) = \partial \mathbf{u}(t)/\partial t$ and $\ddot{\mathbf{u}}(t) = \partial^2 \mathbf{u}(t)/\partial t^2$ are the global velocity and acceleration vectors with the dimensions $(ndof \times 1)$. The global system matrices and the load vector have the dimensions $(ndof \times ndof)$ and $(ndof \times 1)$, respectively, with $ndof$ representing the total number of degrees of freedom in the discretized domain. As a result of the Galerkin approach, the system matrices become symmetric. Furthermore, since only elements adjacent to a node give any contributions to the equations for the degrees of freedom related to the node, the system matrices in an FEM scheme become sparse. Preferably the element mesh should be constructed, *i.e.* the nodes should be numbered, so that the bandwidth of $\mathbf{K}$, $\mathbf{C}$ and $\mathbf{M}$ is reduced to a minimum.

The surface traction and the body forces applied to the boundaries and the interior of the finite continuum elements are transformed into nodal forces by use of the shape functions. Contributions from adjacent elements are added to the common nodes. Dirichlet boundary conditions of the kind $u_j(\mathbf{x}, t) = 0$ may be introduced in two different ways:

- In the stiffness matrix, the diagonal term corresponding to the constrained degree of freedom can be set to a very high value, *e.g.* 10^6 times the larger value of the diagonal terms.
- The degree of freedom is removed from the system of equations, that is row $ndof$ and column $ndof$ are eliminated.

Generally the second approach provides the better accuracy. Furthermore, the first approach has the disadvantage that it leads to very high eigenvalues of the system. This is a problem in the time integration, which is subsequently used in order to compute the displacement time series, see discussion later. The reason why the first approach is sometimes taken in the analysis of static problems is that the bookkeeping of the degrees of freedom is somewhat easier than in the second approach since all the original degrees of freedom are kept in the system.

Three-dimensional continuum finite elements

For the purpose of modelling structures with an arbitrary geometry, isoparametric continuum elements are well suited. For *hexahedral*, or brick, elements, the shape functions are defined in a local, or "homogeneous", (ξ_1, ξ_2, ξ_3)-coordinate system with origin at the centre of the element and the dimensions $2 \times 2 \times 2$. Concerning the requirement of *completeness*, a study

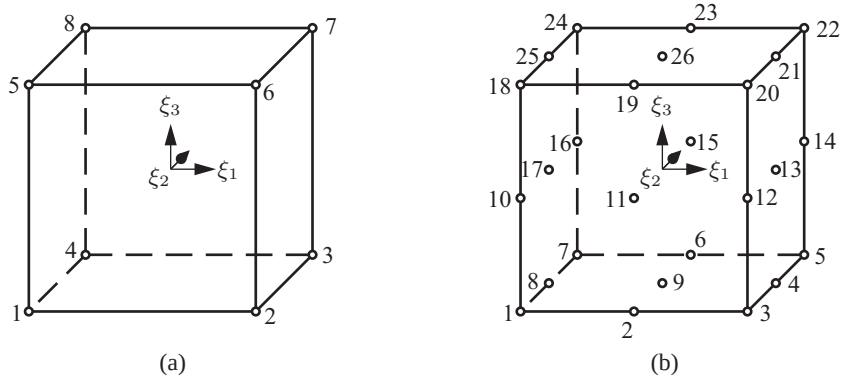

Figure 2–2 Hexahedral element with (a) 8 nodes and (b) 26 nodes.

of the integrals defining the element matrices indicates that the displacement should at least be approximated linearly. This provides a presentation of constant values of the strains within each element. Linear variation of the displacements also fulfills the *conforming requirement*, since linear interpolation of the displacement from both sides of a boundary, which is common to two elements, provides a well-defined integration of the gradients over the boundary. Continuum finite elements with linear and quadratic interpolation are illustrated in Fig. 2–2, and the shape functions for the two finite element types are given in Example 2.1 and 2.2, respectively. In theory, at least four nodes should be used to describe each wave. However, in order to achieve satisfactory results with linear elements, at least 10–12 elements (*i.e.* 10–12 nodes) should be used per wave length in practice. With quadratic interpolation, the minimum requirement is approximately 4–5 elements (8–10 nodes) per wavelength, but the accuracy is usually much higher with quadratic elements than that of linear elements when the same number of nodes is used in the computation grid.

A mapping from the homogeneous coordinates into the physical Cartesian space is carried out by means of the so-called *Jacobian*, the determinant of the matrix $\mathbf{J}$ that relates local derivatives to global derivatives,

$$\mathrm{d}V = \mathrm{d}x_1\,\mathrm{d}x_2\,\mathrm{d}x_3 = \det(\mathbf{J})\;\mathrm{d}\xi_1\,\mathrm{d}\xi_2\,\mathrm{d}\xi_3, \quad \mathbf{J} = \begin{bmatrix} \frac{\partial x_1}{\partial \xi_1} & \frac{\partial x_1}{\partial \xi_2} & \frac{\partial x_1}{\partial \xi_3} \\ \frac{\partial x_2}{\partial \xi_1} & \frac{\partial x_2}{\partial \xi_2} & \frac{\partial x_2}{\partial \xi_3} \\ \frac{\partial x_3}{\partial \xi_1} & \frac{\partial x_3}{\partial \xi_2} & \frac{\partial x_3}{\partial \xi_3} \end{bmatrix}. \tag{2–13}$$

For the isoparametric element, the integrals over the shape functions are usually carried out by means of a Gauss-Legendre quadrature rule. The number of Gauss points in each of the local coordinate directions should be sufficiently high to ensure that the polynomials that are used as the shape functions are integrated accurately. It is recalled that a Gauss quadrature with n points is accurate for polynomials of order $2n-1$. However, more Gauss points may be required in each direction than are necessary due to this condition in order to prevent spurious energy modes in the elements—the so-called *hour-glass effect*, see Fig. 2–3.

Example 2.1 Hexahedron with 8 nodes

The simplest possible hexahedral element that may be used for finite element analysis is the eight-noded element, which has linear interpolation of the geometry and the displacement field in all three local directions, ξ_1, ξ_2 and ξ_3. The shape functions for such linear elements are listed below for the node order given in Fig. 2–2a.

$$\begin{aligned}
\phi_1 &= \tfrac{1}{8}(1-\xi_1)(1-\xi_2)(1-\xi_3), \quad \phi_2 = \tfrac{1}{8}(1+\xi_1)(1-\xi_2)(1-\xi_3), \\
\phi_3 &= \tfrac{1}{8}(1+\xi_1)(1+\xi_2)(1-\xi_3), \quad \phi_4 = \tfrac{1}{8}(1-\xi_1)(1+\xi_2)(1-\xi_3), \\
\phi_5 &= \tfrac{1}{8}(1-\xi_1)(1-\xi_2)(1+\xi_3), \quad \phi_6 = \tfrac{1}{8}(1+\xi_1)(1-\xi_2)(1+\xi_3), \\
\phi_7 &= \tfrac{1}{8}(1+\xi_1)(1+\xi_2)(1+\xi_3), \quad \phi_8 = \tfrac{1}{8}(1-\xi_1)(1+\xi_2)(1+\xi_3).
\end{aligned}$$

Two Gauss points are used in each direction, even if a single Gauss point at the centre of the element would be sufficient to provide an accurate integration of a first-order polynomial. The reason is that two Gauss points are needed to prevent the hour-glass effect, see Fig. 2–3a. □

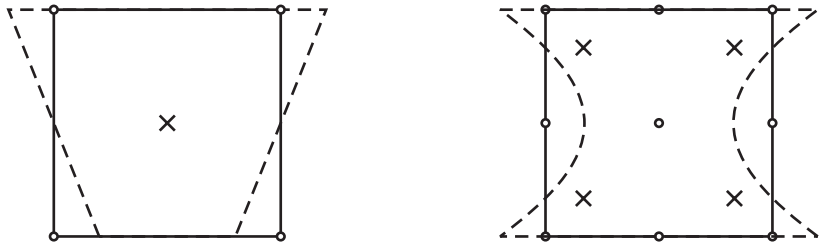

(a) (b)

Figure 2–3 Spurious energy modes (hour-glass effect) in (a) plane linear element with one Gauss point and (b) plane quadratic element with four Gauss points. The Gauss points ($\times$) do not move in the deformed state (— —) when compared with their position in the undeformed state (——).

Example 2.2 Hexahedron with 26 nodes

Continuum finite elements with quadratic interpolation in all directions generally provide better results than can be achieved with linear elements using the same number of degrees of freedom in the global system. In particular it is noted that in finite-element method analysis of elastic continua, only the displacement field is modelled. The stresses are computed from the strains, which are found as the gradients of the displacements. This means that linear interpolation of the displacements over an element implies a constant stress over the element. Therefore linear elements provide poor results in bending problems and related problems, in which the stress variation is of great importance, unless several elements are used over, for example, the thickness.

Often elements are used, which have 20 nodes—eight nodes on each side, *i.e.* one at each corner and 12 mid-edge nodes. Here, however, an alternative element is presented which has nine nodes on either side, *i.e.* including six mid-side nodes. The shape functions are defined below for the node order given in Fig. 2–2b. In order to prevent the existence of spurious energy modes, three Gauss points have to be used in each direction, see Fig. 2–3b.

$$\phi_{\ 1} = -\tfrac{1}{8}(\xi_1 - \xi_1^2)(\xi_2 - \xi_2^2)(\xi_3 - \xi_3^2), \qquad \phi_{\ 2} = \tfrac{1}{4}(1 - \xi_1^2)(\xi_2 - \xi_2^2)(\xi_3 - \xi_3^2),$$

$$\phi_{\ 3} = \tfrac{1}{8}(\xi_1 + \xi_1^2)(\xi_2 - \xi_2^2)(\xi_3 - \xi_3^2), \qquad \phi_{\ 4} = -\tfrac{1}{4}(\xi_1 + \xi_1^2)(1 - \xi_2^2)(\xi_3 - \xi_3^2),$$

$$\phi_{\ 5} = -\tfrac{1}{8}(\xi_1 + \xi_1^2)(\xi_2 + \xi_2^2)(\xi_3 - \xi_3^2), \qquad \phi_{\ 6} = -\tfrac{1}{4}(1 - \xi_1^2)(\xi_2 + \xi_2^2)(\xi_3 - \xi_3^2),$$

$$\phi_{\ 7} = \tfrac{1}{8}(\xi_1 - \xi_1^2)(\xi_2 + \xi_2^2)(\xi_3 - \xi_3^2), \qquad \phi_{\ 8} = \tfrac{1}{4}(\xi_1 - \xi_1^2)(1 - \xi_2^2)(\xi_3 - \xi_3^2),$$

$$\phi_{\ 9} = \tfrac{1}{6}(1 - \xi_1^2)(1 - \xi_2^2)(2\xi_3^2 - 3\xi_3 + 1), \qquad \phi_{10} = \tfrac{1}{4}(\xi_1 - \xi_1^2)(\xi_2 - \xi_2^2)(1 - \xi_3^2),$$

$$\phi_{11} = \tfrac{1}{6}(1 - \xi_1^2)(2\xi_2^2 - 3\xi_2 + 1)(1 - \xi_3^2), \qquad \phi_{12} = -\tfrac{1}{4}(\xi_1 + \xi_1^2)(\xi_2 - \xi_2^2)(1 - \xi_3^2),$$

$$\phi_{13} = \tfrac{1}{6}(2\xi_1^2 + 3\xi_1 + 1)(1 - \xi_2^2)(1 - \xi_3^2), \qquad \phi_{14} = \tfrac{1}{4}(\xi_1 + \xi_1^2)(\xi_2 + \xi_2^2)(1 - \xi_3^2),$$

$$\phi_{15} = \tfrac{1}{6}(1 - \xi_1^2)(2\xi_2^2 + 3\xi_2 + 1)(1 - \xi_3^2), \qquad \phi_{16} = -\tfrac{1}{4}(\xi_1 - \xi_1^2)(\xi_2 + \xi_2^2)(1 - \xi_3^2),$$

$$\phi_{17} = \tfrac{1}{6}(2\xi_1^2 - 3\xi_1 + 1)(1 - \xi_2^2)(1 - \xi_3^2), \qquad \phi_{18} = \tfrac{1}{8}(\xi_1 - \xi_1^2)(\xi_2 - \xi_2^2)(\xi_3 + \xi_3^2),$$

$$\phi_{19} = -\tfrac{1}{4}(1 - \xi_1^2)(\xi_2 - \xi_2^2)(\xi_3 + \xi_3^2), \qquad \phi_{20} = -\tfrac{1}{8}(\xi_1 + \xi_1^2)(\xi_2 - \xi_2^2)(\xi_3 + \xi_3^2),$$

$$\phi_{21} = \tfrac{1}{4}(\xi_1 + \xi_1^2)(1 - \xi_2^2)(\xi_3 + \xi_3^2), \qquad \phi_{22} = \tfrac{1}{8}(\xi_1 + \xi_1^2)(\xi_2 + \xi_2^2)(\xi_3 + \xi_3^2),$$

$$\phi_{23} = \tfrac{1}{4}(1 - \xi_1^2)(\xi_2 + \xi_2^2)(\xi_3 + \xi_3^2), \qquad \phi_{24} = -\tfrac{1}{8}(\xi_1 - \xi_1^2)(\xi_2 + \xi_2^2)(\xi_3 + \xi_3^2),$$

$$\phi_{25} = -\tfrac{1}{4}(\xi_1 - \xi_1^2)(1 - \xi_2^2)(\xi_3 + \xi_3^2), \qquad \phi_{26} = \tfrac{1}{6}(1 - \xi_1^2)(1 - \xi_2^2)(2\xi_3^2 + 3\xi_3 + 1). \qquad \square$$

2.1.3 Finite element formulation of beams

In the analysis of structures composed of beam and plate-like structural elements, continuum finite elements are inefficient because a huge number of elements are required due to the fact that a discretization in all three spatial coordinate directions is necessary. Therefore, elements are used which reduce the problems to two-dimensional (plate/shell) or one-dimensional (beam) problems with respect to the discretization. The material behaviour in the directions, which are not modelled, is described in terms of forces and moments rather than stresses.

Here, an example will be given for the simplest possible beam theory, which is due to Euler and Bernoulli (E-B beam theory). The example only serves as a guide to the finite element formulation of structural elements, well knowing that the E-B beam theory is not well suited for the analysis of dynamic problems, as will be discussed later.

The finite element formulation will be given for an E-B beam resting on a so-called *Kelvin-Pasternak foundation*. A linear Pasternak foundation, which is considered here, includes the linear shear stiffness $K(x)$ in addition to the linear vertical stiffness $\kappa(x)$ that is present in a linear Winkler foundation. The Kelvin part refers to the fact that damping is present in the support, in this case both vertical damping $\gamma(x)$ and shear damping $G(x)$, both of which are assumed to be linear viscous. The model is shown in Fig. 2–4, where $w = w(x,t)$ is the vertical displacement field relative to the state of static equilibrium, t is time, $m(x)$ is the mass per unit length and $f = f(x,t)$ is the additive load. Further, with the directions defined in Fig. 2–4, the rotation, the moment and the shear force are defined as

$$\theta(x,t) = -\frac{\partial w(x,t)}{\partial x}, \quad M(x,t) = -EI\frac{\partial^2 w(x,t)}{\partial x^2}, \quad Q(x,t) = -EI\frac{\partial^3 w(x,t)}{\partial x^3}. \tag{2–16}$$

Normal forces and axial displacements are not considered. For the vertical motion, *i.e.* bending, the *strong formulation* is given as

$$\begin{aligned}&\frac{\partial^2}{\partial x^2}\left(EI(x)\frac{\partial^2 w(x,t)}{\partial x^2}\right) - \frac{\partial}{\partial x}\left(G(x)\frac{\partial^2 w(x,t)}{\partial x \partial t}\right) - \frac{\partial}{\partial x}\left(K(x)\frac{\partial w(x,t)}{\partial x}\right)\\ &\quad + m(x)\frac{\partial^2 w(x,t)}{\partial t^2} + \gamma(x)\frac{\partial w(x,t)}{\partial t} + \kappa(x)w(x,t) = f(x,t).\end{aligned} \tag{2–17}$$

The derivation of Eq. (2–17) is based on a dynamic equilibrium in the vertical direction, *i.e.* perpendicular to the beam axis, of an infinitesimal element of the beam. The mechanical system described by Eq. (2–17) may be applied as a simple model of, for example, a road or a track.

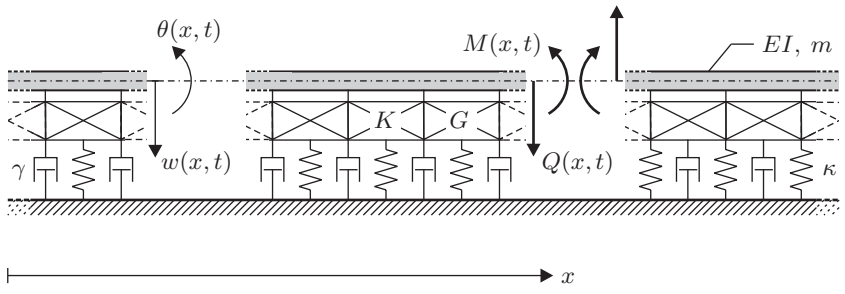

Figure 2–4 Euler-Bernoulli beam on a Kelvin-Pasternak foundation.

The *weak formulation* of the problem is reached by multiplication of Eq. (2–17) with an arbitrary weight function, or virtual field, $\delta w = \delta w(x,t)$, and integration over the length of the beam. Denoting the endpoints of the beam by x_b^- and x_b^+, and integrating the first term by parts, this provides

$$\int_{x_b^-}^{x_b^+} \left\{ \frac{\partial^2 \delta w}{\partial x^2} EI(x) \frac{\partial^2 w}{\partial x^2} + \frac{\partial \delta w}{\partial x} \left(K(x) \frac{\partial w}{\partial x} + G(x) \frac{\partial \dot{w}}{\partial x} \right) \right.$$
$$\left. + \delta w(x,t) \big(m(x) \ddot{w}(x,t) + \gamma(x) \dot{w}(x,t) - \kappa(x) w(x,t) \big) \right\} dx - \left[\delta w \left(G \frac{\partial \dot{w}}{\partial x} + K \frac{\partial w}{\partial x} \right) \right]_{x_b^-}^{x_b^+}$$
$$= \int_{x_b^-}^{x_b^+} \delta w(x,t) f(x,t) dx + \left[\delta w(x,t) Q(x,t) - \frac{\partial \delta w}{\partial x} M(x,t) \right]_{x_b^-}^{x_b^+}, \tag{2–18}$$

where $\dot{w} = \dot{w}(x,t)$ and $\ddot{w} = \ddot{w}(x,t)$ denote the first and second derivative of the displacement with respect to time, *i.e.* the velocity and acceleration.

Next, the physical and the virtual displacement fields are discretized. For an element with the end points x_e^- and x_e^+ an approximation is introduced via the shape and weight functions, $\mathbf{\Phi}_e(x)$ and $\mathbf{\Psi}_e(x)$,

$$w(x,t) = \mathbf{\Phi}_e(x) \mathbf{z}_e(t), \quad \delta w(x,t) = \mathbf{\Psi}_e(x) \delta \mathbf{z}_e(t), \quad x \in [x_e^-, x_e^+]. \tag{2–19}$$

Vectors $\mathbf{z}_e(t)$ and $\delta \mathbf{z}_e(t)$ store the degrees of freedom for the element. Equation (2–19) is inserted into Eq. (2–18) on an element basis. The stationarity condition of the variation principle implies that the integral equation must hold for any choice of the virtual field satisfying the essential boundary conditions and therefore for an arbitrary vector $\delta \mathbf{z}_e(t)$. Thus, the finite element form of the equation of motion for a single finite element becomes

$$\mathbf{M}_e \ddot{\mathbf{z}}_e + \mathbf{C}_e \dot{\mathbf{z}}_e + \mathbf{K}_e \mathbf{z}_e = \mathbf{f}_e + \mathbf{b}_e, \tag{2–20}$$

where the element matrices $\mathbf{M}_e$, $\mathbf{C}_e$, $\mathbf{K}_e$, and the element load vectors $\mathbf{f}_e = \mathbf{f}_e(t)$ and $\mathbf{b}_e = \mathbf{b}_e(t)$ are defined as

$$\mathbf{M}_e = \int_{x_e^-}^{x_e^+} \mathbf{\Psi}_e^T m \mathbf{\Phi}_e \, \mathrm{d}x, \tag{2–21}$$

$$\mathbf{C}_e = \int_{x_e^-}^{x_e^+} \left\{ \mathbf{\Psi}_e^T \gamma \mathbf{\Phi}_e + \frac{\mathrm{d}\mathbf{\Psi}_e^T}{\mathrm{d}x} G \frac{\mathrm{d}\mathbf{\Phi}_e}{\mathrm{d}x} \right\} \mathrm{d}x - \left[\mathbf{\Psi}_e^T G \frac{\mathrm{d}\mathbf{\Phi}_e}{\mathrm{d}x} \right]_{x_e^-}^{x_e^+}, \tag{2–22}$$

$$\mathbf{K}_e = \int_{x_e^-}^{x_e^+} \left\{ \frac{\mathrm{d}^2\mathbf{\Psi}_e^T}{\mathrm{d}x^2} EI \frac{\mathrm{d}^2\mathbf{\Phi}_e}{\mathrm{d}x^2} + \mathbf{\Psi}_e^T \kappa \mathbf{\Phi}_e + \frac{\mathrm{d}\mathbf{\Psi}_e^T}{\partial x} K \frac{\mathrm{d}\mathbf{\Phi}_e}{\mathrm{d}x} \right\} \mathrm{d}x - \left[\mathbf{\Psi}_e^T K \frac{\mathrm{d}\mathbf{\Phi}_e}{\mathrm{d}x} \right]_{x_e^-}^{x_e^+}, \tag{2–23}$$

$$\mathbf{f}_e = \int_{x_e^-}^{x_e^+} \mathbf{\Psi}_e^T f(x,t) \mathrm{d}x, \qquad \mathbf{b}_e = \left[\mathbf{\Psi}_e^T Q(x,t) - \frac{\partial \mathbf{\Psi}_e^T}{\mathrm{d}x} M(x,t) \right]_{x_e^-}^{x_e^+}. \tag{2–24}$$

The *completeness criterion* demands that the *shape functions* for the displacements should be selected so that at least an arbitrary constant stress state in a beam element can be described.

A translation or a rotation of a beam element will not give rise to any internal deformation of the element. Thus the description of an arbitrary constant stress state requires that a constant curvature can be modelled over each element, *i.e.* the displacement should at least be described by a second-order polynomial inside each element.

However, a further study of the weak formulation, *i.e.* Eq. (2–18), shows that the integral of the second derivative of the displacement must be well-defined over the element boundaries. This can only be achieved if not only the displacements, but also the rotations (*i.e.* the first-order derivatives) are continuous over the element boundaries. This requires that the shape functions are at least polynomials of the order three, $w(x,t) = p_0(t) + p_1(t)x + p_2(t)x^2 + p_3(t)x^3$. The calibration of the four coefficients p_i, $i = 0,1,2,3$, requires the presence of four degrees of freedom, or unknowns, in each element. A natural choice is the end-displacements $w_e^-(t) = w(x_e^+,t)$, $w_e^+(t) = w(x_e^-,t)$ and the end-rotations $\theta_e^-(t) = \theta(x_e^-,t)$, $\theta_e^+(t) = \theta(x_e^+,t)$, since in this way the requirements of continuous displacements and rotations over the element boundaries can easily be enforced. With the definition $z_{e,1} = w_e^-(t)$, $z_{e,2} = \theta_e^-(t)$, $z_{e,3} = w_e^+(t)$ and $z_{e,4} = \theta_e^+(t)$, the shape functions become

$$\phi_{e,1}(x_e) = 1 - 3\frac{x_e^2}{L_e^2} + 2\frac{x_e^3}{L_e^3}, \qquad \phi_{e,2}(x_e) = x_e\left(1 - 2\frac{x_e}{L_e} + \frac{x_e^2}{L_e^2}\right), \tag{2–25}$$

$$\phi_{e,3}(x_e) = \frac{x_e^2}{L_e^2}\left(3 - 2\frac{x_e}{L_e}\right), \qquad \phi_{e,4}(x_e) = \frac{x_e^2}{L_e}\left(\frac{x_e}{L_e} - 1\right), \tag{2–26}$$

where $L_e = |x_e^+ - x_e^-|$ is the element length and $x_e = x - x_e^-$ is a local coordinate ranging between 0 and L_e. The integrals defining the system matrices can now be evaluated analytically. The *Hermite* shape functions given by Eqs. (2–25) and (2–26) are cubic. Thus, generally the number of Euler beam elements required per wave length is small when compared to the required number of linear or quadratic elements used in continuum dynamics. Three elements (*i.e.* six nodes) are in most cases sufficient.

Example 2.3 Wave components in an Euler-Bernoulli beam on a Kelvin-Pasternak foundation

An analytical solution for the wave propagation in an Euler-Bernoulli beam on a Kelvin-Pasternak foundation is to be established in the frequency–wavenumber domain. For this purpose, the following definition of the Fourier transforms with respect to space and time will be used:

$$A(k,\omega) = \int_{-\infty}^{\infty} \breve{A}(x,\omega)\mathrm{e}^{-\mathrm{i}kx}dx, \quad \breve{A}(x,\omega) = \int_{-\infty}^{\infty} a(x,t)\mathrm{e}^{+\mathrm{i}\omega t}dt, \tag{a}$$

where, with reference to Eq. (2–17), $a = u$ or $a = f$. The inverse transforms are given as

$$a(x,t) = \frac{1}{2\pi}\int_{-\infty}^{\infty} \breve{A}(x,\omega)\mathrm{e}^{-\mathrm{i}\omega t}d\omega, \quad \breve{A}(x,\omega) = \frac{1}{2\pi}\int_{-\infty}^{\infty} A(k,\omega)\mathrm{e}^{+\mathrm{i}kx}dk. \tag{b}$$

As discussed in Subsection 1.3.2 the harmonic variation of type $\mathrm{e}^{+\mathrm{i}\omega t}$ is not standard in Fourier transformation. However, a positive real wavenumber k leads to wave propagation in the positive x-direction, since the circular frequency ω is supposed to be real and positive.

Carrying out the Fourier transform with respect to time only, the equation of motion for the beam is reduced to an ordinary differential equation in x, *(continued)*

$$EI\frac{\mathrm{d}^4\breve{U}}{\mathrm{d}x^4} - m\omega^2\breve{U} - K\frac{\mathrm{d}^2\breve{U}}{\mathrm{d}x^2} + \mathrm{i}\omega G\frac{\mathrm{d}^2\breve{U}}{\mathrm{d}x^2} - \mathrm{i}\omega\gamma\breve{U} + \kappa\breve{U} = \breve{F}. \tag{c}$$

In the following, the solution will be established for a point force, which is assumed to vary harmonically with time at the circular frequency ω, thereby giving rise to bending waves in the beam that may, or may not, propagate as travelling waves into the far-field. In other words, we are aiming at the *frequency-domain Green's function* for the beam on the viscoelastic foundation, similar to the Green's function for the elastic half-space derived in Example 1.6. The solution for a distributed load may easily be derived by an integration over the length of the loaded region. Likewise, if the load is periodic with more than one frequency, a solution may be derived by means of Fourier transformation. Without loss of generality, the load is assumed to be located at $y = 0$, *i.e.* $f(x,t) = P\delta(x)\mathrm{e}^{-\mathrm{i}\omega t}$ or $\breve{F}(x,\omega) = P\delta(x)$.

A fundamental solution set to the homogeneous part of Eq. (c) may be found in the form

$$\breve{U}_n(x,\omega) = U_n\mathrm{e}^{\mathrm{i}k_n x}, \qquad n = 1,2,3,4. \tag{d}$$

Here $U_n = U_n(\omega)$ are the amplitudes of the wave components at $x = 0$ (which in the homogeneous equation are arbitrary integration constants) and $k_n = k_n(\omega)$ are the corresponding wavenumbers. Both U_n and k_n are generally complex. Since the excitation, and therefore also the response, is assumed to be harmonic, the corresponding solutions to Eq. (2–17) are given in the form

$$u_n(x,t) = U_n\mathrm{e}^{\mathrm{i}(k_n x - \omega t)}, \qquad n = 1,2,3,4. \tag{e}$$

Note that only the real part of $u_n(x,t)$ is interpreted as the physical displacement field.

Insertion of a solution component of type (d) into Eq. (c) leads to the characteristic polynomial

$$k_n^4 + \frac{G - \mathrm{i}\omega D}{EI}k_n^2 + \frac{\kappa - m\omega^2 - \mathrm{i}\omega\gamma}{EI} = 0, \tag{f}$$

from which the four wavenumbers k_n, $n = 1,2,3,4$, are determined. Evidently, the wavenumbers form two pairs of complex conjugates.

Alternatively, the complex wavenumbers are written in terms of their real and imaginary parts,

$$k_n = k_n^p + \mathrm{i}k_n^a, \qquad k_n^p = \Re(k_n), \qquad k_n^a = \Im(k_n), \qquad n = 1,2,3,4, \tag{g}$$

where $\Re(\cdot)$ and $\Im(\cdot)$ denote the real and imaginary part of the argument, respectively. With the chosen definition of the wave field, k_n^p represents propagation and k_n^a represent attenuation of the nth wave component. It turns out that one of the wavenumbers always has a nonpositive imaginary part. This wavenumber will be referred to as k_1. Another wavenumber, k_2, has either a negative imaginary part or is positive and real. More interestingly, however, k_2 is a monotone decreasing function of ω. A third wavenumber always has a nonnegative imaginary part. This wavenumber will be addressed k_3. Finally k_4 has either a positive imaginary part or is a positive real and monotone increasing function of ω. The nature of the wavenumbers is further discussed below.

Physically, only solutions with finite displacement amplitudes in the far-field are acceptable. Further, waves without attenuation, or rather the energy contained therein, must propagate away from the source. The direction of energy transportation is dictated by the so-called group velocity $c_{g\,n}$ and not by the phase velocity c_n. With reference to Eqs. (1–108) and (1–109), the following definitions apply:

$$c_n = \frac{\omega}{k_n^p}, \qquad c_{g\,n} = \frac{\partial\omega}{\partial k_n^p}, \qquad n = 1,2,3,4. \tag{h}$$

It is noted that, in the case of the beam on the elastic foundation, the phase velocities are frequency dependent, *i.e.* the waves are dispersive, and the phase and group velocities are generally not identical. This is expected since the beam serves as a wave guide in the same manner as an elastic layer over bedrock. Further similarities exist between the two models as will be discussed below. *(continued)*

Given the requirements on the wavenumbers, the displacement fields on either side of the source contain two of the mathematically valid solutions,

$$u(x,t) = \begin{cases} U_1(\omega)\mathrm{e}^{-k_1^a x + \mathrm{i}\left(k_1^p x - \omega t\right)} + U_2(\omega)\mathrm{e}^{-k_2^a x + \mathrm{i}\left(k_2^p x - \omega t\right)} & \text{for} \quad x \leqslant 0 \\ U_3(\omega)\mathrm{e}^{-k_3^a x + \mathrm{i}\left(k_3^p x - \omega t\right)} + U_4(\omega)\mathrm{e}^{-k_4^a x + \mathrm{i}\left(k_4^p x - \omega t\right)} & \text{for} \quad x > 0 \end{cases} \tag{i}$$

where, to summarize, the following characteristics apply:

$$\left.\begin{array}{llll} k_1^a \leqslant 0, & k_2^a < 0 & \vee & k_2^a = 0,\ k_2^p < 0 \\ k_3^a \geqslant 0, & k_4^a > 0 & \vee & k_4^a = 0,\ k_4^p > 0 \end{array}\right\}. \tag{j}$$

Alternatively the 3rd and 4th wave component could be used for $x = y$. A summation of all four components is inappropriate, since this would imply a discontinuity of the displacement field under the load. Once the wave components, which are present on either side of the load, have been identified, the amplitudes $U_n(\omega)$, $n = 1, 2, 3, 4$, can be determined. The displacement field $u(x,t)$, the rotation $\theta(x,t)$ and the moment $M(x,t)$ must be continuous across the source point $y = 0$, whereas a jump of the magnitude P must be present in the shear force $Q(x,t)$. With the definitions given by Eq. 2–16, the requirements formulated above may be written as

$$\begin{bmatrix} -1 & -1 & 1 & 1 \\ -\mathrm{i}k_1 & -\mathrm{i}k_2 & \mathrm{i}k_3 & \mathrm{i}k_4 \\ -(\mathrm{i}k_1)^2 & -(\mathrm{i}k_2)^2 & (\mathrm{i}k_3)^2 & (\mathrm{i}k_4)^2 \\ -(\mathrm{i}k_1)^3 & -(\mathrm{i}k_2)^3 & (\mathrm{i}k_3)^3 & (\mathrm{i}k_4)^3 \end{bmatrix} \begin{bmatrix} U_1 \\ U_2 \\ U_3 \\ U_4 \end{bmatrix} = \begin{bmatrix} 0 \\ 0 \\ 0 \\ P/EI \end{bmatrix}. \tag{k}$$

With the amplitudes defined by Eq. (k), the full solution given in Eq. (i) satisfies the inhomogeneous equation of motion. □

One of the main results of the analytic solution for a point force on a beam system given in Ex. 2.3 is the fact that waves in an Euler-Bernoulli beam are dispersive. A further study of the special case with no material dissipation indicates the presence of two characteristic frequencies,

$$\omega_{cn} = \sqrt{\frac{\kappa}{m}}, \quad \omega_{cf} = \omega_{cn}\left(1 - \chi^2\right), \quad \chi = \frac{K}{\sqrt{4EI\kappa}}. \tag{2–28}$$

Here ω_{cn} is identified as the *cut-on frequency*. Only for excitation with a frequency higher than ω_{cn} do travelling waves exist which, in the case of no material dissipation, propagate into the far field without attenuation. As discussed in Subsection 1.6.1, such a cut-on frequency has also been identified for an elastic layer over bedrock. Alternatively, ω_{cn} may be regarded as a *critical frequency*, since the amplitude of the total response becomes infinite when the excitation is applied with a frequency equal to ω_{cn}. ω_{cf} serves as a *cut-off frequency* which is lower than ω_{cn} when shear stiffness is present in the foundation. For excitation with a frequency lower than ω_{cf}, the waves will be evanescent waves, but with wavenumbers containing a real part. However, for an excitation frequency $\omega_{cf} < \omega < \omega_{cn}$ the wavenumbers are purely imaginary. Note that the cut-on frequency only depends on the vertical stiffness of the Pasternak foundation, whereas the cut-off frequency also depends on the shear stiffness.

2.2 Solution in the time domain

Transient dynamic problems are either solved directly in the time domain, or an indirect solution is carried out in the frequency domain by means of Fourier transformation of the governing equation of motion. The latter technique implies that the time history of the displacements must be found subsequently be inverse Fourier transformation. In this section, only time-domain solutions are discussed, while the second approach involving a solution in frequency domain is treated in the next section.

The finite element formulation of a dynamic system with mass, linear viscous damping and linear stiffness may be written as:

$$\mathbf{M}\ddot{\mathbf{z}}(t) + \mathbf{C}\dot{\mathbf{z}}(t) + \mathbf{K}\mathbf{z}(t) = \mathbf{f}(t), \quad \mathbf{z}(0) = \mathbf{z}_0, \quad \dot{\mathbf{z}}(0) = \dot{\mathbf{z}}_0, \tag{2–29}$$

where $\mathbf{M}$, $\mathbf{C}$ and $\mathbf{K}$ denote the mass, damping and stiffness matrices, while $\mathbf{z}(t)$, $\dot{\mathbf{z}}(t)$ and $\ddot{\mathbf{z}}(t)$ are the displacement, velocity and acceleration vectors. $\mathbf{z}_0$ and $\dot{\mathbf{z}}_0$ are the initial conditions for the displacements and velocities, respectively. These must be given for each degree of freedom in the system. Equation (2–29) represents a static equilibrium of the inertia forces, the viscous forces, the elastic forces (which are all internal forces) and the additive, or external, forces.

In a continuum problem, the degrees of freedom are typically the three displacements at each node. Thus, in this case $\mathbf{z}(t) = \mathbf{u}(t)$ etcetera. On the other hand, in analyses involving structural elements such as beam elements, $\mathbf{z}(t)$ may also store rotations in addition to the displacements at each node. For this reason, $\mathbf{z}(t)$ will be referred to as the *generalized* displacements.

In the finite element formulation of the equation of motion given by Eq. (2–29), the continuous field has been discretized in space, *i.e.* and approximation of the field quantities is carried out over the spatial coordinates by means of shape, or interpolation, functions. The idea of a time-domain solution by means of numerical time integration is to further discretize the displacements etc. in time. Thus, in addition to the element dimensions $\Delta\mathbf{x}$ (which in the FE beam model is equal to the element length), a temporal increment, Δt is introduced. Subsequently, the generalized displacements and velocities are computed at a certain time step t_{j+1} from the displacements and velocities at the previous time step(s), at which the displacements and velocities are known.

When performing the time integration over the time interval Δt from the time t_j to the succeeding time t_{j+1}, the variation of $\dot{\mathbf{Z}}(t)$ may be selected in different ways. This is analogous to the fact that different shape function may be used in the spatial discretization process. Depending on the choice of "temporal shape function", different integration schemes are produced, which give different approximations of the Taylor expansions of the generalized acceleration and velocity vectors. The integration scheme is referred to as

- an *explicit* scheme if only previous values of the displacements, velocities and external loads are required for the computation of the similar quantities at a subsequent time step,
- an *implicit* scheme if the degrees of freedom at a given time step depend on each other.

Further, the terminology *direct* time integration is used when Eq. (2–29) is solved in its original form, while *indirect* time integration implies that Eq. (2–29) has to be transformed into the state-space equivalent. A number of integration schemes will be presented below. Firstly, however, some general considerations in time integration will be discussed.

2.2.1 Selecting the time step

In the same way that a finite element scheme for static analysis provides an exact solution in the limit as $\Delta\mathbf{x} \to \mathbf{0}$, any dynamic FEM scheme leads to an accurate solution for $\Delta\mathbf{x} \to \mathbf{0}$ and $\Delta t \to 0$. The challenge is to formulate a time integration scheme that will still provide an accurate solution when a large time step is used. In this respect, a number of considerations should be made with concern to both the physics of the problem and the numerical solution.

Accuracy of a numerical integration scheme

As the ratio $\Delta t/T$ (T being the characteristic wave period) increases, the accuracy of a numerical integration scheme decreases. In particular, two phenomenons may be observed:

- *Period elongation* involves that the numerical scheme predicts a wave period which is too long when compared to the wave period in the exact solution.
- *Numerical dissipation* involves that the amplitudes of the response predicted by the numerical scheme decay with time, even if no material dissipation is present in the physical problem.

These numerical errors are quite pronounced in some schemes, *i.e.* with certain choices of the temporal shape functions, whereas other schemes will lead to smaller numerical errors, *i.e.* larger time steps can be used with the same accuracy.

The Courant condition

In order to ensure an accurate and stable solution in wave propagation problems, Δt must be sufficiently small to ensure that a wave does not move through an element without being noticed. For wave propagation in a given direction, the largest allowable time step is provided by the *Courant condition*,

$$\frac{c\Delta t}{h} = C, \quad C \leq 1, \tag{2–30}$$

where c and h represent a characteristic set of wave propagation speed and spatial increment (*i.e.* element size), and C is the *Courant number*. In acoustics, only a single wave type exists. Hence, Eq. (2–30) is uniquely defined. In problems involving different wave types, such as the P- and S-waves in elastic media, the time step is dictated by the highest wave velocity, whereas the element size depends on the lowest wave velocity, since the wave length is given as $L = cT$. Consequently, if there is a great difference between the highest and the lowest velocity of the waves in a given problem, the numerical solution in time domain by means of time integration requires relatively small element sizes and small time steps. However, depending on the kind of numerical integration being used, further requirements may be put on the time step in order to achieve a stable and accurate solution.

2.2.2 Indirect time integration

Standard numerical solvers for differential equations, such as the Euler method, may be used for the time integration in dynamic finite-element analysis. However, this involves a reformulation of the original system of ordinary second-order differential equations in time into first-order differential equations. Thus, defining the state vector $\mathbf{Z}(t) = [\mathbf{z}(t)\ \dot{\mathbf{z}}(t)]^T$, Eq. (2–29) for a system with N degrees of freedom may be rewritten in the form

$$\dot{\mathbf{Z}}(t) = \mathbf{A}\mathbf{Z}(t) + \mathbf{B}\mathbf{F}(t), \tag{2–31}$$

where

$$\mathbf{A} = \begin{bmatrix} \mathbf{0}_{(N\times N)} & \mathbf{I}_{(N\times N)} \\ -\mathbf{M}^{-1}\mathbf{K} & -\mathbf{M}^{-1}\mathbf{C} \end{bmatrix}, \quad \mathbf{F}(t) = \begin{bmatrix} \mathbf{0}_{(N\times 1)} \\ \mathbf{M}^{-1}\mathbf{f}(t) \end{bmatrix}. \tag{2–32}$$

Here $\mathbf{0}_{(N\times N)}$ and $\mathbf{I}_{(N\times N)}$ are the zero matrix and identity matrix, respectively, of the same dimensions as $\mathbf{M}$, $\mathbf{C}$ and $\mathbf{K}$. $\mathbf{0}_{(N\times 1)}$ is the zero vector of the same dimension as $\mathbf{z}(t)$ and $\mathbf{f}(t)$. Thus the subscripts in the parentheses indicate dimensions of the matrices/vectors.

Low-order explicit time integration methods such as the Euler method (based on a rectangular rule) necessitate the use of an extremely small time step in order to achieve a stable and accurate solution. Therefore, only higher-order explicit solutions and implicit solutions are of practical interest from a computational point of view. In the following, two examples will be given of indirect time integration techniques in order to illustrate the explicit and implicit methods.

The Runge-Kutta fourth order algorithm

A fourth-order integration technique based on the Simpson rule was suggested by Runge and Kutta (Kreyszig 1999) and provides an integration scheme which is explicit in time. For each time step, $t = t_j$, the following vectorial quantities are computed:

$$\mathbf{k}_1 = \Delta t\dot{\mathbf{Z}}(t, \mathbf{Z}(t)) = \Delta t\dot{\mathbf{Z}}(t_j, \mathbf{Z}_j), \tag{2–33}$$

$$\mathbf{k}_2 = \Delta t\dot{\mathbf{Z}}(t + 0.5\Delta t, \mathbf{Z}(t) + 0.5\mathbf{k}_1) = \Delta t\dot{\mathbf{Z}}(t_j + 0.5\Delta t, \mathbf{Z}_j + 0.5\mathbf{k}_1), \tag{2–34}$$

$$\mathbf{k}_3 = \Delta t\dot{\mathbf{Z}}(t + 0.5\Delta t, \mathbf{Z}(t) + 0.5\mathbf{k}_2) = \Delta t\dot{\mathbf{Z}}(t_j + 0.5\Delta t, \mathbf{Z}_j + 0.5\mathbf{k}_2), \tag{2–35}$$

$$\mathbf{k}_4 = \Delta t\dot{\mathbf{Z}}(t + \Delta t, \mathbf{Z}_j + \mathbf{k}_3) = \Delta t\dot{\mathbf{Z}}(t_{j+1}, \mathbf{Z}_j + \mathbf{k}_3), \tag{2–36}$$

where $\mathbf{Z}_j = \mathbf{Z}(t_j)$. Next, the (generalized) displacement vector for time step t_{j+1} is found as

$$\mathbf{Z}(t_{j+1}) = \mathbf{Z}_{j+1} = \mathbf{Z}_j + \frac{1}{6}\left(\mathbf{k}_1 + 2\mathbf{k}_2 + 2\mathbf{k}_3 + \mathbf{k}_4\right). \tag{2–37}$$

The primary disadvantage of the Runge-Kutta scheme is that the numerical solution is only *conditionally stable*. This implies that the time step has to be selected smaller than a certain critical value depending on the smallest eigenperiod of the system, *i.e.* $\Delta t \leqslant \Delta t_{cr}$. If a time step larger than the critical time step is used, an unstable solution is achieved. Unfortunately the critical time step in a conditionally stable integration scheme is usually much smaller than the time step dictated by the Courant condition.

The Crank-Nicolson scheme

Another approach to the indirect time integration is to formulate a numerical solution as a Taylor series expansion of an analytic solution. This leads to a solution, which is implicit in time,

$$\mathbf{Z}_{j+1} = \mathbf{D}_Z\mathbf{Z}_j + \mathbf{D}_F\left(\mathbf{F}_j + \mathbf{F}_{j+1}\right), \tag{2–38}$$

$$\mathbf{D}_Z = \left(2\mathbf{I} - \mathbf{A}\Delta t\right)^{-1}\left(2\mathbf{I} + \mathbf{A}\Delta t\right), \quad \mathbf{D}_F = \frac{1}{6}\left(2\mathbf{I} - \mathbf{A}\Delta t\right)^{-1}\left(6\mathbf{I} + \mathbf{A}\Delta t\right)\mathbf{B}\Delta t. \tag{2–39}$$

A derivation of this so-called *Crank-Nicolson* scheme is given in Example 2.4.

The integration scheme defined by Eq. (2–38) implies that the external forces must be known, not only at the current time step t_j, but also at the succeeding time step t_{j+1} at which the state is to be found. In practice, this means that the entire history of the additive load has to be known beforehand. The Crank-Nicolson scheme has the advantage when compared to the Runge-Kutta method that it is unconditionally stable. Therefore the time step only has to satisfy the Courant condition. However, a large time step will still lead to an inaccurate numerical solution. One of the reasons is the increasing period elongation with increasing time step.

Example 2.4 Derivation of the Crank-Nicolson scheme

Let λ_j and $\mathbf{v}_j$, $j = 1, 2, \ldots, 2N$, denote the $2N$ eigenvalues and the corresponding eigenvectors of the system matrix $\mathbf{A}$. It then follows that

$$\mathbf{AV} = \mathbf{V}\boldsymbol{\Lambda}^1, \quad \mathbf{V} = \begin{bmatrix} \mathbf{v}_1 & \mathbf{v}_2 & \cdots & \mathbf{v}_{2N} \end{bmatrix}, \quad \boldsymbol{\Lambda}^n = \begin{bmatrix} \lambda_1^n & & & \\ & \lambda_2^n & & \\ & & \ddots & \\ & & & \lambda_{2N}^n \end{bmatrix}, \tag{a}$$

from which it is readily seen that $\mathbf{A} = \mathbf{V}\boldsymbol{\Lambda}\mathbf{V}^{-1}$. Thus, the product of n system matrices becomes $\prod_{j=1}^{n} \mathbf{A} = \mathbf{V}\boldsymbol{\Lambda}^n\mathbf{V}^{-1}$. Next, the matrix exponential function $\mathrm{e}^{\mathbf{A}t}$ is defined in terms of its Maclaurin expansion,

$$\mathrm{e}^{\mathbf{A}t} = \mathbf{I} + \mathbf{A}t + \frac{1}{2}\mathbf{AA}t^2 + \frac{1}{6}\mathbf{AAA}t^3 + \ldots = \mathbf{V}\left(\mathbf{I} + \boldsymbol{\Lambda}t + \frac{1}{2}\boldsymbol{\Lambda}^2t^2 + \frac{1}{6}\boldsymbol{\Lambda}^3t^3 + \ldots\right)\mathbf{V}^{-1}, \tag{b}$$

from which it follows that $\mathrm{e}^{\mathbf{A}t} = \mathbf{V}\mathrm{e}^{\boldsymbol{\Lambda}t}\mathbf{V}^{-1}$, where $\mathrm{e}^{\boldsymbol{\Lambda}t}$ is a diagonal matrix with the components $\mathrm{e}^{\lambda_j t}$, $j = 1, 2, \ldots, 2N$, along the diagonal. The commutative rule applies to the product of two diagonal matrices. Hence, $\mathbf{A}\mathrm{e}^{\mathbf{A}t} = \mathbf{V}\boldsymbol{\Lambda}\mathrm{e}^{\boldsymbol{\Lambda}t}\mathbf{V}^{-1} = \mathbf{V}\mathrm{e}^{\boldsymbol{\Lambda}t}\boldsymbol{\Lambda}\mathbf{V}^{-1} = \mathrm{e}^{\mathbf{A}t}\mathbf{A}$. Further, from Eq. (b) it may easily be proved that $d(\mathrm{e}^{\mathbf{A}t})/dt = \mathbf{A}\mathrm{e}^{\mathbf{A}t}$ and that $\mathrm{e}^{\mathbf{A}t_1}\mathrm{e}^{\mathbf{A}t_2} = \mathrm{e}^{\mathbf{A}(t_1+t_2)}$. Consequently, an analytical solution to the state-space form of the equation of motion, *i.e.* Eq. (2–31), is given as

$$\mathbf{Z}(t) = \mathrm{e}^{\mathbf{A}(t-t_0)}\mathbf{Z}_0 + \int_{t_0}^{t} \mathrm{e}^{\mathbf{A}(t-\tau)}\mathbf{BF}(\tau)d\tau, \quad \mathbf{Z}_0 = \mathbf{Z}(t_0). \tag{c}$$

Here t_0 denotes a time at which the state vector $\mathbf{Z}(t)$ is known. This solution is easily verified by differentiation with respect to the time and subsequent insertion on the left side of Eq. (2–31).

In Eq. (c), let $t = t_{j+1}$ and $t_0 = t_j$. A time-stepping algorithm, which can be used to determine the state vector $\mathbf{Z}_{j+1} = \mathbf{Z}(t_{j+1})$ from the previous state vector $\mathbf{Z}_j = \mathbf{Z}(t_j)$, is then expressed as

$$\mathbf{Z}_{j+1} = \mathrm{e}^{\mathbf{A}\Delta t}\mathbf{Z}_j + \int_{t_j}^{t_{j+1}} \mathrm{e}^{\mathbf{A}\left(t_{j+1}-\tau\right)}\mathbf{BF}(\tau)d\tau \Rightarrow \tag{d}$$

$$\mathrm{e}^{-\frac{1}{2}\mathbf{A}\Delta t}\mathbf{Z}_{j+1} = \mathrm{e}^{\frac{1}{2}\mathbf{A}\Delta t}\left\{\mathbf{Z}_j + \int_0^{\Delta t} \mathrm{e}^{-\mathbf{A}\tau}\mathbf{BF}(t_j+\tau)d\tau\right\}, \tag{e}$$

where $\Delta t = t_{j+1} - t_j$ is the time step, and it has been used that $\mathrm{e}^{\mathbf{A}\Delta t} = \mathrm{e}^{\frac{1}{2}\mathbf{A}\Delta t}\mathrm{e}^{\frac{1}{2}\mathbf{A}\Delta t}$. Next, the load function is approximated over the interval between the times t_j and t_{j+1}. Linear variation is assumed,

$$\mathbf{F}(t_j+\tau) = (1 - (\tau/\Delta t))\,\mathbf{F}_j + (\tau/\Delta t)\mathbf{F}_{j+1}. \tag{f}$$

The integration from $\tau = 0$ to $\tau = \Delta t$ is then carried out analytically. *(continued)*

Subsequently the matrix exponential functions are written as their Maclaurin expansions. The following truncated series are used:

$$e^{\frac{1}{2}\mathbf{A}\Delta t} \approx \left(\mathbf{I} + \frac{1}{2}\mathbf{A}\Delta t\right), \quad e^{-\frac{1}{2}\mathbf{A}\Delta t} \approx \left(\mathbf{I} - \frac{1}{2}\mathbf{A}\Delta t\right), \tag{g}$$

$$e^{-\mathbf{A}\Delta t} \approx \left(\mathbf{I} - \mathbf{A}\Delta t + \frac{1}{2}\mathbf{A}\mathbf{A}\Delta t^2 - \frac{1}{6}\mathbf{A}\mathbf{A}\mathbf{A}\Delta t^3\right). \tag{h}$$

Third- and higher-order terms with respect to Δt are discarded in the approximate solution. This provides the implicit solution given by Eq. (2–38). □

2.2.3 Direct time integration

The main disadvantage of the indirect time integration methods is the demand of array storage space because of the fact that the system matrices are converted into the form given by Eq. 2–31. A solution algorithm that requires much less computer memory can be formulated if the nature of the system matrices in the FEM form of the governing equations is utilized. This leads to a *direct integration scheme* which works on the original FEM form of the governing equations.

An integration scheme may be derived by means of central differences for the acceleration and the velocity vectors in time. However, this provides a solution which is only conditionally stable. On the other hand, the Houbolt and Wilson θ methods, which are both widely used in commercial FEM codes, may be calibrated to be unconditionally stable. However, both the unconditionally stable Houbolt and Wilson θ methods provide a solution with numerical dissipation, which is not present in the direct integration scheme proposed by Newmark (1959). At the same time, the Newmark method leads to a smaller degree of period elongation than the two other methods. Therefore, only the Newmark method will be described in the following. The other methods are described in, for example, (Bathe 1996).

The Newmark method

The following variations of the velocity and displacement vectors are introduced (Bathe 1996):

$$\dot{\mathbf{z}}_{j+1} = \dot{\mathbf{z}}_j + \left[(1-\gamma)\,\ddot{\mathbf{z}}_j + \gamma\ddot{\mathbf{z}}_{j+1}\right]\Delta t, \tag{2–41}$$

$$\mathbf{z}_{j+1} = \mathbf{z}_j + \dot{\mathbf{z}}_j\Delta t + \left[(1/2-\beta)\,\ddot{\mathbf{z}}_j + \beta\ddot{\mathbf{z}}_{j+1}\right]\Delta t^2, \tag{2–42}$$

where β and γ are weight functions. These parameters determine how the acceleration is approximated within each time step. The combination $(\beta = 1/6, \gamma = 1/2)$ corresponds to linear variation of the acceleration over the time step Δt. In this case the Newmark scheme is identical to the Wilson θ scheme with the parameter $\theta = 1$—see *e.g.* (Bathe 1996)—and a solution is provided, which becomes unstable when Δt is too large. On the other hand, an unconditionally stable numerical solution is provided when the acceleration is assumed to be constant and equal to $\ddot{\mathbf{z}} = (\ddot{\mathbf{z}}_j + \ddot{\mathbf{z}}_{j+1})/2$. This approximation, which is also referred to as a trapezoidal rule, is obtained with the weights $(\beta = 1/4, \gamma = 1/2)$, and it may be shown that is this case the eigenvibration part of the Newmark scheme becomes identical to the eigenvibration part of the Crank-Nicolson scheme when the original discretized equations are rewritten in state-space form. However, the additive load part is different in the two schemes.

It is noted that the Newmark method is implicit. In particular, the acceleration vector for the time step t_{j+1} enters the right-hand sides of Eqs. (2–41) and (2–42). The solution for the new time step therefore requires an additional matrix equation, which is obtained from the FEM equation of motion, *i.e.* Eq. (2–31), at time step $j+1$,

$$\mathbf{M}\ddot{\mathbf{z}}_{j+1} + \mathbf{C}\dot{\mathbf{z}}_{j+1} + \mathbf{K}\mathbf{z}_{j+1} = \mathbf{f}_{j+1}. \tag{2–43}$$

Together with Eqs. (2–41) and (2–42), Eq. (2–43) forms a system of equations which can be used to find the three unknown states $\mathbf{z}_{j+1}$, $\dot{\mathbf{z}}_{j+1}$ and $\ddot{\mathbf{z}}_{j+1}$. After a few manipulations, the following scheme is achieved:

$$\ddot{\mathbf{z}}_{j+1} = \ddot{\mathbf{z}}_j + \widehat{\mathbf{M}}^{-1}\left(\mathbf{f}_{j+1} - \mathbf{C}\dot{\mathbf{z}}^*_{j+1} - \mathbf{K}\mathbf{z}^*_{j+1}\right), \tag{2–44}$$

$$\dot{\mathbf{z}}_{j+1} = \dot{\mathbf{z}}^*_{j+1} + \gamma\left(\ddot{\mathbf{z}}_{j+1} - \ddot{\mathbf{z}}_j\right)\Delta t, \tag{2–45}$$

$$\mathbf{z}_{j+1} = \mathbf{z}^*_{j+1} + \beta\left(\ddot{\mathbf{z}}_{j+1} - \ddot{\mathbf{z}}_j\right)\Delta t^2, \tag{2–46}$$

where

$$\widehat{\mathbf{M}} = \mathbf{M} + \gamma\mathbf{C}\Delta t + \beta\mathbf{K}\Delta t^2, \quad \dot{\mathbf{z}}^*_{j+1} = \dot{\mathbf{z}}_j + \ddot{\mathbf{z}}_j\Delta t, \quad \mathbf{z}^*_{j+1} = \mathbf{z}_j + \dot{\mathbf{z}}_j\Delta t + \frac{1}{2}\ddot{\mathbf{z}}_j\Delta t^2. \tag{2–47}$$

It is noted that $\dot{\mathbf{z}}^*_{j+1}$ and $\mathbf{z}^*_{j+1}$ are predicted values of the velocity and displacement vectors, respectively. Hence, the Newmark may be interpreted as a predictor–corrector method analogous to the Adams-Moulton-Bashforth method, cf. (Kreyszig 1999).

2.3 Frequency-domain solution

Alternatively to the solution of linear transient response directly in the time domain, the solution may be found indirectly in the frequency domain. The procedure has the following steps:

1 The discrete time series of additive load vectors is Fourier transformed, preferably utilizing the Fast Fourier Transformation (FFT) algorithm.

2 The frequency-domain equivalent of the FEM equation of motion, Eq. (2–31), is solved for each of the circular frequencies $\omega_j = 2\pi\left(j-1\right)/T$, $j = 1, 2, \ldots, J$, where J is the number of time steps and T is the total "integration time".

3 The time-domain solution is found by inverse Fourier transformation of the frequency-domain solution.

The Fourier transforms of the discrete time series of the displacement and the additive load vectors are denoted $\mathbf{Z}_j$ and $\mathbf{F}_j$, respectively. Hence, for each of the frequencies, Eq. (2–31) is reduced to a matrix equation in the form

$$\widehat{\mathbf{K}}_j\mathbf{Z}_j = \mathbf{F}_j, \quad \widehat{\mathbf{K}}_j = -\omega_j^2\mathbf{M} + \mathrm{i}\omega_j\mathbf{C} + \mathbf{K}. \tag{2–48}$$

$\widehat{\mathbf{K}}_j$ may be interpreted as a dynamic stiffness matrix for the circular frequency ω_j. Consequently, the computation effort in the frequency-domain solution of a dynamic problem corresponds to J times the static solution, one time for each frequency or time step.

Thus, the analysis of dynamic and acoustic problems in the frequency domain may seem appealing. However, there are a few considerations that have to be made in order to achieve satisfactory results:

When a dynamic problem is solved in frequency domain, the element size must be sufficiently small so that an accurate solution is provided for all frequencies. In elastodynamics, the wavenumbers depend linearly on the frequency, whereas in beam problems the waves are dispersive, see Example 2.3. In any case, the smaller wavelengths which dictate the element size occur for the highest frequency.

If the steady-state response to a periodic excitation is analysed, there are no problems involved in the Fourier–inverse-Fourier-transformation process. However, if the transient response to, for example, a pulse load is to be identified, it must be ensured that the "integration time" is sufficiently long so that there is no response after the time T. Otherwise a non-causal response is observed in the time domain after the inverse Fourier transformation.

It is noted that the Fourier transformation of the excitation time series will produce a frequency spectrum which is symmetric around the *Nyquist frequency*, $\omega_{nq} = \pi (J-1)/T$. Only the wave propagation related to frequencies below ω_{nq} has physical meaning. However, the frequency-domain analysis must be carried out for all frequencies in order to be able to perform the inverse Fourier transformation, which provides the response time series.

2.4 Steady state analysis of moving loads

Convection is present in a variety of problems related to fluids and acoustics. However, convection will also arise in an elastic medium if we apply a formulation in the local frame of reference following a moving source. This kind of model is advantageous for the analysis of the steady state response to a vehicle, *e.g.* a train. The analysis of such problems in a fixed-frame-of-reference description requires the use of an extremely large element grid, unless the velocity of the source is low and the duration of the transient phase is, at the same time, short. However, the formulation in the moving frame of reference is restricted to the analysis of problems, in which the geometry is constant along the direction of the negative convection. This implies that an infinite domain, or structure, is considered, which again necessitates the use of transmitting boundary conditions in the FEM formulation of the problem. This problem will be returned to in Section 2.5.

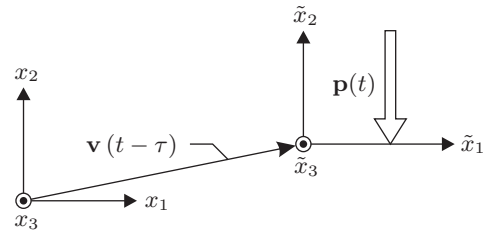

Figure 2–5 The Galilean transformation from fixed Cartesian (x_1, x_2, x_3)-coordinates into moving co-directional $(\tilde{x}_1, \tilde{x}_2, \tilde{x}_3)$-coordinates.

In the following, it will be assumed that the load is moving with the constant velocity $\mathbf{v}$ with components v_j and magnitude $|\mathbf{v}| = v$. A transformation from the fixed Cartesian (x_1, x_2, x_3)-coordinate system into the co-directional convected $(\tilde{x}_1, \tilde{x}_2, \tilde{x}_3)$-coordinate system following the

load is then carried out by means of the three-dimensional *Galilean transformation*,

$$\tilde{\mathbf{x}} = \mathbf{x} - \mathbf{v}\,(t - \tau)\,. \tag{2–49}$$

The two coordinate systems coincide at $t = \tau$ as illustrated in Fig. 2–5. Partial derivatives in the two coordinate systems are related in the following manner:

$$\frac{\partial}{\partial x_j} = \frac{\partial}{\partial \tilde{x}_j}, \quad \left.\frac{\partial}{\partial t}\right|_{x_j} = \left.\frac{\partial}{\partial t}\right|_{\tilde{x}_j} - v_j \frac{\partial}{\partial \tilde{x}_j}, \tag{2–50}$$

This implies that convection gives rise to additional terms in the governing partial differential equations. Hence, the system matrices of the finite element scheme—and possibly also the nodal force vectors—will change. The convection terms are, in contrast to the terms which are usually present in the FEM formulation of a problem, not symmetrical when standard Galerkin variation is used. In other words, the differential operators in the governing equations are not self-adjoint. As a consequence of this, the convection may lead to an unstable numerical solution—in particular when the analysis is carried out directly in the time domain using low-order spatial interpolation functions, *e.g.* linear elements, and large time steps. This calls for a variational approach, in which the shape functions for the virtual field, *i.e.* the weight functions, are changed, or another means of counteracting the instability has to be provided. Different methods of counteracting the instabilities due to convection are discussed in Subsection 2.4.1.

Furthermore, due to the *Dobbler effect*, the propagation velocity will be different in various directions. The degree of distortion of the wavefronts when compared to a stationary source depend on the convection speed relative to the wave speed. The situation for the elastic full-space is illustrated in Fig. 2–6, and here three different situations can be identified:

Subsonic motion — $v < c_S$, implying that the source remains within the S-wavefronts as well as the P-wavefronts, cf. Fig. 2–6a.

Transonic motion — $c_S < v < c_P$, whereby the source passes through the S-wavefronts but remains within the P-wavefronts, cf. Fig. 2–6b.

Supersonic motion — $c_P < v$, and the source passes both wavefront systems, cf. Fig. 2–6c.

Passage of the vibration source through one of the wavefront types generates a corresponding Mach-cone, the angle of which is determined by

$$\varphi_S \;=\; 2\,\mathrm{asin}\Big(\frac{c_S}{v}\Big), \qquad \varphi_P \;=\; 2\,\mathrm{asin}\Big(\frac{c_P}{v}\Big). \tag{2–51}$$

As the wavefronts line up along Mach cones, large response is expected along these. In the general case, in which interfaces and surfaces are present, the situation is more complicated. Here several transonic cases exist, since the load speed will surpass one phase speed in the system at a time. Even for a single layer over a half-space or rigid rock, infinitely many wave types exist, so there is no real supersonic case.

Note that for optimal performance of the FEM scheme, the variation of wavelengths with different directions necessitates the use of elements with different sizes depending on the position of the element relative to the source. A further discussion is given in Subsection 2.4.2

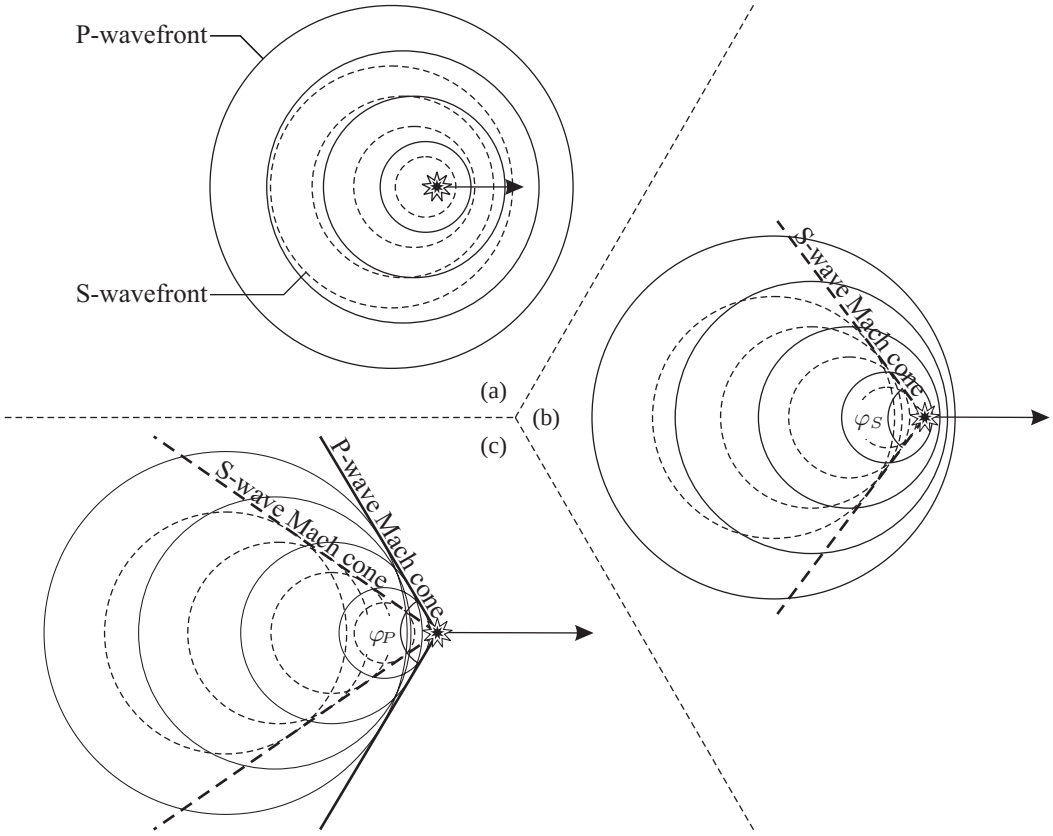

Figure 2–6 Propagation of P- and S-wavefronts from a moving point source for (a) subsonic, (b) transsonic and (c) supersonic convection.

2.4.1 Stabilization of finite element schemes with convection

The problem of unstable numerical solutions for problems involving convection was first encountered in the finite difference solution of the transport equation. The various methods that have been proposed for the stabilization of this and related problems are covered, for example, in the work by Zienkiewicz and Taylor (2000).

As a first illustration of the problems arising in systems subject to convection, consider the idealized one-dimensional diffusion–convection problem (or the dispersion–transport problem),

$$\frac{\partial \varphi}{\partial t} + v\frac{\partial \varphi}{\partial x} - \frac{\partial}{\partial x}\left(k\frac{\partial \varphi}{\partial x}\right) + Q = 0, \tag{2–52}$$

where v is the convection velocity, k is the conductivity and Q is a source term. In the steady state, the weak formulation reads

$$\int_0^L \left\{\frac{1}{2}\left(\delta\varphi v\frac{\partial \varphi}{\partial x} - \frac{\partial \delta\varphi}{\partial x}v\varphi\right) + \frac{\partial \delta\varphi}{\partial x}k\frac{\partial \varphi}{\partial x} + \delta\varphi Q\right\} dx + \left[\frac{1}{2}\delta\varphi\varphi - \delta\varphi k\frac{\partial \varphi}{\partial x}\right]_0^L = 0. \tag{2–53}$$

Linear weight and shape functions are assumed in the form $\mathbf{\Psi} = \mathbf{\Phi} = [1-\xi \;\; \xi], \xi = (x - x_j)/h$. Here x_j is the coordinate of the first node in the element, and h is the element length. Thus the

contribution to the system of equations from a single *internal* element is given as

$$\mathbf{K}_e\boldsymbol{\varphi}_e = \mathbf{f}_e, \quad \mathbf{K}_e = \frac{v}{2}\begin{bmatrix} 0 & 1 \\ -1 & 0 \end{bmatrix} - \frac{k}{h}\begin{bmatrix} 1 & -1 \\ -1 & 1 \end{bmatrix}, \quad \mathbf{f}_e = -\frac{Qh}{2}\begin{bmatrix} 1 \\ 1 \end{bmatrix}. \tag{2–54}$$

Assembling two neighbouring elements provides the equation for a single *internal* node j,

$$Pe\,(\varphi_{j+1} - \varphi_{j-1}) - (\varphi_{j+1} - 2\varphi_j + \varphi_{j-1}) + \frac{Qh^2}{k} = 0, \quad Pe = \frac{vh}{2k}. \tag{2–55}$$

Pe is the so-called *Peclet* number for the element, indicating the relative amount of convection. If $Pe = 0$, the problem is purely diffusive, whereas $Pe = \infty$ corresponds to pure convection. It is immediately seen that Eq. (2–55) obtained by linear finite element discretization is identical to the equations that would be achieved using a finite difference approximation with central differences for both the first and second order derivatives of φ.

In the formulation provided by Eq. (2–55), the weight of φ_{j+1} is not negative for all Peclet numbers. Thus, when $Pe > 1$, the weight of φ_{j+1} becomes positive. This induces an instability of the numerical solution that has an oscillating nature in space. For high Peclet numbers, the solution provided by the numerical scheme becomes purely oscillatory, *i.e.* all information about the physical problem is lost.

The idea in a finite difference scheme would be to approximate the first derivative with a backwards difference rather than the central difference used in Eq. (2–55). Assuming that v is positive, this provides the difference approximation for node j given by

$$2Pe\,(\varphi_j - \varphi_{j-1}) - (\varphi_{j+1} - 2\varphi_j + \varphi_{j-1}) + \frac{Qh^2}{k} = 0. \tag{2–56}$$

Clearly, now the sign of the weight for all discrete values φ_i occurring in the equation for node j are constant independent of the Peclet number. This provides a stable algorithm. However, the question arises as to whether the formulation given by Eq. (2–56) produces accurate results. Unfortunately it turns out that not only the oscillatory terms, but also the physical response is damped in the backward-difference scheme, an therefore it may be interesting to find a weighting somewhere between the weighting corresponding to the central and the backwards difference. This is achieved, if the following interpretation of the first-order derivative is used:

$$\left.\frac{\partial\varphi}{\partial x}\right|_j \approx \frac{\varphi_{j+1} - \varphi_{j-1}}{2h} + \lambda h' \frac{\varphi_{j+1} - 2\varphi_j + \varphi_{j-1}}{h^2}. \tag{2–57}$$

Here h' is a spatial increment in the upwind direction, *i.e.* in the opposite direction of convection, and λ is the *upwind parameter*. A natural choice is $h' = -hv/|v|$. With this definition, the central difference approximation is obtained with $\lambda = 0$, whereas $\lambda = 1/2$ corresponds to the backwards difference, also referred to as *full upwind differencing*, or *full upwinding*.

In the finite-element method, the weighting given by Eq. (2–57) is achieved by using different shape functions for the virtual field and the physical field. Provided that linear shape functions are used for φ, the weight functions, *i.e.* the shape functions for $\delta\varphi$, must satisfy the condition that

$$\boldsymbol{\Psi} = \boldsymbol{\Phi} + \lambda\boldsymbol{\Phi}^*, \quad \int_0^1 \boldsymbol{\Phi}^* d\xi = [-h' \;\; h'], \quad h' = -\frac{hv}{|v|}, \quad 0 \le \lambda \le \frac{1}{2}. \tag{2–58}$$

This alternative to standard Galerkin variation is referred to as *Petrov-Galerkin* variation and is a standard method in stationary fluid dynamics. A simple approach satisfying Eq. (2–58) is to used a discontinuous weight function including the asymmetric contribution achieved as the derivative of the shape function, *i.e.*

$$\boldsymbol{\Psi} = \boldsymbol{\Phi} + \lambda h' \frac{\partial \boldsymbol{\Phi}}{\partial x}. \tag{2–59}$$

For relatively simple problems, such as the problem defined by Eq. (2–52), an optimal value of λ can be found analytically. In more involved problems, and in the two- and three-dimensional cases, λ is usually a heuristic parameter. Further, in a two- or three-dimensional problem, the same technique implies that this difference has to be taken along a streamline, hence the name *upwind differencing along a streamline*. A detailed description of the various approaches to the stabilization of two- and three-dimensional scalar and vector field problems involving convection, namely in the time domain, is beyond the scope of this text. A further explanation can be found, for example, in the book by Zienkiewicz and Taylor (2000). However, the treatment of elastic waves subject to convection in three dimensions will be given below, cf. Example 2.5.

A closer look at Eq. (2–57) reveals that the correction introduced via the the second term on the right hand side does in fact correspond to the inclusion of an additional term in the Taylor expansion used to approximate $\Delta\varphi_j = \varphi_{j+1} - \varphi_j$ over element j. Linear Galerkin variation corresponds, approximately, to a truncated Taylor expansion of the kind

$$\Delta\varphi \approx \frac{\partial \varphi}{\partial x}\Delta x, \tag{2–60}$$

where $\Delta x = h$, while Eq. (2–57) corresponds to the approximation

$$\Delta\varphi \approx \frac{\partial \varphi}{\partial x}\Delta x + \frac{1}{2}\frac{\partial^2 \varphi}{\partial x^2}\Delta x^2, \tag{2–61}$$

where the spatial increment is replaced with $\lambda h'$.

In the wave equation, a term of the kind $v\frac{\partial^2 \varphi}{\partial t \partial x}$ arises when convection is introduced. This term is similar to the problematic term in the diffusion-convection problem, except that the potential velocity, rather than the potential itself, is included. A stable solution may be achieve by application of a method similar to the Petrov-Galerkin method (Krenk *et al.* 1999; Kirkegaard *et al.* 1999), see Example 2.5, or alternatively the so-called *Taylor-Galerkin* approach may be applied. Here the idea is to get a better approximation of the mixed derivative by including more terms in the Taylor expansion with respect to time in stead of expanding the Taylor series with respect to space with one additional term. For a detailed description of the method, cf. (Zienkiewicz and Taylor 2000).

Example 2.5 Elastodynamics in a moving frame of reference

The strong formulation for wave propagation in elastic materials is achieved by means of the Galerkin coordinate transformation (2–49). This way, the *convective Navier equations* are established in the form

$$\begin{aligned}(\lambda+\mu)\,&\frac{\partial^2 \tilde{u}_j(\tilde{\mathbf{x}},t)}{\partial \tilde{x}_i \partial \tilde{x}_j} + \mu \frac{\partial^2 \tilde{u}_i(\tilde{\mathbf{x}},t)}{\partial \tilde{x}_j \partial \tilde{x}_j} + \rho \tilde{b}_i(\tilde{\mathbf{x}},t) \\ &= \rho\left(\frac{\partial^2}{\partial t^2} - 2v_j\frac{\partial^2}{\partial \tilde{x}_j \partial t} + v_j v_k \frac{\partial^2}{\partial \tilde{x}_j \partial \tilde{x}_k}\right)\tilde{u}_i(\tilde{\mathbf{x}},t),\end{aligned} \tag{a}$$

(continued)

where $\tilde{u}_i(\tilde{\mathbf{x}},t) = u_i(\tilde{\mathbf{x}} + \mathbf{v}\,(t-\tau)\,,t)$ and $\tilde{b}_i(\tilde{\mathbf{x}},t)$ are the displacements in the moving frame of reference, respectively. Here $u_i(\mathbf{x},t)$ is the displacement field in the fixed frame of reference governed by the usual Navier equations (1–10). It is noted that the convection arising in the moving-frame-of-reference description is in the opposite direction of the velocity of the moving load, *i.e.* the convection velocity is $-v_j$ when the velocity the moving source, or vehicle, is v_j. In order to achieve a stable numerical scheme, the original partial differential equation given by Eq. (a) is modified. In particular, the mixed temporal-spatial derivative term appearing on the right-hand side of the equation is replaced, based on a Taylor expansion including the second-order term, *i.e.*

$$\Delta\tilde{u}_i \approx \frac{\partial\tilde{u}_i}{\partial\tilde{x}_j}\Delta\tilde{x}_j + \frac{1}{2}\frac{\partial^2\tilde{u}_i}{\partial\tilde{x}_j\partial\tilde{x}_k}\Delta\tilde{x}_j\Delta\tilde{x}_k. \tag{b}$$

where *tilde* signifies quantities related to the local frame of reference. This involves the substitution

$$2\rho v_j\frac{\partial\dot{\tilde{u}}_i}{\partial\tilde{x}_j} \;\curvearrowright\; 2\rho v_j\frac{\partial\dot{\tilde{u}}_i}{\partial\tilde{x}_j} + \rho v_j\frac{\partial^2\dot{\tilde{u}}_i}{\partial\tilde{x}_j\partial\tilde{x}_k}\Delta\tilde{x}_k = 2\rho v_j\frac{\partial\dot{\tilde{u}}_i}{\partial\tilde{x}_j} + \frac{\rho\lambda h}{v}v_jv_k\frac{\partial^2\dot{\tilde{u}}_i}{\partial\tilde{x}_j\partial\tilde{x}_k}. \tag{c}$$

Linear Galerkin variation is used, defined in terms of the "global" shape functions, which in the case of the elastic medium are defined for each of the spatial coordinate directions,

$$\tilde{u}_j(\tilde{\mathbf{x}},t) = \mathbf{\Phi}_j(\tilde{\mathbf{x}})\tilde{\mathbf{u}}(t), \quad \delta\tilde{u}_j(\tilde{\mathbf{x}},t) = \mathbf{\Phi}_j(\tilde{\mathbf{x}})\delta\tilde{\mathbf{u}}(t). \tag{d}$$

The convection velocity is assumed to be constant in time, *i.e.* $\dot{v}_j = 0$. Thus, insertion of Eq. (c) into Eq. (a), the finite element solution becomes

$$\mathbf{M}\ddot{\tilde{\mathbf{u}}}(t) + \mathbf{C}\dot{\tilde{\mathbf{u}}}(t) + \mathbf{K}\tilde{\mathbf{u}}(t) = \tilde{\mathbf{f}}(t), \tag{e}$$

where the following system matrices and load vectors can be identified:

$$\mathbf{M} = \int_V \rho\mathbf{\Phi}_i^T\mathbf{\Phi}_i\,dV, \tag{f}$$

$$\begin{aligned}\mathbf{C} = &\int_V \rho v_j\left\{\frac{\partial\mathbf{\Phi}_i^T}{\partial x_j}\mathbf{\Phi}_i - \mathbf{\Phi}^T\frac{\partial\mathbf{\Phi}_i}{\partial x_j} + \lambda h\frac{v_k}{v}\frac{\partial\mathbf{\Phi}_i^T}{\partial x_j}\frac{\partial\mathbf{\Phi}_i}{\partial x_k}\right\}dV \\ &- \int_S \rho v_j\left\{n_j\mathbf{\Phi}_i^T\mathbf{\Phi}_i + \lambda h n_j\frac{v_k}{v}\mathbf{\Phi}_i^T\frac{\partial\mathbf{\Phi}_i}{\partial x_k}\right\}dS,\end{aligned} \tag{g}$$

$$\mathbf{K} = \int_V\left\{E_{ijkl}\frac{\partial\mathbf{\Phi}_i^T}{\partial x_j}\frac{\partial\mathbf{\Phi}_k}{\partial x_l} - \rho v_jv_k\frac{\partial\mathbf{\Phi}_i^T}{\partial x_j}\frac{\partial\mathbf{\Phi}_i}{\partial x_k}\right\}dV + \int_S \rho n_jv_jv_k\mathbf{\Phi}_i^T\frac{\partial\mathbf{\Phi}_i}{\partial x_k}\,dS, \tag{h}$$

$$\tilde{\mathbf{f}}(t) = \int_V \mathbf{\Phi}_i^T\tilde{f}_i(\mathbf{x},t)\,dV + \int_S \mathbf{\Phi}_i^T\tilde{\tau}_i(x,t)\,dS. \tag{i}$$

$\tilde{\tau}_i(x,t)$ is the surface traction from exterior, or added, load. Both the volume and the surface integral in vector $\tilde{\mathbf{f}}(t)$ reduce to nodal forces which are applied at the inner nodes and the surface nodes, respectively. It is noted that an anisotropic term arises in the stiffness matrix due to convection. This is in good correspondence with the fact that the wavelengths in the moving frame of reference are different in different directions.

In practice, Eq. (e) is formulated for a single finite element at a time, and the element matrices and load vectors are subsequently assembled into the system matrices and load vectors. In the 3-D case, and assuming linear isotropic material behaviour, the element elasticity tensor $\mathbf{E}_j$ given by Eq. (2–9) is used. The 2-D formulation involves the equivalent matrix with dimensions (4×4). □

2.4.2 Choosing the mesh size in convection-dominated problems

As already discussed in Section 2.1.2, a certain number of elements are required per wavelength in order to achieve an accurate numerical solution. In convection dominated problems, the example above illustrate that the stiffness matrix in the FEM form of the equation of motion becomes anisotropic. As a result of this, wave propagation in different directions takes place with different phase velocities and therefore with different wavelengths. Hence, the allowable element size in a given region depends on the directions, in which waves are travelling in that particular region.

In the interior of an elastic plane subject to out-of-plane excitation, only SH-waves are present. The relative velocity of the convection with respect to the S-wave speed may conveniently be expressed in terms of the *Mach number* $\vartheta = v/c_S$. The convection is referred to as subsonic if $\vartheta < 1$, and supersonic if $\vartheta > 1$. When the motion of the source is subsonic, the wavelengths in front of the source relative to the direction of motion will be shorter than in the situation of a stationary source, whereas longer wavelengths are present behind the source. If the motion is supersonic, but with a Mach number close to Mach 1, smaller elements have to be used behind the source in the moving frame of reference than are necessary when no convection is present. This is a result of the fact that two waves propagate behind the source with the phase velocities $c_{S,fast} = v + c$ and $c_{S,slow} = v - c_S$, respectively. The element size is dictated by $c_{S,slow}$, since this phase velocity involves the shortest wavelengths. When the convection velocity becomes sufficiently high, that is when $v > 2c$, elements of the same or even a greater size can be used behind the source, since in this case $c_{S,slow} > c_S$. In any case, in SH-wave propagation problems involving supersonic convection, no waves propagate in front of the moving source. Therefore, this part of the domain should not be modelled. However, it should be noted that in practice it may be a difficult task to produce a finite element scheme, which is stable for high Mach numbers.

In plane strain or three-dimensional elastodynamics, the situation is a bit more complicated since both P- and S-waves are present. Thus two Mach numbers may be defined, namely the P-wave Mach number $\vartheta_P = v/c_P$ and the S-wave Mach number $\vartheta_S = v/c_S$. As discussed in the beginning of this section, the convection is subsonic if $\vartheta_P < \vartheta_S < 1$, transonic if $\vartheta_P < 1 < \vartheta_S$, and supersonic if $1 < \vartheta_P < \vartheta_S$. In the subsonic velocity range, the S-wavelength defines the element size at all points. In the transonic range, only P-waves propagate in front of the source. Thus the P-wavelength defines the element size in this region. Behind the source, the element size depends on the phase velocity of the "slow S-wave", $c_{S,slow} = v - c_S$.

When the convection speed is close to Mach 1, problems arise from both a physical and a computational point of view. Physically, the problem is that the response in the undamped case will go towards infinity in the limit as the convection speed goes to Mach 1—at least in the case of a homogeneous half-space. Computationally, the problem is that extremely small elements should be used in parts of the model or, possibly, in the entire model, depending on the position of sources. It has to be noted that it is always the smaller wavelength at a given point that dictates the element size. For example, if several sources are present in a FEM model subject to subsonic convection, small elements have to be used in any part of the model that lies in the upwind direction from just one of the sources. If a free surface or an interface between two regions consisting of different fluids, is present, surface, or interface, waves are also present. Further, in stratified media, layer waves, such as Love waves, should be taken into consideration when the mesh size is selected. This requires a good understanding of the physics in the problem, or the mesh size must be selected heuristically.

Example 2.6 Simple Euler-Bernoulli beam track model in moving coordinates

As discussed in Subsection 2.1.3, two wave components exist on either side of a point load applied to an Euler-Bernoulli (E-B) beam on a Kelvin-Pasternak foundation. When non-moving load is considered in the fixed frame of reference, the wave propagation is symmetric around the point force. Thus, in this case, the four wave components will be defined by wavenumbers and amplitudes forming 2×2 pairs of complex conjugates. When defining the element size in different parts of the FEM model, the wave components which are present in that part of the model should be taken into consideration.

When a moving force is applied on the beam, a description in the moving frame of reference is adequate for analysis of the response in the steady state. The Galilean transformation implies that the equation of motion for the E-B beam on the viscoelastic foundation in the moving frame of reference reads

$$\frac{\partial^2}{\partial\tilde{x}^2}\left(EI\frac{\partial^2\tilde{u}(\tilde{x},t)}{\partial\tilde{x}^2}\right) - \frac{\partial}{\partial\tilde{x}}\left(G\left(\frac{\partial^2\tilde{u}(\tilde{x},t)}{\partial\tilde{x}\partial t} - v\frac{\partial^2\tilde{u}(\tilde{x},t)}{\partial\tilde{x}^2}\right)\right) - \frac{\partial}{\partial\tilde{x}}\left(K\frac{\partial\tilde{u}(\tilde{x},t)}{\partial\tilde{x}}\right) + \kappa\tilde{u}(\tilde{x},t)$$
$$+ m\left(\frac{\partial^2\tilde{u}(\tilde{x},t)}{\partial t^2} - 2v\frac{\partial^2\tilde{u}(\tilde{x},t)}{\partial\tilde{x}\partial t} + v^2\frac{\partial^2\tilde{u}(\tilde{x},t)}{\partial\tilde{x}^2}\right) + \gamma\left(\frac{\partial\tilde{u}(\tilde{x},t)}{\partial t} - v\frac{\partial\tilde{u}(\tilde{x},t)}{\partial\tilde{x}}\right) = \delta(\tilde{x},t). \qquad \text{(a)}$$

where $\tilde{x}$ is the local spatial coordinate and $\tilde{u}$ is the displacement field, both defined in the moving frame of reference following the load, see Fig. A. Following the same procedure as in Example 2.3, the wavenumbers are the solutions to the characteristic polynomial equation

$$\tilde{k}_n^4 - \frac{\mathrm{i}Gv}{EI}\tilde{k}_n^3 + \frac{K - \mathrm{i}\omega G - mv^2}{EI}\tilde{k}_n^2 - \frac{2\omega mv + \mathrm{i}\gamma v}{EI}\tilde{k}_n + \frac{\kappa - m\omega^2 - \mathrm{i}\omega\gamma}{EI} = 0, \qquad \text{(b)}$$

where $\tilde{k}_n$, $n = 1, 2, 3, 4$, are the wavenumbers as seen in the moving frame of reference.

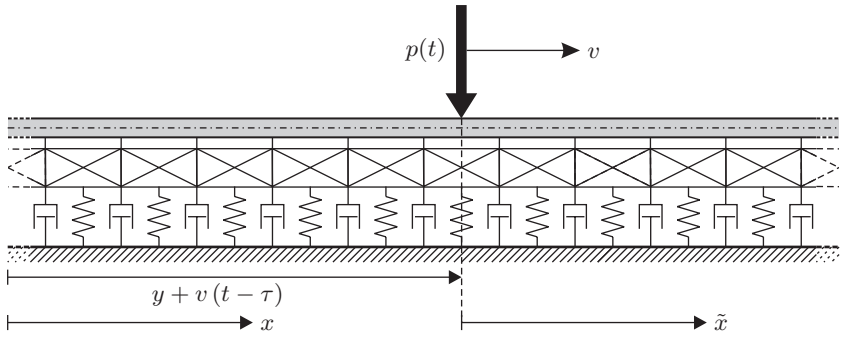

Figure A The Galilean coordinate transformation in one dimension.

The wavenumbers in the moving frame of reference are related to the wavenumbers in the fixed frame of reference via

$$\tilde{k}_n = \left(k_n^{-1} - k_v^{-1}\right)^{-1}, \quad k_v = \frac{\omega}{v}, \quad n = 1, 2, 3, 4. \qquad \text{(c)}$$

Correspondingly, the phase velocities in the two coordinate systems are related as

$$\tilde{c}_n = c_n - v, \qquad \text{(d)}$$

from which it is obvious that the speed of travelling waves *behind* the load will increase with increasing convection. On the other hand, wave components that have a positive phase velocity for low convection will eventually get a negative phase velocity. In particular it is noted that the wave component that propagates as a travelling wave *in front of* the load for $v = 0$, and for $\omega > \omega_{cn}$, where

(continued)

ω_{cn} is the cut-on frequency, will have a phase velocity equal to zero for a certain convection speed. This is a problem from a computational point of view when the finite-element method is used, since a phase velocity equal to zero involves a wavelength equal to zero. However, Andersen (2002) showed that the wave component with $\tilde{c} = 0$ may simply be disregarded when determining the element size. This does not deteriorate the accuracy of the numerical solution.

It is noted that the phase velocities of the four wave components in the E-B beam are not finite in the limit as the frequency goes to infinity. This follows from the fact that the wavenumbers are proportional to $\sqrt{\omega}$ in the high-frequency limit. Thus the phase velocities $\tilde{c}_n = \omega/\tilde{k}_n$ become infinite as $\omega \to \infty$. From a physical point of view, this does not make sense. A comparison with the beam theory proposed by Timoshenko (1921) indicates, that the infinite phase velocities in the high-frequency limit are a result of the fact that the shear deformation of the beam is not included in the E-B beam theory. Therefore it may be concluded that the E-B beam theory is only applicable in the low-frequency range.

Similar to the fixed-frame-of-reference formulation presented in Subsection 2.1.3, the finite element formulation in the moving frame of reference reads

$$\mathbf{M}\ddot{\mathbf{z}} + \mathbf{C}\dot{\mathbf{z}} + \mathbf{K}\mathbf{z} = \mathbf{f} + \mathbf{f_b}, \tag{e}$$

where the system matrices and the boundary load vector are now defined as

$$\mathbf{M} = \int_{\tilde{x}_b^-}^{\tilde{x}_b^+} \mathbf{\Psi}^T m \mathbf{\Phi} d\tilde{x}, \tag{f}$$

$$\mathbf{C} = \int_{\tilde{x}_b^-}^{\tilde{x}_b^+} \left\{ \mathbf{\Psi}^T \left(\gamma \mathbf{\Phi} - 2mv \frac{\partial \mathbf{\Phi}}{\partial \tilde{x}} \right) + \frac{\partial \mathbf{\Psi}}{\partial \tilde{x}} G \frac{\partial \mathbf{\Phi}}{\partial \tilde{x}} \right\} d\tilde{x} - \left[\mathbf{\Psi}^T G \frac{\partial \mathbf{\Phi}}{\partial \tilde{x}} \right]_{\tilde{x}_b^-}^{\tilde{x}_b^+}, \tag{g}$$

$$\begin{aligned} \mathbf{K} = \int_{\tilde{x}_b^-}^{\tilde{x}_b^+} & \left\{ \frac{\partial^2 \mathbf{\Psi}^T}{\partial \tilde{x}^2} EI \frac{\partial^2 \mathbf{\Phi}}{\partial \tilde{x}^2} + \mathbf{\Psi}^T \left(\kappa \mathbf{\Phi} - \gamma v \frac{\partial \mathbf{\Phi}}{\partial \tilde{x}} \right) \right. \\ & \left. + \frac{\partial \mathbf{\Psi}}{\partial \tilde{x}} \left(\left(K - mv^2 \right) \frac{\partial \mathbf{\Phi}}{\partial \tilde{x}} + vG \frac{\partial^2 \mathbf{\Phi}}{\partial \tilde{x}^2} \right) \right\} d\tilde{x} - \left[\mathbf{\Psi}^T K \frac{\partial \mathbf{\Phi}}{\partial \tilde{x}} \right]_{\tilde{x}_b^-}^{\tilde{x}_b^+}, \end{aligned} \tag{h}$$

$$\mathbf{f} = \mathbf{f}(t) = \int_{\tilde{x}_b^-}^{\tilde{x}_b^+} \mathbf{\Psi}^T \tilde{f}(\tilde{x}, t) d\tilde{x}, \quad \mathbf{f_b} = \mathbf{f_b}(t) = \left[\mathbf{\Psi}^T \tilde{Q}(\tilde{x}, t) - \frac{\partial \mathbf{\Psi}^T}{\partial \tilde{x}} \tilde{M}(\tilde{x}, t) \right]_{\tilde{x}_b^-}^{\tilde{x}_b^+}. \tag{i}$$

Here $\mathbf{\Phi}$ and $\mathbf{\Psi}$ are the "global" shape and weight functions assembled from the local element-wise Hermite shape functions defined in (2–25) and (2–26). Subscript b indicates the global boundary, *i.e.* the endpoints of the FEM model. Only the mass matrix is unchanged from the situation in the fixed frame of reference. Convection terms enter both the damping and the stiffness matrix. However, it is noted that there has not been introduced any additional terms in order to stabilize the numerical solution. This is due to the fact that the finite element scheme defined by (e), (f), (g) and (h) has been found to be stable for relatively high convection speeds (Andersen 2002).

As mentioned in Subsection 2.1.3, the system matrices can be found analytically when the cubic Hermite shape functions are used, both for the interpolation over each element and as the weight functions. Thus, using the Galerkin approach, the following matrices are obtained for a single element of the length L_e and with x_e denoting a local coordinate ranging between 0 and L_e:

$$\int_0^{L_e} \mathbf{\Phi}^T \mathbf{\Phi} \, dx_e = \frac{L_e}{420} \begin{bmatrix} 156 & 22\,L_e & 54 & -13\,L_e \\ 22\,L_e & 4\,L_e^2 & 13\,L_e & -3\,L_e^2 \\ 54 & 13\,L_e & 156 & -22\,L_e \\ -13\,L_e & -3\,L_e^2 & -22\,L_e & 4\,L_e^2 \end{bmatrix}, \tag{j}$$

(continued)

$$\int_0^{L_e} \mathbf{\Phi}^T \frac{\partial \mathbf{\Phi}}{\partial x_e} dx_e = \frac{1}{60} \begin{bmatrix} -30 & 6\,L_e & 30 & -6\,L_e \\ -6\,L_e & 0 & 6\,L_e & -L_e^2 \\ -30 & -6\,L_e & 30 & 6\,L_e \\ 6\,L_e & L_e^2 & -6\,L_e & 0 \end{bmatrix}, \tag{k}$$

$$\int_0^{L_e} \frac{\partial \mathbf{\Phi}^T}{\partial x_e} \frac{\partial \mathbf{\Phi}}{\partial x_e} dx_e = \frac{1}{30\,L_e} \begin{bmatrix} 36 & 3\,L_e & -36 & 3\,L_e \\ 3\,L_e & 4\,L_e^2 & -3\,L_e & -L_e^2 \\ -36 & -3\,L_e & 36 & -3\,L_e \\ 3\,L_e & -L_e^2 & -3\,L_e & 4\,L_e^2 \end{bmatrix}, \tag{l}$$

$$\int_0^{L_e} \frac{\partial \mathbf{\Phi}^T}{\partial x_e} \frac{\partial^2 \mathbf{\Phi}}{\partial x_e^2} dx_e = \frac{1}{2\,L_e} \begin{bmatrix} 0 & 2 & 0 & -2 \\ -2 & -L_e & 2 & -L_e \\ 0 & -2 & 0 & 2 \\ 2 & L_e & -2 & L_e \end{bmatrix}, \tag{m}$$

$$\int_0^{L_e} \frac{\partial^2 \mathbf{\Phi}^T}{\partial x_e^2} \frac{\partial^2 \mathbf{\Phi}}{\partial x_e^2} dx_e = \frac{2}{L_e^3} \begin{bmatrix} 6 & 3\,L_e & -6 & 3\,L_e \\ 3\,L_e & 2\,L_e^2 & -3\,L_e & L_e^2 \\ -6 & -3\,L_e & 6 & -3\,L_e \\ 3\,L_e & L_e^2 & -3\,L_e & 2\,L_e^2 \end{bmatrix}. \tag{n}$$

Naturally, if the material properties are not constant, or homogeneous, inside each element, the matrices defined in (j)–(n) do not apply. However, it is usually a reasonable assumption, that the material is homogeneous over each element, since small elements should be used in any case if local inhomogeneities are of importance. □

2.5 Transmitting boundary conditions

As stated in the introduction, the FEM is a convenient way of solving PDEs describing a physical problem in a finite domain bounded with an arbitrary shape. Also exterior domain problems related to radiation problems can be handled by the FEM when appropriate boundary conditions are included at the artificial boundaries delimiting the modelled domain. Provided that there is no reflection from the surrounding domain back into the computation domain these artificial boundaries should simulate outward radiation of energy. The following section will outline different approaches to the formulation of absorbing boundary conditions for FEM computations of infinite domains and structures with an emphasis on elastodynamics and beams.

Figure 2–7 shows a structure interacting with a half-space made up of a nonlinear or linear elastic nonhomogeneous or anisotropic near field, D^+, and a linear elastic, homogeneous and isotropic exterior domain, D^-, defined by the Lamé constants λ^-, μ^- and the mass density ρ^-. The nonlinearities in the near field may be due to large strains caused by heavy reaction forces from the structure or by pore pressure build-up in the soil (liquefaction). Linear nonhomogeneous or anisotropic response in the near field may be caused by a layered structure of the sediments.

The structure itself is usually analysed by the FEM. In cases as the one indicated, where the domain D^+ may not be homogeneous and isotropic linear elastic (and a few other cases) the FEM is also the most useful method for numerical analysis of this part of the subsoil. In any case, the finite element mesh must be of limited extension. However, since the subsoil is taken

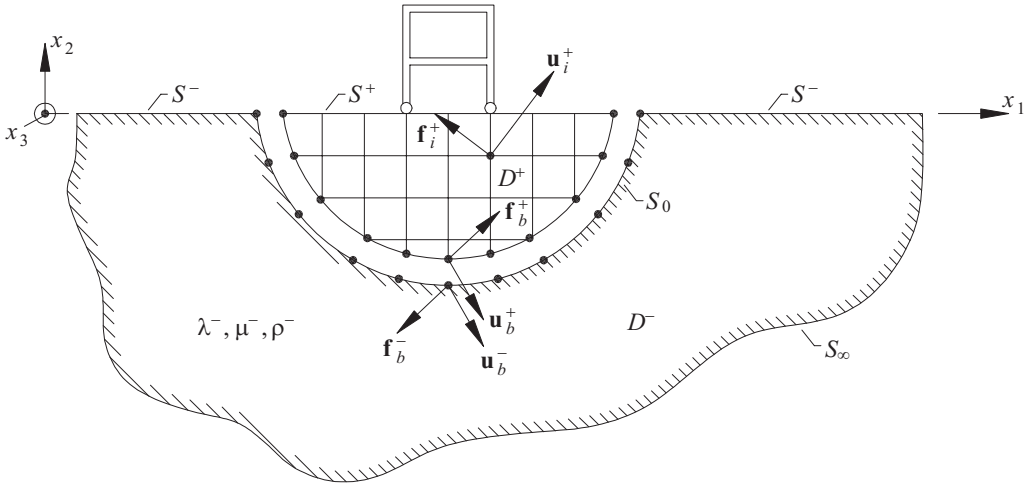

Figure 2–7 Finite domain interacting with an infinite surrounding medium.

as an infinite half space, boundary conditions must be specified along the interface S_0 which give a correct representation of the interaction forces between the modelled region D^+ and the surrounding infinite domain D^-.

The nodal displacements of the finite element scheme along the interface S_0 are assembled in the vector $\mathbf{u}_b^+(t)$ of dimension n_b. The suffix b stands for "boundary" and refers to the common interface S_0 between D^+ and D^-. The parts of the surface of D^+ and D^- not belonging to S_0 are denoted S^+ and S^-, respectively. The conjugated nodal forces are denoted $\mathbf{f}_b^+(t)$. $\mathbf{f}_b^+(t)$ and $\mathbf{u}_b^+(t)$ are related to the reaction forces $\mathbf{f}_b^-(t)$ and the corresponding nodal displacements $\mathbf{u}_b^-(t)$ on the part of the boundary S_0 belonging to D^- as follows, see Fig. 2–7,

$$\mathbf{f}_b^-(t) = -\mathbf{f}_b^+(t), \qquad \mathbf{u}_b^-(t) = \mathbf{u}_b^+(t). \tag{2–64}$$

Temporarily, the material of the exterior domain D^- is merely assumed to be linear elastic as defined by the generalized Hooke's law. The assumption of homogeneous and isotropic material within D^- is not necessary for the validity of the following statements. Then, if the field D^- is not subject to any body forces and the surface S^- is free from surface traction, the forces $\mathbf{f}_b^-(t)$ may be related to the time history of the nodal displacements $\mathbf{u}_b^-(t)$ by the convolution integral,

$$\mathbf{f}_b^-(t) = \int_{-\infty}^{t^+} \mathbf{g}_{bb}^-(t-\tau)\mathbf{u}_b^-(\tau)d\tau. \tag{2–65}$$

The upper integration limit t^+ indicates that summation is performed up to and including the time t to include an instantaneous response component. $\mathbf{g}_{bb}^-(t)$ represents a kind of impulse response matrix function of dimensions $n_b \times n_b$ for the forces $\mathbf{f}_b^-(t)$. It has a slight resemblance of a relaxation modulus, cf. Section 1.6.3, but it provides a hereditary relationship between the interaction forces and the interface displacements rather than the stresses and the strains. Causality requires that $\mathbf{g}_{bb}^-(t) = \mathbf{0}$ for $t < 0$, and that $\mathbf{g}_{bb}^-(t)$ is absolutely integrable on the interval $[0, \infty)$. $\mathbf{g}_{bb}^-(t)$ only depends on the mechanical properties of the domain D^-. If body loads are applied in D^-,

or surface traction is applied on S^-, an additional memory integral must be included in Eq. (2–65) that represents the contribution to $\mathbf{f}_b^-(t)$ from these forces. From Eqs. (2–64) and (2–65) the following boundary condition for the nodal forces $\mathbf{f}_b^+(t)$ in terms of the nodal displacements $\mathbf{u}_b^+(t)$ is obtained:

$$\mathbf{f}_b^+(t) = -\int_{-\infty}^{t^+} \mathbf{g}_{bb}^-(t-\tau)\mathbf{u}_b^+(\tau)d\tau. \tag{2–66}$$

S_0 is referred to as the *interaction boundary*, $\mathbf{f}_b^+(t)$ and $\mathbf{f}_b^-(t)$ are termed the *interaction forces* and Eq. (2–66) is denoted the *interaction boundary condition*.

If the boundary conditions are specified otherwise than given by Eq. (2–66), partial reflection of stress waves back into the computation domain D^+ takes place. Hence, to the level of errors related to the spatial discretization, correctly specified interaction forces make the interaction boundary transparent for any stress wave propagating in D^+. For this reason the boundary condition (2–66) is synonymously denoted a *transmitting* or a *transparent boundary condition*. In some applications the domains D^+ and D^- are made up of the same material, so the boundary S_0 merely represents a more or less arbitrary limitation of the FEM mesh. In these cases S_0 is known as an *artificial boundary* and Eq. (2–66) is called an *artificial boundary condition*. Since a perfect specification of the interaction forces insures that all wave energy is radiated into the surrounding continuum, the name *radiation boundary condition* has also been coined. Finally, since Eq. (2–66) shifts known values of displacements, $\mathbf{u}_b^+(t)$, to nodal forces, $\mathbf{f}_b^+(t)$, Eq. (2–66) represents a general form of a Dirichlet to Neumann condition (DtN condition) in discretized elastodynamics. Here it is recalled that Dirichlet conditions prescribe the field quantity itself, whereas Neumann conditions prescribe its spatial derivative in the direction of the outward normal to the surface.

The boundary condition provided by Eq. (2–66) is *global in space* and *global in time*. This means that the interaction forces at a given node depend on the displacements at all nodes on the boundary (the global in space part) to all instants of time in the past and the present (the global in time part). A boundary condition of this type may be achieved by a coupling of the local FE scheme with a so-called *boundary element* (BE) scheme for the surrounding infinite domain (Andersen 2002). This provides a boundary condition of a very high accuracy, but computationally this is a very expensive solution. In particular, the hereditary approach involves that matrices of the same dimensions as $\mathbf{g}_{bb}^-(t)$ must be stored for all instants of time in the entire discretized time history. Therefore it may be interesting to apply a boundary condition which is *local in time* and *local in space*, even if this comes at the cost that the accuracy is reduced. Thus, various approximate but numerically faster alternatives to the BEM for evaluating the interaction forces $\mathbf{f}_b^-(t)$ are available, as described in the following. Due to their inherent approximate nature, these methods all lead to a partial reflection of waves back into D^+ as stated above.

2.5.1 Rational approximations to transmitting boundary conditions

The frequency response matrix $\mathbf{G}_{bb}^-(\mathrm{i}\omega)$ related to the impulse response matrix $\mathbf{g}_{bb}^-(t)$ is determined by the Fourier transform,,

$$\mathbf{G}_{bb}^-(\mathrm{i}\omega) = \int_{-\infty}^{\infty} \mathbf{g}_{bb}^-(t)\mathrm{e}^{-\mathrm{i}\omega t}dt. \tag{2–67}$$

Assume that the system is under steady state harmonic excitation. Then

$$\mathbf{f}_b^-(t) = \Re\Big(\mathbf{F}_b^-(\omega)\mathrm{e}^{\mathrm{i}\omega t}\Big), \qquad \mathbf{u}_b^-(t) = \Re\Big(\mathbf{U}_b^-(\omega)\mathrm{e}^{\mathrm{i}\omega t}\Big), \tag{2–68}$$

where the complex amplitudes $\mathbf{F}_b^-(\omega)$ and $\mathbf{U}_b^-(\omega)$ are related by

$$\mathbf{F}_b^-(\omega) = \mathbf{G}_{bb}^-(\mathrm{i}\omega)\mathbf{U}_b^-(\omega). \tag{2–69}$$

More generally, let $\mathbf{F}_b^-(\omega)$ and $\mathbf{U}_b^-(\omega)$ signify the Fourier transforms of $\mathbf{f}_b^-(t)$ and $\mathbf{u}_b^-(t)$. Then these are equally related by (2–69), as follows from application of the convolution theorem of Fourier transformation to Eq. (2–65). $\mathbf{G}_{bb}^-(z)$ is assumed to be analytic in the entire z-plane, where $z = x + \mathrm{i}\omega$, save at a discrete number of poles $z_j,\ j = 1, \ldots, s$, where $\det\big(\mathbf{G}_{bb}^-(z_j)\big) = 0$. Then, the following *Laurent series* applies outside the singular points of the z-plane:

$$\mathbf{G}_{bb}^-(z) = \sum_{j=1}^{s} \sum_{k=-\infty}^{\infty} \big(z - z_j\big)^k \mathbf{G}_{jk}. \tag{2–70}$$

In order that Eq. (2–70) represents a real impulse response function in the time domain, it can be shown that the poles z_j and their related Laurent expansion matrices $\mathbf{G}_{jk}$ must either be real or appear as pairwise complex conjugates. Further, in order that the frequency response matrix $\mathbf{g}_b^-(t)$ is causal, *i.e.* zero for negative time arguments, all poles must have negative real parts. In what follows, only the terms with $k = -1, 0, 1, 2$ are withhold in the expansion. Then, upon assemblage of terms of equal power in $\mathrm{i}\omega$ the following approximation is obtained

$$\mathbf{G}_{bb}^-(\mathrm{i}\omega) \simeq \mathbf{K}_{bb}^- + \big(\mathrm{i}\omega\big)\mathbf{C}_{bb}^- + \big(\mathrm{i}\omega\big)^2\mathbf{M}_{bb}^- + \sum_{j=1}^{s} \left(\frac{1}{\mathrm{i}\omega - z_j} + \frac{1}{z_j}\right) \mathbf{G}_j^-, \tag{2–71}$$

where the coefficient matrices $\mathbf{K}_{bb}^-$, $\mathbf{C}_{bb}^-$, and $\mathbf{M}_{bb}^-$ are real matrices of the dimension $n_b \times n_b$, and $\mathbf{G}_j^- = \mathbf{G}_{j,-1}$. The expansion (2–71) is only valid at small circular frequencies. As indicated by Eq. (2–75), the expansion at large circular frequencies has a completely different form. Below, the matrices $\mathbf{K}_{bb}^-$, $\mathbf{C}_{bb}^-$ and $\mathbf{M}_{bb}^-$ defining the first three terms of the expansion will be given a physical interpretation. Equation (2–71) corresponds to the following differential relationships in the time domain,

$$\mathbf{f}_b^-(t) = \left(\mathbf{K}_{bb}^- + \sum_{j=1}^{s} \frac{1}{z_j}\mathbf{G}_j^-\right)\mathbf{u}_b^-(t) + \mathbf{C}_{bb}^-\dot{\mathbf{u}}_b^-(t) + \mathbf{M}_{bb}^-\ddot{\mathbf{u}}_b^-(t) + \sum_{j=1}^{s} \mathbf{G}_j^-\mathbf{v}_j(t), \tag{2–72}$$

where the auxiliary filter variables $\mathbf{v}_j(t)$ of dimension n_b are determined by the 1st order filter differential equations

$$\frac{d}{dt}\mathbf{v}_j(t) - z_j\mathbf{v}_j(t) = \mathbf{u}_b^-(t), \qquad j = 1, \ldots, s. \tag{2–73}$$

Evidently, the boundary condition provided by Eqs. (2–72) and (2–73) is local in time. This comes partly at the expense of loss of accuracy due to the truncation of the series expansion (2–70), and partly at the extra computation effort brought forward by the augmentation of the state vector of the solution domain D^+ with the filter variables $\mathbf{v}_j(t)$. Further, if the matrices $\mathbf{K}_{bb}^-$, $\mathbf{C}_{bb}^-$, $\mathbf{M}_{bb}^-$, $\mathbf{G}_j^-$ are (tri)diagonal (or at most contain coupling to the neighbouring nodes on S_0) the boundary condition (2–72) is local in space.

In general the poles z_j of $\mathbf{G}_{bb}^-(z)$ are complex, for which reason the filter variables $\mathbf{v}_j$ become complex as well. Equation (2–73) is integrated along with the FEM equations by the degrees of freedom $\mathbf{u}_i^+(t)$ for the interior domain D^+, and the degrees of freedom $\mathbf{u}_b^+(t) = \mathbf{u}_b^-(t)$ on the

interface S_0, see Fig. 2–7. As seen from Eq. (2–71) the interaction forces in the static case, *i.e.* for $\omega = 0$, become

$$\mathbf{f}_b^-(t) = \mathbf{K}_{bb}^- \mathbf{u}_b^-(t). \tag{2–74}$$

Hence, $\mathbf{K}_{bb}^-$ may be interpreted as the stiffness matrix of the interaction forces under quasi-static motions of the interface nodes.

The second term on the right hand side of Eq. (2–72) determines the interaction force due to interface nodal velocities $\dot{\mathbf{u}}_b^-(t)$. In Example 2.8 it will be shown that an interaction force of the form $\mathbf{f}_b^-(t) = \mathbf{C}_{bb}^- \dot{\mathbf{u}}_b^-(t)$ appears in the case of plane wave propagation in a linear elastic medium. Here the matrix $\mathbf{C}_{bb}^-$ represents a linear viscous damping matrix of the interaction forces. Adopting the designation used in electronics, we shall generally refer to boundary conditions of the kind $\mathbf{f}_b^-(t) = \mathbf{C}_{bb}^- \dot{\mathbf{u}}_b^-(t)$ as *impedance boundary conditions*. In electronics the impedance defines the amount of voltage that is needed in order to produce a unit current. In elastodynamics it defines the stress to particle velocity ratio—or the nodal force to nodal velocity ratio in the discrete FEM description.

The third term indicates the interaction forces from induced inertial forces in the domain D^- adjacent to the boundary S_0 due to nodal accelerations $\ddot{\mathbf{u}}_b^-(t)$. $\mathbf{M}_{bb}^-$ may thus be interpreted as a kind of added mass matrix, similar to the added mass contributions in incompressible fluids.

The approximate frequency response matrix $\mathbf{G}_{bb}^-(\mathrm{i}\omega)$ as given by Eq. (2–71) is denoted rational, similar to the approximate version of the viscoelastic stress–strain relation ship provided by Eq. (1–125). The determination of $\mathbf{K}_{bb}^-$, $\mathbf{C}_{bb}^-$, $\mathbf{M}_{bb}^-$, $\mathbf{G}_j^-$ and z_j from given input–output data of $\mathbf{u}_b^-(t)$ and $\mathbf{f}_b^-(t)$ in the time or frequency domain has been considered by Wolf (1991b).

As the frequency ω increases, the corresponding wavelength decreases. Generally, the part of D^-, which influences the interaction forces, has an extent of approximately one wavelength. Hence, as $\omega \to \infty$ the interaction tends to become more and more local in space, only involving a small sub-domain in D^- adjacent to S_0. Further, waves propagating from sources in D^+ placed a few wavelengths from the interaction boundary may locally be considered as plane waves impinging on S_0. As shown in Example 2.8, the interaction forces from plane P- and S-waves can be represented by impedance boundary conditions. In the same way, surface and interface waves (Rayleigh-, Love- and Stonely waves) will only have local influence as $\omega \to \infty$. Consequently, the frequency response matrix $\mathbf{G}_{bb}^-(\mathrm{i}\omega)$ has the following asymptotic behaviour as $\omega \to \infty$:

$$\mathbf{G}_{bb}^-(\mathrm{i}\omega) = \big(\mathrm{i}\omega\big)\mathbf{C}_{bb}^-. \tag{2–75}$$

For ease, the same symbol has been applied for the expansion matrix $\mathbf{C}_{bb}^-$ in Eqs. (2–70) and (2–75), although these matrices are generally different, since the expansions are performed at different extremes. Actually, $\mathbf{C}_{bb}^-$ in Eq. (2–75) is local in space, which is not the case for the corresponding matrix in Eq. (2–70). Wolf and Song (1996) have suggested the following so-called *double asymptotic expansion* for the interaction forces:

$$\mathbf{G}_{bb}^-(\mathrm{i}\omega) = \mathbf{K}_{bb}^- + \big(\mathrm{i}\omega\big)\mathbf{C}_{bb}^-, \tag{2–76}$$

where $\mathbf{K}_{bb}^-$ is the stiffness matrix in Eq. (2–70), and $\mathbf{C}_{bb}^-$ is the damping matrix matrix in Eq. (2–75). Hence, Eq. (2–76) will be correct at very small circular frequencies, where the first term in Eq. (2–76) dominates, and at very large circular frequencies, where the second term dominates. In the following, various approaches for approximate calculation of the interaction forces in a finite element formulation will be demonstrated.

Example 2.7 Similarity-based forecasting calculation of interaction forces

As demonstrated in Chapter 4, the boundary-element method may be applied for the establishment of a transmitting boundary condition in an FE based analysis of infinite domains. However, this is fairly cumbersome, since a fundamental solution for the material of the outer domain must be available. To circumvent these problems, Wolf and Song (1996) have suggested several methods for calculating the interaction forces based on the concept of *similarity*, which they explain in the following way, see Fig. A. A so-called *similarity centre* O is defined on the ground surface of D^+. All nodes on the interaction surface S_0 then have a certain distance r_0 from O. Next, in D^- a FEM mesh is defined with a node pattern, which is affine to the node pattern on S_0 with respect to O, *i.e.* the position of the nodes in a certain layer is in the same angular direction as the corresponding nodes on S_0, and the distance is obtained by multiplication of the distance of the node on S_0 by a factor $\frac{r}{r_0} > 1$, which is common to all nodes of the layer. Only a few element layers are normally needed. The value of r for the outer nodal layer is denoted r_1. Generally, quantities referring to the inner and outer nodal layers are indicated by the indices 0 and 1, respectively, whereas quantities referring to the interior nodes of the element mesh are referred to by the index i. In a similarity based formulation, inhomogeneity or anisotropy in D^- can only be taken into consideration in the form of piecewise homogeneous or isotropic angular sectors as shown in Fig. A. Based on the similarity principle, the so-called *forecasting method* was devised by Wolf and Song (1996) for calculating the impulse response matrix of the interaction forces in the time-domain. Instead, in what follows the principle will be used for calculating the corresponding frequency response matrix $\mathbf{G}_{bb}^{-}(\mathrm{i}\omega)$.

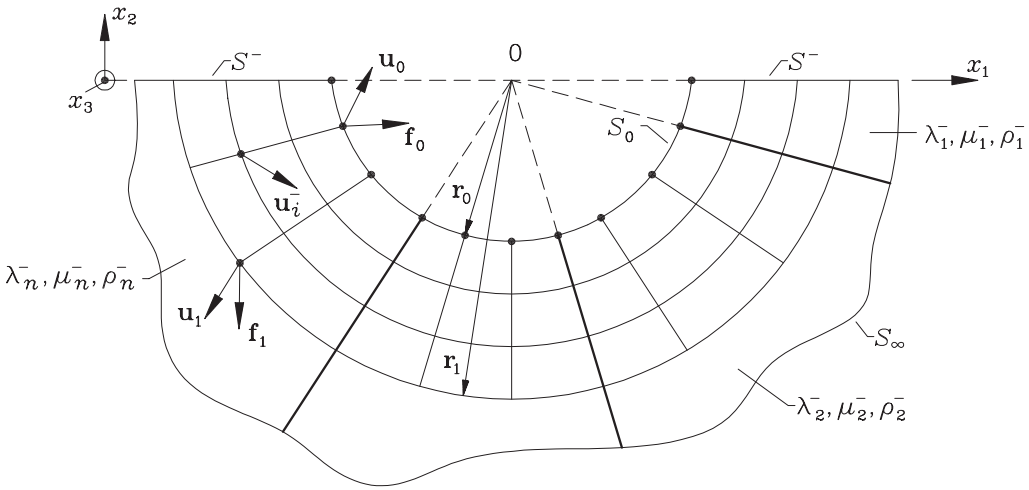

Figure A Similarity-based formulation. Definition of parameters.

The equations of motion for the modelled part of D^- read

$$\mathbf{M}^-\ddot{\mathbf{u}}^- + \mathbf{C}^-\dot{\mathbf{u}}^- + \mathbf{K}^-\mathbf{u}^- = \mathbf{f}^-(t), \tag{a}$$

where $\mathbf{u}^-(t)$ is the displacement vector, $\mathbf{f}^-(t)$ is the load vector, and $\mathbf{M}^-$, $\mathbf{C}^-$ and $\mathbf{K}^-$ are the mass-, damping- and stiffness matrices. In this case $\mathbf{u}^-(t)$ is partitioned into sub-vectors $\mathbf{u}_0(t) = \mathbf{u}_b^-(t)$ and $\mathbf{u}_1(t)$ of the dimension n_b belonging to the inner and outer nodal layers, and into the sub-vector $\mathbf{u}_i(t)$ of the dimension n_i for the internal nodes of the mesh. Similar partitionings of the system matrices and the load vector are performed as follows:

(continued)

$$\left.\begin{aligned} \mathbf{u}^-(t) &= \begin{bmatrix}\mathbf{u}_0(t)\\ \mathbf{u}_1(t)\\ \mathbf{u}_i(t)\end{bmatrix},\ \mathbf{f}^-(t) = \begin{bmatrix}\mathbf{f}_0(t)\\ \mathbf{f}_1(t)\\ \mathbf{0}\end{bmatrix},\ \mathbf{M}^- = \begin{bmatrix}\mathbf{M}_{00} & \mathbf{M}_{01} & \mathbf{M}_{0i}\\ \mathbf{M}_{10} & \mathbf{M}_{11} & \mathbf{M}_{1i}\\ \mathbf{M}_{i0} & \mathbf{M}_{i1} & \mathbf{M}_{ii}\end{bmatrix}\\ \mathbf{C}^- &= \begin{bmatrix}\mathbf{C}_{00} & \mathbf{C}_{01} & \mathbf{C}_{0i}\\ \mathbf{C}_{10} & \mathbf{C}_{11} & \mathbf{C}_{1i}\\ \mathbf{C}_{i0} & \mathbf{C}_{i1} & \mathbf{C}_{ii}\end{bmatrix},\ \mathbf{K}^- = \begin{bmatrix}\mathbf{K}_{00} & \mathbf{K}_{01} & \mathbf{K}_{0i}\\ \mathbf{K}_{10} & \mathbf{K}_{11} & \mathbf{K}_{1i}\\ \mathbf{K}_{i0} & \mathbf{K}_{i1} & \mathbf{K}_{ii}\end{bmatrix} \end{aligned}\right\} \tag{b}$$

Then, in the frequency domain, (a) obtains the form

$$\begin{bmatrix}\mathbf{F}_0\\ \mathbf{F}_1\\ \mathbf{0}\end{bmatrix} = \begin{bmatrix}\mathbf{D}_{00} & \mathbf{D}_{01} & \mathbf{D}_{0i}\\ \mathbf{D}_{10} & \mathbf{D}_{11} & \mathbf{D}_{1i}\\ \mathbf{D}_{i0} & \mathbf{D}_{i1} & \mathbf{D}_{ii}\end{bmatrix}\begin{bmatrix}\mathbf{U}_0\\ \mathbf{U}_1\\ \mathbf{U}_i\end{bmatrix}, \tag{c}$$

where uppercase symbols represent the amplitudes of corresponding lowercase quantities under harmonic response, and where

$$\begin{bmatrix}\mathbf{D}_{00} & \mathbf{D}_{01} & \mathbf{D}_{0i}\\ \mathbf{D}_{10} & \mathbf{D}_{11} & \mathbf{D}_{1i}\\ \mathbf{D}_{i0} & \mathbf{D}_{i1} & \mathbf{D}_{ii}\end{bmatrix} = (\mathrm{i}\omega)^2\begin{bmatrix}\mathbf{M}_{00} & \mathbf{M}_{01} & \mathbf{M}_{0i}\\ \mathbf{M}_{10} & \mathbf{M}_{11} & \mathbf{M}_{1i}\\ \mathbf{M}_{i0} & \mathbf{M}_{i1} & \mathbf{M}_{ii}\end{bmatrix} + (\mathrm{i}\omega)\begin{bmatrix}\mathbf{C}_{00} & \mathbf{C}_{01} & \mathbf{C}_{0i}\\ \mathbf{C}_{10} & \mathbf{C}_{11} & \mathbf{C}_{1i}\\ \mathbf{C}_{i0} & \mathbf{C}_{i1} & \mathbf{C}_{ii}\end{bmatrix} + \begin{bmatrix}\mathbf{K}_{00} & \mathbf{K}_{01} & \mathbf{K}_{0i}\\ \mathbf{K}_{10} & \mathbf{K}_{11} & \mathbf{K}_{1i}\\ \mathbf{K}_{i0} & \mathbf{K}_{i1} & \mathbf{K}_{ii}\end{bmatrix}. \tag{d}$$

From the matrix equation in the lowest row of (c), $\mathbf{U}_i$ can be expressed in terms of $\mathbf{U}_0$ and $\mathbf{U}_1$. $\mathbf{U}_i$ can then be condensed from the first two rows leading to

$$\begin{bmatrix}\mathbf{F}_0\\ \mathbf{F}_1\end{bmatrix} = \begin{bmatrix}\mathbf{L}_{00} & \mathbf{L}_{01}\\ \mathbf{L}_{10} & \mathbf{L}_{11}\end{bmatrix}\begin{bmatrix}\mathbf{U}_0\\ \mathbf{U}_1\end{bmatrix}, \tag{e}$$

$$\begin{bmatrix}\mathbf{L}_{00} & \mathbf{L}_{01}\\ \mathbf{L}_{10} & \mathbf{L}_{11}\end{bmatrix} = \begin{bmatrix}\mathbf{D}_{00} - \mathbf{D}_{0i}\mathbf{D}_{ii}^{-1}\mathbf{D}_{i0} & \mathbf{D}_{01} - \mathbf{D}_{0i}\mathbf{D}_{ii}^{-1}\mathbf{D}_{i1}\\ \mathbf{D}_{10} - \mathbf{D}_{1i}\mathbf{D}_{ii}^{-1}\mathbf{D}_{i0} & \mathbf{D}_{11} - \mathbf{D}_{1i}\mathbf{D}_{ii}^{-1}\mathbf{D}_{i1}\end{bmatrix}. \tag{f}$$

The amplitudes of the forces and displacements on the inner and outer interfaces are related as, cf. Eqs. (2–64) and (2–69),

$$\mathbf{F}_0(\omega) = \mathbf{G}_0(\mathrm{i}\omega)\mathbf{U}_0(\omega), \tag{g}$$

$$\mathbf{F}_1(\omega) = -\mathbf{G}_1(\mathrm{i}\omega)\mathbf{U}_1(\omega), \tag{h}$$

where $\mathbf{G}_0(\mathrm{i}\omega) = \mathbf{G}_{bb}^-(\mathrm{i}\omega)$, and $\mathbf{G}_1(\mathrm{i}\omega)$ is the corresponding frequency response matrix for the interaction forces on the outer periphery. Based on dimensional analysis, Wolf and Song (1996) have derived the following relation between $\mathbf{G}_1(\mathrm{i}\omega)$ and $\mathbf{G}_0(\mathrm{i}\omega)$:

$$\mathbf{G}_1(\mathrm{i}\omega) = \left(\frac{r_1}{r_0}\right)^{d-1}\mathbf{G}_0\left(\frac{r_1}{r_0}\mathrm{i}\omega\right). \tag{i}$$

d signifies the spatial dimension of the problem ($d = 2$ or $d = 3$). Insertion of (h) into the lower matrix equation of (e) provides an expression for $\mathbf{U}_1$ in terms of $\mathbf{U}_0$ and $\mathbf{G}_1$. Condensation of $\mathbf{U}_1$ from the upper matrix equation (e) and use of (i) then provides the following expression for the determination of $\mathbf{G}_0(\mathrm{i}\omega) = \mathbf{G}_{bb}^-(\mathrm{i}\omega)$:

$$\mathbf{G}_0(\mathrm{i}\omega) = \mathbf{L}_{00}(\mathrm{i}\omega) - \mathbf{L}_{01}(\mathrm{i}\omega)\left(\left(\frac{r_1}{r_0}\right)^{d-1}\mathbf{G}_0\left(\frac{r_1}{r_0}\mathrm{i}\omega\right) + \mathbf{L}_{11}(\mathrm{i}\omega)\right)^{-1}\mathbf{L}_{10}(\mathrm{i}\omega). \tag{j}$$

(continued)

Assume that an approximate value of $\mathbf{G}_0(\mathrm{i}\omega)$ is known for some high frequency $\omega = \omega_0$, which may be taken as the asymptotic impedance solution (2–75). Next, values at the lower frequencies $\omega = \omega_0 r_0/r_1$, $\omega = \omega_0 r_0^2/r_1^2, \ldots$ can be calculated recursively from Eq. (j). By varying ω_0, arbitrarily many frequencies can be considered. □

Example 2.8 Impedance boundary conditions in elastodynamics

The elastic P- and S-waves from a given point source will locally behave as plane waves as the distance to the artificial boundary increases. In practice, adjustment to this condition is already achieved at a distance of a few wavelengths between the source and observation point. This forms the background for a local radiation boundary condition of the impedance type (2–75) formulated by Krenk and Kirkegaard (2001), which will be indicated below. Krenk and Kirkegaard derived their boundary condition in a fixed coordinate system. Using an identical approach, the radiation boundary condition will here be derived for P- and S-wave propagation in a $(\tilde{x}_1, \tilde{x}_2, \tilde{x}_3)$-coordinate system moving with the constant velocity v_j relative to a fixed (x_1, x_2, x_3)-coordinate system. The original solution by Krenk and Kirkegaard is obtained for the special choice of $v_j = 0$.

The material of the surrounding medium D^- is assumed to be homogeneous, isotropic and linear elastic with the Lamé constants (λ^-, μ^-) and the mass density ρ^-. With the constant convection velocity v_j of the moving coordinate system, the convective Navier equation for the domain D^- reads

$$\big(\lambda^- + \mu^-\big)\frac{\partial^2 \tilde{u}_j}{\partial \tilde{x}_i \partial \tilde{x}_j} + \mu^- \frac{\partial^2 \tilde{u}_i}{\partial \tilde{x}_j \partial \tilde{x}_j} - \rho^- \Big(\frac{\partial^2 \tilde{u}_i}{\partial t^2} - 2v_j \frac{\partial^2 \tilde{u}_i}{\partial \tilde{x}_j \partial t} + v_j v_k \frac{\partial^2 \tilde{u}_i}{\partial \tilde{x}_j \partial \tilde{x}_k} \Big) = 0. \tag{a}$$

Consider the following plane P- and S-waves, propagating in the directions $p_{j,P}$ and $p_{j,S}$, and with the amplitude vectors $A_{j,P}$ and $A_{j,S}$,

$$\left.\begin{aligned} \tilde{u}_{i,P}(\tilde{\mathbf{x}}, t) &= A_{i,P} f_P\big(\Psi_P\big) \quad , \quad \Psi_P = \tilde{x}_j p_{j,P} - \big(c_P - v_j p_{j,P}\big)t \\ \tilde{u}_{i,S}(\tilde{\mathbf{x}}, t) &= A_{i,S} f_S\big(\Psi_S\big) \quad , \quad \Psi_S = \tilde{x}_j p_{j,S} - \big(c_S - v_j p_{j,S}\big)t \end{aligned}\right\}. \tag{b}$$

It should be noticed that the components $p_{j,P}$ and $p_{j,S}$ denote the directional cosines of the propagation directions as seen in the fixed coordinate system. As explained later, the corresponding directional cosines as seen in the moving coordinate system are different. c_P and c_S denote the phase velocities corresponding to the Lamé constants (λ^-, μ^-) in a fixed coordinate system. Following the approach of Subsection 1.3.2, it may relatively easily be shown that the displacement fields defined in Eq. (b) are both solutions to the convective Navier equation (a).

The total displacement is assumed to consist of plane P- and S-wave components only, so

$$\tilde{u}_i(\tilde{\mathbf{x}}, t) = \tilde{u}_{i,P}(\tilde{\mathbf{x}}, t) + \tilde{u}_{i,S}(\tilde{\mathbf{x}}, t). \tag{c}$$

Since, $\tilde{u}_{i,P}$ is parallel to $p_{i,P}$, and $\tilde{u}_{i,S}$ is orthogonal to $p_{i,S}$, it follows from (c) that

$$\tilde{u}_i^P = \frac{p_{i,P}\, p_{k,S}}{p_{m,P} p_{m,S}} \tilde{u}_k, \tag{d}$$

$$\tilde{u}_{i,S} = \tilde{u}_i - \tilde{u}_{i,P} = \left(\delta_{ik} - \frac{p_{i,P}\, p_{k,S}}{p_{m,P} p_{m,S}} \right) \tilde{u}_k. \tag{e}$$

The small strain tensors corresponding to the displacement fields $\tilde{u}_{i,P}$ and $\tilde{u}_{i,S}$ become, cf. Eqs. (1–3), (d) and (e),

(continued)

$$\tilde{\epsilon}_{ij,P} = \frac{1}{2}\big(A_{i,P}\, p_{j,P} + A_{j,P}\, p_{i,P}\big) f'_P(\Psi_P)$$
$$= -\frac{1}{c_P - v_l p_{l,P}} \cdot \frac{1}{2}\big(A_{i,P}\, p_{j,P} + A_{j,P}\, p_{i,P}\big) \frac{\partial}{\partial t} f_P(\Psi_P)$$
$$= -\frac{1}{c_P - v_l p_{l,P}} \cdot \frac{1}{2}\big(\dot{\tilde{u}}_{i,P}\, p_{j,P} + \dot{\tilde{u}}_{j,P}\, p_{i,P}\big) = -\frac{p_{i,P}\, p_{j,P}\, p_{k,S}}{\Big(c_P - v_l p_{l,P}\Big) p_{m,P} p_{m,S}} \dot{\tilde{u}}_k, \tag{f}$$

$$\tilde{\epsilon}_{ij,S} = -\frac{1}{c_S - v_l p_{l,S}} \cdot \frac{1}{2}\big(\dot{\tilde{u}}_{i,S}\, p_{j,S} + \dot{\tilde{u}}_{j,S}\, p_{i,S}\big)$$
$$= -\frac{1}{c_S - v_l p_{l,S}} \cdot \frac{1}{2}\left(\Big(\delta_{ik} - \frac{p_{i,P}\, p_{k,S}}{p_{l,P} p_{l,S}}\Big)\dot{\tilde{u}}_k p_{j,S} + \Big(\delta_{jk} - \frac{p_{j,P}\, p_{k,S}}{p_{l,P} p_{l,S}}\Big)\dot{\tilde{u}}_k p_{i,S}\right)$$
$$= -\frac{1}{2}\frac{1}{c_S - v_l p_{l,S}}\left(p_{i,S}\delta_{jk} + p_{j,S}\delta_{ik} - \frac{p_{i,P}\, p_{j,S} + p_{j,P} p_{i,S}}{p_{l,P}\, p_{l,S}} p_{k,S}\right)\dot{\tilde{u}}_k. \tag{g}$$

The corresponding stress tensors become, cf. Eq. (1–5),

$$\tilde{\sigma}_{ij,P} = -\frac{1}{\Big(c_P - v_l p_{l,P}\Big) p_{m,P} p_{m,S}}\Big(\lambda^- \delta_{ij} + 2\mu^- p_{i,P}\, p_{j,P}\Big) p_{k,S} \dot{\tilde{u}}_k, \tag{h}$$

$$\tilde{\sigma}_{ij,S} = -\frac{\mu^-}{c_S - v_l p_{l,S}}\left(p_{i,S}\delta_{jk} + p_{j,S}\delta_{ik} - \frac{p_{i,P}\, p_{j,S} + p_{j,P}\, p_{i,S}}{p_{l,P} p_{l,S}} p_{k,S}\right)\dot{\tilde{u}}_k. \tag{i}$$

The total stress tensor is obtained as the sum of (h) and (i),

$$\tilde{\sigma}_{ij} = -\Bigg[\frac{1}{\Big(c_P - v_l p_{l,P}\Big) p_{m,P} p_{m,S}}\Big(\lambda^- \delta_{ij} + 2\mu^- p_{i,P}\, p_{j,P}\Big) p_{k,S}$$
$$+ \frac{\mu^-}{c_S - v_l p_{l,S}}\left(p_{i,S}\delta_{jk} + p_{j,S}\delta_{ik} - \frac{p_{i,P}\, p_{j,S} + p_{j,P}\, p_{i,S}}{p_{l,P} p_{l,S}} p_{k,S}\right)\Bigg]\dot{\tilde{u}}_k. \tag{j}$$

The surface tractions $\tilde{\tau}_i^-$ and $\tilde{\tau}_i^+$ on the parts of the interface S_0 belonging to D^- and D^+ become

$$\left.\begin{aligned} \tilde{\tau}_i^- &= \tilde{\sigma}_{ij} n_j^- \\ \tilde{\tau}_i^+ &= -\tilde{\tau}_i^- = -\tilde{\sigma}_{ij} n_j^- = \tilde{\sigma}_{ij} n_j^+ \end{aligned}\right\}, \tag{k}$$

where n_i^+ and $n_i^- = -n_i^+$ signify the outward directed normal unit vectors to the domains D^- and D^+ at the same position on S_0. From (j) and (k) it follows that the surface tractions $\tilde{\tau}_i^+$ is given by the following impedance boundary condition, which is local in space,

$$\tilde{\tau}_i^+ = -\tilde{c}_{ij}^- \dot{\tilde{u}}_j, \tag{l}$$

$$\tilde{c}_{ij}^- = \frac{1}{\Big(c_P - v_l p_{l,P}\Big) p_{m,P} p_{j,S}}\Big(\lambda^- n_i^+ p_{j,S} + 2\mu^- n_k^+ p_{k,P}\, p_{i,P}\, p_{j,S}\Big)$$
$$+ \frac{\mu^-}{c_S - v_l p_{l,S}}\left(p_{i,S} n_j^+ + n_k^+ p_{k,S}\delta_{ij} - n_k^+ \frac{p_{k,S}\, p_{i,P} + p_{k,P}\, p_{i,S}}{p_{l,P} p_{l,S}} p_{j,S}\right). \tag{m}$$

So far the directional cosines of the propagation directions, $p_{i,P}$ and $p_{i,S}$, in the fixed coordinate system have not been specified. In what follows these will be determined for a certain observation point

(continued)

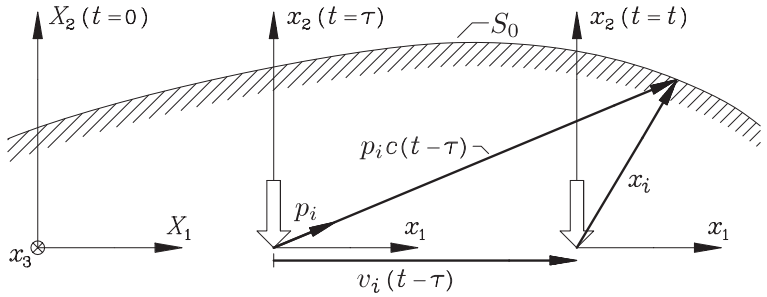

Figure A Determination of propagation directions in fixed coordinate system.

with the moving coordinates $\tilde{x}_i$. As seen in Fig. A, a wave reaching the observation point with the moving coordinates $\tilde{x}_i$ at the time t is generated by the force at a previous instant of time τ. During the elapsed time interval $t-\tau$ the wave has moved the distance $c(t-\tau)$ in the fixed direction p_i, and the force has moved $v_i(t-\tau)$. Then, the following relation is established:

$$\tilde{x}_i = p_i c(t-\tau) - v_i(t-\tau). \tag{n}$$

From (n) the following relation is derived for the elapsed time interval

$$t-\tau = \frac{|\tilde{\mathbf{x}}|}{\sqrt{c^2 - 2v_i p_i c + v^2}}, \tag{o}$$

where $v = |\mathbf{v}|$. From (n) and (o) the following expression is obtained for the determination of p_i:

$$p_i = \tilde{p}_i \sqrt{1 - 2\frac{v_i}{c}p_i + \left(\frac{v}{c}\right)^2} + \frac{v_i}{c} \quad , \quad \tilde{p}_i = \frac{\tilde{x}_i}{|\tilde{\mathbf{x}}|}. \tag{p}$$

Equation (p) can be solved analytically in two dimensions, where $p_i = [\cos\theta, \sin\theta]^T$ is defined by the angle of inclination, θ. This is not possible in three dimensions, where cyclic iteration must be used. The impedance boundary condition (l), (m) will make the interface S_0 transparent to plane P- and S-waves only. All other wave types, *e.g.* Rayleigh waves, Stonely waves, Love waves or non-plane P- and S-waves, will be partly reflected at the boundary.

Upon discretization of Eq. (l) by means of FE-interpolation between nodal values of the interface surface tractions and velocities, the following impedance boundary condition is obtained, cf. Eq. (2–75):

$$\tilde{\mathbf{f}}_b^+(t) = -\tilde{\mathbf{C}}_{bb}^- \dot{\tilde{\mathbf{u}}}_b^+(t). \tag{q}$$

In the special case of $v_i = 0$, one has $p_{i,S} = p_{i,P} = p_i$, and Eq. (m) reduces to

$$\tilde{c}_{ij} = \frac{1}{c_P}\left(\lambda^- n_i^+ p_j + 2\mu^- n_k^+ p_k p_i p_j\right) + \frac{\mu^-}{c_S}\left(p_i n_j^+ + n_k^+ p_k \delta_{ij} - 2n_k^+ p_k p_i p_j\right). \tag{r}$$

Equation (r) is the solution derived by Krenk and Kirkegaard (2001). The marked difference between the tensor expressions (m) and (r) is that the former contains singularities in the denominators, which become increasingly important as the convection velocity approaches the phase velocities. Krenk *et al.* (1999) formulated a transmitting boundary condition in moving coordinates based on the fixed coordinate solution (r), merely by changing the fixed coordinates of the velocity $\partial u_j/\partial t$ of a moving point of the interphase into the corresponding total time derivative coordinates $\partial\tilde{u}_j/\partial t - v_k \partial\tilde{u}_j/\partial\tilde{x}_k$, cf. Eq. (2–50). This is believed to be admissible as long as the convection velocity is small compared to the phase velocities, but may give problems at larger convection velocities. □

Example 2.9 Transmitting boundary conditions for Euler-Bernoulli beams

In Example 2.3 the analytic solution for the Euler-Bernoulli beam on a Kelvin-Pasternak foundation was derived in the fixed frame of reference, based on the assumptions that the response is linear and that the beam is homogeneous. The wavenumbers in the moving frame of reference were derived in Example 2.6, and the corresponding amplitudes of the four wave components comprising the total displacement field in the beam are obtained by insertion of these wavenumbers in Eq. (k) of Example 2.3. Then,

$$\tilde{u}(\tilde{x},t) = \begin{cases} \tilde{U}_1(\omega)\mathrm{e}^{-\tilde{k}_1^a\tilde{x}+\mathrm{i}\left(\tilde{k}_1^p\tilde{x}-\omega t\right)} + \tilde{U}_2(\omega)\mathrm{e}^{-\tilde{k}_2^a\tilde{x}+\mathrm{i}\left(\tilde{k}_2^p\tilde{x}-\omega t\right)} & \text{for} \quad \tilde{x} \leqslant 0 \\ \tilde{U}_3(\omega)\mathrm{e}^{-\tilde{k}_3^a\tilde{x}+\mathrm{i}\left(\tilde{k}_3^p\tilde{x}-\omega t\right)} + \tilde{U}_4(\omega)\mathrm{e}^{-\tilde{k}_4^a\tilde{x}+\mathrm{i}\left(\tilde{k}_4^p\tilde{x}-\omega t\right)} & \text{for} \quad \tilde{x} > 0 \end{cases} \tag{a}$$

In order to analyse problems involving, for example, local inhomogeneities along the track or nonlinear response in the vicinity of a vehicle or moving load, a numerical solution is needed. A finite element scheme combined with transparent boundary conditions based on the analytic solution may be applied. The idea is that at a certain distance from the loaded region the parameters of the track may be replaced by their mean values without significant loss of accuracy, and the response in the far-field is linear, as discussed in introduction to this section.

Transparent boundary conditions for Euler-Bernoulli beams were derived by Wang and Lai (2000). However, the authors did not base the transmitting boundary conditions on the entire analytic solution, but only on the wave components corresponding to the travelling waves. Therefore the artificial ends of the track had to be placed far from the source of vibration. This is not the case for the transmitting boundary conditions derived below.

Subsequently a finite part of an infinite beam, *i.e.* in the interval $[\tilde{x}_b^-, \tilde{x}_b^+]$, will be considered. Transmitting boundary conditions are to be derived for the artificial boundaries $\tilde{x}_b^-$ and $\tilde{x}_b^+$, which will constitute the end points of the FEM model. The idea is to apply a moment $\tilde{M}_b^-(t)$ and a shear force $\tilde{Q}_b^-(t)$ at $\tilde{x}_b^-$, which correspond exactly to the forces that would be present if the FE modelled part of the track was connected to a semi-infinite beam at $\tilde{x}_b^-$, see Fig. A. Likewise, the moment and shear force $\tilde{M}_b^+(t)$ and $\tilde{Q}_b^+(t)$ are applied at $\tilde{x}_b^+$. If the correct reactions are established at the interfaces, the boundaries become perfectly transparent.

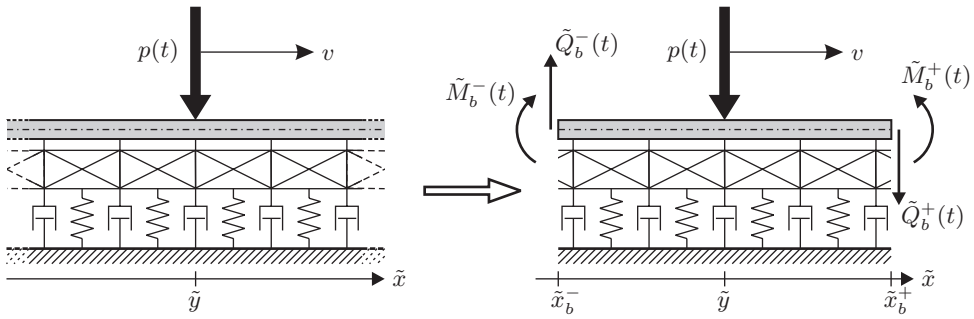

Figure A Infinite beam on Kelvin-Pasternak foundation and equivalent finite beam with moments and shear forces applied at the artificial boundaries.

As discussed in Subsection 2.1.3, the degrees of freedom in the finite element model of the beam are the displacement and the rotations at each node, since the Hermite shape functions are used for the interpolation of the field quantities. Hence, the unknown variables at the artificial boundaries are the displacements $\tilde{u}_b^-$ and $\tilde{u}_b^+$ and the rotations $\tilde{\theta}_b^-$ and $\tilde{\theta}_b^+$. Transparent boundary conditions, which are automatically updated with time, can be achieved by a formulation of the moment and the shear force at the artificial boundaries in terms of the boundary displacements and rotations. *(continued)*

Formulation in the frequency domain

With the definitions of the rotation, the moment and the shear force given in Eq. (2–16) and the displacement fields given by Eq. (a), the following relationships are given in the frequency domain for a boundary located at positive abscissas:

$$\begin{bmatrix} \tilde{\Theta}_b^+(\omega) \\ \tilde{U}_b^+(\omega) \end{bmatrix} = \mathbf{L}_0^+ \begin{bmatrix} \tilde{U}_3 \\ \tilde{U}_4 \end{bmatrix}, \quad \mathbf{L}_0^+ = \begin{bmatrix} \tilde{k}_3^a - \mathrm{i}\tilde{k}_3^p & \tilde{k}_4^a - \mathrm{i}\tilde{k}_4^p \\ 1 & 1 \end{bmatrix}, \tag{b}$$

$$\begin{bmatrix} \tilde{\mathcal{M}}_b^+(\omega) \\ \tilde{\mathcal{Q}}_b^+(\omega) \end{bmatrix} = \mathbf{L}_1^+ \begin{bmatrix} \tilde{U}_3 \\ \tilde{U}_4 \end{bmatrix}, \quad \mathbf{L}_1^+ = -EI \begin{bmatrix} (\tilde{k}_3^a - \mathrm{i}\tilde{k}_3^p)^2 & (\tilde{k}_4^a - \mathrm{i}\tilde{k}_4^p)^2 \\ (\tilde{k}_3^a - \mathrm{i}\tilde{k}_3^p)^3 & (\tilde{k}_4^a - \mathrm{i}\tilde{k}_4^p)^3 \end{bmatrix}. \tag{c}$$

The amplitude functions $\tilde{U}_b^+(\omega)$, $\tilde{\Theta}_b^+(\omega)$, $\tilde{\mathcal{Q}}_b^+(\omega)$ and $\tilde{\mathcal{M}}_b^+(\omega)$ are defined by

$$\left.\begin{aligned} \tilde{u}_b^+(t) &= \tilde{U}_b^+(\omega)\mathrm{e}^{-\mathrm{i}\omega t}, \quad \tilde{\theta}_b^+(t) = \tilde{\Theta}_b^+(\omega)\mathrm{e}^{-\mathrm{i}\omega t}, \\ \tilde{Q}_b^+(t) &= \tilde{\mathcal{Q}}_b^+(\omega)\mathrm{e}^{-\mathrm{i}\omega t}, \quad \tilde{M}_b^+(t) = \tilde{\mathcal{M}}_b^+(\omega)\mathrm{e}^{-\mathrm{i}\omega t}. \end{aligned}\right\} \tag{d}$$

The interface parameters at negative abscissas are expressed in a similar manner. In this case the $\tilde{U}_1$ and $\tilde{U}_2$ terms are included and the signs on the interface reactions are changed in accordance with the definitions in Fig. A.

From Eqs. (b) and (c) it follows that the interface reaction forces can be formulated as functions of the displacement and rotation. Hence, the following frequency response relation arises:

$$\begin{bmatrix} \tilde{\mathcal{M}}_b(\omega) \\ \tilde{\mathcal{Q}}_b(\omega) \end{bmatrix} = \mathbf{B}(\omega) \begin{bmatrix} \tilde{\Theta}_b(\omega) \\ \tilde{U}_b(\omega) \end{bmatrix}, \quad \mathbf{B}(\omega) = \begin{cases} \mathbf{L}_1^-(\mathbf{L}_0^-)^{-1} & \text{for} \quad \tilde{x}_b < \tilde{y} \\ \mathbf{L}_1^+(\mathbf{L}_0^+)^{-1} & \text{for} \quad \tilde{x}_b > \tilde{y} \end{cases}. \tag{e}$$

The coefficients of the frequency response matrix, $\mathbf{B}(\omega)$, are generally complex. Subsequently, Eq. (e) is approximated in the following manner:

$$\begin{bmatrix} \tilde{\mathcal{M}}_b(\omega) \\ \tilde{\mathcal{Q}}_b(\omega) \end{bmatrix} \approx \left(\Re(\mathbf{B}(\omega_1)) + \frac{\mathrm{i}\omega}{\omega_1} \Im(\mathbf{B}(\omega_1)) \right) \begin{bmatrix} \tilde{\Theta}_b(\omega) \\ \tilde{U}_b(\omega) \end{bmatrix}. \tag{f}$$

For harmonic excitation with the circular frequency $\omega = \omega_1$, Eq. (f) represents a set of completely transparent boundary conditions in the frequency domain, *i.e.* for a single-frequency signal no reflection occurs. However, when the response is not purely harmonic with a single frequency, some reflection takes place at the interfaces.

Formulation in the time domain

Introducing the matrices

$$\mathbf{K}_b = \Re(\mathbf{B}(\omega_1))), \quad \mathbf{C}_b = -\frac{1}{\omega_1}\Im(\mathbf{B}(\omega_1))), \tag{g}$$

Eq. (f) may be formulated as the following transmitting boundary conditions in the time domain:

$$\begin{bmatrix} \tilde{M}_b(t) \\ \tilde{Q}_b(t) \end{bmatrix} = \mathbf{K}_b \begin{bmatrix} \tilde{\theta}_b(t) \\ \tilde{u}_b(t) \end{bmatrix} + \mathbf{C}_b \begin{bmatrix} \dot{\tilde{\theta}}_b(t) \\ \dot{\tilde{u}}_b(t) \end{bmatrix}. \tag{h}$$

The components k_{ij} and c_{ij}, $\{i,j\} \in \{1,2\}$, of the matrices $\mathbf{K}_b$ and $\mathbf{C}_b$ may be interpreted as a system of springs and dashpots as illustrated in Fig. B. For example, $k_{11}^- = l_1^2 k_1^- + l_2^2 k_2^-$, $k_{12}^- = l_2 k_2^-$ and $k_{22}^- = k_3^-$. It is noted that the model suggested by Wang and Lai (2000) only includes the vertical spring and dashpot. These are calibrated to the wave component, which is a travelling wave in the case of $\vartheta = \zeta = \xi = \chi = 0$ and $\Omega > 1$. *(continued)*

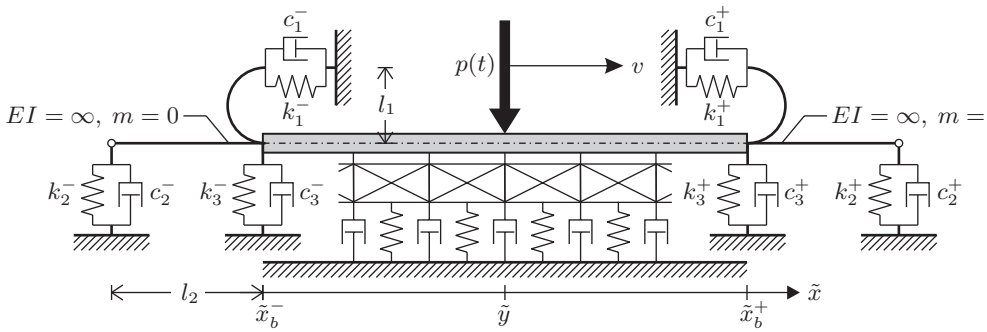

Figure B Interpretation of transmitting boundary conditions in terms of springs and dashpots.

Nevertheless, combinations of the material properties and the loading frequency exist where Eq. (h) will not be physically correct. The problem is that in order to obtain a stable FEM scheme, the system matrices have to be positive definite. This means that the diagonal terms as well as the determinants of the boundary condition matrices must be positive. No problem arises in the imaginary part of $\mathbf{B}$, *i.e.* the damping matrix. However, for frequencies above some factor (typically in the range 1.1-2.6) times the cut-on frequency, in the absence of shear stiffness, the b_{22} component of $\mathbf{B}$ relating $\tilde{Q}_b(t)$ to $\tilde{u}_b(t)$ will have negative real part. A solution to the problem is obtained by replacing the first-order boundary condition by an equivalent second-order boundary condition. Hence, if and only if $k_{22} < 0$, Eq. (h) is modified to

$$\begin{bmatrix} \tilde{M}_b(t) \\ \tilde{Q}_b(t) \end{bmatrix} = \mathbf{K}_b' \begin{bmatrix} \tilde{\theta}_b(t) \\ \tilde{u}_b(t) \end{bmatrix} + \mathbf{C}_b \begin{bmatrix} \dot{\tilde{\theta}}_b(t) \\ \dot{\tilde{u}}_b(t) \end{bmatrix} + \mathbf{M}_b' \begin{bmatrix} \ddot{\tilde{\theta}}_b(t) \\ \ddot{\tilde{u}}_b(t) \end{bmatrix}, \tag{i}$$

where

$$\mathbf{K}_b' = \begin{bmatrix} 2\,k_{11} & 0.5\,k_{12} \\ 0.5\,k_{21} & -k_{22} \end{bmatrix}, \quad \mathbf{M}_b' = -\frac{1}{\omega_1^2} \begin{bmatrix} -k_{11} & 0.5\,k_{12} \\ 0.5\,k_{21} & 2\,k_{22} \end{bmatrix}. \tag{j}$$

The mass terms correspond to point masses and inertial masses in the mechanical systems applied to the artificial boundaries in Fig. B.

Similar to Eq. (f), Eqs. (h) and (i) will only be exact for harmonic variation at the circular frequency ω_1. When the excitation frequency ω diverges from ω_1, the performance of the boundary conditions decreases correspondingly.

One idea of how to overcome the problem with frequency dependence is simply to use a higher order approximation of Eq. (e) in $\mathrm{i}\omega$ corresponding to a transmitting boundary condition in the form,

$$\begin{bmatrix} \tilde{M}_b(t) \\ \tilde{Q}_b(t) \end{bmatrix} = \mathbf{G}_0 \begin{bmatrix} \tilde{\theta}_b(t) \\ \tilde{u}_b(t) \end{bmatrix} + \mathbf{G}_1 \begin{bmatrix} \dot{\tilde{\theta}}_b(t) \\ \dot{\tilde{u}}_b(t) \end{bmatrix} + \cdots + \mathbf{G}_n \begin{bmatrix} \tilde{\theta}_b^{(j)}(t) \\ \tilde{u}_b^{(j)}(t) \end{bmatrix}, \tag{k}$$

with $\tilde{\theta}_b^{(j)}$ and $\tilde{u}_b^{(j)}$ denoting the jth derivatives of $\tilde{\theta}_b$ and $\tilde{u}_b$ with respect to time. Note that rational filters like (k) can still only be valid for ω in a confined interval since it does not provide the correct asymptotic behaviour. Moreover it has not been possible to calibrate Eq. (k) to get a stable FE scheme (*i.e.* a differential filter with all eigenvalues having nonpositive real parts) that provides a more accurate solution than is obtained from Eqs. (h) and (i)—even within a narrow frequency band. □

2.5.2 FEM implementation of artificial boundary conditions

In the previous section, a number of examples have been given of transmitting, or partially transmitting, boundary conditions for acoustic and elastic media and for structural elements in the form of Euler-Bernoulli beams. In most cases the idea is to formulate the pressure, the traction or the generalized interface forces at the artificial boundary in terms of the interface displacements and time-derivatives thereof. A special case is the impedance boundary condition, which related the pressure, or traction, to the interface velocities only. In the examples given below, it will be illustrated how the boundary conditions are applied in an FEM scheme, and some of the shortcomings of the suggested boundary conditions will be discussed.

The discretized equations of motion for the modelled domain D^+ read

$$\mathbf{M}^+\ddot{\mathbf{u}}^+ + \mathbf{C}^+\dot{\mathbf{u}}^+ + \mathbf{K}^+\mathbf{u}^+ = \mathbf{f}^+(t), \tag{2–80}$$

where $\mathbf{u}^+(t)$ is the displacement vector, $\mathbf{f}^+(t)$ is the load vector, and $\mathbf{M}^+$, $\mathbf{C}^+$ and $\mathbf{K}^+$ are the mass-, damping- and stiffness matrices. The components of $\mathbf{u}^+(t)$ are partitioned into subvector components $\mathbf{u}_i^+(t)$ of the dimension n_i^+, and $\mathbf{u}_b^+(t)$ of the dimension n_b with components belonging to the interior of D^+ and to the interface S_0, see Fig. 2–7. Similar partitionings of the system matrices and the load vector are performed as follows,

$$\left.\begin{aligned} &\mathbf{u}^+(t) = \begin{bmatrix}\mathbf{u}_i^+(t)\\ \mathbf{u}_b^+(t)\end{bmatrix}\ ,\ \mathbf{f}^+(t) = \begin{bmatrix}\mathbf{f}_i^+(t)\\ \mathbf{f}_b^+(t)\end{bmatrix} \\ &\mathbf{M}^+ = \begin{bmatrix}\mathbf{M}_{ii}^+ & \mathbf{M}_{ib}^+\\ \mathbf{M}_{bi}^+ & \mathbf{M}_{bb}^+\end{bmatrix}\ ,\ \mathbf{C}^+ = \begin{bmatrix}\mathbf{C}_{ii}^+ & \mathbf{C}_{ib}^+\\ \mathbf{C}_{bi}^+ & \mathbf{C}_{bb}^+\end{bmatrix}\ ,\ \mathbf{K}^+ = \begin{bmatrix}\mathbf{K}_{ii}^+ & \mathbf{K}_{ib}^+\\ \mathbf{K}_{bi}^+ & \mathbf{K}_{bb}^+\end{bmatrix} \end{aligned}\right\}. \tag{2–81}$$

Assume, that the interaction forces are given by the rational approximation (2–72), (2–73). Then, from (2–80) and (2–81) the following system of equations of motion, corrected for the transmitting boundary conditions $\mathbf{f}_b^+(t) = -\mathbf{f}_b^-(t)$ and $\mathbf{u}_b^+(t) = \mathbf{u}_b^-(t)$ at the interface S_0, are obtained:

$$\left.\begin{aligned} &\tilde{\mathbf{M}}^+\ddot{\mathbf{u}}^+ + \tilde{\mathbf{C}}^+\dot{\mathbf{u}}^+ + \tilde{\mathbf{K}}^+\mathbf{u}^+ + \sum_{j=1}^{s}\tilde{\mathbf{G}}_j\mathbf{v}_j = \tilde{\mathbf{f}}^+(t) \\ &\dot{\mathbf{v}}_j(t) - z_j\mathbf{v}_j(t) = \tilde{\mathbf{I}}\mathbf{u}^+(t) \quad , \quad j = 1,\ldots,s \end{aligned}\right\}, \tag{2–82}$$

where

$$\left.\begin{aligned} &\tilde{\mathbf{M}}^+ = \begin{bmatrix}\mathbf{M}_{ii}^+ & \mathbf{M}_{ib}^+\\ \mathbf{M}_{bi}^+ & \mathbf{M}_{bb}^+ + \mathbf{M}_{bb}^-\end{bmatrix},\quad \tilde{\mathbf{C}}^+ = \begin{bmatrix}\mathbf{C}_{ii}^+ & \mathbf{C}_{ib}^+\\ \mathbf{C}_{bi}^+ & \mathbf{C}_{bb}^+ + \mathbf{C}_{bb}^-\end{bmatrix},\quad \tilde{\mathbf{G}}_j = \begin{bmatrix}\mathbf{0}\\ \mathbf{G}_j^-\end{bmatrix} \\ &\tilde{\mathbf{K}}^+ = \begin{bmatrix}\mathbf{K}_{ii}^+ & \mathbf{K}_{ib}^+\\ \mathbf{K}_{bi}^+ & \mathbf{K}_{bb}^+ + \mathbf{K}_{bb}^- + \sum_{j=1}^{s}\frac{1}{z_j}\mathbf{G}_j^-\end{bmatrix},\quad \tilde{\mathbf{f}}^+(t) = \begin{bmatrix}\mathbf{f}_i^+(t)\\ \mathbf{0}\end{bmatrix},\quad \tilde{\mathbf{I}} = [\mathbf{0}\quad \mathbf{I}] \end{aligned}\right\}. \tag{2–83}$$

Equation (2–82) may be written in terms of the following coupled system of 1st order differential equations on state vector form:

$$\frac{d}{dt}\mathbf{z}(t) = \mathbf{A}\mathbf{z}(t) + \mathbf{F}(t), \tag{2–84}$$

$$\mathbf{z}(t) = \begin{bmatrix} \mathbf{u}^+(t) \\ \dot{\mathbf{u}}^+(t) \\ \mathbf{v}_1(t) \\ \vdots \\ \mathbf{v}_s(t) \end{bmatrix} \quad , \quad \mathbf{F}(t) = \left(\tilde{\mathbf{M}}^+\right)^{-1} \begin{bmatrix} \mathbf{0} \\ \mathbf{f}^+(t) \\ \mathbf{0} \\ \vdots \\ \mathbf{0} \end{bmatrix},$$

$$\mathbf{A} = \begin{bmatrix} \mathbf{0} & \mathbf{I} & \mathbf{0} & \cdots & \mathbf{0} \\ -\left(\tilde{\mathbf{M}}^+\right)^{-1}\tilde{\mathbf{K}}^+ & -\left(\tilde{\mathbf{M}}^+\right)^{-1}\mathbf{C}^+ & -\left(\tilde{\mathbf{M}}^+\right)^{-1}\mathbf{G}_1 & \cdots & -\left(\tilde{\mathbf{M}}^+\right)^{-1}\mathbf{G}_s \\ \tilde{\mathbf{I}} & \mathbf{0} & z_1\mathbf{I} & \cdots & \mathbf{0} \\ \vdots & \vdots & \vdots & \ddots & \vdots \\ \tilde{\mathbf{I}} & \mathbf{0} & \mathbf{0} & \cdots & z_s\mathbf{I} \end{bmatrix}. \tag{2–85}$$

Next, assume that the interaction forces are given by an impedance boundary condition. Then, only the damping matrix in Eq. (2–83) is modified, resulting in the equations of motion

$$\mathbf{M}^+\ddot{\mathbf{u}}^+ + \tilde{\mathbf{C}}^+\dot{\mathbf{u}}^+ + \mathbf{K}^+\mathbf{u}^+ = \tilde{\mathbf{f}}^+(t). \tag{2–86}$$

Let $\mathbf{u}_0^+(t)$ be any stiff-body motion of the volume D^+ (or any other displacement in external quasi-static equilibrium). Since, the stiffness matrix has not been modified for support conditions, it follows that $\mathbf{K}^+\mathbf{u}_0^+(t) \equiv \mathbf{0}$. Then, integration of Eq. (2–86) provides the following result for the permanent displacement of the body ($\mathbf{u}_0^+(-\infty) = \dot{\mathbf{u}}_0^+(-\infty) = \dot{\mathbf{u}}_0^+(\infty) = \mathbf{0}$):

$$\tilde{\mathbf{u}}_0^+(\infty) = \left(\tilde{\mathbf{C}}^+\right)^{-1} \int_{-\infty}^{\infty} \tilde{\mathbf{f}}^+(t)dt. \tag{2–87}$$

If a net impulse is applied to the body, so $\int_{-\infty}^{\infty} \tilde{\mathbf{f}}^+(t)dt \neq \mathbf{0}$, permanent stiff-body displacements of the calculation domain appears. Hence, in order to prevent such offsets, the impedance boundary condition should only be used for loads with zero net impulse. Of course static loads cannot be supported by impedance boundary conditions at all.

Next, assume that the system is under stationary harmonic excitation. Then

$$\mathbf{f}_i^+(t) = \Re\left(\mathbf{F}_i^+(\omega)\mathrm{e}^{\mathrm{i}\omega t}\right) \quad , \quad \mathbf{u}^+(t) = \Re\left(\mathbf{U}^+(\omega)\mathrm{e}^{\mathrm{i}\omega t}\right). \tag{2–88}$$

Use of the boundary condition (2–69) provides the following frequency response solution $\mathbf{U}^+(\omega)$ of the systems (2–80):

$$\mathbf{U}^+(\omega) = \left((\mathrm{i}\omega)^2\mathbf{M}^+ + \mathrm{i}\omega\mathbf{C}^+ + \tilde{\mathbf{K}}^+(\omega)\right)^{-1}\tilde{\mathbf{F}}^+(\omega), \tag{2–89}$$

$$\tilde{\mathbf{K}}^+(\omega) = \begin{bmatrix} \mathbf{K}_{ii}^+ & \mathbf{K}_{ib}^+ \\ \mathbf{K}_{bi}^+ & \mathbf{K}_{bb}^+ + \mathbf{G}_{bb}^-(\omega) \end{bmatrix} \quad , \quad \tilde{\mathbf{F}}^+(\omega) = \begin{bmatrix} \mathbf{F}_i^+(\omega) \\ \mathbf{0} \end{bmatrix}. \tag{2–90}$$

Example 2.10 Impedance boundary conditions in elastodynamics

As illustrated in Example 2.8, a relationship between the nodal forces and the nodal velocities can be established on a local-in-time, local-in-space basis for the nodes along the artificial boundary in an FEM scheme for an infinite elastic domain. This elastic impedance boundary condition may be introduced in the FEM formulation given in Example 2.5. Thus, the boundary load vector along the interaction boundary S_0,

$$\tilde{\mathbf{f}}_b^+(t) = \int_{S_0} \mathbf{\Phi}_i^T \tilde{\tau}_i^+(x,t)\, dS, \tag{a}$$

is replaced by the product

$$\tilde{\mathbf{f}}_b^+(t) = -\tilde{\mathbf{C}}_{bb}^- \dot{\tilde{\mathbf{u}}}_b^+(t). \tag{b}$$

Subsequently, the "load" from the surrounding domain V^- is moved to the right-hand side of Eq. (e) of Example 2.5 by adding the components of the impedance matrix $\tilde{\mathbf{C}}_{bb}^-$ into the positions of matrix $\mathbf{C}$ corresponding to the degrees of freedom in $\tilde{\mathbf{u}}_b^+(t)$.

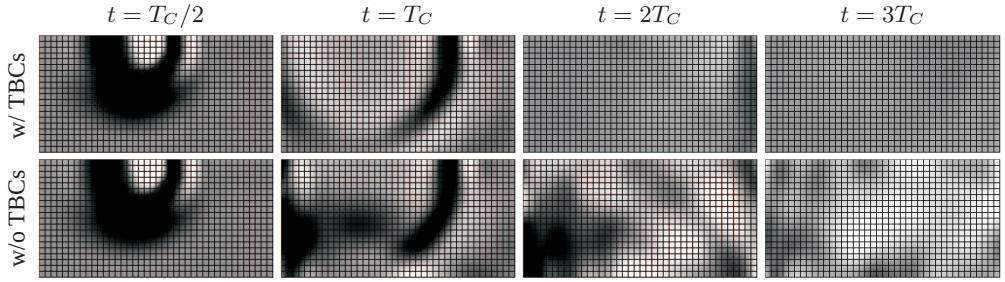

Figure A Finite element model of plane elastic wave propagation. Time-domain solution *with* (top) and *without* (bottom) transmitting boundary conditions.

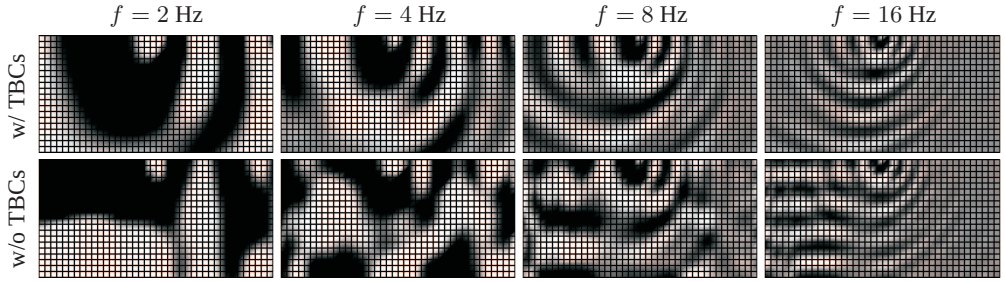

Figure B Finite element model of plane elastic wave propagation. Frequency-domain solution *with* (top) and *without* (bottom) transmitting boundary conditions.

In order to test the transmitting boundary condition, the response has been computed of a half-plane to a point force moving along its surface with subsonic speed. The load is applied as a vertical pulse with no net impulse, and the results are indicated in Fig. A. Clearly, the implementation of TBCs provides an efficient means of avoiding reflection of waves back into the computation domain. The accuracy of the TBCs becomes evident when a frequency-domain analysis is carried out, cf. Fig. B. Here any reflection of waves would lead to an accumulation of energy in the model. □

2.6 Summary

In this chapter, the formulation of finite element models for elastic wave propagation problems has been discussed. Both the case of P- and S-waves propagating in a continuum and flexural waves travelling along a beam have been studied, and the formulation in a local frame of reference following a moving load or vehicle has been given.

The main points in the formulation and application of the FEM for elastodynamics problems may be summarized in the following points, which may be added to the list given in Subsection 2.1.1.

Element size — The spatial increment, *i.e.* the element size, is defined by the shortest wavelength in the system. The number of elements that is required per wavelength in order to ensure a satisfactory accuracy of the numerical results depend on the order of interpolation. Thus, if linear shape/weight functions are applied, approximately 10 elements are needed, whereas only 3–4 elements are necessary per wavelength when cubic elements are utilized.

Time step — The Courant condition determines the maximum time step that may be utilized in a time-marching algorithm. If the time step becomes too large, waves cannot propagate in the numerical model. In time integration schemes that are not unconditionally stable, much smaller time steps should be used than are given by the Courant condition.

Moving loads — The steady state response to moving loads or vehicles may be analysed in a local frame of reference following the wave source. This involves the introduction of negative convection in the wave field that tends to destabilize the numerical solution in the time domain. The problem may be treated in different ways, *e.g.* by the Petrov-Galerkin or the Taylor-Galerkin methods.

Artificial boundaries — Wave propagation problems usually deal with (semi-)infinite domains, *e.g.* an elastic half-space. In the FEM this involves that artificial, or interaction, boundaries are introduced at the edges of the computation mesh.

Transmitting boundary conditions — In order to ensure radiation of waves through the artificial boundaries, transmitting boundary conditions (TBCs) must be implemented. These boundary conditions can be local or global in time and space. The local TBCs are the most efficient from a computational point of view. However, the global TBCs provide the higher accuracy.

Impedance conditions — The transmission of P- and S-waves from an FE model of an elastic medium into the surrounding infinite medium may be established by means of impedance conditions. Since the impedance describes a relationship between interaction forces and particle velocities, this kind of TBCs cannot be applied in the static case.

The finite-element method is considered the state of the art for the numerical analysis of problems involving local nonlinearities, inhomogeneities and complex geometries. However, since a discretization over the volume is required, it is needless to say that three-dimensional FE models of wave propagation require huge amount of computer array storage space, and the solution time may be very long. In Chapter 5, an alternative method is described, which is much more efficient than the FEM. However, it is restricted to the analysis of horizontally layered strata.

CHAPTER 3
Boundary-integral equations in elastodynamics

Boundary-integral equations are a useful mathematical tool for the analytic solution of wave propagation problems. Further, they form the basis for the boundary-element method (BEM) presented in the next chapter. In the following, a number of theorems are derived with regard to the reciprocity of two states governed by the Cauchy equation or the scalar wave equation. Subsequently, the Green's functions are presented for a variety of problems. Only the so-called full-space solution is concerned; however, this solution is derived for three-dimensional as well as plane and anti-plane wave propagation problems in time and frequency domain. Finally, the Green's functions and the reciprocity theorems are combined to form the so-called Somigliana identity which is the starting point for discretization in the BEM.

3.1 Introduction

The starting point of the finite-element method is the weak formulation of the governing partial differential equation which, in the case of elastodynamics, is obtained by multiplication of the Cauchy equation with a weight function in terms of a variational displacement field and subsequent integration by parts over the considered domain. The variational field must conform to the Dirichlet boundary conditions, *i.e.* the variational field vanishes on parts of the boundary with prescribed displacements. However, in the interior of the domain the weight function is arbitrary. Following the standard procedure of displacement-based finite-element discretization presented in Chapter 2, only the displacements are directly represented in the numerical model. Hence, stresses are derived by partial differentiation of the interpolated displacement field.

Now, in this chapter an alternative approach is taken, in which two states are defined on the same domain but with different boundary and initial conditions. Instead of applying an arbitrary weight function, the two states are then applied as weight functions in the governing equation for the other state. In this case, integration by parts over the domain forms a mutual relationship between the two states known as a *reciprocity relation*. In particular, if one of the two states is selected as the Green's function, or fundamental solution, a simple integral equation is obtained. This may be used for an analytical solution of certain problems involving a simple geometry and boundary conditions of the physical problem—or it may be utilised as the starting point for discretization, leading to the boundary-element method described in the next chapter.

3.2 Dynamic reciprocity theorems in elasticity

Firstly, in this section the so-called dynamic reciprocity theorem is derived for three-dimensional elastic wave propagation as well as plane and antiplane shear.

3.2.1 Three-dimensional wave propagation

Consider an elastic body Ω which has the surface Γ with outward unit normal vector $\mathbf{n}$, see Fig. 3–1. In fixed Cartesian coordinates x_j, $j = 1, 2, 3$, the time-domain equation of motion for a three-dimensional elastic continuum with mass density ρ may be written

$$\frac{\partial}{\partial x_j}\sigma_{ij}(\mathbf{x},t) + \rho b_i(\mathbf{x},t) = \rho\frac{\partial^2}{\partial t^2}u_i(\mathbf{x},t) = \rho\ddot{u}_i(\mathbf{x},t), \qquad i,j = 1,2,3, \tag{1–1}$$

where $\sigma_{ij}(\mathbf{x},t)$ are the Cartesian components of the Cauchy stress tensor, $u_i(\mathbf{x},t)$ are the components of the displacement field and $b_i(\mathbf{x},t)$ is the load per unit mass in coordinate direction i. Vector $\mathbf{x}$ is the position in space and t is the time. Finally, $\ddot{u}_i(\mathbf{x},t)$ is the second local time derivative of the displacement, *i.e.* the local acceleration. The summation convention applies, *i.e.* summation is performed over repeated indices.

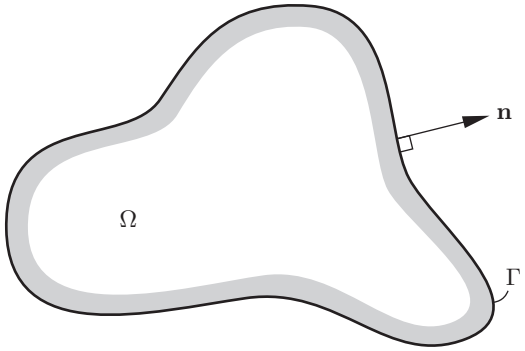

Figure 3–1 Elastic body Ω bounded by the surface Γ with the outward unit normal vector $\mathbf{n}$.

Equation (1–1) is subject to the boundary and initial conditions

$$\left.\begin{array}{ll} u_j(\mathbf{x},t) = \bar{u}_j(\mathbf{x},t) & \text{for} \quad \mathbf{x}\in\Gamma_1 \\ p_j(\mathbf{x},t) = \bar{p}_j(\mathbf{x},t) & \text{for} \quad \mathbf{x}\in\Gamma_2 \end{array}\right\}, \quad \Gamma = \Gamma_1 \cup \Gamma_2, \tag{3–1a}$$

$$\left.\begin{array}{ll} u_j(\mathbf{x},0) = v_j(\mathbf{x}) & \text{for} \quad \mathbf{x}\in\Omega \\ \dot{u}_j(\mathbf{x},0) = \dot{v}_j(\mathbf{x}) & \text{for} \quad \mathbf{x}\in\Omega \end{array}\right\}, \tag{3–1b}$$

Here $\dot{u}_i(\mathbf{x},t)$ is the first local time derivative of the displacement, *i.e.* the local velocity. Further, $p_i(\mathbf{x},t) = \sigma_{ij}(\mathbf{x},t)n_j(\mathbf{x})$ are the components of the surface traction, which is defined on the surface Γ in terms of the Cauchy stress tensor and the outward unit normal $\mathbf{n}(\mathbf{x})$ having the components $n_j(\mathbf{x})$. The boundary conditions are illustrated in Fig. 3–2.

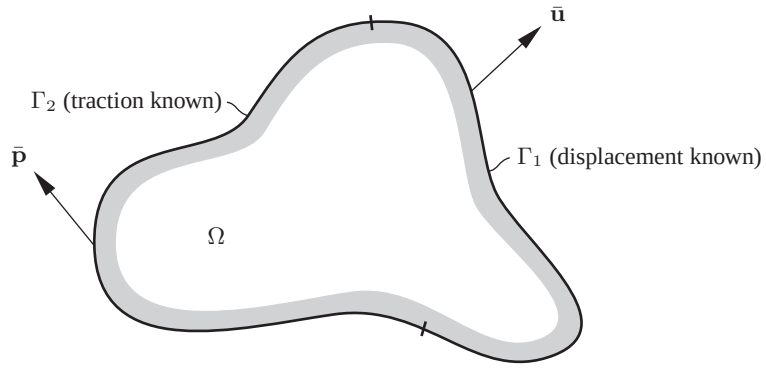

Figure 3–2 Boundary conditions for the elastic body Ω.

Next, on the domain Ω with boundary Γ, let two states be given which satisfy the Cauchy equation (1–1) at the times $t = t_1$ and $t = t_2$, respectively. For any point $\mathbf{x}$, the following identities apply:

$$\frac{\partial}{\partial x_j}\sigma_{ij}^{(1)}(\mathbf{x},t_1) + \rho b_i^{(1)}(\mathbf{x},t_1) = \rho\ddot{u}_i^{(1)}(\mathbf{x},t_1), \tag{3–2a}$$

$$\frac{\partial}{\partial x_j}\sigma_{ij}^{(2)}(\mathbf{x},t_2) + \rho b_i^{(2)}(\mathbf{x},t_2) = \rho\ddot{u}_i^{(2)}(\mathbf{x},t_2). \tag{3–2b}$$

Multiplication of Eq. (3–2a) with $u_i^{(2)}(\mathbf{x},t_2)$, multiplication of Eq. (3–2b) with $u_i^{(1)}(\mathbf{x},t_1)$ and integration over the volume lead to the equations

$$\int_\Omega \frac{\partial}{\partial x_j}\sigma_{ij}^{(1)}(\mathbf{x},t_1)u_i^{(2)}(\mathbf{x},t_2)\mathrm{d}\Omega + \int_\Omega \rho b_i^{(1)}(\mathbf{x},t_1)u_i^{(2)}(\mathbf{x},t_2)\mathrm{d}\Omega - \int_\Omega \rho\ddot{u}_i^{(1)}(\mathbf{x},t_1)u_i^{(2)}(\mathbf{x},t_2)\mathrm{d}\Omega = 0, \tag{3–3a}$$

$$\int_\Omega \frac{\partial}{\partial x_j}\sigma_{ij}^{(2)}(\mathbf{x},t_2)u_i^{(1)}(\mathbf{x},t_1)\mathrm{d}\Omega + \int_\Omega \rho b_i^{(2)}(\mathbf{x},t_2)u_i^{(1)}(\mathbf{x},t_1)\mathrm{d}\Omega - \int_\Omega \rho\ddot{u}_i^{(2)}(\mathbf{x},t_2)u_i^{(1)}(\mathbf{x},t_1)\mathrm{d}\Omega = 0. \tag{3–3b}$$

With $E_{ijkl}(\mathbf{x})$ denoting the components or the fourth-order elasticity tensor, cf. Eq. (1–2), the Cauchy stress tensor is written as $\sigma_{ij}(\mathbf{x},t) = E_{ijkl}(\mathbf{x})\,\partial u_k(\mathbf{x},t)/\partial x_l$. Application of the divergence theorem (see Appendix A) to the first term in Eqs. (3–3a) and (3–3b) then provides

$$\int_\Omega \frac{\partial}{\partial x_j}\sigma_{ij}^{(1)}(\mathbf{x},t_1)\,u_i^{(2)}(\mathbf{x},t_2)\,\mathrm{d}\Omega = \int_\Gamma p_i^{(1)}(\mathbf{x},t_1)\,u_i^{(2)}(\mathbf{x},t_2)\,\mathrm{d}\Gamma - \int_\Omega \frac{\partial}{\partial x_l}u_k^{(1)}(\mathbf{x},t_1)\,E_{ijkl}(\mathbf{x})\,\frac{\partial}{\partial x_j}u_i^{(2)}(\mathbf{x},t_2)\,\mathrm{d}\Omega, \tag{3–4a}$$

$$\int_\Omega \frac{\partial}{\partial x_j}\sigma_{ij}^{(2)}(\mathbf{x},t_2)\,u_i^{(1)}(\mathbf{x},t_1)\,\mathrm{d}\Omega = \int_\Gamma p_i^{(2)}(\mathbf{x},t_2)\,u_i^{(1)}(\mathbf{x},t_1)\,\mathrm{d}\Gamma - \int_\Omega \frac{\partial}{\partial x_l}u_k^{(2)}(\mathbf{x},t_2)\,E_{ijkl}(\mathbf{x})\,\frac{\partial}{\partial x_j}u_i^{(1)}(\mathbf{x},t_1)\,\mathrm{d}\Omega, \tag{3–4b}$$

where it has been utilised that the surface traction is defined as $p_i(\mathbf{x},t) = \sigma_{ij}(\mathbf{x},t)\,n_j(\mathbf{x})$. As discussed in Section 1.2, the elasticity tensor is symmetric in the sense that $E_{ijkl}(\mathbf{x}) = E_{klij}(\mathbf{x})$. Hence, a subtraction of Eq. (3–3a) from Eq. (3–3b) with the substitutions defined in Eqs. (3–4a) and (3–4b) leads to the dynamic *Betti reciprocal theorem*,

$$\int_\Gamma p_i^{(1)}(\mathbf{x},t_1)\,u_i^{(2)}(\mathbf{x},t_2)\,\mathrm{d}\Gamma + \int_\Omega \rho\left(b_i^{(1)}(\mathbf{x},t_1) - \ddot{u}_i^{(1)}(\mathbf{x},t_1)\right)u_i^{(2)}(\mathbf{x},t_2)\,\mathrm{d}\Omega = \int_\Gamma p_i^{(2)}(\mathbf{x},t_2)\,u_i^{(1)}(\mathbf{x},t_1)\,\mathrm{d}\Gamma + \int_\Omega \rho\left(b_i^{(2)}(\mathbf{x},t_2) - \ddot{u}_i^{(2)}(\mathbf{x},t_2)\right)u_i^{(1)}(\mathbf{x},t_1)\,\mathrm{d}\Omega, \tag{3–5}$$

also known as the *Betti-Rayleigh theorem* (Achenbach 1973).

So far the instants of time t_1 and t_2 have not been specified. Now, let $t_1 = \tau$ and $t_2 = t - \tau$. Then, by integration over time with respect to τ, Eq. (3–5) obtains the alternative form

$$\begin{aligned}
&\int_0^t\int_\Gamma p_i^{(1)}(\mathbf{x},\tau)\,u_i^{(2)}(\mathbf{x},t-\tau)\,\mathrm{d}\Gamma\mathrm{d}\tau - \int_0^t\int_\Gamma p_i^{(2)}(\mathbf{x},t-\tau)\,u_i^{(1)}(\mathbf{x},\tau)\,\mathrm{d}\Gamma\mathrm{d}\tau \\
&\quad + \int_0^t\int_\Omega \rho b_i^{(1)}(\mathbf{x},\tau)\,u_i^{(2)}(\mathbf{x},t-\tau)\,\mathrm{d}\Omega\mathrm{d}\tau - \int_0^t\int_\Omega \rho b_i^{(2)}(\mathbf{x},t-\tau)\,u_i^{(1)}(\mathbf{x},\tau)\,\mathrm{d}\Omega\mathrm{d}\tau \\
&\quad = \int_\Omega \rho\left\{\dot{u}_i^{(1)}(\mathbf{x},t)\,v_i^{(2)}(\mathbf{x}) - u_i^{(2)}(\mathbf{x},t)\,\dot{v}_i^{(1)}(\mathbf{x})\right\}\mathrm{d}\Omega \\
&\quad + \int_\Omega \rho\left\{u_i^{(1)}(\mathbf{x},t)\,\dot{v}_i^{(2)}(\mathbf{x}) - \dot{u}_i^{(2)}(\mathbf{x},t)\,v_i^{(1)}(\mathbf{x})\right\}\mathrm{d}\Omega,
\end{aligned} \tag{3–6}$$

where use has been made of the fact that

$$\begin{aligned}
&\int_0^t \left\{\ddot{u}_i^{(1)}(\mathbf{x},\tau)\,u_i^{(2)}(\mathbf{x},t-\tau) - \ddot{u}_i^{(2)}(\mathbf{x},t-\tau)\,u_i^{(1)}(\mathbf{x},\tau)\right\}\mathrm{d}\tau \\
&\quad = \int_0^t \frac{\partial}{\partial\tau}\left\{\dot{u}_i^{(1)}(\mathbf{x},\tau)\,u_i^{(2)}(\mathbf{x},t-\tau) + \dot{u}_i^{(2)}(\mathbf{x},t-\tau)\,u_i^{(1)}(\mathbf{x},\tau)\right\}\mathrm{d}\tau \\
&\quad = \dot{u}_i^{(1)}(\mathbf{x},t)\,v_i^{(2)}(\mathbf{x}) + \dot{v}_i^{(2)}(\mathbf{x})\,u_i^{(1)}(\mathbf{x},t) - \dot{v}_i^{(1)}(\mathbf{x})\,u_i^{(2)}(\mathbf{x},t) - \dot{u}_i^{(2)}(\mathbf{x},t)\,v_i^{(1)}(\mathbf{x})\,.
\end{aligned}$$

Equation (3–6) provides a reciprocal theorem which includes the influence of initial conditions, *i.e.* the displacements $v_i^{(1)}(\mathbf{x})$ and $v_i^{(2)}(\mathbf{x})$, and the velocities $\dot{v}_i^{(1)}(\mathbf{x})$ and $\dot{v}_i^{(2)}(\mathbf{x})$.

3.2.2 Plane and antiplane elastic wave propagation

The wave-propagation problem related to plane strain, cf. Section 1.3.2, may be represented by a governing equation identical to Eq. (1–1) but with indices $1, 2$ rather than $1, 2, 3$. On the other hand, the equation of motion simplifies to a scalar wave equation when the so-called antiplane wave-propagation problem is considered.

Plane elastic wave propagation (P- and SV-waves)

In the case of plane strain in the (x_1, x_2)-plane, the displacement component u_3 is identically equal to zero. Further, any partial derivatives with respect to x_3 vanish and Eq. (1–1) reduces to

$$\frac{\partial}{\partial x_\beta}\sigma_{\alpha\beta}(\mathbf{x},t) + \rho b_\alpha(\mathbf{x},t) = \rho\frac{\partial^2}{\partial t^2}u_\alpha(\mathbf{x},t) = \rho\ddot{u}_\alpha(\mathbf{x},t), \qquad \alpha,\beta = 1,2, \tag{3–7}$$

with the boundary and initial conditions

$$\left.\begin{array}{ll} u_\alpha(\mathbf{x},t) = \bar{u}_\alpha(\mathbf{x},t) & \text{for} \quad \mathbf{x}\in\Gamma_1 \\ p_\alpha(\mathbf{x},t) = \bar{p}_\alpha(\mathbf{x},t) & \text{for} \quad \mathbf{x}\in\Gamma_2 \end{array}\right\}, \quad \Gamma = \Gamma_1\cup\Gamma_2, \tag{3–8a}$$

$$\left.\begin{array}{ll} u_\alpha(\mathbf{x},0) = v_\alpha(\mathbf{x}) & \text{for} \quad \mathbf{x}\in\Omega \\ \dot{u}_\alpha(\mathbf{x},0) = \dot{v}_\alpha(\mathbf{x}) & \text{for} \quad \mathbf{x}\in\Omega \end{array}\right\}, \tag{3–8b}$$

where $p_\alpha(\mathbf{x},t) = \sigma_{\alpha\beta}(\mathbf{x},t)n_\beta(\mathbf{x})$ are the components of the surface traction vector related to plane strain, and the summation convention applies with $\beta = 1,2$. Accordingly, the reciprocal theorems for plane strain are identical to the reciprocal theorems (3–5) and (3–6) but with the index i replaced by the index α ranging over 1 and 2. Further, Ω and Γ represent a two-dimensional domain and its boundary. It is noted that the dynamic plane-strain problem corresponds to the propagation of P- and SV-waves as discussed in Section 1.3.2.

Antiplane elastic wave propagation (SH-waves)

Similarly to plane strain, we now define antiplane shear as the problem in which the displacement components u_1 and u_2 are identically equal to zero and partial derivatives with respect to x_3 vanish, *i.e.* only the displacement component u_3 in the direction out of the (x_1, x_2)-plane exists and it is constant in along the x_3-direction. In the case of elastodynamics this corresponds to the propagation of SH-waves in the (x_1, x_2)-plane, and as described in Section 1.3.2 these waves are completely decoupled from the P- and SV-waves propagating in the same plane. In the particular case of SH-waves propagating in an isotropic linear elastic material, the governing equation reads

$$\mu\frac{\partial^2 u_3(\mathbf{x},t)}{\partial x_\alpha \partial x_\alpha} + \rho b_3(\mathbf{x},t) = \rho\frac{\partial^2 u_3(\mathbf{x},t)}{\partial t^2} = \rho\ddot{u}_3(\mathbf{x},t), \qquad \alpha = 1,2, \tag{3–9}$$

where $u_3(\mathbf{x},t)$ is the displacement field and $b_3(\mathbf{x},t)$ is the load per unit mass related to the SH-wave field. Finally, $\mathbf{x}$ is a point in the (x_1, x_2)-plane, and μ is the shear modulus of the material. Equation (3–9) is subject to the boundary and initial conditions

$$\left.\begin{array}{ll} u_3(\mathbf{x},t) = \bar{u}_3(\mathbf{x},t) & \text{for} \quad \mathbf{x}\in\Gamma_1 \\ p_3(\mathbf{x},t) = \bar{p}_3(\mathbf{x},t) & \text{for} \quad \mathbf{x}\in\Gamma_2 \end{array}\right\}, \quad \Gamma = \Gamma_1\cup\Gamma_2, \tag{3–10a}$$

$$\left.\begin{array}{ll} u_3(\mathbf{x},0) = v_3(\mathbf{x}) & \text{for} \quad \mathbf{x}\in\Omega \\ \dot{u}_3(\mathbf{x},0) = \dot{v}_3(\mathbf{x}) & \text{for} \quad \mathbf{x}\in\Omega \end{array}\right\}, \tag{3–10b}$$

where $p_3(\mathbf{x},t) = \mu n_\alpha(\mathbf{x})\partial u_3(\mathbf{x},t)/\partial x_\alpha = n_\alpha(\mathbf{x})\sigma_{3\alpha}(\mathbf{x},t)$ is the surface traction corresponding to antiplane shear, and the summation convention applies with $\alpha = 1,2$.

Since we are dealing with scalar wave field, Eq. (3–5) simplifies to

$$\int_\Gamma p_3^{(1)}(\mathbf{x},t_1)\,u_3^{(2)}(\mathbf{x},t_2)\,\mathrm{d}\Gamma + \int_\Omega \rho\left(b_3^{(1)}(\mathbf{x},t_1) - \ddot{u}_3^{(1)}(\mathbf{x},t_1)\right) u_3^{(2)}(\mathbf{x},t_2)\,\mathrm{d}\Omega$$
$$= \int_\Gamma p^{(2)}(\mathbf{x},t_2)\,u_3^{(1)}(\mathbf{x},t_1)\,\mathrm{d}\Gamma + \int_\Omega \rho\left(b_3^{(2)}(\mathbf{x},t_2) - \ddot{u}_3^{(2)}(\mathbf{x},t_2)\right) u_3^{(1)}(\mathbf{x},t_1)\,\mathrm{d}\Omega. \quad (3\text{–}11)$$

Likewise, the reciprocal theorem including the influence of initial conditions, *i.e.* Eq. (3–6), enters the scalar form

$$\int_0^t\int_\Gamma p_3^{(1)}(\mathbf{x},\tau)\,u_3^{(2)}(\mathbf{x},t-\tau)\,\mathrm{d}\Gamma\mathrm{d}\tau - \int_0^t\int_\Gamma p_3^{(2)}(\mathbf{x},t-\tau)\,u_3^{(1)}(\mathbf{x},\tau)\,\mathrm{d}\Gamma\mathrm{d}\tau$$
$$+ \int_0^t\int_\Omega \rho b_3^{(1)}(\mathbf{x},\tau)\,u_3^{(2)}(\mathbf{x},t-\tau)\,\mathrm{d}\Omega\mathrm{d}\tau - \int_0^t\int_\Omega \rho b_3^{(2)}(\mathbf{x},t-\tau)\,u_3^{(1)}(\mathbf{x},\tau)\,\mathrm{d}\Omega\mathrm{d}\tau$$
$$= \int_\Omega \rho\left\{\dot{u}_3^{(1)}(\mathbf{x},t)\,v_3^{(2)}(\mathbf{x}) - u_3^{(2)}(\mathbf{x},t)\,\dot{v}_3^{(1)}(\mathbf{x})\right\}\mathrm{d}\Omega$$
$$+ \int_\Omega \rho\left\{u_3^{(1)}(\mathbf{x},t)\,\dot{v}_3^{(2)}(\mathbf{x}) - \dot{u}_3^{(2)}(\mathbf{x},t)\,v_3^{(1)}(\mathbf{x})\right\}\mathrm{d}\Omega. \quad (3\text{–}12)$$

Equations (3–6) and (3–12) are identical to the reciprocal theorems for an acoustic field, given that the scalar quantity p_3 is interpreted as the acoustic pressure, p.

3.3 The Green's function

A cornerstone in the further development of boundary-integral equations is the so-called *fundamental solution* or *Green's function*. In the time domain and Cartesian spatial coordinates, the Green's function for a scalar field is of the general form $g(\mathbf{x},t;\mathbf{y},\tau)$. It provides the response at the *observation point* $\mathbf{x}$ and observation time t due to a unit magnitude load acting at the *source point* $\mathbf{y}$ and emission time τ. Typically, the load is applied as a concentrated force $\delta(\mathbf{x}-\mathbf{y})\delta(t-\tau)$ acting at $\mathbf{y}$ an time τ. However, the it is possible to derive a Green's function for a load which is distributed in time and space. We shall return to this in Chapter 5. However, only concentrated forces are considered in this chapter.

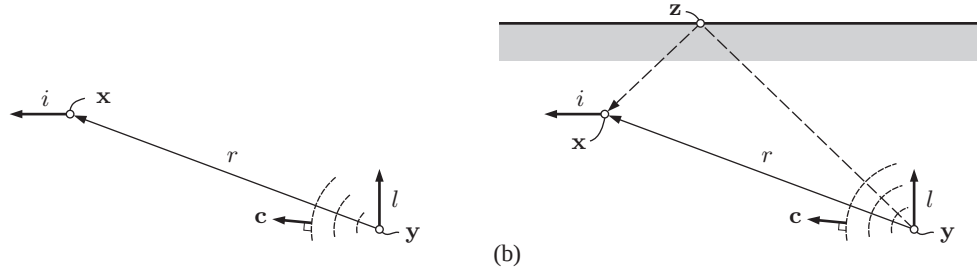

Figure 3–3 Illustration of the Green's function $g_{il}(\mathbf{x},t;\mathbf{y},\tau)$ which provides the response in direction i at point $\mathbf{x}$ to a load in direction l at point $\mathbf{y}$. In the full space (a), a wave is observed after the time $t-\tau = r/c$, where $r = |\mathbf{x}-\mathbf{y}|$ is the distance between the two points and $c = |\mathbf{c}|$ is the wave speed with $\mathbf{c}$ denoting the wave velocity. In a half-space (b) a second contribution is observed due to a reflection of the waves at the point $\mathbf{z}$ on the free boundary.

The Green's function is strongly dependent on the boundary conditions. For example, the Green's function for the displacement in a half-space is different from the corresponding function for the displacement in a full space, *i.e.* an unbounded domain. This problem is illustrated in Fig. 3–3. Whereas the full-space solution is relatively easily obtained in time–space domain, a fundamental solution for a layered half-space (*e.g.* soil) can only be derived in the frequency–wavenumber domain. A further introduction to the solution in frequency–wavenumber domain is given in Chapter 5. Here we shall focus on the much simpler full-space solution for elastodynamic problems. However, in Chapter 4 the discussion of Green's functions is briefly revisited.

Now, in the case of general three-dimensional elastic wave propagation (or coupled P- and SV-waves propagating in a plane) we are dealing with vector fields with regard to displacements, body forces and surface traction. The Green's function for a vector field is a second-order tensor with the components $g_{il}(\mathbf{x}, t; \mathbf{y}, \tau)$ which provides the response at the point $\mathbf{x}$ and time t in coordinate direction i due to a unit magnitude concentrated force acting at the point $\mathbf{y}$ and time τ in coordinate direction l, see Fig. 3–3. Hence, whereas the displacement field $\mathbf{u}(\mathbf{x}, t)$ is a vector field with the components $u_i(\mathbf{x}, t)$, the corresponding Green's function is a tensor field $\mathbf{u}^*(\mathbf{x}, t; \mathbf{y}, \tau)$ with the doubly indexed components $u^*_{il}(\mathbf{x}, t; \mathbf{y}, \tau)$.

3.3.1 Reciprocity relations for the Green's function

In the case of wave propagation in a homogeneous elastic unbounded domain, the full-space Green's function for the displacement in time-domain is found as the solution to the Cauchy equation

$$\frac{\partial}{\partial x_j}\sigma^*_{ijl}(\mathbf{x}, t; \mathbf{y}, \tau) + \rho b^*_{il}(\mathbf{x}, t; \mathbf{y}, \tau) = \rho \frac{\partial^2}{\partial t^2} u^*_{il}(\mathbf{x}, t; \mathbf{y}, \tau), \tag{3–13a}$$

where the body forces per unit volume are given as

$$\rho b^*_{il}(\mathbf{x}, t; \mathbf{y}, \tau) = \delta_{il}\delta(\mathbf{x} - \mathbf{y})\delta(t - \tau). \tag{3–13b}$$

Note that in three dimensions we are actually dealing with nine equations, one for each combination of the free indices i and l. However, the equations for each value of l are decoupled form the equations for the two other coordinate direction in which the load $b^*_{il}(\mathbf{x}, t; \mathbf{y}, \tau)$ may be applied, *i.e.* only three equations are considered at a time.

Evidently, the response $u^*_{il}(\mathbf{x}, t; \mathbf{y}, \tau)$ must fulfill the causality condition that the medium has a quiescent past, *i.e.*

$$u^*_{il}(\mathbf{y}, t; \mathbf{x}, \tau) = 0, \qquad \frac{\partial}{\partial t} u^*_{il}(\mathbf{y}, t; \mathbf{x}, \tau) = 0 \qquad \text{for} \qquad t \leq \tau, \tag{3–14}$$

since no load is applied before the occurrence of the Dirac delta spike $\delta(t - \tau)$ at the time $t = \tau$. Further, the load in the fundamental-solution state only depends on the arguments t and τ through the difference $t - \tau$, and the response is linear. Consequently, the fundamental solution is also invariant to time translation, *i.e.*

$$u^*_{il}(\mathbf{x}, t; \mathbf{y}, \tau) = u^*_{il}(\mathbf{x}, 0; \mathbf{y}, \tau - t) = u^*_{il}(\mathbf{x}, t - \tau; \mathbf{y}, 0) = u^*_{il}(\mathbf{x}, -\tau; \mathbf{y}, -t)\,. \tag{3–15}$$

This equation forms a purely *temporal reciprocity relation* for the displacement Green's function. Obviously, a similar statement applies to the fundamental solution for the stress tensor, that is $\sigma^*_{ijl}(\mathbf{x}, t; \mathbf{y}, \tau) = \sigma^*_{ijl}(\mathbf{x}, -\tau; \mathbf{y}, -t)$.

Next, let us consider the unbounded linear elastic domain Ω. Two states are now defined on this domain with $\rho b_i^{(1)}(\mathbf{x},t) = \delta_{ik}\delta(\mathbf{x}-\mathbf{y}_1)\delta(t-\tau_1)$, $\rho b_i^{(2)}(\mathbf{x},t) = \delta_{il}\delta(\mathbf{x}-\mathbf{y}_2)\delta(t-\tau_2)$. Accordingly, $u_i^{(1)}(\mathbf{x},t) = u_{ik}^*(\mathbf{x},t;\mathbf{y}_1,\tau_1)$ and $u_i^{(2)}(\mathbf{x},t) = u_{il}^*(\mathbf{x},t;\mathbf{y}_2,\tau_2)$. Since the domain is unbounded and has a quiescent past, the integrals over Γ and any influence of initial conditions vanish. Hence, the Betti-Rayleigh theorem (3–6) reduces to

$$\int_0^t \int_\Omega \rho b_i^{(1)}(\mathbf{x},\tau)\, u_i^{(2)}(\mathbf{x},t-\tau)\,\mathrm{d}\Omega\mathrm{d}\tau = \int_0^t \int_\Omega \rho b_i^{(2)}(\mathbf{x},t-\tau)\, u_i^{(1)}(\mathbf{x},\tau)\,\mathrm{d}\Omega\mathrm{d}\tau \qquad \Rightarrow$$

$$\int_0^t \int_\Omega \delta_{ik}\delta(\mathbf{x}-\mathbf{y}_1)\delta(\tau-\tau_1) u_{il}^*(\mathbf{x},t-\tau;\mathbf{y}_2,\tau_2)\,\mathrm{d}\Omega\mathrm{d}\tau$$

$$= \int_0^t \int_\Omega \delta_{il}\delta(\mathbf{x}-\mathbf{y}_2)\delta(t-\tau-\tau_2) u_{ik}^*(\mathbf{x},\tau;\mathbf{y}_1,\tau_1)\,\mathrm{d}\Omega\mathrm{d}\tau \qquad \Rightarrow$$

$$u_{kl}^*(\mathbf{y}_1,t-\tau_1;\mathbf{y}_2,\tau_2) = u_{lk}^*(\mathbf{y}_2,t-\tau_2;\mathbf{y}_1,\tau_1)\,.$$

Exploiting the fact that u_{kl}^* is invariant to time translation, we may add τ_1 to the time arguments on the left-hand side of this equation. Similarly, τ_2 is added to the time arguments on the right-hand side. Then, introducing the substitutions $\tau = \tau_1 + \tau_2$, $\mathbf{y}_1 = \mathbf{x}$ and $\mathbf{y}_2 = \mathbf{y}$, we obtain a purely *spatial reciprocity relation*,

$$u_{kl}^*(\mathbf{x},t;\mathbf{y},\tau) = u_{lk}^*(\mathbf{y},t;\mathbf{x},\tau)\,. \tag{3–16}$$

In particular, if the material is homogeneous in the direction provided by the unit vector $\hat{\mathbf{r}} = \mathbf{x}-\mathbf{y}/|\mathbf{x}-\mathbf{y}|$, the spatial reciprocity

$$u_{kl}(\mathbf{x},t;\mathbf{y},\tau) = u_{kl}(\mathbf{x}-\mathbf{y},t;\mathbf{0},\tau) = u_{lk}(\mathbf{0},t;\mathbf{x}-\mathbf{y},\tau) = u_{lk}(\mathbf{y},t;\mathbf{x},\tau) \tag{3–17}$$

applies. Thus, the Green's function is invariant to a spatial translation in any direction in which the material is homogeneous. Obviously, in the homogeneous full-space, this applies to any direction, $\hat{\mathbf{r}}$.

Finally, Eqs. (3–15) and (3–16) may be combined to form the *spatial–temporal reciprocity relation*

$$u_{kl}^*(\mathbf{x},t;\mathbf{y},\tau) = u_{lk}^*(\mathbf{y},-\tau;\mathbf{x},-t)\,. \tag{3–18}$$

The reciprocity relations play an important part in the derivation of the Green's functions and the development of boundary integral equations discussed in the forthcoming sections.

Reciprocity relations for a scalar field (SH-waves)

In the case of antiplane shear, we consider the scalar wave equation with respect to the displacement in the direction out of the plane. In this case, the reciprocity relations simplify to

$$u_{33}^*(\mathbf{x},t;\mathbf{y},\tau) = u_{33}^*(\mathbf{x},-\tau;\mathbf{y},-t), \tag{3–19a}$$

$$u_{33}^*(\mathbf{x},t;\mathbf{y},\tau) = u_{33}^*(\mathbf{y},t;\mathbf{x},\tau), \tag{3–19b}$$

$$u_{33}^*(\mathbf{x},t;\mathbf{y},\tau) = u_{33}^*(\mathbf{y},-\tau;\mathbf{x},-t), \tag{3–19c}$$

$$u_{33}^*(\mathbf{x},t;\mathbf{y},\tau) = u_{33}^*(\mathbf{x}-\mathbf{y},t-\tau;\mathbf{0},0), \tag{3–19d}$$

where Eq. (3–19d) only applies to a material which is homogeneous in the direction defined by the unit vector $\hat{\mathbf{r}} = (\mathbf{x}-\mathbf{y})/|\mathbf{x}-\mathbf{y}|$.

3.3.2 Green's functions for three-dimensional elastodynamics

For a homogeneous isotropic linear elastic material, the generalised Hooke's law (1–2) forming the relation between stresses, $\sigma_{ij}(\mathbf{x},t)$, and strains, $\epsilon_{ij}(\mathbf{x},t)$, simplifies to

$$\sigma_{ij}(\mathbf{x},t) = \lambda\Delta(\mathbf{x},t)\delta_{ij} + 2\mu\epsilon_{ij}(\mathbf{x},t), \tag{1–5}$$

where λ and μ are the Lamé constants, cf. Section 1.2, and $\Delta(\mathbf{x},t) = \epsilon_{kk}(\mathbf{x},t)$ is the dilation. Hence, wave propagation in the full space is governed by the *Navier equations*,

$$(\lambda+\mu)\,\frac{\partial^2 u_j(\mathbf{x},t)}{\partial x_i \partial x_j} + \mu\frac{\partial^2 u_i(\mathbf{x},t)}{\partial x_j \partial x_j} + \rho b_i(\mathbf{x},t) = \rho\frac{\partial^2 u_i(\mathbf{x},t)}{\partial t^2} = \rho\ddot{u}_i(\mathbf{x},t). \tag{1–10}$$

No boundary conditions apply, as we are dealing with an infinite domain. However, it should be evident that waves may only propagate away from a given source; likewise, according to Section 1.6.2, the magnitude of the displacement field should diminish with increasing distance from the source. This constitutes a radiation condition that replaces the boundary conditions in the case of an unbounded domain.

Governing equations for the Green's functions in time and frequency domain

Inserting the specific body forces $b^*_{il}(\mathbf{x},t;\mathbf{y},\tau)$ defined by Eq. (3–13b) into the Navier equations (1–10), we arrive at the expression

$$(\lambda+\mu)\,\frac{\partial^2 u^*_{jl}(\mathbf{x},t;\mathbf{y},\tau)}{\partial x_i \partial x_j} + \mu\frac{\partial^2 u^*_{il}(\mathbf{x},t;\mathbf{y},\tau)}{\partial x_j \partial x_j} + \delta_{il}\delta(\mathbf{x}-\mathbf{y})\delta(t-\tau) = \rho\ddot{u}^*_{il}(\mathbf{x},t;\mathbf{y},\tau) \tag{3–20}$$

that defines a governing equation for the time-domain Green's function $u^*_{il}(\mathbf{x},t;\mathbf{y},\tau)$. The solution for a concentrated force applied continuously over time is established by convolution.

On the other hand, if the specific body forces are replaced by a harmonically varying function of the kind $B^*_{il}(\mathbf{x},\omega;\mathbf{y})\mathrm{e}^{\mathrm{i}\omega t} = \delta_{il}\delta(\mathbf{x}-\mathbf{y})\mathrm{e}^{\mathrm{i}\omega t}$, it should be evident that the response will also vary harmonically at the same circular frequency, ω. Thus, the displacement in time domain may be written as $U^*_{il}(\mathbf{x},\omega;\mathbf{y})\mathrm{e}^{\mathrm{i}\omega t}$, where $U^*_{il}(\mathbf{x},\omega;\mathbf{y})$ is a complex amplitude field identified as the frequency-domain Green's function. Accordingly, after elimination of the term $\mathrm{e}^{\mathrm{i}\omega t}$, we arrive at the governing equation

$$(\lambda+\mu)\,\frac{\partial^2 U^*_{jl}(\mathbf{x},\omega;\mathbf{y})}{\partial x_i \partial x_j} + \mu\frac{\partial^2 U^*_{il}(\mathbf{x},\omega;\mathbf{y})}{\partial x_j \partial x_j} + \delta_{il}\delta(\mathbf{x}-\mathbf{y}) = -\rho\omega^2 U^*_{il}(\mathbf{x},\omega;\mathbf{y}). \tag{3–21}$$

In this case, the solution for a concentrated force that varies arbitrarily with time may be found by Fourier transformation/inverse Fourier transformation as discussed in Section 2.3 with regard to the finite-element method.

Solution for a concentrated force with arbitrary variation over time

Before we return to the Green's functions in time and frequency domain, we will pay attention to the Navier equation with the inhomogeneity $\rho b_{il}(\mathbf{x},t) = \delta_{il}\delta(\mathbf{x})h(t)$,

$$(\lambda+\mu)\,\frac{\partial^2 u_{jl}(\mathbf{x},t)}{\partial x_i \partial x_j} + \mu\frac{\partial^2 u_{il}(\mathbf{x},t)}{\partial x_j \partial x_j} + \delta_{il}\delta(\mathbf{x})h(t) = \rho\ddot{u}_{il}(\mathbf{x},t) \tag{3–22}$$

where $u_{il}(\mathbf{x},t)$ corresponds to $u^*_{il}(\mathbf{x},t;\mathbf{0},0)$ if $h(t)=\delta(t)$. Likewise, the frequency-domain solution is obtained via the relation $u_{il}(\mathbf{x},t)=U^*_{il}(\mathbf{x},\omega;\mathbf{0})\mathrm{e}^{\mathrm{i}\omega t}$ if $h(t)$ is set to $\mathrm{e}^{\mathrm{i}\omega t}$. Hence, the solutions to Eqs. (3–20) and (3–21) may be established by a simple substitution of variables and utilisation of the reciprocity relations of Section 3.3.1, given that we are able to solve the slightly more general equation (3–22). As discussed in the following, this can be done by application of the Helmholtz decomposition theorem (cf. Sections 1.3.2 and A.2).

Firstly, the function $B_{il}(\mathbf{x},t)$ is defined by

$$\rho B_{il}(\mathbf{x},t)=\frac{1}{4\pi}\int_\Omega\frac{\rho b_{il}(\mathbf{y},t)}{|\mathbf{x}-\mathbf{y}|}\,\mathrm{d}\Omega(\mathbf{y})=\frac{1}{4\pi}\int_\Omega\frac{\delta(\mathbf{y})h(t)}{|\mathbf{x}-\mathbf{y}|}\delta_{il}\,\mathrm{d}\Omega(\mathbf{y})\qquad\Rightarrow$$
$$\rho B_{il}(\mathbf{x},t)=\frac{1}{4\pi}\frac{h(t)}{|\mathbf{x}|}\delta_{il}=\frac{1}{4\pi}\frac{h(t)}{r}\delta_{il},\qquad r=|\mathbf{x}|. \tag{3–23}$$

The Helmholtz potentials for the load $\rho b_{il}(\mathbf{x},t)=\delta_{il}\delta(\mathbf{x})h(t)$ are then given as

$$\Phi_l(\mathbf{x},t)=\quad-\frac{\partial B_{jl}(\mathbf{x},t)}{\partial x_j}=\quad-\frac{1}{4\pi\rho}\frac{\partial}{\partial x_l}\frac{h(t)}{r}, \tag{3–24a}$$
$$\Psi_{il}(\mathbf{x},t)=\varepsilon_{ijk}\frac{\partial B_{kl}(\mathbf{x},t)}{\partial x_j}=\varepsilon_{ijl}\frac{1}{4\pi\rho}\frac{\partial}{\partial x_j}\frac{h(t)}{r}. \tag{3–24b}$$

Secondly, it may be proved that the Helmholtz potentials $\varphi_l(\mathbf{x},t)$ and $\psi_{il}(\mathbf{x},t)$ for the displacement field $u_{il}(\mathbf{x},t)$ are solutions to the inhomogeneous scalar wave equations

$$c_P^2\frac{\partial\varphi_l(\mathbf{x},t)}{\partial x_j\partial x_j}+\ \Phi_l(\mathbf{x},t)=\ \frac{\partial^2\varphi_l(\mathbf{x},t)}{\partial t^2},\qquad c_P^2=\frac{\lambda+2\mu}{\rho}, \tag{3–25a}$$
$$c_S^2\frac{\partial\psi_{il}(\mathbf{x},t)}{\partial x_j\partial x_j}+\Psi_{il}(\mathbf{x},t)=\frac{\partial^2\psi_{il}(\mathbf{x},t)}{\partial t^2},\qquad c_S^2=\frac{\mu}{\rho}, \tag{3–25b}$$

which, after insertion of Eq. (3–24), may be recast as

$$c_P^2\frac{\partial\varphi_l(\mathbf{x},t)}{\partial x_j\partial x_j}-\qquad\frac{1}{4\pi\rho}\frac{\partial}{\partial x_l}\frac{h(t)}{r}=\ \frac{\partial^2\varphi_l(\mathbf{x},t)}{\partial t^2}, \tag{3–26a}$$
$$c_S^2\frac{\partial\psi_{il}(\mathbf{x},t)}{\partial x_j\partial x_j}+\varepsilon_{ijl}\frac{1}{4\pi\rho}\frac{\partial}{\partial x_j}\frac{h(t)}{r}=\frac{\partial^2\psi_{il}(\mathbf{x},t)}{\partial t^2}. \tag{3–26b}$$

Now, to solve these equations we introduce the auxiliary functions $f_P(\mathbf{x},t)$ and $f_S(\mathbf{x},t)$,

$$\varphi_l(\mathbf{x},t)=-\frac{\partial}{\partial x_l}f_P(\mathbf{x},t),\qquad\psi_{il}(\mathbf{x},t)=\varepsilon_{ijl}\frac{\partial}{\partial x_j}f_S(\mathbf{x},t). \tag{3–27}$$

It then follows that $\varphi_l(\mathbf{x},t)$ and $\psi_{il}(\mathbf{x},t)$ are the solutions to Eq. (3–26) given that the auxiliary functions $f_P(\mathbf{x},t)$ and $f_S(\mathbf{x},t)$ fulfill the equations

$$c_P^2\frac{\partial f_P(\mathbf{x},t)}{\partial x_j\partial x_j}+\frac{1}{4\pi\rho}\frac{h(t)}{r}=\frac{\partial^2 f_P(\mathbf{x},t)}{\partial t^2}, \tag{3–28a}$$
$$c_S^2\frac{\partial f_S(\mathbf{x},t)}{\partial x_j\partial x_j}+\frac{1}{4\pi\rho}\frac{h(t)}{r}=\frac{\partial^2 f_S(\mathbf{x},t)}{\partial t^2}. \tag{3–28b}$$

Next, the Laplace operator is rewritten in spherical coordinates. In the general case

$$\nabla^2 f = \frac{\partial^2 f}{\partial x_j \partial x_j} = \frac{\partial^2 f}{\partial r^2} + \frac{2}{r}\frac{\partial f}{\partial r} + \frac{1}{r^2 \sin^2 \vartheta}\frac{\partial^2 f}{\partial \theta^2} + \frac{1}{r^2}\frac{\partial^2 f}{\partial \vartheta^2} + \frac{\cot \vartheta}{r^2}\frac{\partial f}{\partial \vartheta}, \tag{3–29}$$

where r is the distance from the origin, whereas θ and ϑ are the azimuthal and polar angle, respectively. The Cartesian coordinates are related to the spherical coordinates via the relation

$$x_1 = r \sin \vartheta \cos \theta, \qquad x_2 = r \sin \vartheta \sin \theta, \qquad x_3 = r \cos \vartheta. \tag{3–30}$$

However, since the problem defined by Eq. (3–28) is spherically symmetrical, the solution is independent of θ and ϑ, and only the derivatives with respect to r remain, *i.e.*

$$c_P^2 \left(\frac{\partial^2 f_P}{\partial r^2} + \frac{2}{r}\frac{\partial f_P}{\partial r} \right) + \frac{1}{4\pi\rho}\frac{h(t)}{r} = \frac{\partial^2 f_P}{\partial t^2}, \tag{3–31a}$$

$$c_S^2 \left(\frac{\partial^2 f_S}{\partial r^2} + \frac{2}{r}\frac{\partial f_S}{\partial r} \right) + \frac{1}{4\pi\rho}\frac{h(t)}{r} = \frac{\partial^2 f_S}{\partial t^2}. \tag{3–31b}$$

These equations may be further simplified by introduction of the quantities F_P and F_S,

$$f_P(\mathbf{x}, t) = \frac{F_P(r,t)}{r}, \qquad f_S(\mathbf{x}, t) = \frac{F_S(r,t)}{r}. \tag{3–32}$$

Thus, Eq. (3–31) is rewritten in the form

$$c_P^2 \frac{\partial^2 F_P(r,t)}{\partial r^2} + \frac{h(t)}{4\pi\rho} = \frac{\partial^2 F_P(r,t)}{\partial t^2}, \qquad c_S^2 \frac{\partial^2 F_S(r,t)}{\partial r^2} + \frac{h(t)}{4\pi\rho} = \frac{\partial^2 F_S(r,t)}{\partial t^2}. \tag{3–33}$$

Except for the phase velocities of P- and S-waves, *i.e.* c_P and c_S, these equations are identical.

Skipping the indices P and S, a particular solution to Eq. (3–33) is found as

$$F_p(t) = \frac{1}{4\pi\rho}\int_0^t (t-s)\, h(t)\, \mathrm{d}s. \tag{3–34}$$

To prove this, we integrate Eq. (3–34) by parts,

$$F_p(t) = \frac{1}{4\pi\rho}\left[(t-s)\, \tilde{h}(s) \right]_0^t + \frac{1}{4\pi\rho}\int_0^t \tilde{h}(s)\, \mathrm{d}s = \frac{1}{4\pi\rho}\left\{ \tilde{\tilde{h}}(t) - \tilde{\tilde{h}}(0) - t\tilde{h}(0) \right\}, \tag{3–35}$$

where $\tilde{h}(t)$ is the antiderivative of $h(t)$. Accordingly, $\tilde{\tilde{h}}(t)$ is the antiderivative of $\tilde{h}(t)$. Then, by insertion of F_p into Eq. (3–33) and skipping the indices P and S, we get the result

$$\frac{\partial^2 F_p}{\partial s^2} - c^2 \frac{\partial^2 F_p}{\partial r^2} = \frac{1}{4\pi\rho}\left\{ \frac{\partial^2}{\partial s^2} - c^2 \frac{\partial^2}{\partial r^2} \right\}\left\{ \tilde{\tilde{h}}(s) - \tilde{\tilde{h}}(0) - s\tilde{h}(0) \right\} = \frac{1}{4\pi\rho}\frac{\partial^2 \tilde{\tilde{h}}(s)}{\partial s^2} = \frac{h(s)}{4\pi\rho},$$

where it has been utilised that $h(t)$ is independent of r and $h(0)$ is constant with regard to t.

It is readily proved by insertion that the solution to the homogeneous part of Eq. (3–33) has the general form $F_h(t - r/c_P)$ for the first equation and $F_h(t - r/c_P)$ for the second equation, where F_h is an arbitrary function. Note that terms with the arguments $t + r/c_P$ and $t + r/c_S$ are

physically invalid, since they correspond to waves propagating towards the source point. Thus, again skipping the indices P and S, the full solution to any of the equations achieves the form $F(r,t) = F_h(t - r/c) + F_p(t)$.

Evidently, a physically valid solution is only obtained if the auxiliary functions $f_P(\mathbf{x},t)$ and $f_S(\mathbf{x},t)$ are finite at $r = 0$. This is only the case if $F_P(0,t) = F_S(0,t) = 0$, *i.e.*

$$F(0,t) = F_h(t) + F_p(t) = 0 \qquad \Rightarrow \qquad F_h(t) = -\frac{1}{4\pi\rho}\int_0^t (t-s)\,h(s)\,\mathrm{d}s. \tag{3–36}$$

It the follows that the full solution $F(r,t)$ may be written in the form

$$F(r,t) = \frac{1}{4\pi\rho}\int_0^t (t-s)\,h(s)\,\mathrm{d}s - \frac{1}{4\pi\rho}\int_0^{t-r/c}\left(t - \frac{r}{c} - s\right)h(s)\,\mathrm{d}s, \tag{3–37}$$

and by a simple rearrangement of the terms, $F_P(r,t)$ and $F_S(r,t)0$ are obtained as

$$F_P(r,t) = \frac{1}{4\pi\rho}\int_{t-t_P}^t (t-s)\,h(s)\,\mathrm{d}s - \frac{r}{4\pi\rho c_P}\int_0^{t-t_P} h(s)\,\mathrm{d}s, \qquad t_P{=}\frac{r}{c_P}, \tag{3–38a}$$

$$F_S(r,t) = \frac{1}{4\pi\rho}\int_{t-t_S}^t (t-s)\,h(s)\,\mathrm{d}s - \frac{r}{4\pi\rho c_S}\int_0^{t-t_S} h(s)\,\mathrm{d}s, \qquad t_S{=}\frac{r}{c_S}, \tag{3–38b}$$

where t_P and t_S are identified as the arrival times of the P- and S-waves, respectively.

The next step is to employ the variable substitutions (3–32) and, subsequently, (3–27). Thus, the Helmholtz potentials are achieved as

$$\varphi_l(\mathbf{x},t) = -\frac{\partial}{\partial x_l}\left(\frac{F_P(r,t)}{r}\right), \qquad \psi_{il}(\mathbf{x},t) = \varepsilon_{ijl}\frac{\partial}{\partial x_j}\left(\frac{F_S(r,t)}{r}\right), \qquad r = |\mathbf{x}|, \tag{3–39}$$

which, by insertion of $F_P(r,t)$ and $F_S(r,t)$ from Eq. (3–38), provides the result

$$\varphi_l(\mathbf{x},t) = \quad -\frac{1}{4\pi\rho}\frac{\partial}{\partial x_l}\left(\frac{1}{r}\right)\int_0^{t_P} \tau h(t-\tau)\,\mathrm{d}\tau, \tag{3–40a}$$

$$\psi_{il}(\mathbf{x},t) = \varepsilon_{ijl}\frac{1}{4\pi\rho}\frac{\partial}{\partial x_j}\left(\frac{1}{r}\right)\int_0^{t_S} \tau h(t-\tau)\,\mathrm{d}\tau, \tag{3–40b}$$

where the substitution $\tau = t - s$ has been employed.

Finally, the displacement field $u_{il}(\mathbf{x},t)$ is obtained as

$$u_{il}(\mathbf{x},t) = u_{il}^P(\mathbf{x},t) + u_{il}^S(\mathbf{x},t) = \frac{\partial\varphi_l(\mathbf{x},t)}{\partial x_i} + \varepsilon_{ijk}\frac{\partial\psi_{kl}(\mathbf{x},t)}{\partial x_j}, \tag{3–41}$$

where the contributions from the P- and S-waves are given as

$$u_{il}^P(\mathbf{x},t) = -\frac{1}{4\pi\rho}\frac{\partial}{\partial x_i}\left\{\frac{\partial}{\partial x_l}\left(\frac{1}{r}\right)\int_0^{t_P}\tau h(t-\tau)\,\mathrm{d}\tau\right\} \qquad \Rightarrow$$

$$u_{il}^P(\mathbf{x},t) = \frac{1}{4\pi\rho c_P^2}\frac{r_i r_l}{r^3}h(t-t_P) + \frac{1}{4\pi\rho}\left(\frac{\delta_{il}}{r^3} - 3\frac{r_i r_l}{r^5}\right)\int_0^{t_P}\tau h(t-\tau)\,\mathrm{d}\tau, \tag{3–42a}$$

$$u_{il}^S(\mathbf{x},t) = \varepsilon_{ijm}\varepsilon_{mkl}\frac{1}{4\pi\rho}\frac{\partial}{\partial x_j}\left\{\frac{\partial}{\partial x_k}\left(\frac{1}{r}\right)\int_0^{t_S}\tau h(t-\tau)\,\mathrm{d}\tau\right\} = (\delta_{il}\delta_{jk}-\delta_{ik}\delta_{jl})$$
$$\times\left\{\frac{1}{4\pi\rho c_S^2}\frac{r_j r_k}{r^3}h(t-t_S)+\frac{1}{4\pi\rho}\left(\frac{\delta_{jk}}{r^3}-3\frac{r_j r_k}{r^5}\right)\int_0^{t_S}\tau h(t-\tau)\,\mathrm{d}\tau\right\} \qquad \Rightarrow$$

$$u_{il}^S(\mathbf{x},t) = \frac{1}{4\pi\rho c_S^2}\left(\frac{\delta_{il}}{r}-\frac{r_i r_l}{r^3}\right)h(t-t_S)-\frac{1}{4\pi\rho}\left(\frac{\delta_{il}}{r^3}-3\frac{r_i r_l}{r^5}\right)\int_0^{t_S}\tau h(t-\tau)\,\mathrm{d}\tau, \quad \text{(3–42b)}$$

where the δ–ε identity (A–6) has been employed. Further, the substitution $r_i = x_i$ has been introduced, and use has been made of the fact that $\partial r/\partial x_i = x_i/r = r_i/r$. Then, by insertion of Eq. (3–42) into Eq. (3–41) we get the total displacement field

$$u_{il}(\mathbf{x},t) = \frac{1}{4\pi\rho c_P^2}\frac{r_i r_l}{r^3}h(t-t_P)+\frac{1}{4\pi\rho c_S^2}\left(\frac{\delta_{il}}{r}-\frac{r_i r_l}{r^3}\right)h(t-t_S)$$
$$-\frac{1}{4\pi\rho}\left(\frac{\delta_{il}}{r^3}-3\frac{r_i r_l}{r^5}\right)\int_{t_P}^{t_S}\tau h(t-\tau)\,\mathrm{d}\tau. \qquad \text{(3–43)}$$

Thus, we have established the solution to the Navier equation (3–22) with the body force specified as $\rho b_{il}(\mathbf{x},t) = \delta_{il}\delta(\mathbf{x})h(t)$.

Time-domain Green's function

Firstly, we establish the fundamental solution $u_{il}^*(\mathbf{x},t;\mathbf{0},0)$ by insertion of $h(t) = \delta(t)$ into Eq. (3–43). With $H(t)$ denoting the Heaviside unit step function, cf. Eq. (1–116), we get the result

$$u_{il}^*(\mathbf{x},t;\mathbf{0},0) = \frac{1}{4\pi\rho c_P^2}\frac{r_i r_l}{r^3}\delta(t-t_P)+\frac{1}{4\pi\rho c_S^2}\left(\frac{\delta_{il}}{r}-\frac{r_i r_l}{r^3}\right)\delta(t-t_S)$$
$$-\frac{1}{4\pi\rho}\left(\frac{\delta_{il}}{r^3}-3\frac{r_i r_l}{r^5}\right)t\big(H(t-t_P)-H(t-t_S)\big).$$

Secondly, we replace t by $t-\tau$ and $\mathbf{r} = \mathbf{x}$ with $\mathbf{r} = \mathbf{x}-\mathbf{y}$. Exploiting the spatial–temporal reciprocity of the Green's function, $u_{il}^*(\mathbf{x}-\mathbf{y},t-\tau;\mathbf{0},0) = u_{il}^*(\mathbf{x},t;\mathbf{y},\tau)$, the time-domain Green's function for the displacement in an unbounded homogeneous and isotropic elastic domain achieves the form

$$u_{il}^*(\mathbf{x},t;\mathbf{y},\tau) = \frac{1}{4\pi\rho c_P^2}\frac{r_i r_l}{r^3}\delta(t-t_P-\tau)+\frac{1}{4\pi\rho c_S^2}\left(\frac{\delta_{il}}{r}-\frac{r_i r_l}{r^3}\right)\delta(t-t_S-\tau)$$
$$-\frac{1}{4\pi\rho}\left(\frac{\delta_{il}}{r^3}-3\frac{r_i r_l}{r^5}\right)(t-\tau)\big(H(t-t_P-\tau)-H(t-t_S-\tau)\big), \qquad \text{(3–44)}$$

where $t_P = r/c_P$, $t_S = r/c_S$, $r = |\mathbf{x}-\mathbf{y}|$, and $r_i = x_i - y_i$, $i = 1,2,3$.

Frequency-domain Green's function

The fundamental solution in the frequency domain may be found in different ways. One approach is to replace $h(t)$ in Eq. (3–43) with the complex exponential harmonic function $\mathrm{e}^{\mathrm{i}\omega t}$. This provides the solution

$$
\begin{aligned}
u_{il}(\mathbf{x},t) &= \frac{1}{4\pi\rho c_P^2}\frac{r_i r_l}{r^3}\mathrm{e}^{\mathrm{i}\omega t}\mathrm{e}^{-\mathrm{i}k_P r} + \frac{1}{4\pi\rho c_S^2}\left(\frac{\delta_{il}}{r} - \frac{r_i r_l}{r^3}\right)\mathrm{e}^{\mathrm{i}\omega t}\mathrm{e}^{-\mathrm{i}k_S r} \\
&\quad - \frac{1}{4\pi\rho}\left(\frac{\delta_{il}}{r^3} - 3\frac{r_i r_l}{r^5}\right)\mathrm{e}^{\mathrm{i}\omega t}\left[\frac{1+\mathrm{i}\omega\tau}{\omega^2}\mathrm{e}^{-\mathrm{i}\omega\tau}\right]_{t_P}^{t_S} \qquad \Rightarrow \\
u_{il}(\mathbf{x},t) &= \frac{1}{4\pi\rho c_P^2}\left\{\frac{r_i r_l}{r^3} + \left(\frac{\delta_{il}}{r^3} - 3\frac{r_i r_l}{r^5}\right)\frac{1+\mathrm{i}k_P r}{k_P^2}\right\}\mathrm{e}^{\mathrm{i}\omega t}\mathrm{e}^{-\mathrm{i}k_P r} \\
&\quad + \frac{1}{4\pi\rho c_S^2}\left\{\frac{\delta_{il}}{r} - \frac{r_i r_l}{r^3} - \left(\frac{\delta_{il}}{r^3} - 3\frac{r_i r_l}{r^5}\right)\frac{1+\mathrm{i}k_S r}{k_S^2}\right\}\mathrm{e}^{\mathrm{i}\omega t}\mathrm{e}^{-\mathrm{i}k_S r}.
\end{aligned}
$$

Here $k_P = \omega/c_P$ and $k_S = \omega/c_S$ are identified as the wavenumbers of the P- and S-waves, respectively. The frequency-domain Green's function, *i.e.* the solution to Eq. (3–21), is obtained by division of $u_{il}(\mathbf{x},t)$ by $\mathrm{e}^{\mathrm{i}\omega t}$ and replacement of $\mathbf{r} = \mathbf{x}$ with $\mathbf{r} = \mathbf{x} - \mathbf{y}$. Hence, by utilisation of the spatial reciprocity $U_{il}^*(\mathbf{x}-\mathbf{y},\omega;\mathbf{0}) = U_{il}^*(\mathbf{x},\omega;\mathbf{y})$, we find

$$
\begin{aligned}
U_{il}^*(\mathbf{x},\omega;\mathbf{y}) &= \frac{1}{4\pi\rho c_P^2}\left\{\frac{r_i r_l}{r^3} + \left(\frac{\delta_{il}}{r^3} - 3\frac{r_i r_l}{r^5}\right)\frac{1+\mathrm{i}k_P r}{k_P^2}\right\}\mathrm{e}^{-\mathrm{i}k_P r} \\
&\quad + \frac{1}{4\pi\rho c_S^2}\left\{\frac{\delta_{il}}{r} - \frac{r_i r_l}{r^3} - \left(\frac{\delta_{il}}{r^3} - 3\frac{r_i r_l}{r^5}\right)\frac{1+\mathrm{i}k_S r}{k_S^2}\right\}\mathrm{e}^{-\mathrm{i}k_S r}.
\end{aligned} \tag{3–45}
$$

Alternatively, the frequency-domain Green's function (3–45) can be derived by Fourier transformation of the time-domain Green's function, *i.e.*

$$
U_{il}^*(\mathbf{x},\omega;\mathbf{y}) = \int_{-\infty}^{\infty} u_{il}^*(\mathbf{x},t;\mathbf{y},0)\mathrm{e}^{-\mathrm{i}\omega t}\,\mathrm{d}t. \tag{3–46}
$$

It is left as an exercise to the reader to prove this. Finally, the Green's function $U_{il}^*(\mathbf{x},\omega;\mathbf{y})$ may be found directly as the solution to Eq. (3–21) by utilisation of the Helmholtz decomposition theorem. This approach has been illustrated in Example 1.6.

3.3.3 Green's functions for elastic waves in plane strain

Consider a homogeneous isotropic linear elastic full space subject to a line load acting along the x_3-axis. If the body forces only act in the x_1- or x_2-directions, *i.e.* with no excitation in the x_3-direction, and the body forces along the given line act in phase and with a homogeneous magnitude, it should be evident that no response is generated in the x_3-direction. Thus, the applied body forces give rise to a state of plane strain, which in the case of elastodynamics corresponds to the problem of combined P- and SV-wave propagation. Hence, wave propagation in the full space is governed by the plane-strain Navier equation,

$$
(\lambda+\mu)\frac{\partial^2 u_\beta(\mathbf{x},t)}{\partial x_\alpha \partial x_\beta} + \mu\frac{\partial^2 u_\alpha(\mathbf{x},t)}{\partial x_\beta \partial x_\beta} + \rho b_\alpha(\mathbf{x},t) = \rho\frac{\partial^2 u_\alpha(\mathbf{x},t)}{\partial t^2} = \rho\ddot{u}_\alpha(\mathbf{x},t), \tag{3–47}
$$

where $\alpha, \beta = 1, 2$ and $\mathbf{x} = (x_1, x_2)$. Equation (3–47) is obtained directly from its three-dimensional counterpart Eq. (1–10) by letting $u_3 \equiv 0$. The Lamé constants λ and μ are given by Eq. (1–5), *i.e.* the Lamé constants in the plane-strain problem are identical to those in the three-dimensional problem.

Governing equations for the Green's functions in time and frequency domain

In the governing equation for the Green's function, the main difference from the three-dimensional case is the definition of the specific body forces. More precisely, the concentrated force with unit magnitude is replaced by a line load with unit intensity per unit length along the x_3-axis. This corresponding to a reinterpretation of the Dirac delta function in vector form leading to the equation

$$(\lambda+\mu)\,\frac{\partial^2 u^*_{\beta\delta}(\mathbf{x},t;\mathbf{y},\tau)}{\partial x_\alpha \partial x_\beta} + \mu \frac{\partial^2 u^*_{\alpha\delta}(\mathbf{x},t;\mathbf{y},\tau)}{\partial x_\beta \partial x_\beta} + \rho b^*_{\alpha\delta}(\mathbf{x},t;\mathbf{y},\tau) = \rho \ddot{u}^*_{\alpha\delta}(\mathbf{x},t;\mathbf{y},\tau), \quad \text{(3–48a)}$$

$$\rho b^*_{\alpha\delta}(\mathbf{x},t;\mathbf{y},\tau) = \delta_{\alpha\delta}\delta(\mathbf{x}-\mathbf{y})\delta(t-\tau) = \delta_{\alpha\delta}\delta(x_1-y_1)\delta(x_2-y_2)\delta(t-\tau). \quad \text{(3–48b)}$$

All Greek indices range over $1, 2$, *i.e.* the Green's function $u^*_{\alpha\delta}(\mathbf{x},t;\mathbf{y},\tau)$ has four components in contrast to the nine components of the Green's function for three-dimensional elastodynamics.

Similarly to the three-dimensional case, the Green's function in the frequency domain is governed by the equation that is obtained by replacing the specific body forces by a harmonically varying function of the kind $B^*_{\alpha\delta}(\mathbf{x},\omega;\mathbf{y})\mathrm{e}^{\mathrm{i}\omega t} = \delta_{\alpha\delta}\delta(\mathbf{x}-\mathbf{y})\mathrm{e}^{\mathrm{i}\omega t} = \delta_{\alpha\delta}\delta(x_1-y_1)\delta(x_2-y_2)\mathrm{e}^{\mathrm{i}\omega t}$. Again, after elimination of the term $\mathrm{e}^{\mathrm{i}\omega t}$, we arrive at the governing equation

$$(\lambda+\mu)\,\frac{\partial^2 U^*_{\beta\delta}(\mathbf{x},\omega;\mathbf{y})}{\partial x_\alpha \partial x_\beta} + \mu \frac{\partial^2 U^*_{\beta\delta}(\mathbf{x},\omega;\mathbf{y})}{\partial x_\beta \partial x_\beta} + \delta_{\alpha\delta}\delta(\mathbf{x}-\mathbf{y}) = -\rho\omega^2 U^*_{\alpha\delta}(\mathbf{x},\omega;\mathbf{y}). \quad \text{(3–49)}$$

Time-domain solution

In order to obtain the Green's function for the plane-strain problem in the time domain, we need to determine the response in the x_α-direction at the time t and at the *observation line* with the

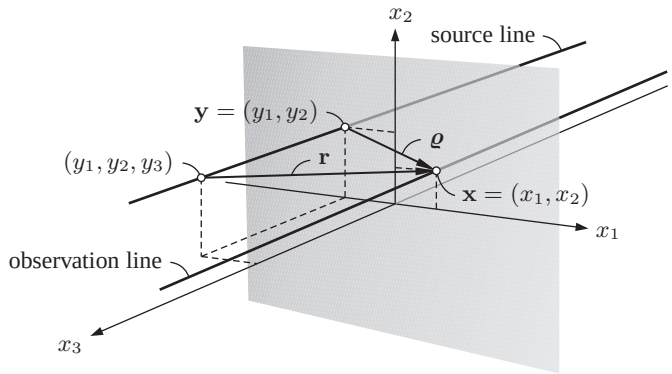

Figure 3–4 Definition of source and receiver lines in plane and strain. Integration is performed over the contributions along the source line with $\mathbf{r}$ and $\boldsymbol{\varrho}$ denoting the distance vectors in two and three dimensions, respectively.

plane coordinates $\mathbf{x} = (x_1, x_2)$ to a line load applied in the x_δ-direction at the time τ and at the *source line* with the plane coordinates $\mathbf{y} = (y_1, y_2)$, see Fig. 3–4. To do this, we interpret the line source as the superposition of infinitely many point sources acting along the line with the plane coordinates $\mathbf{y} = (y_1, y_2)$. Then, the plane-strain Green's function may be found be integration of the three-dimensional Green's function (3–44) with respect to the y_3-coordinate.

Especially, if we consider the response in the (x_1, x_2)-plane, *i.e.* the plane defined by $x_3 = 0$, to a line load acting at time $\tau = 0$ and $\mathbf{y} = \mathbf{0}$, *i.e.* $(y_1, y_2) = (0, 0)$, we get

$$u^*_{\alpha\delta}(\mathbf{x}, t; \mathbf{0}, 0) = \frac{1}{4\pi\rho}\int_{-\infty}^{\infty}\left\{\frac{1}{c_P^2}\frac{\varrho_\alpha\varrho_\delta}{r^3}\delta\!\left(t-\frac{r}{c_P}\right) - \left(\frac{\delta_{\alpha\delta}}{r^3} - 3\frac{\varrho_\alpha\varrho_\delta}{r^5}\right)tH\!\left(t-\frac{r}{c_P}\right)\right\}\mathrm{d}y_3$$
$$+\frac{1}{4\pi\rho}\int_{-\infty}^{\infty}\left\{\frac{1}{c_S^2}\left(\frac{\delta_{\alpha\delta}}{r} - \frac{\varrho_\alpha\varrho_\delta}{r^3}\right)\delta\!\left(t-\frac{r}{c_S}\right) + \left(\frac{\delta_{\alpha\delta}}{r^3} - 3\frac{\varrho_\alpha\varrho_\delta}{r^5}\right)tH\!\left(t-\frac{r}{c_S}\right)\right\}\mathrm{d}y_3,$$

where $\varrho_\alpha = r_\alpha = x_\alpha$, $\varrho = \sqrt{\varrho_1^2 + \varrho_2^2}$ and $r = \sqrt{\varrho^2 + y_3^2}$, *i.e.* ϱ denotes the distance in the (x_1, x_2)-plane whereas r is the distance in the three-dimensional (x_1, x_2, x_3)-space.

Now, instead of y_3 we apply r as the integration variable. With $r = \sqrt{\varrho^2 + y_3^2}$, we get that

$$\frac{\mathrm{d}r}{\mathrm{d}y_3} = \frac{y_3}{r} \qquad \Rightarrow \qquad \frac{\mathrm{d}y_3}{r} = \frac{\mathrm{d}r}{y_3} = \frac{\mathrm{d}r}{\sqrt{r^2-\varrho^2}},$$

where it has been utilised that $r^2 = \varrho^2 + y_3^2$, *i.e.* $y_3^2 = r^2 - \varrho^2$. Furthermore, the integration limits must be changed to ∞ and ϱ. The upper limit for r is obtained for both $y_3 \to -\infty$ and $y_3 \to \infty$, whereas the lower limit $r = \varrho$ is achieved when $y_3 = 0$. Thus, the problem is symmetric around the (x_1, x_2)-plane and the contributions from each value of r should be counted twice—once for positive y_3 and once for negative y_3. The Green's function for plane strain may then be found as

$$u^*_{\alpha\delta}(\mathbf{x}, t; \mathbf{0}, 0) = \frac{1}{2\pi\rho}\int_{\varrho}^{\infty}\left\{\frac{1}{c_P^2}\frac{\varrho_\alpha\varrho_\delta}{r^2}\delta\!\left(t-\frac{r}{c_P}\right) - \left(\frac{\delta_{\alpha\delta}}{r^2} - 3\frac{\varrho_\alpha\varrho_\delta}{r^4}\right)tH\!\left(t-\frac{r}{c_P}\right)\right\}\frac{\mathrm{d}r}{\sqrt{r^2-\varrho^2}}$$
$$+\frac{1}{2\pi\rho}\int_{\varrho}^{\infty}\left\{\frac{1}{c_S^2}\left(\delta_{\alpha\delta} - \frac{\varrho_\alpha\varrho_\delta}{r^2}\right)\delta\!\left(t-\frac{r}{c_S}\right) + \left(\frac{\delta_{\alpha\delta}}{r^2} - 3\frac{\varrho_\alpha\varrho_\delta}{r^4}\right)tH\!\left(t-\frac{r}{c_S}\right)\right\}\frac{\mathrm{d}r}{\sqrt{r^2-\varrho^2}}.$$

It should be clear that no contributions arise in the two integrals for $t < \varrho/c_P$ and $t < \varrho/c_S$, respectively. Likewise, at the time t no contributions exist from source points that are farther away than $r = c_P t$ and $r = c_S t$, respectively. Waves emanating from such points have not yet reached the observation point with the coordinates $(x_1, x_2, 0)$. Thus, making use of the results

$$\int_{\varrho}^{ct}\frac{t\mathrm{d}r}{r^2\sqrt{r^2-\varrho^2}} = t\left[\frac{\sqrt{r^2-\varrho^2}}{r\varrho^2}\right]_{\varrho}^{ct} = \frac{\sqrt{c^2t^2-\varrho^2}}{c\varrho^2}, \tag{3–50a}$$

$$\int_{\varrho}^{ct}\frac{t\mathrm{d}r}{r^4\sqrt{r^2-\varrho^2}} = t\left[\sqrt{r^2-\varrho^2}\frac{2r^2+\varrho^2}{3r^3\varrho^4}\right]_{\varrho}^{ct} = \sqrt{c^2t^2-\varrho^2}\frac{2c^2t^2+\varrho^2}{3t^2c^3\varrho^4}, \tag{3–50b}$$

$$\int_{\varrho}^{\infty}\delta\!\left(t-\frac{r}{c}\right)\frac{\mathrm{d}r}{r^2\sqrt{r^2-\varrho^2}} = \frac{1}{c^2}\int_{\varrho/c}^{\infty}\frac{\delta(t-s)\mathrm{d}s}{s^2\sqrt{s^2-\varrho^2/c^2}} = \frac{c}{c^2t^2\sqrt{c^2t^2-\varrho^2}}, \tag{3–50c}$$

$$\int_{\varrho}^{\infty}\delta\!\left(t-\frac{r}{c}\right)\frac{\mathrm{d}r}{r^4\sqrt{r^2-\varrho^2}} = \frac{1}{c^4}\int_{\varrho/c}^{\infty}\frac{\delta(t-s)\mathrm{d}s}{s^4\sqrt{s^2-\varrho^2/c^2}} = \frac{c}{c^4t^4\sqrt{c^2t^2-\varrho^2}} \tag{3–50d}$$

the Green's function for plane strain in the time domain becomes:

$$u^*_{\alpha\delta}(\mathbf{x},t;\mathbf{y},\tau)=\frac{H(c_P\,(t-\tau)-\varrho)}{2\pi\rho c_P}\left\{\frac{\varrho_\alpha\varrho_\delta}{\varrho^4}\frac{2c_P^2\,(t-\tau)^2-\varrho^2}{\sqrt{c_P^2\,(t-\tau)^2-\varrho^2}}-\frac{\delta_{\alpha\delta}}{\varrho^2}\sqrt{c_P^2\,(t-\tau)^2-\varrho^2}\right\}$$
$$-\frac{H(c_S\,(t-\tau)-\varrho)}{2\pi\rho c_S}\left\{\frac{\varrho_\alpha\varrho_\delta}{\varrho^4}\frac{2c_S^2\,(t-\tau)^2-\varrho^2}{\sqrt{c_S^2\,(t-\tau)^2-\varrho^2}}-\frac{\delta_{\alpha\delta}}{\varrho^2}\frac{c_S^2\,(t-\tau)^2}{\sqrt{c_S^2\,(t-\tau)^2-\varrho^2}}\right\},\quad(3\text{–}51)$$

where ϱ_α has been replaced by $\varrho_\alpha=x_\alpha-y_\alpha$, t has been replaced by $t-\tau$, and use has been made of the temporal reciprocity relation (3–15). Further, the Heaviside unit step functions have been included to ensure that the terms are all real. Physically, this corresponds to the fact that no response is observed at the point $\mathbf{x}$ before the arrival of the first P- and S-waves.

Frequency-domain solution

As in the three-dimensional case, different possibilities exist for the development of the frequency-domain Green's function for plane-strain. Thus,

$$U^*_{\alpha\delta}(\mathbf{x},\omega;\mathbf{y})=\int_{-\infty}^{\infty}u^*_{\alpha\delta}(\mathbf{x},t;\mathbf{y},0)\mathrm{e}^{-\mathrm{i}\omega t}\,\mathrm{d}t=\int_{-\infty}^{\infty}U^*_{\alpha\delta}(\mathbf{x},\omega;\mathbf{z})\,\mathrm{d}z_3,\quad(3\text{–}52)$$

corresponding to either a Fourier transformation of the time-domain solution or integration of the three-dimensional Frequency-domain solution along the x_3-axis. Again, in the plane-strain problem, $\mathbf{x}=(x_1,x_2)$ and $\mathbf{y}=(y_1,y_2)$ are points in the plane. However, $\mathbf{z}$ is a point in three-dimensional space with $z_\alpha=y_\alpha$, $\alpha=1,2$. Proceeding by the first of these methods, *i.e.* Fourier transformation of the time-domain solution, we get the frequency-domain solution

$$U^*_{\alpha\delta}(\mathbf{x},\omega;\mathbf{y})=\frac{1}{4\mathrm{i}\rho c_P^2}\left\{\frac{\varrho_\alpha\varrho_\delta}{\varrho^2}H_0^{(2)}(k_P\varrho)+\left(\frac{\delta_{\alpha\delta}}{k_P\varrho}-\frac{2\varrho_\alpha\varrho_\delta}{k_P\varrho^3}\right)H_1^{(2)}(k_P\varrho)\right\}$$
$$+\frac{1}{4\mathrm{i}\rho c_S^2}\left\{\left(\delta_{\alpha\delta}-\frac{\varrho_\alpha\varrho_\delta}{\varrho^2}\right)H_0^{(2)}(k_S\varrho)-\left(\frac{\delta_{\alpha\delta}}{k_S\varrho}-\frac{2\varrho_\alpha\varrho_\delta}{k_S\varrho^3}\right)H_1^{(2)}(k_S\varrho)\right\},\quad(3\text{–}53)$$

where $k_P=\omega/c_P$ and $k_S=\omega/c_S$ are the P- and S-wavenumbers, respectively, and $H_n^{(2)}$ is the Hankel function of the second kind and order n. Further, the following results have been used:

$$\int_\varrho^\infty\frac{1}{\sqrt{c^2t^2-\varrho^2}}\mathrm{e}^{-\mathrm{i}\omega t}\mathrm{d}t=\frac{1}{c}\frac{\pi}{2\mathrm{i}}H_0^{(2)}(k\varrho),\quad(3\text{–}54a)$$

$$\int_\varrho^\infty\sqrt{c^2t^2-\varrho^2}\mathrm{e}^{-\mathrm{i}\omega t}\mathrm{d}t=-\frac{\varrho^2}{c}\frac{\pi}{2\mathrm{i}}\frac{1}{k\varrho}H_1^{(2)}(k\varrho),\quad(3\text{–}54b)$$

$$\int_\varrho^\infty\frac{2c^2t^2-\varrho^2}{\sqrt{c^2t^2-\varrho^2}}\mathrm{e}^{-\mathrm{i}\omega t}\mathrm{d}t=\frac{\varrho^2}{c}\frac{\pi}{2\mathrm{i}}\Big(k\varrho H_0^{(2)}(k\varrho)-2H_1^{(2)}(k\varrho)\Big),\quad(3\text{–}54c)$$

where c is equal to c_P or c_S, and k is either k_P or k_S. Finally, exploiting the fact that

$$k\varrho H_0^{(2)}(k\varrho)-2H_1^{(2)}(k\varrho)=-k\varrho H_2^{(2)}(k\varrho),$$

and making use of the relations $\pi H_n^{(2)}(x) = 2\mathrm{i}^{n+1} K_n(\mathrm{i}x)$, where $K_n(x)$ is the modified Bessel function of the second kind and order n, Domínguez (1993) gave the alternative formulation

$$U_{il}^*(\mathbf{x},\omega;\mathbf{y}) = \frac{1}{2\pi\rho c_S^2}\left(\alpha\delta_{il} - \beta\frac{\partial r}{\partial x_i}\frac{\partial r}{\partial x_l}\right) \tag{3–55a}$$

with

$$\alpha = K_0(\mathrm{i}k_S r) + \frac{1}{\mathrm{i}k_S r}\left(K_1(\mathrm{i}k_S r) - \frac{c_S}{c_P}K_1(\mathrm{i}k_P r)\right), \tag{3–55b}$$

$$\beta = K_2(\mathrm{i}k_S r) - \frac{c_S^2}{c_P^2}K_2(\mathrm{i}k_P r). \tag{3–55c}$$

This formulation may be preferred, since the complex arguments $\mathrm{i}k_P\varrho$ and $\mathrm{i}k_S\varrho$ are similar to those in the exponential functions appearing in the three-dimensional Green's function (3–45).

3.3.4 Green's functions for elastic waves in antiplane shear

As already discussed, the antiplane shear problem corresponds to SH-wave propagation in the plane. This, with $\mathbf{x}$ and $\mathbf{y}$ denoting two points in the considered plane, the governing equation in time domain is simply the plane scalar wave equation,

$$\mu\frac{\partial^2 u_{33}^*(\mathbf{x},t;\mathbf{y},\tau)}{\partial x_\beta \partial x_\beta} + \delta(\mathbf{x}-\mathbf{y})\delta(t-\tau) = \rho\ddot{u}_{33}^*(\mathbf{x},t;\mathbf{y},\tau), \tag{3–56}$$

where the body forces are now applied as a line load acting along the x_3-axis and in the x_3-direction. Similarly, after a Fourier transformation, the governing equation in the frequency domain obtains the form

$$\mu\frac{\partial^2 U_{33}^*(\mathbf{x},\omega;\mathbf{y})}{\partial x_\beta \partial x_\beta} + \delta(\mathbf{x}-\mathbf{y}) = -\rho\omega^2 U_{33}^*(\mathbf{x},\omega;\mathbf{y}), \tag{3–57}$$

which is identified as the two-dimensional Helmholtz equation. In accordance with the previous subsection, the natural approach is to find the two-dimensional solution by integration of the three-dimensional solution. Unfortunately, this requires a preliminary study in which the full-space Green's function for the scalar wave equation is determined in the time domain.

Green's function for the three-dimensional wave equation

The time-domain Green's function for scalar wave propagation in a homogeneous isotropic full space is defined by the equation

$$\rho c^2\frac{\partial^2 u^*(\mathbf{x},t;\mathbf{y},\tau)}{\partial x_j \partial x_j} + \delta(\mathbf{x}-\mathbf{y})\delta(t-\tau) = \rho\frac{\partial^2 u^*(\mathbf{x},t;\mathbf{y},\tau)}{\partial t^2} = \rho\ddot{u}^*(\mathbf{x},t;\mathbf{y},\tau), \tag{3–58}$$

where c is the phase velocity of the waves spreading from the concentrated load applied at the point $\mathbf{y}$ and time τ, and ρ is the mass density of the material. Now, similarly to the derivation of the fundamental solution for the elastodynamic problem, we start by assuming that the load is applied at the origin, *i.e.* $\mathbf{y} = \mathbf{0}$, and consider the slightly more general scalar wave equation

$$c^2\frac{\partial^2 u(\mathbf{x},t)}{\partial x_j \partial x_j} + \delta(\mathbf{x})h(t) = \ddot{u}(\mathbf{x},t). \tag{3–59}$$

The Laplace operator may advantageously be recast by application of Eq. (3–29). Further, exploiting the spherical symmetry of the problem, Eq. (3–59) enters the form

$$c^2\left(\frac{\partial^2 w(r,t)}{\partial r^2}+\frac{2}{r}\frac{\partial w(r,t)}{\partial r}\right)+\delta(r)h(t)=\ddot{w}(r,t), \tag{3–60}$$

where $r=|\mathbf{x}|$ is the distance from the source point $\mathbf{y}=\mathbf{0}$ to the receiver point $\mathbf{x}$, and $w(r,t)=w(|\mathbf{x}|,t)=u(\mathbf{x},t)$. This equation may be further simplified by introduction of the scalar field $\varphi(r,t)=rw(r,t)$, which provides the one-dimensional wave equation

$$c^2\frac{\partial^2\varphi(r,t)}{\partial r^2}+\delta(r)h(t)=\ddot{\varphi}(r,t). \tag{3–61}$$

The homogeneous part of this equation has the solution $\varphi(r,t)=f(t-r/c)+g(t+r/c)$, where f and g are continuous and differentiable functions of their respective arguments. However, the second term corresponds to waves propagating towards the source point and must be disregarded for physical reasons. Hence, the solution to the homogeneous part of Eq. (3–60) reduces to $w(r,t)=f(t-r/c)/r$, *i.e.* the solution to Eq. (3–59) is given as $u(\mathbf{x},t)=f(t-|\mathbf{x}|/c)/|\mathbf{x}|$.

Next, in order to determine $f(t-r/c)$ we integrate Eq. (3–59) over a sphere Ω_ε with radius ε and centre at the origin. Then, by utilisation of the divergence theorem and insertion of $w(r,t)=f(t-r/c)/r$ we get

$$\begin{aligned}
&c^2\int_{\Omega_\varepsilon}\frac{\partial^2 u(\mathbf{x},t)}{\partial x_j\partial x_j}\mathrm{d}\Omega_\varepsilon+\int_{\Omega_\varepsilon}\delta(\mathbf{x})h(t)\mathrm{d}\Omega_\varepsilon=\int_{\Omega_\varepsilon}\ddot{u}(\mathbf{x},t)\mathrm{d}\Omega_\varepsilon && \Rightarrow\\
&c^2\int_{\Gamma_\varepsilon}n_j(\mathbf{x})\frac{\partial u(\mathbf{x},t)}{\partial x_j}\mathrm{d}\Gamma_\varepsilon+h(t)=\int_{\Omega_\varepsilon}\ddot{u}(\mathbf{x},t)\mathrm{d}\Omega_\varepsilon && \Rightarrow\\
&c^2\int_{\Gamma_\varepsilon}\frac{\partial w(r,t)}{\partial r}\mathrm{d}\Gamma_\varepsilon+h(t)=\int_{\Omega_\varepsilon}\ddot{u}(r,t)\mathrm{d}\Omega_\varepsilon && \Rightarrow\\
&4\pi\varepsilon^2c^2\left.\frac{\partial w(r,t)}{\partial r}\right|_{r=\varepsilon}+h(t)=\int_{\Omega_\varepsilon}\ddot{u}(r,t)\mathrm{d}\Omega_\varepsilon && \Rightarrow\\
&4\pi\varepsilon^2c^2\left\{\frac{1}{\varepsilon^2}f\Big(t-\frac{\varepsilon}{c}\Big)+\frac{1}{\varepsilon c}f'\Big(t-\frac{\varepsilon}{c}\Big)\right\}-h(t)+\int_{\Omega_\varepsilon}\frac{1}{r}f''\Big(t-\frac{r}{c}\Big)\mathrm{d}\Omega_\varepsilon=0, && (3–62)
\end{aligned}$$

where Γ_ε signifies the boundary of the sphere Ω_ε and $n_j(\mathbf{x})$ denote the components of the unit outward normal to Γ_ε. It has been used that the outward normal at a given point on the surface Γ_ε points in the direction defined by the coordinate r. In the limit $\varepsilon\to 0$, Eq. (3–62) reads

$$\begin{aligned}
&\lim_{\varepsilon\to0}\left(4\pi\varepsilon^2c^2\left\{\frac{1}{\varepsilon^2}f\Big(t-\frac{\varepsilon}{c}\Big)+\frac{1}{\varepsilon c}f'\Big(t-\frac{\varepsilon}{c}\Big)\right\}-h(t)+\int_{\Omega_\varepsilon}\frac{1}{r}f''\Big(t-\frac{r}{c}\Big)\mathrm{d}\Omega_\varepsilon\right)=0 && \Rightarrow\\
&4\pi c^2f(t)-h(t)+0=0 \quad\Rightarrow\quad f(t)=\frac{1}{4\pi c^2}h(t) \quad\Rightarrow\quad f\Big(t-\frac{r}{c}\Big)=\frac{1}{4\pi c^2}h\Big(t-\frac{r}{c}\Big).
\end{aligned}$$

Hence, by the definition $w(r,t)=f(t-r/c)/r$ we arrive at the result

$$w(r,t)=\frac{1}{4\pi c^2r}h\Big(t-\frac{r}{c}\Big) \quad\Rightarrow\quad u(\mathbf{x},t)=\frac{1}{4\pi c^2r}h\Big(t-\frac{r}{c}\Big), \quad r=|\mathbf{x}|. \tag{3–63}$$

Finally, in the particular case $\rho h(t) = \delta(t)$, substituting t with $t - \tau$ and replacing $r = |\mathbf{x}|$ by $r = |\mathbf{x} - \mathbf{y}|$ leads to the Green's function

$$u^*(\mathbf{x}, t; \mathbf{y}, \tau) = \frac{1}{4\pi\rho c^2 r}\delta\Big(t - \tau - \frac{r}{c}\Big), \quad r = |\mathbf{x} - \mathbf{y}|, \tag{3–64}$$

where the time–space reciprocal relation (3–19d) has been employed.

Time-domain solution

After this small sidestep, we are ready to proceed with the derivation of the Green's function for the antiplane shear problem. The time-domain solution follows immediately by integration of Eq. (3–64) along the x_3-axis and inserting $c = c_S$:

$$u^*_{33}(\mathbf{x}, t; \mathbf{y}, \tau) = \int_{-\infty}^{\infty} \frac{1}{4\pi\rho c_S^2 r}\delta\Big(t - \tau - \frac{r}{c_S}\Big)\mathrm{d}y_3 = \frac{1}{2\pi\rho c_S}\int_{\varrho/c_S}^{\infty} \frac{\delta(t - \tau - s)}{\sqrt{c_S^2 s^2 - \varrho^2}}\mathrm{d}s, \tag{3–65}$$

where it is understood that $\mathbf{x} = (x_1, x_2)$ and $\mathbf{y} = (y_1, y_2)$ are two points in the considered plane. Further, with reference to Fig. 3–4, $\varrho = |\boldsymbol{\varrho}| = |\mathbf{x} - \mathbf{y}|$ signifies the distance between the source and receiver points in the plane, whereas $r = |\mathbf{r}| = \sqrt{\varrho^2 + y_3^2}$ is a distance in three-dimensional space. Finally, the substitution $r = c_S s$ has been employed, and in the change of integration variable it has been utilised that

$$\frac{\mathrm{d}r}{\mathrm{d}y_3} = \frac{y_3}{r} \qquad \Rightarrow \qquad \frac{\mathrm{d}y_3}{r} = \frac{\mathrm{d}r}{y_3} = \frac{\mathrm{d}r}{\sqrt{r^2 - \varrho^2}} = \frac{c_S\mathrm{d}s}{\sqrt{c_S^2 s^2 - \varrho^2}}.$$

As in the case of the plane-strain problem, the lower limit with respect to r is ϱ corresponding to the limit $s = \varrho/c_S$—and as a result of the symmetry around the plane defined by $y_3 = 0$, the upper limit $s = \infty$ corresponds to both $y_3 = \infty$ and $y_3 = -\infty$.

Evaluation of Eq. (3–65) provides the Green's function for antiplane strain,

$$u^*_{33}(\mathbf{x}, t; \mathbf{y}, \tau) = \frac{1}{2\pi\rho c_S}\frac{1}{\sqrt{c_S^2(t - \tau)^2 - \varrho^2}}H\Big(t - \tau - \frac{\varrho}{c_S}\Big), \qquad \varrho = |\mathbf{x} - \mathbf{y}|, \tag{3–66}$$

where the Heaviside unit step function ensures that a real value is obtained. Physically, this is justified by the fact that no waves arrive at the source point $\mathbf{x}$ for $t - \tau < \varrho/c_S$ which is the time it takes the wave to travel along the direct path from the source point $\mathbf{y}$ to the receiver point $\mathbf{x}$.

Frequency-domain solution

The frequency-domain Green's function for the antiplane shear problem is obtained by Fourier transformation of the equivalent time-domain solution (3–66) with $\tau = 0$, *i.e.*

$$U^*_{33}(\mathbf{x}, \omega; \mathbf{y}) = \int_{-\infty}^{\infty} u^*_{33}(\mathbf{x}, t; \mathbf{y}, 0)\mathrm{e}^{-\mathrm{i}\omega t}\,\mathrm{d}t = \frac{1}{2\pi\rho c_S}\int_{\varrho/c_S}^{\infty} \frac{1}{\sqrt{c_S^2 t^2 - \varrho^2}}\mathrm{e}^{-\mathrm{i}\omega t}\,\mathrm{d}t,$$

which provides the fundamental solution

$$U^*_{33}(\mathbf{x}, \omega; \mathbf{y}) = \frac{1}{4\mathrm{i}\rho c_S^2}H_0^{(2)}(k_S\varrho) = \frac{1}{2\pi\rho c_S^2}K_0(\mathrm{i}k_S\varrho), \tag{3–67}$$

where $H_0^{(2)}$ is the Hankel function of the second kind and order zero, whereas K_0 is the modified Bessel function of order zero. It is noted that $\pi H_0^{(2)}(x) = 2\mathrm{i}K_0(\mathrm{i}x)$.

Thus, we have derived the Green's function for general three-dimensional elastodynamics in time and frequency domain, and subsequently the time- and frequency-domain Green's functions have been established for plane strain as well as antiplane shear. These fundamental solutions will be applied as the second state in the integral identities of Section 3.2 to establish a pure boundary-integral formulation.

3.4 Somigliana's identity

The fundamental equation in the direct boundary-element method described in the next chapter is the so-called *Somigliana identity*. In this section, we shall derive this boundary-integral equation for the general three-dimensional case as well as plane strain and antiplane shear. The identity is presented in both the time and the frequency domain.

3.4.1 Somigliana's identity for three-dimensional elastodynamics

In Section 3.2, dynamic reciprocity theorems were derived for wave propagation in elastic materials. So far, the two elastodynamic states $\{u_l^{(1)}, p_l^{(1)}, b_l^{(1)}\}$ and $\{u_l^{(2)}, p_l^{(2)}, b_l^{(2)}\}$ have not been specified. However, we now define the first state as the state of physical displacements, u_i, specific body forces, b_i, and surface tractions, p_i, whereas the second state is chosen as the fundamental-solution state for a load applied at time $\tau = 0$. Thus, in the general three-dimensional case, and with reference to Eq. (3–6), we have:

$$u_i^{(1)}(\mathbf{x},t) = u_i(\mathbf{x},t)\,, \qquad u_i^{(2)}(\mathbf{x},t) = u_{il}^*(\mathbf{x},t;\mathbf{y},0)\,, \tag{3–68a}$$

$$p_i^{(1)}(\mathbf{x},t) = p_i(\mathbf{x},t)\,, \qquad p_i^{(2)}(\mathbf{x},t) = p_{il}^*(\mathbf{x},t;\mathbf{y},0)\,, \tag{3–68b}$$

$$b_i^{(1)}(\mathbf{x},t) = b_i(\mathbf{x},t)\,, \qquad b_i^{(2)}(\mathbf{x},t) = b_{il}^*(\mathbf{x},t;\mathbf{y},0)\,. \tag{3–68c}$$

Then Eq. (3–6) may be rewritten as

$$\begin{aligned}
&\int_0^t \int_\Gamma p_i(\mathbf{x},\tau) u_{il}^*(\mathbf{x},t-\tau;\mathbf{y},0)\mathrm{d}\Gamma(\mathbf{x})\mathrm{d}\tau - \int_0^t \int_\Gamma p_{il}^*(\mathbf{x},t-\tau;\mathbf{y},0) u_i(\mathbf{x},\tau)\mathrm{d}\Gamma(\mathbf{x})\mathrm{d}\tau \\
&\quad + \int_0^t \int_\Omega \rho b_i(\mathbf{x},\tau) u_{il}^*(\mathbf{x},t-\tau;\mathbf{y},0)\mathrm{d}\Omega(\mathbf{x})\mathrm{d}\tau - \int_0^t \int_\Omega \rho b_{il}^*(\mathbf{x},t-\tau;\mathbf{y},0) u_i(\mathbf{x},\tau)\mathrm{d}\Omega(\mathbf{x})\mathrm{d}\tau \\
&\quad = \int_\Omega \rho \Big\{ \dot{u}_i(\mathbf{x},t) v_{il}^*(\mathbf{x}) - u_{il}^*(\mathbf{x},t;\mathbf{y},0)\dot{v}_i(\mathbf{x}) \Big\} \mathrm{d}\Omega(\mathbf{x}) \\
&\quad + \int_\Omega \rho \Big\{ u_i(\mathbf{x},t)\dot{v}_{il}^*(\mathbf{x}) - \dot{u}_{il}^*(\mathbf{x},t;\mathbf{y},0) v_i(\mathbf{x}) \Big\} \mathrm{d}\Omega(\mathbf{x}),
\end{aligned} \tag{3–69}$$

where $\mathrm{d}\Gamma(\mathbf{x})$ and $\mathrm{d}\Omega(\mathbf{x})$ indicate that the integration variable is actually the spatial coordinates $\mathbf{x}$ on the boundary and in the domain, respectively.

Now, utilising the first integral term in Eq. (3–69) as an example, it should be evident that the following rearrangements may be applied:

$$\int_0^t \int_\Gamma p_i(\mathbf{x},\tau) u_{il}^*(\mathbf{x},t-\tau;\mathbf{y},0)\mathrm{d}\Gamma(\mathbf{x})\mathrm{d}\tau = \int_0^t \int_\Gamma p_i(\mathbf{y},\tau) u_{il}^*(\mathbf{y},t;\mathbf{x},\tau)\mathrm{d}\Gamma(\mathbf{y})\mathrm{d}\tau =$$
$$\int_0^t \int_\Gamma p_l(\mathbf{y},\tau) u_{li}^*(\mathbf{y},t;\mathbf{x},\tau)\mathrm{d}\Gamma(\mathbf{y})\mathrm{d}\tau = \int_0^t \int_\Gamma u_{il}^*(\mathbf{x},t;\mathbf{y},\tau) p_l(\mathbf{y},\tau)\mathrm{d}\Gamma(\mathbf{y})\mathrm{d}\tau.$$

Firstly, the coordinates have been renamed (not changed places!) as $\mathbf{x} \to \mathbf{y}$ and $\mathbf{y} \to \mathbf{x}$, and the temporal reciprocity relation (3–15), *i.e.* $u_{il}^*(\mathbf{x},t-\tau;\mathbf{y},0) = u_{il}^*(\mathbf{x},t;\mathbf{y},\tau)$, has been employed. Secondly, the indices have been renamed as $i \to l$ and $l \to i$, so that the free index is now i. Finally, use has been made of the spatial reciprocity relation (3–16), *i.e.* $u_{il}^*(\mathbf{x},t;\mathbf{y},\tau) = u_{li}^*(\mathbf{y},t;\mathbf{x},\tau)$. Proceeding in a similar manner for the remaining terms of Eq. (3–69), we arrive at the integral identity

$$\begin{aligned}
&\int_0^t \int_\Gamma u_{il}^*(\mathbf{x},t;\mathbf{y},\tau) p_l(\mathbf{y},\tau)\mathrm{d}\Gamma(\mathbf{y})\mathrm{d}\tau - \int_0^t \int_\Gamma p_{il}^*(\mathbf{x},t;\mathbf{y},\tau) u_l(\mathbf{y},\tau)\mathrm{d}\Gamma(\mathbf{y})\mathrm{d}\tau \\
&\quad + \int_0^t \int_\Omega u_{il}^*(\mathbf{x},t;\mathbf{y},\tau)\rho b_l(\mathbf{y},\tau)\mathrm{d}\Omega(\mathbf{y})\mathrm{d}\tau - \int_0^t \int_\Omega \rho b_{il}^*(\mathbf{x},t;\mathbf{y},\tau) u_l(\mathbf{y},\tau)\mathrm{d}\Omega(\mathbf{y})\mathrm{d}\tau \\
&\quad = \int_\Omega \rho\Big\{ v_{il}^*(\mathbf{x};\mathbf{y})\dot{u}_l(\mathbf{y},t) - u_{il}^*(\mathbf{x},t;\mathbf{y},0)\dot{v}_l(\mathbf{y})\Big\}\mathrm{d}\Omega(\mathbf{y}) \\
&\quad + \int_\Omega \rho\Big\{ \dot{v}_{il}^*(\mathbf{x};\mathbf{y}) u_l(\mathbf{y},t) - \dot{u}_{il}^*(\mathbf{x},t;\mathbf{y},0) v_l(\mathbf{y})\Big\}\mathrm{d}\Omega(\mathbf{y}).
\end{aligned} \tag{3–70}$$

Thus, the integration over the domain Ω and its boundary Γ is now carried out with respect to $\mathbf{y}$ instead of $\mathbf{x}$.

Subsequently, it is recalled that the body forces in the fundamental-solution state take the form of a Dirac delta spike, $b_{il}^*(\mathbf{x},t;\mathbf{y},\tau) = \delta_{il}\delta(\mathbf{x}-\mathbf{y})\delta(t-\tau)$. This makes integration over terms involving $b_{il}^*(\mathbf{x},t;\mathbf{y},\tau)$ particularly simple. Further, since no load is applied before the time τ, the initial-condition terms involving $v_{il}^*(\mathbf{x};\mathbf{y})$ and its temporal derivative $\dot{v}_{il}^*(\mathbf{x};\mathbf{y})$ vanish. Hence, Eq. (3–70) simplifies to

$$\begin{aligned}
&C(\mathbf{x})u_i(\mathbf{x},t) + \int_0^{t^+} \int_\Gamma p_{il}^*(\mathbf{x},t;\mathbf{y},\tau) u_l(\mathbf{y},\tau)\mathrm{d}\Gamma(\mathbf{y})\mathrm{d}\tau \\
&\quad = \int_0^{t^+} \int_\Gamma u_{il}^*(\mathbf{x},t;\mathbf{y},\tau) p_l(\mathbf{y},\tau)\mathrm{d}\Gamma(\mathbf{y})\mathrm{d}\tau + \int_0^{t^+} \int_\Omega u_{il}^*(\mathbf{x},t;\mathbf{y},\tau)\rho b_l(\mathbf{y},\tau)\mathrm{d}\Omega(\mathbf{y})\mathrm{d}\tau \\
&\quad + \int_\Omega \rho\Big\{ u_{il}^*(\mathbf{x},t;\mathbf{y},0)\dot{v}_l(\mathbf{y}) + \dot{u}_{il}^*(\mathbf{x},t;\mathbf{y},0) v_l(\mathbf{y})\Big\}\mathrm{d}\Omega(\mathbf{y}),
\end{aligned} \tag{3–71}$$

where the upper integration limit t^+ indicates that the delta spike at the integration time $\tau = t$ must be included. Further, $C(\mathbf{x})$ is a scalar constant that only depends on the local geometry at the receiver point $\mathbf{x}$. In particular, for any interior point within the domain Ω, the constant takes the value $C(\mathbf{x}) = 1$. Actually, the value of $C(\mathbf{x})$ simply corresponds to the part of the point that is included in the domain Ω. Hence, $C(\mathbf{x}) = 0$ at an exterior point, and $C(\mathbf{x}) = \frac{1}{2}$ for a point on a smooth part of the boundary Γ, see Fig. 3–5. Further, at the apex of a cone or pyramid with the internal solid angle ϕ, the geometry constant is $C(\mathbf{x}) = \frac{\phi}{4\pi}$ and at a wedge point with the internal angle Φ, $C(\mathbf{x}) = \frac{\Phi}{2\pi}$. The latter value of $C(\mathbf{x})$ also refers to a corner in two dimensions. A mathematically sound proof regarding the values of $C(\mathbf{x})$ for different

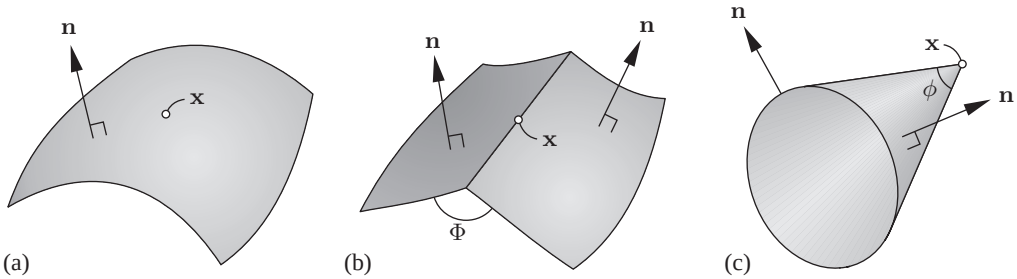

Figure 3–5 Geometry constant at different parts of a surface: (a) a smooth surface with $C(\mathbf{x}) = \frac{1}{2}$; (b) a wedge point with $C(\mathbf{x}) = \frac{\Phi}{2\pi}$; (c) an apex point with $C(\mathbf{x}) = \frac{\phi}{4\pi}$.

geometries of the surface is beyond the scope of the present text. A detailed derivation for a smooth part of a surface can be found in the work by Domínguez (Domínguez 1993). Finally, in the general case, finding $C(\mathbf{x})$ may be difficult—especially at the intersection of multiple curved surfaces. A practical way of dealing with this is discussed in the next chapter.

The integral equation (3–71) is known as *Somigliana's identity* and is the starting point for the boundary-element method, much in the same way that the weak formulation of the governing equation is the basis of the finite-element method. Instead of an arbitrary variation field, we may argue that the Green's function is applied as weight function. It is noted that Eq. (3–71) contains boundary integrals as well as volume integrals. However, only the boundary integrals depend on the unknown field quantities $u_i(\mathbf{x}, t)$ and $p_i(\mathbf{x}, t)$, *i.e.* the displacements and the traction. On the other hand, the volume integrals evaluate the influence of initial conditions and external body forces, both of which are known.

Unfortunately, inspection of Eq. (3–44) reveals that the Green's function for the displacement, $u^*_{il}(\mathbf{x}, t; \mathbf{y}, \tau)$, is singular at the point $\mathbf{x} = \mathbf{y}$. Therefore, a special treatment is necessary for source points $\mathbf{y}$ near the receiver point $\mathbf{x}$ when the first term on the right-hand side of Eq. (3–71) is evaluated by numerical integration. A similar problem arises with regard to the second term on the left-hand side of the equation, since the Green's function for the traction, $p^*_{il}(\mathbf{x}, t; \mathbf{y}, \tau)$, is strongly singularity at $\mathbf{x} = \mathbf{y}$. We shall return to this discussion in Chapter 4.

Next, assume that the physical state is observed at the time t infinitely long after the initial values were applied. Then any influence of the initial conditions has diminished and the lower integration limit on the time may be changed to $-\infty$. Accordingly, Eq. (3–71) simplifies to

$$\begin{aligned} C(\mathbf{x})u_i(\mathbf{x}, t) + \int_{-\infty}^{t^+} \int_\Gamma p^*_{il}(\mathbf{x}, t; \mathbf{y}, \tau) u_l(\mathbf{y}, \tau)\, \mathrm{d}\Gamma(\mathbf{y}) \mathrm{d}\tau \\ = \int_{-\infty}^{t^+} \int_\Gamma u^*_{il}(\mathbf{x}, t; \mathbf{y}, \tau) p_l(\mathbf{y}, \tau)\, \mathrm{d}\Gamma(\mathbf{y}) \mathrm{d}\tau \\ + \int_{-\infty}^{t^+} \int_\Omega u^*_{il}(\mathbf{x}, t; \mathbf{y}, \tau) \rho b_l(\mathbf{y}, \tau)\, \mathrm{d}\Omega(\mathbf{y}) \mathrm{d}\tau \end{aligned} \tag{3–72}$$

Further, assume that the field and surface quantities in the physical state vary harmonically with at the circular frequency ω, *i.e.*

$$u_l(\mathbf{x}, t) = U_l(\mathbf{x}, \omega)\mathrm{e}^{\mathrm{i}\omega t}, \quad p_l(\mathbf{x}, t) = P_l(\mathbf{x}, \omega)\mathrm{e}^{\mathrm{i}\omega t}, \quad b_l(\mathbf{x}, t) = B_l(\mathbf{x}, \omega)\mathrm{e}^{\mathrm{i}\omega t}. \tag{3–73}$$

Then the first integral term on the right-hand side of Eq. (3–72) may be rewritten as

$$\int_{-\infty}^{t^+}\int_\Gamma u_{il}^*(\mathbf{x},t;\mathbf{y},\tau)p_l(\mathbf{y},\tau)\,\mathrm{d}\Gamma(\mathbf{y})\mathrm{d}\tau = \int_\Gamma\int_{-\infty}^{t^+} u_{il}^*(\mathbf{x},t-\tau;\mathbf{y},0)P_l(\mathbf{y},\omega)\,\mathrm{e}^{\mathrm{i}\omega\tau}\,\mathrm{d}\tau\mathrm{d}\Gamma(\mathbf{y})$$
$$= \mathrm{e}^{\mathrm{i}\omega\tau}\int_\Gamma\int_{-\infty}^{\infty} u_{il}^*(\mathbf{x},t;\mathbf{y},0)\,\mathrm{e}^{-\mathrm{i}\omega t}\,\mathrm{d}tP_l(\mathbf{y},\omega)\,\mathrm{d}\Gamma(\mathbf{y}), \tag{3–74}$$

where it has been take into account that $u_{il}^*(\mathbf{x},t;\mathbf{y},0)=0$ for $t<0$ so that it makes no difference whether the lower integration limit is taken as 0^- or $-\infty$. Further, use has been made of the fact that $\partial/\partial t = -\partial/\partial\tau$.

Carrying out the procedure in Eq. (3–74) for the remaining terms in Eq. (3–72), and disregarding the term $\mathrm{e}^{\mathrm{i}\omega\tau}$ which will appear in front of all integrals, the following frequency-domain version of Somigliana's identity is obtained:

$$C(\mathbf{x})U_i(\mathbf{x},\omega) + \int_\Gamma P_{il}^*(\mathbf{x},\omega;\mathbf{y})U_l(\mathbf{y},\omega)\,\mathrm{d}\Gamma(\mathbf{y})$$
$$= \int_\Gamma U_{il}^*(\mathbf{x},\omega;\mathbf{y})P_l(\mathbf{y},\omega)\,\mathrm{d}\Gamma(\mathbf{y}) + \int_\Omega U_{il}^*(\mathbf{x},\omega;\mathbf{y})\rho B_l(\mathbf{y},\omega)\,\mathrm{d}\Omega(\mathbf{y}), \tag{3–75}$$

where

$$U_{il}^*(\mathbf{x},\omega;\mathbf{y}) = \int_{-\infty}^{\infty} u_{il}^*(\mathbf{x},t;\mathbf{y},0)\mathrm{e}^{-\mathrm{i}\omega t}\,\mathrm{d}t, \tag{3–76a}$$

$$P_{il}^*(\mathbf{x},\omega;\mathbf{y}) = \int_{-\infty}^{\infty} p_{il}^*(\mathbf{x},t;\mathbf{y},0)\mathrm{e}^{-\mathrm{i}\omega t}\,\mathrm{d}t. \tag{3–76b}$$

These are identified as the Fourier transforms of $u_{il}^*(\mathbf{x},t;\mathbf{y},0)$ and $p_{il}^*(\mathbf{x},t;\mathbf{y},0)$, respectively. As discussed in Section 3.3.2 this is actually the Green's functions for the displacements and the surface traction in the frequency domain.

3.4.2 Somigliana's identity for plane strain

In the case of plane strain, the third component of the physical displacement field is equal to zero. The same applies to the third component of the displacement field in the fundamental-solution state, and therefore Somigliana's identity is simply obtained by skipping the third component in the summation. Consequently, with $\alpha,\beta=1,2$, Eqs. (3–71) and (3–75) reduce to

$$C(\mathbf{x})u_\alpha(\mathbf{x},t) + \int_0^{t^+}\int_\Gamma p_{\alpha\beta}^*(\mathbf{x},t;\mathbf{y},\tau)u_\beta(\mathbf{y},\tau)\mathrm{d}\Gamma(\mathbf{y})\mathrm{d}\tau$$
$$= \int_0^{t^+}\int_\Gamma u_{\alpha\beta}^*(\mathbf{x},t;\mathbf{y},\tau)p_\beta(\mathbf{y},\tau)\mathrm{d}\Gamma(\mathbf{y})\mathrm{d}\tau + \int_0^{t^+}\int_\Omega u_{\alpha\beta}^*(\mathbf{x},t;\mathbf{y},\tau)\rho b_\beta(\mathbf{y},\tau)\mathrm{d}\Omega(\mathbf{y})\mathrm{d}\tau$$
$$+ \int_\Omega \rho\Big\{u_{\alpha\beta}^*(\mathbf{x},t;\mathbf{y},0)\dot v_\beta(\mathbf{y}) + \dot u_{\alpha\beta}^*(\mathbf{x},t;\mathbf{y},0)v_\beta(\mathbf{y})\Big\}\mathrm{d}\Omega(\mathbf{y}), \tag{3–77}$$

in the time domain, and

$$C(\mathbf{x})U_\alpha(\mathbf{x},\omega) + \int_\Gamma P^*_{\alpha\beta}(\mathbf{x},\omega;\mathbf{y})U_\beta(\mathbf{y},\omega)\,\mathrm{d}\Gamma(\mathbf{y}) = \int_\Gamma U^*_{\alpha\beta}(\mathbf{x},\omega;\mathbf{y})P_\beta(\mathbf{y},\omega)\,\mathrm{d}\Gamma(\mathbf{y}) + \int_\Omega U^*_{\alpha\beta}(\mathbf{x},\omega;\mathbf{y})\rho B_\beta(\mathbf{y},\omega)\,\mathrm{d}\Omega(\mathbf{y}), \tag{3–78}$$

in the frequency domain, respectively. The Green's functions $u^*_{\alpha\beta}(\mathbf{x},t;\mathbf{y},\tau)$ and $U^*_{\alpha\beta}(\mathbf{x},\omega;\mathbf{y})$ are defined by Eq. (3–51) and Eq. (3–55), respectively, and the Green's functions for the surface traction follow by application of the constitutive equation.

3.4.3 Somigliana's identity for antiplane shear

When antiplane shear is considered, only the third component of the displacement field is different from zero. This holds for both the physical field and the Green's function. Hence, Somigliana's identity simplifies to a scalar integral equation. In the time-domain

$$\begin{aligned} C(\mathbf{x})u_3(\mathbf{x},t) + \int_0^{t^+}\int_\Gamma p^*_{33}(\mathbf{x},t;\mathbf{y},\tau)u_3(\mathbf{y},\tau)\mathrm{d}\Gamma(\mathbf{y})\mathrm{d}\tau \\ = \int_0^{t^+}\int_\Gamma u^*_{33}(\mathbf{x},t;\mathbf{y},\tau)p_3(\mathbf{y},\tau)\mathrm{d}\Gamma(\mathbf{y})\mathrm{d}\tau + \int_0^{t^+}\int_\Omega u^*_{33}(\mathbf{x},t;\mathbf{y},\tau)\rho b_3(\mathbf{y},\tau)\mathrm{d}\Omega(\mathbf{y})\mathrm{d}\tau \\ + \int_\Omega \rho\Big\{u^*_{33}(\mathbf{x},t;\mathbf{y},0)\dot v_\beta(\mathbf{y}) + \dot u^*_3(\mathbf{x},t;\mathbf{y},0)v_3(\mathbf{y})\Big\}\mathrm{d}\Omega(\mathbf{y}), \end{aligned} \tag{3–79}$$

and in the frequency domain

$$C(\mathbf{x})U_3(\mathbf{x},\omega) + \int_\Gamma P^*_{33}(\mathbf{x},\omega;\mathbf{y})U_3(\mathbf{y},\omega)\,\mathrm{d}\Gamma(\mathbf{y}) = \int_\Gamma U^*_{33}(\mathbf{x},\omega;\mathbf{y})P_3(\mathbf{y},\omega)\,\mathrm{d}\Gamma(\mathbf{y}) + \int_\Omega U^*_{33}(\mathbf{x},\omega;\mathbf{y})\rho B_3(\mathbf{y},\omega)\,\mathrm{d}\Omega(\mathbf{y}). \tag{3–80}$$

The Green's functions $u^*_{33}(\mathbf{x},t;\mathbf{y},\tau)$ and $U^*_{33}(\mathbf{x},\omega;\mathbf{y})$ are defined by Eq. (3–66) and (3–67), respectively, and again the Green's functions for the surface traction follow by application of the constitutive equation.

Example 3.1 Solution for an infinite cylinder

Consider an elastic full-space with material density ρ and shear modulus μ. As depicted on Fig. A the full-space is divided into two domains by an infinitely long circular cylinder, the centre axis of which coincides with the x_3-axis. The interior domain is coined Ω_1, and the remaining part of the full-space, *i.e.* the exterior domain, is coined Ω_2. The boundary of Ω_1 is denoted Γ_1 and has the outward unit normal $\hat{\mathbf{n}}_1(\mathbf{x})$, whereas the boundary of Ω_2 is denoted Γ_2 and has the outward unit normal $\hat{\mathbf{n}}_2(\mathbf{x})$. Evidently, Γ_1 coalesces with Γ_2, and $\hat{\mathbf{n}}_1(\mathbf{x}) = -\hat{\mathbf{n}}_2(\mathbf{x})$ along the cylindrical interface, cf. Fig. A.

The cylindrical interface between Ω_1 and Ω_2 is subject to a harmonically varying forced displacement with the cyclic frequency ω and applied in the x_3-direction, *i.e.* along the centre axis. This leads to pure antiplane shear wave propagation (SH-waves) in the elastic material, *i.e.* there is no displacement in the x_1- or x_2-direction. Depending on ω, the geometry of the cylinder and the wave propagation velocity $c_S = \sqrt{\mu/\rho}$, the excitation may lead to resonance or antiresonance as illustrated in Fig. A. *(continued)*

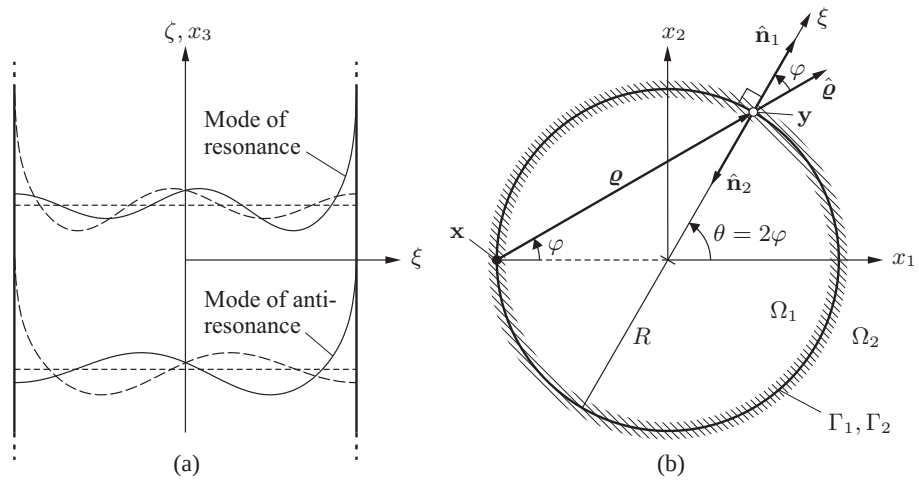

Figure A Geometry of infinite cylinder and definition of polar coordinates: (a) (ξ,ζ)-plane and (b) (ξ,θ)-plane. An observation point $\mathbf{x}$ with the plane coordinates $(x_1,x_2)=(-1,0)$ is considered, and material is present on both sides of the cylindrical interface.

Further, since the surface is smooth along the entire interface, the boundary integral equations (3–80) for the two domains are reduced to

$$\frac{1}{2}U_3^{(1)}(\mathbf{x},\omega)+\int_{\Gamma_1}P_{33}^*(\mathbf{x},\omega;\mathbf{y})U_3^{(1)}(\mathbf{y},\omega)\mathrm{d}\Gamma_{\mathbf{y}}=\int_{\Gamma_1}U_{33}^*(\mathbf{x},\omega;\mathbf{y})P_3^{(1)}(\mathbf{y},\omega)\mathrm{d}\Gamma_{\mathbf{y}}, \tag{a}$$

$$\frac{1}{2}U_3^{(2)}(\mathbf{x},\omega)+\int_{\Gamma_2}P_{33}^*(\mathbf{x},\omega;\mathbf{y})U_3^{(2)}(\mathbf{y},\omega)\mathrm{d}\Gamma_{\mathbf{y}}=\int_{\Gamma_2}U_{33}^*(\mathbf{x},\omega;\mathbf{y})P_3^{(2)}(\mathbf{y},\omega)\mathrm{d}\Gamma_{\mathbf{y}}, \tag{b}$$

where $U_3^{(1)}(\mathbf{x},\omega)$ and $U_3^{(2)}(\mathbf{x},\omega)$ are the displacements in the x_3-direction along the boundaries Γ_1 and Γ_2, respectively, whereas $P_3^{(1)}(\mathbf{x},\omega)$ and $P_3^{(2)}(\mathbf{x},\omega)$ are the corresponding surface tractions. In the derivation of Eqs. (a) and (b) it has been utilised that the surface of the circular cylinder is smooth, *i.e.* $C(\mathbf{x})=1/2$ at all points on the surface.

Obviously, since $\rho c_S^2=\mu$, Eq. (3–67) may be rewritten in terms of the shear modulus, μ. Hence, the fundamental solutions for the antiplane displacements and surface shear stresses become

$$U_{33}^*(\mathbf{x},\omega;\mathbf{y})=\frac{1}{2\pi\mu}K_0(\mathrm{i}k_S\varrho),\quad P_{33}^*(\mathbf{x},\omega;\mathbf{y})=-\frac{k_S}{2\pi}\frac{\partial\varrho}{\partial n}K_1(\mathrm{i}k_S\varrho),\quad \boldsymbol{\varrho}=|\mathbf{x}-\mathbf{y}|, \tag{c}$$

where K_m is the modified Bessel function of the second kind and order m, whereas $\partial\varrho/\partial n$ defines the partial derivative of the distance ϱ between the source and observation points, $\mathbf{x}$ and $\mathbf{y}$, in the direction of the outward normal.

With the definitions given on Fig. A, and further introducing $\hat{\mathbf{n}}(\mathbf{y})=\hat{\mathbf{n}}_1(\mathbf{y})=-\hat{\mathbf{n}}_2(\mathbf{y})$, it becomes evident that

$$\frac{\partial\varrho}{\partial n}=\begin{cases}\hat{\boldsymbol{\varrho}}(\mathbf{x},\mathbf{y})\cdot\hat{\mathbf{n}}(\mathbf{y})=\cos(\varphi) & \text{for } \mathbf{x}\in\Gamma_1\\ -\hat{\boldsymbol{\varrho}}(\mathbf{x},\mathbf{y})\cdot\hat{\mathbf{n}}(\mathbf{y})=-\cos(\varphi) & \text{for } \mathbf{x}\in\Gamma_2\end{cases}\qquad \text{where}\qquad \hat{\boldsymbol{\varrho}}(\mathbf{x},\mathbf{y})=\frac{\mathbf{x}-\mathbf{y}}{|\mathbf{x}-\mathbf{y}|}. \tag{d}$$

Here φ is the angle between the distance vector $\boldsymbol{\varrho}=\varrho\hat{\boldsymbol{\varrho}}$ and the normal vector $\hat{\mathbf{n}}$. Finally, in Eqs. (a) and (b), k_S is the wavenumber of S-waves.

In the case of hysteretic material damping with the loss factor η, the wavenumber and the phase velocity of the shear waves become complex, according to the definitions *(continued)*

$$k_S = \frac{\omega}{c_S}, \quad c_S^2 = (1 + \mathrm{i}\eta)\,\frac{\mu}{\rho}. \tag{e}$$

Now, the forced displacement is applied with constant amplitude $\hat{U}_3(\omega)$ and in phase along the cylindrical interface, $\Gamma \equiv \Gamma_1$. Accordingly, the traction on either side of the interface will be uniform and in phase. Continuity of the displacements across the interface then provides the result:

$$U_3^{(1)}(\mathbf{x},\omega) = U_3^{(2)}(\mathbf{x},\omega) = \hat{U}_3(\omega), \quad P_3^{(1)}(\mathbf{x},\omega) = \hat{P}_3^{(1)}(\omega), \quad P_3^{(2)}(\mathbf{x},\omega) = \hat{P}_3^{(2)}(\omega), \quad \mathbf{x} \in \Gamma. \tag{f}$$

Hence, Eqs. (a) and (b) may be rewritten as

$$\hat{U}_3(\omega)\left(\frac{1}{2} + \int_\Gamma P_{33}^*(\mathbf{x},\omega;\mathbf{y})\mathrm{d}\Gamma_\mathbf{y}\right) = \hat{P}_3^{(1)}(\omega)\int_\Gamma U_{33}^*(\mathbf{x},\omega;\mathbf{y})\mathrm{d}\Gamma_\mathbf{y}, \tag{g}$$

$$\hat{U}_3(\omega)\left(\frac{1}{2} - \int_\Gamma P_{33}^*(\mathbf{x},\omega;\mathbf{y})\mathrm{d}\Gamma_\mathbf{y}\right) = \hat{P}_3^{(2)}(\omega)\int_\Gamma U_{33}^*(\mathbf{x},\omega;\mathbf{y})\mathrm{d}\Gamma_\mathbf{y}, \tag{h}$$

where use has been made of Eq. (d). Addition of Eqs. (g) and (h) provides a measure of the dynamic stiffness per unit surface of the interface related to displacement along the cylinder axis. The stiffness per unit length of the infinite cylinder then becomes

$$S_{33}(\omega) = 2L_\Gamma\frac{\hat{P}_3(\omega)}{\hat{U}_3(\omega)} = \frac{L_\Gamma}{\alpha}, \quad \hat{P}_3(\omega) = \frac{1}{2}\left(\hat{P}_3^{(1)}(\omega) + \hat{P}_3^{(2)}(\omega)\right), \tag{i}$$

where L_Γ is the length of the interface Γ, measured in the (x_1, x_2)-plane, and

$$\alpha = \frac{1}{2}\frac{\hat{U}_3(\omega)}{\hat{P}_3(\omega)} = \int_\Gamma U_3^*(\mathbf{x},\omega;\mathbf{y})\mathrm{d}\Gamma_\mathbf{y}. \tag{j}$$

Equations (i)–(j) hold for arbitrary geometries of the infinite cylinder. However, in what follows, a restriction is made to an infinite circular cylinder with the radius R, that is with $L_\Gamma = 2\pi R$. In order to compute α, the cylindrical polar coordinates (ξ, θ, ζ) are introduced (see Fig. A) such that

$$x_1 = \xi\cos\theta, \quad x_2 = \xi\sin\theta, \quad x_3 = \zeta. \tag{k}$$

In these coordinates, the boundary Γ is defined by $\xi = R$, $0 \le \theta < 2\pi$, $-\infty < \zeta < \infty$.

In particular, when an observation point $\mathbf{x}$ with the plane coordinates $(x_1, x_2) = (-1, 0)$ is considered (see Fig. A), the distance ϱ between the source and observation point becomes

$$\varrho = R\frac{\sin 2\varphi}{\sin\varphi} = 2R\cos\varphi. \tag{l}$$

Making use of the fact that $\theta = 2\varphi$, Eq. (j) may then be evaluated as

$$\alpha = \frac{1}{2\pi\mu}\int_0^{2\pi} K_0(\mathrm{i}k_S\varrho)R\mathrm{d}\theta = \frac{1}{\pi}\frac{R}{\mu}\int_0^{\pi} K_0(2\mathrm{i}k_S R\cos\varphi)\mathrm{d}\varphi = -\frac{R}{\mu}J_0(k_S R)K_0(\mathrm{i}k_S R). \tag{m}$$

Here J_0 is the Bessel function of the first kind and order 0. It is noted that $K_0(\mathrm{i}k_S R) \to \infty$ for $k_S \to 0$. Hence, $S_{33}(\omega) \to 0$ for $\omega \to 0$. Furthermore, $J_0(k_S R)$ has a number of zeros for $\eta = 0$ and $k_S > 0$. At the corresponding frequencies, $S_{33}(\omega)$ becomes singular as reported by Kitahara (1984).

In the high-frequency limit, the complex stiffness becomes a pure impedance. In accordance with Section **??**, the impedance at a point on the inside or the outside of the cylinder is $z = \rho c_S$. Integrating over the area of the cylinder, including the interior as well as the exterior surface, the impedance of the cylinder per unit length in the axial direction becomes $Z = 2L_\Gamma z = 4\pi R\rho c_S$. *(continued)*

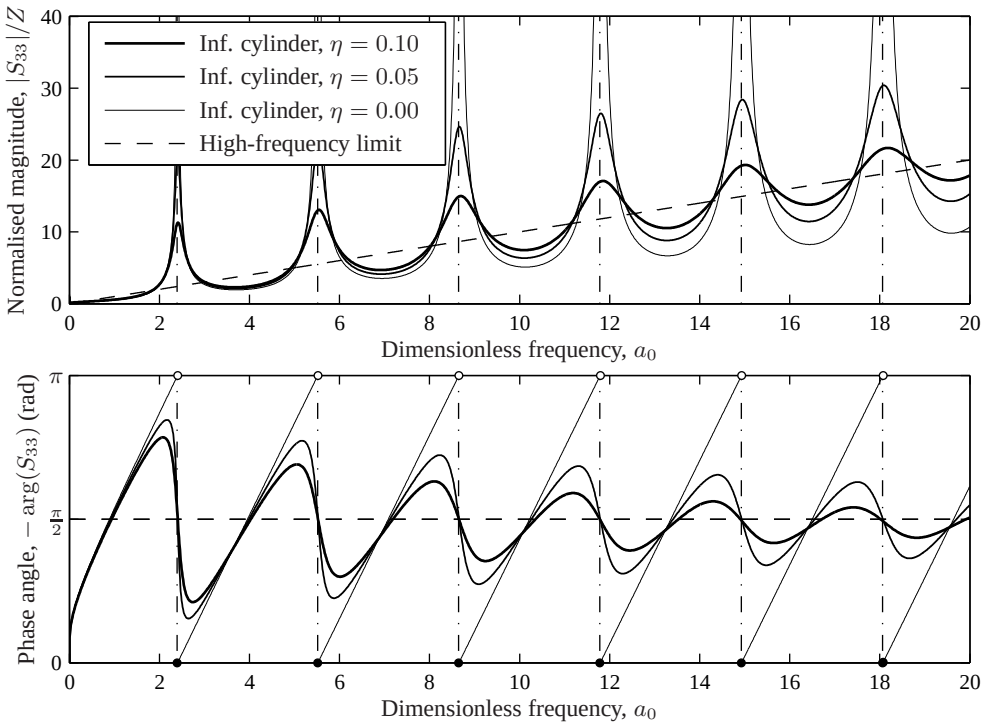

Figure B Dynamic stiffness per unit length of an infinite cylinder subjected to dynamic vertical excitation in the axial direction.

The dynamic stiffness in the high-frequency limit is derived from the definition of the impedance. In the time domain, the surface traction is related to the particle velocity as $\hat{p}_3^\infty(t) = -z\dot{\hat{u}}_3^\infty(t)$, where the superscript ∞ indicates that we consider the limit $\omega \to \infty$. Accordingly, in the frequency domain the relationship becomes $\hat{P}_3^\infty(\omega) = -\mathrm{i}\omega z\hat{U}_3^\infty(\omega)$. Hence, including the contributions from both sides of the cylinder, *i.e.* from Γ_1 as well as Γ_2, the dynamic stiffness may be written as

$$S_{33}^\infty(\omega) = 2L_\Gamma \frac{\hat{P}_3^\infty(\omega)}{\hat{U}_3^\infty(\omega)} = -\mathrm{i}\omega Z = -4\mathrm{i}\omega\pi R\rho c_S. \tag{n}$$

The general solution provided by Eqs. (i) and (m) is plotted in Fig. B as function of the non-dimensional frequency $a_0 = \omega R/c_S$ for different values of the loss factor, η. For comparison, the high-frequency solution is included in the figure. It is noted that the phase angle of the dynamic stiffness is always negative. Hence, $-\arg(S_{33}(\omega))$ has been plotted in the figure. Finally, the absolute value of $S_{33}(\omega)$ has been normalised with respect to the impedance Z.

From Fig. B it is observed that the dynamic stiffness $S_{33}(\omega)$ approaches the high-frequency solution $S_{33}^\infty(\omega)$ for $\omega \to \infty$ and increasing values of the loss factor. Hence, when $\eta = 0.1$ the dynamic stiffness is almost identical to $S_{33}^\infty(\omega)$—even at relatively low values of the non-dimensional frequency a_0. Further, it is clearly seen that the solution for $\eta = 0$ is singular at a number of frequencies within the considered frequency interval. As mentioned above, these singularities occur at the roots of $J_0(k_S R)$, indicated by the vertical lines (— · — ·) in the figure. □

3.5 Summary

In the present chapter, a presentation has been given of integral indenties for elastodynamic problems. The main results are listed below.

Betti's reciprocal theorem forms an integral relationship between two elastodynamic states that are defined on the same domain, but with different boundary and initial conditions.

Green's functions are the fundamental solutions obtained for a particularly simple geometry and load. In this chapter, the Green's functions for elastodynamic wave propagation in a linear elastic isotropic homogeneous full space have been derived. The load has been applied as a concentrated force—or as a line load acting along the x_3-axis and in the direction perpendicular to this axis (plane strain) or parallel to the x_3-axis (antiplane shear).

Reciprocity relations have been derived for the different Green's functions. In the time domain as well as the frequency domain, a purely spatial reciprocity has been demonstrated. Furthermore, purely temporal and mixed spatial/temporal reciprocity relations have been found in the time domain. These reciprocity relations provide insight into the physics of the Green's functions and they are useful in the derivation of boundary integral equations.

Somigliana's identity is obtained by application of the Green's function and the corresponding body forces and surface tractions as one of the states in Betti's reciprocal theorem. This takes the integral to the boundary and forms the basis for the boundary-element method, treated in the next chapter.

Plane strain in elastodynamics corresponds to the propagation of P- and SV-waves. The Green's function for plane strain is obtained by integration of the three-dimensional solution along the axis normal to the considered plane. In other words, a line source is regarded as the sum of infinitely many point sources.

Antiplane strain in elastodynamics corresponds to the propagation of SH-waves which are fully decoupled from the P- and SV-waves. The Green's function for antiplane strain is obtained by integration of the three-dimensional wave equation with the wave speed c_S along the axis normal to the considered plane.

Finally it is noted that results have been provided for frequency-domain as well as time-domain analysis, and in addition to the general three-dimensional problem, integral identities and Green's functions have been presented for plane strain and antiplane shear.

CHAPTER 4
Boundary-element analysis of elastodynamic problems

In Chapter 3, the formulation of boundary-integral equations (BIEs) for the solution of elastodynamic problems was discussed. The *boundary-element method* (BEM) is in essence the discretized version of the BIE. The aim of this chapter is to give a brief overview of the formulation of the BEM. A limitation to the so-called direct formulation is made. This formulation is based on the Somigliana identity derived in the previous chapter for a number of problems. The formulation will be given in both the frequency and the time domain and for closed interior and exterior as well as open domains.

4.1 Introduction to the boundary-element method

The boundary-element method (BEM) is a discretized version of the boundary-integral-equation method. Basically, the idea of the BEM is to partition the boundary Γ of the domain Ω into a number of sub-boundaries Γ_j, referred to as *boundary elements*, see Fig. 4–1. Parallel to this, the continuous fields on the boundary are discretized into their values at a finite number of so-called *collocation nodes*. These nodes may, or may not, coincide with the *extreme points* of the elements. The field quantities on each of the boundary elements are interpolated with the use of shape functions, employing a technique similar to that of the finite-element method. However, the weight functions are not selected on a local, element-wise basis as it is custom in the FEM. Instead, an adequate fundament solution, *i.e.* Green's function, is used for the weighting. As it will be explained below, the choice of Green's function defines which part of the boundary that has to be discretized, and thus the size of the numerical model, *i.e.* the number of degrees of freedom.

Obviously, if there are any body forces, an integration over the volume Ω has to be carried out in excess to that over the boundary Γ. Numerically this problem is treated by a discretization of Ω into a number of sub-domains, which in the context of the BEM are referred to as *interior cells*. It is noted that the interior cells should not be mistaken for finite elements, as the Green's functions are also used as weight functions in the interior of the domain. Further, the interior cells are only used for the evaluation of the contributions from loads applied inside the domain and as such they do not involve the introduction of additional degrees of freedom in the system. Anyway, in this chapter it shall be assumed that there are no contributions in the interior of the domain. Moreover, in the time-domain solutions that will be presented, zero initial conditions are assumed. A study of the boundary-integral equation (BIE) formulations in Chapter 3 reveals that this reduces the problems to pure boundary integral problems.

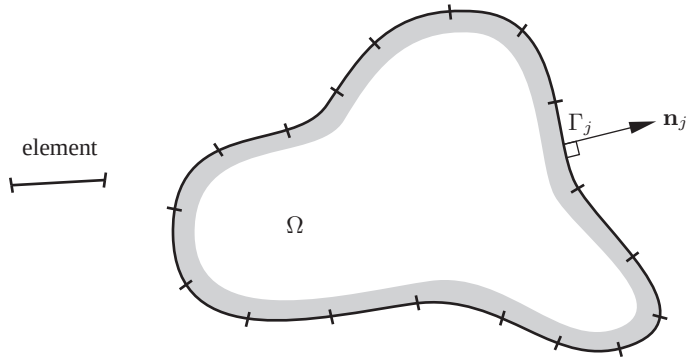

Figure 4–1 Discretization of the boundary into boundary elements representing the surface Γ_j with outward unit normal vector $\mathbf{n}_j$.

4.1.1 Direct formulation in the frequency domain

In the absence of body forces, the frequency-domain boundary-integral equation (3–75) for the general three-dimensional elastodynamic problem may be written in the form

$$C_{il}(\mathbf{x})U_l(\mathbf{x},\omega) + \int_\Gamma P^*_{il}(\mathbf{x},\omega;\mathbf{y})U_l(\mathbf{y},\omega)\mathrm{d}\Gamma(\mathbf{y}) = \int_\Gamma U^*_{il}(\mathbf{x},\omega;\mathbf{y})P_l(\mathbf{y},\omega)\mathrm{d}\Gamma(\mathbf{y}). \tag{4–1}$$

Here $U_i(\mathbf{x},\omega)$ and $U^*_{il}(\mathbf{x},\omega;\mathbf{y})$ signify the displacements in the physical state and the fundamental-solution state, respectively. Likewise, $P_i(\mathbf{y},\omega)$ and $P^*_{il}(\mathbf{x},\omega;\mathbf{y})$ are the surface traction in the physical state and the Green's function for the surface traction, respectively. Further, $C_{il}(\mathbf{x}) = C(\mathbf{x})\delta_{il}$ is a doubly indexed scalar. As discussed in Section 3.4, $C(\mathbf{x})$ depends solely on the geometry of the surface Γ at the point $\mathbf{x}$. In particular, $C_{il}(\mathbf{x}) = \frac{1}{2}\delta_{il}$ if the surface is smooth at $\mathbf{x}$. As discussed in Section 3.4, other values of $C(\mathbf{x})$, an therefore $C_{il}(\mathbf{x})$, are obtained for any other configuration of the surface geometry at the observation point.

A discretization of Eq. (4–1) provides the following equation for a single collocation node i:

$$\begin{aligned}\mathbf{C}(\mathbf{x}_i)\mathbf{U}(\mathbf{x}_i,\omega) + \sum_{j=1}^{NE}\left\{\int_{\Gamma_j}\mathbf{P}^*(\mathbf{x}_i,\omega;\mathbf{y})\mathbf{\Phi}_j(\mathbf{y})\mathrm{d}\Gamma_j(\mathbf{y})\right\}\mathbf{U}_j(\omega)\\ = \sum_{j=1}^{NE}\left\{\int_{\Gamma_j}\mathbf{U}^*(\mathbf{x}_i,\omega;\mathbf{y})\mathbf{\Phi}_j(\mathbf{y})\mathrm{d}\Gamma_j(\mathbf{y})\right\}\mathbf{P}_j(\omega),\end{aligned} \tag{4–2}$$

where NE is the number of boundary elements in the domain, and $\mathbf{\Phi}_j$ contains the shape functions used to interpolate the fields over the sub-boundary defined by element j,

$$\mathbf{U}(\mathbf{x},\omega) = \mathbf{\Phi}_j(\mathbf{x})\mathbf{U}_j(\omega), \quad \mathbf{P}(\mathbf{x},\omega) = \mathbf{\Phi}_j(\mathbf{x})\mathbf{P}_j(\omega). \tag{4–3}$$

In Eqs. (4–2) and (4–3), $\mathbf{U}_j(\omega)$ and $\mathbf{P}_j(\omega)$ are vectors storing all displacement and surface-traction degrees of freedom for element j, respectively.

As indicated by Eq. (4–2), the discretized form of the BIE for a single collocation node i on the surface of the domain Ω involves two sums of integrals over the boundary elements. For convenience, the element matrices defined by these boundary element integrals are denoted

$$\int_{\Gamma_j} \mathbf{P}^*(\mathbf{x}_i,\omega;\mathbf{y})\mathbf{\Phi}_j(\mathbf{y})\mathrm{d}\Gamma_j(\mathbf{y}) = \hat{\mathbf{H}}_{ij}, \quad \int_{\Gamma_j} \mathbf{U}^*(\mathbf{x}_i,\omega;\mathbf{y})\mathbf{\Phi}_j(\mathbf{y})\mathrm{d}\Gamma_j(\mathbf{y}) = \mathbf{G}_{ij}. \tag{4–4}$$

Subsequently, let an element matrix $\mathbf{H}_{ij}$ be defined so that

$$\mathbf{H}_{ij}(\omega) = \begin{cases} \hat{\mathbf{H}}_{ij}(\omega) + \mathbf{C}(\mathbf{x}_i) & \text{for} \quad i = j \\ \hat{\mathbf{H}}_{ij}(\omega) & \text{for} \quad i \neq j \end{cases}. \tag{4–5}$$

It then follows that Eq. (4–2) may be rewritten as

$$\sum_{j=1}^{NE} \mathbf{H}_{ij}(\omega)\mathbf{U}_j(\omega) = \sum_{j=1}^{NE} \mathbf{G}_{ij}(\omega)\mathbf{P}_j(\omega). \tag{4–6}$$

The equations for each collocation node may be assembled into a global system of equations for the entire domain,

$$\mathbf{H}(\omega)\mathbf{U}(\omega) = \mathbf{G}(\omega)\mathbf{P}(\omega). \tag{4–7}$$

Here, $\mathbf{U}(\omega)$ and $\mathbf{P}(\omega)$ are vectors storing all nodal values of the displacements and the traction. As it will be discussed later, $\mathbf{P}(\omega)$ may have more components than $\mathbf{U}(\omega)$, since the traction may be discontinuous over element borders, *e.g.* at corners, whereas the displacement is discontinuous. Accordingly, $\mathbf{G}(\omega)$ may be a rectangular rather than a square matrix.

The boundary conditions in a physical problem are usually given in terms of Dirichlet conditions along one part of the boundary and Neumann conditions on the remaining part of the boundary. Denoting the quantities belonging to the two parts of the boundary with the subscripts 1 and 2, respectively, it is obvious that the vectors $\mathbf{U}_1(\omega)$ and $\mathbf{P}_2(\omega)$ are known. Therefore, the system of equations as given by Eq. (4–7) may be written as

$$\mathbf{A}(\omega)\mathbf{Z}(\omega) = \mathbf{F}(\omega), \tag{4–8a}$$

where

$$\mathbf{A}(\omega) = \begin{bmatrix} -\mathbf{G}_{11} & \mathbf{H}_{12} \\ -\mathbf{G}_{21} & \mathbf{H}_{22} \end{bmatrix}, \quad \mathbf{Z}(\omega) = \begin{bmatrix} \mathbf{P}_1 \\ \mathbf{U}_2 \end{bmatrix}, \quad \mathbf{F}(\omega) = \begin{bmatrix} -\mathbf{H}_{11} & \mathbf{G}_{12} \\ -\mathbf{H}_{21} & \mathbf{G}_{22} \end{bmatrix} \begin{bmatrix} \mathbf{U}_1 \\ \mathbf{P}_2 \end{bmatrix}. \tag{4–8b}$$

Once the BIE is discretized, the solution of the boundary problem reduces to the problem of applying spatial shape functions providing a suitable order of interpolation and then computing the integrals over each element, either analytically or numerically.

In most problem, the formulation of the system of equations in the form (4–8) requires a reordering of the degrees of freedom on the boundary. However, this is merely a bookkeeping problem. Further it is noted that any contributions from body forces would enter Eq. (4–8) as a second term on the right-hand side.

The linear system of equations given by Eq. (4–8) is different from the system of equations obtained in the frequency domain for a finite-element domain. In particular it is noted that $\mathbf{A}(\omega)$ is nonsymmetric and fully populated. Furthermore, the assembly of $\mathbf{A}(\omega)$ requires much more computation time than is the case for the system matrices in the FEM. This is in fact the case, even if only the surface has to be discretized, mainly due to the fact that the fundamental solutions are used as weight functions. A glance at Section 3.3 reveals that these are much more complicated than the polynomial interpolation functions usually applied in the FEM.

4.1.2 Direct formulation in the time domain

Similarly to Eq. (4–1), the time-domain formulation of the BIE (3–71) for a three-dimensional elastic domain with a quiescent past becomes

$$C_{il}(\mathbf{x})u_l(\mathbf{x},t) + \int_0^{t^+}\int_\Gamma p^*_{il}(\mathbf{x},t;\mathbf{y},\tau)u_l(\mathbf{y},t)\mathrm{d}\Gamma(\mathbf{y})\,\mathrm{d}\tau = \int_0^{t^+}\int_\Gamma u^*_{il}(\mathbf{x},t;\mathbf{y},\tau)p_l(\mathbf{y},t)\mathrm{d}\Gamma(\mathbf{y})\,\mathrm{d}\tau, \tag{4–9}$$

assuming that no body forces are applied in the physical state. Here $u_i(\mathbf{x},\omega)$ and $p_i(\mathbf{x},\omega)$ are the physical displacement and surface traction, respectively, whereas $u^*_{il}(\mathbf{x},t;\mathbf{y},\tau)$ and $p^*_{il}(\mathbf{x},\omega;\mathbf{y})$ are the corresponding Green's functions.

A discretization in space and time is carried out. Thus the continuous fields $u_i(\mathbf{x},\omega)$ and $p_i(\mathbf{x},\omega)$ are discretized into their values at the nodal points $\mathbf{x}_j$, $j = 1,2,\ldots,NN$, and at the equally spaced discrete time instants $t^k = k\Delta t$, $k = 1,2,\ldots,NT$. An interpolation over space and time is applied in the form

$$\mathbf{C}(\mathbf{x}_i)\mathbf{u}(\mathbf{x}_i,t^j) + \sum_{m=1}^{j}\sum_{k=1}^{NE}\left\{\int_{\Gamma_k}\left(\int_{\Delta t^m}\mathbf{p}^*(\mathbf{x}_i,t^j;\mathbf{y},\tau)T^m\mathrm{d}\tau\right)\mathbf{\Phi}_k(\mathbf{y})\mathrm{d}\Gamma_k(\mathbf{y})\right\}\mathbf{u}^m_k = \sum_{m=1}^{j}\sum_{k=1}^{NE}\left\{\int_{\Gamma_j}\left(\int_{\Delta t^m}\mathbf{u}^*(\mathbf{x}_i,t^j;\mathbf{y},\tau)\check{T}^m\mathrm{d}\tau\right)\mathbf{\Psi}_k(\mathbf{y})\mathrm{d}\Gamma_k(\mathbf{y})\right\}\mathbf{p}^m_k, \tag{4–10}$$

where $\mathbf{u}^m_k$, $\mathbf{p}^m_k$ are vectors storing all displacement and traction degrees of freedom for element k at time step m, respectively. Further, $\mathbf{\Phi}_k(\mathbf{y})$, $\mathbf{\Psi}_k(\mathbf{y})$ are the spatial shape functions for element k related to the displacement and the traction, respectively. T^j and $\check{T}^j$ are temporal shape functions for time step j for the same physical quantities. Usually, the spatial shape functions are selected so that $\mathbf{\Phi}_k(\mathbf{y}) = \mathbf{\Psi}_k(\mathbf{y})$, whereas the temporal shape functions may advantageously be different. It should be noted that the local integrals over each time step may actually be computed analytically. However this involves a reformulation of the integral over the traction fundamental solution. It is evident, that the accuracy and stability of the numerical solution is highly dependent on the time step Δt. The evaluation of the integrals and the criteria for selecting the time step and the temporal shape functions will be discussed later.

Analogously to Eq. (4–6), the equation for a single collocation node i for the time up till time step j may be written

$$\sum_{k=1}^{NE}\sum_{m=1}^{j}\mathbf{H}^{jm}_{ik}(\omega)\mathbf{u}^m_k = \sum_{k=1}^{NE}\sum_{m=1}^{j}\mathbf{G}^{jm}_{ik}(\omega)\mathbf{p}^m_k. \tag{4–11}$$

where the subscripts relate to space and the superscripts relate to time. Similar to the case of the frequency-domain solution, the geometry constants contained in the matrix $\mathbf{C}(\mathbf{x}_i)$ are absorbed into $\mathbf{H}^{jj}_{ii}$. The total system of equations, equivalent to the frequency-domain solution given by Eq. (4–7), then becomes

$$\sum_{m=1}^{j}\mathbf{H}^{jm}\mathbf{U}^m = \sum_{m=1}^{j}\mathbf{G}^{jm}\mathbf{P}^m, \tag{4–12}$$

where $\mathbf{U}^m$ and $\mathbf{P}^m$ are vectors storing all values of the displacement and traction, respectively, for the entire surface Γ, *i.e.* for all collocation nodes, at time step m.

At any given time step j, the values of all components in $\mathbf{U}^m$ and $\mathbf{P}^m$ will be known for $m = 1, 2, \ldots, j-1$. Thus, for the evaluation of the unknowns at time step j, Eq. (4–12) is solved in the form

$$\mathbf{H}^{jj}\mathbf{U}^j = \mathbf{G}^{jj}\mathbf{P}^j - \sum_{m=1}^{j-1} \left\{ \mathbf{H}^{jm}\mathbf{U}^m - \mathbf{G}^{jm}\mathbf{P}^m \right\}, \tag{4–13}$$

which, after a reordering of vectors $\mathbf{U}^j$ and $\mathbf{P}^j$ into known and unknown quantities, may again be written in the form

$$\mathbf{A}^j\mathbf{Z}^j = \mathbf{F}^j. \tag{4–14}$$

Evidently, the solution in time domain by means of the procedure described above is very expensive in terms of both computation time and memory consumption, as Eq. (4–14) must be evaluated several times per period of the wave component with the highest frequency.

4.1.3 Choice of Green's function

The boundary integral equations presented in Chapter 3 are all based on the assumption that the fundamental solution for the full space (in three dimensions) or the full plane (in two dimensions) is used. However, it is possible to formulate a BIE, in which specialised fundamental solutions are applied. These Green's functions may, for example, include the influence of a free surface at a given location, or they may take into account that the medium is stratified. This may have the advantage that a smaller part of the boundaries present in the physical problem needs to be described in the BIE. Hence, in the BEM, fewer degrees of freedom are necessary. The drawback of a BEM formulation with a specialised fundamental solution is that the evaluation of each of the components in the system matrices becomes a time consuming process, since fundamental solutions like, for example, the one for an elastic half-space cannot be formulated in closed form.

One of the classical examples is the difference between the *Kelvin* and *Mindlin* solutions in elastostatics:

- The *Kelvin* solution is the Green's function for the elastic full-space subject to static loading. In order to evaluate the response due to a load on a half space with an excavation and a cavity, see Fig. 4–2, the entire surface must be included in the BIE. Therefore the surface $\Gamma_1 \cup \Gamma_2 \cup \Gamma_3 \cup \Gamma_4$ must be discretized in the BEM.

- The Mindlin solution is the Green's function for an elastic half-space under static loading. Therefore the Mindlin solution takes into account the surfaces Γ_1 and Γ_3, and as a result of this only $\Gamma_2 \cup \Gamma_4$ should be discretized.

A half-space is an example of an open domain, in the sense that the surface does not form a closed boundary. This, of course, is a problem when a full-space solution is applied, since the free surface can only be discretized to a certaindistance from the region of interest. However, accurate results are usually obtained, except for in a small region close to the artificial edge.

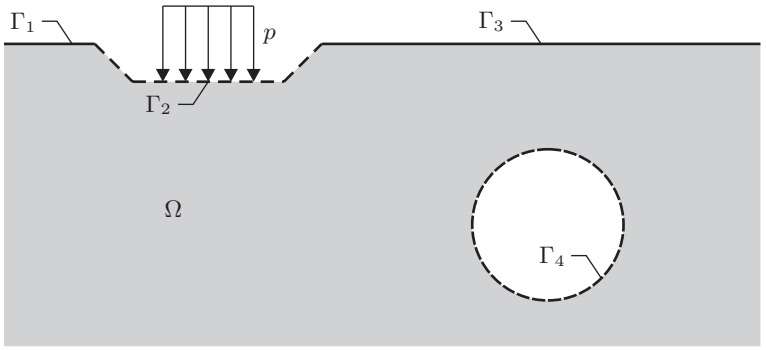

Figure 4–2 Half-space with excavation and cavity.

4.1.4 Boundary element types

In the FEM for elastodynamics, only the displacement is described directly. Hence, the computation of the stresses or the gradients of the displacement implies that the spatial derivatives of the shape functions should exist and be different from zero. E contrario, in the BEM for elastodynamics, the displacement field as well as the surface traction are discretized. Consequently, in the BEM, the lowest possible order of spatial shape functions is zero-order interpolation, *i.e.* the field quantity over each element is assumed to be constant, typically described by the value at the centre of the element.

Due to the fact that the traction is described independently of the displacement, and further since the fundamental solutions are used as weight functions, a very high accuracy is achieved in the BEM when compared with a FEM analysis based on the same order of interpolation. Therefore, interpolation with an order higher than quadratic is unusual in BEM analysis. Thus, the following three types of elements are usually applied:

- *Constant elements*. The displacement and the traction are constant over the entire surface Γ_j of element j, which is taken as the flat surface between the extreme points. The reference point, *i.e.* the collocation node, is placed in the middle of the element, see Fig. 4–3.

- *Linear element*. The element surface is again assumed to be flat. However, the extreme points of the element are now also used as the collocation nodes. This means that the collocation nodes may lie at a corner, or on an edge, see Fig. 4–4.

- *Quadratic elements*. In addition to the nodes in the linear element, nodes are placed at the middle of the element. Further, nodes are placed on the middle of the element edges. This allows elements to be curved, see Fig. 4–5.

The constant and quadratic shape functions, which are used for the interpolation of the field quantities as well as the geometry over each element in two and three dimensions, will be described in the sections below in the discussion of the numerical implementation of the BEM in elastodynamics. Linear elements will not be treated since the quality of the solution obtained with linear elements is usually much lower than the quality of the solution with quadratic interpolation. However, the programming effort in the implementation of quadratic elements is not much bigger than that in the implementation of linear elements.

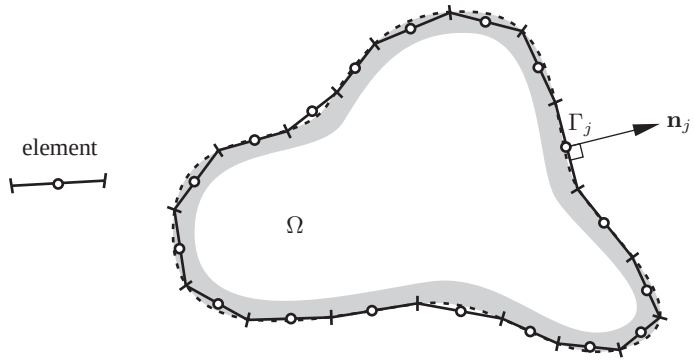

Figure 4–3 Discretization of the boundary into *constant* boundary elements representing the surface Γ_j with outward unit normal $\mathbf{n}_j$. Circles (○) indicate collocation points and lines (|) indicate extreme points of the element.

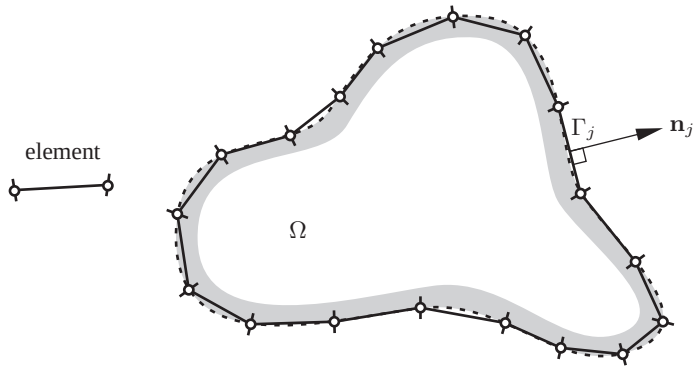

Figure 4–4 Discretization of the boundary into *linear* boundary elements representing the surface Γ_j with outward unit normal $\mathbf{n}_j$. Circles (○) indicate collocation points and lines (|) indicate extreme points of the element.

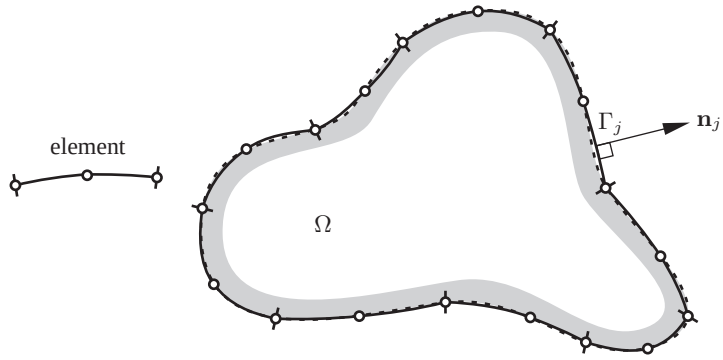

Figure 4–5 Discretization of the boundary into *quadratic* boundary elements representing the surface Γ_j with outward unit normal $\mathbf{n}_j$. Circles (○) indicate collocation points and lines (|) indicate extreme points of the element.

4.2 Frequency-domain solution in two dimensions

In this section, the boundary-element method in the frequency domain and in two dimensions is explained in detail. Firstly, the formulation for scalar field quantities is discussed. This formulation applies to horizontally polarized shear waves in two-dimensional elastodynamics and may alternatively be applied in acoustics. Secondly, the formulation for plane strain is given, whereas a treatment of the equivalent problems in three dimensions may be found in the next section.

4.2.1 Constant boundary elements in antiplane shear

In the frequency domain, the propagation of horizontally polarized shear waves is governed by the two-dimensional Helmholtz equation, Eq. (3–57). The fundamental solution is given by Eq. (3–67) and repeated here for convenience,

$$U^*_{33}(\mathbf{x},\omega;\mathbf{y}) = \frac{1}{2\pi\mu} K_0(\mathrm{i}k_S r), \qquad k_S = \frac{\omega}{c_S}, \qquad r = |\mathbf{x}-\mathbf{y}|, \tag{4–15}$$

where it has been utilised that $\rho c_S^2 = \mu$.

The antiplane shear-wave propagation is described by a scalar field. Further, when constant elements are used, the shape functions are simply 1 over the entire surface of the element, given that the field quantities at any point in the element are taken as the value at the collocation node placed at the middle of the element. Therefore the matrices given by Eq. (4–4) reduce to scalars,

$$\int_{\Gamma_j} P^*_{33}(\mathbf{x}_i,\omega;\mathbf{y})\mathrm{d}\Gamma_j(\mathbf{y}) = \hat{H}_{ij}, \quad \int_{\Gamma_j} U^*_{33}(\mathbf{x}_i,\omega;\mathbf{y})\mathrm{d}\Gamma_j(\mathbf{y}) = G_{ij}, \tag{4–16}$$

where $P^*_{33}(\mathbf{x},\omega;\mathbf{y})$ is the fundamental solution for the traction, which is found as μ times the spatial derivative of $U^*_{33}(\mathbf{x},\omega;\mathbf{y})$ in the direction of the outward unit normal, *i.e.*

$$P^*_{33}(\mathbf{x},\omega;\mathbf{y}) = -\frac{\mathrm{i}k_S}{2\pi}\frac{\partial r}{\partial n} K_1(\mathrm{i}k_S r). \tag{4–17}$$

As pointed out in Subsection 4.1.1, the remaining task in the formulation of the BEM solution lies in the evaluation of the integrals (4–16), so that the system of equations (4–7) can be assembled.

Contribution from elements, $i \neq j$

The contributions from any element to which the collocation node does not belong, *i.e.* $i \neq j$, can be found by numerical integration. For this purpose, a standard Gauss quadrature rule can be used. In this respect, the basic difference from the case of the FEM is that, in the BEM, the fundamental solution is used as the weight function. Since the fundamental solutions are definitely not polynomials, additional accuracy will always be obtained by using more Gauss points in the integration over each element. However, a reasonably high accuracy is usually provided with 10 Gauss points per element in a two dimensional scheme.

The main difficulty in the evaluation of the contributions from elements defined by $i \neq j$ consists in an accurate computation of the modified Bessel functions, $K_0(\mathrm{i}k_S r)$ and $K_1(\mathrm{i}k_S r)$. Domínguez (1993) pointed out that this demands the use of different series expansions for different arguments. Thus, for arguments $|\mathrm{i}k_S r| < 5$, Maclaurin expansions in the form

$$K_0(z) = -\ln\!\left(\frac{z}{2}\right) I_0(z) - \gamma + \frac{(z^2/4)}{(1!)^2}(1-\gamma) + \frac{(z^2/4)^2}{(2!)^2}\left(1+\frac{1}{2}-\gamma\right) + \ldots, \tag{4–18}$$

$$K_1(z) = \frac{1}{2}\left(\frac{z}{2}\right)^{-1} + \ln\!\left(\frac{z}{2}\right) I_1(z) - \frac{1}{2}\left(\frac{z}{2}\right) \sum_{n=0}^{\infty} \left\{\vartheta(n+1) + \vartheta(n+2)\right\} \frac{(z^2/4)^n}{n!\,(n+1)!}, \quad (4\text{–}19)$$

where

$$\vartheta(m) = -\gamma + \sum_{n=1}^{m-1} n^{-1}, \quad (4\text{–}20)$$

are used. Here $\gamma = 0.577215664\ldots$ is Euler's constant, and $I_0(z)$, $I_1(z)$ are two functions defined by the series expansions

$$I_0(z) = 1 + \frac{z^2/4}{(1!)^2} + \frac{(z^2/4)^2}{(2!)^2} + \ldots, \quad I_1(z) = \frac{z}{2}\left\{1 + \sum_{n=0}^{\infty} \frac{(z^2/4)^n}{n!\,\Gamma(n+2)}\right\}. \quad (4\text{–}21)$$

For $|\mathrm{i}k_S r| \geq 5$, the following expansions are used (Domínguez 1993):

$$K_n(z) = \sqrt{\frac{\pi}{2z}}\,\mathrm{e}^{-z}\left\{1 + \frac{(m-1^2)}{1!\,(8z)^1} + \frac{(m-1^2)(m-3^2)}{2!\,(8z)^2} + \ldots\right\}, \quad (4\text{–}22)$$

where $m = 4n^2$ and $n = 1, 2, \ldots$, etc.

Contribution from elements, $i = j$

When $i = j$, *i.e.* when the collocation node belongs to the element over which the integration is carried out, the Gauss quadrature rule does not provide results of an acceptable accuracy. This is due to the fact that the fundamental solutions are singular in the limit as $r \to 0$. In the case of constant elements, the evaluation of the singular terms is however relatively easy. In particular, $\hat{H}_{ii} = 0$, which follows from the fact that the normal vector is orthogonal to the distance vector, so that $\partial r/\partial n = 0$. Further, since a collocation point at the middle of a constant element belongs to a smooth, flat part of the surface, the geometry constant takes the value $C(\mathbf{x}_i) = 0.5$ at all points on the surface. On the other hand, the displacement Green's function needs special treatment when $i = j$.

When constant elements are used for the discretization, a minimum of six elements per wavelength L should be used in order to get results that have any physical validity. Therefore, denoting the element length L_e, any point belonging to element i should lie within the distance $r = L_e/2 = L/12$ from the collocation node. Given that $k = 2\pi/L$, this means that the small-argument expansion of K_0 given by Eq. (4–18) is valid on the entire element. Consequently, using the symmetry of $U^*_{33}(\mathbf{x}_i, \omega; \mathbf{y})$ with respect to r, G_{ii} is found as

$$2\pi\mu G_{ii} = \int_0^z K_0(s)\,ds = -\left\{\gamma + \ln\!\left(\frac{z}{2}\right)\right\} z \sum_{n=0}^{\infty} \frac{(z^2/4)^n}{(n!)^2(2n+1)} + z\sum_{n=0}^{\infty} \frac{(z^2/4)^n}{(n!)^2(2n+1)^2} + z\sum_{n=1}^{\infty} \frac{(z^2/4)^n}{(n!)^2(2n+1)} \left(\sum_{m=1}^{n} \frac{1}{m}\right). \quad (4\text{–}23)$$

In practice, only a finite number of terms are included in the series expansions listed in this section. The expansions are all convergent, so that after a given number of terms have been included in the approximation, additional terms will only contribute a very little.

Usual steps in a frequency-domain boundary element code

At this point it should be clear, that the computation of the complex amplitude spectres of the response, *i.e.* the Fourier transforms of the unknown displacements and surface tractions, involves a number of steps. Thus, a computer code for the frequency-domain BEM should contain the following procedures:

1 An input procedure reading the geometry, the material properties and the boundary conditions defining the problem.

2 A procedure utilised for the assembly of the matrices $\mathbf{G}$ and $\mathbf{H}$, or rather $\mathbf{A}$ and $\mathbf{F}$, for the domain Ω.

3 Subroutines for the computation of the element contributions for the case $i \neq j$.

4 Subroutines for the computation of the element contributions for the case $i = j$.

5 A solver that computes the unknowns from the global system of equations.

6 A routine which can be used for the computation of field quantities at interior points of the domain.

7 An output procedure which saves the results for further use.

In the frequency domain, the computation of the response for multiple frequencies requires a global loop over the procedures listed above.

Evaluation of quantities at internal points

Concerning item 6 of the list of procedures given in the previous subsection, the computation of field quantities at interior points, *i.e.* points within the domain Ω, may be considered postprocessing of the data provided by the BEM model. Thus, once the field quantities are known for all nodes on the boundary, the displacement at a point $\mathbf{x}_i$ which is interior to Ω may be found as

$$U_3(\mathbf{x}_i, \omega) = \sum_{j=1}^{NE} G_{ij}(\omega) U_{3\,j}(\omega) - \sum_{j=1}^{NE} H_{ij}(\omega) P_{3\,j}(\omega), \tag{4–24}$$

where $U_{3\,j}(\omega)$ and $P_{3\,j}(\omega)$ are the nodal values of the antiplane displacements and shear stresses, respectively. Note, that additional contributions must be included if body forces are applied within the domain. A similar procedure may be utilised to find the stresses at interior points.

Numbering convention for two-dimensional boundary elements

In the BEM, the direction of the normal vector is crucial in the evaluation of the integrals over the traction fundamental solutions. A simple means of making sure that the normal vector is always pointing out from the considered domain, is to number the extreme points of an element in the direction indicated on Fig. 4–6. Thus, in a two-dimensional boundary element scheme for an interior domain, the extreme points of an element are numbered clockwise when looking in the direction of the out-of-plane coordinate axis. By contrast, for an exterior domain, the extreme points are numbered counterclockwise. In other words, the material is always on the left when you ‘walk along the boundary’.

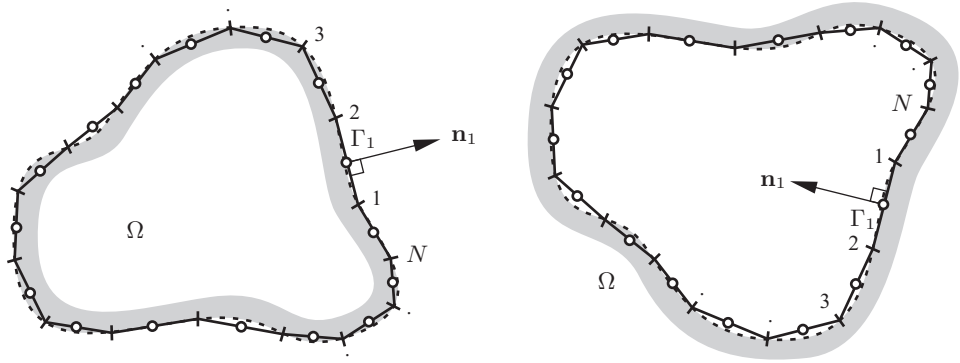

Figure 4–6 Numbering of the extreme points in two-dimensional boundary element analysis with constant elements for: (a) interior domains and (b) exterior domains.

4.2.2 Constant boundary elements in plane strain

The Green's function tensor for the displacements in plane-strain elastodynamics was derived in Section 3.3.3 and repeated here for convenience:

$$U^*_{il}(\mathbf{x},\omega;\mathbf{y}) = \frac{1}{2\pi\rho c_S^2}\left(\alpha\delta_{il} - \beta\frac{\partial r}{\partial x_i}\frac{\partial r}{\partial x_l}\right), \tag{3–55a}$$

where

$$\alpha = K_0(\mathrm{i}k_S r) + \frac{1}{\mathrm{i}k_S r}\left(K_1(\mathrm{i}k_S r) - \frac{c_S}{c_P}K_1(\mathrm{i}k_P r)\right), \tag{3–55b}$$

$$\beta = K_2(\mathrm{i}k_S r) - \frac{c_S^2}{c_P^2}K_2(\mathrm{i}k_P r). \tag{3–55c}$$

Here $k_P = \omega/c_P$, $k_S = \omega/c_S$ are the wavenumbers for the P- and S-waves. Similarly, the traction Green's function tensor is given as

$$P^*_{il}(\mathbf{x},\omega;\mathbf{y}) = \frac{1}{2\pi}\left[\left(\frac{c_P^2}{c_S^2}-2\right)\left(\frac{\partial\alpha}{\partial r} - \frac{\partial\beta}{\partial r} - \frac{2\beta}{r}\right)\frac{\partial r}{\partial x_l}n_i(\mathbf{x}) + \frac{\partial\alpha}{\partial r}\left(\frac{\partial r}{\partial x_i}n_l(\mathbf{x}) + \frac{\partial r}{\partial n}\delta_{il}\right)\right.$$
$$\left. -\frac{\beta}{r}\left(\frac{\partial r}{\partial x_i}n_l(\mathbf{x}) + \frac{\partial r}{\partial n}\delta_{il} + 2\frac{\partial r}{\partial x_l}n_i(\mathbf{x}) - 4\frac{\partial r}{\partial x_i}\frac{\partial r}{\partial x_l}\frac{\partial r}{\partial n}\right) - 2\frac{\partial\beta}{\partial r}\frac{\partial r}{\partial x_i}\frac{\partial r}{\partial x_l}\frac{\partial r}{\partial n}\right], \tag{4–26a}$$

where

$$\frac{d\alpha}{dr} = \mathrm{i}k_S K_1(\mathrm{i}k_S r)\left(\frac{2}{k_S^2 r^2} - 1\right) + K_1(\mathrm{i}k_P r)\frac{c_S}{c_P}\frac{2}{\mathrm{i}k_P r^2}$$
$$-\left(K_0(\mathrm{i}k_S r) - \frac{c_S^2}{c_P^2}K_0(\mathrm{i}k_P r)\right)\frac{1}{r}, \tag{4–26b}$$

$$\frac{d\beta}{dr} = -\mathrm{i}k_S K_1(\mathrm{i}k_S r) - \frac{2}{r}K_2(\mathrm{i}k_S r) + \frac{c_S^2}{c_P^2}\mathrm{i}k_P K_1(\mathrm{i}k_P r) + \frac{c_S^2}{c_P^2}\frac{2}{r}K_2(\mathrm{i}k_P r). \tag{4–26c}$$

In the case of two-dimensional elastodynamics, the frequency domain BEM is given by Eq. (4–7), where the submatrices given by Eq. (4–4) now have the dimensions (2×2). The evaluation of $\mathbf{G}_{ij}$ and $\hat{\mathbf{H}}_{ij}$, $i \neq j$, is straightforward and may be carried out using a standard Gauss quadrature rule. The series expansions for the modified Bessel functions given in Subsection 4.2.1 can be used in the computation. Concerning the case of the traction Green's function, the fact that $\partial r/\partial n = 0$ along the element to which the collocation node belongs means that component lk of $\hat{\mathbf{H}}_{ii}$ is given as

$$\hat{H}_{ii,\,lk} = \frac{1}{2\pi} \int_{\Gamma_i} \left\{ \left(\frac{d\alpha}{dr} - \frac{1}{r}\beta \right) n_l \frac{\partial r}{\partial x_k} - \frac{2}{r} \frac{\partial r}{\partial x_l} n_k \beta \right. \\ \left. - \left(\frac{c_P^2}{c_S^2} - 2 \right) \left(\frac{d\alpha}{dr} - \frac{d\beta}{dr} - \frac{\beta}{r} \right) \frac{\partial r}{\partial x_l} n_k \right\} \mathrm{d}\Gamma. \tag{4–27}$$

Since $\partial r/\partial x_l = r_l/r$, it is evident that $\hat{H}_{ii,\,ll} = 0$. In this case, the dot product between two orthogonal vectors is taken. When $k \neq l$, the contributions from the two halves of the element, that is on either side of the collocation node, will be of the same magnitude, but with opposite sign. Thus, in this case the integral also becomes zero. Therefore, similar to the case in constant-element BEM analysis of antiplane shear, $\hat{\mathbf{H}}_{ii} = \mathbf{0}$.

A local coordinate system is now introduced, in which the element lies along the x_1-axis and with the normal vector pointing in the x_2-direction. In this frame of reference, the components $G_{ii,\,lk}^{local}$ of the element matrix $\mathbf{G}_{ii}^{local}$ are zero when $l \neq k$, since $r_2^{local} = 0$. However, nonzero values are obtained for the diagonal terms in the local-frame-of-reference description. With reference to Eq. (3–55), the following values of $G_{ii,\,ll}^{local}$ are achieved:

$$G_{ii,\,11}^{local} = \frac{1}{\pi \rho c_S^2} \left\{ \int_0^z K_0(\mathrm{i}k_S r)\, dr + \frac{1}{\mathrm{i}k_S} K_1(\mathrm{i}k_S z) - \frac{c_S^2}{c_P^2} \frac{1}{\mathrm{i}k_P} K_1(\mathrm{i}k_P z) \right\}, \tag{4–28a}$$

$$G_{ii,\,22}^{local} = \frac{1}{\pi \rho c_S^2} \left\{ \frac{c_S^2}{c_P^2} \int_0^z K_0(\mathrm{i}k_P r)\, dr - \frac{1}{\mathrm{i}k_S} \left(K_1(\mathrm{i}k_S z) - \frac{c_S^2}{c_P^2} K_1(\mathrm{i}k_P z) \right) \right\}, \tag{4–28b}$$

where $z = L_e/2$ with L_e denoting the element length. The evaluation of the modified Bessel function K_1 and the integration of K_0 are carried out numerically by means of the series expansions given in Subsection 4.2.1. Finally, in the global coordinate system, $\mathbf{G}_{ii}$ is found as

$$\mathbf{G}_{ii} = \mathbf{T} \mathbf{G}_{ii}^{local} \mathbf{T}^T, \quad \mathbf{T} = \begin{bmatrix} \cos\theta & -\sin\theta \\ \sin\theta & \cos\theta \end{bmatrix}. \tag{4–29}$$

$\mathbf{T}$ is the transformation matrix from the local to the global coordinate system with θ denoting the angle between the two systems, measured positive from the global to the local system.

4.2.3 Quadratic boundary elements in antiplane shear

In two-dimensional boundary-element analysis, the quadratic shape functions for a scalar field are given as

$$\phi_1(\xi) = \frac{1}{2}\xi\,(\xi - 1)\,, \quad \phi_2(\xi) = (1 - \xi)\,(1 + \xi)\,, \quad \phi_3(\xi) = \frac{1}{2}\xi\,(\xi + 1)\,, \tag{4–30}$$

in a local coordinate system with ξ varying between -1 and 1 along the piece of boundary defined by an element. In the frequency domain, the displacement and traction fields on element j are then given as

$$U_3(\mathbf{x},\omega) = \mathbf{\Phi}(\xi)\mathbf{U}_j(\omega), \quad P_3(\mathbf{x},\omega) = \mathbf{\Phi}(\xi)\mathbf{P}_j(\omega), \quad \mathbf{x}(\xi) = \mathbf{x}_j^T\mathbf{\Phi}(\xi), \tag{4–31}$$

where $\mathbf{U}_j(\omega)$ and $\mathbf{P}_j(\omega)$ are column vectors of length 3 storing the nodal values of the displacement and traction for element j, respectively, while $\mathbf{\Phi}(\xi)$ is a row vector with the same length storing the shape functions defined by Eq. (4–30). $\mathbf{x}_j$ is a matrix of the dimensions (3×2) storing the (x_1, x_2)-coordinates for each of the three nodes in element j, one node in each row.

Due to the coordinate transformation from the physical (x_1, x_2)-coordinate system into the so-called homogeneous ξ-coordinate system, the length of an element will not be interpreted correctly. A correction of the integrals over each element is carried out by multiplication with the Jacobian $|J|$ of the mapping, *i.e.*

$$\mathrm{d}\Gamma = \sqrt{\left(\frac{\mathrm{d}x_1}{\mathrm{d}\xi}\right)^2 + \left(\frac{\mathrm{d}x_2}{\mathrm{d}\xi}\right)^2}\,\mathrm{d}\xi = |J|\,\mathrm{d}\xi. \tag{4–32}$$

Insertion of Eq. (4–30) into Eq. (4–32) provides the result

$$|J| = \left(\left\{ \left(x_1^{(3)} - 2x_1^{(2)} + x_1^{(1)}\right)\xi + \frac{1}{2}\left(x_1^{(3)} - x_1^{(1)}\right) \right\}^2 + \left\{ \left(x_2^{(3)} - 2x_2^{(2)} + x_2^{(1)}\right)\xi + \frac{1}{2}\left(x_2^{(3)} - x_2^{(1)}\right) \right\}^2 \right)^{1/2}, \tag{4–33}$$

where $(x_1^{(n)}, x_2^{(n)})$ are the coordinates of element node n, $n = 1, 2, 3$. Thus, similar to Eq. (4–16), the contributions to the system matrices from each element become

$$\hat{\mathbf{H}}_{ij} = \int_{-1}^{1} P_{33}^*(\mathbf{x}_i, \omega; \mathbf{y}(\xi))\mathbf{\Phi}_j(\xi)|J|\mathrm{d}\xi, \quad \mathbf{G}_{ij} = \int_{-1}^{1} U_{33}^*(\mathbf{x}_i, \omega; \mathbf{y}(\xi))\mathbf{\Phi}_j(\xi)|J|\mathrm{d}\xi. \tag{4–34}$$

Here, $\mathbf{G}_{ij}$ and $\hat{\mathbf{H}}_{ij}$ are row vectors with the length 3.

Treatment of corners

When linear or quadratic elements are used in the BEM, the possibility arises that nodes may be placed at a corner. This means that a collocation node will belong to two parts of the boundary that will be defined by different normal vectors. As a result of this, the traction on either side of the corner will in general have different directions and magnitude. This may even be the case for nodes belonging to two different elements on a smooth part of the surface when, for example, a nonzero traction is applied to one of the elements, whereas the neighbouring element is free. The fact that the traction need not be the same on adjacent elements means that the system traction vector $\mathbf{P}$ will have the length $3NE$ in a BEM scheme for plane strain when quadratic elements are utilised. In this vector, the traction for each node is stored separately for each element. Correspondingly, $\mathbf{G}$ has the dimensions $(NN \times 3NE)$, where NN is the number of nodes. By contrast, $\mathbf{H}$ is still a square matrix with the dimensions $(NN \times NN)$, because the displacements are continuous at the nodes.

Thus, when the constant elements are abandoned, a means of treating discontinuous tractions at the nodes should be provided. The following situations may have to be accounted for:

1 The traction is known on either side of the node. Therefore the unknown is the displacement.

2 The traction on one side of the node and the displacement are known. Thus, the unknown is the traction on the other side of the node.

3 Only the displacement is known. In this case the traction on both sides of the node are unknown.

In the first two cases listed above, there is only one unknown per node. Therefore, the system of equations may be rearranged into the form (4–8) without any further problems. In the third case, however, the problem arises that the formulation (4–7) only provides a single equation for two unknowns. Therefore, an auxiliary equation is required. This case shall not be discussed in detail in the present work. Note that it is not possible that both the displacement and the traction on one side of the node are unknown, since this would correspond to the situation in which neither Dirichlet nor Neumann conditions are specified on that part of the boundary. Further, note that the discussion of discontinuities does also apply to plane strain and three-dimensional elastodynamics. In this case the situation is slightly more complicated, since each component of the displacements and traction, *i.e.* in each of the coordinate directions, must be treated separately.

Naturally, in the constant element model, both the traction and the displacements will be discontinuous. Since the field quantities are assumed to be constant over each element, the discontinuities will however arise between the elements. This provides a very poor model from a physical point of view, which explains that the constant-element BEM is unusable in many situations. Actually, it turns out that the analysis of, for example, problems involving bending, requires the use of elements with quadratic interpolation in order to get a model with a reasonably low amount of degrees of freedom. The fact that linear elements are associated with almost the same amount of work from a programming point of view, whereas they are still not appropriate for all kinds of analysis, explains why the very simple constant boundary elements or the more adaptable quadratic boundary elements are usually implemented.

The evaluation of the terms for $i \neq j$ is straightforward—here a Gauss quadrature rule may be applied. However, as usual a special treatment of the terms is required for $i = j$. A way of dealing with the singularities of the displacement and the traction Green's functions will be presented in the following subsections.

Evaluation of the singular terms in the fundamental solution for the displacement

The fundamental solution for the displacement contains a weak singularity of the kind $-\ln r$ in the limit as $r \to 0$. This allows a numerical evaluation of $\mathbf{G}_{ii}$, given that a further mapping of the local ξ-coordinate system into an η-coordinate system is performed, such that the Jacobian of the mapping cancels out the singularity.

(1) When the collocation node is the first node out of the three nodes in the quadratic element, the fundamental solution for the displacement becomes singular for $r \to 0$, where r is now the distance given as

$$r = \sqrt{\left(x_1 - x_1^{(1)}\right)^2 + \left(x_2 - x_2^{(1)}\right)^2}, \tag{4–35}$$

where $(x_1^{(1)}, x_2^{(1)})$ are the coordinates of the collocation node. Alternatively, the distance r may be written as

$$r = \eta A, \quad \eta = \frac{1+\xi}{2}, \quad A = 2\sqrt{(a_1\xi + b_1)^2 + (a_2\xi + b_2)^2}, \tag{4–36}$$

$$a_1 = \frac{1}{2}\left(r_1^{(3)} - 2r_1^{(2)}\right), \quad b_1 = r_1^{(2)}, \quad a_2 = \frac{1}{2}\left(r_2^{(3)} - 2r_2^{(2)}\right), \quad b_2 = r_2^{(2)}. \tag{4–37}$$

Here $r_n^{(m)} = x_n^{(m)} - x_n^{(1)}$, $n = 1, 2$, $m = 2, 3$.

In the limit as $r \to 0$, the fundamental solution for the displacement becomes

$$\lim_{r\to 0} \frac{1}{2\pi\mu} K_0(\mathrm{i}k_S r) = -\frac{1}{2\pi\mu}\ln(\mathrm{i}k_S r) = -\frac{1}{2\pi\mu}\ln(\mathrm{i}k_S A) - \frac{1}{2\pi\mu}\ln(\eta). \tag{4–38}$$

The term $-\ln(\mathrm{i}k_S A)$ is nonsingular with the definition of A given in Eq. (4–36). Thus the entire singularity is contained in the term $-\ln(\eta)$. Therefore, the integral over element j may advantageously be split into two contributions,

$$\mathbf{G}_{ii}^{(1)} = \int_{-1}^{1} \frac{1}{2\pi\mu}\left\{K_0(\mathrm{i}k_S r(\xi)) + \ln\left(\frac{1+\xi}{2}\right)\right\}\mathbf{\Phi}_j(\xi)|J|\mathrm{d}\xi + \int_0^1 \frac{1}{2\pi\mu}\ln\left(\frac{1}{\eta}\right)|J_\eta| d\eta, \tag{4–39}$$

where the Jacobian of the mapping into the η-coordinate system is given as

$$J_\eta = J_\eta(\eta) = 2\sqrt{\left(4a_1\eta - 2a_1 + 0.5r_1^{(3)}\right)^2 + \left(4a_2\eta - 2a_2 + 0.5r_2^{(3)}\right)^2}. \tag{4–40}$$

The first integral in Eq. (4–39) may be evaluated with the use of a standard Gauss quadrature rule, while the second integral may be evaluated with the use of a specialised Gauss quadrature rule, cf. (Domínguez 1993).

(2) When the collocation node is node 2 of the element, *i.e.* the centre node, a subdivision of the element is carried out into the part between nodes 1 and 2 and the part between nodes 2 and 3. Accordingly, the integral over the boundary is evaluated as

$$\begin{aligned}\mathbf{G}_{ii}^{(2)} &= \int_{-1}^{1} U_{33}^*(\mathbf{x}_i, \omega; \mathbf{y}(\xi))\mathbf{\Phi}_j(\xi)|J|\mathrm{d}\xi \\ &= \int_{-1}^{0} U_{33}^*(\mathbf{x}_i, \omega; \mathbf{y}(\xi))\mathbf{\Phi}_j(\xi)|J|\mathrm{d}\xi + \int_0^1 U_{33}^*(\mathbf{x}_i, \omega; \mathbf{y}(\xi))\mathbf{\Phi}_j(\xi)|J|\mathrm{d}\xi.\end{aligned} \tag{4–41}$$

A mapping into an η-coordinate system is now carried out over each of the subsurfaces. In the interval between nodes 1 and 2, the transformation $\eta = -\xi$ is applied, whereas the transformation $\eta = \xi$ is used in the interval between nodes 2 and 3.

(3) Finally, when the collocation point lies at node 3 of the element, the logarithmic integration variable is chosen as $\eta = (1-\xi)/2$. In this case the procedure for the computation of $\mathbf{G}_{ii}^{(3)}$ is otherwise equivalent to the procedure for the collocation node lying at node 1.

Evaluation of the singular terms in the the fundamental solution for the traction

A study of Eq. (4–19) reveals that the traction fundamental solution has a strong singularity of the order $1/r$ in the limit as $r \to 0$. In principle, the integrals leading to the matrices $\hat{\mathbf{H}}_{ii}$ may be found by application of a mapping into a local coordinate system which is associated with a Jacobian of the order r. However, when quadratic interpolation is used, the problem would still remain that the geometry constants had to be computed.

Alternatively, a method may be applied, in which the singular terms of $\hat{\mathbf{H}}_{ii}$ and the geometry constants $\mathbf{C}(\mathbf{x}_i)$ are found simultaneously. The method is based on the fact that the singularity of the traction in the dynamic state governed by the Helmholtz equation is the same as the singularity in the static case, *i.e.* for $\omega = 0$, which is governed by the Poisson equation. This follows immediately by a comparison of Eqs. (4–17) and (4–19) with the fundamental solution for the traction in the static case, $P^*_{33\,S}(r)$, which is found as μ times the normal derivative of the Green's function for the two-dimensional Poisson equation, $U^*_{33\,S}(r) = \ln(r)/(2\pi\mu)$, *i.e.*

$$P^*_{33\,S}(r) = n_j \frac{\partial}{\partial x_j} U^*_{33\,S}(r) = \frac{1}{2\pi} \frac{\partial r}{\partial n} \frac{\partial}{\partial r} \ln(r) = -\frac{1}{2\pi r} \frac{\partial r}{\partial n}. \tag{4–42}$$

Now, in the static case, consider a state in which the traction is zero along the entire boundary Γ of the interior domain Ω. In this case, the displacement is constant over the entire domain Ω, *i.e.* $U_{3\,S}(\mathbf{x}) = U_0$, and the equation for the boundary-element domain, that is Eq. (4–7), reduces to

$$\mathbf{H}_S \mathbf{U}_0 = \mathbf{0}. \tag{4–43}$$

In particular, the equation for a single collocation node, Eq. (4–6), becomes

$$\left(C(\mathbf{x}_i) + \sum_{j=1}^{NN} \hat{H}_{S,\,ij} \right) U_0 = 0 \quad \Rightarrow \quad H_{S,\,ii} = C(\mathbf{x}_i) + \hat{H}_{S,\,ii} = -\sum_{j=1,\,j\neq i}^{NN} \hat{H}_{S,\,ij}, \tag{4–44}$$

where, for example, $H_{S,\,ij}$ is component ij of the global matrix $\mathbf{H}_S$. Addition of $\hat{H}_{ii}$ and subtraction of $\hat{H}_{S,\,ii}$ on both sides of the equation leads to the formulation

$$H_{ii} = C(\mathbf{x}_i) + \hat{H}_{ii} = -\sum_{j=1,\,j\neq i}^{NN} \hat{H}_{S,\,ij} + \left(\hat{H}_{ii} - \hat{H}_{S,\,ii} \right). \tag{4–45}$$

Since the singularities of $P^*_{33\,S}(r)$ and $P^*_{33}(r)$ are the same, the matrix defined by the difference $\hat{H}_{ii} - \hat{H}_{S,\,ii}$ is nonsingular. The appropriate way to compute this nonsingular term is to evaluate the element-wise surface integrals over the series expansion (4–19) minus the term corresponding to the static solution.

Hence, a direct evaluation of the singular terms of the traction Green's function can be avoided. However, the procedure described above is only valid for an interior domain. If an exterior domain is considered, it may be argued that in this case Ω is bounded by the surface $\Gamma \cup \Gamma_\infty$, where Γ_∞ is the radiation boundary lying at an infinite distance from the collocation node. Since the Green's function provides a traction of the magnitude 1 at the collocation node, this is the traction that should 'radiate' through Γ_∞, meaning that

$$\int_{\Gamma_\infty} P^*_{33}(\mathbf{x}_i, \mathbf{y}) \mathrm{d}\Gamma(\mathbf{y}) = -1. \tag{4–46}$$

Therefore, for an exterior domain, Eq. (4–45) reads

$$H_{ii} = C(\mathbf{x}_i) + \hat{H}_{ii} = 1 - \sum_{j=1,\, j\neq i}^{NN} \hat{H}_{S,\,ij} + \left(\hat{H}_{ii} - \hat{H}_{S,\,ii}\right). \tag{4–47}$$

In practice, since the term H_{ii} is never evaluated directly, only the vector G_{ii} is computed in the subroutine used to evaluate the singular terms. The computation of H_{ii} is better included in the global routine used to assemble the system matrices for the entire domain, while each of the nonsingular terms in Eqs. (4–45) and (4–47) may be calculated in the subroutine used to compute the nonsingular contributions, which should for this purpose also be called for the case $i = j$.

Unfortunately, neither Eq. (4–45) nor Eq. (4–47) can be used for the evaluation of the singular traction fundamental solution terms in an *open* domain, *i.e.* a domain where only a part of the boundary can be discretized due to the fact that the surface is (semi-)infinite. Here an alternative procedure is necessary. This will be further discussed in Subsection 4.3.2. In any case it is evident that a boundary element code for quadratic interpolation elements is much more complicated than that for constant elements, the main reasons being that discontinuities at corners have to be accounted for and that the singularities of the fundamental solutions need a numerical treatment.

4.2.4 Quadratic boundary elements in plane strain

When quadratic interpolation is used in the boundary-element analysis of plane P- and SV-waves, it is convenient to order the degrees of freedom for element j, so that the following definitions apply for the displacement, the traction and the global coordinate at a point on the subsurface defined by the element:

$$\mathbf{U}(\mathbf{x},\omega) = \begin{bmatrix} U_1(\mathbf{x},\omega) \\ U_2(\mathbf{x},\omega) \end{bmatrix} = \begin{bmatrix} \phi_1 & 0 & \phi_2 & 0 & \phi_3 & 0 \\ 0 & \phi_1 & 0 & \phi_2 & 0 & \phi_3 \end{bmatrix} \begin{bmatrix} U_1^{(1)} \\ U_2^{(1)} \\ U_1^{(2)} \\ U_2^{(2)} \\ U_1^{(3)} \\ U_2^{(3)} \end{bmatrix}_j = \mathbf{\Phi}(\xi)\mathbf{U}_j(\omega), \tag{4–48}$$

$$\mathbf{P}(\mathbf{x},\omega) = \begin{bmatrix} P_1(\mathbf{x},\omega) \\ P_2(\mathbf{x},\omega) \end{bmatrix} = \begin{bmatrix} \phi_1 & 0 & \phi_2 & 0 & \phi_3 & 0 \\ 0 & \phi_1 & 0 & \phi_2 & 0 & \phi_3 \end{bmatrix} \begin{bmatrix} P_1^{(1)} \\ P_2^{(1)} \\ P_1^{(2)} \\ P_2^{(2)} \\ P_1^{(3)} \\ P_2^{(3)} \end{bmatrix}_j = \mathbf{\Phi}(\xi)\mathbf{P}_j(\omega), \tag{4–49}$$

$$\mathbf{x} = \begin{bmatrix} x_1 \\ x_2 \end{bmatrix} = \begin{bmatrix} \phi_1 & 0 & \phi_2 & 0 & \phi_3 & 0 \\ 0 & \phi_1 & 0 & \phi_2 & 0 & \phi_3 \end{bmatrix} \begin{bmatrix} x_1^{(1)} \\ x_2^{(1)} \\ x_1^{(2)} \\ x_2^{(2)} \\ x_1^{(3)} \\ x_2^{(3)} \end{bmatrix}_j = \mathbf{\Phi}(\xi)\mathbf{x}_j(\omega). \tag{4–50}$$

Here $U_n^{(m)} = U_n^{(m)}(\omega)$, $P_n^{(m)} = P_n^{(m)}(\omega)$, and $\phi_m = \phi_m(\xi)$. Index $n = 1, 2$ denotes the components in the two coordinate directions, while $m = 1, 2, 3$ refers to the local node number in the element. Obviously, with the definitions given in Eq. (4–48) and (4–49), the element matrices computed in Eq. (4–4) now have the dimensions (2×6).

When compared to the two-dimensional analysis of acoustic problems in frequency domain using quadratic interpolation, the main difference lies in the fact that the scalar terms related to each node are now matrices of the dimension (2×2). Accordingly, the routines used to compute the singular terms of the traction fundament solution matrices become

$$\mathbf{H}_{ii} = \mathbf{C}(\mathbf{x}_i) + \hat{\mathbf{H}}_{ii} = -\sum_{j=1,\, j\neq i}^{NN} \hat{\mathbf{H}}_{S,\,ij} + (\mathbf{H}_{ii} - \mathbf{H}_{S,\,ii}) \tag{4–51}$$

for an *interior* domain, and

$$\mathbf{H}_{ii} = \mathbf{C}(\mathbf{x}_i) + \hat{\mathbf{H}}_{ii} = \mathbf{I} - \sum_{j=1,\, j\neq i}^{NN} \hat{\mathbf{H}}_{S,\,ij} + (\mathbf{H}_{ii} - \mathbf{H}_{S,\,ii}) \tag{4–52}$$

for an *exterior* domain. Here $\mathbf{I}$ is the identity matrix with the dimension (2×2). In this case the idea behind the indirect evaluation of the terms $\mathbf{H}_{ii}$ is the a rigid-body displacement (translation) is associated with zero traction on the entire boundary. As it was also the case in plane acoustics, the nonsingular term $\mathbf{H}_{ii} - \mathbf{H}_{S,\,ii}$ is computed from the series expansion of the traction Green's function minus the term corresponding to the static solution.

The singular terms of the displacement fundamental solution are found by a mapping into a local η-coordinate system that involves a Jacobian that cancels out the weak singularity. With reference to Eq. (3–55), the fundamental solution for the displacement may be divided into two parts. The β-part contains no singularities, whereas the singularity of the α-part is given as

$$\lim_{r\to 0} \alpha = -\frac{3 - 4\nu}{4\,(1-\nu)} \ln r, \tag{4–53}$$

where ν is the Poisson ratio for the material. Evidently, a strategy equivalent to that for the singular terms of U_{33}^* may be used, *i.e.* the specialized Gauss quadrature may be applied to the singular term in the η-coordinate description, while a standard Gauss quadrature rule is used for the nonsingular part. The procedure will not be described any further in the present work. Details on the method can be found in the book by Domínguez (1993).

4.3 Frequency-domain solution in three dimensions

In a three-dimensional problem analysed with the BEM, two-dimensional elements are used for the discretization of the surface. In principle, any geometry of the boundary elements can be used, but usually isoparametric triangular or quadrilateral elements are used. Analogous to the case of two-dimensional analysis, elements with constant, linear or quadratic interpolation are typically applied. Here, however, we shall concentrate on the constant and quadratic elements, since linear interpolation is much more complicated to handle than constant elements from a computational point of view, whereas they are far less adaptable than the quadratic elements which may be implemented in a computer code with little additional effort.

4.3.1 Constant boundary elements in three dimensions

When constant interpolation is used in three-dimensional boundary element analyses, the collocation nodes are placed at the centres of the quadrilateral or triangular elements as illustrated in Fig. 4–7. The assembly procedure in three dimensions is exactly the same as that in two dimensions. Thus, the only difference lies in the evaluation of the element-wise surface integrals defined by Eq. (4–4). Again, a numerical integration in terms of a standard Gauss quadrature rule may be applied to the nonsingular terms, which arise when the collocation node does not belong to the element, whereas the singular terms arising in the contributions from a collocation node to itself have to be determined in a different manner.

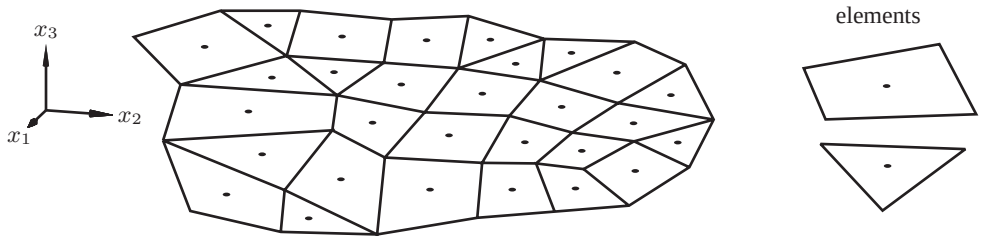

Figure 4–7 Surface of a three-dimensional domain discretized into quadrilateral and triangular boundary elements with constant interpolation. The collocation nodes (•) are placed at the centres of the elements.

Evaluation of nonsingular integrals

When a numerical integration by means of a standard Gauss quadrature must be carried out over an element, in which constant interpolation is used for the physical displacement and traction, a mapping into a homogeneous (ξ_1, ξ_2)-coordinate system is necessary, see Fig. 4–8. In the case of the quadrilateral element, the four extreme points of the elements lie at the coordinates

$$\boldsymbol{\xi}_1 = (-1,-1), \quad \boldsymbol{\xi}_2 = (1,-1), \quad \boldsymbol{\xi}_3 = (1,1), \quad \boldsymbol{\xi}_4 = (-1,1). \tag{4–54}$$

Likewise, the three extreme points for the triangular element have the positions

$$\boldsymbol{\xi}_1 = (1,0), \quad \boldsymbol{\xi}_2 = (0,1), \quad \boldsymbol{\xi}_3 = (0,0). \tag{4–55}$$

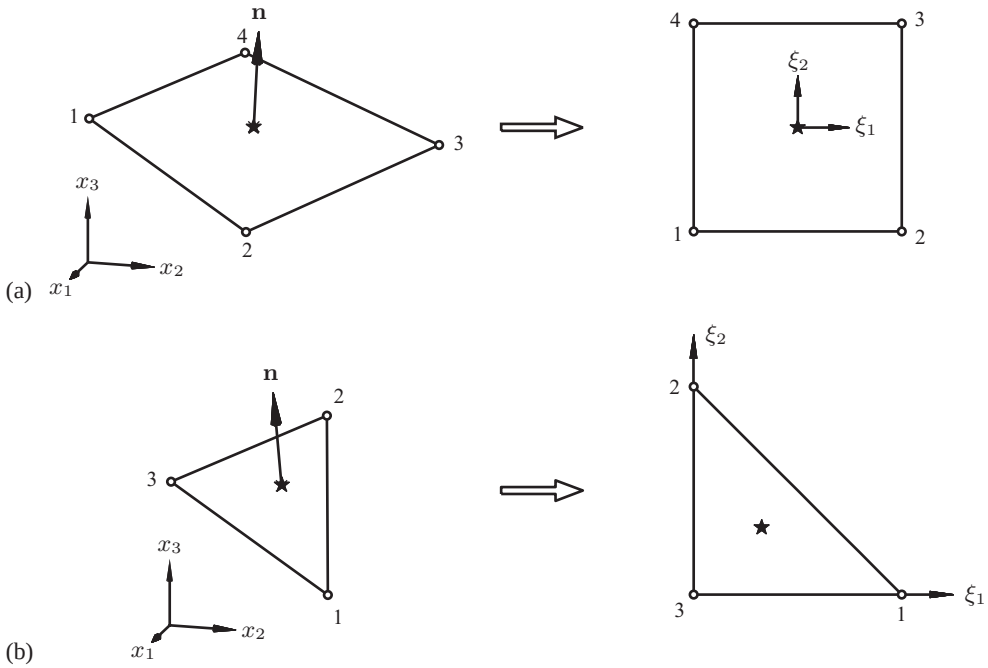

Figure 4–8 Mapping from global Cartesian coordinates into local homogeneous coordinates for constant elements. The extreme points are indicated with circles (○), while the collocation nodes are marked with stars (⋆).

The coordinates in the physical space are found as

$$\mathbf{x} = \begin{bmatrix} \phi_1 & 0 & 0 & \phi_2 & 0 & 0 & \cdots & \phi_n & 0 & 0 \\ 0 & \phi_1 & 0 & 0 & \phi_2 & 0 & \cdots & 0 & \phi_n & 0 \\ 0 & 0 & \phi_1 & 0 & 0 & \phi_2 & \cdots & 0 & 0 & \phi_n \end{bmatrix} \begin{bmatrix} x_1^{(1)} \\ x_2^{(1)} \\ x_3^{(1)} \\ x_1^{(2)} \\ x_2^{(2)} \\ x_3^{(2)} \\ \vdots \\ x_1^{(n)} \\ x_2^{(n)} \\ x_3^{(n)} \end{bmatrix}_j = \mathbf{\Phi}(\xi)\mathbf{x}_j(\omega), \tag{4–56}$$

where n is the number of extreme points in an element, *i.e.* 3 or 4 depending on whether a triangular or a quadrilateral element is considered. Actually, when constant interpolation is used for the field quantities, linear interpolation is used for the geometry. With the local coordinates defined in Fig. 4–8, the linear shape functions for a quadrilateral element are:

$$\phi_1(\xi_1, \xi_2) = \frac{1}{4}(1 - \xi_1)(1 - \xi_2), \qquad \phi_2(\xi_1, \xi_2) = \frac{1}{4}(1 + \xi_1)(1 - \xi_2), \tag{4–57a}$$

$$\phi_3(\xi_1,\xi_2) = \frac{1}{4}(1+\xi_1)(1+\xi_2), \qquad \phi_4(\xi_1,\xi_2) = \frac{1}{4}(1-\xi_1)(1+\xi_2), \tag{4–57b}$$

and the shape functions for a triangular element are:

$$\phi_1(\xi_1,\xi_2) = \xi_1, \qquad \phi_2(\xi_1,\xi_2) = \xi_2, \qquad \phi_3(\xi_1,\xi_2) = 1-\xi_1-\xi_2 = \xi_3, \tag{4–58}$$

where ξ_3 is a dependent coordinate that has only been introduced for convenience.

The mapping into the local homogeneous coordinate system means that a differential area of the element surface is evaluated as

$$\mathrm{d}\Gamma(\mathbf{x}) = \left|\frac{\partial \mathbf{r}}{\partial \xi_1} \times \frac{\partial \mathbf{r}}{\partial \xi_2}\right| \mathrm{d}\xi_1 \mathrm{d}\xi_2 = |\mathbf{J}| \mathrm{d}\xi_1 \mathrm{d}\xi_2, \qquad \mathbf{r} = [x_1 \;\; x_2 \;\; x_3]^T, \tag{4–59}$$

where $\mathbf{J}$ is the reduced Jacobian of the mapping and $|\mathbf{J}|$ is its magnitude, which is actually equal to the length of the normal vector (not the unit outward normal) at the point $\mathbf{x}$. After a bit of work, the following results is obtained:

$$\mathbf{J} = \begin{bmatrix} \mathbf{x}_{j,2}^T \left[\mathbf{Q} - \mathbf{Q}^T\right] \mathbf{x}_{j,3} \\ \mathbf{x}_{j,3}^T \left[\mathbf{Q} - \mathbf{Q}^T\right] \mathbf{x}_{j,1} \\ \mathbf{x}_{j,1}^T \left[\mathbf{Q} - \mathbf{Q}^T\right] \mathbf{x}_{j,2} \end{bmatrix}, \quad \mathbf{Q} = \begin{bmatrix} Q_{11} & Q_{12} & \cdots & Q_{1n} \\ Q_{21} & Q_{22} & \cdots & Q_{2n} \\ \vdots & \vdots & \ddots & \vdots \\ Q_{n1} & Q_{n2} & \cdots & Q_{nn} \end{bmatrix}, \quad Q_{ik} = \frac{\partial \phi_i}{\partial \xi_1}\frac{\partial \phi_k}{\partial \xi_2}, \tag{4–60}$$

where $\mathbf{x}_{j,m}$, $m = 1,2,3$, are three vectors of length n storing the Cartesian coordinates for the extreme points of element j. Subsequently, the integrals over the element surfaces become

$$\hat{\mathbf{H}}_{ij} = \int_{\xi_1}\int_{\xi_2} \mathbf{P}^*(\mathbf{x}_i,\omega;\mathbf{y}(\boldsymbol{\xi}))|\mathbf{J}|\mathrm{d}\xi_2\mathrm{d}\xi_1, \quad \mathbf{G}_{ij} = \int_{\xi_1}\int_{\xi_2} \mathbf{U}^*(\mathbf{x}_i,\omega;\mathbf{y}(\boldsymbol{\xi}))|\mathbf{J}|\mathrm{d}\xi_2\mathrm{d}\xi_1, \tag{4–61}$$

where $\boldsymbol{\xi} = [\xi_1 \;\; \xi_2]^T$. In particular, for a quadrilateral element, the integration limits become $\xi_1 \in [-1,1]$, $\xi_2 \in [-1,1]$, while the integration limits for the triangular element are $\xi_1 \in [0,1]$, $\xi_2 \in [0, 1-\xi_1]$, where it is assumed that the integration in the ξ_2-direction is carried out before the integration in the ξ_1-direction as indicated by Eq. (4–61).

It is noted that in three-dimensional BEM codes for elastodynamics, the Green's functions in the frequency domain include the exponential function. In contrast to the modified Bessel functions, the exponential function is generally computed with satisfactory accuracy in most programming languages.

Evaluation of singular integrals

As it was also the case in two dimensions, the singular terms of the traction Green's function vanish in the three-dimensional model with constant elements. This is due to the fact that each collocation node lies on a flat part of the surface, and therefore the normal derivative of the distance vector $\mathbf{r}$ to an integration point is zero on the entire element. Consequently, $\mathbf{H}_{ii} = \frac{1}{2}\mathbf{I}$ for all nodes, where $\mathbf{I}$ is the identity matrix of dimension 3.

Contrarily, the singularities of the fundamental solution for the displacement do not cancel out. Thus, with reference to Eq. (3–45), a singularity of the order $1/r$ has to be treated. In Section 4.3.2 a method of dealing with the singularities is presented, in which a standard Gauss quadrature rule may be used for the integration.

4.3.2 Quadratic boundary elements in three dimensions

Rather than going through the theory for constant elements in three-dimensional elastodynamics and quadratic elements for three-dimensional acoustics, we shall skip directly to quadratic elements for three-dimensional elastodynamics.

The frequency-domain Green's function for the propagation of waves in the elastic full space was derived in Section 3.3.2 and, by a slightly different approach, in Example 1.6. Instead of applying Eq. (3–45) directly as it is, we shall write the the fundamental solutions for the displacement and the traction in three-dimensional elastodynamics is a form similar to Eqs. (3–55) and (4–26a) for the plane strain, *i.e.*

$$U_{il}^{*}(\mathbf{x},\omega;\mathbf{y}) = \frac{1}{4\pi\rho c_S^2}\left(\alpha\delta_{il} - \beta\frac{\partial r}{\partial x_i}\frac{\partial r}{\partial x_l}\right), \tag{4–62a}$$

$$P_{il}^{*}(\mathbf{x},\omega;\mathbf{y}) = \frac{1}{4\pi}\left[\left(\frac{c_P^2}{c_S^2}-2\right)\left(\frac{\partial\alpha}{\partial r}-\frac{\partial\beta}{\partial r}-\frac{2\beta}{r}\right)\frac{\partial r}{\partial x_l}n_i(\mathbf{x}) + \frac{\partial\alpha}{\partial r}\left(\frac{\partial r}{\partial x_i}n_l(\mathbf{x})+\frac{\partial r}{\partial n}\delta_{il}\right)\right.$$
$$\left. -\frac{\beta}{r}\left(\frac{\partial r}{\partial x_i}n_l(\mathbf{x})+\frac{\partial r}{\partial n}\delta_{il}+2\frac{\partial r}{\partial x_l}n_i(\mathbf{x})-4\frac{\partial r}{\partial x_i}\frac{\partial r}{\partial x_l}\frac{\partial r}{\partial n}\right)-2\frac{\partial\beta}{\partial r}\frac{\partial r}{\partial x_i}\frac{\partial r}{\partial x_l}\frac{\partial r}{\partial n}\right]. \tag{4–62b}$$

where

$$\alpha = \left(\frac{1}{r}+\frac{1}{\mathrm{i}k_S r^2}-\frac{1}{k_S^2 r^3}\right)\mathrm{e}^{-\mathrm{i}k_S r} - \frac{c_S^2}{c_P^2}\left(\frac{1}{\mathrm{i}k_P r^2}-\frac{1}{k_P^2 r^3}\right)\mathrm{e}^{-\mathrm{i}k_P r}, \tag{4–62c}$$

$$\beta = \left(\frac{1}{r}+\frac{3}{\mathrm{i}k_S r^2}-\frac{3}{k_S^2 r^3}\right)\mathrm{e}^{-\mathrm{i}k_S r} - \frac{c_S^2}{c_P^2}\left(\frac{1}{r}+\frac{3}{\mathrm{i}k_P r^2}-\frac{3}{k_P^2 r^3}\right)\mathrm{e}^{-\mathrm{i}k_P r}, \tag{4–62d}$$

$$\frac{\partial\alpha}{\partial r} = \left(-\frac{\mathrm{i}k_S}{r}-\frac{2}{r^2}-\frac{3}{\mathrm{i}k_S r^3}+\frac{3}{k_S^2 r^4}\right)\mathrm{e}^{-\mathrm{i}k_S r} + \frac{c_S^2}{c_P^2}\left(\frac{1}{r^2}+\frac{3}{\mathrm{i}k_P r^3}-\frac{3}{k_P^2 r^4}\right)\mathrm{e}^{-\mathrm{i}k_P r}, \tag{4–62e}$$

$$\frac{\partial\beta}{\partial r} = \left(-\frac{\mathrm{i}k_S}{r}-\frac{4}{r^2}-\frac{9}{\mathrm{i}k_S r^3}+\frac{9}{k_S^2 r^4}\right)\mathrm{e}^{-\mathrm{i}k_S r} + \frac{c_S^2}{c_P^2}\left(\frac{\mathrm{i}k_P}{r}+\frac{4}{r^2}+\frac{9}{\mathrm{i}k_P r^3}-\frac{9}{k_P^2 r^4}\right)\mathrm{e}^{-\mathrm{i}k_P r}. \tag{4–62f}$$

In the case of quadratic interpolation, the quadrilateral and triangular elements are described by nine and six nodes, respectively, as illustrated in Fig. 4–9. Since the displacement and traction over each element is now weighted between the values at $n = 9$ or $n = 6$ nodes, an interpolation in the form (4–56) introduced for the geometry of the constant element should also be used for $\mathbf{U}(\mathbf{x},\omega)$ and $\mathbf{P}(\mathbf{x},\omega)$. However, the shape functions now refer to the nodes of the element rather than the extreme points.

In the local, homogeneous coordinate system, see Fig. 4–9a, the shape functions related to each of the nodes in the quadrilateral element are:

$$\phi_1 = \frac{1}{4}\left(\xi_1^2-\xi_1\right)\left(\xi_2^2-\xi_2\right),\ \phi_2 = \frac{1}{2}\left(1-\xi_1^2\right)\left(\xi_2^2-\xi_2\right),\quad \phi_3 = \frac{1}{4}\left(\xi_1+\xi_1^2\right)\left(\xi_2^2-\xi_2\right),$$
$$\phi_4 = \frac{1}{2}\left(\xi_1+\xi_1^2\right)\left(1-\xi_2^2\right),\quad \phi_5 = \frac{1}{4}\left(\xi_1+\xi_1^2\right)\left(\xi_2+\xi_2^2\right),\ \phi_6 = \frac{1}{2}\left(1-\xi_1^2\right)\left(\xi_2+\xi_2^2\right),$$
$$\phi_7 = \frac{1}{4}\left(\xi_1^2-\xi_1\right)\left(\xi_2+\xi_2^2\right),\ \phi_8 = \frac{1}{2}\left(\xi_1^2-\xi_1\right)\left(1-\xi_2^2\right),\quad \phi_9 = \left(1-\xi_1^2\right)\left(1-\xi_2^2\right). \tag{4–63}$$

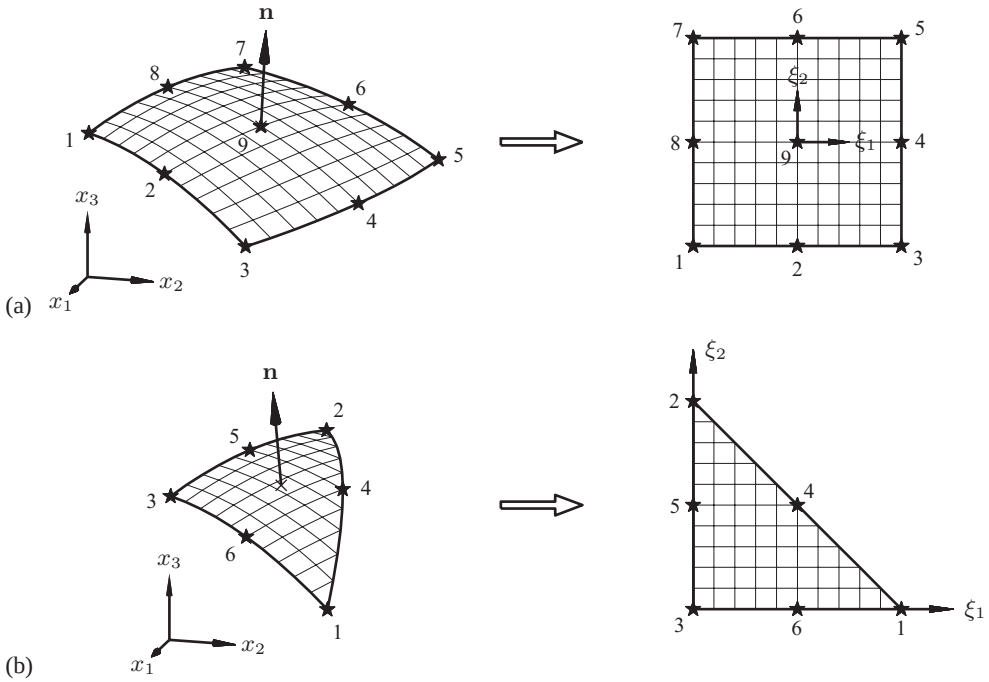

Figure 4–9 Mapping from three-dimensional Cartesian coordinate space (x_1, x_2, x_3) into plane local coordinates (ξ_1, ξ_2): (a) nine-noded quadrilateral element with biquadratic interpolation, (b) six-noded triangular element with quadratic interpolation. The normal vectors $\mathbf{n}$ are pointing out from the domain.

Similarly, for the triangular elements the six quadratic shape functions are defined for a local plane coordinate system as illustrated in Fig. 4–9b. The six shape functions are:

$$\begin{aligned} &\phi_1 = \xi_1\left(2\xi_1 - 1\right), \quad \phi_2 = \xi_2\left(2\xi_2 - 1\right), \quad \phi_3 = \xi_3\left(2\xi_3 - 1\right), \\ &\phi_4 = 4\xi_1\xi_2, \qquad\quad \phi_5 = 4\xi_2\xi_3, \qquad\quad \phi_6 = 4\xi_3\xi_1, \end{aligned} \tag{4–64}$$

where $0 \leqslant \xi_1 \leqslant 1$ and $0 \leqslant \xi_2 \leqslant 1 - \xi_1$. The third local coordinate $\xi_3 = 1 - \xi_1 - \xi_2$ is dependent on the first two coordinates and has been introduced for convenience only.

For the main part of the numerical integration, a six-point Gauss quadrature rule provides results of satisfactory accuracy for the quadrilateral elements, while a total of 16 Gauss points should be used per triangular element. Thus, only small improvements in the numerical integration are achieved if more Gauss points are used; the computation time is however increased dramatically. As usual, when the collocation node is one of the nodes in the element, over which the integration is carried out, the standard integration is not satisfactory as singularities arise in the Green's functions for the displacement and the traction. Therefore, a specialized integration method must be used as will be discussed in the following.

Singularities of the displacement fundamental solution

As mentioned in the previous subsection, the diagonal terms of $\mathbf{G}$ contain *weak singularities* of the kind $1/r$. To carry out the numerical integration using a standard Gauss quadrature over

an element where the collocation node is one of the element nodes, Domínguez (1993) used a coordinate-transformation method proposed by Lachat (1975). The main steps are:

1 The element is divided into a number of triangles, each having one of the corners at the collocation node (see Fig. 4–10). In the case of triangular elements, no subdivision is necessary.

2 The integral over each of the triangles is performed using a standard Gauss quadrature rule over an equivalent *collapsed quadratic element*, but only for the shape function belonging to the element node which is also the collocation node. The technique is further explained below.

3 For all other shape functions, an integration is carried out in the same way that is used for elements, in which the collocation node is not one of the element nodes.

The collapsed quadrilateral elements are quadrilateral elements where two of the corner nodes coincide so that one of the element sides has a length of zero, see Fig. 4–11. When performing the numerical integration over an element with such a geometry, the Jacobian of the mapping will tend to zero with r as $r \to 0$. This zero of the order r cancels out the singularity of the order $1/r$. Hence the accuracy of the Gauss quadrature is satisfactory.

It is clear that a procedure of the same kind is applicable to the boundary element scheme with constant elements. In that case, however, the collocation node can only take the position of the centre node in the quadrilateral element, and thus the subdivision shown in Fig. 4–10c should be used. For the triangular element, the situation is a bit more complicated than in the case of quadratic interpolation, since the collocation node is now placed at the centre of the element. Therefore, a subdivision similar to that of the quadrilateral element is required.

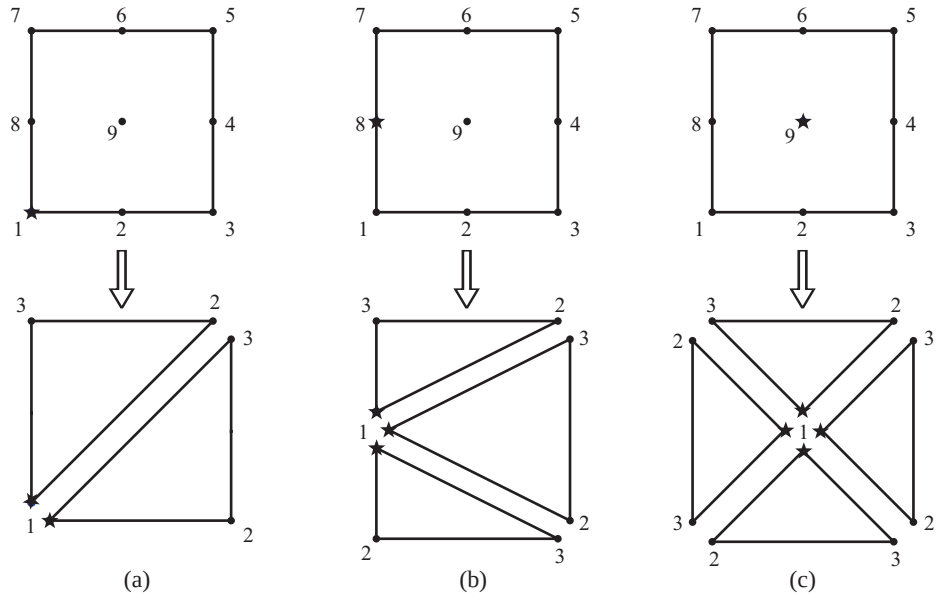

Figure 4–10 Sub-division of a quadrilateral element when (a) the collocation node is at a corner, (b) the collocation node is at a side and (c) the collocation node is at the centre of the element.

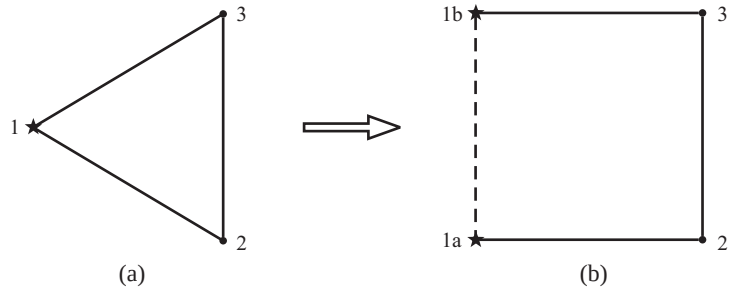

Figure 4–11 Sub-element for integration of $1/r$ singularities: (a) triangular sub-element and (b) equivalent collapsed quadrilateral element.

Singularities of the traction fundamental solution

The traction Green's function contains *strong singularities* of the kind $1/r^2$ when the observation point coincides with the integration point. Therefore the method proposed by Lachat does not provide a means of dealing with the diagonal terms of the matrix $\mathbf{H}$. To treat singularities of higher order than $1/r$ an alternative method has to be used. In the present work, a numerical method is proposed, based on static equilibrium considerations for the surface traction, which normally only apply to closed domains (Domínguez 1993). To generalize the method to cover open domains, in which parts of the boundary are not discretized, a modified version of the *enclosing elements* technique proposed by Ahmad and Banerjee (1988) is developed.

As discussed in Subsections 4.2.3 and 4.2.4, a numerical method may be applied to any closed interior or exterior domain, building on the fact that the singularity in the dynamic frequency domain solution is the same as that of the static solution. Hence, writing the total dynamic Green's function matrix $\hat{\mathbf{H}}$ for the stress as the sum of the static part $\hat{\mathbf{H}}_S$ and the dynamic residue matrix $\mathbf{H}_R$,

$$\hat{\mathbf{H}} = \hat{\mathbf{H}}_S + \mathbf{H}_R, \tag{4–65}$$

only the singularities of the static part $\hat{\mathbf{H}}_S$ need to be treated in a special way. The remainder $\mathbf{H}_R$ may be determined using a standard Gauss quadrature, since it contains no singularities. In the three-dimensional case the rest term is derived by writing the exponential terms of the full elastodynamic solution as series expansions and subtracting the terms corresponding to the elastostatic Green's function (Domínguez 1993).

The three-dimensional elastostatic traction Green's function is the special case of the elastodynamic fundamental solution given by Eq. (4–62b) that is obtained for the frequency $\omega = 0$. After rearranging the terms, the following solution is obtained:

$$P^*_{S\,il}(\mathbf{x},\omega;\mathbf{y}) = -\frac{1}{8\pi\,(1-\nu)}\frac{1}{r^2}\left\{\frac{\partial r}{\partial n}\left((1-2\nu)\,\delta_{il} + 3\frac{\partial r}{\partial x_i}\frac{\partial r}{\partial x_l}\right)\right.$$
$$\left. + (1-2\nu)\left(n_i\frac{\partial r}{\partial x_l} - n_l\frac{\partial r}{\partial x_i}\right)\right\}. \tag{4–66}$$

Here $P^*_{S\,il}(\mathbf{x},\omega;\mathbf{y})$ is expressed in terms of the Poisson ratio ν. The singularity of order $1/r^2$ is obvious in the static Green's function. As the static part $\hat{\mathbf{H}}_S$ is constant, regardless of the

frequency, it may be evaluated once and for all and added to the dynamic residue term $\mathbf{H}_R$, which is calculated for each individual frequency.

For an open domain the method described in Subsections 4.2.3 and 4.2.4 for scalar and vectorial fields, respectively, obviously makes no sense as parts of the boundary are not described in the model. To overcome this problem, Ahmad and Banerjee (1988) proposed that an artificial, enclosing boundary is constructed, merely for the evaluation of the singular diagonal terms of $\mathbf{H}_S$ and the geometry constants. This is plausible because the geometry constants only depend on the local geometry of the surface. This also applies to the singularities of $\hat{\mathbf{H}}_S$ since they arise in the contributions from a node to itself. Hence, any *closed* region which has the correct local geometry for the true surface may be used instead of the original *open* region for the purpose of determining $\mathbf{H}_{S\,ii}$. Any shape of the domain will do for the evaluation of the diagonal terms of $\hat{\mathbf{H}}_S$, given that the following requirements are met:

1 The distance between original elements and new, opposing elements must be at least one element length to ensure sufficient precision. Otherwise singularities may arise in the contributions from new nodes to existing nodes and vice versa.

2 The original geometry is modelled correctly at the nodes, for which the $\mathbf{H}_{S\,ii}$ terms are to be found. In principle this only requires that the elements adjacent to the node in question are taken from the original model.

The first point is a general rule of thumb for BE discretization and hence does not impose any restrictions that are not already there. From the second point, it may be concluded that it is not necessary to model the entire original open region and then add a number of extra elements to establish a single, global closed domain. Instead the terms for each node may be evaluated by creating a small closed domain around that specific node. This method of *local enclosing elements*, which was first proposed by Jones and Thompson (1999) for the two dimensional case, has the following advantages compared to the original fully enclosing elements technique:

- It may be faster/more efficient to find the solution to numerous small systems of equations than to a single big system of equations.
- A local geometry for enclosing elements may easily be established automatically, whereas the construction of an enclosing boundary for the entire domain may require an extensive amount of error checking to ensure that the enclosing elements do not intersect the true surface.
- The method may be applied to closed domains as well as open domains. This simplifies the programming of a general routine to find the $\mathbf{H}_{S\,ii}$ terms.

Several ways to pick out a local part of the entire surface may be suggested. The method implemented in the program BEASTS (Andersen and Jones 2001a) has the following steps:

1 A loop is performed over all nodes, $i = 1, \ldots, N$, disregarding nodes that are not at the corner of an element.

2 The NE_i elements in the original model to which the selected corner node i belongs are identified.

3 A copy of the original elements adjacent to the corner node is offset a distance of approximately one element length in the direction of the inward normal (that is $-\mathbf{n}$).

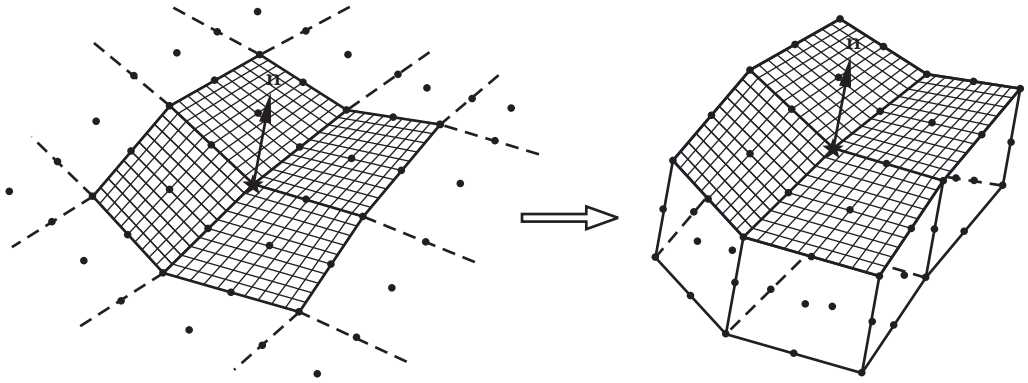

Figure 4–12 Construction of a false surface for a closed local domain. Firstly, a corner node on the original surface is picked (*left*); secondly, the local domain is formed (*right*).

4 The gap between the original surface elements and the copy is filled with NE_i elements, thereby producing a closed domain.

5 $\mathbf{H}_{S\,ii}$ is calculated using Eq. (4–51) for the corner node i and the neighbouring mid-side or centre nodes. These nodes are all on a part of the surface where the geometry is unchanged from the original open domain and will thus be determined correctly.

The method has been illustrated in Fig. 4–12 and the five points in the procedure will be explained in the following.

Ad. 1 Generally corner nodes are identified as nodes that belong to three or more elements. A centre node of a nine-noded quadrilateral element belongs to only one element, and a mid-side node of either a six-noded triangular element or a nine-noded quadrilateral element belongs to two elements. Only at the edge, *i.e.* where the model of the open domain ends, does special care have to be shown.

Ad. 2 When identifying the elements to which the selected node belongs, it should be checked if the node is not a corner node in one/some of the elements. Definitely the node should not be the centre-node of a quadrilateral element, but also it is bad discretization practice to join side-nodes with corner nodes. This would mean that the displacements along the element junctions are inconsistent as the shape functions for corner and side-nodes are not the same.

Ad. 3 By copying the original elements in the direction of the inward normal vector it is assured that the local closed domain is on the correct side of the true surface. When the surface is not flat at the selected corner node, the normal vector at the node is different for each element. To ensure that the projection vector points away from all adjacent elements and into the domain, the projection vector may be taken as a weighted average of the inward normal vectors.

Ad. 4 The distance between the two parts of the local surface consisting of the original NE_i elements and the copy thereof need only be of the same order as the distance across these two surfaces. Hence, one element in the $-\mathbf{n}$ direction should be sufficient to fill in the gap. By experiment it has been shown that adding another "layer" of elements will not improve the accuracy significantly, whereas the calculation time is increased significantly.

Ad. 5 $\mathbf{H}_{S\,ii}$ is determined twice for mid-side nodes, and for centre nodes $\mathbf{H}_{S\,ii}$ may be determined multiple times. To reduce computation time it is advantageous to keep track of nodes which have already been analysed. However, the method described ensures that $\mathbf{H}_{S\,ii}$ is determined for each node at least once.

For some geometries of the surface in the model of the original open domain, the method described above may lead to significant errors in the determination of $\mathbf{H}_{S\,ii}$ and thus in the solution to the entire problem. Generally, to get an accurate solution the following conditions should apply:

- all sides of an element should have lengths of the same order of magnitude,
- contiguous elements must be of similar size,
- the angle between two elements should not be close to 2π,
- only slightly curved elements should be used.

In any case these conditions represent good practice for BE analysis of wave propagation problem. Hence, the fact that the method will only produce accurate results in these circumstances should not cause a difficulty in practice.

As an alternative to the described method, a bigger part of the boundary (*i.e.* more elements) may be picked out at a time, meaning that the local closed domain would consist of more elements and that the $\mathbf{H}_{S\,ii}$ terms would be determined for more nodes simultaneously. However, this would complicate the construction of the false surface since a general means of establishing the projection vector cannot be found. Moreover the described method has been tested for several different geometries and has been found to work satisfactorily.

4.4 Coupling of boundary and finite element domains

This section describes how multiple boundary element domains and a finite element region may be coupled to form a global system of equations representing the entire model for a given frequency. The coupling is established on the basis of continuity of the displacement and equilibrium of the forces at the interfaces. The main problem in performing the coupling of a boundary element domain and finite element domain is that the forces at the interface in the boundary-element method are described in terms of *tractions* distributed over the element surface, whereas a description in terms of *nodal forces* is used in the finite element method. This leads to three approaches to the coupling of BE and FE matrices. In any case the nodes of the neighbouring BE and/or FE sub-domains are assumed to coincide, see Fig. 4–13.

1 The coupling may be carried out in the finite element sense by transforming each of the boundary element domains to a *macro finite element*, *i.e.* a large multi-noded finite element. An equivalent dynamic finite element stiffness matrix is derived from the BE system matrices $\mathbf{G}_{ibed}$ and $\mathbf{H}_{ibed}$, and the surface tractions are transformed into nodal forces.

2 The coupling may be carried out on the basis of equilibrium of the tractions on the interfaces. For this purpose, the FE dynamic stiffness matrix must be transformed to one in terms of tractions on the boundary.

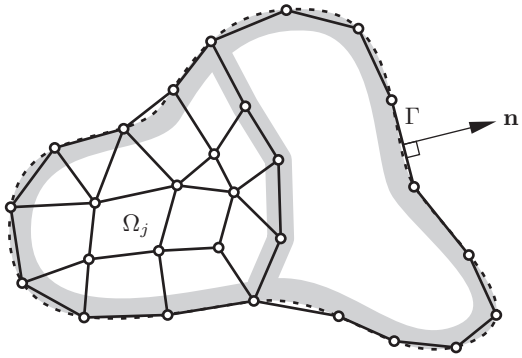

Figure 4–13 Coupled boundary element–finite element model.

3 The coupling may be carried out as an iterative process, in which the interaction forces or tractions are kept in their original form in the FE and BE parts of the model. An iteration is then performed until a satisfactory equilibrium of the boundary forces is reached.

The first of these options seems to be the most popular. This may be due to the fact that it allows the resulting dynamic stiffness matrices for the individual BE domains to be coupled in the finite element sense and for the response of the whole model to applied nodal forces to be calculated. The method is described in Subsection 4.4.1. The second approach has computational advantages but does not provide a simple means of dealing with the problem of coupling at points where the implied tractions are discontinuous. The third method, *i.e.* the iterative coupling procedure, may be efficient for the coupling of a single BE domain with an FE region. However, a generalization of the method to multi-domain BE–FE may be inconvenient. A further argumentation is given below.

4.4.1 Coupling in a finite-element sense

In the time domain, the work done by the surface tractions $\mathbf{p}(\mathbf{x},t)$ at a part Γ_p of the boundary in applying a virtual displacement field $\delta\mathbf{u}(\mathbf{x},t)$ is given as

$$\delta w = \int_{\Gamma_p} \{\delta\mathbf{u}(\mathbf{x},t)\}^T \mathbf{p}(\mathbf{x},t)\mathrm{d}\Gamma. \tag{4–67}$$

The vectors describing the traction and virtual displacement fields are column vectors with the three components $p_j(\mathbf{x},t)$ and $u_j(\mathbf{x},t)$, $j=1,2,3$, respectively.

Consider a single finite, or boundary, element on which tractions are applied at the boundary $\Gamma_j \in \Gamma_p$. The nodal displacements and tractions may be stacked in two column vectors $\mathbf{u}_j(t)$ and $\mathbf{p}_j(t)$. Using the element shape functions to interpolate the displacements and the tractions, the field quantities at any point on the element surface become $\mathbf{u}(\mathbf{x},t) = \mathbf{\Phi}_j(\mathbf{x})\mathbf{u}_j(t)$ and $\mathbf{p}(\mathbf{x},t) = \mathbf{\Phi}_j(\mathbf{x})\mathbf{p}_j(t)$, respectively. Thus the work done for element j may be written

$$\delta w_j = \{\delta\mathbf{u}_j(t)\}^T \int_{\Gamma_j} \{\mathbf{\Phi}_j(\mathbf{x})\}^T \mathbf{\Phi}_j(\mathbf{x})\mathrm{d}\Gamma\, \mathbf{p}_j(t). \tag{4–68}$$

The work done by the surface tractions is equal to the work done by the equivalent nodal forces $\mathbf{f}_j(t)$ that would imply the same virtual displacement values, $\delta\mathbf{u}_j(t)$, at the nodes, that is,

$$\delta w_j = \{\delta\mathbf{u}_j(t)\}^T \mathbf{f}_j(t). \tag{4–69}$$

Combining Eqs. (4–68) and (4–69), the following relationship is derived,

$$\mathbf{f}_j(t) = \int_{\Gamma_j} \{\mathbf{\Phi}_j(\mathbf{x})\}^T \mathbf{\Phi}_j(\mathbf{x}) \mathrm{d}\Gamma\, \mathbf{p}_j(t). \tag{4–70}$$

This provides a matrix expression where the shape functions are used to transform the surface tractions $\mathbf{p}_j(t)$ on element j into the equivalent nodal forces $\mathbf{f}_j(t)$. In the frequency domain the transformation process becomes

$$\mathbf{F}_j(\omega) = \int_{\Gamma_j} \{\mathbf{\Phi}_j(\mathbf{x})\}^T \mathbf{\Phi}_j(\mathbf{x}) \mathrm{d}\Gamma\, \mathbf{P}_j(\omega), \tag{4–71}$$

where $\mathbf{F}_j(\omega)$ and $\mathbf{P}_j(\omega)$ are the complex amplitudes of the nodal forces and tractions, respectively.

Calculating the element transformation matrices represented by the integral in Eq. (4–71) for all elements $j = 1, 2, \ldots, J$ in BE domain $ibed$ and assembling them into a global system for the domain yields a transformation matrix $\mathbf{T}_{ibed}$ such that

$$\mathbf{F}_{ibed} = \mathbf{T}_{ibed}\mathbf{P}_{ibed}. \tag{4–72}$$

Here $\mathbf{F}_{ibed}$ is a vector of nodal forces equivalent to the nodal tractions $\mathbf{P}_{ibed}$ applied on the domain. The dimension of the system (*i.e.* the number of rows in $\mathbf{F}_{ibed}$, $\mathbf{T}_{ibed}$ and $\mathbf{P}_{ibed}$ as well as the number of columns in $\mathbf{T}_{ibed}$) is equal to the number of degrees of freedom in the domain. For a three-dimensional, elastodynamic BE domain that is three times the number of nodes in the domain. The transformation matrix $\mathbf{T}_{ibed}$ is sparse. Due to the nature of the element shape function matrices $\mathbf{\Phi}_j$ two out of three components are in all cases equal to zero, and furthermore only parts of the matrix $\mathbf{T}_{ibed}$ that belong to nodes of the same element will be filled.

Now consider the frequency-domain boundary element equation for a single domain, *i.e.* Eq. (4–7) with subscript $ibed$ on each of the matrices and vectors. Premultiplication with the matrix $\mathbf{T}_{ibed}\{\mathbf{G}_{ibed}\}^{-1}$ leads to the formulation

$$\left[\mathbf{T}_{ibed}\{\mathbf{G}_{ibed}\}^{-1}\mathbf{H}_{ibed}\right]\mathbf{U}_{ibed} = \mathbf{T}_{ibed}\mathbf{P}_{ibed} = \mathbf{F}_{ibed}. \tag{4–73}$$

This defines $\left[\mathbf{T}_{ibed}\{\mathbf{G}_{ibed}\}^{-1}\mathbf{H}_{ibed}\right] = \mathbf{K}_{ibed}$ as the dynamic stiffness matrix for boundary element domain $ibed$. The matrix $\mathbf{K}_{ibed}$ relates the nodal displacements to the nodal forces applied to the domain instead of the nodal tractions, as is the case in the original BE formulation. For a number of BE domains the $ibed = 1, 2, \ldots, nbed$ stiffness matrices $\mathbf{K}_{ibed}$ may therefore be assembled in the FE sense along with any finite elements into a global stiffness matrix $\mathbf{K}$ representing the entire model.

As already mentioned, the present transformation method turns each boundary element domain into a kind of macro finite element, that is a finite element with as many nodes as are used in the BE domain. Since the Green's functions are used as weighting functions, all degrees of freedom in the individual BE domains are coupled, meaning that the matrices $\mathbf{K}_{ibed}$ are full.

However, the global system matrix $\mathbf{K}$ will only have a limited bandwidth, as is common for FE matrices, given that only some of the nodes are coupled at the interface.

Another thing worth mentioning is that the BE stiffness matrices produced in this way do not have the usual FE property of symmetry, which is a disadvantage with respect to memory storage space. Mustoe (1980) suggested a method by which a symmetric boundary element stiffness matrix can be produced. The method is however slightly more complicated than the method presented in this section, and furthermore the inversion of a matrix twice the size of $\mathbf{K}_{ibed}$ has to be carried out. This is a major disadvantage as inverting the $\mathbf{G}_{ibed}$ matrix is already a time consuming process.

Tullberg and Bolteus (1982) conducted a study of seven different stiffness matrices for a BE domain, including the original non-symmetric stiffness matrix and six symmetric matrices. The main conclusions from their study is:

1 The direct non-symmetric stiffness matrix, *i.e.* the matrix derived above, is the best in terms of accuracy.

2 The direct non-symmetric stiffness matrix is as good as, or better than, a stiffness matrix based on a finite element discretization with the same number of degrees of freedom. The same conclusion was drawn by Jones *et al.* (1999).

3 The manipulated methods involving symmetric matrices show a very poor rate of convergence compared to the direct BE.

Therefore it is advisable to implement the non-symmetric stiffness matrix, the derivation of which has been given in this section, in a BEM code.

4.4.2 Coupling in a boundary-element sense

Instead of transforming the BE system matrices to an equivalent FE stiffness matrix and performing the coupling in a finite element sense, the boundary element method formulation may be used. This means that equilibrium of the tractions has to be ensured on the interface, rather than equilibrium of nodal forces. For a coupling with finite elements, this implies that a reformulation of the FE system matrices has to be carried out, but even for a pure BE model problems arise in this method as will be described in the next subsection.

First, consider a single boundary element domain, $ibed$. Reordering the rows and columns into components belonging to the interface (superscript I) and the rest of the domain (superscript R) the matrix equation (4–7) takes the form

$$\begin{bmatrix} \mathbf{H}_{ibed}^{RR} & \mathbf{H}_{ibed}^{RI} \\ \mathbf{H}_{ibed}^{IR} & \mathbf{H}_{ibed}^{II} \end{bmatrix} \begin{bmatrix} \mathbf{U}_{ibed}^{R} \\ \mathbf{U}_{ibed}^{I} \end{bmatrix} = \begin{bmatrix} \mathbf{G}_{ibed}^{RR} & \mathbf{G}_{ibed}^{RI} \\ \mathbf{G}_{ibed}^{IR} & \mathbf{G}_{ibed}^{II} \end{bmatrix} \begin{bmatrix} \mathbf{P}_{ibed}^{R} \\ \mathbf{P}_{ibed}^{I} \end{bmatrix}. \tag{4–74}$$

Next, for a finite element domain, similarly the system of equations becomes

$$\begin{bmatrix} \mathbf{K}_{FE}^{RR} & \mathbf{K}_{FE}^{RI} \\ \mathbf{K}_{FE}^{IR} & \mathbf{K}_{FE}^{II} \end{bmatrix} \begin{bmatrix} \mathbf{U}_{FE}^{R} \\ \mathbf{U}_{FE}^{I} \end{bmatrix} = \begin{bmatrix} \mathbf{F}_{FE}^{R} \\ \mathbf{F}_{FE}^{I} \end{bmatrix} = \begin{bmatrix} \mathbf{T}_{FE}^{RR} & \mathbf{T}_{FE}^{RI} \\ \mathbf{T}_{FE}^{IR} & \mathbf{T}_{FE}^{II} \end{bmatrix} \begin{bmatrix} \mathbf{P}_{FE}^{R} \\ \mathbf{P}_{FE}^{I} \end{bmatrix}, \tag{4–75}$$

where the transformation matrix $\mathbf{T}_{FE}$ has been defined on the finite element domain.

The conditions of continuity of the displacements and equilibrium of the tractions at the interface between the BE and FE domains are now satisfied by

$$\mathbf{U}^I_{ibed} = \mathbf{U}^I_{FE} = \mathbf{U}^I, \quad \mathbf{P}^I_{ibed} = -\mathbf{P}^I_{FE} = \mathbf{P}^I. \tag{4–76}$$

Thus, Equations (4–74) and (4–75) can be rearranged in the forms,

$$\begin{bmatrix} \mathbf{H}^{RR}_{ibed} & \mathbf{H}^{RI}_{ibed} & -\mathbf{G}^{RI}_{ibed} \\ \mathbf{H}^{IR}_{ibed} & \mathbf{H}^{II}_{ibed} & -\mathbf{G}^{II}_{ibed} \end{bmatrix} \begin{bmatrix} \mathbf{U}^R_{ibed} \\ \mathbf{U}^I \\ \mathbf{P}^I \end{bmatrix} = \begin{bmatrix} \mathbf{G}^{RR}_{ibed} \\ \mathbf{G}^{IR}_{ibed} \end{bmatrix} \left[\mathbf{P}^R_{ibed} \right], \tag{4–77}$$

$$\begin{bmatrix} \mathbf{K}^{RR}_{FE} & \mathbf{K}^{RI}_{FE} & \mathbf{T}^{RI}_{FE} \\ \mathbf{K}^{IR}_{FE} & \mathbf{K}^{II}_{FE} & \mathbf{T}^{II}_{FE} \end{bmatrix} \begin{bmatrix} \mathbf{U}^R_{FE} \\ \mathbf{U}^I \\ \mathbf{P}^I \end{bmatrix} = \begin{bmatrix} \mathbf{T}^{RR}_{FE} \\ \mathbf{T}^{IR}_{FE} \end{bmatrix} \left[\mathbf{P}^R_{FE} \right], \tag{4–78}$$

which may eventually be written together to form one single matrix equation,

$$\underset{(N_F+N_B)\times(N_F+N_B)}{\begin{bmatrix} \mathbf{H}^{RR}_{ibed} & \mathbf{H}^{RI}_{ibed} & -\mathbf{G}^{RI}_{ibed} & \mathbf{0} \\ \mathbf{H}^{IR}_{ibed} & \mathbf{H}^{II}_{ibed} & -\mathbf{G}^{II}_{ibed} & \mathbf{0} \\ \mathbf{0} & \mathbf{K}^{RI}_{FE} & \mathbf{T}^{RI}_{FE} & \mathbf{K}^{RR}_{FE} \\ \mathbf{0} & \mathbf{K}^{II}_{FE} & \mathbf{T}^{II}_{FE} & \mathbf{K}^{IR}_{FE} \end{bmatrix}} \begin{bmatrix} \mathbf{U}^R_{ibed} \\ \mathbf{U}^I \\ \mathbf{P}^I \\ \mathbf{U}^R_{FE} \end{bmatrix} = \underset{(N_F+N_B)\times(N_F^R+N_B^R)}{\begin{bmatrix} \mathbf{G}^{RR}_{ibed} & \mathbf{0} \\ \mathbf{G}^{IR}_{ibed} & \mathbf{0} \\ \mathbf{0} & \mathbf{T}^{RR}_{FE} \\ \mathbf{0} & \mathbf{T}^{IR}_{FE} \end{bmatrix}} \begin{bmatrix} \mathbf{P}^R_{ibed} \\ \mathbf{P}^R_{FE} \end{bmatrix}. \tag{4–79}$$

The first column of matrices on the left hand side consists of terms from the BE domain only, the second and third column consist of terms for the interface part of both domains and the fourth column has terms which solely relate the displacements and tractions in the FE domain to one another. The dimensions of the matrices on the left and right hand sides of the equation are indicated using the symbols N_F, N_B, N_F^R and N_B^R, to represent the number of degrees of freedom of the finite element domain, of the boundary element domain, of the non-interface part of the finite element domain and the non-interface part of the boundary element domain, respectively. If the tractions are known (notice that tractions may not be applied at the interface) Eq. (4–79) may be solved to find the displacements.

4.4.3 Iterative coupling

Alternatively to any of the methods described in the previous subsections, Elleithy *et al.* (2001) proposed the use of an iterative coupling procedure having the following steps:

1 Initial values of the displacements at the common interface are set.

2 The equations for the boundary element domain are solved in order to find the interface traction.

3 The traction at the interface is converted to nodal forces and the equations for the finite element region are solved to find the interface displacements.

4 If the differences between the initial displacements and the displacements found in the FE analysis are below a certain level, convergence has been reached. Otherwise the process is repeated with revised initial values of the interface displacements.

The procedure suggested by Elleithy *et al.* (2001) seems quite awkward, since several iterations may be necessary before convergence is achieved. However, no inversion of the BE system matrices is involved, and the system matrices for the BE domain and the FE region may be stored separately. This, combined with the fact that two smaller systems of equations are solved in stead of one larger system of equations, is an advantage in terms of memory consumption and, possibly, computation time. The main drawback of the technique is that a generalization to the analysis of problems involving multiple BE domains may be unattractive, since the equilibrium of tractions has to be reached simultaneous for multiple interfaces between the individual domains, but only a single interface can be treated at a time. Thus the iterative process for the global system may become very time consuming.

4.4.4 Discussion of coupling method

The equivalent BE matrix method has been developed for the case of coupling a single FE and single BE domain (Subsection 4.4.2). The complexity in implementing the method in a computer program is greater where an arbitrary number of boundary element domains is involved. So is the required effort in data preparation, since the interface and non-interface nodes of the FE and BE domains must be identified, and the matrices repartitioned to introduce each new domain.

The BE matrix method has the advantage over the FE matrix, or equivalent-nodal-forces, method that there is no matrix inversion involved in producing the global system of equations. This is the step (Eq. (4–73)) which, for most practical problems, takes the greatest amount of computing time. Thus, for problems involving a single BE domain with almost as many degrees of freedom as the global system, the solution time may be doubled. The equivalent BE matrix method is therefore considerably more time efficient. However from Eq. (4–79), it is seen that the equivalent BE matrix method requires more computer array storage space and thus is less memory efficient. It also carries the minor disbenefit that tractions cannot be applied at the interfaces of the domains.

No method has been developed here to solve the problem of discontinuous tractions in the BE coupling method. One way to overcome this problem is to define multiple coincident nodes where the discontinuities are present, hereby adding extra degrees of freedom to the global system of equations. Alternatively extra equations may be implemented to ensure equilibrium of the surface tractions (Stamos and Beskos 1995).

For a coupling with FE regions, extra terms would have to be derived. Mustoe (1980) outlines four methods of dealing with this problem in two dimensions. This would add considerable complexity to the implementation of this method as well as its use. The method of expressing the BE matrices in terms of nodal forces on a finite element basis avoids having to allow for traction discontinuities at corners as well as at any point on smooth parts of the surface of the boundary element domains. It has been found that this does not generate erroneous results compared to those obtained by a pure BE scheme where discontinuous tractions are allowed (Andersen 2002).

Finally, a judgement also arises as to whether it is preferable to apply the loads in terms of tractions over finite areas of boundary element (or finite element) surfaces or if it is more convenient to specify the load in terms of nodal forces.

Regarding the iterative process, it seems unlikely that a method of coupling multiple boundary element domains and finite element regions can be formulated in a simple manner, which provides an efficient coupling in terms of computation time. The reasons given above may explain why the coupling in a finite element sense is usually preferred.

4.5 Boundary element analysis of symmetric structures

Many problems of wave propagation through soil and solids involve structures and layered ground that have at least one plane of geometric symmetry. Examples include tunnels, tracks and many types of foundations. When the geometry is symmetric the load and the corresponding response may, in any case, be split into a symmetric and an antisymmetric part. The total displacements may then be found as a linear combination of the displacements obtained by the two analyses involving, respectively:

1 symmetry of the load and response around the plane of geometric symmetry,

2 antisymmetry of the load and response around the plane of geometric symmetry.

Since the size of the system matrices depends on the number of degrees of freedom squared, the demand for computer memory is quartered when a symmetric description is used. Furthermore it is often much faster to make the two analyses for the reduced system than one analysis for the original (the full) system. Naturally, if the load is purely symmetric/antisymmetric the benefit from a symmetric description is even more pronounced.

In a finite element scheme only half the model needs to be analysed when a plane of symmetry exists. Usually the degrees of freedom which are known to be zero at the plane of symmetry are eliminated in the system of equations to satisfy the conditions at the interface between the modelled and the non-modelled part. Alternatively a very high stiffness (orders of magnitude higher than the average stiffness of the system) may be applied for those degrees of freedom so that the displacements here become insignificant relative to the displacements elsewhere. The second approach has the advantage that no reordering of the degrees of freedom is necessary. However, it is not physically correct, and numerically the first method is more efficient.

The introduction of a plane of symmetry in a boundary element scheme is slightly more complicated than the implementation in a finite element scheme. One way to proceed is to discretize the plane of symmetry so that the conditions that apply here can be introduced in the same way as it is usually done in a FE scheme. However, this implies the introduction of degrees of freedom that are not present in the original model. Thus the results may be less accurate and, depending on the geometry of the model, there may be no or only a little net reduction of the number of unknowns in the system of equations. Especially, if a half-space is considered, only half the surface has to be discretized. However, the interface at the plane of symmetry has to be discretized a similar distance into the soil to obtain the same degree of accuracy in the model, see Fig. 4–14.

Instead, a method has to be developed where a discretization of the plane of symmetry is not necessary. For that purpose, consider the original BE system of equations for a single domain with identical, but mirrored discretizations of the surface on either side of the plane of geometrical symmetry $x_2 = 0$,

$$\begin{bmatrix} \mathbf{H}^{++} & \mathbf{H}^{+-} \\ \mathbf{H}^{-+} & \mathbf{H}^{--} \end{bmatrix} \begin{bmatrix} \mathbf{U}^{+} \\ \mathbf{U}^{-} \end{bmatrix} = \begin{bmatrix} \mathbf{G}^{++} & \mathbf{G}^{+-} \\ \mathbf{G}^{-+} & \mathbf{G}^{--} \end{bmatrix} \begin{bmatrix} \mathbf{P}^{+} \\ \mathbf{P}^{-} \end{bmatrix}. \tag{4–80}$$

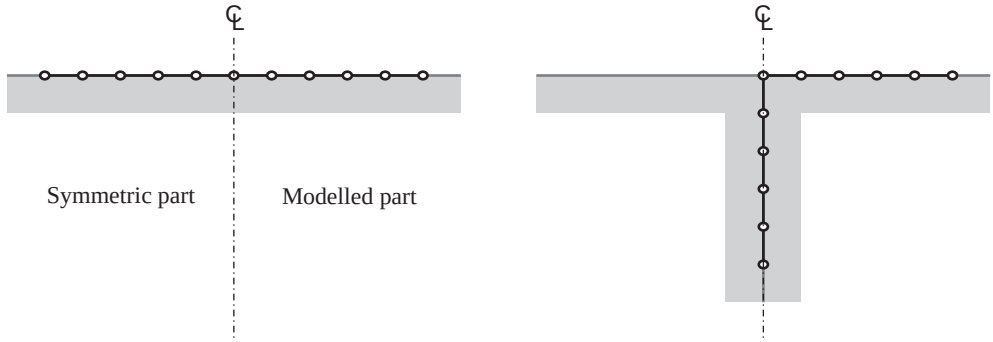

Figure 4–14 Original boundary element model (left) and use of symmetry without loss of accuracy (right).

Superscripts $+$ and $-$ denote terms belonging to the half-spaces defined by $x_2 > 0$ and $x_2 < 0$, respectively. Subsequent superscripts $+-$, for instance, indicate the influence to degrees of freedom at $x_2 > 0$ from degrees of freedom at $x_2 < 0$. It is assumed that all sub-matrices are square (which disallows discontinuous tractions) and that $N/2$ nodes are located on either side of the plane of symmetry.

When the load, and thus also the response, is symmetric around the $x_2 = 0$ plane, the following conditions apply for the displacements and the surface traction:

$$\begin{aligned}
U_1(x_1,-x_2,x_3,\omega) &= U_1(x_1,x_2,x_3,\omega)\,, \quad P_1(x_1,-x_2,x_3,\omega) = P_1(x_1,x_2,x_3,\omega)\,,\\
U_2(x_1,-x_2,x_3,\omega) &= -U_2(x_1,x_2,x_3,\omega)\,, \quad P_2(x_1,-x_2,x_3,\omega) = -P_2(x_1,x_2,x_3,\omega)\,,\\
U_3(x_1,-x_2,x_3,\omega) &= U_3(x_1,x_2,x_3,\omega)\,, \quad P_3(x_1,-x_2,x_3,\omega) = P_3(x_1,x_2,x_3,\omega)\,.
\end{aligned} \tag{4–81}$$

Thus the displacements and tractions in the x_1 and x_3 directions are the same on both sides of the $x_2 = 0$ plane of symmetry, whereas the x_2 components are reflected. The degrees of freedom are now assumed to be ordered so that the "mirror image" of degree of freedom j appears as degree of freedom $j + N/2$. Furthermore rows and columns are reordered so that all x_1 degrees of freedom appear first, and all x_3 degrees of freedom appear last on either side of the $x_2 = 0$ plane. The arrays storing the displacements and tractions for the part of the model located at $x_2 < 0$ may then be written as:

$$\mathbf{U}^- = \mathbf{R}_S\mathbf{U}^+, \quad \mathbf{P}^- = \mathbf{R}_S\mathbf{P}^+, \quad \mathbf{R}_S = \begin{bmatrix} \mathbf{I} & \mathbf{0} & \mathbf{0} \\ \mathbf{0} & -\mathbf{I} & \mathbf{0} \\ \mathbf{0} & \mathbf{0} & \mathbf{I} \end{bmatrix}. \tag{4–82}$$

Here $\mathbf{I}$ is the identity matrix with dimensions $(N/6 \times N/6)$ and $\mathbf{0}$ is the null matrix with the same dimensions. $\mathbf{R}_S$ is denoted *the reflection matrix* for symmetric load/response. In the case of antisymmetric load and response, the reflection matrix becomes

$$\mathbf{R}_A = \begin{bmatrix} -\mathbf{I} & \mathbf{0} & \mathbf{0} \\ \mathbf{0} & \mathbf{I} & \mathbf{0} \\ \mathbf{0} & \mathbf{0} & -\mathbf{I} \end{bmatrix} = -\mathbf{R}_S. \tag{4–83}$$

With the assumed order of the degrees of freedom, the original system of equations may eventually be reduced to:

$$\left(\mathbf{H}^{++} + \mathbf{R}\mathbf{H}^{+-}\right)\mathbf{U}^{+} = \left(\mathbf{G}^{++} + \mathbf{R}\mathbf{G}^{+-}\right)\mathbf{P}^{+}. \tag{4–84}$$

The reflection matrix $\mathbf{R}$ is equal to $\mathbf{R}_S$ and $\mathbf{R}_A$ in case of symmetric and antisymmetric load and response, respectively, and only the first row of sub-matrices in Eq. (4–80) is taken into account. Thus the system of equations may be halved in size by "adding" the contributions from the reflected part of the model to the part which is kept in the discretization.

In the present case only the part of the model present in the $x_2 > 0$ half-space has to be modelled, and the following steps have to be carried out in the integration process:

1 The influence from integration points on the part of the surface at $x_2 > 0$ to collocation points at $x_2 > 0$ are found in the usual manner.

2 The influence from the "mirror images" of the integration points to the collocation points are found by evaluating the same elements again, but with a change of sign on the x_2 coordinates for the nodes. The contributions are then assembled into the existing system matrices.

Since the elements, and thus the local node order, will be mirrored in the process, a reordering of the nodes in each of the elements produced in this manner at $x_2 < 0$ is necessary to ensure the correct direction of the normal vector. Alternatively, the model may be reduced to only include the part of the domain present at $x_2 < 0$. In that case the reduced system is established from the second line of sub-matrices in Eq. (4–80). The reflection matrix remains the same.

So far it has been assumed that half of the nodes are present on either side of the plane of symmetry. This may be the case when constant elements are used, and is even possible with linear elements. However, when quadratic interpolation is used, some of the nodes will definitely have an x_2-coordinate equal to zero when the discretization is strictly symmetric around the plane defined by $x_2 = 0$. This leads to some numerical problems which will be discussed below.

For the nodes on the plane of symmetry the contributions from a node and its "mirror image" are exactly the same. However, depending on the kind of symmetry, the sign on either the x_2 degree of freedom or the x_1 and the x_3 degrees of freedom will be opposite. Since the contributions are added into *one* component in the $\mathbf{G}$ and $\mathbf{H}$ matrices, not stored separately (as they are in the original description), this eventually means that some of the rows in the reduced system matrices contain nothing but zeros. Notice that the diagonal term is zero, even if it only stores the influence from a single node, namely the node itself. The reason is that half the influence is obtained from one side of $x_2 = 0$ and the other half is obtained by integration over elements on the other side of $x_2 = 0$ to which the node also belongs. For the same reason, the contribution to other degrees of freedom will also be very small. The terms in the columns corresponding to the problematic degrees of freedom may even be zero if the other degree of freedom belongs to a node which is also on the plane of symmetry.

As explained in the previous subsection, the solution for a multi-domain BEM model, or a coupled BEM–FEM model, is often carried out in a finite element manner. This implies that each boundary element domain is transformed into a macro finite element described by an equivalent stiffness matrix, the derivation of which involves an inversion of the $\mathbf{G}$ matrix. When some of the rows contain nothing but zeros, the system is ill-conditioned. In theory, the inversion of such a system is impossible. However, due to the small errors introduced in the numerical integration,

the terms in the problematic columns are not identically equal to zero. Hence, a solution of the system of equations is still possible in practice; but the solution algorithm is unstable and the results produced are erroneous unless the zero-terms are in one or another way removed/avoided in the $\mathbf{G}$ matrix.

To obtain a stable system of equations, the following approaches may be suggested:

1 A certain amount of asymmetry is introduced so that the contributions from the original and the reflected elements are not exactly the same.

2 The rows and columns corresponding to the degrees of freedom which are known to be zero are eliminated.

Of these two method, the second approach is preferable due to the reasons that are given below.

Ad. 1 One way of introducing asymmetry is to disregard some of the nodes or elements in the reflected part of the model. However the major problem is that some of the diagonal terms become zero. Since these terms are calculated entirely from the elements adjacent to the plane of symmetry, it is these elements (or the nodes of elements) that have to be disregarded to avoid the problematic zeros in the diagonal of $\mathbf{G}$. Just disregarding the elements/nodes that are farthest away from the plane of symmetry, as it is common practice when the entire model is considered, will not stabilize the solution. Alternatively the asymmetry may be introduced in an arbitrary way, simply buy adding small numbers to the zero-terms in the $\mathbf{G}$ matrix. Mathematically this may be as good as leaving out elements or nodes in the reflected part of the domain. However, it is impossible to give any physical interpretation of the error which is introduced in this manner. The conclusion is that the first approach cannot be used, since the changes that are necessary to produce a stable system are conflicting with the initial assumption that the model should be symmetric (or antisymmetric) with respect to the x_2-coordinate, at least in the vicinity of the plane defined by $x_2 = 0$.

Ad. 2 The rows that contain values which are infinite to working precision in all columns may be eliminated in the equivalent stiffness matrix. In this way the "infinite" stiffness terms associated with the degrees of freedom that are known to be zero are avoided. However, even if the system of equations is, in this way, not badly scaled, erroneous results will still be produced. The reason is that the remaining stiffness terms for all other degrees of freedom are already determined inaccurately because the $\mathbf{G}$ matrix is ill-conditioned. Actually the inversion is only possible in the first place because a small numerical error has been introduced in the Gauss integration process. Therefore the reduction of the system must be applied before the matrix inversion. This implies a bit more bookkeeping, especially as it has to be ensured that the same degrees of freedom are removed from all sub-domains in the entire model. However this should not be a problem. Finally it should be noticed that when the degrees of freedom are removed before the matrix inversion, the calculation time may be reduced significantly if a large fraction of the nodes are on the plane of symmetry.

Hisatake *et al.* (1983) proposed an alternative method which may be used to avoid an ill-conditioned matrix for inversion. Basically, their idea was to establish the equivalent stiffness matrix from the full system of equations, where the rows with nothing but zeros do not occur. However this requires the assembly of the double amount of terms in $\mathbf{G}$ and $\mathbf{H}$ and a matrix of the quadruple size has to be stored and inverted. Hence, the method suggested by Hisatake *et al.* is not as efficient as the second method, which has been proposed in this section.

The method of dealing with symmetric structures that has been developed in the present section may easily be generalised to the case where more than one plane of symmetry exist, or a formulation may be given where the plane of symmetry has an arbitrary position and orientation. However, for most practical purposes it is sufficient with a code that allows the utilisation of symmetry around two predefined planes, say the (x_1, x_3)-plane and the (x_2, x_3)-plane.

4.6 Boundary element solution in the time domain

The direct time-domain formulation of the BEM was introduced in the introduction to the chapter. Here, the method will be further discussed, and an alternative approach, namely the so-called *dual reciprocity boundary-element method*, will be presented.

4.6.1 Direct time-domain formulation

The direct time-domain boundary-element method is a very complex computation method. We shall therefore restrict ourselves to looking at the simplest possible case, namely the two-dimensional scalar problem, concerning antiplane shear with constant-spatial-interpolation elements.

The fundamental solution to the displacement in the antiplane shear wave problem was found in Eq. (3–66) and is repeated here for convenience. We consider the slightly different case, in which a unit impulse of the kind $b^*(\mathbf{x}, t; \mathbf{y}, \tau) = c_S^2 \delta(\mathbf{x} - \mathbf{y})\delta(t - \tau)$, rather than a load of the type $\rho b^*(\mathbf{x}, t; \mathbf{y}, \tau) = \delta(\mathbf{x} - \mathbf{y})\delta(t - \tau)$, is applied. Then,

$$u_{33}^*(\mathbf{x}, t; \mathbf{y}, \tau) = \frac{c_S \, H(c_S \, (t - \tau) - r)}{2\pi \big(c_S^2 \, (t - \tau)^2 - r^2\big)^{1/2}}, \qquad r = |\mathbf{x} - \mathbf{y}|, \tag{4–85}$$

where $\mathbf{x}$ and $\mathbf{y}$ are points in the plane, and $H(\cdot)$ is the Heaviside unit step function. The Green's function for the traction is defined as the normal derivative of $u_{33}^*(\mathbf{x}, t; \mathbf{y}, \tau)$,

$$\begin{aligned} p_{33}^*(\mathbf{x}, t; \mathbf{y}, \tau) &= \frac{\partial}{\partial n} u_{33}^*(\mathbf{x}, t; \mathbf{y}, \tau) = \frac{\partial r}{\partial n} \frac{\partial}{\partial r} u_{33}^*(\mathbf{x}, t; \mathbf{y}, \tau) \\ &= \frac{\partial r}{\partial n} \frac{c_S r \, H(c_S \, (t - \tau) - r)}{2\pi \big(c_S^2 \, (t - \tau)^2 - r^2\big)^{3/2}} + \frac{\partial r}{\partial n} \frac{c_S \frac{\partial}{\partial r} H(c_S \, (t - \tau) - r)}{2\pi \big(c_S^2 \, (t - \tau)^2 - r^2\big)^{1/2}}. \end{aligned} \tag{4–86}$$

Making use of the fact the spatial and temporal derivatives of the Heaviside function are related as

$$\frac{\partial}{\partial r} H(c_S \, (t - \tau) - r) = \frac{1}{c_S} \frac{\partial}{\partial \tau} H(c_S \, (t - \tau) - r), \tag{4–87}$$

a reformulation of the time integral over the product $p_{33}^*(\mathbf{x}, t; \mathbf{y}, \tau) u_3(\mathbf{y}, \tau)$ may be carried out.

Thus, by means of partial integration, it becomes evident that

$$\begin{aligned}
&\int_0^{t^+} u_3(\mathbf{y},\tau)\frac{c_S}{2\pi\left(c_S^2\,(t-\tau)^2-r^2\right)^{1/2}}\,\frac{\partial r}{\partial n}\,\frac{\partial}{\partial r}H(c_S\,(t-\tau)-r)\,\mathrm{d}\tau \\
&\quad=\frac{\partial r}{\partial n}\,\int_0^{t^+} u_3(\mathbf{y},\tau)\,\frac{1}{2\pi\left(c_S^2\,(t-\tau)^2-r^2\right)^{1/2}}\,\frac{\partial}{\partial \tau}H(c_S\,(t-\tau)-r)\,\mathrm{d}\tau \\
&\quad=-\frac{\partial r}{\partial n}\,\int_0^{t^+} \frac{1}{2\pi\left(c_S^2\,(t-\tau)^2-r^2\right)^{1/2}}\,\frac{\partial}{\partial \tau}u_3(\mathbf{y},\tau)\;H(c_S\,(t-\tau)-r)\,\mathrm{d}\tau \\
&\quad-\frac{\partial r}{\partial n}\,\int_0^{t^+} u_3(\mathbf{y},\tau)\,\frac{c_S^2\,(t-\tau)^2}{2\pi\left(c_S^2\,(t-\tau)^2-r^2\right)^{3/2}}\;H(c_S\,(t-\tau)-r)\,\mathrm{d}\tau, \qquad (4\text{–}88)
\end{aligned}$$

where use has been made of the assumption that the domain has a quiescent past, *i.e.* $u_3(\mathbf{y},0)=0$. With these reformulations, the reciprocal relation given by Eq. (4–9) instead becomes

$$\begin{aligned}
C(\mathbf{x}_i)u_3(\mathbf{x},t)&=\int_0^{t^+}\int_\Gamma u_{33}^*(\mathbf{x}_i,t;\mathbf{y},\tau)\;p_3(\mathbf{y},t)\;\mathrm{d}\Gamma(\mathbf{y})\;\mathrm{d}\tau \\
&-\int_0^{t^+}\int_\Gamma \left\{z^*(\mathbf{x}_i,t;\mathbf{y},\tau)\;u_3(\mathbf{y},t)-w^*(\mathbf{x}_i,t;\mathbf{y},\tau)\;\dot{u}_3(\mathbf{y},t)\right\}\mathrm{d}\Gamma(\mathbf{y})\;\mathrm{d}\tau, \qquad (4\text{–}89)
\end{aligned}$$

where

$$z^*(\mathbf{x}_i,t;\mathbf{y},\tau)=\frac{\partial r}{\partial n}\,\frac{c_S\left\{r-c_S\,(t-\tau)^2\right\}}{2\pi\left(c_S^2\,(t-\tau)^2-r^2\right)^{3/2}}\;H(c_S\,(t-\tau)-r), \qquad (4\text{–}90)$$

$$w^*(\mathbf{x}_i,t;\mathbf{y},\tau)=\frac{\partial r}{\partial n}\frac{\partial 1}{\partial c_S}u_{33}^*(\mathbf{x}_i,t;\mathbf{y},\tau). \qquad (4\text{–}91)$$

This equation is known as Volterra's integral relationship. As already discussed, the primary difference from the equivalent three-dimensional boundary integral identity for acoustics is that contributions from a given point will continue to arrive at a collocation point at all time steps after the first perturbation arrives at the time $t=r/c_S$. This is due to the fact that the Heaviside step functions replace the Dirac delta functions. As a result of this, the data must be kept for all previous time steps. It is noted that this also applies to the plane-strain problem and three-dimensional elastodynamics.

As usual, the next step in the boundary element formulation is to discretize the field quantities on the surface and introduce an interpolation. In the time-domain BEM, the interpolation is carried out both in space and time using the following approximations for the displacement and the traction at the time $t<j\Delta t$:

$$u_3(\mathbf{x},t)=\sum_{k=1}^{N}\sum_{m=1}^{j}\phi_k(\mathbf{x})T^m(t)u_{3\,k}^m,\quad p_3(\mathbf{x},t)=\sum_{k=1}^{N}\sum_{m=1}^{j}\psi_k(\mathbf{x})\check{T}^m(t)p_{3\,k}^m, \qquad (4\text{–}92)$$

where $u_{3\,k}^m$ and $p_{3\,k}^m$ store the displacement and the traction, respectively, at node k and at the time $t_m=m\Delta t$. $\phi_k(\mathbf{x})$ and $\psi_k(\mathbf{x})$ are the spatial shape functions for the displacement and the

traction, respectively. Usually the same shape functions are used for the spatial interpolation of $u_3(\mathbf{x},t)$ and $p_3(\mathbf{x},t)$, *i.e.* $\phi_k(\mathbf{x}) = \psi_k(\mathbf{x})$, as it is also the case in the frequency-domain BEM. On the contrary, it has been found that the temporal shape functions $T^m(t)$ and $\check{T}^m(t)$ may advantageously be selected differently for the displacement and the traction. Thus, piecewise constant temporal interpolation of the traction and piecewise linear interpolation of the displacement seems to provide both stable and accurate results. If linear interpolation is used for the traction, the integration over time tends to be unstable, and a constant interpolation of both the traction and the displacement provides results that are less accurate than those of the constant/linear temporal interpolation scheme. In essence, the problems related to the time integration in the time-domain BEM are equivalent to those in the time-integration schemes discussed in Section 2.2.

With the spatial–temporal interpolation defined by Eq. (4–92), the boundary element equation following from Eq. (4–89) becomes

$$\begin{aligned}\mathbf{C}(\mathbf{x}_i)\varphi(\mathbf{x}_i,t^j) = \sum_{m=1}^{j}\sum_{k=1}^{NE}\Bigg(&\Bigg\{\int_{\Gamma_k}\Bigg(\int_{\Delta t^m} u^*_{33}(\mathbf{x}_i,t^j;\mathbf{y},\tau)T^m(\tau)\mathrm{d}\tau\Bigg)\phi_k(\mathbf{y})\mathrm{d}\Gamma_k(\mathbf{y})\Bigg\}p^m_{3\,k}\\ &-\Bigg\{\int_{\Gamma_j}\Bigg(\int_{\Delta t^m}\big(z^*(\mathbf{x}_i,t^j;\mathbf{y},\tau)\;\check{T}^m(\tau)\\ &-w^*(\mathbf{x}_i,t^j;\mathbf{y},\tau)\;\dot{\check{T}}^m(\tau)\big)\mathrm{d}\tau\Bigg)\psi_k(\mathbf{y})\mathrm{d}\Gamma_k(\mathbf{y})\Bigg\}u^m_{3\,k}\Bigg),\end{aligned} \tag{4–93}$$

NE is the number of elements, which in the case of constant elements is the same as the number of nodes, N. Here the order of integration has been reversed, which has the reason that for local linear or constant temporal shape functions over each time step, a closed-form analytic evaluation of the integrals

$$\varphi^{jm}(\mathbf{x}_i;\mathbf{y}) = \int_{\Delta t^m} u^*_{33}(\mathbf{x}_i,t^j;\mathbf{y},\tau)T^m(\tau)\mathrm{d}\tau, \tag{4–94}$$

$$\chi^{jm}(\mathbf{x}_i;\mathbf{y}) = \int_{\Delta t^m}\big(z^*(\mathbf{x}_i,t^j;\mathbf{y},\tau)\;\check{T}^m(\tau) - w^*(\mathbf{x}_i,t^j;\mathbf{y},\tau)\;\dot{\check{T}}^m(\tau)\big)\mathrm{d}\tau, \tag{4–95}$$

may be carried out. Insertion into Eq. (4–93) provides the formulation

$$\begin{aligned}\mathbf{C}(\mathbf{x}_i)\varphi(\mathbf{x}_i,t^j) = \sum_{m=1}^{j}\sum_{k=1}^{NE}\Bigg(&\Bigg\{\int_{\Gamma_k}\varphi^{jm}(\mathbf{x}_i;\mathbf{y})\phi_k(\mathbf{y})\mathrm{d}\Gamma_k(\mathbf{y})\Bigg\}p^m_{3\,k}\\ &-\Bigg\{\int_{\Gamma_j}\chi^{jm}(\mathbf{x}_i;\mathbf{y})\psi_k(\mathbf{y})\mathrm{d}\Gamma_k(\mathbf{y})\Bigg\}u^m_{3\,k}\Bigg),\end{aligned} \tag{4–96}$$

This equation is easily rewritten into the standard BEM form,

$$\sum_{k=1}^{NE}\sum_{m=1}^{j}\mathbf{H}^{jm}_{ik}(\omega)u^m_{3\,k} = \sum_{k=1}^{NE}\sum_{m=1}^{j}\mathbf{G}^{jm}_{ik}(\omega)p^m_{3\,k}. \tag{4–97}$$

where the subscripts relate to space and the superscripts relate to time, and where the geometry constants contained in the matrix $\mathbf{C}(\mathbf{x}_i)$ are absorbed into $\mathbf{H}^{jj}_{ii}$. The equations for each of the N

nodes may be assembled into the global system of equations

$$\sum_{m=1}^{j} \mathbf{H}^{jm}\mathbf{u}_3^m = \sum_{m=1}^{j} \mathbf{G}^{jm}\mathbf{p}_3^m, \tag{4–98}$$

which must be solved at each time step.

When the local integrals over time are carried out, the main difficulty lies in the tracking of the wavefronts. In particular, there is no reason to include integration points, from which the first perturbation has still not reached the collocation node. Thus, assuming constant temporal shape functions, integrals over the time step Δt^m fall in three categories:

- when $c_S\left(t^j - \tau^{m-1}\right) \leq r$ the first perturbation has not yeat arrived. Therefore, there are no contributions. With reference to Eq. (4–95), $\psi^{jm}(\mathbf{x}_i;\mathbf{y}) = 0$.
- when $c_S\left(t^j - \tau^{m}\right) \leq r < c_S\left(t^j - \tau^{m-1}\right)$ the first perturbation will arrive during the time step Δt^m. The integration should only be carried out for the time interval after the first arrival, *i.e.* after $t = t^j - r/c_S$.
- when $r < c_S\left(t^j - \tau^{m}\right)$ the perturbation has arrived before the beginning of the time step. Hence the integral should be performed over the entire time step.

In the case of linear interpolation, the bookkeeping is a bit more complex. The details of the evaluation of the local integrals over time will not be discussed here. A reference is given to the book by Domínguez (1993).

As a last notice, it is mentioned that the choice of the time step is crucial for the accuracy and the stability of the BEM solution. Domínguez (1993) carried out a study of the two-dimensional elastodynamic response of a rectangular domain with different time steps, measured in terms of the Courant number relative to the P-wave speed. It turns out that numerical damping tends to arise when a courant number larger than 1 is used, which is not very strange as some of the energy cannot propagate in the numerical model. However, if a Courant number smaller than 1 is used, the solution is destabilized. Thus, for very small Courant numbers, the solution becomes purely oscillatory. This problem only seems to get worse, when quadratic spatial interpolation is used.

4.6.2 The dual reciprocity boundary-element method

The main disadvantage of the direct time-domain formulation of the BEM is that the system matrices for each time step have to be stored since a convolution over the entire time history has to be be carried out at each time step. This has to do with the fact that the reciprocal relation given by Eq. (4–9) uses a time-dependent Green's function as the weight function.

A different approach would be to use the Green's function for the static problem. The inertia forces should in this context be treated as body forces. Thus an integral identity is obtained which is local in time. Unfortunately, this comes at the cost that volume integrals enter the BEM formulation. However, as it shall be shown below, it is possible to reduce the problem to a pure boundary problem by application of the reciprocal theorem a second time. This leads to the formulation known as the dual reciprocity boundary-element method.

Approximate reciprocal relation

The starting point of the dual reciprocity BEM for elastodynamics is the variational formulation of the Cauchy equation of motion. However, in stead of the rather arbitrary virtual field applied in the FEM, an elastostatic state $\tilde{u}_i(\mathbf{x})$ is used as the weighting function,

$$\int_\Omega \tilde{\varepsilon}_{ij}(\mathbf{x})\sigma_{ij}(\mathbf{x},t)\mathrm{d}\Omega(\mathbf{x}) + \int_\Omega \tilde{u}_i(\mathbf{x})\rho\ddot{u}_i(\mathbf{x},t)\mathrm{d}\Omega(\mathbf{x}) = \int_\Gamma \tilde{u}_i(\mathbf{x})p_i(\mathbf{x},t)\mathrm{d}\Gamma(\mathbf{x}) + \int_\Omega \tilde{u}_i(\mathbf{x})\rho b_i(\mathbf{x},t)\mathrm{d}\Omega(\mathbf{x}). \tag{4–99}$$

Since $\tilde{\varepsilon}_{ij}(\mathbf{x})\sigma_{ij}(\mathbf{x},t) = \tilde{\sigma}_{ij}(\mathbf{x})\varepsilon_{ij}(\mathbf{x},t)$, and since the elastostatic state is the solution to the equation

Eq. (4–99) may alternatively be written

$$\int_\Gamma \tilde{u}_i(\mathbf{x})p_i(\mathbf{x},t)\mathrm{d}\Gamma(\mathbf{x}) + \int_\Omega \rho\tilde{u}_i(\mathbf{x})\left(b_i(\mathbf{x},t) - \ddot{u}_i(\mathbf{x},t)\right)\mathrm{d}\Omega(\mathbf{x}) = \int_\Gamma \tilde{p}_i(\mathbf{x})u_i(\mathbf{x},t)\mathrm{d}\Gamma(\mathbf{x}) + \int_\Omega \rho\tilde{b}_i(\mathbf{x})u_i(\mathbf{x},t)\mathrm{d}\Omega(\mathbf{x}). \tag{4–100}$$

This equation forms an approximate reciprocal relation, in which the inertia terms are treated as body forces.

Next, the elastostatic state is taken as the fundamental solution for a load applied to an infinite domain at the point $\mathbf{y}$ in the direction l, *i.e.* the following substitutions are applied:

$$\tilde{u}_i(\mathbf{x}) \sim u^*_{li}(\mathbf{x}-\mathbf{y}), \quad \tilde{p}_i(\mathbf{x}) \sim p^*_{li}(\mathbf{x}-\mathbf{y}), \quad \rho\tilde{b}_i(\mathbf{x}) \sim \delta(\mathbf{x}-\mathbf{y})\delta_{li}. \tag{4–101}$$

Assuming that there are no body forces in the physical state, *i.e.* $\rho b_i(\mathbf{x},t) = 0$, and utilising the spatial reciprocity (3–16) of the Green's function, the integral identity becomes

$$C_{il}(\mathbf{x})u_l(\mathbf{x},t) + \int_\Gamma p^*_{il}(\mathbf{x}-\mathbf{y})u_l(\mathbf{y},t)\mathrm{d}\Gamma(\mathbf{y}) = \int_\Gamma u^*_{il}(\mathbf{x}-\mathbf{y})p_l(\mathbf{y},t)\mathrm{d}\Gamma(\mathbf{y}) - \int_\Omega \rho u^*_{il}(\mathbf{x}-\mathbf{y})\ddot{u}_l(\mathbf{y},t)\mathrm{d}\Omega(\mathbf{y}). \tag{4–102}$$

where $C_{il}(\mathbf{x})$ is the geometry constant as defined previously. In particular, on a smooth part of the surface, $C_{il}(\mathbf{x}) = \delta_{il}/2$.

Transformation of the volume integral

The following approximations of the displacements and accelerations in the physical state are introduced:

$$u_i(\mathbf{x},t) = \sum_{m=1}^{M} \alpha_l^m(t)f^m(\mathbf{x}), \quad \ddot{u}_i(\mathbf{x},t) = \sum_{m=1}^{M} \ddot{\alpha}_l^m(t)f^m(\mathbf{x}), \tag{4–103}$$

which is very similar to the method that is usually applied in the Ritz method. The volume integral may now be written as

$$\int_\Omega \rho u^*_{il}(\mathbf{x}-\mathbf{y})\ddot{u}_l(\mathbf{y},t)\mathrm{d}\Omega(\mathbf{y}) = \rho\sum_{m=1}^{M} \ddot{\alpha}_l^m(t)\int_\Omega u^*_{il}(\mathbf{x}-\mathbf{y})f^m(\mathbf{y})\mathrm{d}\Omega(\mathbf{y}). \tag{4–104}$$

The idea is subsequently to establish a second reciprocal relation. For this purpose, an elastic state is considered, in which the body forces $-f^m(\mathbf{x})$ are applied to an infinite domain in direction k, *i.e.*

$$\rho b_i^m(\mathbf{x}) = -f^m(\mathbf{x})\delta_{ik}. \tag{4–105}$$

The resulting displacement and traction fields are represented as

$$u_i^m(\mathbf{x}) = \psi_{ik}^m(\mathbf{x})\mathbf{e}_k, \quad p_i^m(\mathbf{x}) = \eta_{ik}^m(\mathbf{x})\mathbf{e}_k, \tag{4–106}$$

where $\mathbf{e}_k$ is the unit vector in the direction of the body forces. The reciprocal between this new state and the state corresponding to the static fundamental solution may be written:

$$\begin{aligned} &C_{il}(\mathbf{x})\psi_{lk}^m(\mathbf{x}) + \int_\Gamma p_{il}^*(\mathbf{x}-\mathbf{y})\psi_{lk}^m(\mathbf{y})\mathrm{d}\Gamma(\mathbf{y}) \\ &\quad = \int_\Gamma u_{il}^*(\mathbf{x}-\mathbf{y})\eta_{lk}^m(\mathbf{y})\mathrm{d}\Gamma(\mathbf{y}) - \int_\Omega u_{il}^*(\mathbf{x}-\mathbf{y})f^m(\mathbf{y})\delta_{lk}\mathrm{d}\Omega(\mathbf{y}). \end{aligned} \tag{4–107}$$

A comparison of Eq. (4–107) with Eq. (4–104) reveals that the volume integral may now be transformed into the sum of M surface integrals,

$$\begin{aligned} \int_\Omega \rho u_{il}^*(\mathbf{x}-\mathbf{y})\ddot{u}_l(\mathbf{y},t)\mathrm{d}\Omega(\mathbf{y}) &= \rho\sum_{m=1}^{M}\ddot{\alpha}_k^m(t)\Big\{ - C_{il}(\mathbf{x})\psi_{lk}^m(\mathbf{x}) \\ &+ \int_\Gamma u_{il}^*(\mathbf{x}-\mathbf{y})\eta_{lk}^m(\mathbf{y})\mathrm{d}\Gamma(\mathbf{y}) - \int_\Gamma p_{il}^*(\mathbf{x}-\mathbf{y})\psi_{lk}^m(\mathbf{y})\mathrm{d}\Gamma(\mathbf{y})\Big\}. \end{aligned} \tag{4–108}$$

This result may be inserted into the original "reciprocal" relation for the physical and the static fundamental solution states. Thereby a pure boundary integral version of the reciprocal relation is achieved,

$$\begin{aligned} &C_{il}(\mathbf{x})u_l(\mathbf{x},t) + \int_\Gamma p_{il}^*(\mathbf{x}-\mathbf{y})u_l(\mathbf{y},t)\mathrm{d}\Gamma(\mathbf{y}) \\ &\quad = \int_\Gamma u_{il}^*(\mathbf{x}-\mathbf{y})p_l(\mathbf{y},t)\mathrm{d}\Gamma(\mathbf{y}) + \rho\sum_{m=1}^{M}\ddot{\alpha}_k^m(t)\Big\{C_{il}(\mathbf{x})\psi_{lk}^m(\mathbf{x}) \\ &\quad - \int_\Gamma u_{il}^*(\mathbf{x}-\mathbf{y})\eta_{lk}^m(\mathbf{y})\mathrm{d}\Gamma(\mathbf{y}) + \int_\Gamma p_{il}^*(\mathbf{x}-\mathbf{y})\psi_{lk}^m(\mathbf{y})\mathrm{d}\Gamma(\mathbf{y})\Big\}. \end{aligned} \tag{4–109}$$

Combining the equations for all two, or three, load directions, the following matrix equation is achieved for a collocation point placed at the position $\mathbf{x}_i$,

$$\begin{aligned} &\mathbf{C}(\mathbf{x}_i)\mathbf{u}(\mathbf{x}_i,t) + \int_\Gamma \mathbf{p}^*(\mathbf{x}_i-\mathbf{y})\mathbf{u}(\mathbf{y},t)\mathrm{d}\Gamma(\mathbf{y}) \\ &\quad = \int_\Gamma \mathbf{u}^*(\mathbf{x}_i-\mathbf{y})\mathbf{p}(\mathbf{y},t)\mathrm{d}\Gamma(\mathbf{y}) + \rho\sum_{m=1}^{M}\Big\{\mathbf{c}(\mathbf{x}_i)\boldsymbol{\psi}^m(\mathbf{x}_i) \\ &\quad - \int_\Gamma \mathbf{u}^*(\mathbf{x}_i-\mathbf{y})\boldsymbol{\eta}^m(\mathbf{y})\mathrm{d}\Gamma(\mathbf{y}) + \int_\Gamma \mathbf{p}^*(\mathbf{x}_i-\mathbf{y})\boldsymbol{\psi}^m(\mathbf{y})\mathrm{d}\Gamma(\mathbf{y})\Big\}\ddot{\boldsymbol{\alpha}}^m(t). \end{aligned} \tag{4–110}$$

This equation forms the basis for the boundary element formulation. After discretization of the physical field quantities on the boundary and interpolation over each element by means of spatial shape functions, the equation for each collocation node obtains the form

$$\sum_{j=1}^{N} \mathbf{H}_{ij}\ \mathbf{u}_j(t) = \sum_{j=1}^{N} \mathbf{G}_{ij}\ \mathbf{p}_j(t) + \rho \sum_{m=1}^{M} \sum_{j=1}^{N} \left(\mathbf{H}_{ij}\ \boldsymbol{\psi}_j^m - \mathbf{G}_{ij}\ \boldsymbol{\eta}_j^m\right) \ddot{\boldsymbol{\alpha}}^m(t). \tag{4–111}$$

Here N is the number of nodes on the entire surface, while $\mathbf{G}_{ij}$ and $\mathbf{H}_{ij}$ are the submatrices of dimension (3×3) in three dimensions, and (2×2) in two dimensions, relating node i to node j. Since the static fundamental solution is employed, these matrices are independent of time.

The M vectors $\ddot{\boldsymbol{\alpha}}^m(t)$, which all have the length 3 in three dimensions, and 2 in two dimensions, can be combined into a single row vector $\ddot{\boldsymbol{\alpha}}(t)$ with the lenght $3M$ in three dimensions, or $2M$ in two dimensions. Further, with reference to Eq. (4–103), the global acceleration vector with the length $3N$, or $2N$, for the entire surface Γ may be expressed as

$$\ddot{\mathbf{u}}(t) = \mathbf{F}\ddot{\boldsymbol{\alpha}}(t), \tag{4–112}$$

where $\mathbf{F}$ is a matrix of the dimension $(3N \times 3M)$, or $(2N \times 2M)$, which is assembled from the functions $f^m(\mathbf{x})$ evaluated at the nodes with the coordinates $\mathbf{x}_j$, $j = 1, 2, \ldots, N$.

After assembly of the N equations of the kind (4–111), insertion of the inverse relationship of the one defined by Eq. (4–112) provides the global system of equations

$$\mathbf{H}\mathbf{u}(t) = \mathbf{G}\mathbf{p}(t) + \rho \left(\mathbf{H}\boldsymbol{\psi} - \mathbf{G}\boldsymbol{\eta}\right) \mathbf{F}^{-1} \ddot{\mathbf{u}}(t). \tag{4–113}$$

This equation may alternatively be written

$$\mathbf{M}\ddot{\mathbf{u}}(t) + \mathbf{H}\mathbf{u}(t) = \mathbf{G}\mathbf{p}(t), \quad \mathbf{M} = \rho \left(\mathbf{H}\boldsymbol{\psi} - \mathbf{G}\boldsymbol{\eta}\right) \mathbf{F}^{-1}, \tag{4–114}$$

which has a clear similarity with the equation of motion obtained in dynamic finite-element analysis. In fact, if Neumann conditions are given on the entire boundary, the left-hand side reduces to a known load vector, and in this case $\mathbf{M}$ and $\mathbf{H}$ take the form of mass and stiffness matrices. Contrary to the system matrices in FEM, $\mathbf{M}$ and $\mathbf{H}$ are however fully populated. In any case, a direct time integration scheme like the Newmark scheme may be used to compute the values of the displacement and the accelerations at the discrete time t_j, once the states are known at the time t_{j-1}. This is a great advantage when compared to the direct formulation of the BEM in the time domain. However, the accuracy of the dual reciprocity BEM is highly dependent of the approximation over the volume introduced via the shape functions stored in $\boldsymbol{\psi}$ and $\boldsymbol{\eta}$. The choice of $\psi_{lk}^m(\mathbf{x})$ and $\eta_{lk}^m(\mathbf{x})$ shall not be discussed here. It shall only be mentioned that it has been found in several cases that for a suitable choice of the volume shape functions, the dual reciprocity BEM provides results of an accuracy which is comparable to that of the standard time-domain BEM, but with a much smaller computation time.

4.7 Summary

The boundary-element method has been presented for a variety of elastodynamic problems with focus on the discretization procedure. Some of the main conclusions are:

Boundary elements are used to discretize the surface of a given domain. Both the displacement and the surface traction is represented directly, and the Green's functions are applied as weight functions.

Spatial discretization can be carried out with constant, linear or higher-order interpolation. For some problems, constant elements will suffice, whereas accurate results in, for example, problems involving bending demand the use of quadratic interpolation.

System matrices in the boundary-element method are fully populated and great effort is required in their assembly, since the Green's functions are much more complex from a computational point of view than the interpolation functions in the finite-element method.

Singularities arise in the Green's function when the contributions from a collocation node to itself are to be determined. This is only a minor problem with regard to the weakly singular displacement Green's function, but evaluation of the strongly singular Greens' function for the surface traction requires special care. Use can be made of the fact that the singularities of the elastodynamic Green's function and its static counterpart are identical.

Coupling of boundary elements and finite elements can be performed in different ways. The main problem in this regard is that loads are applied as nodal forces in the FEM, whereas surface traction is applied in the BEM. The coupling in terms of nodal forces is particularly simple and allows the boundary-element domains to be treated as macro-finite elements.

Symmetry of boundary-element domains may be exploited to reduce the numerical model significantly. Half the model may simply be removed. However, the influence from the elements in this part of the model to the elements in the other half of the model must be included. Thus, for each element the contributions to the system matrices is also found for the "mirror image" of the element.

Time-domain boundary-element analysis is extremely expensive in terms of computer time and memory. Hence, frequency-domain analysis is generally preferred.

The dual-reciprocity method is an alternative to the direct boundary-element method in the time domain. It produces a numerical scheme in which temporal convolution is avoided, and the system of equations is very similar to the algebraic system of equations obtained in the finite-element method for elastodynamics.

CHAPTER 5
The domain-transformation method for a layered half-space

In this chapter, a semi-analytical solution for the analysis of a horizontally stratified medium is established. The main idea is to transform the original time–space domain problem into the frequency–wavenumber domain, however only with respect to the horizontal spatial coordinates. This leaves a set of equations that may be dealt with individually and analytically in a computationally efficient manner. This is the great advantage of the method when compared to, for example, the finite element method, in which a large system of equations must be solved simultaneously. However, the method only applies to media with horizontal interfaces and surfaces.

5.1 Introduction

The finite element method with transmitting boundary conditions may be applied for the elastodynamic analysis of a layered half-space. However, a discretization over a large volume may be necessary in order to describe wave propagation in three-dimensions—in particular if the far-field response of, for example, a ground surface is of interest, or if interfaces are present deep in the ground. Likewise, if a Green's function is applied in the boundary element method which does not account for the presence of interfaces, all interfaces must be discretized, thus leading to a large numerical model. In both the FEM and the BEM, the major disadvantage, seen from a computational point of view, lies in the fact that the global system of equations must be solved simultaneously.

If a linear viscoelastic half-space with only horizontal interfaces is considered, the computations are simplified significantly when a formulation in the horizontal wavenumber domain is adopted. Here it turns out that an analytical Green's function can be found, and once the solution has been established in the wavenumber domain, a transformation back into Cartesian space is readily achieved by inverse Fourier transformation. Furthermore, the formulation provides a straight forward means of dealing with moving loads.

In the present chapter, a model is considered that consists of a layered medium—a so-called *stratum*—overlaying a rigid foundation or a homogeneous half-space. An illustration of the situation with three layers over a half-space is given in Fig. 5–1, in which a definition of the Cartesian (x_1, x_2, x_3)-coordinate system is provided. The theory is due to Sheng *et al.* (1999a, 1999b).

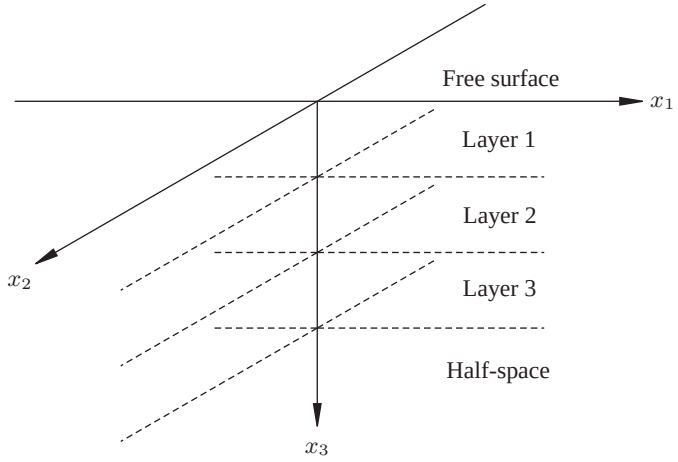

Figure 5–1 Model with three layers overlaying a half-space.

5.2 Response of a layered half-space

The surface displacement in time domain and in Cartesian space is denoted $u_i^{10}(x_1, x_2, t) = u_i(x_1, x_2, 0, t)$. Likewise the surface traction, or the load on the free surface, will be denoted $p_i^{10}(x_1, x_2, t) = p_i(x_1, x_2, 0, t)$. An explanation of the double superscript 10 will be given in the next section. In this section it is just noted that superscript 10 refers to the top of the half-space.

Further, let $g_{ij}(x_1 - y_1, x_2 - y_2, t - \tau)$ be the Green's function relating the displacement at the observation point $(x_1, x_2, 0)$ to the traction applied at the source point $(y_1, y_2, 0)$. Both points are situated on the surface of a stratified half-space with horizontal interfaces. The total displacement at the point $(x_1, x_2, 0)$ on the surface of the half-space is then found as

$$u_i^{10}(x_1, x_2, t) = \int_{-\infty}^{t} \int_{-\infty}^{\infty} \int_{-\infty}^{\infty} g_{ij}(x_1 - y_1, x_2 - y_2, t - \tau) p_j^{10}(y_1, y_2, \tau)\, \mathrm{d}y_1 \mathrm{d}y_2 d\tau. \qquad (5\text{–}1)$$

The displacement at any point on the surface of the half-space and at any instant of time may be evaluated by means of Eq. (5–1) given that $g_{ij}(x_1 - y_1, x_2 - y_2, t - \tau)$, which may be interpreted as the dynamic flexibility, is available. However, an analytical solution cannot be established; therefore, in practice, the temporal–spatial solution expressed by Eq. (5–1) is inadequate.

Assuming that the response of the stratum is linear, the analysis may be carried out in the frequency domain. The Fourier transformation of the surface displacements with respect to time is defined as

$$U_i^{10}(x_1, x_2, \omega) = \int_{-\infty}^{\infty} u_i^{10}(x_1, x_2, t) \mathrm{e}^{-\mathrm{i}\omega t} \mathrm{d}t, \qquad (5\text{–}2)$$

with the inverse Fourier transformation given as

$$u_i^{10}(x_1, x_2, t) = \frac{1}{2\pi} \int_{-\infty}^{\infty} U_i^{10}(x_1, x_2, \omega) \mathrm{e}^{\mathrm{i}\omega t} \mathrm{d}\omega. \qquad (5\text{–}3)$$

Similar definitions apply to the surface load, *i.e.* between the quantities $p_i^{10}(x_1, x_2, t)$ and $P_i^{10}(x_1, x_2, \omega)$, and to the Green's function, *i.e.* between $g_{ij}(x_1 - y_1, x_2 - y_2, t - \tau)$ and

$G_{ij}(x_1 - y_1, x_2 - y_2, \omega)$. It then follows that

$$U_i^{10}(x_1, x_2, \omega) = \int_{-\infty}^{\infty} \int_{-\infty}^{\infty} G_{ij}(x_1 - y_1, x_2 - y_2, \omega) P_j^{10}(y_1, y_2, \omega) \mathrm{d}y_1 \mathrm{d}y_2. \tag{5–4}$$

Thus, in the frequency domain, the temporal–spatial convolution is reduced to a purely spatial convolution.

Next, a transformation is carried out from the Cartesian space domain description into a horizontal wavenumber domain. The following definitions of the double Fourier transformation and inverse Fourier transformation over space apply,

$$\bar{U}_i^{10}(k_1, k_2, \omega) = \int_{-\infty}^{\infty} \int_{-\infty}^{\infty} U_i^{10}(x_1, x_2, \omega) \mathrm{e}^{-\mathrm{i}(k_1 x_1 + k_2 x_2)} \mathrm{d}x_1 \mathrm{d}x_2, \tag{5–5}$$

$$U_i^{10}(x_1, x_2, \omega) = \frac{1}{4\pi^2} \int_{-\infty}^{\infty} \int_{-\infty}^{\infty} \bar{U}_i^{10}(k_1, k_2, \omega) \mathrm{e}^{\mathrm{i}(k_1 x_1 + k_2 x_2)} \mathrm{d}k_1 \mathrm{d}k_2. \tag{5–6}$$

Defining similar transformations for the surface traction and the Green's function, Eq. (5–4) achieves the form

$$\bar{U}_i^{10}(k_1, k_2, \omega) = \bar{G}_{ij}(k_1, k_2, \omega) \bar{P}_j^{10}(k_1, k_2, \omega). \tag{5–7}$$

This equation has the advantage when compared to the previous formulation in space and time domain, that no convolution has to be carried out. Thus, the displacement amplitudes in the frequency–wavenumber domain are related directly to the traction amplitudes for a given set of the circular freqeuncy ω and the horizontal wavenumbers k_1 and k_2 via the Green's function tensor $\bar{G}_{ij}(k_1, k_2, \omega)$. When the load in the time domain varies harmonically in the form $p_i^{10}(x_1, x_2, t) = P_i(x_1, x_2)\mathrm{e}^{\mathrm{i}\omega t}$, the solution simplifies, since no inverse Fourier transformation over the frequency is necessary. $\bar{G}_{ij}(k_1, k_2, \omega)$ needs only be evaluated for a single frequency.

5.3 Flexibility matrix for a layered half-space

The main advantage of the description in the frequency domain and in the horizontal wavenumber domain is that a solution for the stratum may be found analytically. In this section, the derivation of $\bar{G}_{ij}(k_1, k_2, \omega)$ is described. The derivation is based on the assumption that the material within each individual layer is linear elastic, homogeneous and isotropic. Further, material dissipation is confined to hysteretic damping, which has been found to be a reasonably accurate model for materials such as soil, even if the model is invalid from a physical point of view.

5.3.1 Solution for a single layer

The stratum consists of J horizontally bounded layers, each defined by the Young's modulus E^j, the Poisson ratio ν^j, the mass density ρ^j and the loss factor η^j. Further, the layers have the depths h^j, $j = 1, 2, ..., J$. Thus, the equations of motion for each layer may advantageously be established in a coordinate system with the local x_3-coordinate x_3^j defined with the positive direction downwards so that $x_3^j \in [0, h^j]$, see Fig. 5–2.

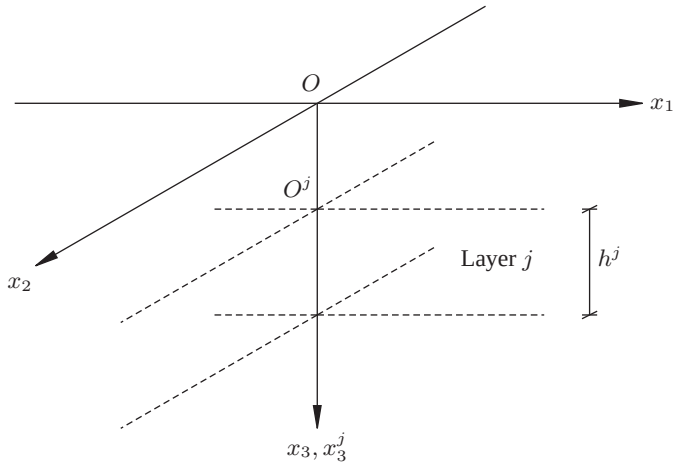

Figure 5–2 Definition of the global and local coordinates for layer j with the depth h^j. The (x_1, x_2, x_3)-coordinate system has the origin O, whereas the local (x_1, x_2, x_3^j)-coordinate system has the origin O^j.

Boundary conditions

In the frequency domain, and in terms of the horizontal wavenumbers, the displacements at the top and at the bottom of the jth layer are given, respectively, as

$$\bar{U}_i^{j0}(k_1, k_2, \omega) = \bar{U}_i(k_1, k_2, x_3^j = 0, \omega), \qquad \bar{U}_i^{j1}(k_1, k_2, \omega) = \bar{U}_i(k_1, k_2, x_3^j = h^j, \omega). \tag{5–8}$$

The meaning of the double superscript 10 applied in the definition of the flexibility or Green's function in the previous section now becomes somewhat clearer. Thus $\bar{U}_i^{10}$ are the displacement components at the top of the uppermost layer which coincides with the surface of the half-space. The remaining layers are counted downwards with $j = J$ referring to the bottommost layer.

Similar to Eq. (5–8) for the displacements, the traction at the top and bottom of layer j are given as

$$\bar{P}_i^{j0}(k_1, k_2, \omega) = \bar{P}_i(k_1, k_2, x_3^j = 0, \omega), \qquad \bar{P}_i^{j1}(k_1, k_2, \omega) = \bar{P}_i(k_1, k_2, x_3^j = h^j, \omega). \tag{5–9}$$

The quantities defined in Eqs. (5–8) and (5–9) may advantageously be stored in vector form as

$$\bar{\mathbf{S}}^{j0} = \begin{bmatrix} \bar{\mathbf{U}}^{j0} \\ \bar{\mathbf{P}}^{j0} \end{bmatrix}, \qquad \bar{\mathbf{S}}^{j1} = \begin{bmatrix} \bar{\mathbf{U}}^{j1} \\ \bar{\mathbf{P}}^{j1} \end{bmatrix}, \tag{5–10}$$

where $\bar{\mathbf{U}}^{j0} = \bar{\mathbf{U}}^{j0}(k_1, k_2, \omega)$ is the column vector with the components $\bar{U}_i^{j0}$, $i = 1, 2, 3$, etcetera.

Equations of motion

In the time domain, and in terms of Cartesian coordinates, the equations of motion for the layer are given in terms of the Cauchy equations, which in the absence of body forces read

$$\frac{\partial}{\partial x_k}\sigma_{ik}^j(x_1, x_2, x_3^j, t) = \rho^j \frac{\partial^2}{\partial t^2} u_i^j(x_1, x_2, x_3^j, t), \tag{5–11}$$

where $\sigma_{ik}^j(x_1, x_2, x_3^j, t)$ is the Cauchy stress tensor. On any part of the boundary, *i.e.* on the top and bottom of the layer, Dirichlet or Neumann conditions apply as defined by Eqs. (5–8) and (5–9), respectively. Initial conditions are of no interest in the present case, since the steady state solution is to be found.

The dynamic stiffness of the homogeneous and isotropic material may conveniently be described in terms of complex Lamé constants defined as

$$\lambda^j = \frac{\nu^j E^j \left(1 + \mathrm{i}\,\mathrm{sign}(\omega)\eta^j\right)}{(1+\nu^j)(1-2\nu^j)}, \qquad \mu^j = \frac{E^j \left(1 + \mathrm{i}\,\mathrm{sign}(\omega)\eta^j\right)}{2(1+\nu^j)}. \tag{5–12}$$

Subsequently, the stress amplitudes $\hat{\sigma}_{ik}^j(x_1, x_2, x_3^j, \omega)$ may be expressed in terms of the dilation amplitudes $\hat{\Delta}^j(x_1, x_2, x_3^j, \omega)$, and the infinitesimal strain tensor amplitudes $\hat{\varepsilon}_{ik}^j(x_1, x_2, x_3^j, \omega)$,

$$\hat{\sigma}_{ik}^j(x_1, x_2, x_3^j, \omega) = \lambda^j \hat{\Delta}^j(x_1, x_2, x_3^j, \omega)\delta_{ik} + 2\mu^j \hat{\varepsilon}_{ik}^j(x_1, x_2, x_3^j, \omega), \tag{5–13}$$

where δ_{ij} is the Kronecker delta and the following definitions apply:

$$\hat{\Delta}^j(x_1, x_2, x_3^j, \omega) = \frac{\partial}{\partial x_k} U_k^j(x_1, x_2, x_3^j, \omega), \tag{5–14}$$

$$\hat{\varepsilon}_{ik}^j(x_1, x_2, x_3^j, \omega) = \frac{1}{2}\left(\frac{\partial}{\partial x_i} U_k^j(x_1, x_2, x_3^j, \omega) + \frac{\partial}{\partial x_k} U_i^j(x_1, x_2, x_3^j, \omega)\right). \tag{5–15}$$

It is noted that $\partial/\partial x_3^j = \partial/\partial x_3$ as the local x_3^j-axes have the same positive direction as the global x_3-axis.

Inserting Eqs. (5–12) to (5–15) into the Fourier transformation of the Cauchy equation given by Eq. (5–11), the Navier equations in the frequency domain are achieved,

$$\left(\lambda^j + \mu^j\right) \frac{\partial \hat{\Delta}^j}{\partial x_i} + \mu^j \frac{\partial^2 U_i^j}{\partial x_k \partial x_k} = -\omega^2 \rho^j U_i^j. \tag{5–16}$$

Applying the double Fourier transformation over the horizontal Cartesian coordinates as defined by Eq. (5–5), the Navier equations in the frequency–wavenumber domain are established,

$$\left(\lambda^j + \mu^j\right) \mathrm{i}k_i \bar{\Delta}^j + \mu^j \left(\frac{\mathrm{d}^2}{\mathrm{d}x_3^2} - k_1^2 - k_2^2\right) \bar{U}_i^j = -\omega^2 \rho^j \bar{U}_i^j, \qquad i = 1, 2, \tag{5–17a}$$

$$\left(\lambda^j + \mu^j\right) \frac{\mathrm{d}\bar{\Delta}^j}{\mathrm{d}x_3} + \mu^j \left(\frac{\mathrm{d}^2}{\mathrm{d}x_3^2} - k_1^2 - k_2^2\right) \bar{U}_3^j = -\omega^2 \rho^j \bar{U}_3^j, \tag{5–17b}$$

where $\bar{\Delta}^j = \bar{\Delta}^j(k_1, k_2, x_3^j, \omega)$ is the double Fourier transform of $\hat{\Delta}^j(x_1, x_2, x_3^j, \omega)$ with respect to the horizontal Cartesian coordinates x_1 and x_2. Obviously,

$$\bar{\Delta}^j(k_1, k_2, x_3^j, \omega) = \mathrm{i}k_1 \bar{U}_1^j(k_1, k_2, x_3^j, \omega) + \mathrm{i}k_2 \bar{U}_2^j(k_1, k_2, x_3^j, \omega) + \frac{\mathrm{d}\bar{U}_3^j(k_1, k_2, x_3^j, \omega)}{\mathrm{d}x_3}. \tag{5–18}$$

Equations (5–17a) and (5–17b) are ordinary differential equations in x_3. When the boundary values at the top and the bottom of the layer expressed in Eqs. (5–8) and (5–9) are known, an analytical solution may be found as will be discussed below.

The solution for compression waves

The phase velocities of compression and shear waves, or P- and S-waves, are identified as

$$c_P = \sqrt{\frac{\lambda^j + 2\mu^j}{\rho^j}}, \qquad c_S = \sqrt{\frac{\mu^j}{\rho^j}}, \tag{5–19}$$

respectively. Accordingly, when the response varies harmonically with time with the circular frequency ω, P- and S-waves in layer j are associated with the wavenumbers k_P^j and k_S^j, respectively, defined as

$$\{k_P^j\}^2 = \frac{\omega^2}{\{c_P^j\}^2}, \qquad \{k_S^j\}^2 = \frac{\omega^2}{\{c_S^j\}^2}. \tag{5–20}$$

Introducing the parameters α_P^j and α_S^j as the larger of the roots to

$$\{\alpha_P^j\}^2 = k_1^2 + k_2^2 - \{k_P^j\}^2, \qquad \{\alpha_S^j\}^2 = k_1^2 + k_2^2 - \{k_S^j\}^2, \tag{5–21}$$

Eqs. (5–17a) and (5–17b) may conveniently be recast as

$$\left(\lambda^j + \mu^j\right) \mathrm{i}k_i \bar{\Delta}^j + \mu^j \left(\frac{\mathrm{d}^2 U_i^j}{\mathrm{d}x_3^2} - \{\alpha_S^j\}^2 U_i^j \right) = 0, \qquad i = 1, 2, \tag{5–22a}$$

$$\left(\lambda^j + \mu^j\right) \frac{\mathrm{d}\bar{\Delta}^j}{\mathrm{d}x_3} + \mu^j \left(\frac{\mathrm{d}^2 U_3^j}{\mathrm{d}x_3^2} - \{\alpha_S^j\}^2 U_3^j \right) = 0. \tag{5–22b}$$

Eq. (5–22a) is now multiplied with $\mathrm{i}k_i$ and Eq. (5–22b) is differentiated with respect to x_3. Adding the three resulting equations and making use of Eq. (5–18), an equation for the dilation is obtained in the form

$$\left(\lambda^j + \mu^j\right) \left(\frac{\mathrm{d}^2}{\mathrm{d}x_3^2} - k_1^2 - k_2^2 \right) \bar{\Delta}^j + \mu^j \left(\frac{\mathrm{d}^2}{\mathrm{d}x_3^2} - \{\alpha_S^j\}^2 \right) \bar{\Delta}^j = 0 \qquad \Rightarrow$$

$$\left(\lambda^j + 2\mu^j\right) \left(\frac{\mathrm{d}^2}{\mathrm{d}x_3^2} - k_1^2 - k_2^2 \right) \bar{\Delta}^j + \mu^j \left(k_1^2 + k_2^2 - \{\alpha_S^j\}^2 \right) \bar{\Delta}^j = 0 \qquad \Rightarrow$$

$$\left(\lambda^j + 2\mu^j\right) \left(\frac{\mathrm{d}^2}{\mathrm{d}x_3^2} - k_1^2 - k_2^2 \right) \bar{\Delta}^j + \mu^j \{k_S^j\}^2 \bar{\Delta}^j = 0. \tag{5–23}$$

The last derivation follows from Eq. (5–21). Further, Eqs. (5–19) and (5–20) involve that

$$\mu^j \{k_S^j\}^2 = \left(\lambda^j + 2\mu^j\right) \{k_P^j\}^2. \tag{5–24}$$

Inserting this result into Eq. (5–23), and once again making use of Eq. (5–21), we finally arrive at the ordinary homogenous differential equation

$$\left(\frac{\mathrm{d}^2}{\mathrm{d}x_3^2} - \{\alpha_P^j\}^2 \right) \bar{\Delta}^j = 0, \tag{5–25}$$

which has the full solution

$$\bar{\Delta}^j = a_1^j \mathrm{e}^{\alpha_P^j x_3^j} + a_2^j \mathrm{e}^{-\alpha_P^j x_3^j}. \tag{5–26}$$

Here a_1^j and a_2^j are integration constants that follow from the boundary conditions. Physically, the two parts of the solution (5–26) describe the decay of P-waves travelling in the negative and positive x_3-direction, respectively.

The solution for compression and shear waves

Insertion of the solution (5–26) into Eqs. (5–22a) and (5–22b) leads to three equations for the displacement amplitudes,

$$\frac{\mathrm{d}^2\bar{U}_i^j}{\mathrm{d}x_3^2} - \{\alpha_S^j\}^2\bar{U}_i^j = -\left(\frac{\lambda^j}{\mu^j}+1\right)\mathrm{i}k_i\left(a_1^j\mathrm{e}^{\alpha_P^j x_3^j} + a_2^j\mathrm{e}^{-\alpha_P^j x_3^j}\right), \qquad i=1,2, \tag{5–27a}$$

$$\frac{\mathrm{d}^2\bar{U}_3^j}{\mathrm{d}x_3^2} - \{\alpha_S^j\}^2\bar{U}_3^j = -\left(\frac{\lambda^j}{\mu^j}+1\right)\alpha_P^j\left(a_1^j\mathrm{e}^{\alpha_P^j x_3^j} - a_2^j\mathrm{e}^{-\alpha_P^j x_3^j}\right). \tag{5–27b}$$

Solutions to Eqs. (5–27a) and (5–27b) are found in the form

$$\bar{U}_1^j = \bar{U}_{1,c}^j + \bar{U}_{1,p}^j = b_1^j\mathrm{e}^{\alpha_S^j x_3^j} + b_2^j\mathrm{e}^{-\alpha_S^j x_3^j} + b_3^j\mathrm{e}^{\alpha_P^j x_3^j} + b_4^j\mathrm{e}^{-\alpha_P^j x_3^j}, \tag{5–28a}$$

$$\bar{U}_2^j = \bar{U}_{2,c}^j + \bar{U}_{2,p}^j = c_1^j\mathrm{e}^{\alpha_S^j x_3^j} + c_2^j\mathrm{e}^{-\alpha_S^j x_3^j} + c_3^j\mathrm{e}^{\alpha_P^j x_3^j} + c_4^j\mathrm{e}^{-\alpha_P^j x_3^j}, \tag{5–28b}$$

$$\bar{U}_3^j = \bar{U}_{3,c}^j + \bar{U}_{3,p}^j = d_1^j\mathrm{e}^{\alpha_S^j x_3^j} + d_2^j\mathrm{e}^{-\alpha_S^j x_3^j} + d_3^j\mathrm{e}^{\alpha_P^j x_3^j} + d_4^j\mathrm{e}^{-\alpha_P^j x_3^j}, \tag{5–28c}$$

where the subscripts c and p denote the complimentary and the particular solutions, respectively. These include S- and P-wave terms, respectively. Like a_1^j and a_2^j, c_1^j, c_2^j, etc. are integration constants given by the boundary conditions at the top and the bottom of layer j.

Apparently, the full solution has fourteen integration constants. However, a comparison of Eqs. (5–18) and (5–26) reveals that

$$\bar{\Delta}^j(k_1,k_2,x_3^j,\omega) = \mathrm{i}k_1\bar{U}_1^j + \mathrm{i}k_2\bar{U}_2^j + \frac{\mathrm{d}\bar{U}_3^j}{\mathrm{d}x_3} = a_1^j\mathrm{e}^{\alpha_P^j x_3^j} + a_2^j\mathrm{e}^{-\alpha_P^j x_3^j}. \tag{5–29}$$

By insertion of the complementary solutions, *i.e.* the first two terms in Eqs. (5–28a) to (5–28c), into Eq. (5–29) it immediately follows that

$$\mathrm{i}k_1 b_1^j + \mathrm{i}k_2 c_1^j + \alpha_S^j d_1^j = 0 \qquad \Rightarrow \qquad d_1^j = -\left(\frac{\mathrm{i}k_1}{\alpha_S^j}b_1^j + \frac{\mathrm{i}k_2}{\alpha_S^j}c_1^j\right), \tag{5–30a}$$

$$\mathrm{i}k_1 b_2^j + \mathrm{i}k_2 c_2^j - \alpha_S^j d_2^j = 0 \qquad \Rightarrow \qquad d_2^j = \frac{\mathrm{i}k_1}{\alpha_S^j}b_2^j + \frac{\mathrm{i}k_2}{\alpha_S^j}c_2^j. \tag{5–30b}$$

Here use has been made of the fact that the exponential functions of different powers are orthogonal. A further reduction of the number of integration constants is achieved by insertion of the particular solutions into the respective differential equations (5–27a) and (5–27b). Thus, after a few manipulations it may be shown that

$$b_3^j = -\frac{\mathrm{i}k_1}{\{k_P^j\}^2}\,a_1^j, \qquad c_3^j = -\frac{\mathrm{i}k_2}{\{k_P^j\}^2}\,a_1^j, \qquad d_3^j = -\frac{\alpha_P^j}{\{k_P^j\}^2}\,a_1^j, \tag{5–31a}$$

$$b_4^j = -\frac{\mathrm{i}k_1}{\{k_P^j\}^2}\,a_2^j, \qquad c_4^j = -\frac{\mathrm{i}k_2}{\{k_P^j\}^2}\,a_2^j, \qquad d_4^j = +\frac{\alpha_P^j}{\{k_P^j\}^2}\,a_2^j, \tag{5–31b}$$

where use has been made of the fact that

$$\frac{\lambda^j+\mu^j}{\mu^j\left(\{\alpha_S^j\}^2-\{\alpha_P^j\}^2\right)}=\frac{\{c_P^j\}^2-\{c_S^j\}^2}{\{c_S^j\}^2\left(\{k_P^j\}^2-\{k_S^j\}^2\right)}=\frac{\{k_S^j\}^2-\{k_P^j\}^2}{\{k_P^j\}^2\left(\{k_P^j\}^2-\{k_S^j\}^2\right)}=-\frac{1}{\{k_P^j\}^2},$$

which follows from the definitions given in Eqs. (5–19) to (5–21). Thus, eventually only six of the original fourteen integration constants are independent, namely a_1^j, a_2^j, b_1^j, b_2^j, c_1^j and c_2^j. As already mentioned, the terms including a_1^j and a_2^j represent P-waves moving up and down in layer j. Inspection of Eqs. (5–28a) to (5–28c) reveals that the b_1^j and b_2^j terms represent S-waves that are polarized in the x_1-direction and which are moving up and down in the layer, respectively. Similarly, the c_1^j and c_2^j terms describe the contributions from S-waves polarized in the x_2-direction and travelling up and down in the layer, respectively. It becomes evident that the previously defined quantities α_P^j and α_S^j may be interpreted as exponential decay coefficients of P- and S-waves, respectively. Obviously, when k_1 and k_2 are both small, α_P^j and α_S^j turns into "wavenumbers", as they become imaginary, cf. Eq. (5–21).

Once the displacement field is known, the stress components on any plane orthogonal to the x_3^j-axis may be found from Eq. (5–13) by letting index $k=3$. The full solution for displacements, $\bar{\mathbf{U}}^j$, and traction, $\bar{\mathbf{P}}^j$, may then be written in matrix form as

$$\bar{\mathbf{S}}^j=\begin{bmatrix}\bar{\mathbf{U}}^j\\ \bar{\mathbf{P}}^j\end{bmatrix}=\mathbf{A}^j\mathbf{E}^j\mathbf{b}^j,\qquad \mathbf{b}^j=\begin{bmatrix}a_1^j & b_1^j & c_1^j & a_2^j & b_2^j & c_2^j\end{bmatrix}^T \tag{5–32}$$

where $\mathbf{E}^j$ is a matrix of dimension (6×6), which has the diagonal terms

$$E_{11}^j=\mathrm{e}^{\alpha_P^j x_3^j},\quad E_{22}^j=E_{33}^j=\mathrm{e}^{\alpha_S^j x_3^j},\quad E_{44}^j=\mathrm{e}^{-\alpha_P^j x_3^j},\quad E_{55}^j=E_{66}^j=\mathrm{e}^{-\alpha_S^j x_3^j}, \tag{5–33}$$

and is otherwise empty. $\mathbf{A}^j$ is a matrix of dimension (6×6), the components of which follow from Eqs. (5–28a) to (5–31b) and (5–13). The computation of matrix $\mathbf{A}^j$ is further discussed below. Finally, the displacements and the traction at the two boundaries of layer j may be expressed as

$$\bar{\mathbf{S}}^{j0}=\mathbf{A}^{j0}\mathbf{b}^j,\qquad \mathbf{A}^{j0}=\mathbf{A}^j, \tag{5–34a}$$

$$\bar{\mathbf{S}}^{j1}=\mathrm{e}^{\alpha_P^j h^j}\mathbf{A}^{j1}\mathbf{b}^j,\qquad \mathbf{A}^{j1}=\mathbf{A}^{j0}\mathbf{D}^j. \tag{5–34b}$$

$\mathbf{D}^j$ is the matrix $\mathrm{e}^{-\alpha_P^j x_3^j}\mathbf{E}^j$ evaluated at $x_3^j=h_j$, *i.e.* a (6×6) matrix with the diagonal terms

$$D_{11}^j=1,\ \ D_{22}^j=D_{33}^j=\mathrm{e}^{(\alpha_S^j-\alpha_P^j)h^j},\ \ D_{44}^j=\mathrm{e}^{-2\alpha_P^j h^j},\ \ D_{55}^j=D_{66}^j=\mathrm{e}^{-(\alpha_P^j+\alpha_S^j)h^j}, \tag{5–35}$$

and zeros at all other positions. Equations (5–34a) and (5–34b) may be combined in order to eliminate vector $\mathbf{b}^j$ which contains unknown integration constants. This provides a transfer matrix for the layer as proposed by Thomson (1950) and Haskell (1953),

$$\bar{\mathbf{S}}^{j1}=\mathrm{e}^{\alpha_P^j h^j}\mathbf{A}^{j1}[\mathbf{A}^{j0}]^{-1}\bar{\mathbf{S}}^{j0}, \tag{5–36}$$

forming a relationship between the displacements and the traction at the top and the bottom of a single layer.

5.3.2 Solution for a static force

When a static load is applied, the circular frequency is identically equal to zero, $\omega \equiv 0$. As a consequence of this, the wavenumbers for P- and S-waves, *i.e.* k_P^j and k_S^j defined by Eq. (5–20), become zero and the integration constants b_3^j etc. given in Eqs. (5–31a) and (5–31b) are undefined. Hence, the solution given in the previous section does not apply in the static case.

The solution for the dilatational part of the displacements

Similar to the solution for the dynamic case $\omega \neq 0$, a solution for the dilatation is first derived. Analogous to Eq. (5–21), the quantity α is defined as

$$\alpha^2 = k_1^2 + k_2^2. \tag{5–37}$$

For $\omega = 0$, Eqs. (5–17a) and (5–17b) may then be rewritten as

$$\left(\lambda^j + \mu^j\right) \mathrm{i}k_i \bar{\Delta}^j + \mu^j \left(\frac{\mathrm{d}^2 U_i^j}{\mathrm{d}x_3^2} - \alpha^2 U_i^j \right) = 0, \qquad i = 1, 2, \tag{5–38a}$$

$$\left(\lambda^j + \mu^j\right) \frac{\mathrm{d}\bar{\Delta}^j}{\mathrm{d}x_3} + \mu^j \left(\frac{\mathrm{d}^2 U_3^j}{\mathrm{d}x_3^2} - \alpha^2 U_3^j \right) = 0. \tag{5–38b}$$

Proceeding in the same manner as before, we arrive at the ordinary homogenous differential equation

$$\left(\frac{\mathrm{d}^2}{\mathrm{d}x_3^2} - \alpha^2 \right) \bar{\Delta}^j = 0 \tag{5–39}$$

defining the dilatation. The full solution reads

$$\bar{\Delta}^j = a_1^j \mathrm{e}^{\alpha x_3^j} + a_2^j \mathrm{e}^{-\alpha x_3^j}, \tag{5–40}$$

where a_1^j and a_2^j are integration constants that follow from the boundary conditions.

The total displacement field

Insertion of the solution (5–40) into Eqs. (5–38a) and (5–38b) leads to the following three inhomogeneous equations for the displacement amplitudes,

$$\frac{\mathrm{d}^2 \bar{U}_i^j}{\mathrm{d}x_3^2} - \alpha^2 \bar{U}_i^j = -\left(\frac{\lambda^j}{\mu^j} + 1 \right) \mathrm{i}k_i \left(a_1^j \mathrm{e}^{\alpha x_3^j} + a_2^j \mathrm{e}^{-\alpha x_3^j} \right), \qquad i = 1, 2, \tag{5–41a}$$

$$\frac{\mathrm{d}^2 \bar{U}_3^j}{\mathrm{d}x_3^2} - \alpha^2 \bar{U}_3^j = -\left(\frac{\lambda^j}{\mu^j} + 1 \right) \alpha \left(a_1^j \mathrm{e}^{\alpha x_3^j} - a_2^j \mathrm{e}^{-\alpha x_3^j} \right). \tag{5–41b}$$

The solutions to the homogeneous parts of Eqs. (5–41a) and (5–41b) are in the same form as the complimentary solutions to Eqs. (5–27a) and (5–27b) with the exception that the exponential terms depend on α rather than α_P^j. However, since $\alpha_P^j = \alpha_S^j = \alpha$ for $\omega = 0$, the particular solutions suggested in Eqs. (5–28a) to (5–28c) fulfil the homogeneous equations, and hence they are invalid. Instead the full solutions are sought in the form

$$\bar{U}_1^j = \bar{U}_{1,c}^j + \bar{U}_{1,p}^j = b_1^j \mathrm{e}^{\alpha x_3^j} + b_2^j \mathrm{e}^{-\alpha x_3^j} + b_3^j x_3^j \mathrm{e}^{\alpha x_3^j} + b_4^j x_3^j \mathrm{e}^{-\alpha x_3^j}, \tag{5–42a}$$

$$\bar{U}_2^j = \bar{U}_{2,c}^j + \bar{U}_{2,p}^j = c_1^j \mathrm{e}^{\alpha x_3^j} + c_2^j \mathrm{e}^{-\alpha x_3^j} + c_3^j x_3^j \mathrm{e}^{\alpha x_3^j} + c_4^j x_3^j \mathrm{e}^{-\alpha x_3^j}, \tag{5–42b}$$

$$\bar{U}_3^j = \bar{U}_{3,c}^j + \bar{U}_{3,p}^j = d_1^j \mathrm{e}^{\alpha x_3^j} + d_2^j \mathrm{e}^{-\alpha x_3^j} + d_3^j x_3^j \mathrm{e}^{\alpha x_3^j} + d_4^j x_3^j \mathrm{e}^{-\alpha x_3^j}. \tag{5–42c}$$

Again, apparently there are fourteen integration constants. However, insertion of $\bar{U}_{1,p}^j$ and $\bar{U}_{2,p}^j$ into Eq. (5–41a) and insertion of Eq. $\bar{U}_{3,p}^j$ into Eq. (5–41b) provide the identities

$$b_3^j = -\frac{1}{2}\frac{\lambda+\mu}{\mu}\frac{\mathrm{i}k_1}{\alpha}\, a_1^j, \qquad c_3^j = -\frac{1}{2}\frac{\lambda+\mu}{\mu}\frac{\mathrm{i}k_2}{\alpha}\, a_1^j, \qquad d_3^j = -\frac{1}{2}\frac{\lambda+\mu}{\mu}\, a_1^j, \tag{5–43a}$$

$$b_4^j = +\frac{1}{2}\frac{\lambda+\mu}{\mu}\frac{\mathrm{i}k_1}{\alpha}\, a_2^j, \qquad c_4^j = +\frac{1}{2}\frac{\lambda+\mu}{\mu}\frac{\mathrm{i}k_2}{\alpha}\, a_2^j, \qquad d_4^j = -\frac{1}{2}\frac{\lambda+\mu}{\mu}\, a_2^j. \tag{5–43b}$$

Similarly, a reduction in the number of independent constants is achieved by a comparison of Eqs. (5–18) and (5–40),

$$\bar{\Delta}^j(k_1, k_2, x_3^j, \omega) = \mathrm{i}k_1 \bar{U}_1^j + \mathrm{i}k_2 \bar{U}_2^j + \frac{\mathrm{d}\bar{U}_3^j}{\mathrm{d}x_3} = a_1^j \mathrm{e}^{\alpha x_3^j} + a_2^j \mathrm{e}^{-\alpha x_3^j}. \tag{5–44}$$

By insertion of the full solutions given by Eqs. (5–42a) to (5–42c) into Eq. (5–44), it follows that

$$\mathrm{i}k_1 b_1^j + \mathrm{i}k_2 c_1^j + \alpha d_1^j + \mathrm{i}k_1 x_3^j b_3^j + \mathrm{i}k_2 x_3^j c_3^j + \left(1 + \alpha x_3^j\right) d_3 = a_1, \tag{5–45a}$$

$$\mathrm{i}k_1 b_2^j + \mathrm{i}k_2 c_2^j - \alpha d_2^j + \mathrm{i}k_1 x_3^j b_4^j + \mathrm{i}k_2 x_3^j c_4^j + \left(1 - \alpha x_3^j\right) d_4 = a_2, \tag{5–45b}$$

which involves a relationship between the integration constants in the form

$$\mathrm{i}k_1 b_1^j + \mathrm{i}k_2 c_1^j + \alpha d_1^j + d_3^j = a_1^j, \qquad \mathrm{i}k_1 b_2^j + \mathrm{i}k_2 c_2^j - \alpha d_2^j + d_4^j = a_2^j. \tag{5–46}$$

Inserting the definitions of d_3^j and d_4^j given by Eqs. (5–43a) and (5–43b), respectively, into Eq. (5–46), the equivalents of Eqs. (5–30a) and (5–30b) in the static case read

$$d_1^j = -\left(\frac{\mathrm{i}k_1}{\alpha} b_1^j + \frac{\mathrm{i}k_2}{\alpha} c_1^j\right) + \frac{\lambda+3\mu}{2\mu\alpha} a_1^j, \qquad d_2^j = \frac{\mathrm{i}k_1}{\alpha} b_2^j + \frac{\mathrm{i}k_2}{\alpha} c_2^j - \frac{\lambda+3\mu}{2\mu\alpha} a_2^j. \tag{5–47}$$

The stress components on a horizontal plane are found from Eq. (5–13) with $k = 3$, and the full solution for displacements and traction is then given in the form provided by Eqs. (5–32) and (5–33). However, in the static case $\alpha_P^j = \alpha_S^j = \alpha$, and the matrix $\mathbf{A}^j$ is replaced by an equivalent matrix denoted $\mathbf{A}_0^j$. Since the solution in the static case contains terms in the form $x_3^j \mathrm{e}^{\alpha x_3^j}$ and $x_3^j \mathrm{e}^{-\alpha x_3^j}$, and since only the exponential functions are accounted for in the matrix $\mathbf{E}^j$, it is evident that the matrix $\mathbf{A}_0^j$ depends on x_3^j. Consequently, the displacements and the traction at the two boundaries of layer j become

$$\bar{\mathbf{S}}^{j0} = \mathbf{A}_0^{j0} \mathbf{b}^j, \qquad \mathbf{A}_0^{j0} = \mathbf{A}_0^j(x_3^j = 0), \tag{5–48a}$$

$$\bar{\mathbf{S}}^{j1} = \mathrm{e}^{\alpha_P^j h^j} \mathbf{A}_0^{j1} \mathbf{b}^j, \qquad \mathbf{A}_0^{j1} = \mathbf{A}_0^j(x_3^j = h^j) \mathbf{D}^j. \tag{5–48b}$$

The definition of $\mathbf{D}^j$ given in Eq. (5–35) applies with $\alpha_P^j = \alpha_S^j = \alpha$, and analogous to the dynamic case, Eqs. (5–48a) and (5–48b) may be combined to form the layer transfer matrix

$$\bar{\mathbf{S}}^{j1} = \mathrm{e}^{\alpha h^j} \mathbf{A}_0^{j1} [\mathbf{A}_0^{j0}]^{-1} \bar{\mathbf{S}}^{j0}. \tag{5–49}$$

5.3.3 Assembly of multiple layers

At an interface between two layers, the displacements should be continuous and there should be equilibrium of the traction. This may be expressed as $\bar{\mathbf{S}}^{j0} = \bar{\mathbf{S}}^{j-1,1}$, $j = 2, 3, ..., J$, *i.e.* the quantities at the top of layer j are equal to those at the bottom of layer $j-1$. Proceeding in this manner, Eq. (5–36) for the single layer may be rewritten for a system of J layers,

$$\begin{aligned}\bar{\mathbf{S}}^{J1} &= \mathrm{e}^{\alpha_P^J h^J}\mathbf{A}^{J1}[\mathbf{A}^{J0}]^{-1}\bar{\mathbf{S}}^{J0} \quad = \quad \mathrm{e}^{\alpha_P^J h^J}\mathbf{A}^{J1}[\mathbf{A}^{J0}]^{-1}\bar{\mathbf{S}}^{J-1,1} \\ &= \mathrm{e}^{\alpha_P^J h^J}\mathrm{e}^{\alpha_P^{J-1} h^{J-1}}\mathbf{A}^{J1}[\mathbf{A}^{J0}]^{-1}\mathbf{A}^{J-1,1}[\mathbf{A}^{J-1,0}]^{-1}\bar{\mathbf{S}}^{J-1,0} \qquad \Rightarrow \\ \bar{\mathbf{S}}^{J1} &= \mathrm{e}^{\Sigma\alpha}\mathbf{A}^{J1}[\mathbf{A}^{10}]^{-1}\mathbf{A}^{J-1,1}[\mathbf{A}^{J-1,0}]^{-1}\cdots\mathbf{A}^{11}[\mathbf{A}^{10}]^{-1}\bar{\mathbf{S}}^{10}, \qquad \Sigma\alpha = \sum_{j=1}^{J}\alpha_P^j h^j. \end{aligned} \quad (5\text{–}50)$$

Introducing the transfer matrix $\mathbf{T}$ defined as

$$\mathbf{T} = \begin{bmatrix}\mathbf{T}_{11} & \mathbf{T}_{12}\\ \mathbf{T}_{21} & \mathbf{T}_{22}\end{bmatrix} = \mathbf{A}^{J1}[\mathbf{A}^{J0}]^{-1}\mathbf{A}^{J-1,1}[\mathbf{A}^{J-1,0}]^{-1}\cdots\mathbf{A}^{11}[\mathbf{A}^{10}]^{-1}, \quad (5\text{–}51)$$

Eq. (5–50) may in turn be written as $\bar{\mathbf{S}}^{J1} = \mathrm{e}^{\Sigma\alpha}\mathbf{T}\bar{\mathbf{S}}^{10}$, or

$$\begin{bmatrix}\bar{\mathbf{U}}^{J1}\\ \bar{\mathbf{P}}^{J1}\end{bmatrix} = \mathrm{e}^{\Sigma\alpha}\begin{bmatrix}\mathbf{T}_{11} & \mathbf{T}_{12}\\ \mathbf{T}_{21} & \mathbf{T}_{22}\end{bmatrix}\begin{bmatrix}\bar{\mathbf{U}}^{10}\\ \bar{\mathbf{P}}^{10}\end{bmatrix}, \qquad \Sigma\alpha = \sum_{j=1}^{J}\alpha_P^j h^j. \quad (5\text{–}52)$$

This formulation is due to Thomson (1950) and Haskell (1953) and establishes a relationship between the traction and the displacements at the free surface of the half-space and the equivalent quantities at the bottom of the stratum. For the frequency $\omega = 0$, Eqs. (5–50) to (5–52) still apply, but the matrices $\mathbf{A}^{j0}$ and $\mathbf{A}^{j1}$ are replaced with $\mathbf{A}_0^{j0}$ and $\mathbf{A}_0^{j1}$, respectively, and $\alpha_P^j = \alpha$.

5.3.4 The solution for a stratum over a rigid foundation

A rigid foundation may underlay the stratum. This model may be applied, for example, in the analysis of a stratified ground consisting of multiple soil layers overlaying bedrock. On the surface of the rigid foundation, the displacements are identically equal to zero and thus, by insertion into Eq. (5–52),

$$\begin{bmatrix}\bar{\mathbf{U}}^{J1}\\ \bar{\mathbf{P}}^{J1}\end{bmatrix} = \begin{bmatrix}\mathbf{0}\\ \bar{\mathbf{P}}^{J1}\end{bmatrix} = \mathrm{e}^{\Sigma\alpha}\begin{bmatrix}\mathbf{T}_{11} & \mathbf{T}_{12}\\ \mathbf{T}_{21} & \mathbf{T}_{22}\end{bmatrix}\begin{bmatrix}\bar{\mathbf{U}}^{10}\\ \bar{\mathbf{P}}^{10}\end{bmatrix}. \quad (5\text{–}53)$$

The first three rows of this matrix equation provide the identity

$$\bar{\mathbf{U}}^{10} = \bar{\mathbf{G}}_{\mathbf{rf}}\bar{\mathbf{P}}^{10}, \qquad \bar{\mathbf{G}}_{\mathbf{rf}} = -\mathbf{T}_{11}^{-1}\mathbf{T}_{12}. \quad (5\text{–}54)$$

$\bar{\mathbf{G}}_{\mathbf{rf}} = \bar{\mathbf{G}}_{\mathbf{rf}}(k_1, k_2, \omega)$ is the flexibility matrix for a stratum over a rigid foundation. It is observed that the exponential function of the power $\Sigma\alpha$, defined in Eq. (5–52), vanishes in the formulation provided by Eq. (5–54). This is a great advantage from a computational point of view, since $\mathrm{e}^{\Sigma\alpha}$ becomes very large for strata of great depths, which may lead to problems on a computer—even when double precision complex variables are employed.

5.3.5 The solution for a homogeneous or stratified half-space

A half-space may be present underneath the stratum consisting of J layers. In this context, the material properties etc. of the half-space will be assigned the superscript $J+1$. The main difference between a semi-infinite half-space and a layer of finite depth is that only an upper boundary is present, *i.e.* the boundary situated at $x_3^{J+1} = 0$. Since the material is assumed to be homogeneous, no reflection of waves will take place inside the half-space. Further assuming that no sources are present in the interior of the half-space, only outgoing, *i.e.* downwards propagating, waves can be present. Dividing the matrices $\mathbf{A}^j$ and $\mathbf{E}^j$ for a layer of finite depth, cf. Eq. (5–32), into four quadrants, and the column vector $\mathbf{b}^j$ into two sub-vectors,

$$\mathbf{A}^j = \begin{bmatrix} \mathbf{A}_{11}^j & \mathbf{A}_{12}^j \\ \mathbf{A}_{21}^j & \mathbf{A}_{22}^j \end{bmatrix}, \qquad \mathbf{E}^j = \begin{bmatrix} \mathbf{E}_{11}^j & \mathbf{E}_{12}^j \\ \mathbf{E}_{21}^j & \mathbf{E}_{22}^j \end{bmatrix}, \qquad \mathbf{b}^j = \begin{bmatrix} \mathbf{b}_1^j \\ \mathbf{b}_2^j \end{bmatrix}, \tag{5–55}$$

it is evident that only half of the solution applies to the half-space, *i.e.*

$$\bar{\mathbf{S}}^{J+1} = \begin{bmatrix} \bar{\mathbf{U}}^{J+1} \\ \bar{\mathbf{P}}^{J+1} \end{bmatrix} = \begin{bmatrix} \mathbf{A}_{12}^{J+1} \\ \mathbf{A}_{22}^{J+1} \end{bmatrix} \mathbf{E}_{22}^{J+1} \mathbf{b}_2^{J+1}, \qquad \mathbf{b}_2^{J+1} = \begin{bmatrix} a_2^{J+1} & b_2^{J+1} & c_2^{J+1} \end{bmatrix}^T. \tag{5–56}$$

The terms including the integration constants a_1^{J+1}, b_1^{J+1} and c_1^{J+1} are physically invalid as they correspond to waves incoming from $x_3^{J+1} = \infty$, *i.e.* from infinite depth.

From Eq. (5–56), the traction on the interface between the bottommost layer and the half-space may be expressed in terms of the corresponding displacements,

$$\bar{\mathbf{U}}^{J+1} = \mathbf{A}_{12}^{J+1} [\mathbf{A}_{22}^{J+1}]^{-1} \bar{\mathbf{P}}^{J+1}. \tag{5–57}$$

The matrix $\mathbf{E}_{22}^{J+1}$ reduces to the identity matrix of order 3, since all the exponential terms are equal to 1 for $x_3^{J+1} = 0$.

Flexibility of a homogeneous half-space

If no layers are present in the model of the stratum, $J = 0$ and it immediately follows from Eq. (5–57) that Eq. (5–7), written in matrix form, becomes

$$\bar{\mathbf{U}}^{10} = \bar{\mathbf{G}}_{\mathbf{hh}} \bar{\mathbf{P}}^{10}, \qquad \bar{\mathbf{G}}_{\mathbf{hh}} = \mathbf{A}_{12}^{10} [\mathbf{A}_{22}^{10}]^{-1}, \tag{5–58}$$

where it is noted that the flexibility matrix for the homogeneous half-space $\bar{\mathbf{G}}_{\mathbf{hh}} = \bar{\mathbf{G}}_{\mathbf{hh}}(k_1, k_2, \omega)$ is given in the horizontal wavenumber–frequency domain.

Flexibility of a stratum over a half-space

When J layers overlay a homogeneous half-space, continuity of the displacements, equilibrium of the traction and application of Eq. (5–57) provides

$$\bar{\mathbf{U}}^{J1} = \bar{\mathbf{U}}^{J+1,0} = \mathbf{A}_{12}^{J+1} [\mathbf{A}_{22}^{J+1}]^{-1} \bar{\mathbf{P}}^{J+1,0} = \mathbf{A}_{12}^{J+1} [\mathbf{A}_{22}^{J+1}]^{-1} \bar{\mathbf{P}}^{J1}. \tag{5–59}$$

Insertion of this result into Eq. (5–52) leads to system of equations

$$\begin{bmatrix} \bar{\mathbf{U}}^{J1} \\ \bar{\mathbf{P}}^{J1} \end{bmatrix} = \begin{bmatrix} \mathbf{A}_{12}^{J+1} [\mathbf{A}_{22}^{J+1}]^{-1} \bar{\mathbf{P}}^{J1} \\ \bar{\mathbf{P}}^{J1} \end{bmatrix} = \mathrm{e}^{\Sigma\alpha} \begin{bmatrix} \mathbf{T}_{11} & \mathbf{T}_{12} \\ \mathbf{T}_{21} & \mathbf{T}_{22} \end{bmatrix} \begin{bmatrix} \bar{\mathbf{U}}^{10} \\ \bar{\mathbf{P}}^{10} \end{bmatrix}. \tag{5–60}$$

From the bottommost three rows of the matrix equation, an expression of $\bar{\mathbf{P}}^{J1}$ is obtained which may be inserted into the first three equations. This leads to the solution

$$\bar{\mathbf{U}}^{10} = \bar{\mathbf{G}}_{\mathbf{lh}}\bar{\mathbf{P}}^{10}, \tag{5–61}$$

where the flexibility matrix for the layered half-space $\bar{\mathbf{G}}_{\mathbf{lh}} = \bar{\mathbf{G}}_{\mathbf{lh}}(k_1, k_2, \omega)$ is given by

$$\bar{\mathbf{G}}_{\mathbf{lh}} = \left(\mathbf{A}_{12}^{J+1}[\mathbf{A}_{22}^{J+1}]^{-1}\mathbf{T}_{21} - \mathbf{T}_{11}\right)^{-1}\left(\mathbf{T}_{12} - \mathbf{A}_{12}^{J+1}[\mathbf{A}_{22}^{J+1}]^{-1}\mathbf{T}_{22}\right), \tag{5–62}$$

where again the exponential function disappears.

5.4 Optimising the numerical computations

In this section, a few methods will be described that may be used to speed up the computations.

5.4.1 Computation of the matrices $\mathbf{A}^{j0}$ and $\mathbf{A}^{j1}$

The computation of the transfer matrix $\mathbf{T}$ involves inversion of the matrices $\mathbf{A}^{j0}$, $j = 1, 2, ..., J$. Further, the flexibility matrix $\bar{\mathbf{G}}(k_1, k_2, \omega)$ has to be evaluated for all combinations (k_1, k_2) before the transformation given by Eq. (5–6) may be applied. However, as pointed out by Sheng *et al.* (1999a), the evaluation of $\mathbf{A}^j$, and therefore also the Green's function matrix $\bar{\mathbf{G}}$, is particularly simple along the line defined by $k_1 = 0$. To take advantage of this, a coordinate transformation is introduced in the form

$$\begin{bmatrix} k_1 \\ k_2 \\ x_3 \end{bmatrix} = \mathbf{R}(\varphi)\begin{bmatrix} \gamma \\ \alpha \\ x_3 \end{bmatrix}, \qquad \mathbf{R}(\varphi) = \begin{bmatrix} \sin\varphi & \cos\varphi & 0 \\ -\cos\varphi & \sin\varphi & 0 \\ 0 & 0 & 1 \end{bmatrix}. \tag{5–63}$$

This corresponds to a rotation of (k_1, k_2, x_3)-basis by the angle $\varphi - \pi/2$ around the x_3-axis as illustrated in Fig. 5–4. It follows from Eq. (5–63) that $R_{ij}(\varphi) = R_{ji}(\pi - \varphi)$, which in matrix–vector notation corresponds to $\{\mathbf{R}(\varphi)\}^T = \mathbf{R}(\pi - \varphi)$.

For any combination of k_1 and k_2, the angle φ is now defined so that $\gamma = 0$. The relationship between the coordinates in the two systems of reference is then given by

$$k_1 = \alpha\cos\varphi, \qquad k_2 = \alpha\sin\varphi, \qquad \alpha = \sqrt{k_1^2 + k_2^2}, \qquad \tan\varphi = \frac{k_2}{k_1}, \qquad \gamma = 0. \tag{5–64}$$

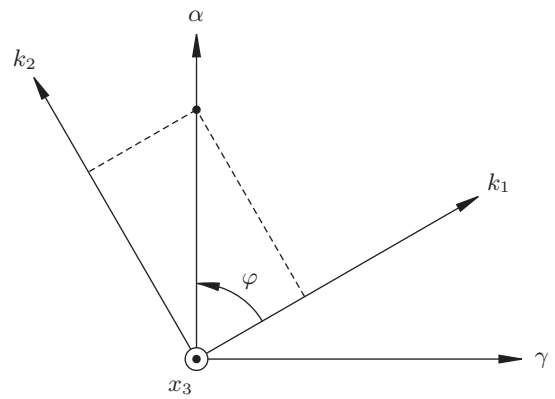

Figure 5–3 Definition of the (k_1, k_2, x_3)- and (γ, α, x_3)-coordinate systems.

The computational advantage of this particular orientation of the (γ, α, x_3)-coordinate system is twofold. Firstly, the flexibility matrix may be evaluated along a line rather than over an area, and for any other combination of the wavenumbers, the Green's function matrix can be computed as

$$\bar{\mathbf{G}}(k_1, k_2, \omega) = \mathbf{R}(\varphi)\hat{\bar{\mathbf{G}}}\{\mathbf{R}(\varphi)\}^T \qquad \text{or} \qquad \bar{G}_{ik}(k_1, k_2, \omega) = R_{il}(\varphi)\hat{\bar{G}}_{lm}R_{km}(\varphi). \tag{5–65}$$

Here $\hat{\bar{\mathbf{G}}} = \hat{\bar{\mathbf{G}}}(\alpha, \omega) = \bar{\mathbf{G}}(0, \alpha, \omega)$. Secondly, the matrices $\mathbf{A}^{j0}$ and $\mathbf{A}^{j1}$—and therefore also $\mathbf{A}_{12}^{J+1}$ and $\mathbf{A}_{22}^{J+1}$—simplify significantly when one of the wavenumbers is equal to zero. Thus, when $k_1 = \gamma = 0$, $k_2 = \alpha$ and $\omega \neq 0$,

$$\hat{\mathbf{A}}^{j0} = \mathbf{A}^{j0}(0, \alpha, \omega) = \begin{bmatrix} 0 & 1 & 0 & 0 & 1 & 0 \\ \hat{A}_{21}^{j0} & 0 & 1 & \hat{A}_{21}^{j0} & 0 & 1 \\ \hat{A}_{31}^{j0} & 0 & \hat{A}_{33}^{j0} & -\hat{A}_{31}^{j0} & 0 & -\hat{A}_{33}^{j0} \\ 0 & \hat{A}_{42}^{j0} & 0 & 0 & -\hat{A}_{42}^{j0} & 0 \\ \hat{A}_{51}^{j0} & 0 & \hat{A}_{53}^{j0} & -\hat{A}_{51}^{j0} & 0 & -\hat{A}_{53}^{j0} \\ \hat{A}_{61}^{j0} & 0 & \hat{A}_{63}^{j0} & \hat{A}_{61}^{j0} & 0 & \hat{A}_{63}^{j0} \end{bmatrix}, \tag{5–66a}$$

where

$$\begin{aligned} &\hat{A}_{21}^{j0} = -\mathrm{i}\alpha/\{k_P^j\}^2, \quad \hat{A}_{31}^{j0} = -\alpha_P^j/\{k_P^j\}^2, \quad \hat{A}_{33}^{j0} = -\mathrm{i}\alpha/\alpha_S^j, \\ &\hat{A}_{42}^{j0} = \alpha_S^j\mu^j, \quad \hat{A}_{51}^{j0} = -2\mathrm{i}\mu^j\alpha_P^j\alpha/\{k_P^j\}^2, \quad \hat{A}_{53}^{j0} = \mu^j(\alpha^2/\alpha_S^j + \alpha_S^j), \\ &\hat{A}_{61}^{j0} = -\mu^j\left(\{k_S^j\}^2 + 2\{\alpha_S^j\}^2\right)/\{k_P^j\}^2, \quad \hat{A}_{63}^{j0} = -2\mathrm{i}\mu^j\alpha. \end{aligned} \tag{5–66b}$$

At the bottom of the layer, the corresponding matrix is evaluated as $\hat{\mathbf{A}}^{j1} = \hat{\mathbf{A}}^{j0}\mathbf{D}^j$, where the components of the matrix $\mathbf{D}^j$ are given by Eq. (5–35)

When $k_1 = \gamma = 0$, $k_2 = \alpha$ and $\omega = 0$ (*i.e.* the static case), $\hat{\mathbf{A}}^{j0}$ is replaced by $\hat{\mathbf{A}}_0^{j0}$. The structure of $\hat{\mathbf{A}}_0^{j0}$ is identical to that of $\hat{\mathbf{A}}^{j0}$ given by Eq. (5–66a), but the nonzero components are different. Thus, for $x_3^j = 0$,

$$\begin{aligned} &\hat{A}_{0,21}^{j0} = 0, \quad \hat{A}_{0,31}^{j0} = \left(\lambda^j + 3\mu^j\right)/\left(2\mu^j\alpha\right), \quad \hat{A}_{0,33}^{j0} = -\mathrm{i}, \quad \hat{A}_{0,42}^{j0} = \alpha\mu^j, \\ &\hat{A}_{0,51}^{j0} = \mathrm{i}\mu^j, \quad \hat{A}_{0,53}^{j0} = 2\mu^j\alpha, \quad \hat{A}_{0,61}^{j0} = \lambda^j + 2\mu^j, \quad \hat{A}_{0,63}^{j0} = -2\mathrm{i}\mu^j\alpha. \end{aligned} \tag{5–67}$$

However, at the bottom of a layer, *i.e.* for $x_3^j = h^j$, the structure of the matrix $\hat{\mathbf{A}}_0^{j0}$ to be applied in the operation $\hat{\mathbf{A}}_0^{j1} = \hat{\mathbf{A}}_0^{j0}\mathbf{D}^j$ is different from that of $\hat{\mathbf{A}}^{j0}$ provided by Eq. (5–66a). Hence, instead

$$\hat{\mathbf{A}}_0^{j1} = \begin{bmatrix} 0 & 1 & 0 & 0 & 1 & 0 \\ \check{A}_{0,21}^{j0} & 0 & 1 & -\check{A}_{0,21}^{j0} & 0 & 1 \\ \check{A}_{0,31}^{j0} & 0 & \check{A}_{0,33}^{j0} & \check{A}_{0,34}^{j0} & 0 & -\check{A}_{0,33}^{j0} \\ 0 & \check{A}_{0,42}^{j0} & 0 & 0 & -\check{A}_{0,42}^{j0} & 0 \\ \check{A}_{0,51}^{j0} & 0 & \check{A}_{0,53}^{j0} & \check{A}_{0,54}^{j0} & 0 & -\check{A}_{0,53}^{j0} \\ \check{A}_{0,61}^{j0} & 0 & \check{A}_{0,63}^{j0} & \check{A}_{0,64}^{j0} & 0 & \check{A}_{0,63}^{j0} \end{bmatrix} \mathbf{D}^j, \tag{5–68a}$$

where

$$\check{A}^{j0}_{0,21} = \left(\lambda^j + \mu^j\right) h^j / \left(2\mathrm{i}\mu^j\right), \quad \check{A}^{j0}_{0,31} = \left(\lambda^j + 3\mu^j\right) / \left(2\mu^j\alpha\right) - \left(\lambda^j + \mu^j\right) h^j / \left(2\mu^j\right),$$
$$\check{A}^{j0}_{0,33} = -\mathrm{i}, \quad \check{A}^{j0}_{0,34} = -\left(\lambda^j + 3\mu^j\right) / \left(2\mu^j\alpha\right) - \left(\lambda^j + \mu^j\right) h^j / \left(2\mu^j\right), \quad \check{A}^{j0}_{0,42} = \alpha\mu^j,$$
$$\check{A}^{j0}_{0,51} = \mathrm{i}\left(\mu^j - (\lambda^j + \mu^j)\alpha h^j\right), \quad \check{A}^{j0}_{0,53} = 2\mu^j\alpha, \quad \check{A}^{j0}_{0,54} = -\mathrm{i}\left(\mu^j + (\lambda^j + \mu^j)\alpha h^j\right),$$
$$\check{A}^{j0}_{0,61} = \left(\lambda^j + 2\mu^j\right) - \left(\lambda^j + \mu^j\right)\alpha h^j, \quad \check{A}^{j0}_{0,63} = -2\mathrm{i}\mu^j\alpha,$$
$$\check{A}^{j0}_{0,64} = \left(\lambda^j + 2\mu^j\right) + \left(\lambda^j + \mu^j\right)\alpha h^j. \tag{5–68b}$$

Inversion of the matrices $\hat{\mathbf{A}}^{j0}$ and $\hat{\mathbf{A}}^{j0}_0$

A result of the many zeros in $\hat{\mathbf{A}}^{j0}$ and $\hat{\mathbf{A}}^{j0}_0$ is that the matrices can be inverted analytically. This may reduce computation time significantly. For $\hat{\mathbf{A}}^{j0}$, the inverted matrix becomes

$$\hat{\mathbf{B}}^{j0} = \left[\mathbf{A}^{j0}(0,\alpha,\omega)\right]^{-1} = \begin{bmatrix} 0 & \hat{B}^{j0}_{12} & \hat{B}^{j0}_{13} & 0 & \hat{B}^{j0}_{15} & \hat{B}^{j0}_{16} \\ \hat{B}^{j0}_{21} & 0 & 0 & \hat{B}^{j0}_{24} & 0 & 0 \\ 0 & \hat{B}^{j0}_{32} & \hat{B}^{j0}_{33} & 0 & \hat{B}^{j0}_{35} & \hat{B}^{j0}_{36} \\ 0 & \hat{B}^{j0}_{12} & -\hat{B}^{j0}_{13} & 0 & -\hat{B}^{j0}_{15} & \hat{B}^{j0}_{16} \\ \hat{B}^{j0}_{21} & 0 & 0 & -\hat{B}^{j0}_{24} & 0 & 0 \\ 0 & \hat{B}^{j0}_{32} & -\hat{B}^{j0}_{33} & 0 & -\hat{B}^{j0}_{35} & \hat{B}^{j0}_{36} \end{bmatrix}, \quad \omega \neq 0, \tag{5–69a}$$

where

$$\hat{B}^{j0}_{12} = \frac{\mathrm{i}\{k^j_P\}^2\alpha}{C_1}, \quad \hat{B}^{j0}_{13} = \frac{\{k^j_P\}^2(\alpha^2 + \alpha^2_S)}{2\alpha_P C_2}, \quad \hat{B}^{j0}_{15} = \frac{\mathrm{i}\{k^j_P\}^2\alpha}{2\alpha_P\mu^j C_2}, \quad \hat{B}^{j0}_{16} = \frac{\{k^j_P\}^2}{2\mu^j C_1},$$
$$\hat{B}^{j0}_{32} = -\frac{\{k^j_S\}^2 + 2\alpha^2_S}{2C_1}, \quad \hat{B}^{j0}_{33} = \frac{\mathrm{i}\alpha_S\alpha}{C_2}, \quad \hat{B}^{j0}_{35} = -\frac{\alpha_S}{2C_2\mu^j}, \quad \hat{B}^{j0}_{36} = \frac{\mathrm{i}\alpha}{2\mu^j C_1},$$
$$\hat{B}^{j0}_{21} = \frac{1}{2}, \quad \hat{B}^{j0}_{24} = \frac{1}{2\mu^j\alpha_S}, \quad C_1 = 2\alpha^2 - k^2_S(j) - 2\alpha^2_S, \quad C_2 = \alpha^2 - \alpha^2_S. \tag{5–69b}$$

Similarly, in the case of $\hat{\mathbf{A}}^{j0}_0$, the inverted matrix reads

$$\hat{\mathbf{B}}^{j0}_0 = \left[\mathbf{A}^{j0}(0,\alpha,0)\right]^{-1} = \begin{bmatrix} 0 & \hat{B}^{j0}_{0,12} & \hat{B}^{j0}_{0,13} & 0 & \hat{B}^{j0}_{0,15} & \hat{B}^{j0}_{0,16} \\ \hat{B}^{j0}_{0,21} & 0 & 0 & \hat{B}^{j0}_{0,24} & 0 & 0 \\ 0 & \hat{B}^{j0}_{0,21} & \hat{B}^{j0}_{0,33} & 0 & \hat{B}^{j0}_{0,35} & 0 \\ 0 & \hat{B}^{j0}_{0,12} & -\hat{B}^{j0}_{0,13} & 0 & -\hat{B}^{j0}_{0,15} & \hat{B}^{j0}_{0,16} \\ \hat{B}^{j0}_{0,21} & 0 & 0 & -\hat{B}^{j0}_{0,24} & 0 & 0 \\ 0 & \hat{B}^{j0}_{0,21} & -\hat{B}^{j0}_{0,33} & 0 & -\hat{B}^{j0}_{0,35} & 0 \end{bmatrix}, \tag{5–70a}$$

where

$$\hat{B}^{j0}_{0,12} = \frac{\mathrm{i}\mu^j\alpha}{C_n 3}, \quad \hat{B}^{j0}_{0,13} = \frac{1}{\mu^j\alpha C_3}, \quad \hat{B}^{j0}_{0,15} = \frac{\mathrm{i}}{2C_3}, \quad \hat{B}^{j0}_{0,16} = \frac{1}{2C_3}, \quad \hat{B}^{j0}_{0,21} = \frac{1}{2},$$
$$\hat{B}^{j0}_{0,24} = \frac{1}{2\mu^j\alpha}, \quad \hat{B}^{j0}_{0,33} = -\frac{\mathrm{i}\mu^j}{2C_3}, \quad \hat{B}^{j0}_{0,35} = \frac{\lambda^j + 3\mu^j}{4\mu^j\alpha C_3}, \quad C_3 = \lambda^j + 2\mu^j. \tag{5–70b}$$

Matrices for a homogeneous half-space

The matrices $\hat{\mathbf{A}}_{12}^{J+1,0}$ and $\hat{\mathbf{A}}_{22}^{J+1,0}$ are readily obtained from the leftmost three columns of $\hat{\mathbf{A}}^{j0}$, whereas $\hat{\mathbf{A}}^{j1}$ is obtained as

$$\hat{\mathbf{A}}^{j1} = \hat{\mathbf{A}}^{j0}\mathbf{D}^{j} \tag{5–71}$$

in accordance with Eq. (5–34b). Similar computations lead to the equivalent matrices for $\omega = 0$. Note that $\mathbf{D}^j$ is symmetric in the (k_1, k_2)-plane and that therefore $\hat{\mathbf{D}}^j = \mathbf{D}^j$. This property follows from the definition of the exponential decay coefficients α_P^j and α_S^j given in Eq. (5–21), or the definition of α given by Eqs. (5–37) and (5–64), along with the definition of $\mathbf{D}^j$, cf. Eq. (5–35). In other words it may be stated that α_P^j and α_S^j are invariant to rotation around the x_3-axis.

Similarly to the case of the matrices for a stratum, the inversion of the matrix $\hat{\mathbf{A}}_{22}^{J+1,0}$ can be expressed analytically. This mathematical exercise is left to the reader.

5.4.2 Numerical procedure

As mentioned above, a direct evaluation of $\bar{\mathbf{G}}$ involves a computation over the entire (k_1, k_2)-space. Making use of the coordinate transformation, the problem is reduced by one dimension since $\hat{\bar{\mathbf{G}}}$ needs only be evaluated along the α-axis. The following procedure is suggested:

1 $\hat{\bar{\mathbf{G}}}$ is computed for $\alpha = 0, \Delta\alpha, 2\Delta\alpha, ..., N\Delta\alpha$. Here $\Delta\alpha$ must be sufficiently small to ensure that local peaks in the Green's function are described. N must be sufficiently large so that $\hat{\bar{\mathbf{G}}}(\alpha, \omega) \approx \mathbf{0}$ for $\alpha > N\Delta\alpha$.

2 The values of $\hat{\bar{\mathbf{G}}}(\alpha, \omega)$ for $\alpha = \sqrt{k_1^2 + k_2^2}$ are computed by linear interpolation between values at the $N + 1$ discrete points.

3 Before the double Fourier transformation given by Eq. (5–6) is carried out, the coordinate transformation is applied.

In order to provide a fast computation of the inverse Fourier transformation it may be advantageous to use $N = 2^n$ wavenumbers in either direction so that that an inverse fast Fourier transformation (iFFT) procedure may be applied. The iFFT provides an efficient transformation of the entire discrete field $\bar{U}_i^{10}(k_1, k_2, \omega)$ into the entire discrete field $U_i^{10}(x_1, x_2, \omega)$. Given that the wavenumber step is $\Delta\alpha$, the area covered in Cartesian space becomes $2\pi/\Delta\alpha \times 2\pi/\Delta\alpha$. Since the number of points on the surface in either coordinate direction in the Cartesian space is identical to the number of points N in the wavenumber domain, the spatial increment $\Delta x = 2\pi/(N\Delta\alpha)$.

In numerical methods based on a spatial discretization, *e.g.* the FEM, the BEM or finite differences, at least 5-10 points should be present per wavelength in order to provide an accurate solution. However, in the domain transformation method, the requirement is that the fourier transformed field is described with satisfactory accuracy in the wavenumber domain. If the results in Cartesian coordinates are subsequently only evaluated at a few points per wavelength, this will only mean that the wave field does not become visible—the few responses that are computed will still be accurate. This is a great advantage when dealing with high frequencies. It

has been found that 2048×2048 wavenumbers are required in order to give a sufficiently accurate description of the response (Sheng *et al.* 1999a). On the other hand, if the displacements are only to be computed over an area which is much smaller than the area spanned by the wavenumbers, say at a few points, it may be more efficient to use the discretized version of Eq. (5–6) directly.

5.4.3 Evaluation of the response in cylindrical coordinates

As discussed on p. 186, the matrices $\mathbf{A}^{j0}$ and $\mathbf{A}^{j1}$ define a relationship between the tractions and displacements at the top and the bottom of a viscoelastic layer. The six columns/rows of these matrices correspond to a decomposition of the displacement field into P-waves and S-waves polarized in the x_1- and x_2-directions, respectively, and moving up and down through the layer.

Some notes on the Green's function tensor

Consider a vertical source or a horizontal source acting in the α-direction, *i.e.* along the axis forming the angle $\varphi - \pi/2$ with the k_1-axis around the x_3-axis, see Fig. 5–3. In accordance with the discussion in Section 1.3.2 this source produces P- and SV-waves. Secondly, if a source is applied in the transverse direction, *i.e.* the γ-direction, only SH-waves are generated. These propagate in a stratum independently of the two other wave types. Therefore, the Green's function $\hat{\bar{\mathbf{G}}}(\alpha, \omega)$ should simplify to the form

$$\hat{\bar{\mathbf{G}}}(\alpha, \omega) = \begin{bmatrix} \hat{\bar{G}}_{11} & 0 & 0 \\ 0 & \hat{\bar{G}}_{22} & \hat{\bar{G}}_{23} \\ 0 & \hat{\bar{G}}_{32} & \hat{\bar{G}}_{33} \end{bmatrix} \tag{5–72}$$

with the zeros indicating the missing interaction between SH-waves and P- and SV-waves. This is exactly the result provided by Eqs. (5–58) and (5–62) for a homogeneous and stratified half-space, respectively, after insertion of the matrices $\hat{\mathbf{A}}^{j0}$, $\hat{\mathbf{A}}_0^{j1}$, etc.. Further, due to reciprocity the matrix $\hat{\bar{\mathbf{G}}}(\alpha, \omega)$ is generally antisymmetric, *i.e.* $\hat{\bar{G}}_{32} = -\hat{\bar{G}}_{23}$ (Auersch 1988). As discussed above, $\bar{\mathbf{G}} = \mathbf{R}\hat{\bar{\mathbf{G}}}\mathbf{R}^T$, where $\mathbf{R} = \mathbf{R}(\varphi)$ is the transformation matrix defined in Eq. (5–63). Hence, the displacement response in the horizontal wavenumber domain may be found as

$$\bar{U}_i^{10} = R_{ij}(\varphi)\, \hat{\bar{G}}_{jk}(\alpha, \omega)\, R_{lk}(\varphi) \bar{P}_l^{10}, \tag{5–73}$$

where $\bar{U}_i^{10} = \bar{U}_i^{10}(k_1, k_2, \omega) = \bar{U}_i^{10}(\alpha \cos\varphi, \alpha \sin\varphi, \omega)$ and a similar definition applies to $\bar{P}_l^{10}$.

Rotation of the Cartesian coordinate frame of reference

Similarly to the transformation of the horizontal wavenumbers from (k_1, k_2) into (γ, α), the Cartesian coordinate system is rotated around the x_3-axis according to transformation

$$\begin{bmatrix} x_1 \\ x_2 \\ x_3 \end{bmatrix} = \mathbf{R} \begin{bmatrix} q \\ r \\ x_3 \end{bmatrix}, \qquad \mathbf{R} = \mathbf{R}(\theta) = \begin{bmatrix} \sin\theta & \cos\theta & 0 \\ -\cos\theta & \sin\theta & 0 \\ 0 & 0 & 1 \end{bmatrix}. \tag{5–74}$$

The displacement amplitude vector in (q, r, x_3)-coordinates is denoted $\hat{\mathbf{U}}(q, r, x_3)$ and has the components $(\hat{U}_q, \hat{U}_r, \hat{U}_3)$. Likewise, the load amplitudes are represented by the vector $\hat{\mathbf{P}}(q, r, x_3)$

with components $(\hat{P}_q, \hat{P}_r, \hat{P}_3)$. According to Eq. (5–74) the corresponding amplitudes in the Cartesian (x_1, x_2, x_3)-coordinates are given as

$$\mathbf{U}(x_1, x_2, x_3) = \mathbf{R}(\theta)\hat{\mathbf{U}}(q, r, x_3), \quad \mathbf{P}(x_1, x_2, x_3) = \mathbf{R}(\theta)\hat{\mathbf{P}}(q, r, x_3). \tag{5–75}$$

For a given observation point $(x_1, x_2, 0)$ on the surface of the half-space, the angle θ is now selected so that $q = 0$, *i.e.* the point lies on the r-axis. Hence, the response to a load applied over an area of rotational symmetry around the x_3-axis may be evaluated in cylindrical coordinates,

$$x_1 = r\cos\theta, \qquad x_2 = r\sin\theta, \qquad r = \sqrt{x_1^2 + x_2^2}, \qquad \tan\theta = \frac{x_2}{x_1}. \tag{5–76}$$

Thus, at any given point $\hat{U}_r(0, r, x_3)$ is the radial displacement amplitude whereas $\hat{U}_q(0, r, x_3)$ is the amplitude of the displacement in the tangential direction.

The coordinate transformations (5–63) and (5–74) are defined by two angles: φ defines the rotation of the wavenumber (k_1, k_2) aligned with the Cartesian (x_1, x_2)-coordinates into the rotated wavenumbers (γ, α). Likewise, a transformation of the Cartesian coordinates (x_1, x_2) into the rotated (q, r)-coordinate frame is provided by the angle θ. However, in order to simplify the analysis in cylindrical coordinates, it is convenient to introduce the angle

$$\vartheta = \pi/2 + \varphi - \theta \tag{5–77}$$

defining the rotation of the wavenumbers (γ, α) relative to the spatial coordinates (q, r). The transformation is illustrated in Fig. 5–4. Evidently $\mathbf{R}(\varphi) = \mathbf{R}(\theta)\,\mathbf{R}(\vartheta)$, and the wavenumbers (k_1, k_2) in the original Cartesian frame of reference may be obtained from the rotated wavenumbers (γ, α) by either of the transformations

$$\begin{bmatrix} k_1 \\ k_2 \\ x_3 \end{bmatrix} = \mathbf{R}(\varphi) \begin{bmatrix} \gamma \\ \alpha \\ x_3 \end{bmatrix} = \mathbf{R}(\theta)\,\mathbf{R}(\vartheta) \begin{bmatrix} \gamma \\ \alpha \\ x_3 \end{bmatrix}, \qquad \mathbf{R}(\vartheta) = \begin{bmatrix} \sin\vartheta & \cos\vartheta & 0 \\ -\cos\vartheta & \sin\vartheta & 0 \\ 0 & 0 & 1 \end{bmatrix}. \tag{5–78}$$

This identity is easily proved by combination of Eqs. (5–63), (5–74), (5–77) and (5–78).

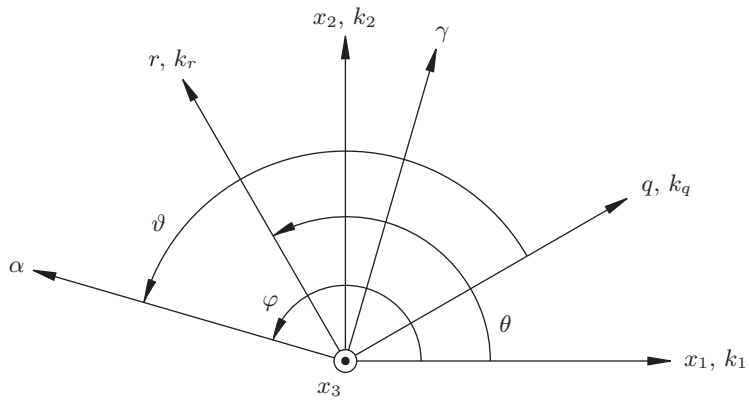

Figure 5–4 Definition of the three angles φ, θ and ϑ.

Firstly, by application of the coordinate transformation (5–74) in Eq. (5–6), the response at the surface of the stratum may be evaluated by a double inverse Fourier transform in polar coordinates, here given in matrix form:

$$\hat{\mathbf{U}}^{10} = \frac{1}{4\pi^2}\int_0^{\infty}\int_0^{2\pi} \mathbf{R}(\vartheta)\,\hat{\tilde{\mathbf{G}}}\,\{\mathbf{R}(\vartheta)\}^T\,\hat{\bar{\mathbf{P}}}^{10}\,\mathrm{e}^{\mathrm{i}\alpha r\sin\vartheta}\mathrm{d}\vartheta\,\alpha\,\mathrm{d}\alpha. \tag{5–79}$$

where $\alpha r\sin\vartheta = k_1x_1 + k_2x_2$ is identified as the dot product of the two-dimensional vectors with lengths α and r, respectively, and $\pi/2-\vartheta$ is the plane angle between these vectors as given by Eq. (5–77). In accordance with Eq. (5–75), the load amplitudes given in terms of x_3 and the horizontal wavenumbers (k_q, k_r) are found from the corresponding load amplitudes in (k_1, k_2, x_3)-space by means of the transformation $\hat{\mathbf{P}}(k_q, k_r, x_3) = \{\mathbf{R}(\theta)\}^T\mathbf{P}(k_1, k_2, x_3)$. Furthermore, transformation of the displacement amplitudes from (q, r, x_3)-coordinates into (x_1, x_2, x_3)-coordinates provide the double inverse Fourier transformation

$$\mathbf{U}^{10} = \frac{1}{4\pi^2}\,\mathbf{R}(\theta)\int_0^{\infty}\int_0^{2\pi} \mathbf{R}(\vartheta)\,\hat{\tilde{\mathbf{G}}}\,\{\mathbf{R}(\vartheta)\}^T\,\{\mathbf{R}(\theta)\}^T\,\bar{\mathbf{P}}^{10}\,\mathrm{e}^{\mathrm{i}\alpha r\sin\vartheta}\mathrm{d}\vartheta\,\alpha\,\mathrm{d}\alpha. \tag{5–80}$$

The component form of Eq. (5–80) reads

$$U_i^{10} = \frac{R_{ik}(\theta)}{4\pi^2}\int_0^{\infty}\int_0^{2\pi} R_{kl}(\vartheta)\,\hat{\tilde{G}}_{lm}(0,\alpha,\omega)\,R_{nm}(\vartheta)\,R_{jn}(\theta)\,\bar{P}_j^{10}\,\mathrm{e}^{\mathrm{i}\alpha r\sin\vartheta}\mathrm{d}\vartheta\,\alpha\,\mathrm{d}\alpha. \tag{5–81}$$

If summation is skipped over index j, this defines the displacement in direction i at a point $(x_1, x_2, 0)$ on the surface of the stratified or homogeneous ground due to a load applied in direction j over an area of rotational symmetry and centred around $(0, 0, 0)$. In the general case, $\bar{\mathbf{P}}^{10}$ depends on both the angle ϑ and the wavenumber α. However, if the complex amplitudes of the load are independent of ϑ, *i.e.* if the load is applied with rotational symmetry around the point $(0, 0, 0)$, the vector $\bar{\mathbf{P}}^{10}$ may be taken outside the integral over ϑ in Eq. (5–80), thus reducing computation time in numerical algorithms considerably:

$$\mathbf{U}^{10} = \frac{1}{2\pi}\,\mathbf{R}(\theta)\int_0^{\infty}\tilde{\mathbf{G}}\,[\mathbf{R}(\theta)]^T\,\bar{\mathbf{P}}^{10}\,\alpha\,\mathrm{d}\alpha, \tag{5–82a}$$

$$\tilde{\mathbf{G}} = \frac{1}{2\pi}\int_0^{2\pi}\mathbf{R}(\vartheta)\,\hat{\tilde{\mathbf{G}}}\,[\mathbf{R}(\vartheta)]^T\,\mathrm{e}^{\mathrm{i}\alpha r\sin\vartheta}\mathrm{d}\vartheta. \tag{5–82b}$$

Examples of the analytical evaluation of axisymmetric loads are given in Subsection 5.4.4.

Evaluation by means of Hankel transforms

Apparently Eq. (5–81) seems more complicated than the corresponding inverse Fourier transform in Cartesian coordinates given by Eq. (5–6). However, the integrals over each of the components with respect to ϑ, *i.e.* the nine integrals involved in the computation of $\tilde{G}_{kn}(\alpha, r, \omega)$ are identified as Hankel transforms which may be evaluated by means of Bessel functions:

$$\frac{1}{2\pi}\int_0^{2\pi}\mathrm{e}^{\mathrm{i}\alpha r\sin\vartheta}\mathrm{d}\vartheta = \mathrm{J}_0(\alpha r),\quad \frac{1}{2\pi}\int_0^{2\pi}\sin^2\vartheta\,\mathrm{e}^{\mathrm{i}\alpha r\sin\vartheta}\mathrm{d}\vartheta = \mathrm{J}_0(\alpha r) - \frac{1}{\alpha r}\,\mathrm{J}_1(\alpha r),$$

$$\frac{1}{2\pi}\int_0^{2\pi}\sin\vartheta\,\mathrm{e}^{\mathrm{i}\alpha r\sin\vartheta}\mathrm{d}\vartheta = \mathrm{i}\,\mathrm{J}_1(\alpha r),\quad \frac{1}{2\pi}\int_0^{2\pi}\cos^2\vartheta\,\mathrm{e}^{\mathrm{i}\alpha r\sin\vartheta}\mathrm{d}\vartheta = \frac{1}{\alpha r}\,\mathrm{J}_1(\alpha r). \tag{5–83}$$

Here, $\mathrm{J}_n(\alpha r)$ is the Bessel function of the first kind and order n. Series expansions of these functions were given by Abramowitz and Stegun (1972), and routines for their evaluation are available in MATLAB and FORTRAN. Alternatively, the integrals may be given in terms of modified Bessel functions or Hankel functions. Note that the remaining kernels of the integrals in Eq. (5–82b) are odd functions of ϑ on the interval $[-\pi;\pi]$. Therefore these integrals vanish.

Application of the Bessel functions in accordance with Eq. (5–83) and further taking into account that the Green's function tensor is skew symmetric with $\hat{\tilde{G}}_{12} = \hat{\tilde{G}}_{13} = \hat{\tilde{G}}_{21} = \hat{\tilde{G}}_{31} = 0$, see Eq. (5–72), the components of the integral in Eq. (5–82b) become

$$\tilde{G}_{11}(\alpha,r,\omega) = \left(\mathrm{J}_0(\alpha r) - \frac{1}{\alpha r}\,\mathrm{J}_1(\alpha r)\right)\,\hat{\tilde{G}}_{11} + \frac{1}{\alpha r}\,\mathrm{J}_1(\alpha r)\,\hat{\tilde{G}}_{22},$$

$$\tilde{G}_{22}(\alpha,r,\omega) = \frac{1}{\alpha r}\,\mathrm{J}_1(\alpha r)\,\hat{\tilde{G}}_{11} + \left(\mathrm{J}_0(\alpha r) - \frac{1}{\alpha r}\,\mathrm{J}_1(\alpha r)\right)\,\hat{\tilde{G}}_{22},$$

$$\tilde{G}_{12}(\alpha,r,\omega) = \tilde{G}_{13}(\alpha,r,\omega) = \tilde{G}_{21}(\alpha,r,\omega) = \tilde{G}_{31}(\alpha,r,\omega) = 0,$$

$$\tilde{G}_{23}(\alpha,r,\omega) = -\tilde{G}_{32}(\alpha,r,\omega) = \mathrm{i}\mathrm{J}_1(\alpha r)\,\hat{\tilde{G}}_{23}, \quad \tilde{G}_{33}(\alpha,r,\omega) = \mathrm{J}_0(\alpha r)\,\hat{\tilde{G}}_{33}. \tag{5–84}$$

Hence, the numerical integration involved in the double inverse Fourier transformation (5–82a) is reduced to a line integral with respect to α. The relations listed in Eq. (5–84) were established by Auersch (1994). As $\alpha\, r \to 0$ the terms $\tilde{G}_{11}(\alpha,r,\omega)$ and $\tilde{G}_{22}(\alpha,r,\omega)$ approach the limit

$$\lim_{\alpha r\to 0} \tilde{G}_{11}(\alpha,r,\omega) = \lim_{\alpha r\to 0} \tilde{G}_{22}(\alpha,r,\omega) = \frac{\hat{\tilde{G}}_{11} + \hat{\tilde{G}}_{22}}{2}. \tag{5–85}$$

5.4.4 Analytical evaluation of loads in the Fourier domain

In order to establish the solution for the displacements in the wavenumber domain, the surface load must first be Fourier transformed over the horizontal Cartesian coordinates. This may be done numerically by application of, for example, an FFT algorithm. However, computation speed my be improved if the Fourier transformations are carried out analytically. In this subsection, the load spectrum in wavenumber domain is derived for a number of surface load distributions.

Example 5.1 A vertical rectangular surface load

In Cartesian coordinates, a vertical surface load is applied over a rectangular area with the dimensions $2a \times 2b$, see Fig. A. Given that the load is in phase, the amplitude function $P_3^{10}(x_1,x_2,\omega)$ may be expressed as

$$P_3^{10}(x_1,x_2,\omega) \;=\; \begin{cases} P_0/(4ab) & \text{for} \quad -a \le x_1 \le a,\ -b \le x_2 \le b \\ 0 & \text{else.} \end{cases}$$

Double Fourier transformation with respect to the horizontal coordinates yields,

$$\bar{P}_3^{10}(k_1,k_2,\omega) \;=\; \int_{-\infty}^{\infty}\int_{-\infty}^{\infty} P_3^{10}(x_1,x_2,\omega)\,\mathrm{e}^{-\mathrm{i}(k_1x_1+k_2x_2)}\,\mathrm{d}x_1\,\mathrm{d}x_2 \quad \Rightarrow$$

(continued)

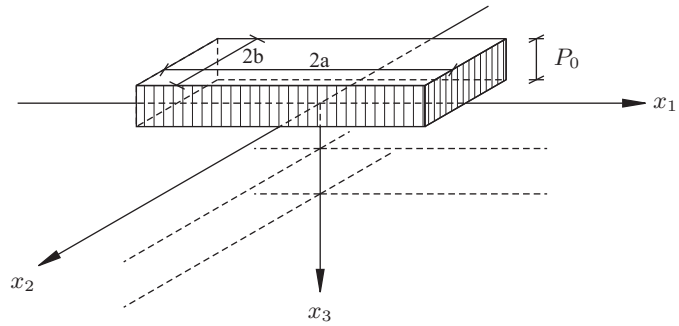

Figure A Rectangular surface load.

$$\bar{P}_3^{10}(k_1,k_2,\omega) \;=\; \frac{P_0}{4ab}\int_{-b}^{b} \mathrm{e}^{-\mathrm{i}k_2 x_2}\int_{-a}^{a} \mathrm{e}^{-\mathrm{i}k_1 x_1}\,\mathrm{d}x_1\,\mathrm{d}x_2$$

$$= \; P_0\,\frac{\mathrm{e}^{\mathrm{i}k_1 a}-\mathrm{e}^{-\mathrm{i}k_1 a}}{2k_1 a}\,\frac{\mathrm{e}^{-\mathrm{i}k_2 b}-\mathrm{e}^{\mathrm{i}k_2 b}}{2k_2 b} \;=\; P_0\,\frac{\sin k_1 a}{k_1 a}\,\frac{\sin k_2 b}{k_2 b}\,.$$

A key feature of $\bar{P}_3^{10}(k_1,k_2,\omega)$ is the inverse proportionality with k_1 and k_2 which means that also the displacements $\bar{U}_i^{10}(k_1,k_2,\omega)$ will be small, given that just a small amount of material damping is present in the layered ground as will be the case for any realistic materials. A similar behaviour is found for a load applied over a circular area, see below. However, if an undamped stratum is considered, the response may "blow up" for certain wavenumbers corresponding to layer waves like the Love wave. □

Example 5.2 A vertical circular surface load

A vertical surface load is applied over a circular area with radius r_0 and centred at the origin of a cylindrical frame of reference. The load is applied axisymmetrically and in phase with the amplitude function $P_3^{10}(r,\omega)$ given as

$$P_3^{10}(r,\omega) \;=\; \begin{cases} P_0/(\pi r_0^2) & \text{for} \quad r \le r_0 \\ 0 & \text{else.} \end{cases}$$

Double Fourier transformation with respect to the polar coordinates (r,θ) yields

$$\bar{P}_3^{10}(\alpha,\omega) \;=\; \int_0^{\infty}\int_0^{2\pi} P_3^{10}(r,\omega)\mathrm{e}^{-\mathrm{i}\alpha r\sin\vartheta}\,\mathrm{d}\vartheta\,r\mathrm{d}r$$

$$= \; \frac{P_0}{\pi r_0^2}\int_0^{r_0}\int_0^{2\pi} \mathrm{e}^{-\mathrm{i}\alpha r\sin\vartheta}\,\mathrm{d}\vartheta\,r\mathrm{d}r \;=\; \frac{P_0}{\pi r_0^2}\int_0^{r_0} 2\pi\,\mathrm{J}_0(\alpha r)\,r\mathrm{d}r \;=\; \frac{2\,P_0}{\alpha\,r_0}\,\mathrm{J}_1(\alpha r_0).$$

Here, α is the radial wavenumber, and $\vartheta = \pi/2 + \varphi - \theta$ is the angle between the wavenumber and the radius vectors in polar coordinates (α,φ) and (r,θ), respectively. As discussed above, $\alpha r\sin\vartheta$ corresponds to the scalar product between the two vectors with the length α and r, respectively.

Clearly, the load spectrum decays rapidly with α which is present both in the denominator of the fraction and in the argument of the Bessel function of the first kind and order 1. The decay rate increases if the load is distributed over a large area in spatial domain, *i.e.* if r_0 is large. However, at $\alpha = 0$, the spectrum has a strong singularity. □

Example 5.3 A vertical point force on the ground surface

The load on the surface of the half-space is applied as a vertical point force with the magnitude P_0 and acting at the origin of the frame of reference. The amplitude function may be expressed in Cartesian coordinates as

$$P_3^{10}(x_1, x_2, \omega) \;=\; P_0\, \delta(x_1)\, \delta(x_2).$$

Double Fourier transformation with respect to the horizontal coordinates provides the load spectrum in wavenumber domain:

$$\bar{P}_3^{10}(k_1, k_2, \omega) \;=\; \int_{-\infty}^{\infty} \int_{-\infty}^{\infty} P_3^{10}(x_1, x_2, \omega)\, \mathrm{e}^{-\mathrm{i}(k_1 x_1 + k_2 x_2)}\, \mathrm{d}x_1\, \mathrm{d}x_2$$

$$= \; P_0 \int_{-\infty}^{\infty} \int_{-\infty}^{\infty} \delta(x_1)\, \delta(x_2)\, \mathrm{e}^{-\mathrm{i}(k_1 x_1 + k_2 x_2)}\, \mathrm{d}x_1\, \mathrm{d}x_2 \;=\; P_0.$$

Thus, the load simply reduces to a constant in the wavenumber domain. While this load spectrum is very simple, it is not very useful seen in a perspective of numerical computation. This will be discussed in the following.

A decrease in the kernel of the plane integral with respect to k_1 and k_2 is present due to the nature of the Green's function tensor. The previous examples show that a distributed load applied over a finite area leads to a further decrease of the integrand with the horizontal wavenumber. However, this is not the situation in the present case. Thus, when a point force is applied with magnitude P_0, the load spectrum has infinite band width in wavenumber domain with the uniform intensity P_0. This is a great disadvantage in numerical computations, since the double inverse Fourier transformation involved in the computation of the response must be carried out over a large interval of the wavenumbers. □

Example 5.4 A vertical "bell-shaped" surface load

The application of a Gaussian distribution of $P_3^{10}(r, \omega)$ leads to a "bell-shaped" load on the surface of the half-space. In polar coordinates, a vertical load of this kind is expressed as

$$P_3^{10}(r, \omega) \;=\; \frac{P_0}{4\pi r_0^2}\, \mathrm{e}^{-\left(\frac{r}{2r_0}\right)^2}.$$

A small value of r_0 (the standard deviation) defines a concentrated force, and in the limit as $r_0 \to 0$, the "bell-shaped" load approaches the delta spike discussed in the previous example.

Double Fourier transformation of $P_3^{10}(r, \omega)$ with respect to the polar coordinates (r, θ) yields:

$$\bar{P}_3^{10}(\alpha, \omega) \;=\; \int_0^{\infty} \int_0^{2\pi} P_3^{10}(r, \omega) \mathrm{e}^{-\mathrm{i}\alpha r \sin\vartheta}\, \mathrm{d}\vartheta\, r \mathrm{d}r$$

$$= \; \frac{P_0}{4\pi r_0^2} \int_0^{\infty} \int_0^{2\pi} \mathrm{e}^{-\left(\frac{r}{2r_0}\right)^2 - \mathrm{i}\alpha r \sin\vartheta}\, \mathrm{d}\vartheta\, r \mathrm{d}r \;=\; P_0 \mathrm{e}^{-\alpha^2 r_0^2},$$

where the usual interpretation of $\alpha r \sin\vartheta$ as a scalar product between two vectors applies. The definition of the angle ϑ is given in Fig. 5–4.

Hence, in the spatial domain, the "bell-shaped" load is subject to an exponential decay with increasing radius r and decreasing standard deviation r_0. In the wavenumber domain, there is an exponential decay of $\bar{P}_3^{10}(\alpha, \omega)$, both with respect to α and r_0 squared. This results in a load that is adequate for numerical evaluation of the inverse Fourier transform of the response in wavenumber domain. □

5.5 Analysis of moving sources

The domain-transformation method described in the previous sections for the analysis of fixed sources acting on the surface of a half-space is easily extended to the analysis of moving sources. In the fixed frame of reference, a point source moving on the surface of the half-space along the x_1-axis with the velocity v is identified as

$$p_i^{10}(x_1, x_2, t) = \delta(x_1 - vt)\delta(x_2)p_i^*(t), \tag{5–102}$$

where it has been assumed that the source is situated at the coordinates $(x_1, x_2, x_3) = (0, 0, 0)$ at the time $t = 0$. When the load varies harmonically with the frequency $\tilde{\omega}$, it follows that $p_i^*(t) = P_i^* \mathrm{e}^{\mathrm{i}\tilde{\omega}t}$.

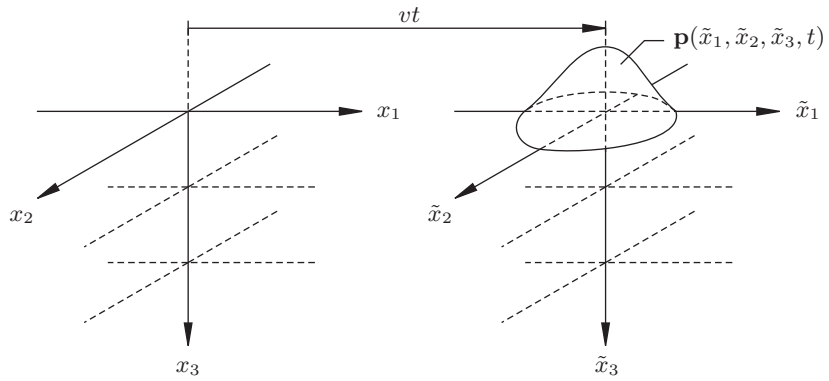

Figure 5–5 Definition of the moving $(\tilde{x}_1, \tilde{x}_2, \tilde{x}_3)$-coordinate frame.

A formulation in the fixed frame of reference becomes complicated since the Fourier transformation over time does not account for the fact that the load is moving. A great simplification of the solution is achieved if a moving frame of reference is adopted which is defined by

$$(\tilde{x}_1, \tilde{x}_2, \tilde{x}_3) = (x_1 - vt, x_2, x_3). \tag{5–103}$$

This relation is identified as a special case of the Galilean coordinate transformation (2–49), and applies for any load speed. The transformation is illustrated in Fig. 5–5. Note that $\tilde{x}_1 = x_1$ for $t = 0$. Further, partial derivatives in the two systems are related as

$$\frac{\partial}{\partial x_i} = \frac{\partial}{\partial \tilde{x}_i}, \qquad \frac{\partial}{\partial t}\Big|_{x_i} = \frac{\partial}{\partial t}\Big|_{\tilde{x}_i} - v\frac{\partial}{\partial \tilde{x}_1}. \tag{5–104}$$

In the moving frame of reference, the response at any point $(\tilde{x}_1, \tilde{x}_2, \tilde{x}_3)$ varies harmonically with the circular frequency $\tilde{\omega}$ of the moving load. This means that the local partial derivative with respect to time corresponds to $\mathrm{i}\tilde{\omega}$. The time derivative at a material point then becomes

$$\frac{\partial}{\partial t}\Big|_{x_i} \sim \mathrm{i}\omega \sim \mathrm{i}\tilde{\omega} - v\frac{\partial}{\partial \tilde{x}_1}. \tag{5–105}$$

Hence, in the moving $(\tilde{x}_1, \tilde{x}_2, \tilde{x}_3)$-coordinate frame and in the frequency domain, the Navier equations (5–16) yield

$$\left(\lambda^j + \mu^j\right)\frac{\partial \hat{\Delta}^j}{\partial \tilde{x}_i} + \mu^j \frac{\partial^2 U_i^j}{\partial \tilde{x}_k \partial \tilde{x}_k} = -\rho^j\left(\tilde{\omega}^2 + 2\mathrm{i}v\tilde{\omega}\frac{\partial}{\partial \tilde{x}_1} - v^2\frac{\partial^2}{\partial \tilde{x}_1^2}\right)\tilde{U}_i^j. \tag{5–106}$$

Further, applying the double Fourier transform over the horizontal coordinates, the Navier equations enter the form

$$\left(\lambda^j + \mu^j\right) \mathrm{i}\tilde{k}_i \tilde{\bar{\Delta}}^j + \mu^j \left(\frac{\mathrm{d}^2}{\mathrm{d}\tilde{x}_3^2} - \tilde{k}_1^2 - \tilde{k}_2^2\right) \tilde{\bar{U}}_i^j = -\omega^2 \rho^j \tilde{\bar{U}}_i^j, \qquad i = 1, 2, \tag{5–107a}$$

$$\left(\lambda^j + \mu^j\right) \frac{\mathrm{d}\tilde{\bar{\Delta}}^j}{\mathrm{d}\tilde{x}_3} + \mu^j \left(\frac{\mathrm{d}^2}{\mathrm{d}\tilde{x}_3^2} - \tilde{k}_1^2 - \tilde{k}_2^2\right) \tilde{\bar{U}}_3^j = -\omega^2 \rho^j \tilde{\bar{U}}_3^j, \tag{5–107b}$$

Here, $\omega = \tilde{\omega} - \tilde{k}_1 v$ is identified as the circular frequency of vibration at a material point. A comparison of Eqs. (5–107a) and (5–107b) with Eqs. (5–17a) and (5–17b) leads to the conclusion that the solution in the moving frame of reference denoted by tilde is identical to the solution in the fixed frame of reference except for the fact that the circular frequency ω is now wavenumber dependent. Unfortunately the asymmetry of ω in the $(\tilde{k}_1, \tilde{k}_2)$-plane implies that the numerical approach suggested in Subsection 5.7.1 is not applicable. However, it may still be useful to evaluate all quantities along the α-axis and then transform them back into the $(\tilde{k}_1, \tilde{k}_2)$-plane; but now the computation must be repeated for each value of $\tilde{k}_1$.

5.6 Dispersion of waves in viscoelastic strata

The domain-transformation method is well-suited for the analysis of dispersion in stratified viscoelastic media. In the following, an example is given, in which the dispersion in half-spaces with different numbers of layers are examined.

Example 5.5 Dispersion in a layered half-space

In Figs. A and B, the dispersion diagrams are plotted for four different half-spaces built up by three materials with the following properties:

Material 1: $E = 50$ MPa, $\nu = 0.25$, $\rho = 1500$ kg/m^3

Material 2: $E = 100$ MPa, $\nu = 0.20$, $\rho = 2000$ kg/m^3

Material 3: $E = 200$ MPa, $\nu = 0.15$, $\rho = 2500$ kg/m^3

An increase of the stiffness and density is usually encountered for increasing depths of a deposit. Low Poisson ratios are descriptive of soils with a high degree of cementation.

The plots in Fig. A represent the dispersion in two layered half-spaces. In the first model, a single layer of material 1 and with a depth of 2 m overlays a homogeneous half-space of material 3. In the second model, two layers of depth 1 m overlay the homogenous half-space of material 3. The top layer consists of material 1, while the bottom layer is made of material 2. The dark shades indicate that a great response is produced for a given combination of the frequency and the wavenumber, whereas light shades indicate a low response. The curves representing P-, S- and Rayleigh wave propagation are included in the figure. In accordance with the discussion in Subsection 1.6.1, these dispersion curves are straight lines.

(continued)

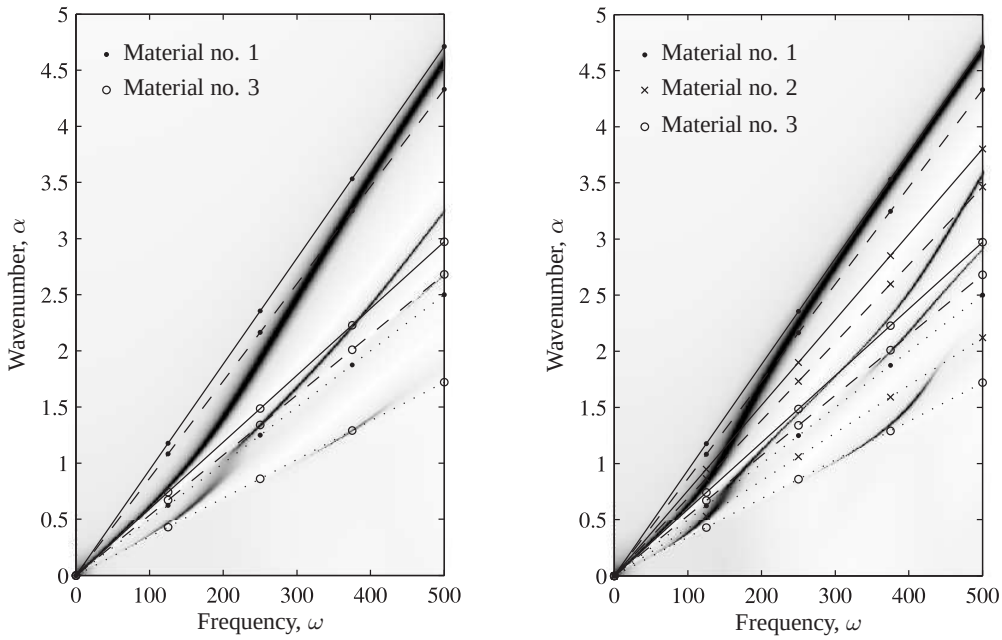

Figure A Dispersion diagrams for layered half-spaces: one layer (left) and two layers (right). The straight lines represent the Rayleigh waves (——), the S-waves (— —) and the P-waves (·····) in the indicated materials.

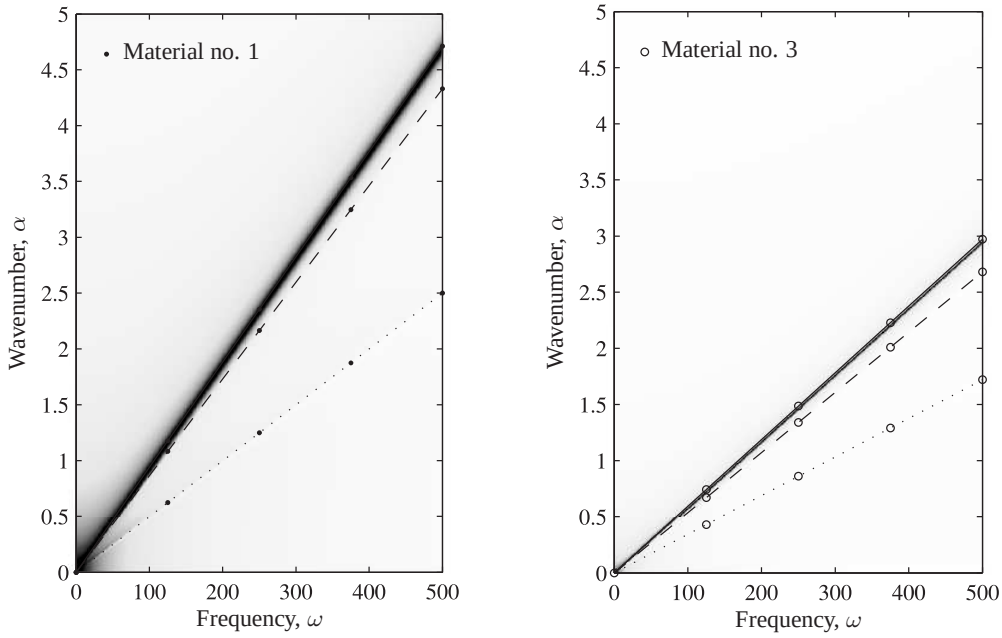

Figure B Dispersion diagrams for homogeneous half-spaces: soft half-space (left) and stiff half-space (right).

(continued)

Figure A clearly shows that the dispersion in the two different layered half-spaces is very different, though some common observations can be made. Thus, in both situations a surface wave with a strong response is identified. In the low-frequency limit, the dispersion curve of this wave defines a phase speed which goes towards the Rayleigh wave speed of the half-space. In the high-frequency limit, the wave travels with a speed that goes asymptotically towards the Rayleigh wave speed of the surface layer. A rapid shift between the two limits is observed for the single layer over the half-space, whereas a slow shift is noticed for the two-layer model.

In addition to the surface wave, several other waves may be identified in the dispersion diagrams for the layered half-spaces. These wave run along the layers or interfaces and are associated with a much smaller response than the surface wave. The layer waves are identified by a cut-on frequency, cf. Subsection 1.6.1, and evidently they bifurcate from the faster P-wave in the system. Thus, no waves exist with a speed higher than the P-wave speed in material 3, and no waves travel with a speed that is lower than the Rayleigh speed in material 1. The dispersion curves for the various layer and interface waves lie inside the angle space provided by the lines representing these two waves. It is noted that if the stratum overlays bedrock, *i.e.* a half-space with infinite stiffness, the lower bound defined by the fast P-wave lies at the frequency axis.

Finally, the dispersion for two different homogeneous half-spaces has been illustrated in Fig. B in order to examine whether such models are able to describe the dynamic behaviour of a real soil deposit. Clearly, the analysis indicates that neither of the homogeneous half-space models are able to describe the complicated dispersion of waves in a soil deposit with even a single layer. Thus soil should at least be modelled as a single layer over a half-space. In many situations this rather simple model has been found to provide useful results. □

5.7 Impedance of rigid foundations

A rigid footing has three translational and three rotational degrees of freedom as shown in Fig. 5–6. In the frequency domain, these are related to the corresponding forces and moments via the impedance matrix $\mathbf{Z}(\omega)$,

$$\mathbf{Z}(\omega)\mathbf{V}(\omega) = \mathbf{F}(\omega), \tag{5–112a}$$

$$\mathbf{V}(\omega) = \begin{bmatrix} V_1 & V_2 & V_3 & \Theta_1 & \Theta_2 & \Theta_3 \end{bmatrix}^T, \tag{5–112b}$$

$$\mathbf{F}(\omega) = \begin{bmatrix} P_1 & P_2 & P_3 & M_1 & M_2 & M_3 \end{bmatrix}^T. \tag{5–112c}$$

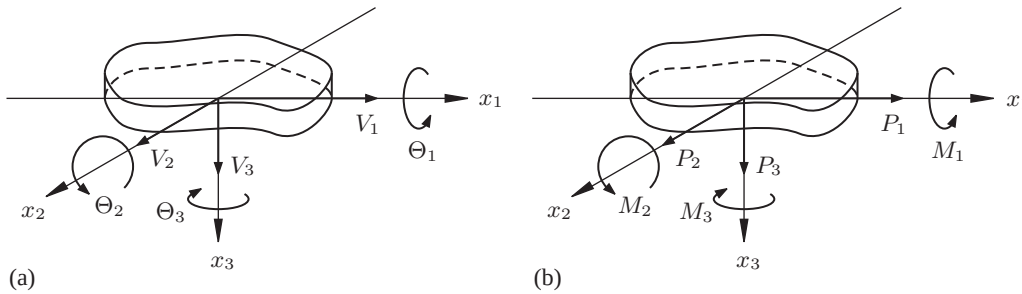

Figure 5–6 Degrees of freedom for a rigid surface footing: (a) displacements and rotations, and (b) forces and moments.

In the most general case, the impedance matrix $\mathbf{Z}(\omega)$ is full, *i.e.* all the rigid-body motions of the footing are interrelated. However, in the present case the footing rests on the surface of a horizontally layered stratum. Further, assuming that the stress resultants act at the centre of the soil–foundation interface, the torsional and vertical displacements are completely decoupled from the remaining degrees of freedom. Thus, the impedance matrix simplifies to

$$\mathbf{Z}(\omega) = \begin{bmatrix} Z_{11} & Z_{12} & 0 & Z_{14} & Z_{15} & 0 \\ Z_{12} & Z_{22} & 0 & Z_{24} & Z_{25} & 0 \\ 0 & 0 & Z_{33} & 0 & 0 & 0 \\ Z_{14} & Z_{24} & 0 & Z_{44} & Z_{45} & 0 \\ Z_{15} & Z_{55} & 0 & Z_{45} & Z_{55} & 0 \\ 0 & 0 & 0 & 0 & 0 & Z_{66} \end{bmatrix}. \tag{5–113}$$

A further simplification of $\mathbf{Z}(\omega)$ is obtained if the moment of inertia around a given horizontal axis is invariant to a rotation of the footing around the z-axis. This is the case for the gravitation foundations that are typically utilised for wind turbines, *i.e.* circular, square, hexagonal and octagonal footings. With reference to Fig. 5–7, the moments of inertia are $I_{x_1} = I_{x_2} = I_\xi = I_\zeta$, where ζ is an arbitrary horizontal axis. As a result of this, $Z_{11} = Z_{22}$, $Z_{44} = Z_{55}$ and $Z_{15} = -Z_{24}$, and the coupling between sliding in the x_1-direction and rocking in the x_2-direction (and vice versa) vanishes, *i.e.*

$$\mathbf{Z}(\omega) = \begin{bmatrix} Z_{11} & 0 & 0 & 0 & -Z_{24} & 0 \\ 0 & Z_{22} & 0 & Z_{24} & 0 & 0 \\ 0 & 0 & Z_{33} & 0 & 0 & 0 \\ 0 & Z_{24} & 0 & Z_{44} & 0 & 0 \\ -Z_{24} & 0 & 0 & 0 & Z_{55} & 0 \\ 0 & 0 & 0 & 0 & 0 & Z_{66} \end{bmatrix}. \tag{5–114}$$

In order to compute the nonzero components of the impedance matrix $\mathbf{Z}(\omega)$, the distribution of the contact stresses at the interface between the footing and the ground due to given rigid body displacements has to be determined. However, Eq. (5–80) provides the displacement field for a known stress distribution. Generally this implies that the problem takes the form of an integral equation. For the particular case of a circular footing on a homogeneous half-space, Krenk and Schmidt (1981) derived a closed-form solution for the vertical impedance. Yong *et al.* (1997) proposed that the total contact stress be decomposed into a number of simple distributions obtained by a Fourier series with respect to the azimuthal angle and a polynomial in the radial direction, *e.g.*

$$P_r^{10}(r, \vartheta, \omega) = \sum_{m=1}^{M} \sum_{n=1}^{N} a_{mn} r^n \cos(m\vartheta) \tag{5–115}$$

for the component in the r-direction and a symmetric contact stress distribution. Similar expressions were given for the components in the q- (or ϑ-) and x_3-direction and for the antisymmetric case. The response to each of the contact stress distributions can be computed, and the coefficients a_{mn} are determined so that the prescribed rigid body displacements are obtained.

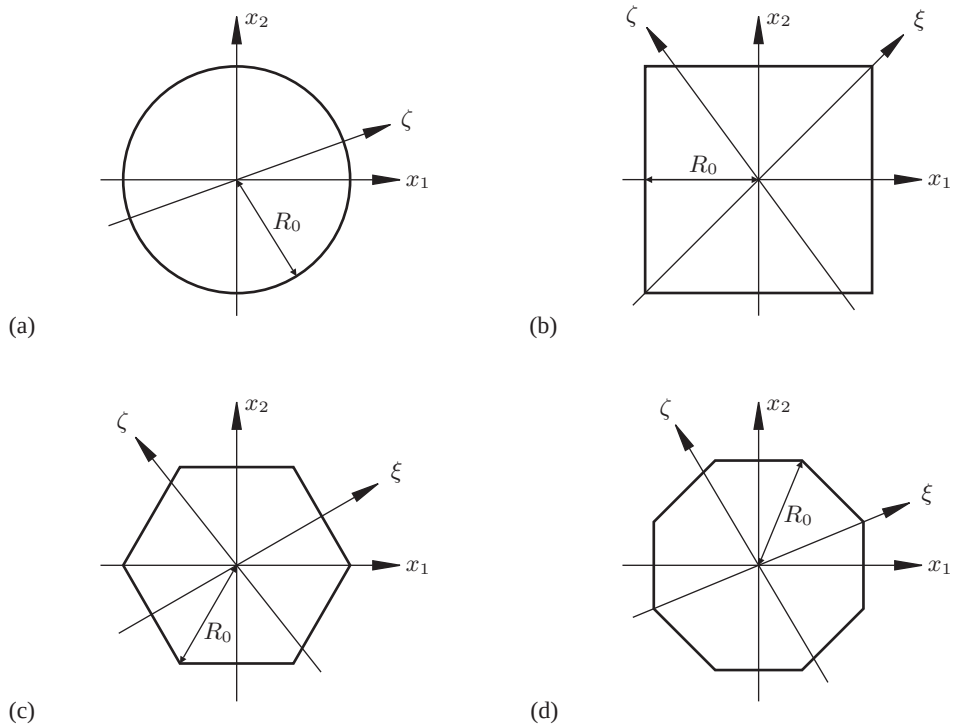

Figure 5–7 Definition of axes for different geometries of a footing: (a) circular, (b) square, (c) hexagonal, and (d) octagonal footing. The horizontal plane is considered, and all the footings have the same characteristic length, R_0.

However, for arbitrary shapes of the footing it may be difficult to follow this idea. Hence, in this study a different approach is taken which has the following steps:

1 The displacement corresponding to each rigid body mode is prescribed at N points distributed uniformly at the interface between the footing and the ground.

2 The Green's function matrix is evaluated in the wavenumber domain along the α-axis, and Eq. (5–82b) is evaluated by application of Eq. (5–84).

3 The wavenumber spectrum for a simple distributed load with unit magnitude and rotational symmetry around a point on the ground surface is computed. As discussed in Example 5.4, a "bell-shaped" load based on a double Gaussian distribution has the advantage that the wavenumber spectrum is a monotonic decreasing function of α.

4 The response at point n to a load centred at point m is calculated for all combinations of $n, m = 1, 2, ..., N$. This provides a flexibility matrix for the footing.

5 The unknown magnitudes of the loads applied around each of the points are computed. Integration over the contact area provides the impedance.

In particular, if the surface traction vector in the wavenumber–frequency domain takes the form $\bar{P}_i^{10}(k_1, k_2, \omega) = \bar{D}(k_1, k_2)\,\tilde{P}_i(\omega)$, $i = 1, 2, 3$, where $\bar{D}(k_1, k_2)$ is a stress distribution

with unit magnitude and $\tilde{P}_i(\omega)$ is an amplitude, Eq. (5–82a) may be computed as

$$\mathbf{U}^{10} = \mathbf{R}(\theta)\,\hat{\mathbf{G}}\,[\mathbf{R}(\theta)]^T\,\tilde{\mathbf{P}}, \tag{5–116a}$$

$$\hat{\mathbf{G}} = \hat{\mathbf{G}}(r,\omega) = \frac{1}{2\pi}\int_0^\infty \tilde{\mathbf{G}}\,\hat{\bar{D}}\,\alpha\,\mathrm{d}\alpha. \tag{5–116b}$$

Here it is noted that $\hat{\bar{D}} = \hat{\bar{D}}(\alpha) = \bar{D}(0,\alpha)$, since an axisymmetric distribution is assumed. The choice of contact stress distribution and various discretization aspects are discussed below. Alternatively, a boundary element model based on the Green's function for the layered half-space may be employed. However, this involves some additional work since the Green's function for traction has to be evaluated.

5.7.1 Discretization considerations

In order to achieve an accurate and efficient computation of the impedance matrix for a footing with the present method, a number of issues need consideration:

1 Equation (5–116) has to be evaluated numerically. This requires a computation of $\hat{\tilde{\mathbf{G}}}(\alpha,\omega)$ for a number of discrete wavenumbers. All peaks in the wavenumber spectrum must be represented well, demanding a fine discretization in the low wavenumber range—in particular for a half-space with little material damping.

2 No significant contributions may exist from the products $\hat{\bar{D}}(\alpha)\,\hat{\tilde{G}}_{ij}(\alpha,\omega)$, $i,j = 1,2,3$, for wavenumbers beyond the truncation point in the numerical evaluation of the integral in Eq. (5–116).

3 Enough points should be employed at the soil–structure interface in order to provide a good approximation of the contact stress distribution.

Concerning item 1 it is of paramount importance to determine the wavenumber below which the wavenumber spectrum may have narrow-banded peaks. Here use can be made of the fact that the longest wave present in a homogeneous half-space is the Rayleigh wave. An approximate upper limit for the Rayleigh wavenumber is provided by the inequality $\alpha_R = \omega/c_R < 1.2\,\omega/c_S$ for $\nu \in [0;0.5]$. For a stratum with J layers overlaying a homogeneous half-space, the idea is now to determine the quantity

$$\alpha_1 = 2\,\omega/\min\left\{c_S^1, c_S^2, ..., c_S^{J+1}\right\}. \tag{5–117}$$

where index $J+1$ refers to the underlying homogeneous half-space. In a stratum, waves with wavenumbers higher than α_1 are generally subject to strong material dissipation since they arise from P- or S-waves being reflected multiple times at the interfaces between layers. Only if the loss factor is $\eta^j = 0$ for all layers, undamped Love waves may exist; but this situation is not likely to appear in real soils.

Concerning item 2 it has been found by numerical experiments that the integral of Eq. (5–116) may be truncated beyond the wavenumber α_2 determined as

$$\alpha_2 = \max\left\{5\,\alpha_1, 20\,\alpha_0\right\}, \quad \alpha_0 = 2\pi/R_0. \tag{5–118}$$

Here R_0 is a characteristic length of the foundation, *e.g.* the diameter of a circular footing. For strata with $\eta^j > 0.01$ for all layers it has been found that accurate results are typically obtained by Simpson integration with 2000 points in the wavenumber range $\alpha \in [0; \alpha_1]$ and 500 points in the range $\alpha \in [\alpha_1; \alpha_2]$. As discussed above, the numerical evaluation of the integral in the range $\alpha \in [\alpha_1; \alpha_2]$ is particularly efficient for the "bell-shaped" load distribution, since $\hat{\tilde{D}}(\alpha)\,\hat{\tilde{G}}_{ij}(\alpha, \omega)$, $i, j = 1, 2, 3$, are all monotone functions beyond α_1 in this case as demonstrated in the example below.

Finally, concerning item 3, $\mathbf{U}^{10}$ must be evaluated for all combinations of receiver and source points. In the present analyses, $\hat{\mathbf{G}}(r, \omega)$ is computed at 250 points on the r-axis from $r = 0$ to $r = 2R_0$, where R_0 is the radius of a circular footing. Subsequently $\mathbf{U}^{10}$ is found by Eq. (5–116) using linear interpolation of $\hat{\mathbf{G}}(r, \omega)$. This provides a fast solution of satisfactory accuracy.

Example 5.6 A circular footing on a homogeneous half-space

The impedance of a circular footing with radius $R_0 = 5$ m is computed. The footing rests on a homogeneous linear viscoelastic half-space consisting of one of the materials listed in Table A. Here G is the shear modulus, ν is the Poisson ratio, ρ is the mass density, and η is the loss factor. Note that G is a real number in contrast to $\mu = (1 + \mathrm{i}\eta)G$ which defines the complex shear stiffness, cf. Eq. (5–12). The three materials may resemble very soft rock, drained sandy soil and undrained soil, respectively.

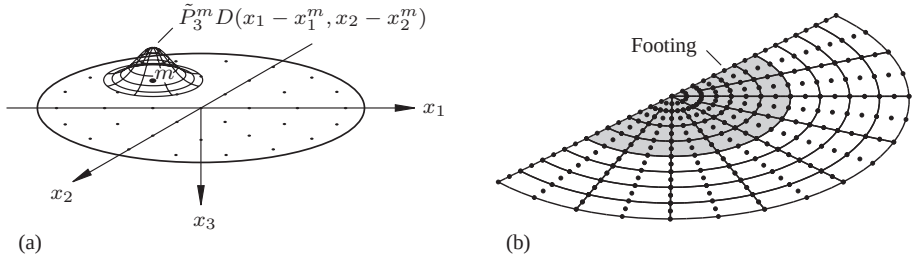

Figure A Models used for computation of the impedance: (a) Present method with "bell-shaped" loads applied at 37 points under the footing, and (b) boundary element model with quadratic interpolation. The shaded elements comprise the footing.

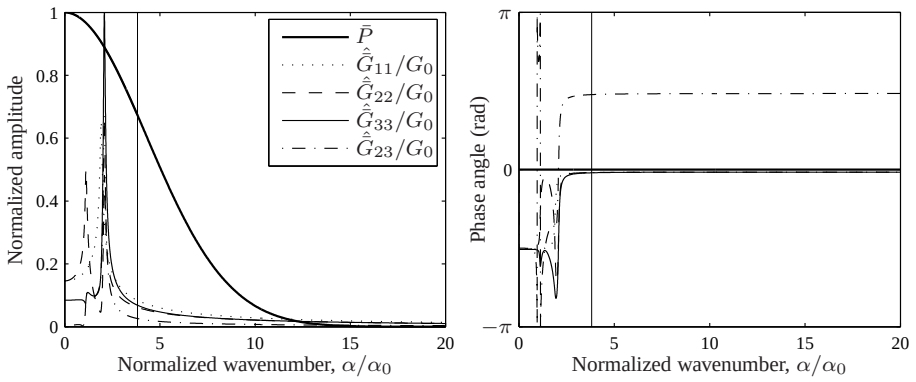

Figure B Wavenumber spectra for the "bell-shaped" load and the components of the Green's function matrix for Material 1 (see Table A) and for $\omega = 6\omega_0$. The vertical lines indicate α/α_0, where $\alpha_0 = 2\pi/R_0$.

(continued)

A model with $N = 91$ uniformly distributed points under the footing has been employed in the present method, and the contact stress is discretized into "bell-shaped" loads applied at these N points with $r_1 = R_0/\sqrt{4N}$, cf. Example 5.4. Alternative, for a load applied over a circular area, *i.e.* according to Example 5.2, the natural choice is $r_0 = R_0/\sqrt{N}$, implying that the areas over which the N loads act add up to the total area of the footing. In any case, for point m the the contribution in direction i is $\tilde{P}_i^m D(x_1 - x_1^m, x_2 - x_2^m)$. The principle has been illustrated in Fig. Aa for a vertical "bell-shaped" load, however for a model with only 37 points.

The results of the present method are compared with those of a three-dimensional boundary element (BE) model employing the full-space Green's function (Domínguez 1993; Andersen and Jones 2001a) and quadrilateral elements with biquadratic interpolation of the displacement and traction fields. Use has been made of the fact that the contact stress distribution due to a rigid body motion of the circular footing is either symmetric or antisymmetric. Thus, only half the footing is included in the model, see Fig. Ab.

The circular frequency of the excitation is normalized with respect to the quantity $\omega_0 = c_S/R_0$, where c_S is the shear wave velocity in the half-space computed according to Eq. (5–19). Figure B shows the wavenumber spectra for the "bell-shaped" load and the components of the Green's function matrix for Material 1 in terms of the normalized wavenumber $\alpha_0 = 2\pi/R_0$ at the circular frequency $\omega = 6\omega_0$. Similar results are obtained at other frequencies and for the other materials listed in Table A. The components of $\hat{\tilde{\mathbf{G}}}(\alpha, \omega)$ have all been normalized with respect to the quantity $G_0 = \hat{\tilde{G}}_{33}(0, \omega)$.

Pronounced peaks are present in the wavenumber spectra for Green's function components in Fig. B at the P-wavenumber and, in particular, at the Rayleigh wavenumber. However, as indicated in the previous subsection, both the load and the Green's function components are monotone functions for wavenumbers beyond the Rayleigh wavenumber. Hence, only a few points are necessary in order to obtain an accurate discrete inverse Fourier transformation of the wavenumber range beyond α_1.

Table A Material properties for homogeneous half-space.

Material no.	G (MPa)	ν	ρ (kg/m^3)	η
Material 1	50	0.250	2000	0.05
Material 2	50	0.400	2000	0.05
Material 3	50	0.495	2000	0.05

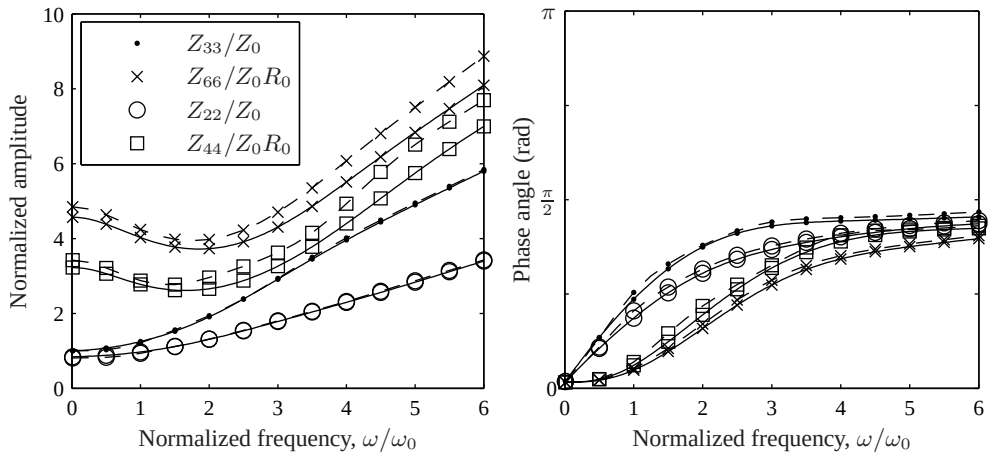

Figure C Impedance of a circular footing on a homogeneous half-space of Material 1 (see Table A): present method (——) and boundary element solution (— —).

(continued)

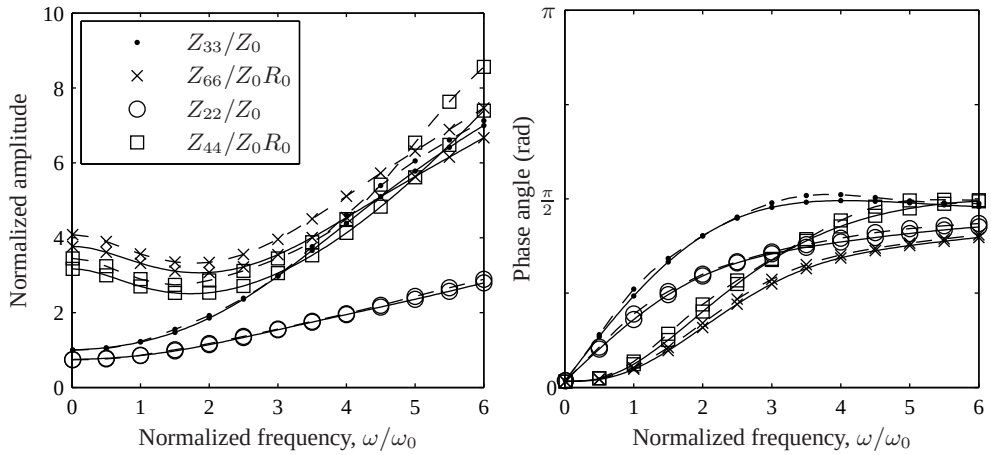

Figure D Impedance of a circular footing on a homogeneous half-space of Material 2 (see Table A): present method (——) and boundary element solution (— —).

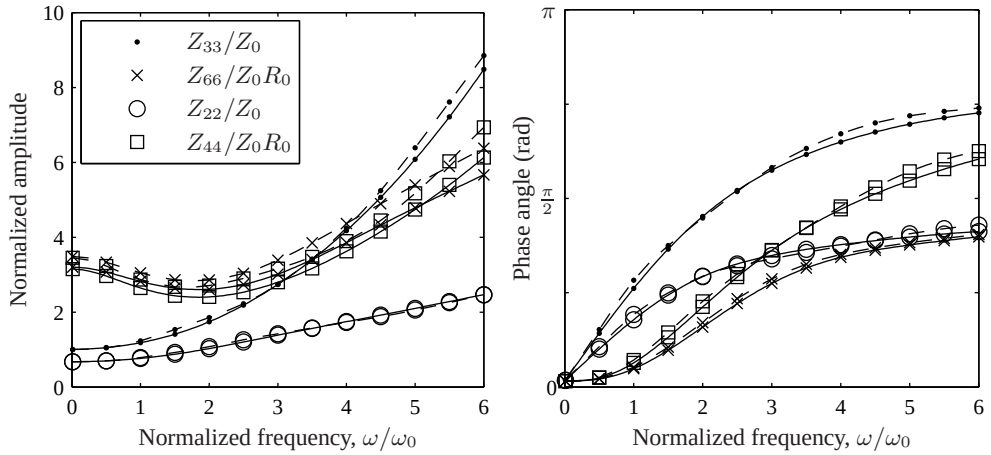

Figure E Impedance of a circular footing on a homogeneous half-space of Material 3 (see Table A): present method (——) and boundary element solution (— —).

Pronounced peaks are present in the wavenumber spectra for Green's function components in Fig. B at the P-wavenumber and, in particular, at the Rayleigh wavenumber. However, as indicated in the previous subsection, both the load and the Green's function components are monotone functions for wavenumbers beyond the Rayleigh wavenumber. Hence, only a few points are necessary in order to obtain an accurate discrete inverse Fourier transformation of the wavenumber range beyond α_1.

Next, the impedance matrix $\mathbf{Z}(\omega)$, cf. Eq. (5–113), is computed for a number of frequencies in the range $\omega_0 \in [0; 6]$. All components are normalized with respect to the static vertical stiffness $Z_0 = Z_{33}(0)$, and the results are plotted in Figs. C to E for the materials listed in Table A. It is noted that the impedances for rocking and torsion, *i.e.* Z_{44} and Z_{66}, have been divided by R_0 in order to get results of the same order of magnitude for all components of $\mathbf{Z}(\omega)$. Further, since the circular footing is doubly symmetric, $Z_{11} = Z_{22}$ and $Z_{44} = Z_{55}$.

(continued)

From Figs. C to E it is concluded that the present method provides results of great accuracy for the components Z_{11} and Z_{33}, *i.e.* horizontal and vertical translation. On the other hand there are some discrepancies in the rocking and torsion impedances predicted with the two methods. Whereas the same phase angle is achieved with the two methods, the amplitude predicted by the present method is approximately 10% smaller than the amplitude obtained with the BE model. However, it is worthwhile to mention that the present method generally provides stiffnesses that are too small, whereas the opposite is the case for the BE solution. A convergence study indicates that a better agreement between the present method and the BE model is achieved when more degrees of freedom are used in both models.

In addition to this, the BE solution took about 100 s per frequency on a 1.6 GHz P4 laptop computer, whereas the computation time for 121 frequencies is 52 s with the present method. For a layered half-space the difference becomes more pronounced. Andersen and Jones (2001b) concluded that the BE computation mesh must be truncated farther away from the load than is necessary in the case of the homogeneous half-space. Further, compared to the model of a half-space, a better discretization is needed due to the existence of waves propagating in the layers. Thus, in comparison to the model illustrated in Fig. Ab, a BE model with more than twice as many degrees of freedom has to be applied for the analysis when a half-space overlaid by a single layer. As the system matrices in the BE formulation are fully populated (Domínguez 1993) this leads to a significant increase in computation time. On the other hand, with the present model the computation time only increases from 52 s to 60 s, *i.e.* by about 15%. □

Example 5.7 Example: A wind turbine foundation on a layered ground

In this example, the impedance of a wind turbine foundation is studied for frequencies in the range 0–3 Hz. This frequency range is relevant for the first vibration modes of both the tower and the wings, which are typically close to 0.25 Hz and 1.0 Hz, respectively, for a 3 GW wind turbine. The foundation is modelled as a circular footing with the radius $R_0 = 10$ m resting on a subsoil with a single layer over a homogeneous half-space. The top layer is assumed to consist of soft undrained soil, and the underlying half-space consists of a stiffer material. The material properties of the top layer and the half-space are listed in Table A. These properties may be representative of, for example, a sandy or clayey deposit overlaying limestone or bedrock.

The results of the analyses are shown in Figs. A to D, and several interesting observations can be made. The main conclusions are given in the following.

Firstly, a comparison of Figs. C to E in Example 5.6 with Fig. D in this example shows that the impedance of the footing on the 80 m deep layer over the half-space resembles that of a footing on a homogeneous half-space, in particular at the higher frequencies. This was to be expected, since the top layer in this situation is deep compared to the radius of the footing. Thus, the normalized frequency $\omega/\omega_0 = 6$ corresponds to an S-wavelength less than 1/10 of the layer depth.

As an exception to the general observation that a deep layer resembles a half-space, it is noticed that the vertical impedance does not increase monotonously at high frequencies. Local tips and dips continue to be present in both the normalized amplitude and the phase angle—even in the case of the 80 m deep layer,

Table A Material properties for layered half-space.

Layer no.	h (m)	μ (MPa)	ν	ρ (kg/m^3)	η
Layer 1	20−80	5	0.497	2000	0.05
Half-space	∞	500	0.250	2500	0.01

(continued)

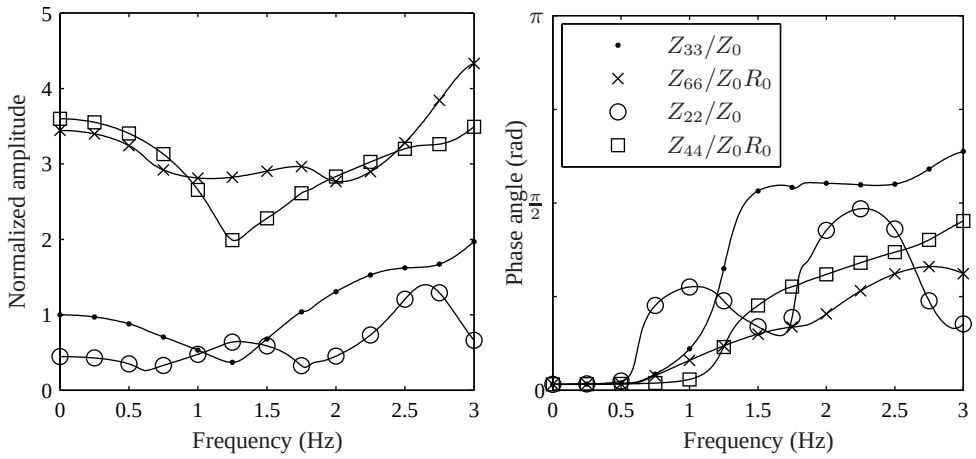

Figure A Impedance of a circular footing on a subsoil with soft sandy soil overlaying a stiffer homogeneous half-space: $h^1 = 20$ m.

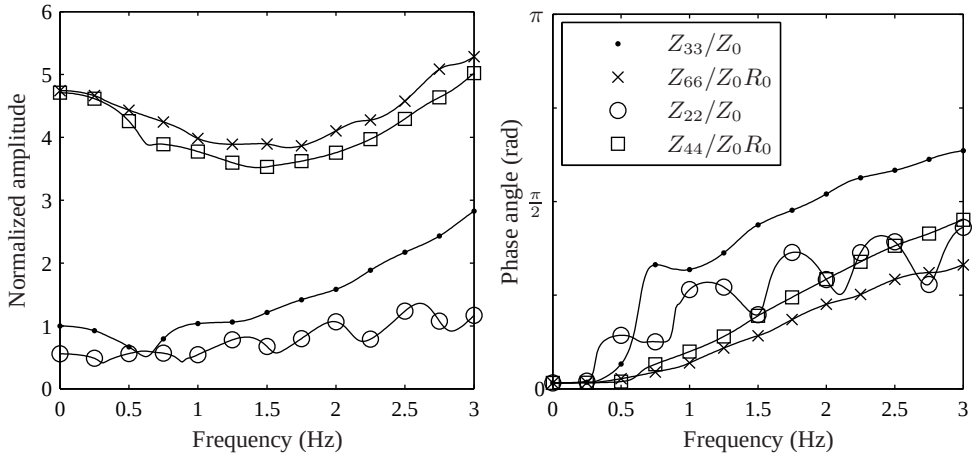

Figure B Impedance of a circular footing on a subsoil with soft sandy soil overlaying a stiffer homogeneous half-space: $h^1 = 40$ m.

cf. Fig. D. These tips and dips correspond to negative and positive interference, respectively, between the outgoing SH-waves generated at the footing and the incoming SH-waves reflected from the interface between the layer and the underlying half-space.

For a homogeneous half-space with a Poisson ratio lower than approximately 0.4, the phase angles of all impedance components are monotone increasing functions of the frequency with the limit $\pi/2$ as the frequency goes to infinity, cf. Fig. C in Example 5.6. For higher Poisson ratios, the phase angles associated with vertical motion and rocking increase to a global maximum and then decrease to the asymptotic value $\pi/2$, cf. Figs. D and E in Example 5.6. The maximum value of the phase shift approaches π for Poisson ratios near $1/2$, since in this case the half-space becomes infinitely stiff with regard to the propagation of P-waves. On the other hand, for the layered half-space the phase angle varies significantly with the frequency. As the depth of the top layer is increased, so is the number of tips and dips in the phase angles of the impedance components within the considered frequency range.

(continued)

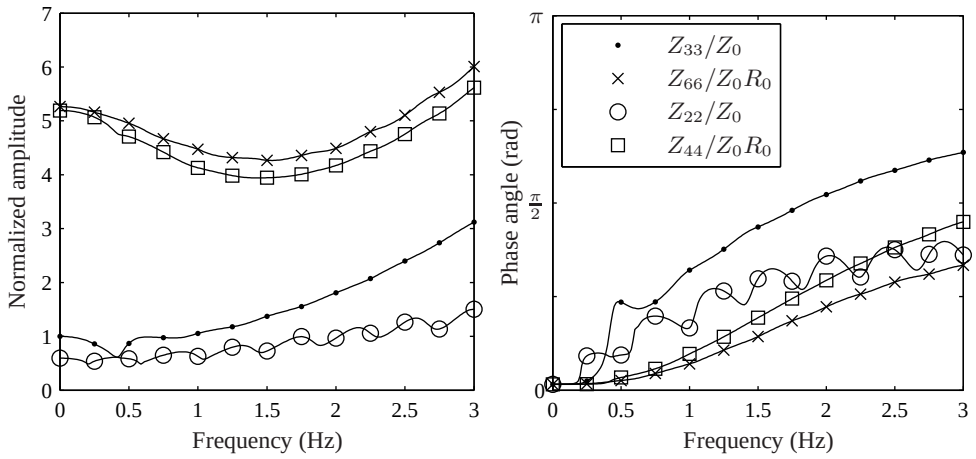

Figure C Impedance of a circular footing on a subsoil with soft sandy soil overlaying a stiffer homogeneous half-space: $h^1 = 60$ m.

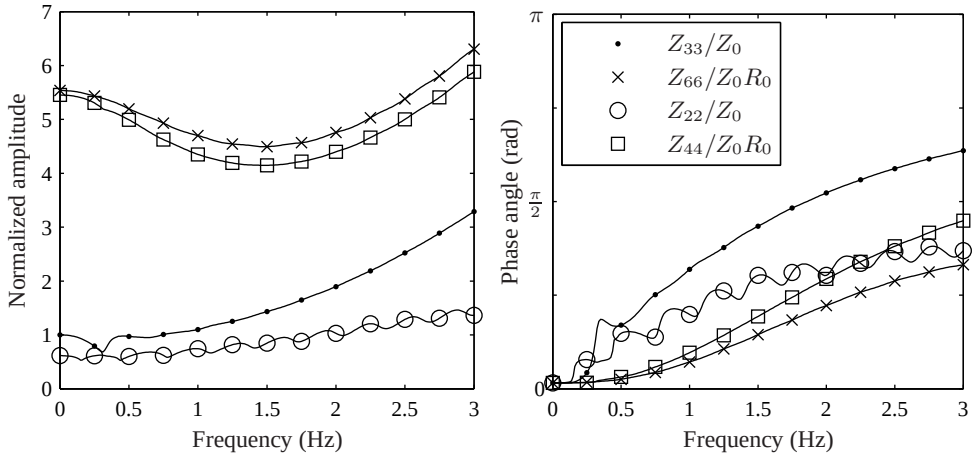

Figure D Impedance of a circular footing on a subsoil with soft sandy soil overlaying a stiffer homogeneous half-space: $h^1 = 80$ m.

With increasing layer depth, the static stiffness related to rocking and torsion increases relatively more than those related to vertical or horizontal translation.

The magnitude of the translation impedances of a footing on a homogeneous half-space increase monotonously with increasing frequency. Figures A to D show that this is not the case for a footing on a layered half-space. In particular it is noted that the 60 and 80 m deep layers give rise to a decrease in the impedance of about 30% at 0.20 to 0.30 Hz, *i.e.* close to the first resonance frequency of a modern wind turbine.

In the case of a homogeneous half-space, there is a slight decrease of the rotational impedances with frequency for low frequencies, cf. Figs. C to E in Example 5.6. This decrease is more pronounced when the half-space is overlaid by a layer with $h^1 = 20$ or 40 metres, in particular with respect to the rocking impedance. For $h^1 = 20$ m the decrease is most significant. However, for $h^1 = 40$ m the dip is located at a lower frequency, which may be critical for the response of a wind turbine.

(continued)

Based on these findings it is concluded that stratification of the subsoil may lead to decreases of both translation and rotation impedances of a wind turbine foundation in the frequency range that is critical to the structural response. □

5.8 Summary

This chapter contains a derivation of the domain-transformation metho, which may be applied for the analysis of a stratum overlaying bedrock or a homogeneous half-space. The method relies on an analytical solution for the wave propagation over depth, and this provides a much faster evaluation of the response to a load on the surface of the ground than may be achieved with the finite element method and other numerical methods. However, the horizontal wavenumber–frequency domain model is confined to the analysis of strata with horizontal interfaces. It has been demonstrated that the method is useful for the examination of dispersion in such deposits.

In the general case, the Fourier transformation and inverse Fourier transformation in space involves the evaluation of double integrals over spatial coordinates and wavenumbers. However, the evaluation of the response to a fixed load applied over an axisymmetric area may be carried out by means of Hankel transforms. Hence, only a line integral must be computed.

Finally, the domain-transformation method is easily adapted to moving sources. The governing equations are unchanged from the situation in case of a fixed load. However, the computation of the response becomes slightly more complicated since the circular frequency of vibration at a material point depends on both the frequency of the moving load (as seen in the moving frame of reference) and the wavenumber in the direction of convection.

Since the response is computed in the frequency–wavenumber domain, the method is ideal for the analysis of wave propagation in viscoelastic media with advanced material models such as fractional time-derivative models. In particular such material models cannot be adapted in the finite element method in convective coordinates, since the wavenumbers for the waves at a given point are unknown.

Finally, examples have been given, in which the domain-transformation method is employed to the analysis of rigid footings. The impedance matrices computed in this way may subsequently be approximated by means of consistent lumped-parameter models (Wolf 1991b) which can be used in time- or frequency-domain analysis of structures. Such simple models are extremely useful in, for example, aero-elastic codes for wind turbines.

CHAPTER 6
Lumped-parameter models

A lumped-parameter model is a simple physical system with few degrees of freedom that may represent the dynamic response of a structure or substructure. Such a model is ideal for the macro modelling of foundations in soil–structure interaction problems, or lumped-parameter models may be fitted to the measured dynamic response of a structure. In this chapter, the main steps of establishing a lumped-parameter model are presented. Firstly, the main reasons for the utilization of lumped-parameter models are discussed. Secondly, simple lumped-parameter models for a foundation are presented, and finally the guidelines for the formulation of advanced higher-order lumped-parameter models are given. Examples are presented in which the lumped-parameter models are applied to the analysis of surface footings or embedded flexible foundations.

6.1 Introduction

As discussed in the previous chapters, dynamic soil–structure interaction may be analysed by the finite-element method (FEM), the boundary-element method (BEM) or the domain-transformation method (DTM), or any combination thereof. These methods are highly adaptable and may be applied to the analysis of wave-propagation problems involving stratified soil, embedded foundations and inclusions or inhomogeneities in the ground. However, this comes at the cost of great computation times, in particular in the case of time-domain analysis of transient structural response over large periods of time. Thus, rigourous numerical models based on the FEM, the BEM, or the DTM, are not useful for real-time simulations or parametric studies in situation where only the structural response is of interest. Alternatively, soil–structure interaction may be analysed by experimental methods. However, the models and equipment required for such analyses are expensive and this approach is not very useful in a predesign phase.

Similarly, in many situations the dynamic response of a substructure (*e.g.* a wall, a floor or a machine part) has to be examined, whereas the response of the remaining structure is of no particular interest. Under such circumstances the need arises for a computationally efficient model which accounts for the interaction with the surrounding/underlying soil or the adjacent substructures. A fairly general solution is the so-called *lumped-parameter model* which may be applied to the analysis in both frequency and time domain. The development of the lumped-parameter model has been reported by Wolf (1991a), Wolf and Paronesso (1991), Wolf (1991b), Wolf and Paronesso (1992), Wolf (1994), Wolf (1997), Wu and Lee (2002), and Wu and Lee (2004). The present chapter is, to a great extent, based on this work.

The basic concept of a lumped-parameter model is to represent the original problem by a simple mechanical system consisting of a few so-called *discrete elements*. This may be springs, dashpots and point masses which are easily implemented in standard finite-element models. This

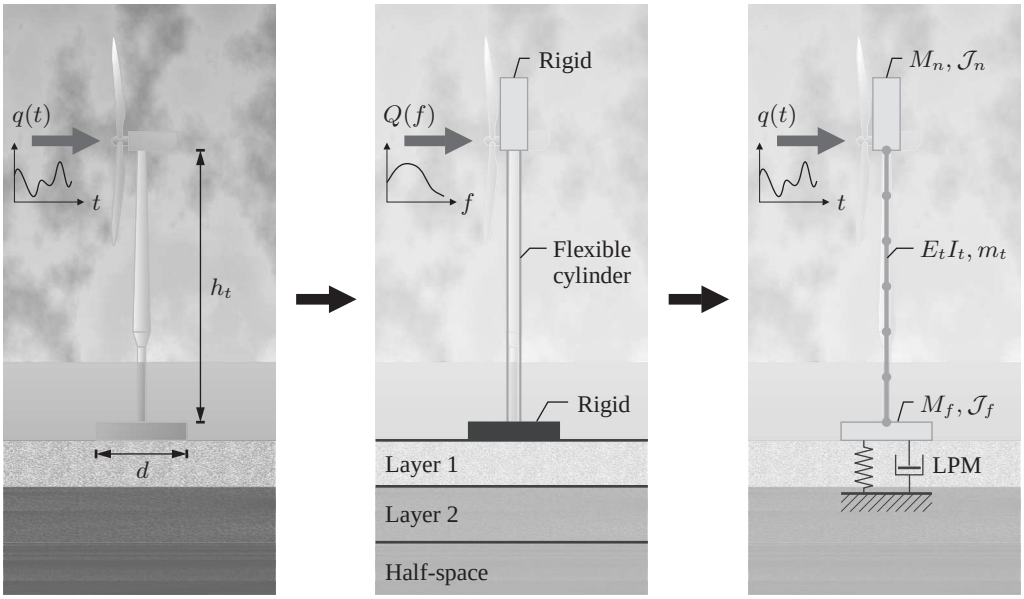

Figure 6–1 From prototype to computational model: Wind turbine on soil stratum (left); rigorous model of the layered half-space (centre); lumped-parameter model of the soil coupled with finite-element model of the structure (right).

is illustrated in Figure 6–1 for a wind turbine on a layered ground. The computational model consists of two parts: a model of the structure (*e.g.* a finite-element model) and a lumped-parameter model (LPM) of the foundation and the subsoil. The formulation of the model has three steps:

1 A rigorous frequency-domain model is applied for the foundation (in this case a footing on a soil stratum) and the frequency response is evaluated at a number of discrete frequencies.

2 A Lumped-parameter model providing approximately the same frequency response is calibrated to the results of the rigorous model.

3 The structure itself (in this case the wind turbine) is represented by a finite-element model (or similar) and soil–structure interaction is accounted for by a coupling with the LPM.

Whereas the application of rigorous models like the BEM or DTM is often restricted to the analysis in the frequency domain—at least for any practical purposes—the LPM may be applied in the freqeuncy domain as well as the time domain. This is ideal for problems involving linear response in the ground and nonlinear behaviour of a structure.

Actually, the transmitting boundary conditions presented in Chapter 2 for wave propagation in an elastic continuum or a beam on a Kelvin foundation may be considered a lumped-parameter model, since the original mechanical system is represented by lumped springs, dashpots and masses. In this regard it should be noted that the geometrical damping present in the original wave-propagation problem is represented as material damping in the discrete-element model. Thus, no distinction is made between material and geometrical dissipation in the final lumped-parameter model—they both contribute to the same parameters, *i.e.* damping coefficients.

Generally, if only few discrete elements are included in the lumped-parameter model, it can only reproduce a simple frequency response, *i.e.* a response with no resonance peaks. This is

useful for homogeneous (semi-)infinite structures and soil. However, inhomogeneous or finite structures and stratified soil have a frequency response that cannot be represented by a model with a few degrees of freedom. Here, a lumped-parameter model with internal degrees of freedom is required. When the number of internal degrees of freedom is increased, so is the computation time. However, so is the quality of the fit to the original frequency response. This is the idea of the so-called *consistent lumped-parameter model* which is presented in Section 6.3. However, before a discussion of consistent lumped-parameter models based on these concepts, in Section 6.2 we shall go through the theory for some particularly simple models that have been developed for the analysis of soil-structure interaction.

6.2 Simple lumped-parameter models for foundations

In many engineering problems, the dynamic response of structures has to be determined and the influence of the underlying soil in this regard has to be quantified. One approach to the analysis of dynamic soil–structure interaction is to model the complete composite soil–structure system by application of, for example, the finite-element method as discussed in Chapter 2. Such an approach is, however, both inconvenient and inefficient for most practical purposes. Instead, a solution may be preferred in which a macro-model of the foundation is applied by means of a lumped-parameter system. The interactions between the foundation and the structure are then expressed purely in terms of force and moment resultants, and their conjugate displacements and rotations, see Fig. 6–2.

In the following subsections, guidelines are given for the construction of simple lumped-parameter models of axisymmetric foundations. These models may, to some extent, account for the frequency dependency of the foundation stiffness—in particular in the low-frequency range which is relevant to such structures as wind turbines, chimneys, high-rise buildings and bridge pylons. Two models are considered: The standard lumped-parameter model and the fundamental lumped-parameter model. The presentation of the models is based on Wolf (1994), and the theory applies to both surface footings and structures which are embedded in a half-space. In both models, the soil is idealized as a homogeneous, isotropic and linear elastic half-space, *i.e.* no stratification or inelastic behaviour of the soil is accounted for in the models. In order to model the behaviour of foundations under such conditions, advanced (consistent) lumped-parameter models may be applied as described in Section 6.3.

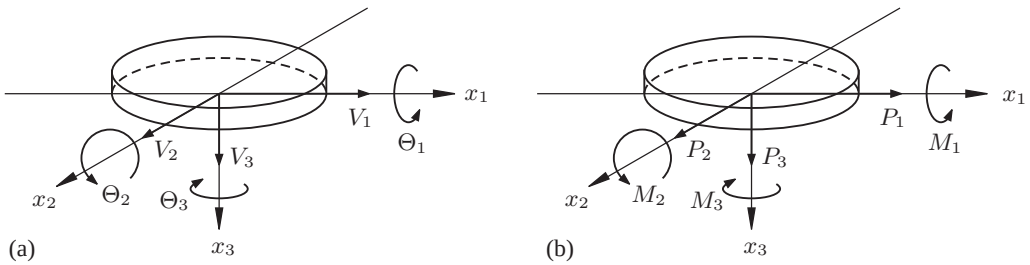

Figure 6–2 Degrees of freedom for a rigid surface footing: (a) displacements and rotations, and (b) forces and moments.

6.2.1 Static stiffness of axisymmetric foundations

The elastic static stiffness of a foundation can be expressed by dimensionless elastic stiffness coefficients corresponding to vertical ($\bar{Z}^0_{33}$), horizontal ($\bar{Z}^0_{11} = \bar{Z}^0_{22}$), rocking ($\bar{Z}^0_{44} = \bar{Z}^0_{55}$) and torsional ($\bar{Z}^0_{66}$) degrees of freedom. As discussed in Section 5.7, the vertical and torsional motion of axisymmetric footings are completely decoupled from the remaining degrees of freedom. However, cross-coupling exists between horizontal and rocking motion; hence, additional terms ($\bar{Z}^0_{15} = \bar{Z}^0_{51} = -\bar{Z}^0_{24} = -\bar{Z}^0_{42}$) are necessary, where the change of sign is a result of the displacement and rotation directions defined in Fig. 6–2.

Under general (combined) static loading (see Fig. 6–2) the elastic stiffness of the foundation system can be expressed as

$$\begin{bmatrix} P_1/\mu R_0^2 \\ P_2/\mu R_0^2 \\ P_3/\mu R_0^2 \\ M_1/\mu R_0^3 \\ M_2/\mu R_0^3 \\ M_3/\mu R_0^3 \end{bmatrix} = \begin{bmatrix} \bar{Z}^0_{11} & 0 & 0 & 0 & -\bar{Z}^0_{24} & 0 \\ 0 & \bar{Z}^0_{22} & 0 & \bar{Z}^0_{24} & 0 & 0 \\ 0 & 0 & \bar{Z}^0_{33} & 0 & 0 & 0 \\ 0 & \bar{Z}^0_{24} & 0 & \bar{Z}^0_{44} & 0 & 0 \\ -\bar{Z}^0_{24} & 0 & 0 & 0 & \bar{Z}^0_{55} & 0 \\ 0 & 0 & 0 & 0 & 0 & \bar{Z}^0_{66} \end{bmatrix} \begin{bmatrix} V_1/R_0 \\ V_2/R_0 \\ V_3/R_0 \\ \Theta_1 \\ \Theta_2 \\ \Theta_3 \end{bmatrix}, \tag{6–1}$$

where R_0 is the radius of the foundation and μ is the shear modulus of the homogeneous half-space, which is related to Young's modulus, E, and Poisson's ratio, ν, as given by Eq. (1–8). Obviously, the components of the normalised static stiffness matrix are related to the components the impedance matrix evaluated at the circular frequency $\omega = 0$. With reference to Eq. (5–114), evidently $\bar{Z}^0_{33} = \mu R_0 Z_{33}(0)$ and similar relationships hold for the remaining non-zero components of $\bar{\mathbf{Z}}^0$ and $\mathbf{Z}(0)$. The main reason for the normalisation provided in Eq. (6–1) is that $\bar{\mathbf{Z}}^0$ only depends on the shear modules of the ground, μ, *i.e.* it is independent of Poisson's ratio, ν. By contrast, $\mathbf{Z}(0)$ depends on both μ and ν. However, it is noted that a simple normalisation of this kind is only possible for an isotropic homogenous elastic half-space. In the case of stratified soils, the material properties of all materials present in the ground influence the static stiffness. Thus, the choice of normalisation stiffness is not straightforward.

6.2.2 Dynamic stiffness of axisymmetric foundations

It is assumed that the foundation is excited with a harmonic vibrating force with the circular frequency ω. The dynamic system for a vertical vibrating surface footing with no mass is shown in Fig. 6–3(a). For each degree of freedom the dynamic stiffness of the system can be represented by a frequency dependent spring and dashpot, as shown in Fig. 6–3(b).

A massless axisymmetric rigid foundation has six degrees of freedom: one vertical, two horizontal, two rocking and one torsional. The six degrees of freedom and the corresponding forces and moments are shown in Fig. 6–2. The normalised dynamic stiffness matrix $\bar{\mathbf{Z}}$ is related to the vector of forces and moments $\mathbf{F}$ and the vector of displacements and rotations $\mathbf{V}$ as follows:

$$\mathbf{F}(\omega) = \bar{\mathbf{Z}}(\omega)\mathbf{V}(\omega) \tag{6–2}$$

The component form of Eq. (6–2) can be written as

$$\begin{bmatrix} P_1/\mu R_0^2 \\ P_2/\mu R_0^2 \\ P_3/\mu R_0^2 \\ M_1/\mu R_0^3 \\ M_2/\mu R_0^3 \\ M_3/\mu R_0^3 \end{bmatrix} = \begin{bmatrix} \bar{Z}_{11} & 0 & 0 & 0 & -\bar{Z}_{24} & 0 \\ 0 & \bar{Z}_{22} & 0 & \bar{Z}_{24} & 0 & 0 \\ 0 & 0 & \bar{Z}_{33} & 0 & 0 & 0 \\ 0 & \bar{Z}_{24} & 0 & \bar{Z}_{44} & 0 & 0 \\ -\bar{Z}_{24} & 0 & 0 & 0 & \bar{Z}_{55} & 0 \\ 0 & 0 & 0 & 0 & 0 & \bar{Z}_{66} \end{bmatrix} \begin{bmatrix} V_1/R_0 \\ V_2/R_0 \\ V_3/R_0 \\ \Theta_1 \\ \Theta_2 \\ \Theta_3 \end{bmatrix}, \tag{6–3}$$

where R_0 is the radius of the foundation and μ is the shear modulus of the soil. The components in $\bar{\mathbf{Z}} = \bar{\mathbf{Z}}(\omega)$ are functions of the cyclic frequency ω and they reflect the dynamic stiffness of the soil for a given shape of the foundation. The components of the normalised dynamic stiffness (or impedance) matrix can be written as

$$\bar{Z}_{ij}(\omega) = K_{ij}(\omega) + \mathrm{i}\omega C_{ij}(\omega), \qquad i,j = 1,2,\ldots,6, \tag{6–4}$$

where K_{ij} and C_{ij} are the dynamic stiffness and damping coefficients with respect to ω, respectively. These coefficients are both real.

It is convenient to introduce the dimensionless frequency $a_0 = \omega R_0/c_S$ that is normalised by the ratio of the foundation radius R_0 and the shear wave velocity of the soil c_S as defined by Eq. (1–17). The dynamic stiffness components can then be recast into the form

$$\tilde{\bar{Z}}_{ij}(a_0) = \bar{Z}^0_{ij}\left[k_{ij}(a_0) + \mathrm{i}a_0 c_{ij}(a_0)\right], \qquad i,j = 1,2,\ldots,6, \tag{6–5}$$

where $\tilde{\bar{Z}}_{ij}(a_0) = \bar{Z}_{ij}(c_S a_0/R_0) = \bar{Z}_{ij}(\omega)$, and $\bar{Z}^0_{ij}$ is the static value of *ij*th stiffness component, cf. Eq. (6–1). Finally, k_{ij} and c_{ij} are the dynamic stiffness and damping coefficients with respect to a_0, respectively. Like K_{ij} and C_{ij}, the coefficients k_{ij} and c_{ij} are both real. Further, it is noted that geometrical damping, *i.e.* the radiation of waves into the subsoil, as well as any material damping contribute to c_{ij}.

In some situations it is useful to examine the magnitude and phase angle of Eq. (6–5) in addition to the real and imaginary parts of the dynamic stiffness. The magnitude (complex modulus) of $\tilde{\bar{Z}}_{ij}$ is given by

$$|\tilde{\bar{Z}}_{ij}| = |\bar{Z}^0_{ij}|\sqrt{(k_{ij})^2 + (a_0 c_{ij})^2}, \tag{6–6a}$$

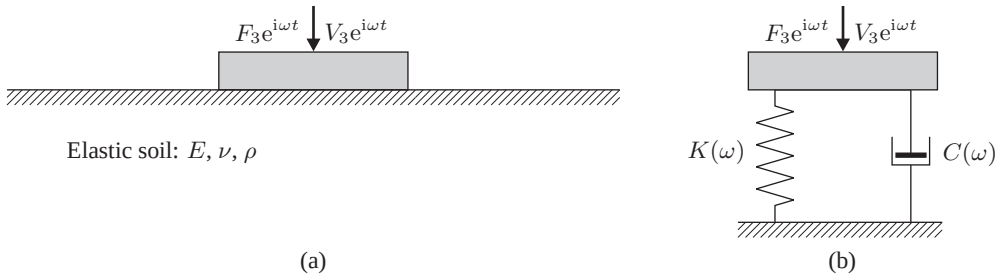

Figure 6–3 Vertical vibration of a massless rigid footing on a homogeneous half-space: (a) continuum model of the soil; (b) analogous frequency-dependent discrete-element model.

and the phase angle ϕ_{ij} of $\tilde{\tilde{Z}}_{ij}$ is given as

$$\phi_{ij} = \operatorname{atan}\left(\frac{a_0 c_{ij}}{k_{ij}}\right). \tag{6–6b}$$

Like the components of the normalised static stiffness matrix, the components in $\tilde{\tilde{\mathbf{Z}}}$ are functions of Poisson's ratio ν, whereas $\tilde{\tilde{\mathbf{Z}}}$ is independent of the shear modulus of the ground, μ. Again it is noted that a normalisation of the stiffness is only possible in the case of footings on a homogeneous half-space. For layered or inhomogeneous subsoils a change in μ implies a change in the resonance frequencies of the ground, see Section 5.7. This prohibits a simple normalisation like the one suggested by Eq. (6–3).

6.2.3 Standard lumped-parameter models

The standard lumped-parameter model contains three coefficients, K, C and M, for each degree of freedom, see Fig. 6–4. The spring stiffness, K, is equal to the static stiffness related to the degree of freedom in question. Thus, K is given by the expressions in Subsection 6.2.1. The dashpot and mass coefficients, C and M, do not have physical meaning but are solely curve fitting parameters, used to reproduce the dynamic stiffness of the foundation.

For a foundation, C and M are given in terms of the non-dimensional coefficients γ and ϱ,

$$C = \frac{R_0}{c_0}\gamma K, \qquad M = \frac{R_0^2}{c_0^2}\varrho K, \tag{6–7}$$

where R_0 and c_0 are a characteristic length of the foundation and a characteristic wave speed. In the case of circular footings on a homogeneous elastic half-space, R_0 and c_0 are chosen as the radius of the footing and the shear wave velocity c_S, cf. Subsection 1.2.1. Further, the values of K, γ and ϱ for a circular disc without mass on an elastic half-space are given in Table 6–1 which is reproduced from Wolf (1994). Note that the inertia of the disk m (mass moment of inertia for rocking vibrations) enters the expressions for γ with respect to rocking and torsional vibrations in the expressions given by Wolf (1994). However, it is possible to construct the parameters for a massless foundation.

Based on the three coefficients, K, C and M, the dynamic stiffness for a each degree of freedom can be formulated as

$$Z(\omega) = K - \omega^2 M + \mathrm{i}\omega C. \tag{6–8}$$

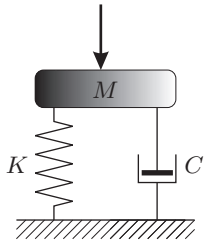

Figure 6–4 Standard lumped-parameter model for translational motion.

Table 6–1 Non-dimensional coefficients for the standard lumped-parameter model. The coefficients corresponds to a circular disc with mass on an elastic half-space.

	Static stiffness K	Dashpot coefficient γ	Mass coefficient ϱ
Horizontal	$\frac{8\varrho R_0}{2-\nu}$	0.58	0.095
Vertical	$\frac{4\varrho R_0}{1-\nu}$	0.85	0.27
Rocking	$\frac{8\varrho R_0^3}{3(1-\nu)}$	$\frac{0.3}{1+\frac{3(1-\nu)m}{8R_0^5\rho}}$	0.24
Torsional	$\frac{16\varrho R_0^3}{3}$	$\frac{0.433}{1+\frac{2m}{R_0^5\rho}}\sqrt{\frac{m}{R_0^5\rho}}$	0.045

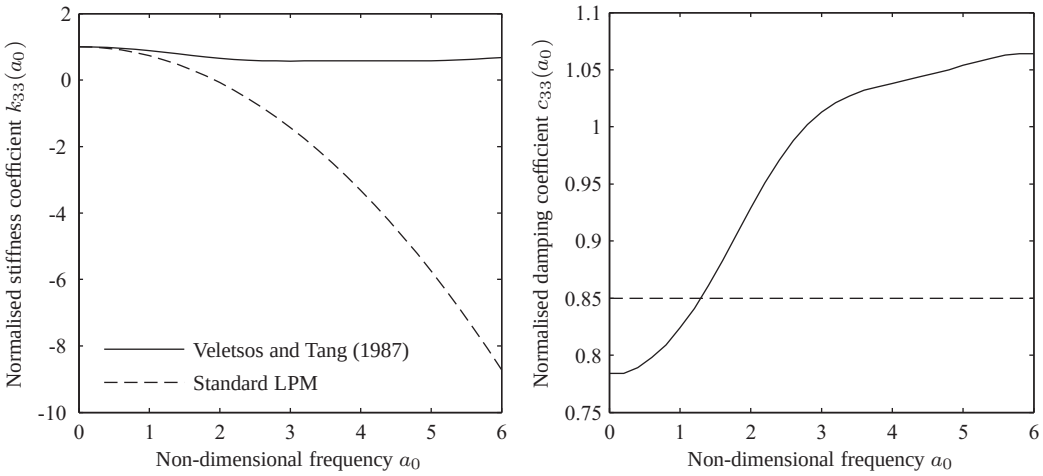

Figure 6–5 Vertical dynamic stiffness of a massless circular footing on an elastic half-space. The rigourous solution is compared with the approximation provided by a standard lumped-parameter model.

This dynamic stiffness can be rewritten in terms of the non-dimensional frequency a_0 as

$$\tilde{Z}(a_0) = K\left[k(a_0) + \mathrm{i}a_0 c(a_0)\right]. \tag{6–9}$$

By comparing Eqs. (6–7) and (6–8) with Eq. (6–9) it becomes evident that the spring and damping coefficients $k(a_0)$ and $c(a_0)$ can be written as

$$k(a_0) = 1 - \varrho a_0^2, \qquad c(a_0) = \gamma. \tag{6–10}$$

It turns out that the damping term $c(a_0)$ of the standard lumped-parameter model is constant. This behaviour is not well-suited to represent the geometrical damping of a footing, in particular with respect to the torsional and rocking vibrations. Further, the normalised real part of Eq. (6–9) given by $k(a_0)$ in Eq. (6–10) describes a parabolic shape of the dynamic stiffness. This may

represent the actual dynamic stiffness of a given foundation at low frequencies, but is inadequate for modelling the dynamic stiffness at intermediate and high frequencies where it provides an extremely poor representation of the dynamic response. This is illustrated in Fig. 6–5, where the standard lumped-parameter approximation of the vertical dynamic stiffness of a massless circular rigid footing is compared with a rigourous solution provided by Veletsos and Tang (1987).

6.2.4 Fundamental lumped-parameter models

The fundamental lumped-parameter model consists of one static stiffness parameter and four free parameters, found by curve fitting. As opposed to the standard lumped-parameter model, this type of model contains one additional internal degree of freedom. The fundamental lumped-parameter model may be assembled in several ways by combining springs, dashpots and masses. Two examples are shown in Fig. 6–6.

The spring stiffness K is equal to the static stiffness coefficient for the elastic half-space, given by the expressions in Section 6.2.1. The remaining four *free parameters* are obtained by curve fitting. The spring-dashpot model in Fig. 6–6a is represented by the parameters M_0, C_0, K_1 and C_1, whereas the monkey-tail model in Fig. 6–6b is represented by the parameters M_0, C_0, M_1 and C_1. For the monkey-tail model, the four free parameters M_0, C_0, M_1 and C_1 can be formulated by means of the non-dimensional coefficients ϱ_0, γ_0, ϱ_1 and γ_1 as

$$M_0 = \frac{r_0^2}{c_S^2}\varrho_0 K, \quad C_0 = \frac{r_0}{c_S}\gamma_0 K, \quad M_1 = \frac{r_0^2}{c_S^2}\varrho_1 K, \quad C_1 = \frac{r_0}{c_S}\gamma_1 K. \tag{6–11}$$

The values of K, ϱ_0, γ_0, ϱ_1 and γ_1 for a circular disk on an elastic half-space are given in Table 6–2 which is reproduced from (Wolf 1994). Most of the coefficients, except for torsional vibrations, depend on ν. Note that some of the non-dimensional coefficients may be missing for some of the vibration modes.

The dynamic stiffness $Z(\omega)$ of the fundamental lumped-parameter model (for harmonic loading) can be established by formulating the equilibrium equation for each of the two degrees of freedom, $V_0(\omega)$ and $V_1(\omega)$ in Fig. 6–6b. The two equilibrium equations are

$$-\omega^2 M_1 V_1(\omega) + \mathrm{i}\omega C_1 \left[V_1(\omega) - V_0(\omega)\right] = 0, \tag{6–12a}$$

$$-\omega^2 M_0 V_0(\omega) + \mathrm{i}\omega \left(C_0 + C_1\right) V_0(\omega) - \mathrm{i}\omega C_1 V_1(\omega) + K V_0(\omega) = P_0(\omega), \tag{6–12b}$$

where $V_0(\omega)$ is the displacement amplitude related to the applied load amplitude $P_0(\omega)$. By eliminating $V_1(\omega)$ in Eqs. (6–12a) and (6–12b) the relation between $P_0(\omega)$ and $V_0(\omega)$ is given as

$$P_0(\omega) = \underbrace{K\left[1 - \frac{\frac{\omega^2 M_1}{K}}{1+\frac{\omega^2 M_1^2}{C_1^2}} - \frac{\omega^2 M_0}{K} + \mathrm{i}\omega\left(\frac{M_1}{C_1}\frac{\frac{\omega^2 M_1}{K}}{1+\frac{\omega^2 M_1^2}{C_1^2}} + \frac{C_0}{K}\right)\right]}_{Z(\omega)} V_0(\omega). \tag{6–13}$$

Table 6–2 Non-dimensional coefficients for the fundamental lumped-parameter model. The coefficients correspond to a circular disc on an elastic half-space.

	Stiffness	Dashpots		Masses		
	K	γ_0	γ_1	ϱ_0		ϱ_1
Horizontal	$\frac{8\mu R_0}{2-\nu}$	0.78-0.4ν	—	—		—
Vertical	$\frac{4\mu R_0}{1-\nu}$	0.8	0.34-4.3ν^4	$\nu < \frac{1}{3}$	0	0.4-4ν^4
				$\nu > \frac{1}{3}$	0.9($\nu - \frac{1}{3}$)	
Rocking	$\frac{8\mu R_0^3}{3(1-\nu)}$	—	0.42-0.3ν^2	$\nu < \frac{1}{3}$	0	0.34-0.2ν^2
				$\nu > \frac{1}{3}$	0.16($\nu - \frac{1}{3}$)	
Torsional	$\frac{16\mu R_0^3}{3}$	0.017	0.291	—		0.171

Figure 6–6 Fundamental lumped-parameter models: (a) spring-dashpot model; (b) monkey-tail model.

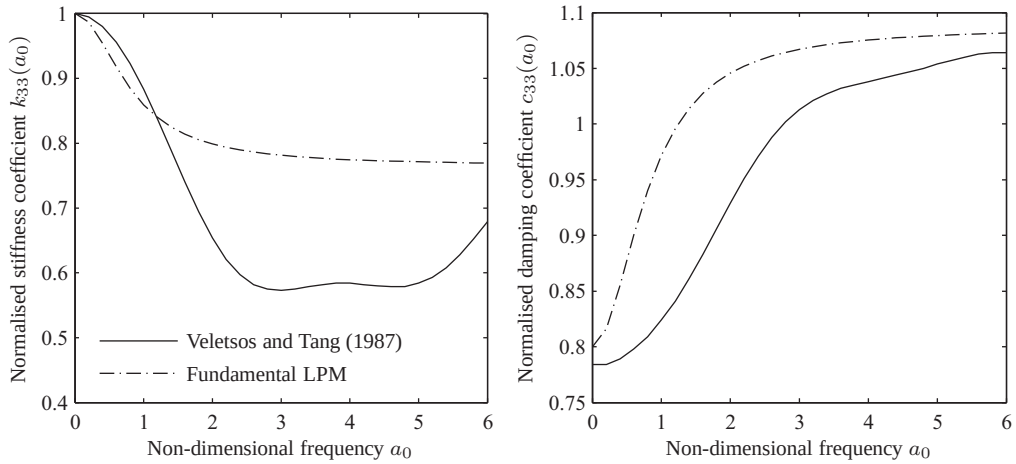

Figure 6–7 Vertical dynamic stiffness of a massless circular footing on an elastic half-space. The rigourous solution is compared with the approximation provided by a fundamental lumped-parameter model.

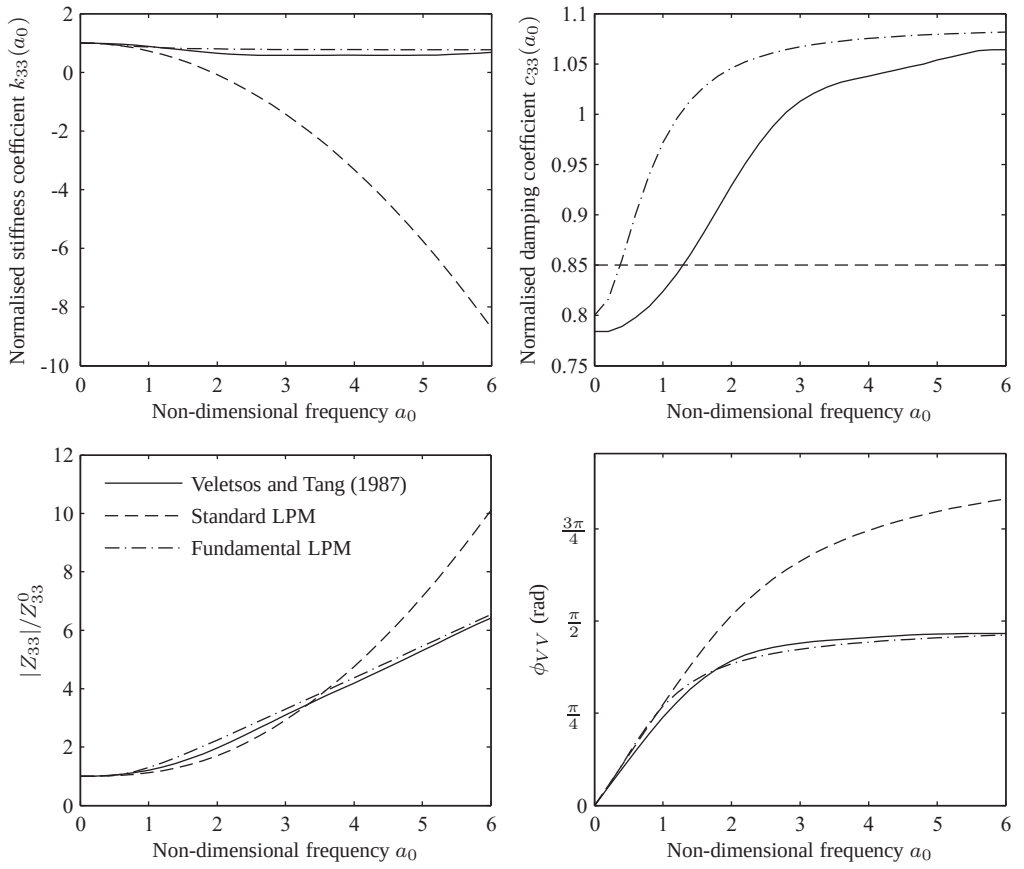

Figure 6–8 Vertical dynamic stiffness of a massless circular footing on an elastic half-space. The rigourous solution is compared with the approximation of both the standard and the fundamental lumped-parameter model.

The dynamic stiffness in Eq. (6–13) can be rewritten in terms of the non-dimensional frequency a_0 as stated in Eq. (6–9). By substituting Eq. (6–11) into Eq. (6–13), the spring and damping coefficients $k(a_0)$ and $c(a_0)$ of the fundamental lumped-parameter model (monkey-tail version) can be determined as

$$k(a_0) = 1 - \frac{\varrho_1 a_0^2}{1 + \frac{\varrho_1^2}{\gamma_1^2} a_0^2} - \varrho_0 a_0^2, \qquad c(a_0) = \frac{\varrho_1}{\gamma_1} \frac{\varrho_1 a_0^2}{1 + \frac{\varrho_1^2}{\gamma_1^2} a_0^2} + \gamma_0. \tag{6–14}$$

Note that the procedure for establishing the formulation for spring-dashpot model is similar to that of the monkey-tail model. The only difference is the characteristics of the non-dimensional coefficients. Further, as opposed to the standard lumped-parameter model, the fundamental lumped-parameter model is double-asymptotic, meaning that the approximation of $\tilde{Z}(a_0)$ is exact for the static limit, $a_0 \to 0$, and for the high-frequency limit, for $a_0 \to \infty$.

The fundamental lumped-parameter approximation of the vertical dynamic stiffness of a massless circular rigid footing is illustrated in Fig. 6–7. The approximation is compared with

a rigorous solution provided by Veletsos and Tang (1987). A comparison of Fig. 6–7 with Fig. 6–5 reveals that the inclusion of an internal degree of freedom improves the quality of lumped-parameter model significantly. Hence, in the high-frequency range the fundamental lumped-parameter model provides a much better fit to the rigourous solution than the standard lumped-parameter model presented in the previous section.

The approximation of the fundamental lumped-parameter model is compared with that of the standard lumped-parameter model in Fig. 6–8. The approximations are shown for the real and imaginary part of the dynamic stiffness, as well as for the magnitude and phase angle.

6.3 Consistent lumped-parameter models

As discussed in Subsection 1.6.3, a fairly general viscoelastic model may be obtained by application of a rational filter approximation, cf. Eq. (1–125). Likewise, Subsection 2.5.1 concerns the formulation of transmitting boundary conditions in terms of rational approximations. In the case of a structure interacting with soil, a similar relationship may be established between a generalised force resultant, $f(t)$, acting at the foundation–soil interface and the corresponding generalised displacement component, $v(t)$:

$$\sum_{i=0}^{k} A_i \frac{\mathrm{d}^i v(t)}{\mathrm{d}t^i} = \sum_{j=0}^{l} B_j \frac{\mathrm{d}^j f(t)}{\mathrm{d}t^j}. \tag{6–15}$$

Here, A_i, $i = 1, 2, \ldots, k$, and B_j, $j = 1, 2, \ldots, l$, are real coefficients found by curve fitting to the exact analytical solution or the results obtained by some numerical method or measurements.

The rational approximation (6–15) suggests a model, in which higher-order temporal derivatives of both the forces and the displacements occur. This is undesired from a computational point of view. However, a much more elegant model only involving the zeroth, the first and the second temporal derivatives may be achieved by a rearrangement of the differential operators. This operation is simple to carry out in the frequency domain; hence, the first step in the formulation of a rational approximation is a Fourier transformation of Eq. (6–15), which provides:

$$\sum_{i=0}^{k} A_i (\mathrm{i}\omega)^i V(\omega) = \sum_{j=0}^{l} B_j (\mathrm{i}\omega)^j P(\omega) \quad \Rightarrow$$

$$P(\omega) = \hat{Z}(\mathrm{i}\omega) V(\omega), \quad \hat{Z}(\mathrm{i}\omega) = \frac{\sum_{i=0}^{k} A_i (\mathrm{i}\omega)^i}{\sum_{j=0}^{l} B_j (\mathrm{i}\omega)^j}, \tag{6–16}$$

where $V(\omega)$ and $F(\omega)$ denote the complex amplitudes of the generalized displacements and forces, respectively. It is noted that in Eq. (6–16) it has been assumed that the reaction force $F(\omega)$ stems from the response to a single displacement degree of freedom. This is generally not the case. For example, as discussed in Subsection 5.7, there is a coupling between the rocking moment–rotation and the horizontal force–translation of a rigid footing. However, the model (6–16) is easily generalised to account for such behaviour by an extension in the form $F_i(\omega) = \hat{Z}_{ij}(\mathrm{i}\omega) V_j(\omega)$, where summation is carried out over index j equal to the degrees of freedom contributing to the response. Each of the complex stiffness terms, $\hat{Z}_{ij}(\mathrm{i}\omega)$, is given by a polynomial fraction as illustrated by Eq. (6–16) for $\hat{Z}(\mathrm{i}\omega)$. This forms the basis for the derivation of so-called consistent lumped-parameter models.

6.3.1 Polynomial-fraction form of a rational filter

In the frequency domain, the dynamic stiffness related to a degree of freedom, or to the interaction between two degrees of freedom, i and j, is given by $\tilde{Z}_{ij}(a_0) = Z^0_{ij} S_{ij}(a_0)$ (no sum on i, j). Here, $Z^0_{ij} = Z_{ij}(0)$ denotes the static stiffness related to the interaction of the two degrees of freedom, and $a_0 = \omega R_0/c_0$ is a dimensionless frequency with R_0 and c_0 denoting a characteristic length and wave velocity, respectively. For example, for a circular footing with the radius R_0 on an elastic half-space with the S-wave velocity c_S, $a_0 = \omega R_0/c_S$ may be chosen. With the given normalisation of the frequency it is noted that $\tilde{Z}_{ij}(a_0) = Z_{ij}(c_0 a_0/R_0) = Z_{ij}(\omega)$.

For simplicity, any indices indicating the degrees of freedom in question are omitted in the following sections, *e.g.* $\tilde{Z}(a_0) \sim \tilde{Z}_{ij}(a_0)$. The frequency-dependent stiffness coefficient $S(a_0)$ for a given degree of freedom is then decomposed into a singular part, $S_s(a_0)$, and a regular part, $S_r(a_0)$, *i.e.*

$$\tilde{Z}(a_0) = Z^0 S(a_0), \qquad S(a_0) = S_s(a_0) + S_r(a_0), \tag{6–17}$$

where Z^0 is the static stiffness, and the singular part has the form

$$S_s(a_0) = k^\infty + \mathrm{i} a_0 c^\infty. \tag{6–18}$$

In this expression, k^∞ and c^∞ are two real-valued constants which are selected so that $Z^0 S_s(a_0)$ provides the entire stiffness in the high-frequency limit $a_0 \to \infty$. Typically, the stiffness term $Z^0 k^\infty$ vanishes and the complex stiffness in the high-frequency range becomes a pure mechanical impedance, *i.e.* $S_s(a_0) = \mathrm{i} a_0 c^\infty$. This is demonstrated below for a number of example structures interacting with soil.

The regular part $S_r(a_0)$ accounts for the remaining part of the stiffness. Generally, a closed-form solution for $S_r(a_0)$ is unavailable. Hence, the regular part of the complex stiffness is usually obtained by the fitting of a rational filter to the results obtained in a numerical or semi-analytical model by the finite-element method (FEM), the boundary-element method (BEM) or the domain-transformation method (DTM). These methods have been discussed in the previous chapters, and further below in this chapter examples are given of their application to the calibration of lumped-parameter models.

Whether an analytical or a numerical solution is established, the output of a frequency-domain analysis is the complex dynamic stiffness $\tilde{Z}(a_0)$. This is taken as the "exact" solution, and the regular part of the stiffness coefficient is found as $S_r(a_0) = \tilde{Z}(a_0)/Z^0 - S_s(a_0)$. A rational approximation, or filter, is now introduced in the form

$$S_r(a_0) \approx \hat{S}_r(\mathrm{i}a_0) = \frac{P(\mathrm{i}a_0)}{Q(\mathrm{i}a_0)} = \frac{p_0 + p_1(\mathrm{i}a_0) + p_2(\mathrm{i}a_0)^2 + \ldots + p_N(\mathrm{i}a_0)^N}{q_0 + q_1(\mathrm{i}a_0) + q_2(\mathrm{i}a_0)^2 + \ldots + q_M(\mathrm{i}a_0)^M}. \tag{6–19}$$

The orders, N and M, and the coefficients, p_n ($n = 0, 1, \ldots, N$) and q_m ($m = 0, 1, \ldots, M$), of the numerator and denominator polynomials $P(\mathrm{i}a_0)$ and $Q(\mathrm{i}a_0)$ are chosen according to the following criteria:

1 To obtain a unique definition of the filter, one of the coefficients in either $P(\mathrm{i}a_0)$ or $Q(\mathrm{i}a_0)$ has to be given a fixed value. For convenience, $q_0 = 1$ is chosen.

2 Since part of the static stiffness is already represented by $S_s(0) = k^\infty$, this part of the stiffness should not be provided by $S_r(a_0)$ as well. Therefore, $p_0/q_0 = p_0 = 1 - k^\infty$.

3 In the high-frequency limit, $S(a_0) = S_s(a_0)$. Thus, the regular part must satisfy the condition that $\hat{S}_r(\mathrm{i}a_0) \to 0$ for $a_0 \to \infty$. Hence, $N < M$, *i.e.* the numerator polynomial $P(\mathrm{i}a_0)$ is at least one order lower than the denominator polynomial, $Q(\mathrm{i}a_0)$.

Based on these criteria, Eq. (6–20) may advantageously be reformulated as

$$S_r(a_0) \approx \hat{S}_r(\mathrm{i}a_0) = \frac{P(\mathrm{i}a_0)}{Q(\mathrm{i}a_0)} = \frac{1 - k^\infty + p_1(\mathrm{i}a_0) + p_2(\mathrm{i}a_0)^2 + \ldots + p_{M-1}(\mathrm{i}a_0)^{M-1}}{1 + q_1(\mathrm{i}a_0) + q_2(\mathrm{i}a_0)^2 + \ldots + q_M(\mathrm{i}a_0)^M}. \quad (6\text{–}20)$$

Evidently, the polynomial coefficients in Eq. (6–20) must provide a physically meaningful filter. By a comparison with Eqs. (6–15) and (6–16) it follows that p_n ($n = 1, 2, \ldots, M-1$) and q_j ($m = 1, 2, \ldots M$) must all be real. Furthermore, no poles should appear along the positive real axis as this will lead to an unstable solution in the time domain. This issue is discussed below.

The total approximation of $S(a_0)$ is found by an addition of Eqs. (6–18) and (6–20) as stated in Eq. (6–17). The approximation of $S(a_0)$ has two important characteristics:

- It is exact in the static limit, since $S(a_0) \approx \hat{S}(\mathrm{i}a_0) + S_s(a_0) \to 1$ for $a_0 \to 0$.
- It is exact in the high-frequency limit. Here, $S(a_0) \to S_s(a_0)$ for $a_0 \to \infty$, because $\hat{S}_r(\mathrm{i}a_0) \to 0$ for $a_0 \to \infty$.

Hence, the approximation is double-asymptotic. For intermediate frequencies, the quality of the fit depends on the order of the rational filter and the nature of the physical problem. Thus, in some situations a low-order filter may provide a very good fit to the exact solution, whereas other problems may require a high-order filter to ensure an adequate match—even over a short range of frequencies. This topic is further discussed in the examples at the end of this chapter.

6.3.2 Partial-fraction form of a rational filter

Whereas the polynomial-fraction form is well-suited for curve fitting to measured or computed responses, it provides little insight into the physics of the problem. To a limited extent, such information is gained by a recasting of Eq. (6–20) into partial-fraction form,

$$\hat{S}_r(\mathrm{i}a_0) = \sum_{m=1}^{M} \frac{R_m}{\mathrm{i}a_0 - s_m}, \quad (6\text{–}21)$$

where s_m, $m = 1, 2, \ldots, M$ are the poles of $\hat{S}_r(\mathrm{i}a_0)$ (*i.e.* the roots of $Q(\mathrm{i}a_0)$), and R_j are the corresponding residues. The conversion of the original polynomial-fraction form into the partial-fraction expansion form may be carried out in MATLAB with the inbuilt function `residue`.

The poles s_m are generally complex. However, as discussed above the coefficients q_m must be real in order to provide a rational approximation that is physically meaningful in the time domain. To ensure this, any complex poles, s_m, and the corresponding residues, R_m, must appear as conjugate pairs. When two such terms are added together, a second-order term with real coefficients appears. Thus, with N conjugate pairs, Eq. (6–21) can be rewritten as

$$\hat{S}_r(\mathrm{i}a_0) = \sum_{n=1}^{N} \frac{\beta_{0n} + \beta_{1n}\mathrm{i}a_0}{\alpha_{0n} + \alpha_{1n}\mathrm{i}a_0 + (\mathrm{i}a_0)^2} + \sum_{n=N+1}^{M-N} \frac{R_n}{\mathrm{i}a_0 - s_n}, \qquad 2N \le M. \quad (6\text{–}22)$$

The coefficients α_{0n}, α_{1n}, β_{0n} and β_{1n}, $n = N+1, N+2, \ldots, M-N$, are given by

$$\alpha_{0n} = \{s_n^{\Re}\}^2 + \{s_n^{\Im}\}^2, \quad \alpha_{1n} = -2s_n^{\Re}, \quad \beta_{0n} = -2(R_n^{\Re} s_n^{\Re} + R_n^{\Im} s_n^{\Im}), \quad \beta_{1n} = 2R_n^{\Re}, \quad (6\text{–}23)$$

where $s_n^{\Re} = \Re(s_n)$ and $s_n^{\Im} = \Im(s_n)$ are the real and imaginary parts of the complex conjugate poles, respectively. Similarly, the real and imaginary parts of the complex conjugate residues are denoted by $R_n^{\Re} = \Re(R_n)$ and $R_n^{\Im} = \Im(R_n)$, respectively.

By adding the singular term in Eq. (6–18) to the expression in Eq. (6–21), the total approximation of the dynamic stiffness coefficient $S(a_0)$ can be written as

$$\hat{S}(\mathrm{i}a_0) = k^{\infty} + \mathrm{i}a_0 c^{\infty} + \sum_{n=1}^{N} \frac{\beta_{0n} + \beta_{1n}\mathrm{i}a_0}{\alpha_{0n} + \alpha_{1n}\mathrm{i}a_0 + (\mathrm{i}a_0)^2} + \sum_{n=N+1}^{M-N} \frac{R_n}{\mathrm{i}a_0 - s_n}. \quad (6\text{–}24)$$

The total approximation of the dynamic stiffness in Eq. (6–24) consists of three characteristic types of terms, namely a constant/linear term, $M - 2N$ first-order terms and N second-order terms. These terms are given as:

Constant/linear term: $$k^{\infty} + \mathrm{i}a_0 c^{\infty} \quad (6\text{–}25a)$$

First-order term: $$\frac{R}{\mathrm{i}a_0 - s} \quad (6\text{–}25b)$$

Second-order term: $$\frac{\beta_1 \mathrm{i}a_0 + \beta_0}{\alpha_0 + \alpha_1 \mathrm{i}a_0 + (\mathrm{i}a_0)^2}. \quad (6\text{–}25c)$$

6.3.3 Physical interpretation of a rational filter

Now, each term in Eq. (6–25) may be identified as the frequency-response function for a simple dynamic system similar to those in Figures 6–4 and 6–6, *i.e.* with no or only few internal degrees of freedom. Physically, the summation of terms (6–24) may then be interpreted as a parallel coupling of $M - N + 1$ of these so-called discrete-element models, and the resulting lumped-parameter model provides a frequency-response function similar to that of the original continuous system. In the subsections below, the calibration of the discrete-element models is discussed.

Constant/linear term

The constant/linear term given by Eq. (6–25a) consists of two known parameters, k^{∞} and c^{∞}, that represent the singular part of the dynamic stiffness. The discrete-element model for the constant/linear term is shown in Fig. 6–9.

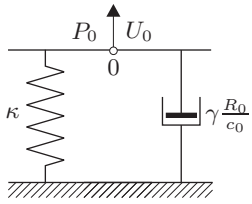

Figure 6–9 The discrete-element model for the constant/linear term.

The equilibrium formulation of Node 0 (for harmonic loading) is as follows:

$$\kappa U_0(\omega) + \mathrm{i}\omega\gamma \frac{R_0}{c_0} U_0(\omega) = P_0(\omega) \tag{6–26}$$

Recalling that the dimensionless frequency is introduced as $a_0 = \omega R_0/c_0$, the equilibrium formulation in Eq. (6–26) results in a force–displacement relation given by

$$P_0(a_0) = (\kappa + \mathrm{i}a_0\gamma)\, U_0(a_0). \tag{6–27}$$

By a comparison of Eqs. (6–25a) and (6–27) it becomes evident that the non-dimensional coefficients κ and γ are equal to k^∞ and c^∞, respectively.

First-order term

The first-order term given by Equation (6–25b) has two parameters, R and s. The layout of the discrete-element model is shown in Fig. 6–10(a). The model is constructed by a spring $(-\kappa)$ in parallel with another spring (κ) and dashpot $(\gamma\frac{R_0}{c_0})$ in series. The serial connection between the spring (κ) and the dashpot $(\gamma\frac{R_0}{c_0})$ results in an internal node (internal degree of freedom). The equilibrium formulations for Nodes 0 and 1 (for harmonic loading) are as follows:

$$\text{Node 0}: \qquad \kappa\big(U_0(\omega) - U_1(\omega)\big) - \kappa U_0(\omega) = P_0(\omega) \tag{6–28a}$$

$$\text{Node 1}: \qquad \kappa\big(U_1(\omega) - U_0(\omega)\big) + \mathrm{i}\omega\gamma \frac{R_0}{c_0} U_1(\omega) = 0. \tag{6–28b}$$

After elimination of $U_1(\omega)$ in Eqs. (6–28a) and (6–28b), it becomes clear that the force–displacement relation of the first-order model is given as

$$P_0(a_0) = \frac{-\frac{\kappa^2}{\gamma}}{\mathrm{i}a_0 + \frac{\kappa}{\gamma}} U_0(a_0). \tag{6–29}$$

By comparing Eqs. (6–25b) and (6–29), κ and γ are identified as

$$\kappa = \frac{R}{s}, \qquad \gamma = -\frac{R}{s^2}. \tag{6–30}$$

It should be noted that the first-order term could also be represented by a monkey-tail model, see Fig. 6–10(b). This turns out to be advantageous in situations where κ and γ in Eq. (6–30) are

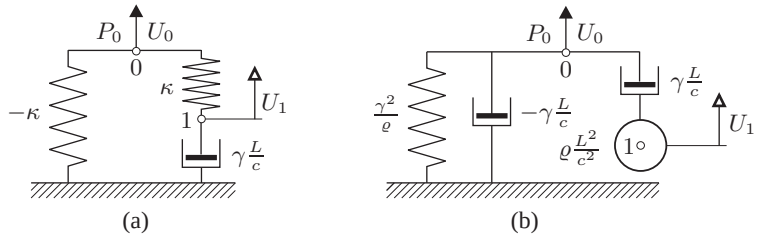

Figure 6–10 The discrete-element model for the first-order term: (a) Spring-dashpot model; (b) monkey-tail model.

negative, which may be the case when R is positive (s is negative). To avoid negative coefficients of springs and dashpots, the monkey-tail model is applied, and the resulting coefficients are positive. By inspecting the equilibrium formulations for Nodes 0 and 1, see Fig. 6–10(b), the coefficients can be identified as

$$\gamma = \frac{R}{s^2}, \qquad \varrho = -\frac{R}{s^3}. \tag{6–31}$$

Second-order term

The second-order term given by Eq. (6–25c) has four parameters: α_0, α_1, β_0 and β_1. An example of a second-order discrete-element model is shown in Fig. 6–11(a). This particular model has two internal nodes. The equilibrium formulations for Nodes 0, 1 and 2 (for harmonic loading) are as follows:

$$\text{Node 0 :} \qquad \kappa_1\big(U_0(\omega) - U_1(\omega)\big) - \kappa_1 U_0(\omega) = P_0(\omega) \tag{6–32a}$$

$$\text{Node 1 :} \qquad \kappa_1\big(U_1(\omega) - U_0(\omega)\big) + \mathrm{i}\omega\gamma_1\frac{R_0}{c_0}\big(U_1(\omega) - U_2(\omega)\big) = 0 \tag{6–32b}$$

$$\text{Node 2 :} \qquad \kappa_2 U_2(\omega) + \mathrm{i}\omega\gamma_2\frac{R_0}{c_0}U_2(\omega) + \mathrm{i}\omega\gamma_1\frac{R_0}{c_0}\big(U_2(\omega) - U_1(\omega)\big) = 0. \tag{6–32c}$$

After some rearrangement and elimination of the internal degrees of freedom, the force-displacement relation of the second-order model is given by

$$P_0(a_0) = \frac{-\kappa_1^2\frac{\gamma_1+\gamma_2}{\gamma_1\gamma_2}\mathrm{i}a_0 - \frac{\kappa_1^2\kappa_2}{\gamma_1\gamma_2}}{(\mathrm{i}a_0)^2 + \left(\kappa_1\frac{\gamma_1+\gamma_2}{\gamma_1\gamma_2} + \frac{\kappa_2}{\gamma_2}\right)\mathrm{i}a_0 + \frac{\kappa_1\kappa_2}{\gamma_1\gamma_2}}U_0(a_0). \tag{6–33}$$

By a comparison of Eqs. (6–25c) and (6–33), the four coefficients in Eq. (6–33) are identified as

$$\kappa_1 = -\frac{\beta_0}{\alpha_0}, \qquad \gamma_1 = -\frac{\alpha_0\beta_1 - \alpha_1\beta_0}{\alpha_0^2}, \tag{6–34a}$$

$$\kappa_2 = \frac{\beta_0}{\alpha_0^2}\frac{(-\alpha_0\beta_1 + \alpha_1\beta_0)^2}{\alpha_0\beta_1^2 - \alpha_1\beta_0\beta_1 + \beta_0^2}, \qquad \gamma_2 = \frac{\beta_0^2}{\alpha_0^2}\frac{-\alpha_0\beta_1 + \alpha_1\beta_0}{\alpha_0\beta_1^2 - \alpha_1\beta_0\beta_1 + \beta_0^2}. \tag{6–34b}$$

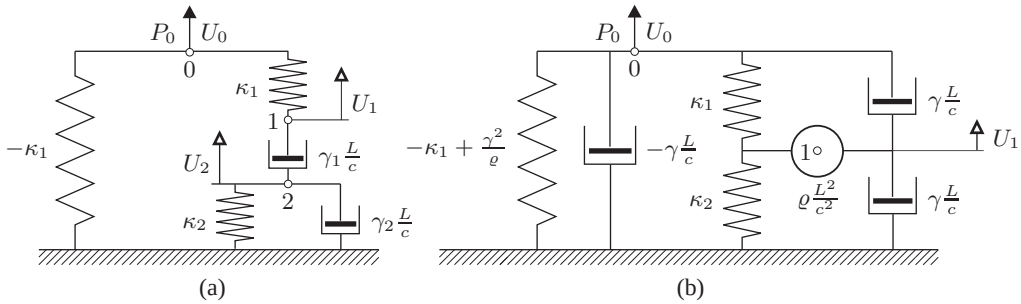

Figure 6–11 The discrete-element model for the second-order term: (a) Spring-dashpot model with two internal degrees of freedom; (b) spring-dashpot-mass model with one internal degree of freedom.

Alternatively, introducing a second-order model with springs, dampers and a point mass, it is possible to construct a second-order model with only one internal degree of freedom. The model is sketched in Fig. 6–11(b). The force–displacement relation of the alternative second-order model is given by

$$P_0(a_0) = \frac{2\left(\frac{\kappa_1\gamma}{\varrho} + \frac{\gamma^3}{\varrho^2}\right)\mathrm{i}a_0 - \frac{\kappa_1^2}{\varrho} + \frac{(\kappa_1+\kappa_2)\gamma^2}{\varrho^2}}{(\mathrm{i}a_0)^2 + 2\frac{\gamma}{\varrho}\mathrm{i}a_0 + \frac{\kappa_1+\kappa_2}{\varrho}} U_0(a_0). \tag{6–35}$$

By equating the coefficients in Eq. (6–35) to the terms of the second-order model in Eq. (6–25c), the four parameters κ_1, κ_2, γ and ϱ can be determined. In order to calculate ϱ, a quadratic equation has to be solved. The quadratic equation for ϱ is

$$a\varrho^2 + b\varrho + c = 0 \quad \text{where} \quad a = \alpha_1^4 - 4\alpha_0\alpha_1^2, \quad b = -8\alpha_1\beta_1 + 16\beta_0, \quad c = 16\frac{\beta_1^2}{\alpha_1^2}. \tag{6–36}$$

Equation (6–36) results in two solutions for ϱ. To ensure real values of ϱ, $b^2 - 4ac \geq 0$ or $\alpha_0\beta_1^2 - \alpha_1\beta_0\beta_1 + \beta_0^2 \geq 0$. When ϱ has been determined, the three remaining coefficients can be calculated by

$$\kappa_1 = \frac{\varrho\alpha_1^2}{4} - \frac{\beta_1}{\alpha_1}, \quad \kappa_2 = \varrho\alpha_0 - \kappa_1, \quad \gamma = \frac{\varrho\alpha_1}{2}. \tag{6–37}$$

6.3.4 Fitting of a rational filter

In order to get a stable solution in the time domain, the poles of $\hat{S}_r(\mathrm{i}a_0)$ should all reside in the second and third quadrant of the complex plane, *i.e.* the real parts of the poles must all be negative. Due to the fact that computers only have a finite precision, this requirement may have to be adjusted to $s_m < -\varepsilon$, $m = 1, 2, \ldots, M$, where ε is a small number, *e.g.* 0.01.

The rational approximation may now be obtained by curve-fitting of the rational filter $\hat{S}_r(\mathrm{i}a_0)$ to the regular part of the dynamic stiffness, $S_r(a_0)$, by a least-squares technique. In this process, it should be observed that:

1 The response should be accurately described by the lumped-parameter model in the frequency range that is important for the physical problem being investigated. For soil–structure interaction of buildings, bridges, wind turbines, chimneys, etc., this is typically the low-frequency range, whereas the analysis of machine foundations may require an accurate lumped-parameter model at higher frequencies.

2 The "exact" values of $S_r(a_0)$ are only measured—or computed—over a finite range of frequencies, typically for $a_0 \in [0; a_{0max}]$ with $a_{0max} = 2 \sim 10$. Further, the values of $S_r(a_0)$ are typically only known at a number of discrete frequencies.

3 Outside the frequency range, in which $S_r(a_0)$ has been provided, the singular part of the dynamic stiffness, $S_s(a_0)$, should govern the response. Hence, no additional tips and dips should appear in the frequency response provided by the rational filter beyond the dimensionless frequency a_{0max}.

Firstly, this implies that the order of the filter, M, should not be too high. Experience shows that orders about $M = 2 \sim 8$ are adequate for most physical problems. Higher-order filters than this are not easily fitted, and lower-order filters provide a poor match to the "exact" results. Secondly, in order to ensure a good fit of $\hat{S}_r(\mathrm{i}a_0)$ to $S_r(a_0)$ in the low-frequency range, it is recommended to employ a higher weight on the squared errors in the low-frequency range, *e.g.* for $a_0 < 0.2 \sim 2$, compared with the weights in the medium-to-high-frequency range. Obviously, the definition of low, medium and high frequencies is strongly dependent on the problem in question. For example, frequencies that are considered high for an offshore wind turbine, may be considered low for a diesel power generator.

For soil-structure interaction of foundations, Wolf (1994) suggested to employ a weight of $w(a_0) = 10^3 \sim 10^5$ at low frequencies and unit weight at higher frequencies. This should lead to a good approximation in most cases. However, numerical experiment indicates that the fitting goodness of the rational filter is highly sensitive to the choice of the weight function $w(a_0)$, and the guidelines provided by Wolf (1994) are not useful in all situations. Hence, as an alternative, the following fairly general weight function is proposed:

$$w(a_0) = \frac{1}{(1 + (\varsigma_1 a_0)^{\varsigma_2})^{\varsigma_3}}. \tag{6–38}$$

The coefficients ς_1, ς_2 and ς_3 are heuristic parameters. Experience shows that values of about $\varsigma_1 = \varsigma_2 = \varsigma_3 = 2$ provide an adequate solution for most foundations in the low-frequency range $a_0 \in [0; 2]$. This recommendation is justified by the examples given at the end of the chapter. For analyses involving high-frequency excitation, lower values of ς_1, ς_2 and ς_3 may have to be employed.

Hence, final result is the optimisation problem defined in Box 6.1. However, the requirement of all poles lying in the second and third quadrant of the complex plane is not easily fulfilled when an optimisation is carried out by least-squares (or similar) curve fitting of $\hat{S}_r(\mathrm{i}a_0)$ to $S_r(a_0)$ as suggested in Box 6.1. Specifically, the choice of the polynomial coefficients q_j, $j = 1, 2, \ldots, m$, as the optimisation variables is unsuitable, since the constraint that all poles of $\hat{S}_r(\mathrm{i}a_0)$ must have negative real parts is not easily incorporated in the optimisation problem. Therefore, instead of the interpretation

$$Q(\mathrm{i}a_0) = 1 + q_1(\mathrm{i}a_0) + q_2(\mathrm{i}a_0)^2 + \ldots + q_M(\mathrm{i}a_0)^M, \tag{6–39}$$

an alternative approach is considered, in which the denominator is expressed as

$$Q(\mathrm{i}a_0) = (\mathrm{i}a_0 - s_1)(\mathrm{i}a_0 - s_2)\cdots(\mathrm{i}a_0 - s_M) = \prod_{m=1}^{M} (\mathrm{i}a_0 - s_m). \tag{6–40}$$

In this representation, s_m, $m = 1, 2, \ldots, M$, are the roots of $Q(\mathrm{i}a_0)$. In particular, if there are N complex conjugate pairs, the denominator polynomial may advantageously be expressed as

$$Q(\mathrm{i}a_0) = \prod_{n=1}^{N} (\mathrm{i}a_0 - s_n)\,(\mathrm{i}a_0 - s_n^*) \cdot \prod_{n=N+1}^{M-N} (\mathrm{i}a_0 - s_n)\,. \tag{6–41}$$

where an asterisk $(*)$ denotes the complex conjugate. Thus, instead of the polynomial coefficients, the roots s_n are identified as the optimisation variables.

Accordingly, in addition to the coefficients of the numerator polynomial $P(\mathrm{i}a_0)$, the variables in the optimisation problem are the real and imaginary parts $s_n^{\Re} = \Re(s_n)$ and $s_n^{\Im} = \Im(s_n)$ of the complex roots s_n, $n = 1, 2, \ldots, N$, and the real roots s_n, $n = N+1, N+2, \ldots, M-N$.

Box 6.1 Fitting of rational filter by optimisation of polynomial coefficients

A rational filter for the regular part of the dynamic stiffness is defined in the form:

$$S_r(a_0) \approx \hat{S}_r(\mathrm{i}a_0) = \frac{P(\mathrm{i}a_0)}{Q(\mathrm{i}a_0)} = \frac{1 - k^{\infty} + p_1(\mathrm{i}a_0) + p_2(\mathrm{i}a_0)^2 + \ldots + p_{M-1}(\mathrm{i}a_0)^{M-1}}{1 + q_1(\mathrm{i}a_0) + q_2(\mathrm{i}a_0)^2 + \ldots + q_M(\mathrm{i}a_0)^M}. \tag{a}$$

Find the optimal polynomial coefficients p_n and q_m which minimize the object function $F(p_n, q_m)$ in a weighted-least-squares sense subject to the constraints $G_1(p_n, q_m), G_2(p_n, q_m), \ldots, G_M(p_n, q_m)$.

Input:

$$\begin{aligned} M:&\quad \text{order of the filter,}\\ p_n^0,&\quad n = 1, 2, \ldots, M-1,\\ q_m^0,&\quad m = 1, 2, \ldots, M,\\ a_{0j},&\quad j = 1, 2, \ldots, J,\\ S_r(a_{0j}),&\quad j = 1, 2, \ldots, J,\\ w(a_{0j}),&\quad j = 1, 2, \ldots, J. \end{aligned}$$

Variables:

$$\begin{aligned} p_n,&\quad n = 1, 2, \ldots, M-1,\\ q_m,&\quad m = 1, 2, \ldots, M. \end{aligned}$$

Object function:

$$F(p_n, q_m) = \sum_{j=1}^{J} w(a_{0j}) \left(\hat{S}_r(\mathrm{i}a_{0j}) - S_r(a_{0j}) \right)^2.$$

Constraints:

$$\begin{aligned} G_1(p_n, q_m) &= \Re(s_1) < -\varepsilon,\\ G_2(p_n, q_m) &= \Re(s_2) < -\varepsilon,\\ &\vdots\\ G_M(p_n, q_m) &= \Re(s_M) < -\varepsilon. \end{aligned}$$

Output:

$$\begin{aligned} p_n,&\quad n = 1, 2, \ldots, M-1,\\ q_m,&\quad m = 1, 2, \ldots, M. \end{aligned}$$

Here, p_n^0 and q_m^0 are the initial values of the polynomial coefficients p_n and q_m, whereas $S_r(a_{0j})$ are the "exact" value of the dynamic stiffness evaluated at the J discrete dimensionless frequencies a_{0j}. These are either measured or calculated by rigourous numerical or analytical methods. Further, $\hat{S}_r(\mathrm{i}a_{0j})$ are the values of the rational filter (a) at the same discrete frequencies, and $w(a_0)$ is a weight function, *e.g.* as defined by Eq. (6–38) with $\varsigma_1 = \varsigma_2 = \varsigma_3 = 2$. Finally, s_m are the poles of the rational filter $\hat{S}_r(\mathrm{i}a_0)$, *i.e.* the roots of the denominator polynomial $Q(\mathrm{i}a_0)$, and ε is a small number, *e.g.* $\varepsilon = 0.01$.

Box 6.2 Fitting of rational filter by optimisation of the poles

A rational filter for the regular part of the dynamic stiffness is defined in the form:

$$S_r(a_0) \approx \hat{S}_r(\mathrm{i}a_0) = \frac{P(\mathrm{i}a_0)}{Q(\mathrm{i}a_0)} = \frac{1 - k^\infty + p_1(\mathrm{i}a_0) + p_2(\mathrm{i}a_0)^2 + \ldots + p_{M-1}(\mathrm{i}a_0)^{M-1}}{\prod_{m=1}^{N}(\mathrm{i}a_0 - s_m)\,(\mathrm{i}a_0 - s_m^*) \cdot \prod_{m=N+1}^{M-N}(\mathrm{i}a_0 - s_m)}. \qquad \text{(a)}$$

Find the optimal polynomial coefficients p_n and the poles s_m which minimize the $F(p_n, s_m)$ subject to the constraints $G_0(p_n, s_m), G_1(p_n, s_m), \ldots, G_M(p_n, s_m)$.

Input:

M : order of the filter,

N : number of complex conjugate pairs, $2N \leq M$

p_n^0, $n = 1, 2, \ldots, M-1$,

$s_m^{\Re 0}$, $m = 1, 2, \ldots, N$,

$s_m^{\Im 0}$, $m = 1, 2, \ldots, N$,

s_m^0, $m = N+1, 2, \ldots, M-N$,

a_{0j}, $j = 1, 2, \ldots, J$,

$S_r(a_{0j})$, $j = 1, 2, \ldots, J$,

$w(a_{0j})$, $j = 1, 2, \ldots, J$.

Variables:

p_n, $n = 1, 2, \ldots, M-1$,

$s_m^{\Re}$, $m = 1, 2, \ldots, N$, $s_m^{\Re} < -\varepsilon$,

$s_m^{\Im}$, $m = 1, 2, \ldots, N$, $s_m^{\Im} > +\varepsilon$,

s_m, $m = N+1, 2, \ldots, M-N$, $s_m < -\varepsilon$.

Object function:

$$F(p_n, s_m) = \sum_{j=1}^{J} w(a_{0j}) \left(\hat{S}_r(\mathrm{i}a_{0j}) - S_r(a_{0j})\right)^2.$$

Constraints:

$$G_0(p_n, s_m) = 1 - \prod_{1}^{M}(-s_m) = 0,$$

$$G_k(p_n, s_m) = s_k^{\Re} < -\varepsilon, \quad k = 1, 2, \ldots, N,$$

$$G_k(p_n, s_m) = \zeta s_k^{\Re} + s_k^{\Im} < 0, \quad k = N+1, 2, \ldots, 2N,$$

$$G_k(p_n, s_m) = \Re(s_k) < -\varepsilon, \quad k = 2N+1, \ldots, M.$$

Output:

p_n, $n = 1, 2, \ldots, M-1$,

$s_m^{\Re}$, $m = 1, 2, \ldots, N$,

$s_m^{\Im}$, $m = 1, 2, \ldots, N$,

s_m, $m = N+1, 2, \ldots, M-N$.

Here, superscript 0 indicates initial values of the respective variables, and $\hat{S}_r(\mathrm{i}a_{0j})$ are the values of the rational filter (a) at the same discrete frequencies. Further, $\zeta \approx 10 \sim 100$ and $\varepsilon \approx 0.01$ are two real parameters. Note that the initial values of the poles must conform with the constraint $G_0(p_n, s_m)$. For additional information, see Box 6.1.

The great advantage of the representation (6–41) is that the constraints on the poles are defined directly on each individual variable, whereas the constraints in the formulation with $Q(\mathrm{i}a_0)$ defined by Eq. (6–39), the constraints are given on functionals of the variables. Hence, the solution is much more efficient and straightforward. However, Eq. (6–41) has two disadvantages when compared with Eq. (6–39):

- The number of complex conjugate pairs has to be estimated. However, experience shows that as many as possible of the roots should appear as complex conjugates—*e.g.* if M is even, $N = M/2$ should be utilized. This provides a good fit in most situations and may, at the same time, generate the lumped-parameter model with fewest possible internal degrees of freedom.

- In the representation provided by Eq. (6–39), the correct asymptotic behaviour is automatically ensured in the limit $\mathrm{i}a_0 \to 0$, *i.e.* the static case, since $q_0 = 1$. Unfortunately, in the representation given by Eq. (6–41) an additional equality constraint has to be implemented to ensure this behaviour. However, this condition is much easier implemented than the constraints which are necessary in the case of Eq. (6–39) in order to prevent the real parts of the roots from being positive.

Eventually, instead of the problem defined in Box 6.1, it may be more efficient to solve the optimisation problem given in Box 6.2. It is noted that additional constraints are suggested, which prevent the imaginary parts of the complex poles to become much (*e.g.* 10 times) bigger than the real parts. This is due to the following reason: If the real part of the complex pole s_m vanishes, *i.e.* $s_m^{\Re} = 0$, this results in a second order pole, $\{s_m^{\Im}\}^2$, which is real and positive. Evidently, this will lead to instability in the time domain. Since the computer precision is limited, a real part of a certain size compared to the imaginary part of the pole is necessary to ensure a stable solution.

Finally, as an alternative to the optimisation problems defined in Box 6.1 and Box 6.2, the function $S(\mathrm{i}a_0)$ may be expressed by Eq. (6–22), *i.e.* in partial-fraction form. In this case, the variables in the optimization problem are the poles and residues of $S(\mathrm{i}a_0)$. In the case of the second-order terms, these quantities are replaced with α_0, α_1, β_0 and β_1. At a first glance, this choice of optimisation variable seems more natural than p_n and s_m, as suggested in Box 6.2. However, from a computational point of view, the mathematical operations involved in the polynomial-fraction form are more efficient than those of the polynomial-fraction form. Hence, the scheme provided in Box 6.2 is recommended.

6.4 Time-domain analysis of soil–structure interaction

In this section, two examples are given in which consistent lumped-parameter models are applied to the analysis of foundations and soil–structure interaction. The first example concerns a rigid hexagonal footing on a homogeneous or layered ground. The frequency-domain solution obtained by the domain-transformation method (DTM) of Chapter 5 is fitted by lumped-parameter models (LPMs) of different orders. Subsequently, the response of the original model and the LPMs are compared in frequency and time domain.

In the second example, LPMs are fitted to the frequency-domain results of a coupled boundary-element/finite-element model (see Chapter 4) of a flexible embedded foundation. As part of the

examples, the complex stiffness of the foundation in the high-frequency limit is discussed, *i.e.* the coefficients k^∞ and c^∞ in Eq. (6–18) are determined for each component of translation and rotation of the foundation. Whereas no coupling exists between horizontal sliding and rocking of surface footings in the high-frequency limit, coupled sliding–rocking is present in the case of embedded foundation—even at high frequencies.

6.4.1 A footing on a homogeneous or layered ground

The foundation is modelled as a regular hexagonal rigid footing with the side length r_0, height h_0 and mass density ρ_0. This geometry is typical for offshore wind turbine foundations. As illustrated in Fig. 6–12, the centre of the soil–foundation interface coincides with the origin of the Cartesian coordinate system. The mass of the foundation and the corresponding mass moments of inertia with respect to the three coordinate axes then become:

$$M_0 = \rho_0 h_0 A_0, \quad \mathcal{J}_1 = \mathcal{J}_2 = \rho_0 h_0 \mathcal{I}_0 + \frac{1}{3}\rho_0 h_0^3 A_0, \quad \mathcal{J}_3 = 2\rho_0 h_0 \mathcal{I}_0, \tag{6–42a}$$

where A_0 is the area of the horizontal cross-section and $\mathcal{I}_0$ is the corresponding geometrical moment of inertia,

$$A_0 = \frac{3\sqrt{3}}{2} r_0^2, \quad \mathcal{I}_0 = \frac{5\sqrt{3}}{16} r_0^4. \tag{6–42b}$$

It is noted that $\mathcal{I}_0$ is invariant to rotation of the foundation around the x_3-axis. This property also applies to circular or quadratic foundations as discussed in Section 5.7.

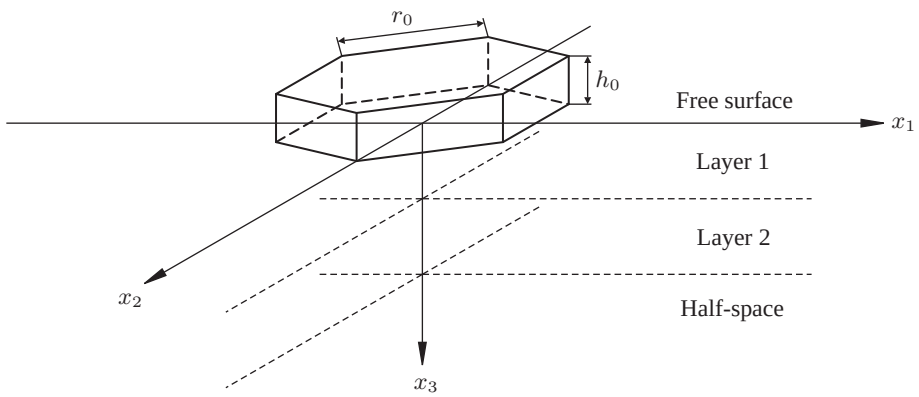

Figure 6–12 Hexagonal footing on a stratum with three layers over a half-space.

A footing on a homogeneous ground

Firstly, we consider a hexagonal footing on a homogeneous visco-elastic half-space. The footing has the side length $r_0 = 10$ m, the height $h_0 = 10$ m and the mass density $\rho_0 = 2000$ kg/m^3, and the mass and mass moments of inertia are computed by Eq. (6–42). The properties of the soil are $\rho^1 = 2000$ kg/m^3, $E^1 = 10^4$ kPa, $\nu^1 = 0.25$ and $\eta^1 = 0.03$. However, in the static limit, *i.e.* for $\omega \to 0$, the hysteretic damping model leads to a complex impedance in the frequency

domain. By contrast, the lumped-parameter model provides a real impedance, since it is based on viscous dashpots. This discrepancy leads to numerical difficulties in the fitting procedure and to overcome this, the hysteretic damping model for the soil is replaced by a linear viscous model at low frequencies, in this case below 1 Hz.

In principle, the time-domain solution for the displacements and rotations of the rigid footing is found by inverse Fourier transformation, *i.e.*

$$v_i(t) = \frac{1}{2\pi}\int_{-\infty}^{\infty} V_i(\omega)\mathrm{e}^{\mathrm{i}\omega t}\mathrm{d}\omega, \quad \theta_i(t) = \frac{1}{2\pi}\int_{-\infty}^{\infty} \Theta_i(\omega)\mathrm{e}^{\mathrm{i}\omega t}\mathrm{d}\omega, \quad i = 1, 2, 3. \tag{6–43}$$

In the numerical computations, the frequency response spectrum is discretized and accordingly, the time-domain solution is found by a Fourier series.

According to Eqs. (5–112a) and (5–114), the vertical motion $v_3(t)$ as well as the torsional motion $\theta_3(t)$ (see Fig. 6–2) are decoupled from the remaining degrees of freedom of the hexagonal footing. Thus, $v_3(t)$ and $\theta_3(t)$ may be fitted by independent lumped-parameter models. In the following, the quality of lumped-parameter models based on rational filters of different orders are tested for vertical and torsional excitation.

For the footing on the homogeneous half-space, rational filters of the order 2–6 are tested. Firstly, the impedance components are determined in the frequency-domain by the domain-transformation method presented in Section 5. The lumped-parameter models are then fitted by application of the procedure described in Section 6.3 and summarised in Box 6.2. The two components of the normalised impedance, S_{33} and S_{66}, are shown in Figs. 6–13 and 6–15 as functions of the physical frequency, f. It is noted that all the LPMs are based on second-order discrete-element models including a point mass, see Fig. 6–11(b). Hence, the LPM for each individual component of the impedance matrix, $\mathbf{Z}(\omega)$, has 1, 2 or 3 internal degrees of freedom.

With reference to Fig. 6–13, a poor fit of the vertical impedance is obtained with $M = 2$ regarding the absolute value of S_{33} as well as the phase angle. A lumped-parameter model with $M = 4$ provides a much better fit in the low-frequency range. However, a sixth-order lumped-parameter model is required to obtain an accurate solution in the medium-frequency range, *i.e.* for frequencies between approximately 1.5 and 4 Hz. As expected, further analyses show that a slightly better match in the medium-frequency range is obtained with the weight-function coefficients $\varsigma_1 = 2$ and $\varsigma_2 = \varsigma_3 = 1$. However, this comes at the cost of a poorer match in the low-frequency range. Finally, it has been found that no improvement is achieved if first-order terms, *e.g.* the "monkey tail" illustrated in Fig. 6–10(b), are allowed in the rational-filter approximation.

Figure 6–15 shows the rational-filter approximations of S_{66}, *i.e.* the non-dimensional torsional impedance. Compared with the results for the vertical impedance, the overall quality of the fit is relatively poor. In particular the LPM with $M = 2$ provides a phase angle which is negative in the low frequency range. Actually, this means that the geometrical damping provided by the second-order LPM becomes negative for low-frequency excitation. Furthermore, the stiffness is generally under-predicted and as a consequence of this an LPM with $M = 2$ cannot be used for torsional vibrations of the surface footing. A significant improvement is achieved with $M = 4$, but even with $M = 6$ some discrepancies are observed between the results provide by the LPM and the rigorous model. Unfortunately, additional studies indicate that an LPM with $M = 8$ does not increase the accuracy beyond that of the sixth-order model.

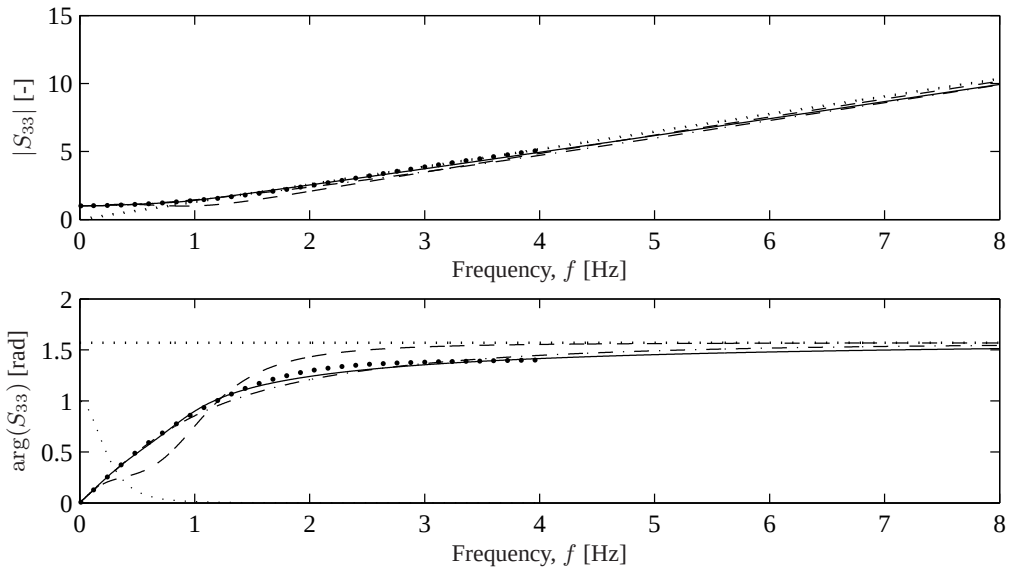

Figure 6–13 Dynamic stiffness coefficient, S_{33}, obtained by the domain-transformation model (the large dots) and lumped-parameter models with $M = 2$ (— —), $M = 4$ (— · — ·), and $M = 6$ (——). The thin dotted line (·····) indicates the weight function w (not in radians), and the thick dotted line (·····) indicates the high-frequency solution, *i.e.* the singular part of S_{33}.

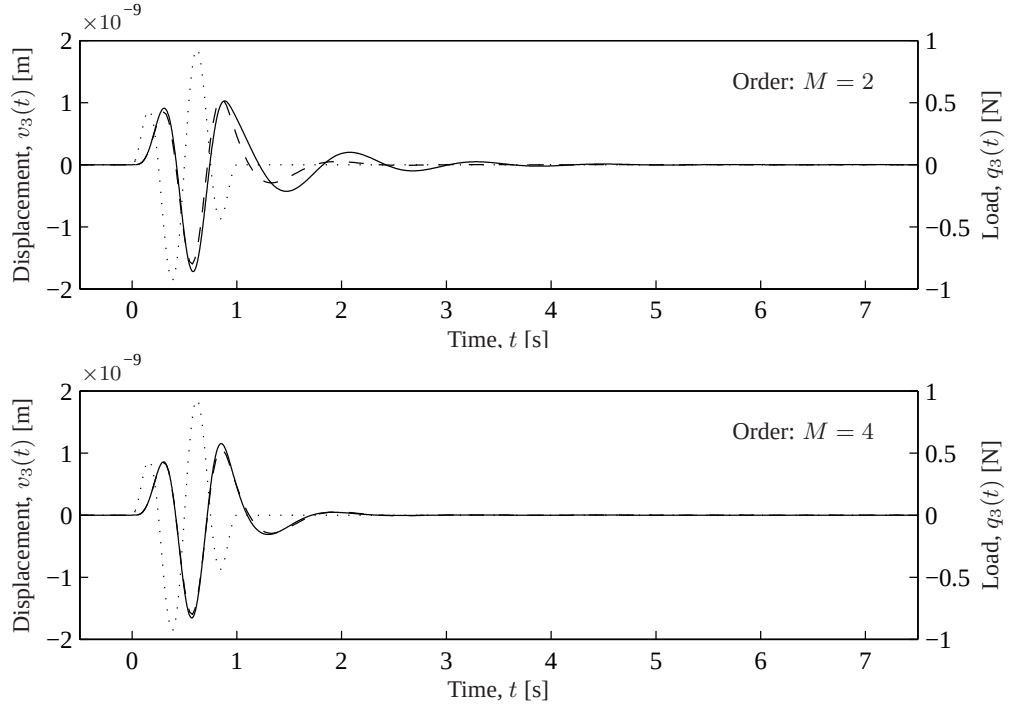

Figure 6–14 Response $v_3(t)$ obtained by inverse Fourier transformation (— —) and lumped-parameter model (——). The dots (·····) indicate the load time history.

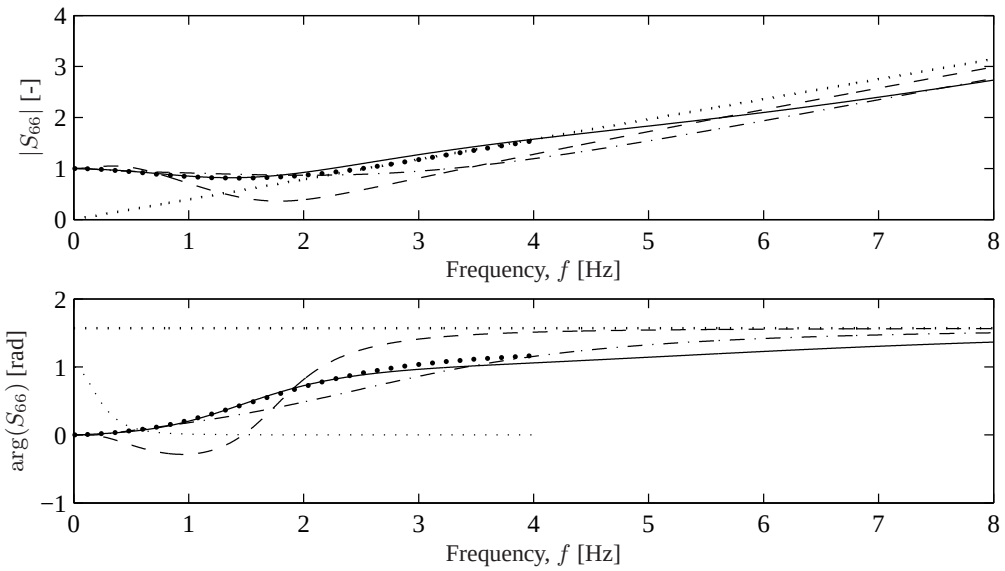

Figure 6–15 Dynamic stiffness coefficient, S_{66}, obtained by the domain-transformation model (the large dots) and lumped-parameter models with $M = 2$ (— —), $M = 4$ (— · — ·), and $M = 6$ (——). The thin dotted line (·····) indicates the weight function w (not in radians), and the thick dotted line (·····) indicates the high-frequency solution, *i.e.* the singular part of S_{66}.

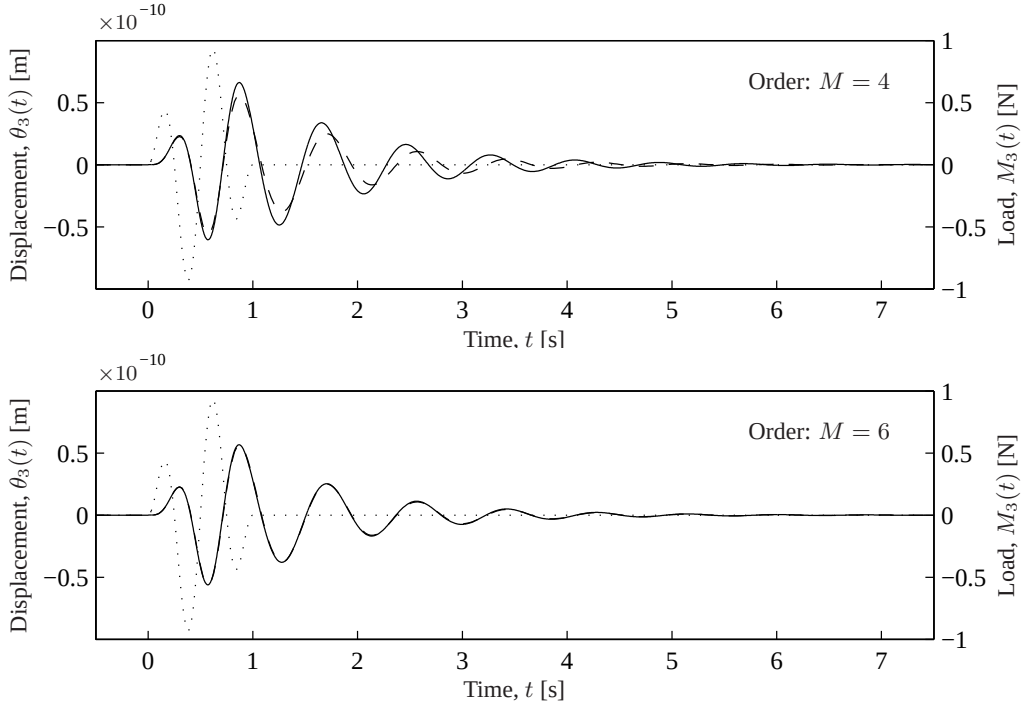

Figure 6–16 Response $\theta_3(t)$ obtained by inverse Fourier transformation (— —) and lumped-parameter model (——). The dots (·····) indicate the load time history.

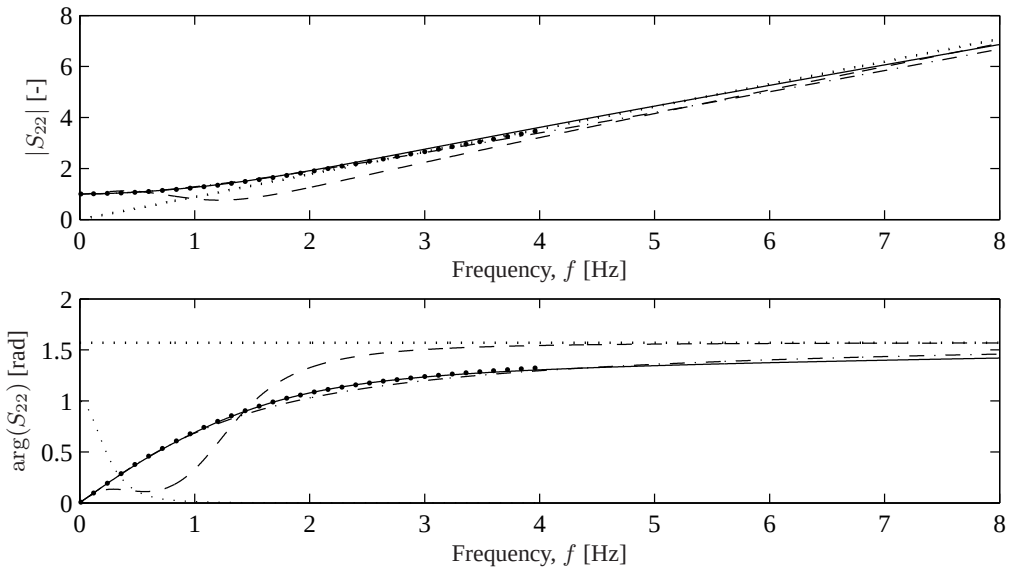

Figure 6–17 Dynamic stiffness coefficient, S_{22}, obtained by the domain-transformation model (the large dots) and lumped-parameter models with $M = 2$ (— —), $M = 4$ (— · — ·), and $M = 6$ (——). The thin dotted line (·····) indicates the weight function w (not in radians), and the thick dotted line (·····) indicates the high-frequency solution, *i.e.* the singular part of S_{22}.

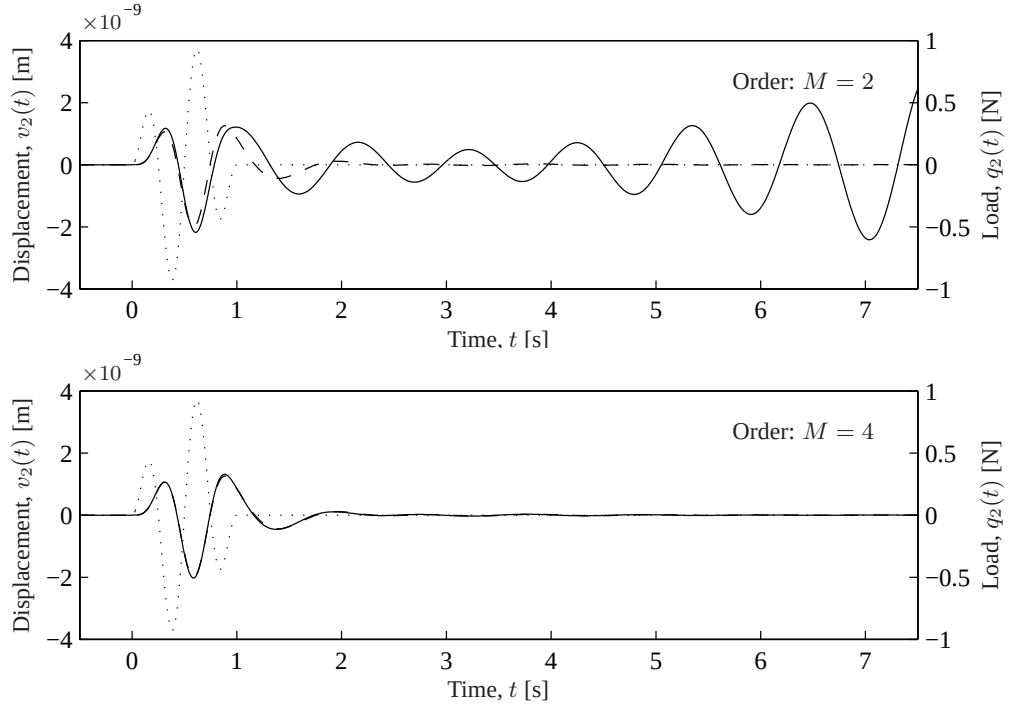

Figure 6–18 Response $v_2(t)$ obtained by inverse Fourier transformation (— —) and lumped-parameter model (——). The dots (·····) indicate the load time history.

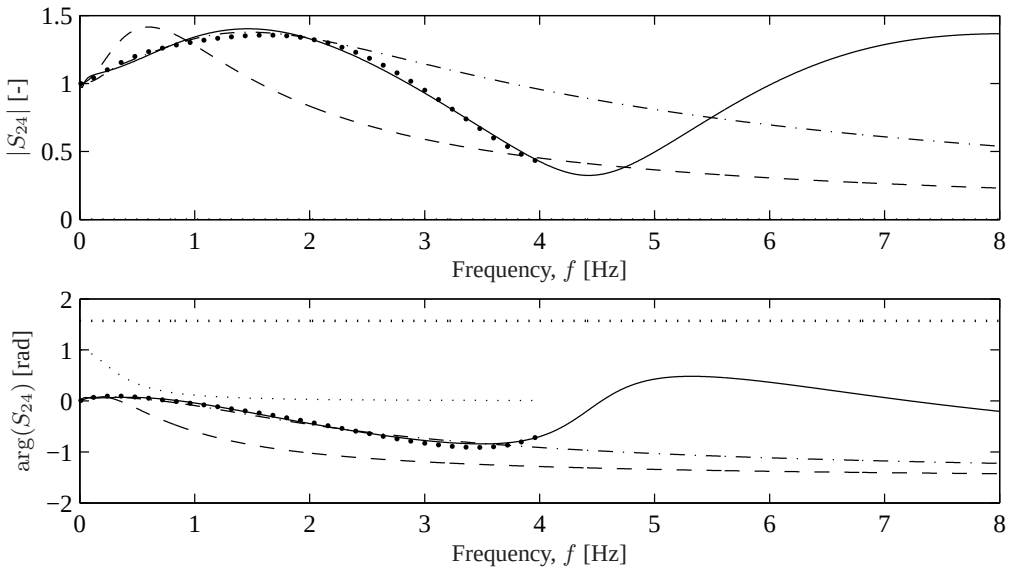

Figure 6–19 Dynamic stiffness coefficient, S_{24}, obtained by the domain-transformation model (the large dots) and lumped-parameter models with $M = 2$ (— —), $M = 4$ (— · — ·), and $M = 6$ (——). The thin dotted line (·····) indicates the weight function w (not in radians), and the thick dotted line (·····) indicates the high-frequency solution, *i.e.* the singular part of S_{24}.

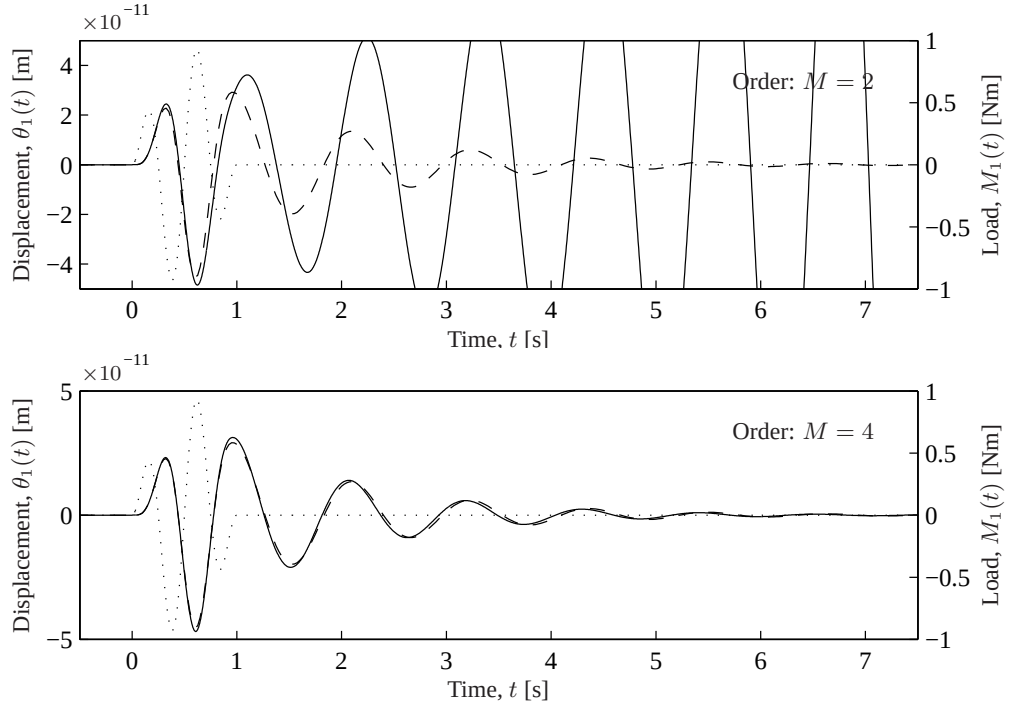

Figure 6–20 Response $\theta_1(t)$ obtained by inverse Fourier transformation (— —) and lumped-parameter model (——). The dots (·····) indicate the load time history.

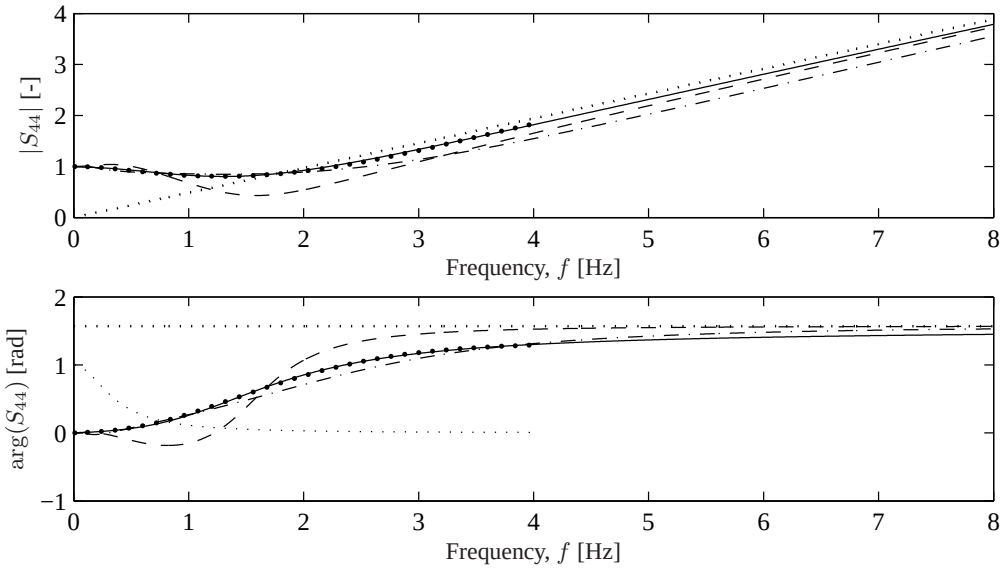

Figure 6–21 Dynamic stiffness coefficient, S_{44}, obtained by the domain-transformation model (the large dots) and lumped-parameter models with $M = 2$ (— —), $M = 4$ (— · — ·), and $M = 6$ (——). The thin dotted line (·····) indicates the weight function w (not in radians), and the thick dotted line (·····) indicates the high-frequency solution, *i.e.* the singular part of S_{44}.

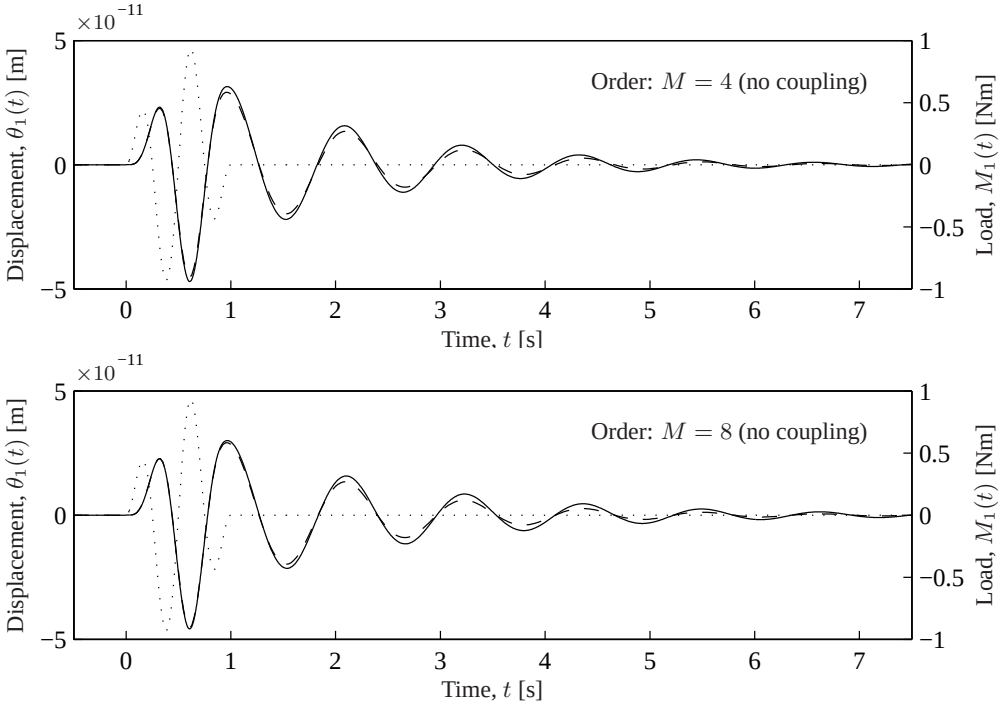

Figure 6–22 Response $\theta_1(t)$ obtained by inverse Fourier transformation (— —) and lumped-parameter model (——). The dots (·····) indicate the load time history.

Next, the dynamic soil–foundation interaction is studied in the time domain. In order to examine the transient response, a pulse load is applied in the form

$$p(t) = \begin{cases} \sin(2\pi f_c t)\sin(0.5\pi f_c t) & \text{for} \quad 0 < t < 2/f_c \\ 0 & \text{otherwise.} \end{cases} \tag{6–44}$$

In this analysis, $f_c = 2$ Hz is utilised, and the responses obtained with the lumped-parameter models of different orders are computed by application of the Newmark β-scheme (see Subsection 2.2.3. Figure 6–14 shows the results of the analysis with $q_3(t) = p(t)$, whereas the results for $M_3(t) = p(t)$ are given in Fig. 6–16.

In the case of vertical excitation, Fig. 6–14 shows that even the LPM with $M = 2$ provides an acceptable match to the "exact" results achieved by inverse Fourier transformation of the frequency-domain solution. In particular, the maximum response occurring during the excitation is well described. However, an improvement in the description of the damping is obtained with $M = 4$. For torsional motion, the second-order LPM is invalid since it provides negative damping. Hence, the models with $M = 4$ and $M = 6$ are compared in Fig. 6–16. It is clearly demonstrated that the fourth-order LPM provides a poor representation of the torsional impedance, whereas an accurate prediction of the response is achieved with the sixth-order model.

Subsequently, lumped-parameter models are fitted for the horizontal sliding and rocking motion of the surface footing, *i.e.* $v_2(t)$ and $\theta_1(t)$ (see Fig. 6–2). As indicated by Eqs. (5–112a) and (5–114), these degrees of freedom are coupled via the impedance component Z_{24}. Hence, two analyses are carried out. Firstly, the quality of lumped-parameter models based on rational filters of different orders are tested for horizontal and moment excitation. Secondly, the significance of coupling is investigated by a comparison of models with and without the coupling terms.

Similarly to the case for vertical and torsional motion, rational filters of the order 2–6 are tested. The three components of the normalised impedance, S_{22}, $S_{24} = S_{42}$ and S_{44}, are shown in Figs. 6–17, 6–19 and 6–21 as functions of the physical frequency, f. Again, the lumped-parameter models are based on discrete-element model shown in Fig. 6–11(b), which reduces the number of internal degrees of freedom to a minimum. Clearly, the lumped-parameter models with $M = 2$ provide a poor fit for all the components S_{22}, S_{24} and S_{44}. However, Figs. 6–17 and 6–21 show that an accurate solution is obtained for S_{22} and S_{44} when a 4th model is applied, and the inclusion of an additional internal degree of freedom, *i.e.* raising the order from $M = 4$ to $M = 6$, does not increase the accuracy significantly. However, for S_{24} an LPM with $M = 6$ is much more accurate than an LPM with $M = 4$ for frequencies $f > 3$ Hz, see Fig. 6–19.

Subsequently, the transient response to the previously defined pulse load with centre frequency $f_c = 2$ Hz is studied. Figure 6–18 shows the results of the analysis with $q_2(t) = p(t)$, and the results for $M_1(t) = p(t)$ are given in Fig. 6–20. Further, the results from an alternative analysis with no coupling of sliding and rocking are presented in Fig. 6–22. In Fig. 6–18 it is observed that the LPM with $M = 2$ provides a poor match to the results of the rigorous model. The maximum response occurring during the excitation is well described by the low-order LPM. However the damping is significantly underestimated by the LPM. Since the loss factor is small, this leads to the conclusion that the geometrical damping is not predicted with adequate accuracy. On the other hand, for $M = 4$ a good approximation is obtained with regard to both the maximum response and the geometrical damping. As suggested by Fig. 6–17, almost no further improvement is gained with $M = 6$. For the rocking produced by a moment applied to the rigid footing, the lumped-parameter model with $M = 2$ is useless. Here, the geometrical damping is

apparently negative. However, $M = 4$ provides an accurate solution (see Fig. 6–20) and little improvement is achieved by raising the order to $M = 6$ (this result is not included in the figure).

Alternatively, Fig. 6–22 shows the result of the time-domain solution for a lumped-parameter model in which the coupling between sliding and rocking is disregarded. This model is interesting because the two coupling components S_{24} and S_{42} must be described by separate lumped-parameter models. Thus, the model with $M = 4$ in Fig. 6–22 has four less internal degrees of freedom than the corresponding model with $M = 4$ in Fig. 6–20. However, the two results are almost identical, *i.e.* the coupling is not pronounced for the footing on the homogeneous half-space. Hence, the sliding–rocking coupling may be disregarded without significant loss of accuracy. Increasing the order of the LPMs for S_{22} and S_{44} from 4 to 8 results in a model with the same number of internal degrees of freedom as the fourth-order model with coupling; but as indicated by Fig. 6–22, this does not improve the overall accuracy. Finally, Fig. 6–19 suggests that the coupling is more pronounced when a load with, for example, $f_c = 1.5$ or 3.5 Hz is applied. However, further analyses, whose results are not presented in this paper, indicate that this is not the case.

In conclusion, for the footing on the homogeneous soil it is found that an LPM with two internal degrees of freedom for the vertical and each sliding and rocking degree of freedom provides a model of great accuracy. This corresponds to fourth-order rational approximations for each of the response spectra obtained by the domain-transformation method. Little improvement is gained by including additional degrees of freedom. Furthermore, it is concluded that little accuracy is lost by neglecting the coupling between the sliding and rocking motion. However, a sixth-order model is necessary in order to get an accurate representation of the torsional impedance.

A footing on a layered half-space

Next, a stratified ground is considered. The soil consists of two layers over homogeneous half-space. Material properties and layer depths are given in Table 6–3. This may correspond to sand over a layer of undrained clay resting on limestone or bedrock. The geometry and density of the footing are unchanged from the analysis of the homogeneous half-space.

The non-dimensional vertical and torsional impedance components, *i.e.* S_{33} and S_{66}, are presented in Figs. 6–23 and 6–25 as functions of the physical frequency, f. In addition to the domain-transformation method results, the LPM approximations are shown for $M = 2$, $M = 6$ and $M = 10$. Clearly, low-order lumped-parameter models are not able to describe the local tips and dips in the frequency response of a footing on a layered ground. However, the LPM with $M = 10$ provides a good approximation of the vertical and torsional impedances for frequencies $f < 2$ Hz. It is worthwhile to note that the lumped-parameter models of the footing on the layered ground are actually more accurate than the models of the footing on the homogeneous ground. This follows by a comparison of Figs. 6–23 and 6–25 with Figs. 6–13 and 6–15.

Table 6–3 Material properties and layer depths for layered half-space.

Layer no.	h (m)	E (MPa)	ν	ρ (kg/m^3)	η
Layer 1	8	10	0.25	2000	0.03
Layer 2	16	5	0.49	2200	0.02
Half-space	∞	100	0.25	2500	0.01

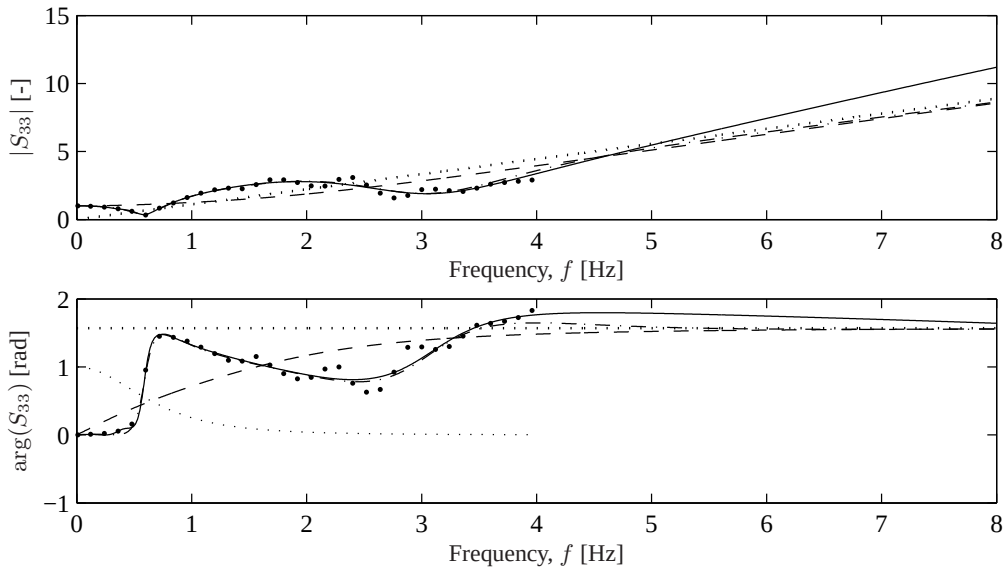

Figure 6–23 Dynamic stiffness coefficient, S_{33}, obtained by the domain-transformation model (the large dots) and lumped-parameter models with $M = 2$ (— —), $M = 6$ (— · — ·), and $M = 10$ (——). The thin dotted line (·····) indicates the weight function w (not in radians), and the thick dotted line (·····) indicates the high-frequency solution, *i.e.* the singular part of S_{33}.

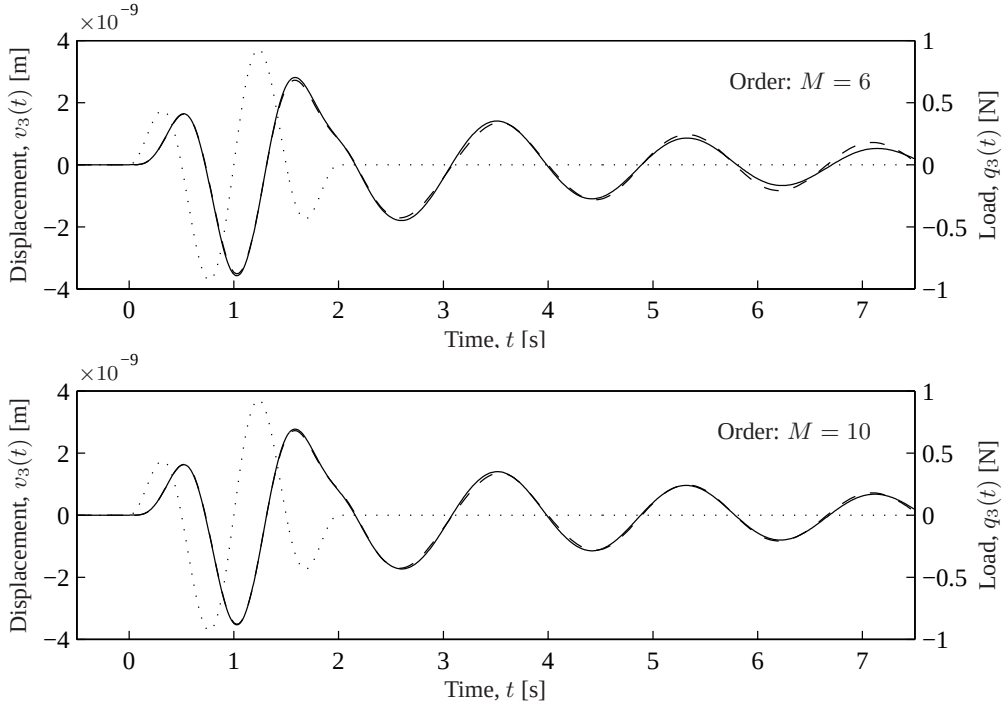

Figure 6–24 Response $v_3(t)$ obtained by inverse Fourier transformation (— —) and lumped-parameter model (——). The dots (·····) indicate the load time history.

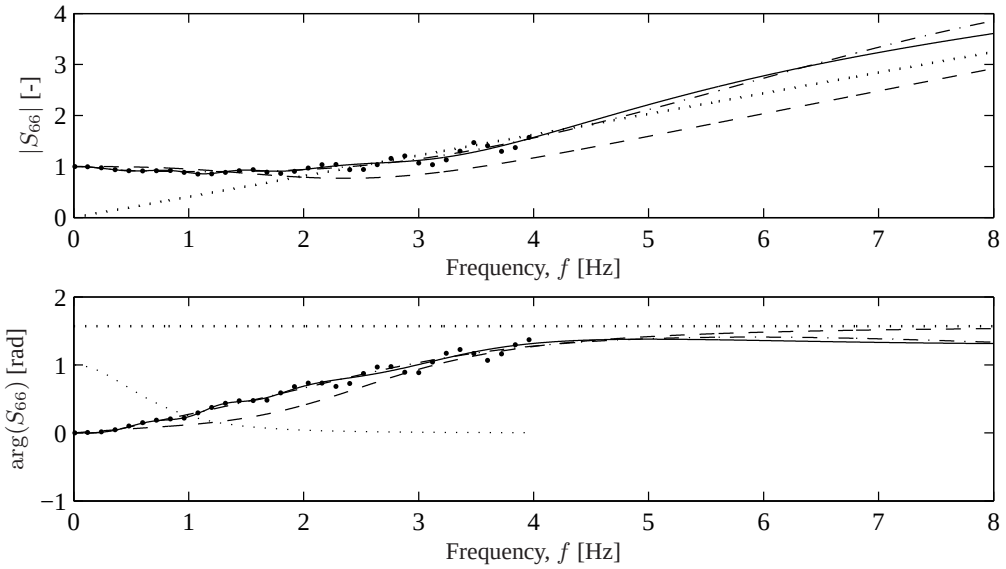

Figure 6–25 Dynamic stiffness coefficient, S_{66}, obtained by the domain-transformation model (the large dots) and lumped-parameter models with $M = 2$ (— —), $M = 6$ (— · — ·), and $M = 10$ (——). The thin dotted line (·····) indicates the weight function w (not in radians), and the thick dotted line (·····) indicates the high-frequency solution, *i.e.* the singular part of S_{66}.

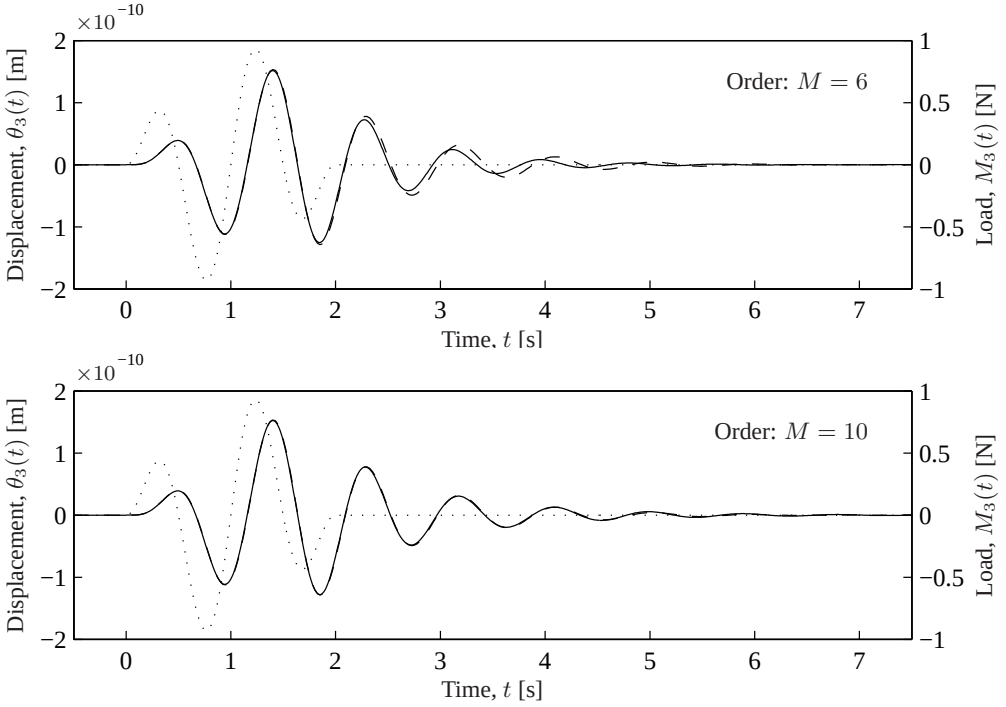

Figure 6–26 Response $\theta_3(t)$ obtained by inverse Fourier transformation (— —) and lumped-parameter model (——). The dots (·····) indicate the load time history.

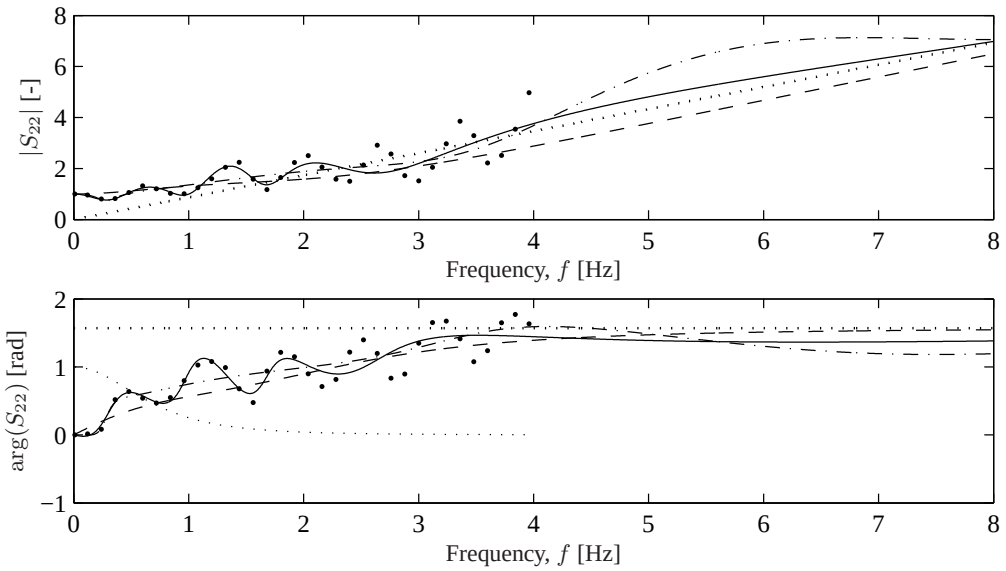

Figure 6–27 Dynamic stiffness coefficient, S_{22}, obtained by the domain-transformation model (the large dots) and lumped-parameter models with $M = 2$ (— —), $M = 6$ (— · — ·), and $M = 10$ (——). The thin dotted line (·····) indicates the weight function w (not in radians), and the thick dotted line (·····) indicates the high-frequency solution, *i.e.* the singular part of S_{22}.

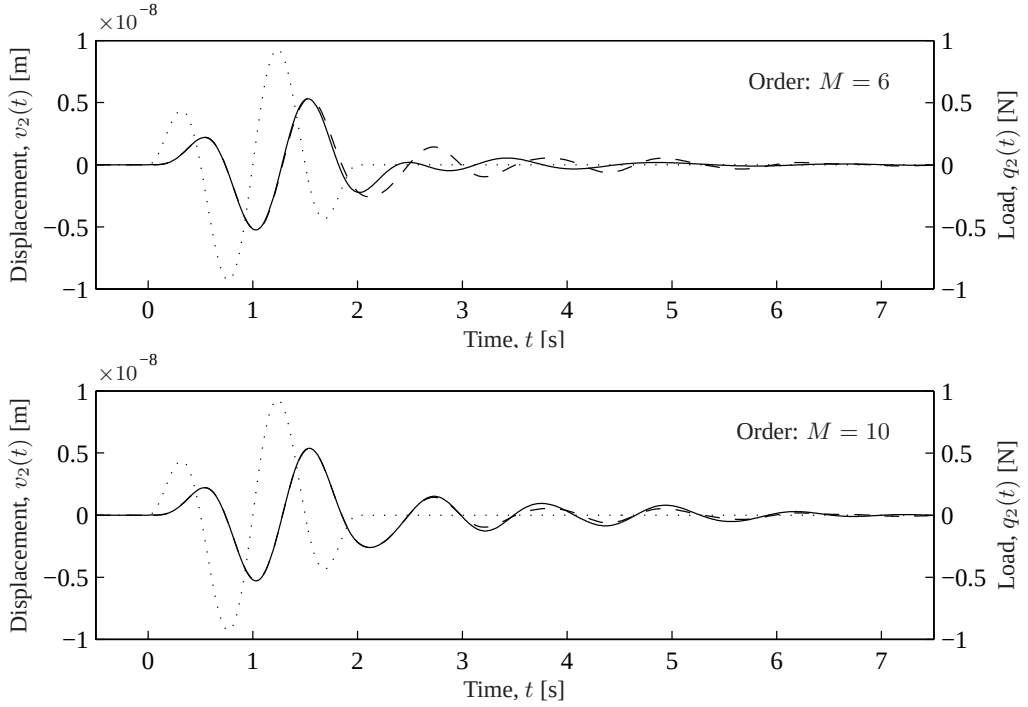

Figure 6–28 Response $v_2(t)$ obtained by inverse Fourier transformation (— —) and lumped-parameter model (——). The dots (·····) indicate the load time history.

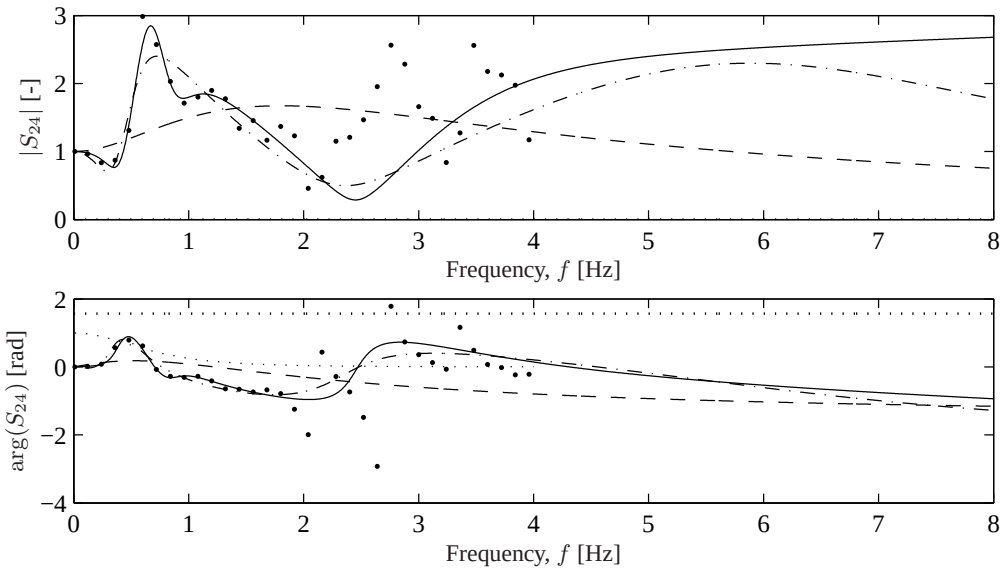

Figure 6–29 Dynamic stiffness coefficient, S_{24}, obtained by the domain-transformation model (the large dots) and lumped-parameter models with $M = 2$ (— —), $M = 6$ (— · — ·), and $M = 10$ (——). The thin dotted line (·····) indicates the weight function w (not in radians), and the thick dotted line (·····) indicates the high-frequency solution, *i.e.* the singular part of S_{24}.

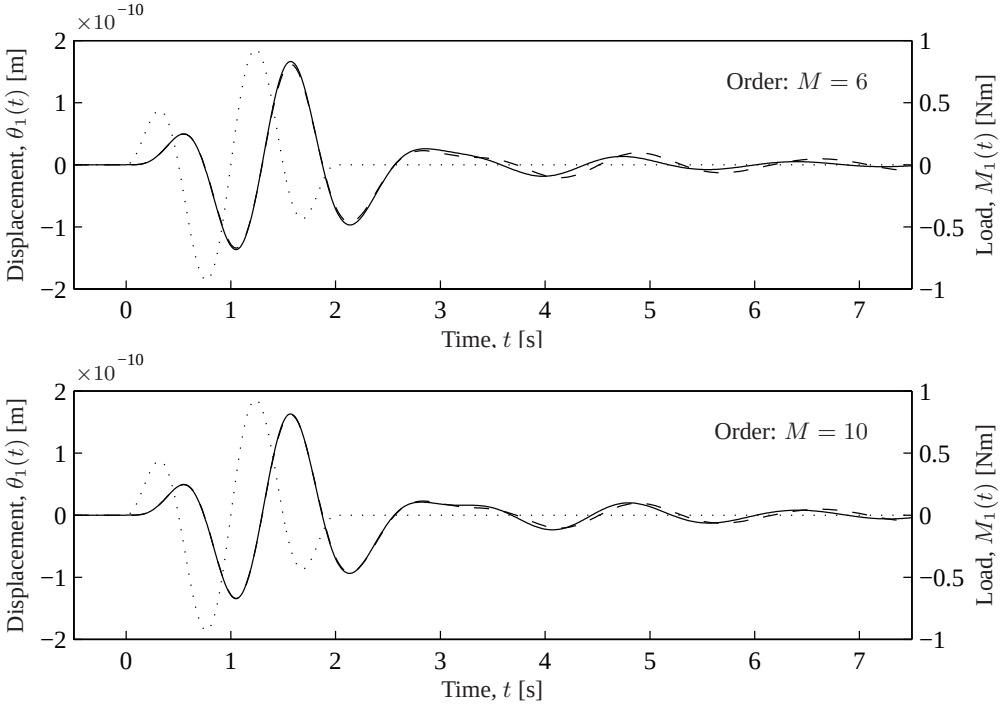

Figure 6–30 Response $\theta_1(t)$ obtained by inverse Fourier transformation (— —) and lumped-parameter model (——). The dots (·····) indicate the load time history.

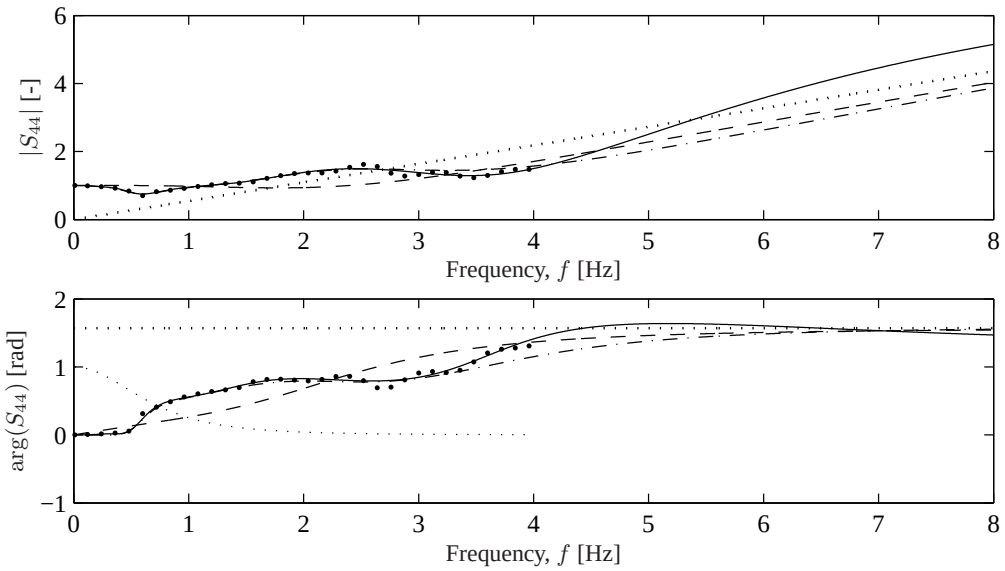

Figure 6–31 Dynamic stiffness coefficient, S_{44}, obtained by the domain-transformation model (the large dots) and lumped-parameter models with $M = 2$ (— —), $M = 6$ (— · — ·), and $M = 10$ (——). The thin dotted line (·····) indicates the weight function w (not in radians), and the thick dotted line (·····) indicates the high-frequency solution, *i.e.* the singular part of S_{44}.

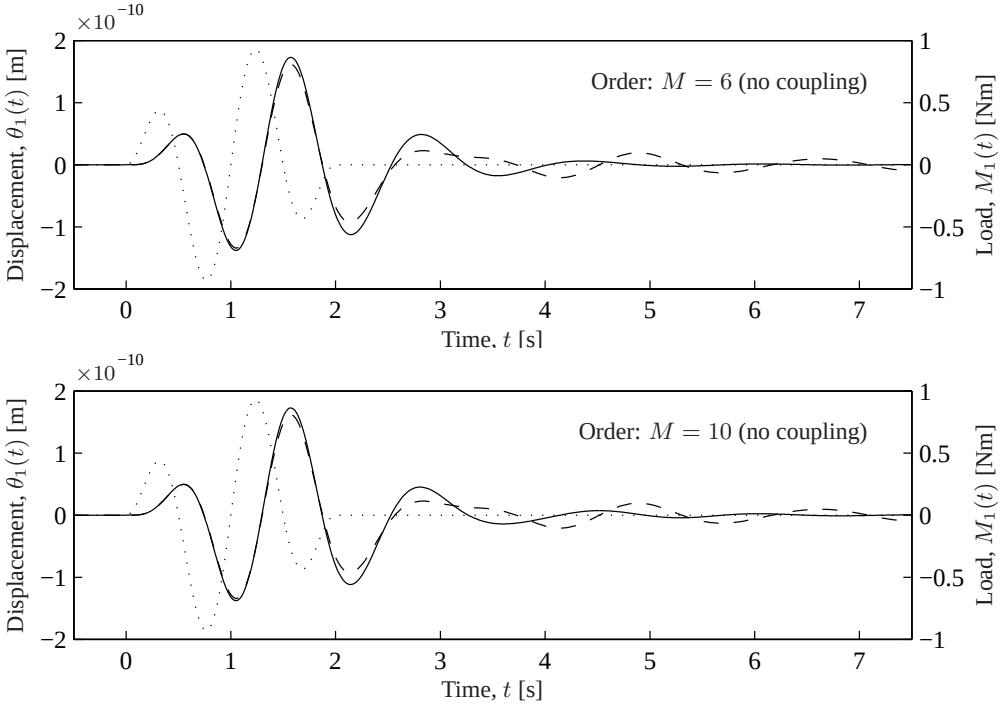

Figure 6–32 Response $\theta_1(t)$ obtained by inverse Fourier transformation (— —) and lumped-parameter model (——). The dots (·····) indicate the load time history.

The time-domain solutions for an applied vertical force, $q_3(t)$, or torsional moment, $M_3(t)$, are plotted in Fig. 6–24 and Fig. 6–26, respectively. Evidently, the LPM with $M = 6$ provides an almost exact match to the solution obtained by inverse Fourier transformation—in particular in the case of vertical motion. However, in the case of torsional motion (see Fig. 6–26), the model with $M = 10$ is significantly better at describing the free vibration after the end of the excitation.

Next, the horizontal sliding and rocking are analysed. The non-dimensional impedance components S_{22}, $S_{24} = S_{42}$ and S_{44} are shown in Figs. 6–27, 6–29 and 6–31 as functions of the physical frequency, f. Again, the LPM approximations with $M = 2$, $M = 6$ and $M = 10$ are illustrated, and the low-order lumped-parameter models are found to be unable to describe the local variations in the frequency response. The LPM with $M = 10$ provides an acceptable approximation of the sliding, the coupling and the rocking impedances for frequencies $f < 2$ Hz, but generally the match is not as good as in the case of vertical and torsional motion.

The transient response to a horizontal force, $q_2(t)$, or rocking moment, $M_1(t)$, are shown in Figs. 6–28 and 6–30. Again, the LPM with $M = 6$ provides an almost exact match to the solution obtained by inverse Fourier transformation. However, the model with $M = 10$ is significantly better at describing the free vibration after the end of the excitation. This is the case for the sliding, $v_2(t)$, as well as the rotation, $\theta_1(t)$.

Finally, in Fig. 6–32 the results are given for the alternative LPM, in which the coupling between sliding and rocking has been neglected. It is observed that the maximum response occurring during loading is predicted with almost the same accuracy as by the model in which the coupling is accounted for. However, the geometrical damping is badly described with regard to the decrease in magnitude and, in particular, the phase of the response during the free vibration.

Hence, the response of the footing on the layered ground cannot be predicted with low order models, and an LPM with 3–5 internal degrees of freedom is necessary for each nonzero term in the impedance matrix, *i.e.* rational approximations of the order 6–10 are required. In particular, it is noted that the impedance term providing the coupling between sliding and rocking is not easily fitted by an LPM of low order, *i.e.* orders below six. The maximum response is well predicted without the coupling term; however, if the coupling is not accounted for, the geometrical damping is poorly described. This may lead to erroneous conclusions regarding the fatigue lifespan of structures exposed to multiple transient dynamic loads, *e.g.* offshore wind turbines.

6.4.2 A flexible foundation embedded in viscoelastic soil

In this example, a skirted circular foundation, also known as a bucket foundation, is analysed using the coupled finite-element and boundary-element methods. The bucket has the radius $r_0 = 10$ m and the skirt length $h_0 = 12$ m, see Fig. 6–33. The lid has a thickness of $t_{lid} = 0.50$ m, whereas the thickness of the skirt is $t_{skirt} = 50$ mm. The bucket consists of steel, and the material properties are given in Table 6–4. The model of the lid is unrealistic and the real structure may be lighter and stiffer than the solid plate but with a complex geometry not easily modelled.

Table 6–4 Material properties of the bucket foundation and the subsoil.

Material	E (MPa)	ν	ρ (kg/m^3)	η
Soil	20	0.25	2000	0.03
Steel (bucket)	200.000	0.30	7850	0.01

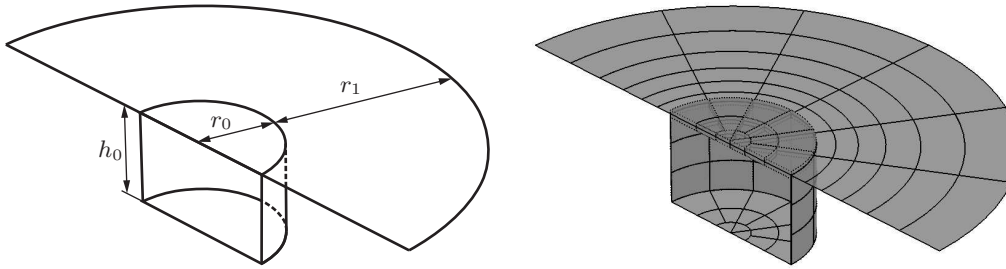

Figure 6–33 Coupled finite-element/boundary-element model of skirted foundation: Geometry (left) and discretization (right). Only half the foundation is discretized, utilising the symmetry of the problem.

The theory is explained in Chapters 2–4 and will not be repeated here. A closed boundary-element (BE) domain is applied for the soil inside the bucket and an open BE domain is utilised for the remaining half-space. In either case, quadratic spatial interpolation is applied. Finally, the lid and the skirt of the bucket foundation are discretized using shell finite elements. The theory for such elements is not presented in this book and the reader should confer the work by, for example, Bathe (1996).

With ρ, c_P and c_S denoting the mass density, the P-wave velocity and the S-wave velocity of the soil, respectively, the high-frequency limit of the impedance components are given as

$$c_{33}^{\infty} = \rho c_P A_{lid} + \rho c_S A_{skirt}, \tag{6–45a}$$

$$c_{66}^{\infty} = 2\rho c_S \mathcal{I}_{lid} + \rho c_S A_{skirt} r_0^2, \tag{6–45b}$$

$$c_{22}^{\infty} = \rho c_S A_{lid} + \frac{1}{2}\left(\rho c_S + \rho c_P\right) A_{skirt}, \tag{6–45c}$$

$$c_{24}^{\infty} = c_{42}^{\infty} = -\frac{1}{2}\left(\rho c_S + \rho c_P\right) A_{skirt} \frac{h_0}{2} = -c_{15}^{\infty} = -c_{51}^{\infty}, \tag{6–45d}$$

$$c_{44}^{\infty} = c_{55}^{\infty} = \rho c_P \mathcal{I}_{lid} + \frac{1}{2}\left(\rho c_S + \rho c_P\right) \mathcal{I}_{skirt} + \frac{1}{2}\rho c_S A_{skirt} r_0^2, \tag{6–45e}$$

where $A_{lid} = \pi r_0^2$ and $A_{skirt} = 4\pi r_0 h_0$ are the areas of the lid and the skirt, respectively. The latter accounts for the inside as well as the outside of the skirt; hence, the factor 4 instead of the usual factor 2. Further, $\mathcal{I}_{lid}$ and $\mathcal{I}_{skirt}$ are the geometrical moments of inertia of the lid and the skirt around the centroid of the lid, defined as

$$\mathcal{I}_{lid} = \frac{\pi}{4} r_0^4, \qquad \mathcal{I}_{skirt} = \frac{4\pi}{3} r_0 h_0^3. \tag{6–46}$$

Again, the contributions from both sides of the skirt are included and it is noted that the torsional moment of inertia of the lid is simply $2\mathcal{I}_{lid}$.

In the following, an explanation is given of the terms in Eq. (6–45). Firstly, the vertical impedance is given as the sum of a contribution from the P-waves emanating from the bottom of the lid, represented by the first term in Eq. (6–45a), and a second contribution from the S-waves produced at the exterior and interior surfaces of the skirt when the foundation moves up and down as a rigid body. This may be an overestimation of the impedance for a flexible foundation and alternatively a high-frequency solution with no contributions from the skirt may be proposed.

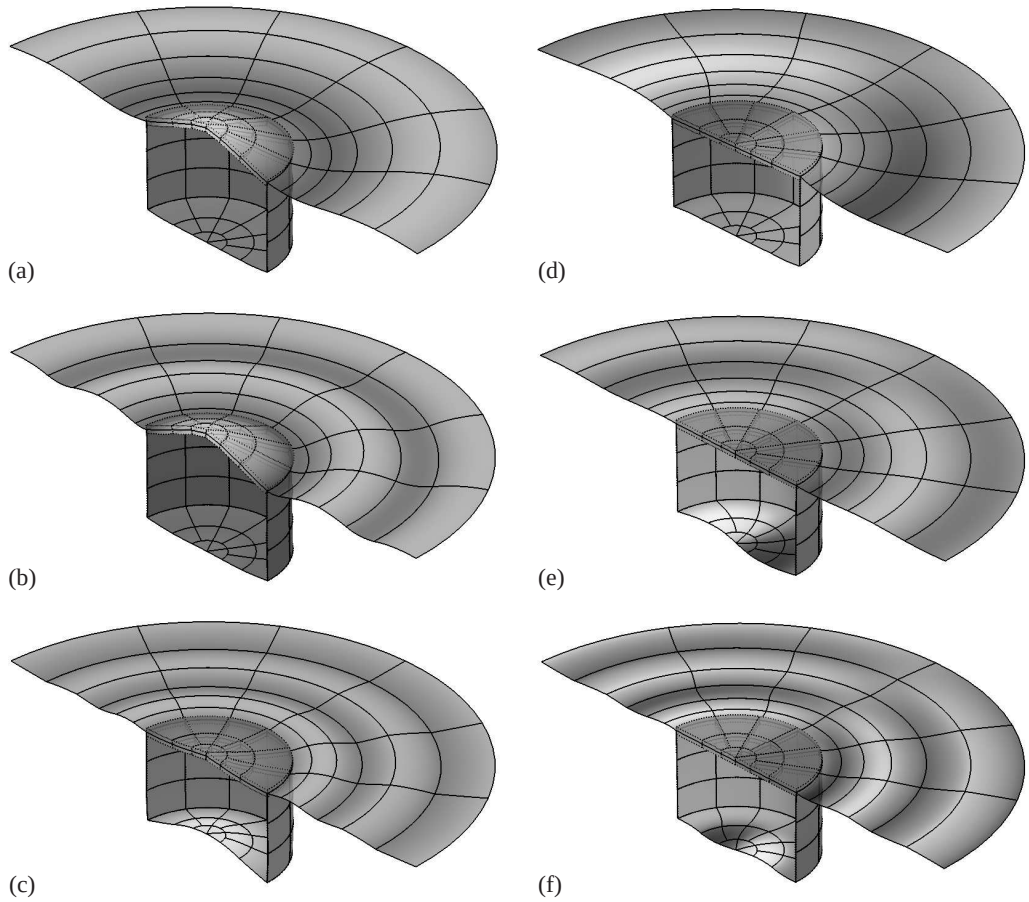

Figure 6–34 Response in phase with the load for the skirted foundation. On the left, the results are shown for a unit-magnitude harmonic vertical force acting at the centre of the foundation at the frequencies (a) $f = 2$ Hz, (b) $f = 4$ Hz and (c) $f = 6$ Hz. The displacements are scaled by a factor of 10^9 and the light and dark shades of grey indicate positive and negative vertical displacements. On the right, the results are shown for a unit-magnitude harmonic torsional moment acting around the centre of the foundation at the frequencies (a) $f = 2$ Hz, (b) $f = 4$ Hz and (c) $f = 6$ Hz. The displacements are scaled by a factor of 10^{10} and the light and dark shades of grey indicate positive and negative displacements in the direction orthogonal to the plane of antisymmetry.

Secondly, the torsional impedance provided by Eq. (6–45b) contains a contribution from the S-waves generated at the bottom of the lid, whereas the second term represents the S-waves stemming from the rotation of the skirt around the vertical axis. Thirdly, the horizontal impedance given by Eq. (6–45c) is composed of three terms. The first term represent S-waves initiated at the bottom of the lid, whereas the second term is due to the S- and P-waves arising at the skirt. Only S-waves are generated at the vertical lines at the "sides" of the foundation, and only P-waves are produced at the vertical lines on the "back" and "front" of the bucket. However, at all other vertical lines, a combination of P- and S-waves are emitted. A formal mathematical proof of Eq. (6–45c) follows by integration along the perimeter of the skirt. However, by physical reasoning one finds that half the area A_{skirt} emits P-waves, concentrating around the "back" and

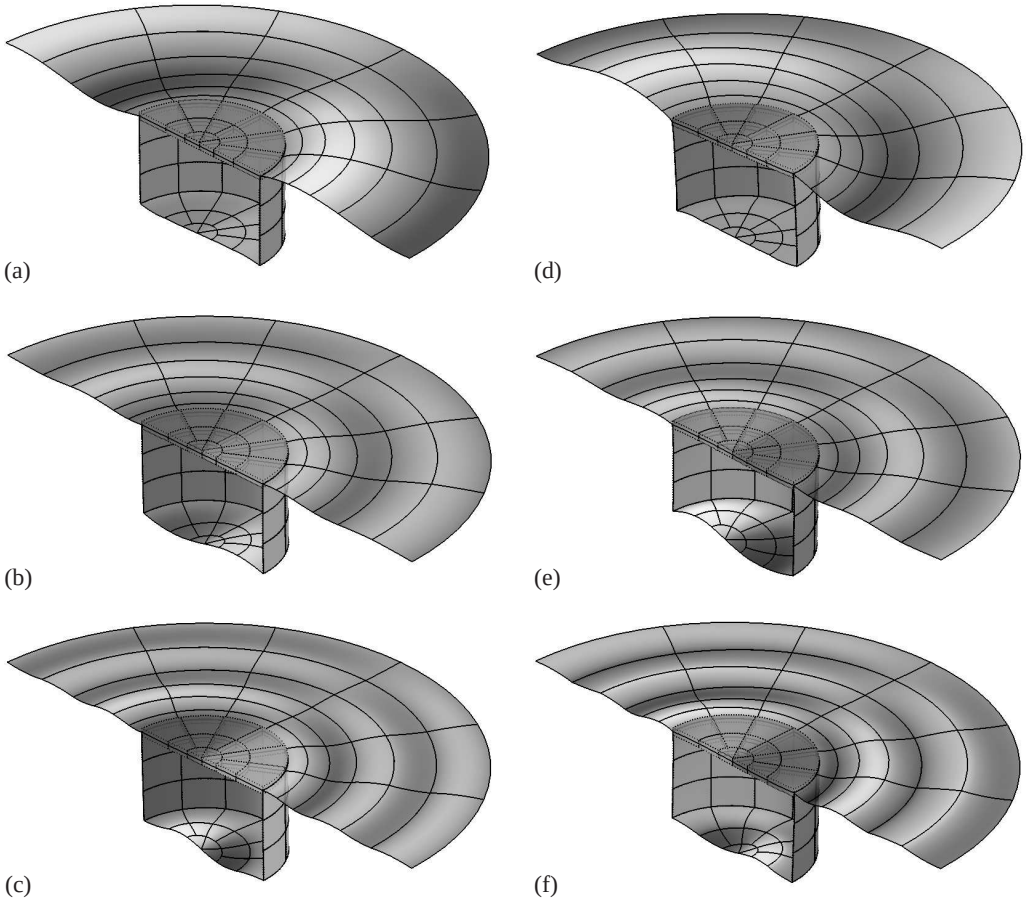

Figure 6–35 Response in phase with the load for the skirted foundation. On the left, the results are shown for a unit-magnitude harmonic horizontal force acting at the centre of the foundation at the frequencies (a) $f = 2$ Hz, (b) $f = 4$ Hz and (c) $f = 6$ Hz. The displacements are scaled by a factor of 10^9 and the light and dark shades of grey indicate positive and negative vertical displacements. On the right, the results are shown for a unit-magnitude harmonic rocking moment acting around the centre of the foundation at the frequencies (a) $f = 2$ Hz, (b) $f = 4$ Hz and (c) $f = 6$ Hz. The displacements are scaled by a factor of 10^{10} and the light and dark shades of grey indicate positive and negative vertical displacements.

"front" of the foundation, whereas the other half of A_{skirt}, *i.e.* the "sides", emits S-waves. A similar reasoning lies behind the derivation of c_{24}^{∞}, and as indicated by Eq. (6–45d) there are no contributions from the lid to the sliding–rocking coupling at high frequencies.

Finally, the rocking impedance provided by Eq. (6–45e) consists of three parts. The first one stems from P-waves originating from the bottom of the lid and the next term is a mixture of P- and S-waves generated at the skirts. However, only the S-waves polarised in the horizontal direction are included in the second term of Eq. (6–45e); but the rocking motion of the foundation also induces S-waves polarised in the vertical direction, in particular at the "back" and "front" of the bucket. Again, a strict proof follows by integration over the surface of the skirts, but a by physical reasoning it is found the half the area contributes to the generation of such S-waves.

The response of the bucket foundation is computed at 31 discrete frequencies from 0 to 6 Hz using the coupled boundary-element–finite-element model. The results for vertical and torsional excitation and three different frequencies are shown in Fig. 6–34, whereas the corresponding results for horizontal sliding and rocking are given in Fig. 6–35. It is noted that the light and dark shades of grey indicate vertical displacements upwards and downwards, respectively, in the plots for the vertical, horizontal and rocking-moment excitation. However, in the case of torsional excitation, no vertical displacements are generated. Hence, in this particular case the light/dark shades indicate horizontal displacements away from/towards the plane of symmetry.

Figures 6–36 to 6–40 show the frequency-domain solution obtained by the coupled finite-element–boundary-element scheme for the five different impedance components. The results of the corresponding lumped-parameter models of orders 2, 6 and 10 are plotted in the same figures. It is clear that the low-order models with $M = 2$, and having only a single internal degree-of-freedom, are inadequate. However, the sixth-order lumped-parameter model provide a good fit to the FE–BE model in the low-frequency range and only an insignificant improvement is obtained by increasing the order of the LPMs to 10.

It is of particular interest that the high-order lumped-parameter model with $M = 10$ does not lead to a better fit at higher frequencies than the sixth-order model. Instead, wiggling occurs at low-frequencies with the tenth-order model, *i.e.* non-physical tips and dips arise in the results from the LPM between frequencies at which the target FE-BE solution has been computed. This behaviour should be avoided and thus the sixth-order model is preferred. In order to obtain a better fit without wiggling, a smaller frequency step should be applied in the FE-BE solution.

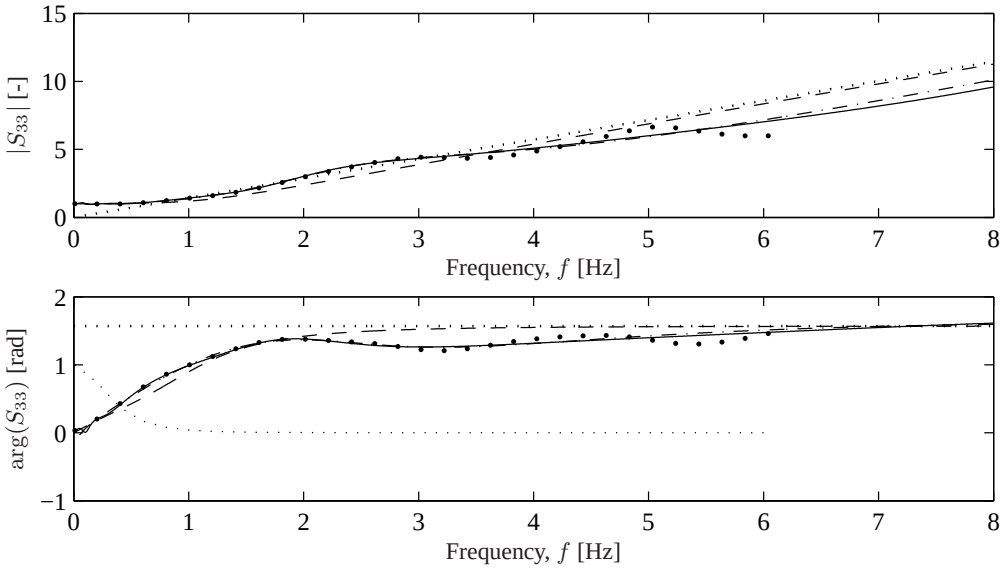

Figure 6–36 Dynamic stiffness coefficient, S_{33}, obtained by the finite-element–boundary-element (the large dots) and lumped-parameter models with $M = 2$ (— —), $M = 6$ (— · — ·), and $M = 10$ (——). The thin dotted line (·····) indicates the weight function w (not in radians), and the thick dotted line (·····) indicates the high-frequency solution, *i.e.* the singular part of S_{33}.

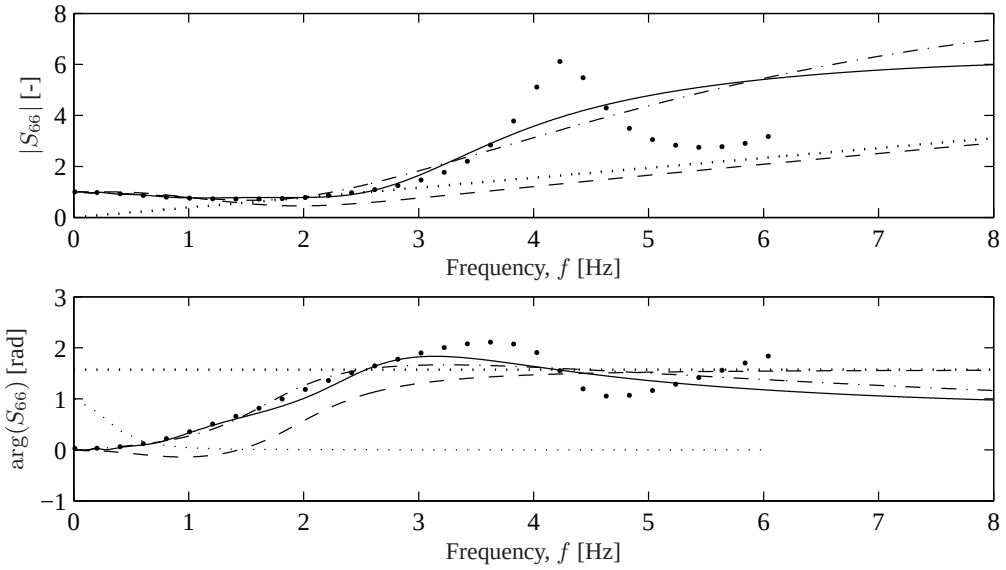

Figure 6–37 Dynamic stiffness coefficient, S_{66}, obtained by the finite-element–boundary-element model (the large dots) and lumped-parameter models with $M = 2$ (— —), $M = 6$ (— · — ·), and $M = 10$ (——). The thin dotted line (·····) indicates the weight function w (not in radians), and the thick dotted line (▪▪▪▪▪) indicates the high-frequency solution, *i.e.* the singular part of S_{66}.

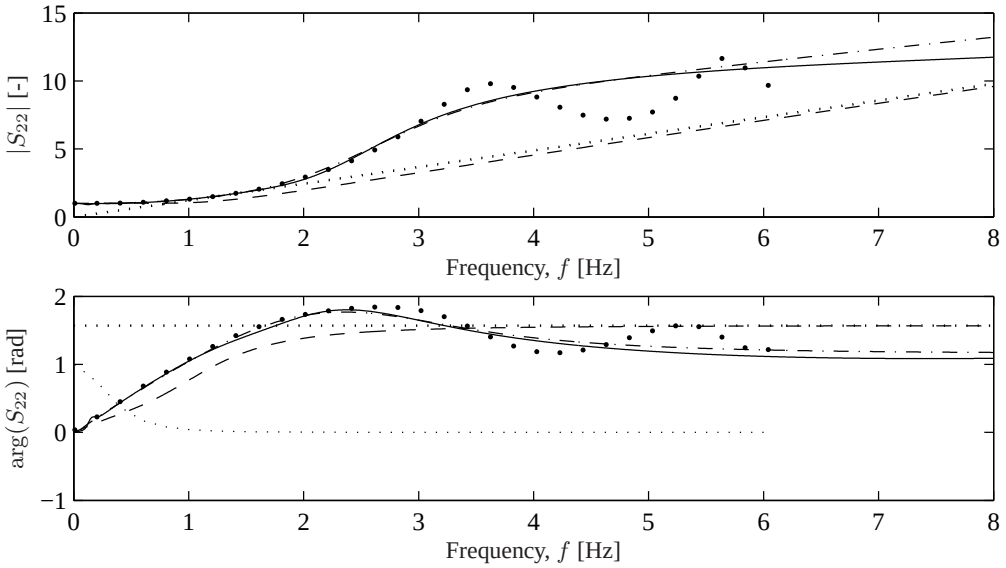

Figure 6–38 Dynamic stiffness coefficient, S_{22}, obtained by the finite-element–boundary-element model (the large dots) and lumped-parameter models with $M = 2$ (— —), $M = 6$ (— · — ·), and $M = 10$ (——). The thin dotted line (·····) indicates the weight function w (not in radians), and the thick dotted line (▪▪▪▪▪) indicates the high-frequency solution, *i.e.* the singular part of S_{22}.

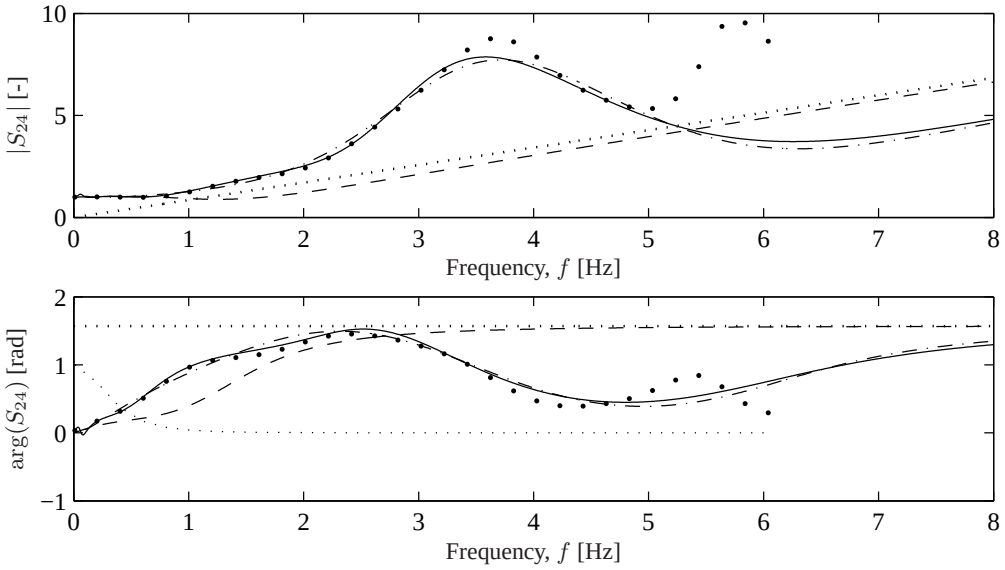

Figure 6–39 Dynamic stiffness coefficient, S_{24}, obtained by the finite-element–boundary-element model (the large dots) and lumped-parameter models with $M = 2$ (— —), $M = 6$ (— · — ·), and $M = 10$ (——). The thin dotted line (·····) indicates the weight function w (not in radians), and the thick dotted line (·····) indicates the high-frequency solution, *i.e.* the singular part of S_{24}.

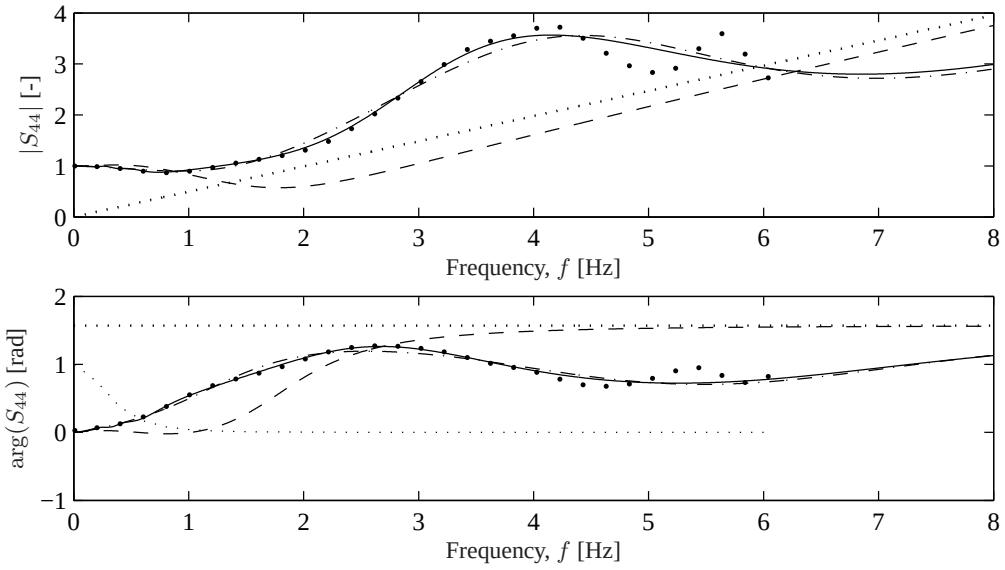

Figure 6–40 Dynamic stiffness coefficient, S_{44}, obtained by the domain-transformation model (the large dots) and lumped-parameter models with $M = 2$ (— —), $M = 6$ (— · — ·), and $M = 10$ (——). The thin dotted line (·····) indicates the weight function w (not in radians), and the thick dotted line (·····) indicates the high-frequency solution, *i.e.* the singular part of S_{44}.

6.5 Summary

In this chapter, the concept of a lumped-parameter model (LPM) has been presented. The basic idea is to adapt a simple mechanical system with few degrees of freedom to the response of a much more complex system, *e.g.* a foundation on a layered ground. For a circular footing on a homogeneous half-space, particularly simple solutions exist. These are

- the standard lumped-parameter model which only introduces a spring stiffness and a viscous dashpot for each degree of freedom, *i.e.* vertical, torsional, horizontal and rocking motion, and
- the fundamental lumped-parameter models which introduces a mass in addition to the spring and dashpot. This mass represents the added mass of the soil and must be added to the mass of the footing itself.

The fundamental LPM is much better than the standard LPM at high frequencies. Here the standard LPM provides useless results. None of the simple models account for coupling between horizontal sliding and rocking. This may be a reasonable assumption for a surface footing on a half-space. However, for footings on a layered half-space or embedded foundations, the coupling has to be accounted for. Furthermore, the simple models are not able to reproduce the resonance and antiresonance occurring in, for example, a soil stratum.

In the general case, a consistent lumped-parameter model may be applied. The use of such a model involves the following steps:

1. The target solution in the frequency domain is computed by a rigorous model, *e.g.* a finite-element or boundary-element model. Alternatively the response of a real structure or footing is measured.
2. A rational filter is fitted to the target results, ensuring that nonphysical resonance is avoided. The order of the filter should by high enough to provide a good fit, but low enough to avoid wiggling.
3. Discrete-element models with few internal degrees of freedom are established based on the rational-filter approximation.

This procedure is carried out for each degree of freedom and the discrete-element models are then assembled with a finite-element, or similar, model of the structure. Typically, lumped-parameter models with a three to four internal degrees of freedom provide results of sufficient accuracy. This has been demonstrated in the present chapter for two different cases, namely a footing on a stratified ground and a flexible skirted foundation in homogeneous soil.

Exercises

Exercise 1: Seismic reflection test

On a given site, the soil is known to consist of a soft soil deposit underlain by a homogeneous half-space of a much stiffer material (bedrock). For low-frequent vibrations at small amplitudes the soil behaves as an elastic continuum. Both the ground surface and the interface between the top layer and the underlying half-space are assumed to be horizontal. However, the depth, h of the top layer is unknown. In order to find h, a so-called *seismic reflection test* is carried out.

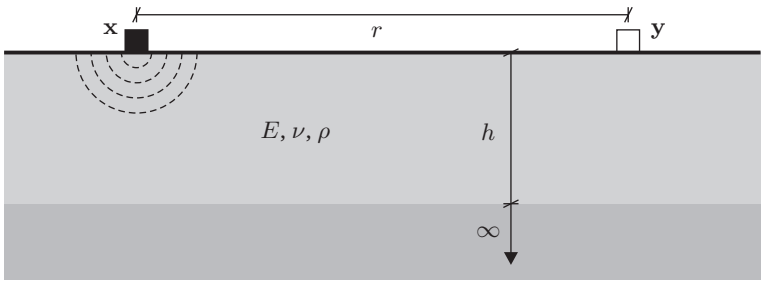

Figure A Seismic reflection test for identification of the depth of a top layer over a subsoil.

An explosive charge is released at the point $\mathbf{x}$ on the surface of the ground, see Fig. A. The resulting vibrations are measured at the receiver point $\mathbf{y}$, which lies the distance r from the source point $\mathbf{x}$. The test is then based on a registration of the arrival times of different waves.

1 Identify the first body wave arriving at the receiver point $\mathbf{y}$ after the explosion at point $\mathbf{x}$.

2 Which body wave is the second to arrive at the receiver point, and which wave is the third and the fourth? Why is there no unique answer to this question?

3 The material properties of the surface layer are assumed to be unknown. This implies that the distance between $\mathbf{x}$ and $\mathbf{y}$ should at least be equal to twice the layer depth in order to provide an unambiguous measurement of h. Prove that this statement is correct.

4 The surface layer has the properties $E = 300$ MPa, $\nu = 0.25$, $\rho = 2000$ kg/m^3 and $h = 5$ m. Make a small MATLAB program that computes the arrival times of the first four body waves as function of the distance between the source and receiver points in the interval $0 \text{ m} \leq r \leq 20 \text{ m}$.

Exercise 2: A constitutive model with four parameters

A one-dimensional viscoelastic model is considered. The model consists of a Kelvin model and a Maxwell model coupled in parallel. The Maxwell part of the model is defined by the parameters E_1 and η_1, whereas the stiffness and the damping terms of the Kelvin part of the model are given as E_2 and η_2, respectively. The complete model with four parameters is illustrated below.

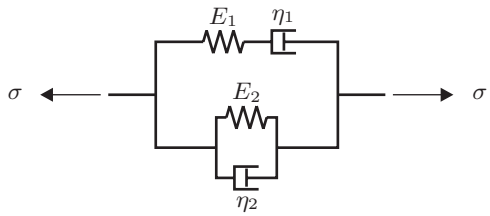

Figure A Four-parameter viscoelastic model.

1 Define the relationship between the total *stress* $\sigma(t)$ in the model and the local stresses in the individual parts of the model. Likewise, define the relationship between the total *strain* $\epsilon(t)$ in the model and the local strains in the individual parts of the model.

2 The relaxation modulus and the creep compliance of the *Maxwell* part of the model are denoted $G_1(t)$ and $J_1(t)$, respectively. Further, the relaxation modulus and the creep compliance of the *Kelvin* part of the model are denoted $G_2(t)$ and $J_2(t)$, respectively. Given that $G_1(t)$, $J_1(t)$, $G_2(t)$ and $J_2(t)$ are all known, how is the creep compliance $J(t)$ and the relaxation modulus $G(t)$ for the entire model defined?

3 Compute the relaxation modulus $G(t)$ of the entire model.

4 Formulate a constitutive relation between the stress $\sigma(t)$ and the strain $\epsilon(t)$ in terms of a rational model, *i.e.* by means of the *differential* approach.

5 On the basis of the relaxation modulus $G(t)$ and the constitutive equation formulated in the answers to questions 3 and 4, establish the hereditary approach.

6 Establish the stress–strain relationship in the frequency domain and identify the rational filter $\hat{G}(\omega)$ for the four-parameter model.

7 Derive the phase velocity and the wavenumber as functions of the frequency and plot dispersion and slowness diagrams for various combinations of the parameters E_1, η_1, E_2, η_2 and the mass density ρ. Which of the damping constants η_1 and η_2 is the more important with respect to the degree of dispersion?

8 Derive the high-frequency limits of the phase and group velocities in the material model. Do you think that the material model is realistic?

Exercise 3: FEM model of an infinite bar

Consider an infinite bar subject to a harmonic excitation applied at $x = 0$ and in the axial direction with the amplitude P and the circular frequency ω. The bar has the Young's modulus E, the mass density ρ and the cross-sectional area A as illustrated below.

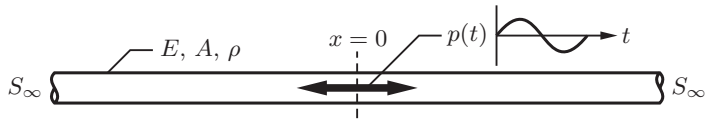

Figure A Infinite bar subjected to the harmonic excitation $p(t) = P\mathrm{e}^{\mathrm{i}\omega t} \sim P\sin\omega t$ applied at $x = 0$.

1 Formulate the equation of motion, *i.e.* the strong form of the governing partial differential equation for the bar.

2 Establish the weak form of the equation of motion and identify the integrals corresponding to the mass and stiffness matrix for an element as well as the nodal force vector.

3 Apply the Galerkin method and compute (analytically) the element matrices for linear shape and weight functions. Assume that the mass is *consistent, i.e.* distributed according to the shape functions.

4 Determine the phase velocity of the waves propagating in the bar. Is the phase velocity the same as that of the pressure waves in 3-D or 2-D elastodynamics? Why/why not?

5 Derive the fundamental solution for the wave propagation in the infinite bar, *i.e.* find the amplitudes and the wavenumbers for the wave components in the system for the load $f(x,t) = P\mathrm{e}^{\mathrm{i}\omega t}\delta(x) \sim P\sin\omega t\delta(x)$.

6 Based on the fundamental solution, derive an impedance boundary condition for the bar to be applied at the artificial end points S_∞. Can this boundary condition be used for any frequency and does it work for any kind of load? In other words, what are the limitations of the boundary condition?

7 Write a MATLAB program which can be used to assemble any number of bar elements with arbitrary, but equal length on either side of a point force.

8 Determine the necessary element length and time step in order to get n elements per wavelength and a Courant number of C.

9 Apply the Newmark method and perform a time-domain solution for the FEM system of equations.

10 Carry out the solution in the frequency domain and compare the results with the analytical solution.

11 Try to change a part of the mass to *lumped* mass. What happens to the numerical solution? How much of the mass should be lumped in order to get the highest possible accuracy of the numerical solution?

12 Use the finite element scheme for bars and loads with different parameters. Furthermore, investigate the influence of the time step and the element size on the accuracy of the numerical solution.

13 Compute the response to a broad-banded load in time and frequency domain. This could for instance be the Ricker pulse defined as:

$$p(t) = \begin{cases} p_0 \frac{5^{2.5}}{4^2} \varphi (1-\varphi^2)^2 & \text{for} \quad 0 < t < T_C \\ 0 & \text{for} \quad T_C \leqslant t \end{cases},$$

where p_0 is the maximum intensity of the load signal and $\varphi = \varphi(t)$ is a linear function,

$$\varphi(t) = \frac{2t}{T_C} - 1.$$

14 Introduce linear viscous or hysteretic material damping in the bar model. How does the damping influence the wave propagation with respect to dissipation and dispersion? How pronounced is the non-causal response of the hysteretic model?

15 Try instead to discretize the bar with quadratic elements. Compare the results with those obtained with the linear finite elements model. How much better are the quadratic elements than the linear ones?

Exercise 4: Seismic analysis of a layered ground

This exercise concerns the formulation of a semi-analytic model of the seismic response of a layered ground and may be considered a simplification of the theory described in Chapter 5. The soil is idealized as a stratum consisting of J homogeneous, isotropic and linear viscoelastic horizontal layers overlaying bedrock. An earthquake emits plane elastic SH-waves which are assumed to impinge vertically, *i.e.* orthogonally, on the interface between the bottommost layer and the bedrock. This approximation is justified by the fact that the seismic waves are refracted on their way through the bedrock due to increasing stiffness over the depth. With no further loss of generality, the particle motion is assumed to be polarized in the x_1-direction.

1 In the general three-dimensional case, the following quantities are all different from zero:

$$u_i^j(\mathbf{x}, t), \quad \frac{\partial u_i^j(\mathbf{x}, t)}{\partial x_k}, \quad i = 1, 2, 3, \quad k = 1, 2, 3, \quad j = 1, 2, ..., J,$$

where superscript j refers to the number of the layer. Identify the two quantities from this list that are different from zero in the present case.

2 Harmonic SH-waves are considered and external body forces are disregarded. Starting from the Navier equations (1–10), and making use of the simplifications from Question 1, show that the governing equation of wave propagation in a layer with the shear modulus μ^j and the mass density ρ^j is given by (no summation over index j)

$$\frac{\partial^2 u^j(z,t)}{\partial z^2} = \frac{1}{\{c_S^j\}^2} \frac{\partial^2 u^j(z,t)}{\partial t^2}, \quad z = x_3, \quad u^j(z,t) = u_1(x_3,t), \quad c_S^j = \sqrt{\frac{\mu^j}{\rho^j}}.$$

3 To analyse the problem in the frequency domain, for each individual layer a Fourier transformation is carried out according to the definition

$$U^j(z,\omega) = \int_{-\infty}^{\infty} u^j(z,t)\mathrm{e}^{-\mathrm{i}\omega t}\mathrm{d}t, \qquad u^j(z,t) = \frac{1}{2\pi}\int_{-\infty}^{\infty} U^j(z,\omega)\mathrm{e}^{\mathrm{i}\omega t}\mathrm{d}t.$$

Instead of the analytic evaluation of the inverse Fourier transformation, the time-domain solution is approximated as a Fourier series with N harmonic wave components,

$$u^j(z,t) \simeq \sum_{n=1}^{N} U_n^j(z)\mathrm{e}^{\mathrm{i}\omega_n t}.$$

Establish the governing equation for a single wave component, $u_n^j(z,t) = U_n^j(z)\mathrm{e}^{\mathrm{i}\omega_n t}$, in the frequency domain. Show that the same result is obtained from Eq. (5–17a) by making use of the fact that the horizontal wavenumbers are equal to zero (why is this true?).

4 As in Chapter 5, a local z-axis may advantageously be applied in the formulation of the solution for a given layer. The coordinate z^j is defined so that $z^j \in [0; h_j]$, where h_j is the depth of the layer, cf. Fig. 5–2. With this definition, the solution to the equation of motion may be given in any of the forms:

$$U_n^j(z^j) = B_n^j\mathrm{e}^{\mathrm{i}k_n^j z^j} + C_n^j\mathrm{e}^{-\mathrm{i}k_n^j z^j} \qquad \text{or} \qquad U_n^j(z^j) = B_n^j\mathrm{e}^{\mathrm{i}k_n^j z^j} + D_n^j\mathrm{e}^{-\mathrm{i}k_n^j (z^j - h_j)},$$

where $k_n^j = \omega_n / c_S^j$. Show that both solutions are valid and find the relation between the integration constants C_n^j and D_n^j.

5 For an isotropic linear and viscoelastic layer with the Lamé constants λ^j and μ^j, the stresses in the frequency domain are generally given by a constitutive law in terms of the strain amplitudes:

$$\hat{\sigma}_{ik}^j = \lambda^j \hat{\Delta}^j \delta_{ik} + 2\mu^j \hat{\epsilon}_{ik}, \qquad \hat{\Delta}^j = \hat{\epsilon}_{ii}, \qquad \hat{\epsilon}_{ik}^j = \frac{1}{2}\left(\frac{\partial U_i^j}{\partial x_k} + \frac{\partial U_k^j}{\partial x_i}\right),$$

with no summation over the index j. Based on this information and the second solution for $U_n^j(z^j)$ in the previous question, express the amplitude function $P_n^j(z^j)$ for the shear stress in layer j corresponding to harmonic SH-wave component n.

6 Similarly to the Haskel–Thompson approach in Chapter 5, the displacement and the shear stress at the local depth z^j are stacked in a vector,

$$\mathbf{S}_n^j(z^j) = \begin{bmatrix} U_n^j(z^j) \\ P_n^j(z^j) \end{bmatrix} = \mathbf{A}_n^j(z^j) \begin{bmatrix} B_n^j \\ D_n^j \end{bmatrix},$$

where $\mathbf{A}_n^j(z^j)$ is a matrix with the dimensions (2×2), the components of which are obtained from the expressions of $U_n^j(z^j)$ and $P_n^j(z^j)$ in terms of the integration constants. Find this matrix and evaluate $\mathbf{A}_n^{j0} = \mathbf{A}_n^j(z^j = 0)$ and $\mathbf{A}_n^{j1} = \mathbf{A}_n^j(z^j = h^j)$.

7 Establish a relationship between the displacement and the shear stress at the top of layer j and the corresponding quantities at the bottom of the layer. This relationship should be given in terms of $\mathbf{A}_n^{j0}$ and $\mathbf{A}_n^{j1}$.

8 Analogously to Subsection 5.3.3, formulate a relationship between the displacement and the traction at the surface of the layered half-space and the similar quantities at the interface between layer J and bedrock. This relationship should have the form $\mathbf{S}_n^{10} = \mathbf{T}_n \mathbf{S}_n^{J1}$, where $\mathbf{S}_n^{10} = \mathbf{S}_n^1(z^1 = 0)$ and $\mathbf{S}_n^{J1} = \mathbf{S}_n^J(z^J = h^J)$, and $\mathbf{T}_n$ is a matrix with the dimensions (2×2). This should depend on the matrices $\mathbf{A}_n^{j0}$ and $\mathbf{A}_n^{j1}$, $j = 1, 2, ..., J$.

9 Show that the displacement U_n^{10} at the free surface of the layered half-space due to a forced displacement $U_n^{J1} = \bar{U}_n$ at the bedrock is given as

$$U_n^{10} = H_n \bar{U}_n, \qquad H_n = T_{11} - \frac{T_{12} T_{21}}{T_{22}},$$

where T_{ik} are the components of $\mathbf{T}_n$. $H_n \sim H(\omega)$ is the frequency response function for the layered half-space, which may be used to compute the response at the free surface of the ground for seismic excitation with a given one-sided amplitude spectrum $S_{\bar{U}}(\omega)$.

10 Make a MATLAB program that calculates the frequency response function for a stratum with the properties listed below. The frequency range 0 to 20 Hz should be considered.

Layer 1:	$G^1 = 50$ MPa,	$\rho^1 = 1600$ kg/m^3,	$\eta^1 = 0.12$,	$h^1 = 5$ m
Layer 2:	$G^2 = 100$ MPa,	$\rho^2 = 1800$ kg/m^3,	$\eta^2 = 0.08$,	$h^2 = 10$ m
Layer 3:	$G^3 = 150$ MPa,	$\rho^3 = 2000$ kg/m^3,	$\eta^3 = 0.04$,	$h^3 = 15$ m
Layer 4:	$G^4 = 200$ MPa,	$\rho^4 = 2200$ kg/m^3,	$\eta^4 = 0.02$,	$h^4 = 20$ m

Note that η^j is the loss factor and that a complex shear modulus should be applied in the form $\mu^j = G^j \left(1 + \mathrm{i}\,\mathrm{sign}(\omega)\eta^j\right)$, where G^j is the real shear modulus.

Exercise 5: Boundary-elements for antiplane shear

The antiplane shear-wave propagation in a homogeneous elastic material is considered. The phase velocity of the shear waves is c_S, and material dissipation is assumed to be present, defined by the loss factor η. Create a boundary-element method program with constant elements that can be used for the frequency-domain analysis of the wave propagation in a half-plane. Here, the loss factor defines the complex phase velocity $c_S^* = c_S\,(1 + \mathrm{i}\eta)$. The program should include the following:

1 An input routine, in which the material properties, the coordinates of the extreme points, the element topology, the frequencies, the boundary conditions and the internal point coordinates are given.

2 A routine which computes the collocation node coordinates and the normal vectors along with the complex phase velocity.

3 A routine that assembles the system matrices $\mathbf{H}$ and $\mathbf{G}$.

4 A subroutine for the evaluation of the nonsingular terms of $\mathbf{H}$ and $\mathbf{G}$. Here a six-point standard Gauss quadrature rule should be used. Hint: the Jacobian is simply the ratio between the element lengths in the global and local coordinate systems.

5 A subroutine for the evaluation of the singular terms in $\mathbf{G}$. Note that the singular terms of $\mathbf{H}$ are 0.5, *i.e.* only the geometry constant contributes along the diagonal of the flux fundamental solution matrix.

6 A routine which reorders $\mathbf{H}$ and $\mathbf{G}$ into the coefficient matrix $\mathbf{A}$ and the vector of known quantities $\mathbf{F}$.

7 A main program that calls the routines 1 and 2 and includes a frequency loop over the remaining routines. Further, inside the loop the system of equations $\mathbf{A}(\omega)\mathbf{Z}(\omega) = \mathbf{F}(\omega)$ should be solved for each frequency.

8 A routine that reorders $\mathbf{Z}(\omega)$ and the known values (*i.e.* the boundary conditions) into $\mathbf{U}(\omega)$ and $\mathbf{P}(\omega)$.

9 A routine that computes the values of the displacements at interior points.

10 An output routine which can be used for the illustration of the results.

Utilise the program for the analysis of a half-space with the properties $c_S = 100$ m/s and $\eta = 0.05$. The following frequencies should be included: 5, 10 and 20 Hz. Fifty elements with a length of 0.5 m may be applied to discretize the surface of the half-space. Is this reasonable?

Solutions

Exercise 1: Seismic reflection test

Question 1

The first body wave to arrive at point $\mathbf{y}$ is the P-wave travelling horizontally along the surface of the ground. This P-wave will arrive at the time $t_1^P = r/c_P$.

Question 2

The order, in which the next P- and S-waves will arrive at the receiver point depends on the fraction r/h and the Poisson ratio of the layer. For high Poisson ratios, the S-wave is extremely slow compared with the P-wave, *i.e.* $c_S \ll c_P$. Hence, the first four waves to arrive at point $\mathbf{y}$ may all be P-waves reflected 0, 1, 2 or 3 times. On the other hand, as the Poisson ratio approaches zero, the S-wave becomes faster, though still not as fast as the P-wave. Thus for deep layers ($h \gg r$) the second wave reaching point $\mathbf{y}$ is the direct S-wave travelling along the surface.

Question 3

In order to "measure" the layer depth by means of the seismic reflection test, the arrival times must be identified for two waves. Further, for each of these waves, the speed and travel path must be known. As discussed in Question 2, the order of arrival of various P- and S-waves (except the first one) become ambiguous. Therefore it may not be possible to distinguish between, for example, the third P-wave and the second S-wave to arrive at the receiver point—in particular since each P-wave is reflected as both a P-wave and an S-wave, and vice versa. However, an unambiguous measure of h is obtained if the first two wave to be registered at $\mathbf{y}$ are the waves shown in Fig. A.

The arrival time of the first S-wave at point $\mathbf{y}$ is $t_1^S = r/c_S$. For a given P-wave speed, the maximum S-wave speed is achieved when the Poisson ratio is equal to zero (see Fig. 1–25). Here $c_P = \sqrt{2}c_S$, and it follows that $t_1^S = \sqrt{2}\,r/c_P$. For any other value of the Poisson ratio, the S-wave will arrive later than this.

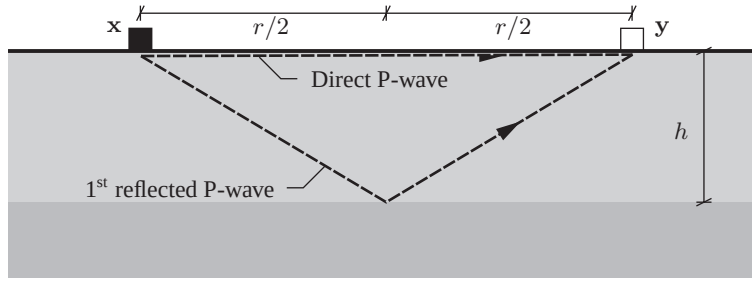

Figure A Direct P-wave and the first reflected P-wave arriving at point $\mathbf{y}$ from point $\mathbf{x}$.

The second P-wave has been reflected at the interface and therefore has to travel the distance $2\sqrt{(r/2)^2+h^2}$. Thus it arrives at time $t_2^P = 2\sqrt{(r/2)^2+h^2}/c_P$. Evidently, in order to ensure that the layer depth is actually measured by the test, the following (in)equality must hold:

$$t_2^P \leqslant t_1^S \quad \Rightarrow \quad \frac{2}{c_P}\sqrt{\left(\frac{r}{2}\right)^2+h^2} \leqslant \sqrt{2}\frac{r}{c_P} \quad \Rightarrow \quad r^2+4h^2 \leqslant 2r^2 \quad \Rightarrow \quad 2h \leqslant r.$$

Hence, the distance between the source and receiver points should at least be equal to twice the layer depth. Note that the reflected P-wave will arrive before the direct S-wave at any point beyond $\mathbf{y}$. However, a very long distance r between the source and receiver points may not be useful since $t_1^P \to t_2^P$ for $r \to \infty$. One may say that the layer depth has to be known in advance in order to measure it with a seismic reflection test.

Question 4

The order, in which the first waves arrive at the receiver point, depends on the distance r between the $\mathbf{x}$ and $\mathbf{y}$. For small values of r, the first two waves to arrive at $\mathbf{y}$ are the direct P- and S-waves. However, at larger distances, the first (and possibly also the second) reflected P-wave arrives sooner than the direct S-wave. Further, waves may start as P-waves and end as SV-waves and vice versa after a phase transition at the interface. These waves will be coined "P-to-S-waves" and "S-to-P-waves", respectively.

In the present case, only the waves that travel most of the way as P-waves are of interest since S-wave travel with a speed that is much lower than the P-wave speed. Thus, according to Eqs. (1–8), (1–14) and (1–17) the following wave speeds are found

$$c_P = 424.26\,\text{m}, \quad c_S = 244.95\,\text{m}.$$

Equation (1–47) then defines the ratio between the angles of incidence of incoming P-waves and reflected S-waves,

$$\alpha = \frac{c_P}{c_S} = \frac{\sin\theta_P}{\sin\theta_S} = 1.7320.$$

Along with the layer depth h and the distance r, this fraction determines the geometry of the wave propagation paths for the waves that travel part of the way from the source point to the receiver point as P-waves and the remaining part of the way as S-waves.

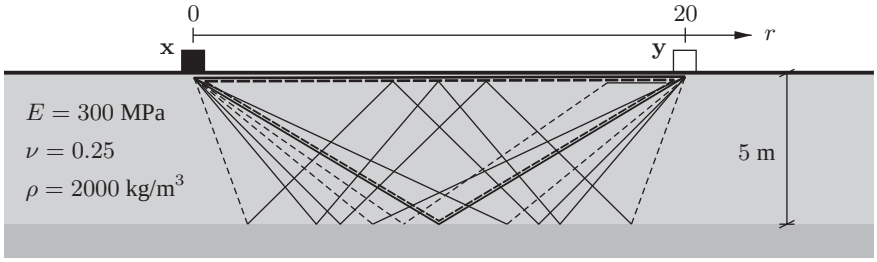

Figure B Propagation paths of the first waves to arrive at the receiver point $\mathbf{y}$. P-waves are indicated with full-drawn lines, and S-waves are plotted with dashed lines.

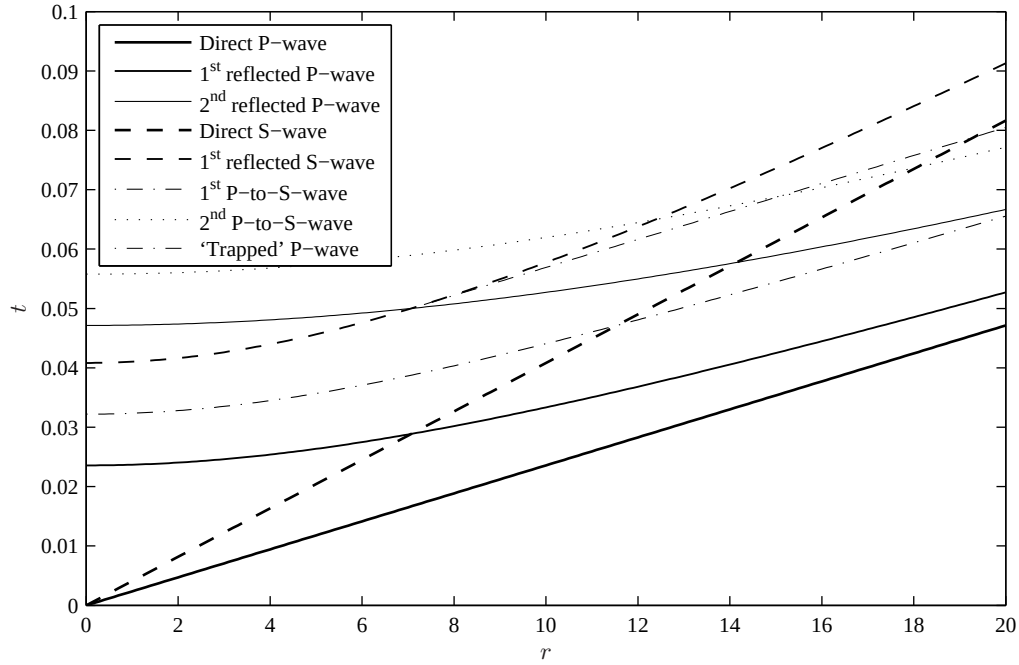

Figure C Arrival times t of the first waves as functions of the distance r between the source and the receiver points.

A MATLAB program (`exercise_01.m`) has been made, in which the travel times are computed for the waves shown in Fig. B. The travel times for the waves that do not change phase from P- to SV-waves or vice versa are straightforward to compute. However, the geometry of the propagation paths for the P-to-S-waves and S-to-P-waves is rather complex. An analytical solution for known values of r, h and α is not easily found, and instead the arrival times of these waves is computed by iteration. In Fig. C the arrival times of the waves at point $\mathbf{y}$ are plotted as functions of r. Note that there are two pairs of waves that arrive at the same time. These are the first and second P-to-S-waves and the corresponding S-to-P-waves. As illustrated in Fig. B, the travel path has the same length for the first P-to-S-wave and the first S-to-P-wave, and the part of the path where the propagation is of P- and S-wave type, respectively, have the same lengths.

Further, when the S-wave impinges on the free surface at an oblique angle greater than $\theta_c = \operatorname{asin}(1/\alpha) = 35.26°$, P-waves are trapped in the surface. Here Snell's law provides values of θ_P greater than $90°$, which has no physical meaning. Hence, a "trapped" P-wave curve bifurcates from the first reflected S-wave curve in the r-t-plot beyond a certain critical distance $r_C = h/\tan\theta_c = 7.071$ m. However, as illustrated in Fig. C, the trapped P-wave is not one of the first four waves to arrive at the receiver point, even though it is a bit faster than the first reflected S-wave at great distances.

Exercise 2: A constitutive model with four parameters

Question 1

The stress and strain in the Maxwell part of the model are denoted σ_1 and ϵ_1, respectively. Likewise, the stress and strain in the Kelvin part of the model are denoted σ_2 and ϵ_2, respectively. Further, stresses and strains associated with elastic parts of the model (the springs) are indicated with the superscript e, and superscript v denotes stresses or strains in the viscous parts of the model (the dashpot). Then the following relationships are identified for the four parameter model:

$$\sigma = \sigma_1 + \sigma_2 = \sigma_1 + \sigma_2^e + \sigma_2^s,$$

$$\epsilon = \epsilon_1 = \epsilon_1^e + \epsilon_1^v = \epsilon_2 = \epsilon_2^e = \epsilon_2^v.$$

Furthermore $\sigma_1^e = \sigma_1^v$ as the spring and dashpot in the Maxwell model are coupled in series.

Question 2

The following quantities are known:

$$J_1 = J_1^e + J_1^v = \frac{1}{E_1} + \frac{t}{\eta_1}, \qquad \text{(Maxwell} \sim \text{series coupling)}$$

$$G_2 = G_2^e + G_2^v = E_2 + \eta_2\,\delta(t). \qquad \text{(Kelvin} \sim \text{parallel coupling)}$$

The full model is achieved by a parallel coupling of part 1 and 2. Therefore, according to Definition 1.4, the relaxation modulus may be found as $G = G_1 + G_2$. The computation of the creep compliance J is far more complicated.

Question 3

In order to calculate G, the relaxation modulus for the Maxwell model has to be known. Here, Eq. (1–114) is utilized. Partial integration provides the result

$$\epsilon(t) = \int_{-\infty}^{t} J(t-\tau)\,\frac{\mathrm{d}\sigma(\tau)}{\mathrm{d}\tau}\,\mathrm{d}\tau = \int_{-\infty}^{t}\left(\frac{1}{E_1} + \frac{t-\tau}{\eta_1}\right)\frac{\mathrm{d}\sigma(\tau)}{\mathrm{d}\tau}\,\mathrm{d}\tau$$

$$= \int_{-\infty}^{t}\frac{1}{E_1}\,\frac{\mathrm{d}\sigma(\tau)}{\mathrm{d}\tau}\,\mathrm{d}\tau + \left[\frac{t-\tau}{\eta_1}\,\sigma_1(\tau)\right]_{-\infty}^{t} + \int_{-\infty}^{t}\frac{\sigma(\tau)}{\eta_1}\,\mathrm{d}\tau = \frac{\sigma(t)}{E_1} + \int_{-\infty}^{t}\frac{\sigma(\tau)}{\eta_1}\,\mathrm{d}\tau. \quad \text{(a)}$$

Here, use has been made of the fact that $\sigma_1(-\infty) = 0$ and $\sigma_1(t) < \infty$ so that $(t - t)\,\sigma_1(t) = 0$. Equation (a) is differentiated with respect to time:

$$\frac{\mathrm{d}\epsilon}{\mathrm{d}t} = \frac{1}{E_1}\,\frac{\mathrm{d}\sigma_1}{\mathrm{d}t} + \frac{1}{\eta_1}\,\sigma_1(t). \tag{b}$$

The relaxation modulus $G_1(t)$ is equal to $\sigma_1(t)$ for a unit strain $\epsilon(t) = 1$ applied at time $t = 0$. The solution to Eq. (b) for a strain of this kind is derived as:

$$0 = \frac{1}{E_1}\,\frac{\mathrm{d}G_1}{\mathrm{d}t} + \frac{1}{\eta_1}\,G_1(t) \;\Rightarrow\; G_1(t) = C\,\mathrm{e}^{-\frac{E_1}{\eta_1}\,t}.$$

The constant C is determined from the initial conditions at $t = 0$. Here the entire strain will be present in the spring, since the dashpot is infinitely stiff for a strain applied with infinite velocity (infinite strain rate). Hence,

$$G_1(0) = C\,\mathrm{e}^0 = C = E_1\,\epsilon(0^+) = E_1 \;\Rightarrow\; C = E_1.$$

Finally, the relaxation module of the entire model is found as

$$G(t) = G_1(t) + G_2(t) = E_1\,\mathrm{e}^{-\frac{E_1}{\eta_1}\,t} + E_2 + \eta_2\,\delta(t). \tag{c}$$

Question 4

The strain vanishes in the limit as $t \to -\infty$. Hence, from Eq. (1–114) follows that the stress may be written as

$$\begin{aligned}\sigma(t) &= \int_{-\infty}^{t} G(t-\tau)\frac{\mathrm{d}\epsilon(\tau)}{\mathrm{d}\tau}\,\mathrm{d}\tau = \int_{-\infty}^{t}\left(E_1\,\mathrm{e}^{-\frac{E_1}{\eta_1}\,(t-\tau)} + E_2 + \eta_2\,\delta(t-\tau)\right)\,\frac{\mathrm{d}\epsilon(\tau)}{\mathrm{d}\tau}\,\mathrm{d}\tau \\ &= E_1\,\mathrm{e}^{-\frac{E_1}{\eta_1}\,t}\,\int_{-\infty}^{t}\mathrm{e}^{-\frac{E_1}{\eta_1}\,\tau}\frac{\mathrm{d}\epsilon(\tau)}{\mathrm{d}\tau}\,\mathrm{d}\tau + E_2\,\epsilon(t) + \eta_2\,\frac{\mathrm{d}\epsilon(t)}{\mathrm{d}t}.\end{aligned} \tag{d}$$

Differentiation of Eq. (d) with respect to time provides the equation:

$$\begin{aligned}\frac{\mathrm{d}\sigma(t)}{\mathrm{d}t} &= \frac{E_1^2}{\eta_1}\,\mathrm{e}^{-\frac{E_1}{\eta_1}\,t}\,\int_{-\infty}^{t}\mathrm{e}^{-\frac{E_1}{\eta_1}\,\tau}\frac{\mathrm{d}\epsilon(\tau)}{\mathrm{d}\tau}\,\mathrm{d}\tau + E_1\,\mathrm{e}^{-\frac{E_1}{\eta_1}\,t}\mathrm{e}^{\frac{E_1}{\eta_1}\,t}\frac{\mathrm{d}\epsilon(t)}{\mathrm{d}t} + E_2\,\frac{\mathrm{d}\epsilon(t)}{\mathrm{d}t} + \eta_2\,\frac{\mathrm{d}^2\epsilon(t)}{\mathrm{d}t^2} \\ &= \frac{E_1^2}{\eta_1}\,\mathrm{e}^{-\frac{E_1}{\eta_1}\,t}\,\int_{-\infty}^{t}\mathrm{e}^{-\frac{E_1}{\eta_1}\,\tau}\frac{\mathrm{d}\epsilon(\tau)}{\mathrm{d}\tau}\,\mathrm{d}\tau + (E_1 + E_2)\,\frac{\mathrm{d}\epsilon(t)}{\mathrm{d}t} + \eta_2\,\frac{\mathrm{d}^2\epsilon(t)}{\mathrm{d}t^2}.\end{aligned} \tag{e}$$

Further, from Eq. (d) follows that

$$\mathrm{e}^{-\frac{E_1}{\eta_1}\,t}\,\int_{-\infty}^{t}\mathrm{e}^{-\frac{E_1}{\eta_1}\,\tau}\frac{\mathrm{d}\epsilon(\tau)}{\mathrm{d}\tau}\,\mathrm{d}\tau = \frac{1}{E_1}\,\left(\sigma(t) - E_2\,\epsilon(t) - \eta_2\,\frac{\mathrm{d}\epsilon(t)}{\mathrm{d}t}\right).$$

Insertion of this result into Eq. (e) leads to an ordinary differential equation in t:

$$\frac{\mathrm{d}\sigma(t)}{\mathrm{d}t} = -\frac{E_1}{\eta_1}\,\left(\sigma(t) - E_2\,\epsilon(t) - \eta_2\,\frac{\mathrm{d}\epsilon(t)}{\mathrm{d}t}\right) + (E_1 + E_2)\,\frac{\mathrm{d}\epsilon(t)}{\mathrm{d}t} + \eta_2\,\frac{\mathrm{d}^2\epsilon(t)}{\mathrm{d}t^2} \;\Rightarrow$$

$$E_1\,\sigma(t) + \eta_1\,\frac{\mathrm{d}\sigma(t)}{\mathrm{d}t} = E_1\,E_2\,\epsilon(t) + (E_1\,\eta_2 + E_1\,\eta_1 + E_2\,\eta_1)\,\frac{\mathrm{d}\epsilon(t)}{\mathrm{d}t} + \eta_1\,\eta_2\,\frac{\mathrm{d}^2\epsilon(t)}{\mathrm{d}t^2}. \tag{f}$$

This is the so-called *differential approach*. In the special case $E_2 = \eta_2 = 0$, Eq. (f) reduces to the relation for a Maxwell model. Likewise, after division of all terms by E_1, a pure Kelvin model is achieved with $E_1 = \infty$ and $\eta_2 = 0$.

Question 5

The creep compliance $J(t)$ of the full material model in Fig. A is the solution to Eq. (f) for a constant stress $\sigma = 1$ applied at time $t = 0$, *i.e.*

$$E_1 = E_1\,E_2\,J(t) + B\frac{\mathrm{d}J(t)}{\mathrm{d}t} + \eta_1\,\eta_2\,\frac{\mathrm{d}^2J(t)}{\mathrm{d}t^2}, \quad B = E_1\,\eta_2 + E_1\,\eta_1 + E_2\,\eta_1. \tag{g}$$

Solutions to Eq. (g) are of the kind

$$J(t) = 1/E_2 + C_1\,\mathrm{e}^{\lambda_1\,t} + C_2\,\mathrm{e}^{\lambda_2\,t}, \tag{h}$$

where $1/E_2$ is the particular solution and the constants C_1 and C_2 are determined from the initial conditions. Finally λ_i, $i = 1, 2$, are the roots to the characteristic polynomial,

$$\eta_1\,\eta_2\,\lambda_i^2 + B\,\lambda_i + E_1\,E_2 = 0 \;\Rightarrow\; \left.\begin{matrix}\lambda_1\\ \lambda_2\end{matrix}\right\} = \frac{-B \pm \sqrt{B^2 - 4\,E_1\,E_2\,\eta_1\,\eta_2}}{2\,\eta_1\,\eta_2}.$$

The dashpot in the Kelvin part of the model does not allow instantaneous strains, *i.e.* infinite strain rates are impossible. As an implication of this, the dashpot in the Kelvin part of the model is responsible for the entire stress $\sigma(t)$ at the time $t = 0^+$, that is just after the application of the unit stress. Hence, Eq. (g) is subject to the initial conditions

$$\epsilon(0^+) = J(0^+) = 0, \quad \sigma(0^+) = 1 = \eta_2\,\left.\frac{\mathrm{d}\epsilon(t)}{\mathrm{d}t}\right|_{t=0^+} = \eta_2\,\left.\frac{\mathrm{d}J(t)}{\mathrm{d}t}\right|_{t=0^+}. \tag{i}$$

Insertion of Eq. (h) into Eq. (i) provides two equations for the determination of C_1 and C_2,

$$\begin{bmatrix} 1 & 1 \\ \lambda_1 & \lambda_2 \end{bmatrix}\begin{bmatrix} C_1 \\ C_2 \end{bmatrix} = \begin{bmatrix} -1/E_2 \\ 1/\eta_2 \end{bmatrix} \quad \Rightarrow \quad \begin{bmatrix} C_1 \\ C_2 \end{bmatrix} = \frac{1}{\lambda_1 - \lambda_2}\begin{bmatrix} \lambda_2/E_2 + 1/\eta_2 \\ -\lambda_1/E_2 - 1/\eta_2 \end{bmatrix}.$$

Finally, now that both $J(t)$ and $G(t)$ are known, the stress–strain relation in terms of the *hereditary approach* is obtained by the equations

$$\sigma(t) = \int_{-\infty}^{t} G(t-\tau)\frac{\mathrm{d}\epsilon(\tau)}{\mathrm{d}\tau}\,\mathrm{d}\tau, \qquad \epsilon(t) = \int_{-\infty}^{t} J(t-\tau)\frac{\mathrm{d}\sigma(\tau)}{\mathrm{d}\tau}\,\mathrm{d}\tau.$$

No attempt will be made here to insert Eqs. (c) and (h) into these equations.

Question 6

In the frequency domain Eq. (f) is rewritten as

$$\{E_1 + \mathrm{i}\omega\,\eta_1\}\;\hat{\sigma}(\omega) = \left\{E_1\,E_2 + \mathrm{i}\omega\;(E_1\,\eta_2 + E_1\,\eta_1 + E_2\,\eta_1) - \omega^2\,\eta_1\,\eta_2\right\}\hat{\epsilon}(\omega).$$

Here ω is the cyclic frequency, and $\hat{\sigma}(\omega)$ and $\hat{\epsilon}(\omega)$ are the Fourier transformed stresses and strains, respectively. Thus, the stress–strain relation in the frequency domain is identified as

$$\hat{\sigma}(\omega) = \hat{G}(\omega)\,\hat{\epsilon}(\omega), \quad \hat{G}(\omega) = \frac{E_1\,E_2 + \mathrm{i}\omega\;(E_1\,\eta_2 + E_1\,\eta_1 + E_2\,\eta_1) - \omega^2\,\eta_1\,\eta_2}{E_1 + \mathrm{i}\omega\,\eta_1}. \tag{j}$$

Question 7

The phase velocities for one-dimensional viscoelastic wave propagation are derived from Eq. (c) in Example 1.5:

$$c(\omega) = \sqrt{\frac{\hat{G}(\omega)}{\rho}},$$

and the wavenumber may then be computed as

$$k(\omega) = \frac{\omega}{c(\omega)} = \omega \sqrt{\frac{\rho}{\hat{G}(\omega)}}. \tag{k}$$

By application of Eqs. (j) and (k), dispersion and slowness diagrams can be made. Numerical experiments (no results are included here) lead to conclusion that η_2 has the most significant influence on the amount of dispersion compared with E_1, E_2 and η_1.

Question 8

The following limits are identified:

$$\lim_{\omega\to\infty} \hat{G}(\omega) = \mathrm{i}\omega\,\eta_2, \quad \lim_{\omega\to\infty} \frac{\mathrm{d}\hat{G}(\omega)}{\mathrm{d}\omega} = \mathrm{i}\,\eta_2.$$

Hence, the limits of the phase and group velocities in the limit $\omega \to \infty$ are found according to Example 1.5:

$$\lim_{\omega\to\infty} c(\omega) = \lim_{\omega\to\infty} \frac{\sqrt{2}}{2}\,(1+\mathrm{i})\,\sqrt{\frac{\eta_2}{\rho}}\,\sqrt{\omega} = \infty\,(1+\mathrm{i})\,,$$

$$\lim_{\omega\to\infty} c_g(\omega) = \lim_{\omega\to\infty} c(\omega)\,\left(1 - \frac{\omega}{2\mathrm{i}\omega\,\eta_2}\,\mathrm{i}\,\eta_2\right)^{-1} = \lim_{\omega\to\infty} 2\,c(\omega) = \infty\,(1+\mathrm{i})\,.$$

Physically, it does not make any sense that the speed of wave and energy propagation through the material becomes infinite for $\omega \to \infty$. However, it is observed that the propagation speeds are complex. As a result of this, waves will propagate with infinite speed for $\omega \to \infty$, but they will at the same time be subject to infinite material dissipation. Therefore the material model provided by the Kelvin and Maxwell models coupled in parallel makes some physical sense.

Exercise 3: FEM model of an infinite bar

Question 1

The bar has the longitudinal stiffness EA and the mass per unit length ρA. Balance of the forces and utilization of d'Alembert's principle then provides the equation of motion

$$EA\,\frac{\partial^2 u(x,t)}{\partial x^2} + p(x,t) = \rho A\,\frac{\partial^2 u(x,t)}{\partial t^2}, \tag{a}$$

where $u(x,t)$ is the longitudinal (or axial) displacement of the bar and $p(x,t)$ is the load applied per unit length in the axial direction.

Question 2

A bar element with the end points $x = x_{e1}$ and $x = x_{e2}$ is considered. The weak form of the equation of motion follows by multiplication of Eq. (a) with the virtual displacement $\delta u(x,t)$ and integration over the element length $L_e = |x_{e2} - x_{e1}|$,

$$\int_{x_{e1}}^{x_{e2}} \delta u(x,t)\, EA\, \frac{\partial^2 u(x,t)}{\partial x^2}\, \mathrm{d}x + \int_{x_{e1}}^{x_{e2}} \delta u(x,t)\, p(x,t)\, \mathrm{d}x = \int_{x_{e1}}^{x_{e2}} \delta u(x,t)\, \rho A\, \frac{\partial^2 u(x,t)}{\partial t^2}\, \mathrm{d}x.$$

Integration by parts with respect to x provides the result

$$\int_{x_{e1}}^{x_{e2}} \frac{\partial \delta u(x,t)}{\partial x}\, EA\, \frac{\partial u(x,t)}{\partial x}\, \mathrm{d}x + \int_{x_{e1}}^{x_{e2}} \delta u(x,t)\, \rho A\, \frac{\partial^2 u(x,t)}{\partial t^2}\, \mathrm{d}x$$

$$= \int_{x_{e1}}^{x_{e2}} \delta u(x,t)\, p(x,t)\, \mathrm{d}x + \left[\delta u(x,t)\, N(x,t)\right]_{x_{e1}}^{x_{e2}}, \quad N(x,t) = EA\, \frac{\partial u(x,t)}{\partial x}. \tag{b}$$

Here $N(x,t)$ is identified as the normal force in the bar. The first integral on the left side of the equation represents the stiffness, and the second term corresponds to the mass matrix. On the right side of Eq. (b) the first term arises from the external forces on the interior of the element. These will later be transferred to the nodes via the weight functions. Finally, the contributions from the normal forces $N(x_{e1},t)$ and $N(x_{e2},t)$ at the ends of the element are represented by the second term on the right side of Eq. (b).

Question 3

When linear interpolation is employed, a bar element is defined by two nodes. The physical displacements at these nodes are denoted $a_{e1}(t)$ and $a_{e2}(t)$, respectively. Likewise, the virtual nodal displacements are coined $\delta a_{e1}(t)$ and $\delta a_{e2}(t)$. The following vectors are then defined:

$$\mathbf{a}_e(t) = \left[\, a_{e1}(t) \quad a_{e2}(t) \,\right]^T, \quad \delta\mathbf{a}_e(t) = \left[\, \delta a_{e1}(t) \quad \delta a_{e2}(t) \,\right]^T. \tag{c}$$

In the interior of the element, the physical displacements are computed from the shape functions,

$$u(x_e,t) = \mathbf{\Phi}(x_e)\, \mathbf{a}_e(t), \quad \mathbf{\Phi}(x_e) = \left[\left(1 - \frac{x_e}{L_e}\right) \frac{x_e}{L_e} \right]. \tag{d}$$

Here $\mathbf{\Phi}(x_e)$ is the shape function vector given in terms of the local coordinate $x_e = x - x_{e1}$ which ranges from 0 at one end of the element to L_e at the other end of the element.

In the Galerkin method, the weight functions $\psi_j(x_e)$ are identical to the shape functions, *i.e.* $\psi_j(x_e) = \phi_j(x_e)$. Thus the virtual displacement field is written as

$$\delta u(x_e,t) = \mathbf{\Psi}(x_e)\, \delta\mathbf{a}_e(t) = \mathbf{\Phi}(x_e)\, \delta\mathbf{a}_e(t). \tag{e}$$

where $\mathbf{\Psi}(x_e)$ is the weight function vector. Insertion of Eqs. (c), (d) and (e) into Eq. (b), and further taking into account that $\delta\mathbf{a}_e(t)$ is arbitrary, the finite element form of the equations of motion for a bar element is achieved,

$$\mathbf{K}_e\, \mathbf{a}_e + \mathbf{M}_e\, \ddot{\mathbf{a}}_e = \mathbf{f}_e + \mathbf{b}_e, \tag{f}$$

where the dots denote the second time derivative (*i.e.* the acceleration) and

$$\mathbf{K}_e = \int_0^{L_e} EA \left\{ \frac{\partial \mathbf{\Phi}(x_e)}{\partial x_e} \right\}^T \frac{\partial \mathbf{\Phi}(x_e)}{\partial x_e} \, \mathrm{d}x_e = \frac{EA}{L_e} \begin{bmatrix} 1 & -1 \\ -1 & 1 \end{bmatrix}, \tag{g}$$

$$\mathbf{M}_e = \int_0^{L_e} \rho A \left\{ \mathbf{\Phi}(x_e) \right\}^T \mathbf{\Phi}(x_e) \, \mathrm{d}x_e = \frac{\rho A L_e}{6} \begin{bmatrix} 2 & 1 \\ 1 & 2 \end{bmatrix}, \tag{h}$$

$$\mathbf{f}_e = \int_0^{L_e} \left\{ \mathbf{\Phi}(x_e) \right\}^T p(x_e + x_{e1}, t) \, \mathrm{d}x_e, \tag{i}$$

$$\mathbf{b}_e = \left[\left\{ \mathbf{\Phi}(x_e) \right\}^T N(x_e + x_{e1}, t) \right]_{x_e=0}^{x_e=L_e} = \begin{bmatrix} N_{e1} \\ N_{e2} \end{bmatrix}. \tag{j}$$

Here, N_{e1} and N_{e2} are the normal forces applied at the end points of the bar element. Given that a consistent mass model should be adapted, the mass matrix provided by Eq. (h) is employed.

Question 4

Equation (a) is identified as the scalar wave equation,

$$\frac{\partial^2 u(x,t)}{\partial x^2} + f(x,t) = \frac{1}{c^2} \frac{\partial^2 u}{\partial t^2}, \quad c = \sqrt{\frac{E}{\rho}}, \quad f(x,t) = \frac{p(x,t)}{EA}. \tag{k}$$

Here c is the phase velocity of longitudinal waves and $f(x,t)$ is a normalized load.

Generally the phase velocity c is different from the P-wave velocity c_P. In order to show this, the Lamé constants are firstly written in terms of the Young's modulus E and Poisson ratio ν:

$$\lambda = \frac{\nu E}{(1+\nu)(1-2\nu)}, \qquad \mu = \frac{E}{2(1+\nu)}. \tag{1–8}$$

Inserting this into Eq. (1–14) provides the result

$$c_P = \sqrt{\frac{\lambda + 2\mu}{\rho}} = \sqrt{\frac{\nu E + (1-2\nu) E}{(1+\nu)(1-2\nu)\rho}} = c \sqrt{\frac{(1-\nu)}{(1+\nu)(1-2\nu)}}. \tag{l}$$

Obviously, if $\nu = 0$ the phase velocity of longitudinal waves in the bar is identical to c_P. For other Poisson ratios, the waves in the bar propagate at a lower velocity. This may be explained in the following manner: P-wave propagation is associated with a particle motion that is constrained in the transverse directions in one-dimensional elastodynamics, *i.e.* geometrical boundary conditions of the kind $v = w = 0$ are applied on the surface of the "constrained bar", where v and w are the displacement components in the y- and z-directions. On the other hand the bar can deform freely in the transverse directions, *i.e.* mechanical boundary condition are applied which define zero traction on the surface of the bar. Therefore the "constrained bar" is stiffer than the bar for all Poisson ratios other than $\nu = 0$, for which the bar does not deform in the transverse direction when a longitudinal load is applied.

Question 5

When the harmonic point load $p(t) = P\,\mathrm{e}^{\mathrm{i}\omega t}$ is applied at the point $x = 0$, the response will eventually become harmonic with the same circular frequency, *i.e.* $u(x,t) = U(x)\,\mathrm{e}^{\mathrm{i}\omega t}$. Hence, Eq. (k) achieves the form

$$\frac{\partial^2 U(x)}{\partial x^2} + k^2\,U(x) + \frac{P}{EA}\,\delta(x) = 0, \quad k^2 = \frac{\omega^2}{c^2}. \tag{m}$$

Here $U(x)$ is an amplitude function, k is the wavenumber of harmonic longitudinal waves travelling along the bar, and the exponential term $\mathrm{e}^{\mathrm{i}\omega t}$ has been left out.

Solutions to the homogeneous part of Eq. (m) are in the form

$$U(x) = U_1\,\mathrm{e}^{\mathrm{i}kx} + U_2\,\mathrm{e}^{-\mathrm{i}kx}. \tag{n}$$

For a finite bar, both terms in Eq. (n) are physically valid. However, in infinite homogeneous bars only outgoing waves are allowed, since no reflection of waves occurs and waves are only generated by the point load at $x = 0$. Since the exponential function with arguments $\mathrm{i}\,(kx + \omega t)$ and $\mathrm{i}\,(kx - \omega t)$ define harmonic waves moving to the left and right, respectively, the term with amplitude U_1 only exists for $x < 0$ and the term with amplitude U_2 is only present for $x \geqslant 0$.

Continuity of the displacements at $x = 0$ provides the condition $U_1 = U_2 = U_0$. In addition to this, a jump of the magnitude P is present in the normal force amplitude at $x = 0$. This leads to the equation

$$\mathrm{i}k\,EA\,U_0 + P = -\mathrm{i}k\,EA\,U_0, \tag{o}$$

where the definition of the normal force given in Eq. (b) has been employed. The solution of Eq. (o) provides the displacement

$$\left.\begin{array}{ll} u(x,t) = U_0\,\mathrm{e}^{\mathrm{i}(\omega t + kx)} & \text{for} \quad x < 0 \\ u(x,t) = U_0\,\mathrm{e}^{\mathrm{i}(\omega t - kx)} & \text{for} \quad x \geqslant 0 \end{array}\right\}, \quad U_0 = \frac{\mathrm{i}P}{2kEA}. \tag{p}$$

The appearance of the imaginary unit i in the displacement amplitude simply means that the response is $\pi/2$ out of phase with the excitation.

Question 6

According to Eq. (p) the fundamental solution for $x < 0$ is given as $u(x,t) = U_0\,\mathrm{e}^{\mathrm{i}(\omega t + kx)}$. The normal force in the bar is given by Eq. (b), and for $x < 0$ insertion of the fundamental solution leads to the result

$$N(x,t) = EA\,\frac{\partial u(x,t)}{\partial x} = \mathrm{i}k\,EA\,U_0\,\mathrm{e}^{\mathrm{i}(\omega t + kx)} = \mathrm{i}k\,EA\,u(x,t) \quad \text{for} \quad x < 0.$$

Likewise, for $x \geqslant 0$ the normal force is $N(x,t) = -\mathrm{i}k\,EA\,u(x,t)$. For both positive and negative values of x the velocity of longitudinal vibrations is given as

$$\frac{\partial u(x,t)}{\partial t} = \mathrm{i}\omega U_0\,\mathrm{e}^{\mathrm{i}(\omega t + kx)} = \mathrm{i}\omega\,u(x,t).$$

Comparing these results, and furthermore taking into account that $c = \omega/k$ and $c^2 = E/\rho$, it becomes evident that

$$N(x,t) = c\rho A \frac{\partial u(x,t)}{\partial t} \quad \text{for} \quad x < 0 \quad \text{and} \quad N(x,t) = -c\rho A \frac{\partial u(x,t)}{\partial t} \quad \text{for} \quad x \geqslant 0. \qquad \text{(q)}$$

Equation (q) constitutes an impedance condition that may be applied at the artificial ends of an FE model of an infinite bar.

However, in an FE model the nodal forces in the x-direction are defined as positive in the positive x-direction. This does not involve any problems for the artificial end located at positive x; but at the end located at negative x the normal force in the bar is defined as positive in the negative x-direction, *i.e.* with the opposite sign of the nodal force. Therefore, for $x < 0$ the sign of the normal force in the impedance condition must be changed, and Eq. (q) simplifies to

$$N(x,t) = -Z \frac{\partial u(x,t)}{\partial t}, \quad Z = c\rho A. \qquad \text{(r)}$$

It is emphasized that the implementation of the impedance condition does not imply a modification of the force vectors $\mathbf{b}_e$ for the two elements at the ends of the FE model. Instead the damping matrices $\mathbf{C}_e$ for the two elements are changed by the inclusion of the term $Z = c\rho A$ in the diagonal terms corresponding to the degrees of freedom of the end nodes. In the FE form of the equation of motion, *i.e.* the global form of Eq. (f), the impedance is likely to be added to the components C_{11} and C_{NN} of the damping matrix, where N is the number of degrees of freedom, which is identical to the number of nodes in the present problem.

Question 7

A MATLAB program is provided on the website `www.civil.aau.dk`.

Question 8

The element length, L_e, that must be used in order to get n elements per wavelength, L, of longitudinal waves in the bar is computed from the relation

$$n\,L_e = L = \frac{2\pi}{k} \quad \Rightarrow \quad L_e = \frac{2\pi}{nk}.$$

The necessary time step follows from the Courant relation,

$$\frac{c\,\Delta t}{L_e} = C \quad \Rightarrow \quad \Delta t = \frac{C\,L_e}{c}.$$

Since there is only longitudinal waves in the bar, these waves determine both the element length and the time step.

Question 9 . . .

To appear.

Exercise 4: Seismic analysis of a layered ground

Question 1

Since the particle motion in the incoming SH-wave field is polarized in the x_1-direction, it follows that $u_2^j(\mathbf{x},t) = u_3^j(\mathbf{x},t) = 0$. Further, the plane waves propagate in the x_3-direction. Thus, at each instance the same particle motion is recorded at all points with the same x_3-coordinate, *i.e.* $\partial u_i^j/\partial x_1 = \partial u_i^j/\partial x_2 = 0$, $i = 1,2,3$. Therefore, only the following two components are different from zero:

$$u^j(z,t) = u_1^j(\mathbf{x},t), \qquad \frac{\partial u^j(z,t)}{\partial z} = \frac{\partial u_1^j(\mathbf{x},t)}{\partial x_3}, \qquad z = x_3.$$

Question 2

In the general three-dimensional case, the Navier equations (1–10) for layer j read

$$\left(\lambda^j + \mu^j\right) \frac{\partial^2 u_k^j}{\partial x_i \partial x_k} + \mu^j \frac{\partial^2 u_i^j}{\partial x_k \partial x_k} + \rho^j b_i^j = \rho^j \frac{\partial^2 u_i^j}{\partial t^2}.$$

In the present case, the body forces $\rho^j b_i^j$ are disregarded. Further, from Question 1 it follows that $\partial u_i^j/\partial x_k = 0$ for $i = k$. This means that the dilation is equal to zero, *i.e.* $\Delta^j = \partial u_k^j/\partial x_k = 0$. Therefore only the middle term on the left-hand side of the Navier equations remains, *i.e.*

$$\mu^j \frac{\partial^2 u_i^j}{\partial x_k \partial x_k} = \rho^j \frac{\partial^2 u_i^j}{\partial t^2}.$$

Since $u_2^j(\mathbf{x},t) = u_3^j(\mathbf{x},t) = \ddot{u}_2^j(\mathbf{x},t) = \ddot{u}_3^j(\mathbf{x},t) = 0$, only the first equation (*i.e.* with $i = 1$) is non-trivial. Further, $\partial u_1^j/\partial x_1 = \partial u_1^j/\partial x_2 = 0$. Thus, the wave propagation in the layered half-space is governed by the one-dimensional wave equation

$$\frac{\partial^2 u^j(z,t)}{\partial z^2} = \frac{1}{\{c_S^j\}^2} \frac{\partial^2 u^j(z,t)}{\partial t^2}, \qquad z = x_3, \qquad u^j(z,t) = u_1^j(x_3,t), \qquad c_S^j = \sqrt{\frac{\mu^j}{\rho^j}}. \qquad \text{(a)}$$

Question 3

A harmonic wave component in the form $u_n^j(z,t) = U_n^j(z)\mathrm{e}^{\mathrm{i}\omega_n t}$ is inserted into Eq. (a). Elimination of the exponential function $\mathrm{e}^{\mathrm{i}\omega_n t}$ leads to the ordinary differential equation

$$\frac{\mathrm{d}^2 U_n^j(z)}{\mathrm{d}z^2} = \left(\frac{i\omega_n}{c_S^j}\right)^2 U_n^j(z) = -\{k_n^j\}^2 U_n^j(z), \qquad k_n^j = \frac{\omega_n}{c_S^j}. \qquad \text{(b)}$$

Alternatively, the governing equation may be derived from Eq. (5–17a) with $i = 1$,

$$\left(\lambda^j + \mu^j\right) \mathrm{i}k_1 \bar{\Delta}^j + \mu^j \left(\frac{\mathrm{d}^2}{\mathrm{d}x_3^2} - k_1^2 - k_2^2\right) \bar{U}_1^j = -\omega^2 \rho \bar{U}_1^j. \qquad \text{(5–17a*)}$$

The products $k_1^2\bar{U}_1^j$ and $k_2^2\bar{U}_1^j$ correspond to the partial derivatives $\partial^2 U_1^j/\partial x_1^2$ and $\partial^2 U_1^j/\partial x_2^2$, respectively. However, according to Question 1, these partial derivatives vanish. Further, the dilation in the horizontal wavenumber domain is found as

$$\bar{\Delta}^j = \mathrm{i}k_1\bar{U}_1^j + \mathrm{i}k_2\bar{U}_2^j + \frac{\mathrm{d}\bar{U}_3^j}{\mathrm{d}x_3} = 0 + 0 + 0 = 0, \qquad \text{(5–18*)}.$$

Here, use has been made of the fact that $\mathrm{i}k_1\bar{U}_1^j \sim \partial U_1^j/\partial x_1 = 0$, $\mathrm{i}k_2\bar{U}_2^j \sim \partial U_2^j/\partial x_2 = 0$ and $\bar{U}_3^j \sim U_3^j = 0$. Thus, Eq. (5–17a*) reduces to

$$\mu^j \frac{\mathrm{d}^2\bar{U}_1^j}{\mathrm{d}x_3^2} = -\omega^2\rho^j\bar{U}_1^j \qquad \Rightarrow \qquad \frac{\mathrm{d}^2 U_n^j}{\mathrm{d}x_3^2} = -\omega^2\frac{\rho^j}{\mu^j}U_n^j,$$

which is identical to Eq. (b). We may arrive at the same conclusion by recalling that the wavenumbers $k_1 = k_2 = 0$ correspond to the wavelengths $L_1 = L_2 = 2\pi/k_1 = 2\pi/k_2 = \infty$. This implies that the same particle motion is observed at all points in a plane parallel with the (x_1, x_2)-plane, *i.e.* with the same x_3-coordinate, which is exactly the case in the present problem.

Question 4

Inserting the wave component $U_n^j(z^j) = B_n^j\mathrm{e}^{\mathrm{i}k_n^j z^j} + C_n^j\mathrm{e}^{-\mathrm{i}k_n^j z^j}$ into Eq. (b), we get

$$\frac{\mathrm{d}^2 U_n^j(z^j)}{\mathrm{d}z^2} = (\mathrm{i}k_n^j)^2 B_n^j\mathrm{e}^{\mathrm{i}k_n^j z^j} + (-\mathrm{i}k_n^j)^2 C_n^j\mathrm{e}^{-\mathrm{i}k_n^j z^j} = -\{k_n^j\}^2\left(B_n^j\mathrm{e}^{\mathrm{i}k_n^j z^j} + C_n^j\mathrm{e}^{-\mathrm{i}k_n^j z^j}\right),$$

which is identically fulfilled for any value of z^j. Similarly, with the alternative solution we get

$$(\mathrm{i}k_n^j)^2 B_n^j\mathrm{e}^{\mathrm{i}k_n^j z^j} + (-\mathrm{i}k_n^j)^2 D_n^j\mathrm{e}^{-\mathrm{i}k_n^j(z^j-h_j)} = -\{k_n^j\}^2\left(B_n^j\mathrm{e}^{\mathrm{i}k_n^j z^j} + D_n^j\mathrm{e}^{-\mathrm{i}k_n^j(z^j-h_j)}\right),$$

which is also identically fulfilled for any value of z^j. Since any of the two solutions provide the full solution to the homogeneous ordinary differential equation (b), they must be identical. Hence, $C_n^j\mathrm{e}^{-\mathrm{i}k_n^j z^j} = D_n^j\mathrm{e}^{-\mathrm{i}k_n^j(z^j-h_j)} = D_n^j\mathrm{e}^{\mathrm{i}k_n^j h_j}\mathrm{e}^{-\mathrm{i}k_n^j z^j}$, which implies that $C_n^j = D_n^j\mathrm{e}^{\mathrm{i}k_n^j h_j}$.

Question 5

In the general, the stresses in the frequency domain are given by the constitutive law

$$\hat{\sigma}_{ik}^j = \lambda^j\hat{\Delta}^j\delta_{ik} + 2\mu^j\hat{\epsilon}_{ik}, \qquad \hat{\Delta}^j = \hat{\epsilon}_{ii}, \qquad \hat{\epsilon}_{ik}^j = \frac{1}{2}\left(\frac{\partial U_i^j}{\partial x_k} + \frac{\partial U_k^j}{\partial x_i}\right).$$

However, in the present case only the partial derivative $\partial U_1^j/\partial x_3 \sim \mathrm{d}U_n^j/\mathrm{d}z^j$ is different from zero. Hence, the dilation vanishes, *i.e.* $\hat{\Delta}^j = 0$, and the stress amplitude simplifies to

$$P_n^j(z^j) = \hat{\sigma}_{13}^j = \mu^j\frac{\partial U_1^j}{\partial x_3} = \mu^j\frac{\mathrm{d}U_n^j}{\mathrm{d}z^j} = \mathrm{i}k_n^j\mu^j\left(B_n^j\mathrm{e}^{\mathrm{i}k_n^j z^j} - D_n^j\mathrm{e}^{-\mathrm{i}k_n^j(z^j-h_j)}\right). \qquad \text{(c)}$$

All other stress components are equal to zero.

Question 6

Employing the second solution suggested in Question 4, the amplitude functions for the displacement and the shear stress, $U_n^j(z^j)$ and $P_n^j(z^j)$, may be represented in the form

$$\mathbf{S}_n^j(z^j) = \begin{bmatrix} U_n^j(z^j) \\ P_n^j(z^j) \end{bmatrix} = \mathbf{A}_n^j(z^j) \begin{bmatrix} B_n^j \\ D_n^j \end{bmatrix}, \quad \mathbf{A}_n^j(z^j) = \begin{bmatrix} \mathrm{e}^{\mathrm{i}k_n^j z^j} & \mathrm{e}^{-\mathrm{i}k_n^j (z^j - h_j)} \\ \mathrm{i}k_n^j \mu^j \mathrm{e}^{\mathrm{i}k_n^j z^j} & -\mathrm{i}k_n^j \mu^j \mathrm{e}^{-\mathrm{i}k_n^j (z^j - h_j)} \end{bmatrix}. \text{(d)}$$

The matrix $\mathbf{A}_n^j(z^j)$ is now evaluated at $z^j = 0$ and $z^j = h^j$, *i.e.* at the top and bottom of layer j, respectively. With $\mathbf{A}_n^{j0} = \mathbf{A}_n^j(z^j = 0)$ and $\mathbf{A}_n^{j1} = \mathbf{A}_n^j(z^j = h^j)$ we get:

$$\mathbf{A}_n^{j0} = \begin{bmatrix} 1 & \mathrm{e}^{\mathrm{i}k_n^j h_j} \\ \mathrm{i}k_n^j \mu^j & -\mathrm{i}k_n^j \mu^j \mathrm{e}^{\mathrm{i}k_n^j h_j} \end{bmatrix}, \qquad \mathbf{A}_n^{j1} = \begin{bmatrix} \mathrm{e}^{\mathrm{i}k_n^j h^j} & 1 \\ \mathrm{i}k_n^j \mu^j \mathrm{e}^{\mathrm{i}k_n^j h^j} & -\mathrm{i}k_n^j \mu^j \end{bmatrix}. \text{(e)}$$

Question 7

Making use of Eqs. (d) and (e), the integration constants B_n^j and D_n^j may be expressed in terms of the displacement and the shear stress at the bottom of layer j. Introducing $U_n^{j1} = U_n^j(z^j = h^j)$ and $P_n^{j1} = P_n^j(z^j = h^j)$ the following relation is derived:

$$\mathbf{S}_n^{j1} = \begin{bmatrix} U_n^{j1} \\ P_n^{j1} \end{bmatrix} = \mathbf{A}_n^{j1} \begin{bmatrix} B_n^j \\ D_n^j \end{bmatrix} \qquad \Rightarrow \qquad \begin{bmatrix} B_n^j \\ D_n^j \end{bmatrix} = \left\{\mathbf{A}_n^{j1}\right\}^{-1} \begin{bmatrix} U_n^{j1} \\ P_n^{j1} \end{bmatrix} = \left\{\mathbf{A}_n^{j1}\right\}^{-1} \mathbf{S}_n^{j1}. \text{(f)}$$

Next, $U_n^{j0} = U_n^j(z^j = 0)$ and $P_n^{j0} = P_n^j(z^j = 0)$ are introduced as the displacement and the shear stress, respectively, at the top of layer j. Equations (d)–(f) then provide the result

$$\mathbf{S}_n^{j0} = \begin{bmatrix} U_n^{j0} \\ P_n^{j0} \end{bmatrix} = \mathbf{A}_n^{j0} \begin{bmatrix} B_n^j \\ D_n^j \end{bmatrix} = \mathbf{A}_n^{j0} \left\{\mathbf{A}_n^{j1}\right\}^{-1} \begin{bmatrix} U_n^{j1} \\ P_n^{j1} \end{bmatrix} = \mathbf{A}_n^{j0} \left\{\mathbf{A}_n^{j1}\right\}^{-1} \mathbf{S}_n^{j1}. \text{(g)}$$

This forms a relationship between the displacement and the shear stress at the top of layer j and the corresponding quantities at the bottom of the layer.

Question 8

At the interfaces between adjacent layers, the displacements and shear stresses should be continuous, *i.e.* $\mathbf{S}_n^{j1} = \mathbf{S}_n^{j+1,0}$. Then, from Eq. (g) it follows that

$$\mathbf{S}_n^{10} = \mathbf{A}_n^{10} \left\{\mathbf{A}_n^{11}\right\}^{-1} \mathbf{S}_n^{11} = \mathbf{A}_n^{10} \left\{\mathbf{A}_n^{11}\right\}^{-1} \mathbf{S}_n^{20} = \mathbf{A}_n^{10} \left\{\mathbf{A}_n^{11}\right\}^{-1} \mathbf{A}_n^{20} \left\{\mathbf{A}_n^{21}\right\}^{-1} \mathbf{S}_n^{21} = \ldots$$

$$= \mathbf{A}_n^{10} \left\{\mathbf{A}_n^{11}\right\}^{-1} \mathbf{A}_n^{20} \left\{\mathbf{A}_n^{21}\right\}^{-1} \cdots \mathbf{A}_n^{J0} \left\{\mathbf{A}_n^{J1}\right\}^{-1} \mathbf{S}_n^{J1},$$

which may conveniently be rewritten in the form

$$\mathbf{S}_n^{10} = \mathbf{T}_n \mathbf{S}_n^{J1}, \qquad \mathbf{T}_n = \mathbf{A}_n^{10} \left\{\mathbf{A}_n^{11}\right\}^{-1} \mathbf{A}_n^{20} \left\{\mathbf{A}_n^{21}\right\}^{-1} \cdots \mathbf{A}_n^{J0} \left\{\mathbf{A}_n^{J1}\right\}^{-1}. \text{(h)}$$

Here $\mathbf{T}_n$ is identified as a the transfer matrix for the layered half-space in the particular case of pure SH-wave propagation. Advantageously, the matrix product $\mathbf{A}_n^{j0} \left\{\mathbf{A}_n^{j1}\right\}^{-1}$ can be evaluated analytically, which will speed up the computations.

Question 9

At a free surface, no traction is applied, *i.e.* $P_n^{10} = 0$. Furthermore, if a forced displacement, $U_n^{J1} = \bar{U}_n$, is applied at the bottom of the stratum, *i.e.* at the interface between the bottommost layer and bedrock, Eq. (h) obtains the form:

$$\begin{bmatrix} U_n^{10} \\ P_n^{10} \end{bmatrix} = \begin{bmatrix} T_{11} & T_{12} \\ T_{21} & T_{22} \end{bmatrix} = \begin{bmatrix} U_n^{J1} \\ P_n^{J1} \end{bmatrix} \qquad \Rightarrow \qquad \begin{bmatrix} U_n^{10} \\ 0 \end{bmatrix} = \begin{bmatrix} T_{11} & T_{12} \\ T_{21} & T_{22} \end{bmatrix} = \begin{bmatrix} \bar{U}_n \\ P_n^{J1} \end{bmatrix},$$

where T_{ik} are the components of $\mathbf{T}_n$. From the second line in this system of equations, the shear stress at the interface between the soil and the bedrock may be expressed as $P_n^{J1} = -\bar{U}_n T_{21}/T_{22}$, which after insertion into the first line of the system of equations yields the result:

$$U_n^{10} = \left(T_{11} - \frac{T_{12}T_{21}}{T_{22}} \right) \bar{U}_n = H_n \bar{U}_n, \qquad H_n = T_{11} - \frac{T_{12}T_{21}}{T_{22}}. \tag{i}$$

Hence, the displacement at the free surface of the ground to a forced shear displacement at bedrock may be computed for each harmonic wave component, $n = 1, 2, ..., N$.

Question 10

A MATLAB program has been written that calculates the frequency response function for SH-waves propagating vertically through a horizontally layered stratum with any number of layers. This program is available online on the address `www.civil.aau.dk`. Figure A shows the results for a stratum with the properties listed below and for the frequency range 0 to 20 Hz.

Layer 1:	$G^1 = 50$ MPa,	$\rho^1 = 1600$ kg/m^3,	$\eta^1 = 0.12$,	$h^1 = 5$ m
Layer 2:	$G^2 = 100$ MPa,	$\rho^2 = 1800$ kg/m^3,	$\eta^2 = 0.08$,	$h^2 = 10$ m
Layer 3:	$G^3 = 150$ MPa,	$\rho^3 = 2000$ kg/m^3,	$\eta^3 = 0.04$,	$h^3 = 15$ m
Layer 4:	$G^4 = 200$ MPa,	$\rho^4 = 2200$ kg/m^3,	$\eta^4 = 0.02$,	$h^4 = 20$ m

In the MATLAB program, a complex shear modulus is introduced as $\mu^j = G^j \left(1 + \mathrm{i}\,\mathrm{sign}(\omega)\eta^j\right)$, where G^j is the real shear modulus and η^j is the loss factor.

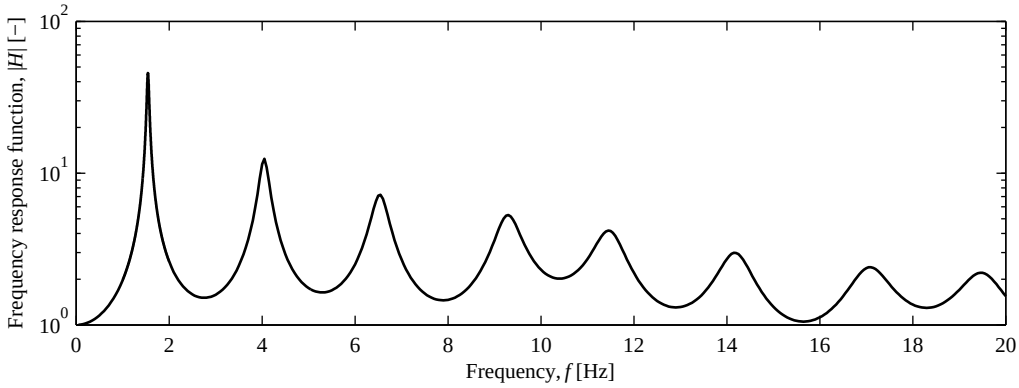

Figure A Frequency response function for SH-waves propagating vertically SH-wave in a stratum with four horizontal layers of increasing stiffness over bedrock.

References

Abramowitz, M and Stegun, IA (1972). *Handbook of mathematical functions with formulas, graphs and mathematical tables* (10 ed.). United States Department of Commerce: National Bureau of Standards.

Achenbach, JD (1973). *Wave Propagation in Elastic Solids* (1 ed.). Amsterdam: North-Holland Publishing Company.

Ahmad, S. and Banerjee, P.K. (1988). Multi-domain BEM for two-dimansional problems of elastodynamics. *International Journal for Numerical Methods in Engineering* **26**, 891–911.

Aki, K and Richards, PG (1980). *Quantitative Seismology — Theory and Methods: Volume I* (1 ed.). New York: W.H. Freeman and Company.

Andersen, L (2002). *Wave propagation in inifinite structures and media*. PhD thesis, Aalborg University, Denmark.

Andersen, L and Jones, CJC (2001a). BEASTS — A Computer Program for Boundary Element Analysis of Soil and Three-dimensional Structures. ISVR Technical Memorandum 868, Institute of Sound and Vibration Research, University of Southampton.

Andersen, L and Jones, CJC (2001b). Three-Dimensional Elastodynamic Analysis Using Multiple Boundary Element Domains. ISVR Technical Memorandum 867, Institute of Sound and Vibration Research, University of Southampton.

Auersch, L (1988). Wechselwirkung starrer und flexibler strukturen mit dem baugrund inbesondere bei anregnung durch bodenerschütterungen. BAM-Forschungsbericht 151, Berlin.

Auersch, L (1994). Wave propagation in layered soils: Theoretical solution in wavenumber domain and experimental results of hammer and railway traffic excitation. *Journal of Sound and Vibration* **173**(2), 233–264.

Bathe, K-J (1996). *Finite-Element Procedures* (1 ed.). Chichester: John Wiley & Sons Ltd.

Berryman, JG (1980). Confirmation of biot's theory. *Applied Physics Letters* **37**, 382–384.

Biot, MA (1941). General theor of three-dimensional consolidation. *Journal of Applied Physics* **12**, 155–164.

Biot, MA (1955). Theory of elasticity and consolidation for a porous anisotropic solid. *Journal of Applied Physics* **26**(2), 182–185.

Biot, MA (1956a). Theory of deformation of a porous viscoelastic anisotropic solid. *Journal of Applied Physics* **27**(5), 459–467.

Biot, MA (1956b). Theory of propagation of elastic waves in a fluid-saturated porous solid. I. Low-frequency range. *The Journal of the Acoustical Society of America* **28**(2), 168–178.

Biot, MA (1956c). Theory of propagation of elastic waves in a fluid-saturated porous solid. II. Higher frequency range. *The Journal of the Acoustical Society of America* **28**(2), 179–191.

Carcione, JM, Cavallini, F, Santos, JE, Ravazzoli, CL, and Gauzellino, PM (2004). Wave propagation in partially saturated porous media: simulation of a second slow wave. *Wave Motion* **39**, 227–240.

Domínguez, J. (1993). *Boundary elements in dynamics*. Southampton: Computational Mechanics Publications.

Elleithy, WM, Al-Gahtani, HJ, and El-Gebeily, M (2001). Iterative coupling of BE and FE method in elastostatics. *Engineering Analysis with Boudnary Elements* **25**, 685–695.

Gaul, L (1999). The influence of damping on waves and vibrations. *Mechanical Systems and Signal Processing* **13**(1), 1–30.

Haskell, N (1953). The dispersion of surface waves on multilayered medium. *Bulletin of the Seismological Society of America* **73**, 17–43.

Hisatake, M., Ito, T., and Ueda, H. (1983). Three dimensional symmetric coupling of boundary and finite element methods. In Brebbia, CA, Futagami, T, and Tanaka, M (Eds.), *Boundary Elements — Proceedings of the Fifth International Conference*, pp. 985–994.

Jones, CJC (1994). Use of numerical models to determine the effectiveness of anti-vibration systems for railways. *Proceedings of the Institute of Civil Engineers, Transportation* **105**(1), 43–51.

Jones, CJC and Thompson, DJ (1999). A boundary Element Model for Two-Dimensional Elastodynamics on a Single Open or Closed Domain. ISVR Technical Memorandum 838, Institute of Sound and Vibration Research, University of Southampton.

Jones, CJC, Thompson, DJ, and Petyt, M. (1999). TEA — a suite of computer programs for elastodynamic analysis using coupled boundary elements and finite elements. ISVR Technical Memorandum 840, Institute of Sound and Vibration Research, University of Southampton.

Kirkegaard, P.H., Nielsen, S.R.K., Krenk, S., and Kellezi, L. (1999). Radiation of air-borne noise in non-homogeneous wind and temperature fields using FEM analysis. In *Proceedings of the 4th European conference on structural dynamics, Eurodyn '99*, Praha, pp. 1069–1074.

Kitahara, M. (1984). Applications of boundary integral equation methods to eigenvalue problems of elastodynamic and thin plates. Research report, University of Kyoto.

Krenk, S., Kellezi, L., Nielsen, S.R.K., and Kirkegaard, P.H. (1999). Finite elements and transmitting boundary conditions for moving loads. In *Proceedings of the 4th European conference on structural dynamics, Eurodyn '99*, Praha, pp. 447–452.

Krenk, S and Kirkegaard, PH (2001). Local tensor radiation conditions for elastic waves. *Journal of Sound and Vibration* **247**(5), 875–896.

Krenk, S and Schmidt, H (1981). Vibration of an elastic circular plate on an elastic half space—a direct approach. *Journal of Applied Mechanics* **48**, 161–168.

Kreyszig, E (1999). *Advanced Engineering Mathematics*. New York: John Wiley & Sons, Inc.

Krätzig, WB and Niemann, H-J (1996). *Dynamics of civil engineering structures*. Rotterdam: A.A. Balkema.

Lachat, JC (1975). *A Further Development of the Boundary Integral Technique for Elastostatics*. PhD thesis, University of Southampton, United Kingdom.

Mustoe, GGW (1980). *A combination of the finite element and boundary integral procedures*. PhD thesis, Swansea University, United Kingdom.

Newmark, NM (1959). A method of computation for structural dynamics. *ASCE Journal of the Engineering Mechanics Division* **85**(EM3), 67–94.

Oldham, KB and Spanier, J (1974). *The fractional calculus*. San Diego: Academic Press.

Sheng, X, Jones, CJC, and Petyt, M (1999a). Ground vibration generated by a harmonic load acting on a railway track. *Journal of Sound and Vibration* **225**(1), 3–28.

Sheng, X, Jones, CJC, and Petyt, M (1999b). Ground vibration generated by a load moving along a railway track. *Journal of Sound and Vibration* **228**(1), 129–156.

Skempton, AW (1960). Effective stress in soil, concrete and rocks. In *Proceedings of the Conference on Pore Pressure and Suction in Soils*, pp. 4–16. Butterworths, London.

Stamos, AA and Beskos, DE (1995). Dynamic analysis of large 3-d underground structures by the BEM. *Earthquake Engineering and Structural Dynamics* **24**, 917–934.

Thomson, W (1950). Transmission of elastic waves through a stratified solid medium. *Journal of Applied Physics* **21**, 89–93.

Timoshenko, SP (1921). On the correction for shear of the differential equation for transverse vibrations of static bars. *Philosophical Magazine, Series 6* **41**, 744–746.

Tullberg, O and Bolteus, L (1982). A critical study of different boundary element stiffness matrices. In Brebbia, CA (Ed.), *Boundary Element Methods in Engineering*, pp. 625–635. Berlin: Springer.

Veletsos, A.S. and Tang, Y. (1987). Vertical vibration of ring foundations. *Earthquake Engineering and Structural Dynamics* **15**, 1–21.

Wang, C and Lai, JCS (2000). Modelling the vibration behaviour of infinite structures by fem. *Journal of Sound and Vibration* **229**(3), 453–466.

Wolf, JP (1991a). Consistent lumped-parameter models for unbounded soil: frequency-independent stiffness, damping and mass matrices. *Earthquake Engineering and Structural Dynamics* **20**, 33–41.

Wolf, JP (1991b). Consistent lumped-parameter models for unbounded soil: physical representation. *Earthquake Engineering and Structural Dynamics* **20**, 11–32.

Wolf, JP (1994). *Foundation Vibration Analysis Using Simple Physical Models*. Englewood Cliffs, NJ: Prentice-Hall.

Wolf, JP (1997). Spring-dashpot-mass models for foundation vibrations. *Earthquake Engineering and Structural Dynamics* **26**(9), 931–949.

Wolf, JP and Paronesso, A (1991). Errata: Consistent lumped-parameter models for unbounded soil. *Earthquake Engineering and Structural Dynamics* **20**, 597–599.

Wolf, JP and Paronesso, A (1992). Lumped-parameter model for a rigid cylindrical foundation in a soil layer on rigid rock. *Earthquake Engineering and Structural Dynamics* **21**, 1021–1038.

Wolf, JP and Song, C (1996). *Finite-Element Modeling of Unbounded Media* (1 ed.). Chichester: John Wiley & Sons Ltd.

Wu, W-H. and Lee, W-H. (2002). Systematic lumped-parameter models for foundations based on polynomial-fraction approximation. *Earthquake Engineering & Structural Dynamics* **31**(7), 1383–1412.

Wu, W-H. and Lee, W-H. (2004). Nested lumped-parameter models for foundation vibrations. *Earthquake Engineering & Structural Dynamics* **33**(9), 1051–1058.

Yong, Y, Zhang, Ruichong, and Yu, J (1997). Motion of foundation on a layered soil medium—I. impedance characteristics. *Soil Dynamics and Earthquake Engineering* **16**, 295–306.

Zienkiewicz, OC and Taylor, RL (2000). *The Finite Element Method, Vol. 3, Fluid Dynamics*. Oxford: Butterworth-Heinemann.

APPENDIX A
Some notes on mathematical formulations in elastodynamics

This abstract contains a short introduction to index notation which is useful for the formulation of governing equations in elastodynamics. Further, a formal proof is given of the Helmholtz decomposition theorem which is widely applied to the analysis of wave-propagation problems. Finally, complex exponential functions are introduced as a means of analysing steady-state harmonic response. An extension to the analysis of transient response is given by Fourier and inverse Fourier transforms in the complex notation. These transforms are applied in wavenumber- and frequency-domain solutions of wave-propagation problems.

A.1 Index notation and differential operators

A Cartesian (x, y, z)-coordinate system is defined by the three base vectors (see Fig. A–1)

$$\mathbf{e}_x = \mathbf{e}_1 = \left\{ \begin{array}{c} 1 \\ 0 \\ 0 \end{array} \right\}, \qquad \mathbf{e}_y = \mathbf{e}_2 = \left\{ \begin{array}{c} 0 \\ 1 \\ 0 \end{array} \right\}, \qquad \mathbf{e}_z = \mathbf{e}_3 = \left\{ \begin{array}{c} 0 \\ 0 \\ 1 \end{array} \right\}, \tag{A–1}$$

i.e. unit vectors pointing in the directions of the respective coordinate axes. With this definition of the Cartesian basis, the position vector $\mathbf{x}$ may be represented in any of the forms

$$\mathbf{x} = \left\{ \begin{array}{c} x \\ y \\ z \end{array} \right\} = x\mathbf{e}_x + y\mathbf{e}_y + z\mathbf{e}_z \qquad \text{or} \qquad \mathbf{x} = \left\{ \begin{array}{c} x_1 \\ x_2 \\ x_3 \end{array} \right\} = x_1\mathbf{e}_1 + x_2\mathbf{e}_2 + x_3\mathbf{e}_3, \tag{A–2}$$

where the coordinates (x_1, x_2, x_3) are equivalent to the coordinates (x, y, z). The first representation of the Cartesian coordinates may be preferred when equations are expressed in component form, whereas the latter representation (*i.e.* with subscripts 1, 2 and 3) is easily developed into the so-called *index notation*. This is explained in the following.

Now, similarly to the second part of Eq. (A–2), an arbitrary vector $\mathbf{v}$ is expressed as

$$\mathbf{v} = \left\{ \begin{array}{c} v_1 \\ v_2 \\ v_3 \end{array} \right\} = v_1\mathbf{e}_1 + v_2\mathbf{e}_2 + v_3\mathbf{e}_3 = \sum_{i=1}^{3} v_i\mathbf{e}_i = v_i\mathbf{e}_i. \tag{A–3}$$

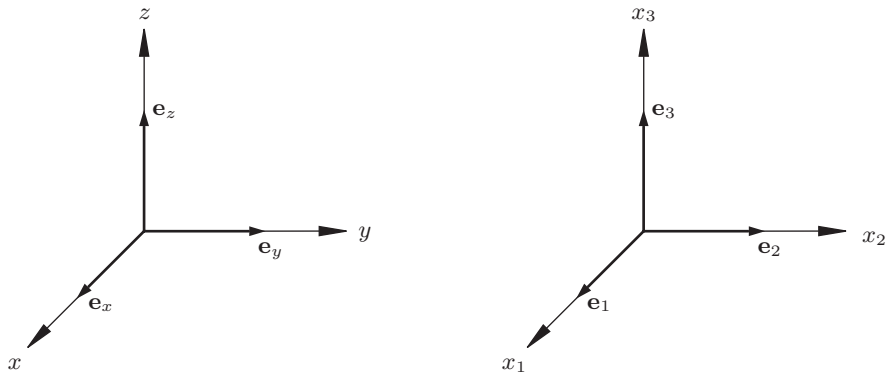

Figure A–1 Cartesian base vectors in (x, y, z)-coordinates (left) and (x_1, x_2, x_3)-coordinates (right).

The definition $\mathbf{v} = v_i \mathbf{e}_i$ is a fundamental concept in index notation. Summation is implicitly carried out with regard to repeated indices, in this case $i = 1, 2, 3$, and the summation symbol is redundant. This principle is coined the *summation convention*. Consequently, many vector and tensor operations may be expressed in a condensed component form. Since summation is always carried out over repeated indices, such indices may be exchanged with any other index, *e.g.* $a_i b_i = a_j b_j$. Therefore, repeated indices are also referred to as *dummy indices*. In contrast to repeated indices, *free indices* only appear once one either side of an equality sign. Such indices must be renamed on both sides of an equation, *e.g.* $a_i = b_{ij} c_j = b_{ik} c_k$ is equivalent to $a_j = b_{jk} c_k$.

Below, some of the basic operations on a vector field are introduced in standard vetor/tensor form and index notation. This is useful for the understanding of the theoretical derivations in Chapters 1 to 5. However, before this some basic definitions are provided.

A.1.1 Kronecker's delta and the permutation symbol

The *Kronecker delta*, δ_{ij}, is defined as

$$\delta_{ij} = \begin{cases} 1 & \text{for} \quad i = j \\ 0 & \text{for} \quad i \neq j \end{cases} \tag{A–4}$$

Evidently, $\mathbf{e}_i \cdot \mathbf{e}_j = \delta_{ij}$, which follows by the definition (A–1), *i.e.* the Cartesian base vectors $\mathbf{e}_i$, $i = 1, 2, 3$, are orthogonal unit vectors. Hence, $\mathbf{e}_i \cdot \mathbf{e}_j = 0$ for $i \neq j$, and $\mathbf{e}_i \cdot \mathbf{e}_j = 1$ for $i = j$.

Next, the *permutation symbol* ε_{ijk} is introduced as

$$\varepsilon_{ijk} = \begin{cases} 1 & \text{if } ijk \text{ is a subsequence of } 12312, \\ -1 & \text{if } ijk \text{ is a subsequence of } 32132, \\ 0 & \text{otherwise.} \end{cases} \tag{A–5}$$

As explained below, the permutation symbol is closely related to the cross product of two vectors. Further, the permutation symbol is related to the Kronecker delta by the so-called δ–ε identity,

$$\varepsilon_{ijk} \varepsilon_{klm} = \delta_{il} \delta_{jm} - \delta_{im} \delta_{jl}, \tag{A–6}$$

which is easily proved. This 'exercise' is left to the reader.

A.1.2 Scalar products, vector products and dyadic products

Firstly, the *scalar product* a of two vectors, $\mathbf{u}$ and $\mathbf{v}$, may be expressed as

$$a = \mathbf{u} \cdot \mathbf{v} = (u_i \mathbf{e}_i) \cdot (v_j \mathbf{e}_j) = u_i v_j \, \mathbf{e}_i \cdot \mathbf{e}_j = u_i v_j \delta_{ij} = u_i v_i. \tag{A–7}$$

Clearly, a is a scalar, since the summation convention applies. Note that Eq. (A–7) may alternatively be derived in the somewhat simpler manner $a = \mathbf{u} \cdot \mathbf{v} = u_1 v_1 + u_2 v_2 + u_3 v_3 = u_i v_i$. The scalar product is also denoted the *dot product*.

Secondly, the *vector product* (or *cross product*) $\mathbf{a}$ of two vectors, $\mathbf{u}$ and $\mathbf{v}$, is defined as

$$\mathbf{a} = \mathbf{u} \times \mathbf{v} = \left\{ \begin{array}{c} u_1 \\ u_2 \\ u_3 \end{array} \right\} \times \left\{ \begin{array}{c} v_1 \\ v_2 \\ v_3 \end{array} \right\} = \left\{ \begin{array}{c} u_2 v_3 - u_3 v_2 \\ u_3 v_1 - u_1 v_3 \\ u_1 v_2 - u_2 v_1 \end{array} \right\} = \mathbf{e}_i \varepsilon_{ijk} u_j v_k. \tag{A–8}$$

For example, the first component of the vector $\mathbf{a}$ is given as $a_1 = \varepsilon_{123} u_2 v_3 + \varepsilon_{132} u_3 v_2 = u_2 v_3 - u_3 v_2$, since $\varepsilon_{123} = 1$ and $\varepsilon_{132} = -1$. In accordance with Eq. (A–5) the remaining components of ε_{1jk} are all equal to zero. Similar derivations can be made with regard to a_2 and a_3. This completes the proof of Eq. (A–8).

Thirdly, a second-order Cartesian tensor $\mathbf{A}$ is obtained by the *dyadic product* of the two vectors, $\mathbf{u}$ and $\mathbf{v}$,

$$\mathbf{A} = \mathbf{u} \otimes \mathbf{v} \sim \mathbf{u}\mathbf{v}^T = u_i v_j \, \mathbf{e}_i \mathbf{e}_j^T = \left[\begin{array}{ccc} u_1 v_1 & u_1 v_2 & u_1 v_3 \\ u_2 v_1 & u_2 v_2 & u_2 v_3 \\ u_3 v_1 & u_3 v_2 & u_3 v_3 \end{array} \right], \tag{A–9}$$

where superscript T denotes the transpose of the vector and it has been assumed that the base vectors are stored as column vectors in accordance with Eq. (A–1). Component ij of $\mathbf{A}$ is then obtained as $[\mathbf{A}]_{ij} = u_i v_j$.

Thus, the scalar product of two vectors reduces to a scalar, and the vector product of two vectors produces a new vector. Finally, a dyadic product of two vectors (first-order Cartesian tensors) expands to a second-order Cartesian tensor which may be represented by an $(n \times n)$-matrix, where n is the spatial dimension, *i.e.* two or three.

A.1.3 Gradient, divergence, curl and Laplacian of a vector field

Firstly, the gradient ∇a of a scalar field a is a vector field $\mathbf{b}$ defined as

$$\mathbf{b} = \mathrm{grad}(a) = \nabla a = \frac{\partial a}{\partial \mathbf{x}} = \left\{ \begin{array}{c} \partial a / \partial x_1 \\ \partial a / \partial x_2 \\ \partial a / \partial x_3 \end{array} \right\} = \mathbf{e}_i \frac{\partial a}{\partial x_i}. \tag{A–10}$$

Consequently, the components of the gradient field $\mathbf{b} = \nabla a$ are

$$b_i = \mathbf{e}_i \cdot \mathbf{v} = \mathbf{e}_i \cdot \mathbf{e}_j \frac{\partial a}{\partial x_j} = \delta_{ij} \frac{\partial a}{\partial x_j} = \frac{\partial a}{\partial x_i}, \tag{A–11}$$

where use has been made of the fact that $\mathbf{e}_i \cdot \mathbf{e}_j = \delta_{ij}$.

Likewise, the gradient of a vector field $\mathbf{a}$ is a second-order Cartesian tensor,

$$\mathbf{B} = \mathrm{grad}(\mathbf{a}) = \nabla\mathbf{a} = \frac{\partial \mathbf{a}}{\partial \mathbf{x}} = \left\{ \begin{array}{c} \partial\mathbf{a}/\partial x_1 \\ \partial\mathbf{a}/\partial x_2 \\ \partial\mathbf{a}/\partial x_3 \end{array} \right\} = \mathbf{e}_i \otimes \mathbf{e}_j \frac{\partial a_j}{\partial x_i}. \tag{A–12}$$

In matrix-vector notation, the dyadic product $\mathbf{e}_i \otimes \mathbf{e}_j$ is interpreted as $\mathbf{e}_i\mathbf{e}_j^T$, *i.e.*

$$\mathbf{B} = \mathrm{grad}(\mathbf{a}) = \nabla\mathbf{a} = \mathbf{e}_i\mathbf{e}_j^T \frac{\partial a_j}{\partial x_i} = \left[\begin{array}{ccc} \partial a_1/\partial x_1 & \partial a_2/\partial x_1 & \partial a_3/\partial x_1 \\ \partial a_1/\partial x_2 & \partial a_2/\partial x_2 & \partial a_3/\partial x_2 \\ \partial a_1/\partial x_3 & \partial a_2/\partial x_3 & \partial a_3/\partial x_3 \end{array} \right]. \tag{A–13}$$

Thus, the gradient field $\mathbf{B} = \nabla\mathbf{a}$ has the components $B_{ij} = \partial a_j/\partial x_i$.

Secondly, the *divergence* of the vector field $\mathbf{a}$ is a scalar field,

$$b = \mathrm{div}(\mathbf{a}) = \nabla \cdot \mathbf{a} = \mathbf{e}_i \cdot \mathbf{e}_j \frac{\partial a_j}{\partial x_i} = \frac{\partial a_i}{\partial x_i}. \tag{A–14}$$

Again it has been exploited that $\mathbf{e}_i \cdot \mathbf{e}_j = \delta_{ij}$.

Thirdly, making use of Eq. (A–8) the *curl* of the vector field $\mathbf{a}$ becomes a new vector field,

$$\mathbf{b} = \mathrm{curl}(\mathbf{a}) = \nabla \times \mathbf{a} = \mathbf{e}_j \times \mathbf{e}_k \frac{\partial a_k}{\partial x_j} = \mathbf{e}_i \varepsilon_{ijk} \frac{\partial a_k}{\partial x_j}, \tag{A–15}$$

with the components $\varepsilon_{ijk}\partial a_k/\partial x_j$. The curl is also denoted *rotation*, $\mathrm{rot}(\mathbf{a})$.

Finally, the so-called *Laplacian* $\nabla^2\mathbf{a}$ of the vector field $\mathbf{a}$ is the vector field defined as

$$\mathbf{b} = \nabla^2\mathbf{a} = \nabla \cdot \nabla\mathbf{a} = \mathbf{e}_i\mathbf{e}_j \cdot \mathbf{e}_k \frac{\partial^2 a_i}{\partial x_j \partial x_k} = \mathbf{e}_i \frac{\partial^2 a_i}{\partial x_j \partial x_j}. \tag{A–16}$$

For a single component $a = a_j$, Eq. (A–16) reduces to

$$b = \nabla^2 a = \nabla \cdot \nabla a = \mathbf{e}_j \cdot \mathbf{e}_k \frac{\partial^2 a}{\partial x_j \partial x_j} = \frac{\partial^2 a}{\partial x_j \partial x_j}. \tag{A–17}$$

Note that the scalar equation $\nabla^2 a = 0$ is known as the Laplace equation.

A.1.4 The divergence theorem

The vector field $\mathbf{a} = \mathbf{a}(\mathbf{x})$ is defined on the domain Ω which has the surface S with outward unit normal $\mathbf{n} = \mathbf{n}(\mathbf{x})$. In vector notation, Gauss's divergence theorem may be expressed as

$$\int_\Omega \mathrm{div}(\mathbf{a})\,\mathrm{d}\Omega = \int_\Gamma \mathbf{n} \cdot \mathbf{a}\,\mathrm{d}\Gamma. \tag{A–18a}$$

Alternatively, index notation may be applied:

$$\int_\Omega \frac{\partial a_i}{\partial x_i}\,\mathrm{d}\Omega = \int_\Gamma n_i a_i\,\mathrm{d}\Gamma. \tag{A–18b}$$

A formal proof of Eq. (A–18) is not given here but may be found, for example, in the book by Kreyszig (1999).

A.1.5 Cauchy equation in component form and index notation

Consider a continuum with the mass density ρ. At an interior point $\mathbf{x}$ and instant t the displacement is defined by the vector $\mathbf{u} = \mathbf{u}(\mathbf{x}, t)$. In the current configuration, an infinitesimal cube with the volume $\mathrm{d}x \cdot \mathrm{d}y \cdot \mathrm{d}z$ is subject to the stresses $\boldsymbol{\sigma} = \boldsymbol{\sigma}(\mathbf{x}, t)$ acting on its surface and the specific body forces $\mathbf{b} = \mathbf{b}(\mathbf{x}, t)$ acting per unit mass.

Now, consider the forces acting on the infinitesimal cube in the x-direction. Firstly, the normal stress σ_{xx} acts in the the negative x-direction on the side with unit normal in the same direction and area $\mathrm{d}y\mathrm{d}z$. On the opposite side of the cube, the normal stress is changed by the increment $\mathrm{d}\sigma_{xx} = \mathrm{d}x\partial\sigma_{xx}/\partial x$. Similar contributions are obtained from the shear stress components σ_{xy} and σ_{xz}, see Fig. A–2. Finally, the specific body force b_x acts on the mass $\rho\mathrm{d}x\mathrm{d}y\mathrm{d}z$, and the net forces provide an acceleration $\partial^2 u/\partial t^2$ in the x-direction. Hence,

$$\left(\sigma_{xx} + \frac{\partial \sigma_{xx}}{\partial x}\mathrm{d}x\right)\mathrm{d}y\mathrm{d}z + \left(\sigma_{yx} + \frac{\partial \sigma_{yx}}{\partial y}\mathrm{d}y\right)\mathrm{d}x\mathrm{d}z + \left(\sigma_{zx} + \frac{\partial \sigma_{zx}}{\partial z}\mathrm{d}z\right)\mathrm{d}x\mathrm{d}y$$
$$+ \rho b_x \mathrm{d}x\mathrm{d}y\mathrm{d}z - \sigma_{xx}\mathrm{d}y\mathrm{d}z - \sigma_{yx}\mathrm{d}x\mathrm{d}z - \sigma_{zx}\mathrm{d}x\mathrm{d}y = \rho\frac{\partial^2 u_x}{\partial t^2}\mathrm{d}x\mathrm{d}y\mathrm{d}z. \tag{A–19}$$

Since $\mathrm{d}x$ is infinitesimal, any higher-order terms in the Taylor expansions for the stresses on the surfaces with unit outward normals in the positive x-, y- and z-direction are disregarded.

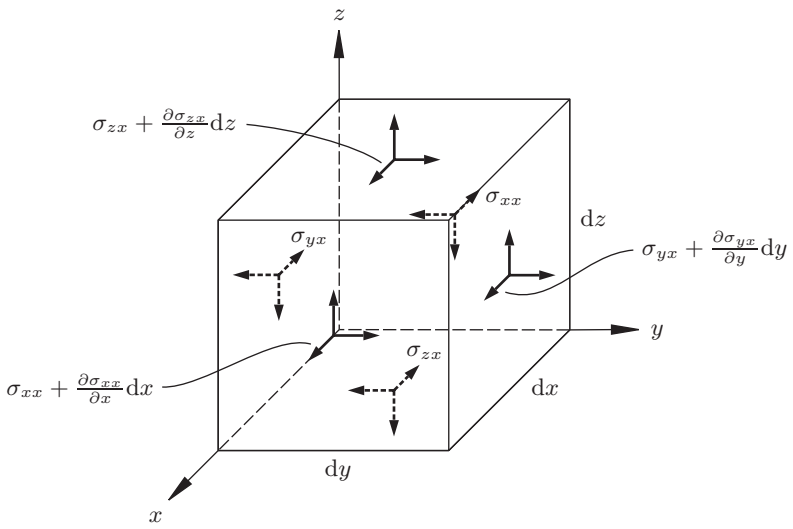

Figure A–2 Stresses acting on an infinitesimal cube in the x-direction.

It is observed that the terms $\sigma_{xx}\mathrm{d}y\mathrm{d}z$, $\sigma_{yx}\mathrm{d}x\mathrm{d}z$ and $\sigma_{zx}\mathrm{d}x\mathrm{d}y$ vanish on the left-hand side of Eq. (A–19). The infinitesimal volume $\mathrm{d}x\mathrm{d}y\mathrm{d}z$ appears in all other terms. Consequently, the equation is divided by $\mathrm{d}x\mathrm{d}y\mathrm{d}z$. Performing a similar operation with regard to the coordinate directions y and z, three equations are obtained:

$$\frac{\partial \sigma_{xx}}{\partial x} + \frac{\partial \sigma_{yx}}{\partial y} + \frac{\partial \sigma_{zx}}{\partial z} + \rho b_x = \rho\frac{\partial^2 u_x}{\partial t^2}, \tag{A–20a}$$

$$\frac{\partial \sigma_{xy}}{\partial x} + \frac{\partial \sigma_{yy}}{\partial y} + \frac{\partial \sigma_{zy}}{\partial z} + \rho b_y = \rho \frac{\partial^2 u_y}{\partial t^2}, \tag{A–20b}$$

$$\frac{\partial \sigma_{xz}}{\partial x} + \frac{\partial \sigma_{yz}}{\partial y} + \frac{\partial \sigma_{zz}}{\partial z} + \rho b_z = \rho \frac{\partial^2 u_z}{\partial t^2}. \tag{A–20c}$$

Introducing $x_1 = x$, $x_2 = y$ and $x_3 = z$, these equations may be recast in index notation,

$$\frac{\partial \sigma_{ij}}{\partial x_j} + \rho b_i = \rho \frac{\partial^2 u_i}{\partial t^2}, \tag{A–21a}$$

or tensor notation,

$$\mathrm{div}(\boldsymbol{\sigma}) + \rho \mathbf{b} = \rho \frac{\partial^2 \mathbf{u}}{\partial t^2}, \tag{A–21b}$$

where it has been utilized that the stress tensor is symmetric, *i.e.* $\sigma_{ij} = \sigma_{ji}$. This follows by the fact that the moment around the mass midpoint of the infinitesimal cube must be zero to prevent rotational acceleration of a material point. It is noted that Eq. (A–21a) is actually *three* equations, one for each index $i = 1, 2, 3$, corresponding to the components of the vector in Eq. (A–21b). This is common practice in index notation. Finally it is noted that the tensor notation (A–21b) is extremely compact. This is both the advantage and the disadvantage of tensor notation.

A.2 The Helmholtz decomposition theorem

In elastodynamic problems, it is often useful to apply the theorem of *Helmholtz decomposition* which states that any piecewise continuous vector field $f_i = f_i(\mathbf{x})$ defined on the open or closed domain Ω may be decomposed into the gradient of a scalar field and the curl of a divergence-free vector field,

$$f_i = \frac{\partial \Phi}{\partial x_i} + \varepsilon_{ijk} \frac{\partial \Psi_k}{\partial x_j}, \tag{A–22a}$$

where the *Helmholtz potentials* $\Phi = \Phi(\mathbf{x})$ and $\Psi_i = \Psi_i(\mathbf{x})$ are defined as

$$\Phi(\mathbf{x}) = -\frac{\partial F_j}{\partial x_j}, \qquad \Psi_i(\mathbf{x}) = \varepsilon_{ijk} \frac{\partial F_k}{\partial x_j}, \qquad F_i = F_i(\mathbf{x}) = \frac{1}{4\pi} \int_\Omega \frac{f_i(\mathbf{y})}{|\mathbf{x} - \mathbf{y}|} \, \mathrm{d}\Omega(\mathbf{y}), \tag{A–22b}$$

where the notation $\Omega(\mathbf{y})$ indicates that the integration variable is $\mathbf{y}$ rather than $\mathbf{x}$. The Helmholtz decomposition theorem is proved in the following.

A.2.1 Fundamental solution to the Poisson equation

At any point $\mathbf{x}$ within the three-dimensional domain Ω, the scalar field $G = G(\mathbf{x})$ is governed by the Poisson equation $\nabla^2 G + g(\mathbf{x}) = 0$, or

$$\frac{\partial^2 G}{\partial x_j \partial x_j} + g(\mathbf{x}) = 0, \tag{A–23}$$

where $\nabla^2 G$ is the Laplacian of G, cf. Eq. (A–16). The solution in the particular case $g(\mathbf{x}) = \delta(\mathbf{x})$ is known as the *Green's function* or *fundamental solution*. Here, $\delta(\mathbf{x})$ is the three-dimensional Dirac delta function which is defined by the identity

$$\delta(\mathbf{x}) = \delta(x_1)\,\delta(x_2)\,\delta(x_3), \qquad \int_{-\infty}^{\infty} \delta(x-y)a(y)\,\mathrm{d}y = a(x), \tag{A–24}$$

where $\delta(x)$ is the Dirac delta function in one dimension and $a(x)$ is a continuous function of x. An explanation of the notion fundamental solution is given below.

However, firstly the function $G(\mathbf{x})$ is derived. In order to do this, Eq. (A–23) is integrated over the domain Ω. This provides the equation

$$\int_\Omega \frac{\partial^2 G}{\partial x_j \partial x_j}\,\mathrm{d}\Omega = -\int_\Omega \delta(\mathbf{x})\,\mathrm{d}\Omega = -1, \tag{A–25}$$

where it is assumed that Ω includes the point $\mathbf{x} = \mathbf{0}$, *i.e.* the origin of the coordinate system, where the inhomogeneity $\delta(\mathbf{x})$ is applied. Utilization of the divergence theorem then yields

$$\int_\Omega \frac{\partial^2 G}{\partial x_j \partial x_j}\,\mathrm{d}\Omega = \int_\Omega \frac{\partial}{\partial x_j}\left(\frac{\partial G}{\partial x_j}\right)\mathrm{d}\Omega = \int_\Gamma n_j \frac{\partial G}{\partial x_j}\,\mathrm{d}\Gamma = \int_\Gamma \frac{\partial G}{\partial n}\,\mathrm{d}\Gamma = -1, \tag{A–26}$$

where Γ is the boundary of Ω and n_j are the components of its unit outward normal $\mathbf{n} = \mathbf{n}(\mathbf{x})$. Further, $\partial G/\partial n$ is the partial derivative of the scalar field $G(\mathbf{x})$ in the direction of the normal,

$$\frac{\partial G}{\partial n} = \frac{\partial G}{\partial x_1}\frac{\partial x_1}{\partial n} + \frac{\partial G}{\partial x_2}\frac{\partial x_2}{\partial n} + \frac{\partial G}{\partial x_3}\frac{\partial x_3}{\partial n} = \frac{\partial G}{\partial x_1}n_1 + \frac{\partial G}{\partial x_2}n_2 + \frac{\partial G}{\partial x_3}n_3 = n_j\frac{\partial G}{\partial x_j}. \tag{A–27}$$

Note that $\partial x_j/\partial n = \mathbf{n}\cdot\mathbf{e}_j = n_j$, where $\mathbf{e}_j$, $j = 1, 2, 3$, are the Cartesian base vectors.

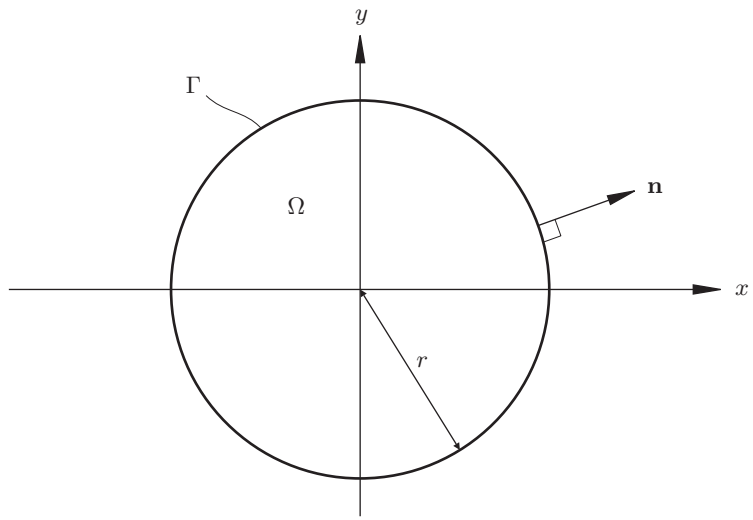

Figure A–3 Spherical domain Ω with the radius r and bounded by the surface Γ with outward unit normal $\mathbf{n}$.

The inhomogeneity $g(\mathbf{x}) = \delta(\mathbf{x})$ and the Laplacian operator are spherically symmetric around $\mathbf{x} = \mathbf{0}$. Consequently this will also be the case for the Green's function. Thus, G does only depend on $\mathbf{x}$ via the distance $r = |\mathbf{x}|$. Hence, G is constant at all points on the surface S of the sphere Ω with the radius r and centre at the point $\mathbf{x} = \mathbf{0}$, see Fig. A–3. Furthermore, the partial derivative in the direction of the outward normal may be replaced by $\partial G/\partial n = \partial G/\partial r$, since the normal points in the direction of the position vector $\mathbf{x}$ at any point on the surface of the sphere. Thus,

$$\int_\Gamma \frac{\partial G}{\partial n}\,\mathrm{d}\Gamma = \int_\Gamma \frac{\partial G}{\partial r}\,\mathrm{d}\Gamma = 4\pi r^2 \frac{\partial G}{\partial r} = -1 \quad \Rightarrow \quad G = \frac{1}{4\pi r} = \frac{1}{4\pi|\mathbf{x}|}, \tag{A–28}$$

where it has been used that the surface area of a sphere is $4\pi r^2$.

A.2.2 General solution to the Poisson equation

The function $G(\mathbf{x})$ has been established as the solution to the equation $\nabla^2 G + \delta(\mathbf{x}) = 0$. Now, the Dirac delta function $\delta(\mathbf{x})$ may be interpreted as a concentrated force with unit magnitude acting at the origin. Similarly, a concentrated force with the magnitude $f_i(\mathbf{y})$ acting at the point $\mathbf{y}$ in direction i may be represented by $\delta(\mathbf{x}-\mathbf{y})f_i(\mathbf{y})$, which provides the solution $G(\mathbf{x}-\mathbf{y})f_i(\mathbf{y})$. For a linear problem the contributions from infinitely many such forces may be integrated over the domain Ω to form the solution to the general Poisson equation $\nabla^2 F_i + f_i(\mathbf{x}) = 0$, *i.e.*

$$\frac{\partial^2 F_i}{\partial x_j \partial x_j} + f_i(\mathbf{x}) = 0 \quad \Rightarrow \quad F_i(\mathbf{x}) = \int_\Omega G(\mathbf{x}-\mathbf{y}) f_i(\mathbf{y})\,\mathrm{d}\Omega(\mathbf{y}) = \frac{1}{4\pi}\int_\Omega \frac{f_i(\mathbf{y})}{|\mathbf{x}-\mathbf{y}|}\,\mathrm{d}\Omega(\mathbf{y}). \tag{A–29}$$

Thus, once the Green's function has been established, the solution to any other force, or inhomogeneity, is found by the convolution (A–29). This justifies the notion 'fundamental solution'.

A.2.3 Helmholtz potentials

Finally, by the δ–ε identity (A–6) it follows that the Laplace equation (A–29) may be recast as

$$\begin{aligned}
&\frac{\partial^2 F_i}{\partial x_j \partial x_j} + f(\mathbf{x}) = 0 \qquad \Leftrightarrow \qquad \delta_{im}\delta_{jl}\frac{\partial^2 F_m}{\partial x_j \partial x_l} + f(\mathbf{x}) = 0 \qquad \Leftrightarrow \\
&\left(\delta_{il}\delta_{jm} - \varepsilon_{ijk}\varepsilon_{klm}\right)\frac{\partial^2 F_m}{\partial x_j \partial x_l} + f(\mathbf{x}) = 0 \qquad \Leftrightarrow \\
&f(\mathbf{x}) = \frac{\partial}{\partial x_i}\left(-\frac{\partial F_j}{\partial x_j}\right) + \varepsilon_{ijk}\frac{\partial}{\partial x_j}\left(\varepsilon_{klm}\frac{\partial F_m}{\partial x_l}\right)
\end{aligned} \tag{A–30}$$

which may be reformulated as

$$f(\mathbf{x}) = \frac{\partial \Phi}{\partial x_i} + \varepsilon_{ijk}\frac{\partial \Psi_k}{\partial x_j} \qquad \text{where} \qquad \Phi(\mathbf{x}) = -\frac{\partial F_j}{\partial x_j}, \qquad \Psi_i(\mathbf{x}) = \varepsilon_{ijk}\frac{\partial F_k}{\partial x_j}. \tag{A–31}$$

Together with Eq. (A–29), this provides a formal proof of the Helmholz decomposition theorem (A–22). The scalar field $\Phi(\mathbf{x})$ and the vector field $\boldsymbol{\Psi}(\mathbf{x})$ with components $\Psi_i(\mathbf{x})$ are referred to as *Helmholtz potentials*. Since $\boldsymbol{\Psi}(\mathbf{x})$ is the rotation of the vector field $\mathbf{F}(\mathbf{x})$ with components $F_j(\mathbf{x})$, it is divergence free.

A.3 Complex exponential notation

For a continuous and differential function, the value $f(x)$ at the point $x = x_0 + \Delta x$ may be found by the *Taylor series expansion* with base x_0,

$$f(x) = \sum_{n=0}^{\infty} \frac{1}{n!}(\Delta x)^n \left.\frac{\partial^n f}{\partial x^n}\right|_{x=x_0} = f(x_0) + \Delta x \left.\frac{\partial f}{\partial x}\right|_{x=x_0} + \frac{1}{2}(\Delta x)^2 \left.\frac{\partial^2 f}{\partial x^2}\right|_{x=x_0} + \ldots, \quad \text{(A–32)}$$

where $n!$ denotes the faculty of n, *e.g.* $0! = 1$ and $4! = 24$.

The *Maclaurin series expansion* is a special case of the Taylor expansion with base $x_0 = 0$. Thus, the function value at the point x is obtained as

$$f(x) = f(0) + x \left.\frac{\partial f}{\partial x}\right|_{x=0} + \frac{x^2}{2} \left.\frac{\partial^2 f}{\partial x^2}\right|_{x=0} + \frac{x^3}{6} \left.\frac{\partial^3 f}{\partial x^3}\right|_{x=0} + \ldots. \quad \text{(A–33)}$$

Obviously, if $|x| \gg 0$ several terms must be included in the series expansion to achieve an accurate approximation.

Now, the trigonometrical functions $\cos(x)$ and $\sin(x)$ may be expanded as Maclaurin series,

$$\cos(x) = 1 - \frac{x^2}{2} + \frac{x^4}{24} - \frac{x^6}{720} + \ldots, \quad \text{(A–34a)}$$

$$\sin(x) = x - \frac{x^3}{6} + \frac{x^5}{120} - \frac{x^7}{5040} + \ldots, \quad \text{(A–34b)}$$

whereas the exponential function e^x may be represented as

$$\mathrm{e}^x = 1 + x + \frac{x^2}{2} + \frac{x^3}{6} + \frac{x^4}{24} + \frac{x^5}{120} + \frac{x^6}{720} + \frac{x^7}{5040} + \ldots. \quad \text{(A–35)}$$

However, if the argument x in the exponential function is replaced by the complex argument $\mathrm{i}x$, the resulting Maclaurin series expansion reads

$$\mathrm{e}^{\mathrm{i}x} = 1 + \mathrm{i}x - \frac{x^2}{2} - \mathrm{i}\frac{x^3}{6} + \frac{x^4}{24} + \mathrm{i}\frac{x^5}{120} - \frac{x^6}{720} - \mathrm{i}\frac{x^7}{5040} + \ldots, \quad \text{(A–36)}$$

which may be recast as

$$\mathrm{e}^{\mathrm{i}x} = \left(1 - \frac{x^2}{2} + \frac{x^4}{24} - \frac{x^6}{720} + \ldots\right) + \mathrm{i}\left(x - \frac{x^3}{6} + \frac{x^5}{120} - \frac{x^7}{5040} + \ldots\right). \quad \text{(A–37)}$$

A comparison of Eq. (A–37) with Eq. (A–34) provides the *Euler formula*

$$\mathrm{e}^{\mathrm{i}x} = \cos(x) + \mathrm{i}\sin(x) \qquad \text{and} \qquad \mathrm{e}^{-\mathrm{i}x} = \cos(x) - \mathrm{i}\sin(x). \quad \text{(A–38)}$$

Addition of these equations and division by 2 provides a definition of $\cos(x)$ in terms of the complex exponential functions. Similarly, a definition of $\sin(x)$ is obtained by subtraction of the equations and division by 2i, *i.e.*

$$\cos(x) = \frac{\mathrm{e}^{\mathrm{i}x} + \mathrm{e}^{-\mathrm{i}x}}{2} \qquad \text{and} \qquad \sin(x) = \frac{\mathrm{e}^{\mathrm{i}x} - \mathrm{e}^{-\mathrm{i}x}}{2\mathrm{i}}. \quad \text{(A–39)}$$

Clearly, all other trigonometric functions, *e.g.* $\tan(x)$ and $\sec(x)$, may also be interpreted by means of exponential functions with complex argument.

A.4 Fourier series and Fourier transform

Fourier transformation is often applied in elastodynamics to go from time domain into frequency domain or, alternatively, from space domain into wavenumber domain. In this section, the basic formulations of the Fourier transform and its inverse are presented. However, firstly the concept of orthogonal basis functions is discussed, and an introduction is given to Fourier series.

A.4.1 Orthogonality of trigonometric functions

The *trigonometric system* $1\ (=\cos 0)$, $\sin x$, $\cos x$, $\sin 2x$, $\cos 2x$, $\sin 3x$, $\cos 3x$, etc. is *orthogonal* on the interval $x \in [-\pi;\pi]$, or indeed on any other interval of length 2π due to the periodicity of the trigonometric functions. By definition, this is equivalent to the statement that the integral over the interval $x \in [-\pi;\pi]$ of the product of two different functions in the trigonometric system should be equal to zero, *i.e.* for any integers m and n (except $m = n$)

$$\int_{-\pi}^{\pi} \cos mx \cos nx \,\mathrm{d}x = 0 \qquad \text{for} \qquad m \neq n, \tag{A–40a}$$

$$\int_{-\pi}^{\pi} \sin mx \sin nx \,\mathrm{d}x = 0 \qquad \text{for} \qquad m \neq n, \tag{A–40b}$$

and for any integers m and n (including $m = n$)

$$\int_{-\pi}^{\pi} \cos mx \sin nx \,\mathrm{d}x = 0. \tag{A–40c}$$

The notion 'orthogonal functions' stems from the fact that the trigonometric system may be interpreted as a basis for any piecewise continuous and differentiable function—just like a vector may be expressed in terms of the base vectors in a Cartesian coordinate system. The contribution to the vector $\mathbf{u}$ from the base vector $\mathbf{e}_1$ cannot be expressed in terms of $\mathbf{e}_2$ and $\mathbf{e}_3$, and in a similar manner the functions constituting the trigonometric system are linearly independent.

We now prove Eqs. (A–40a) and (A–40b), which may be rewritten as

$$\int_{-\pi}^{\pi} \cos mx \cos nx \,\mathrm{d}x = \frac{1}{2}\int_{-\pi}^{\pi} \cos{(m-n)x} \,\mathrm{d}x + \frac{1}{2}\int_{-\pi}^{\pi} \cos{(m+n)x} \,\mathrm{d}x, \tag{A–41a}$$

$$\int_{-\pi}^{\pi} \sin mx \sin nx \,\mathrm{d}x = \frac{1}{2}\int_{-\pi}^{\pi} \cos{(m-n)x} \,\mathrm{d}x - \frac{1}{2}\int_{-\pi}^{\pi} \cos{(m+n)x} \,\mathrm{d}x. \tag{A–41b}$$

Firstly, if $m = n$ we get

$$\int_{-\pi}^{\pi} \cos mx \cos mx \,\mathrm{d}x = \frac{1}{2}\int_{-\pi}^{\pi} \mathrm{d}x + \frac{1}{2}\int_{-\pi}^{\pi} \cos 2mx \,\mathrm{d}x = \pi, \tag{A–42a}$$

$$\int_{-\pi}^{\pi} \sin mx \sin mx \,\mathrm{d}x = \frac{1}{2}\int_{-\pi}^{\pi} \mathrm{d}x - \frac{1}{2}\int_{-\pi}^{\pi} \cos 2mx \,\mathrm{d}x = \pi.$$

Here, use has been made of the fact that cosine is an even function, *i.e.* $\cos x = \cos(-x)$. Hence, the integral of the term $\cos 2mx$ over the symmetric interval $x \in [-\pi;\pi]$ vanishes. For $\cos mx \cos nx$ the same result is obtained if $m = -n$. However, in accordance with the definition of the trigonometric system, m and n are nonnegative integers.

Secondly, if not $m = n$ or $m = -n$ the integrands are of the kind $\cos lx$, where l is a nonzero integer. Again, since cosine is an even function of its argument, all integrals in Eq. (A–41) vanish. Therefore, only the result for $m = n$ is different from zero. A similar proof is easily provided for Eq. (A–40c). However, this 'exercise' is left to the reader.

A.4.2 Fourier-series representation of periodic functions

As a result of the fact that the trigonometric functions are orthogonal on the interval $x \in [-\pi; \pi]$, any integrable function $f(x)$ that is periodic with the period 2π, *i.e.* $f(x) = f(x + 2\pi)$, may be represented by a trigonometric series,

$$f(x) = a_0 + \sum_{n=1}^{\infty} (a_n \cos nx + b_n \sin nx) \tag{A–43}$$

also known as a *Fourier series*.. Accordingly, a_0, a_n and b_n, $n = 1, 2, \ldots$, are called as the *Fourier coefficients*. These are given by the *Euler formulas*:

$$a_0 = \frac{1}{2\pi} \int_{-\pi}^{\pi} f(x)\, \mathrm{d}x, \tag{A–44a}$$

$$a_n = \frac{1}{\pi} \int_{-\pi}^{\pi} f(x) \cos nx\, \mathrm{d}x, \qquad n = 1, 2, \ldots, \tag{A–44b}$$

$$b_n = \frac{1}{\pi} \int_{-\pi}^{\pi} f(x) \sin nx\, \mathrm{d}x, \qquad n = 1, 2, \ldots, \tag{A–44c}$$

In the following, a proof is given for each of the Euler formulas (A–44).

Firstly, a_0 is determined by integration of Eq. (A–43) over the interval $x \in [-\pi; \pi]$;

$$\int_{-\pi}^{\pi} f(x)\, \mathrm{d}x = \int_{-\pi}^{\pi} a_0\, \mathrm{d}x + \sum_{n=1}^{\infty} \left\{ \int_{-\pi}^{\pi} a_n \cos nx\, \mathrm{d}x + \int_{-\pi}^{\pi} b_n \sin nx\, \mathrm{d}x \right\} = 2\pi a_0, \tag{A–45}$$

where it has been exploited that $\cos n\pi = \cos(-n\pi)$ and $\sin n\pi = \sin(-n\pi) = 0$ for any integer value of n. Secondly, since the trigonometric functions are orthogonal,

$$\int_{-\pi}^{\pi} f(x) \cos mx\, \mathrm{d}x = \int_{-\pi}^{\pi} a_0 \cos mx\, \mathrm{d}x + \sum_{n=1}^{\infty} \left\{ \int_{-\pi}^{\pi} a_n \cos mx \cos nx\, \mathrm{d}x + \int_{-\pi}^{\pi} b_n \cos mx \sin nx\, \mathrm{d}x \right\} = \pi a_m, \tag{A–46a}$$

and

$$\int_{-\pi}^{\pi} f(x) \sin mx\, \mathrm{d}x = \int_{-\pi}^{\pi} a_0 \sin mx\, \mathrm{d}x + \sum_{n=1}^{\infty} \left\{ \int_{-\pi}^{\pi} a_n \sin mx \cos nx\, \mathrm{d}x + \int_{-\pi}^{\pi} b_n \sin mx \sin nx\, \mathrm{d}x \right\} = \pi b_m, \tag{A–46b}$$

where the result of Eq. (A–42a) has been applied. This concludes the proof of Eq. (A–44).

The principle provided by Eqs. (A–43) and (A–44) is easily generalised to integrable functions $f(x)$ that are periodic with the period $2L$, *i.e.* $f(x) = f(x + 2L)$. In this case,

$$f(x) = a_0 + \sum_{n=1}^{\infty} \left\{ a_n \cos \frac{n\pi x}{L} + b_n \sin \frac{n\pi x}{L} \right\} \tag{A–47}$$

with the Fourier coefficients

$$a_0 = \frac{1}{2L} \int_{-L}^{L} f(x)\,\mathrm{d}x, \tag{A–48a}$$

$$a_n = \frac{1}{L} \int_{-L}^{L} f(x) \cos \frac{n\pi x}{L}\,\mathrm{d}x, \qquad n = 1, 2, \ldots, \tag{A–48b}$$

$$b_n = \frac{1}{L} \int_{-L}^{L} f(x) \sin \frac{n\pi x}{L}\,\mathrm{d}x, \qquad n = 1, 2, \ldots, \tag{A–48c}$$

A proof of Eqs. (A–47) and (A–48) is achieved by the substitution $y = \pi x/L$. Then $x = yL/\pi$, $\mathrm{d}x = L/\pi\,\mathrm{d}y$, and the interval $x \in [-L; L]$ corresponds to the interval $y \in [-\pi; \pi]$. Finally, defining $g(y) = f(x)$ it becomes evident that $g(y)$ is periodic with the period 2π and its Fourier coefficients are given by the Euler formulas (A–44), *i.e.* Eqs. (A–47) and (A–48) correspond exactly to Eqs. (A–43) and (A–44) given in terms of $y = \pi x/L$.

Moreover, based on the findings of Section A.3, the trigonometric series may be replaced by a complex Fourier series in the form

$$f(x) = \sum_{n=-\infty}^{\infty} c_n \mathrm{e}^{\mathrm{i}n\pi x/L}, \qquad c_n = \frac{1}{2L} \int_{-L}^{L} f(x) \mathrm{e}^{\mathrm{i}n\pi x/L}\,\mathrm{d}x, \qquad n = \pm 1, \pm 2, \ldots. \tag{A–49}$$

The development of Eqs. (A–47) and (A–48) into Eq. (A–49) follows directly by utilisation of Eq. (A–39). It is observed that the complex Fourier series is, in some sense, simpler than the trigonometric series. A similar conclusion can be made regarding the equivalent representations of the Fourier transform provided in the next subsection.

A.4.3 Fourier-integral representation of nonperiodic functions

According to Eq. (A–47) any piecewise continuous and differentiable periodic function $f_L(x)$ with period $2L$ may be represented by a Fourier series,

$$f_L(x) = a_0 + \sum_{n=1}^{\infty} \left\{ a_n \cos w_n x + b_n \sin w_n x \right\}, \qquad w_n = \frac{n\pi}{L}. \tag{A–50}$$

Inserting the definition of the Fourier coefficients (A–48) we obtain the result

$$f_L(x) = \frac{1}{2L} \int_{-L}^{L} f_L(x)\,\mathrm{d}x + \frac{1}{L} \sum_{n=1}^{\infty} \left\{ \cos w_n x \int_{-L}^{L} f_L(y) \cos w_n y\,\mathrm{d}y + \sin w_n x \int_{-L}^{L} f_L(y) \sin w_n y\,\mathrm{d}y \right\}, \tag{A–51}$$

where y has been applied as integration variable in the expressions for the Fourier coefficients.

Next, introducing $\Delta w = w_{n+1} - w_n = \pi/L$, Eq. (A–51) may be recast as

$$f_L(x) = \frac{\Delta w}{2\pi}\int_{-L}^{L} f_L(x)\,\mathrm{d}x + \frac{1}{\pi}\sum_{n=1}^{\infty}\Big\{\Delta w\cos w_n x\int_{-L}^{L} f_L(y)\cos w_n y\,\mathrm{d}y + \Delta w\sin w_n x\int_{-L}^{L} f_L(y)\sin w_n y\,\mathrm{d}y\Big\}. \tag{A–52}$$

We then consider the limit $L\to\infty$ and assume that the resulting nonperiodic function,

$$f(x) = \lim_{L\to\infty} f_L(x), \tag{A–53}$$

is absolutely integrable, *i.e.* the integral over $|f(x)|$ from $-\infty$ to∞ exists. Since $\Delta w\to 0$, the first term in Eq. (A–52), *i.e.* the term corresponding to a_0, vanishes and

$$f(x) = \frac{1}{\pi}\int_0^{\infty}\Big\{\cos wx\int_{-\infty}^{\infty} f(y)\cos wy\,\mathrm{d}y + \sin wx\int_{-\infty}^{\infty} f(y)\sin wy\,\mathrm{d}y\Big\}\mathrm{d}w. \tag{A–54}$$

Thus, analogously to a Fourier series for a periodic function, a nonperiodic function can be represented by a *Fourier integral*,

$$f(x) = \frac{1}{\pi}\int_0^{\infty}\big(A(w)\cos wx + B(w)\sin wx\big)\mathrm{d}w, \tag{A–55a}$$

with

$$A(w) = \int_{-\infty}^{\infty} f(y)\cos wy\,\mathrm{d}y, \qquad B(w) = \int_{-\infty}^{\infty} f(y)\sin wy\,\mathrm{d}y. \tag{A–55b}$$

It is noted that the normalisation factor $1/\pi$ may alternatively be placed in the definition of $A(w)$ and $B(w)$. This is a matter of taste, but the current choice is consistent with the definition of the complex Fourier transform derived below and applied elsewhere in this book.

A.4.4 The Fourier transform and its inverse

Equation (A–54) is rewritten as

$$f(x) = \frac{1}{\pi}\int_0^{\infty}\int_{-\infty}^{\infty} f(y)\big\{\cos wx\cos wy + \sin wx\sin wy\big\}\,\mathrm{d}y\,\mathrm{d}w,$$

or, making use of the fact that $\cos a\cos b + \sin a\sin b = \cos(a-b) = \cos(b-a)$,

$$f(x) = \frac{1}{\pi}\int_0^{\infty} F(w)\,\mathrm{d}w, \qquad F(w) = \int_{-\infty}^{\infty} f(y)\cos(wx - wy)\,\mathrm{d}y$$

The function $F(w)$ is an even function of w, since cosine is an even function of its argument. Consequently, we may represent $f(x)$ by the Fourier integral

$$f(x) = \frac{1}{2\pi}\int_{-\infty}^{\infty} F(w)\,\mathrm{d}w, \qquad F(w) = \int_{-\infty}^{\infty} f(y)\cos(wx - wy)\,\mathrm{d}y.$$

We now define the functions $g(x)$ and $G(w)$ which are similar to $f(x)$ and $F(w)$ but with $\mathrm{i}\sin(wx - wy)$ instead of $\cos(wx - wy)$, *i.e.*

$$g(x) = \frac{1}{2\pi}\int_{-\infty}^{\infty} G(w)\,\mathrm{d}w, \qquad G(w) = \int_{-\infty}^{\infty} g(y)\mathrm{i}\sin(wx - wy)\,\mathrm{d}y.$$

Since $\sin(wx - wy)$ is an odd function of w, $G(w)$ is also and odd function of w and it follows that $g(x) = 0$. Hence, $f(x)$ may be recast as

$$f(x) = \frac{1}{2\pi}\int_{-\infty}^{\infty} F(w)\,\mathrm{d}w, \qquad F(w) = \int_{-\infty}^{\infty} f(y)h(wx - wy)\,\mathrm{d}y, \tag{A–56}$$

where $h(wx - wy) = \cos(wx - wy) + \mathrm{i}\sin(wx - wy)$. Next, by utilisation of the Euler formula (A–39a), we may express the transformation (A–56) in complex form,

$$f(x) = \frac{1}{2\pi}\int_{-\infty}^{\infty} F(w)\,\mathrm{d}w, \qquad F(w) = \int_{-\infty}^{\infty} f(y)\mathrm{e}^{\mathrm{i}(wx-wy)}\,\mathrm{d}y,$$

which is reorganised into the form

$$f(x) = \frac{1}{2\pi}\int_{-\infty}^{\infty} \hat{f}(w)\mathrm{e}^{\mathrm{i}wx}\,\mathrm{d}w, \qquad \hat{f}(w) = \int_{-\infty}^{\infty} f(x)\mathrm{e}^{-\mathrm{i}wx}\,\mathrm{d}x. \tag{A–57}$$

Here, $\hat{f}(w)$ is known as the *Fourier transform* of $f(x)$. Accordingly, $f(x)$ is the *inverse Fourier transform* of $\hat{f}(w)$.

Finally, it is noted that Fourier transformation is often applied in order to go from time domain to frequency domain. In this case the variables x and w correspond to time, t, and circular frequency, ω, respectively. Another typical example is the mapping from space domain to wavenumber domain. Here, x is a spatial coordinate and w is replaced by the wavenumber k. The circular frequency and the wavenumber are defined as $\omega = 2\pi/T$ and $k = 2\pi/L$, where T and L are the period and the wavelength of a wave, respectively.

Index

D

E

F

G

H

Q

R

S

T

U

V

W

ISSN 1901-7278
DCE Lecture Notes No. 3